

This item is held in Loughborough University's Institutional Repository (<https://dspace.lboro.ac.uk/>) and was harvested from the British Library's EThOS service (<http://www.ethos.bl.uk/>). It is made available under the following Creative Commons Licence conditions.



For the full text of this licence, please go to:  
<http://creativecommons.org/licenses/by-nc-nd/2.5/>

---

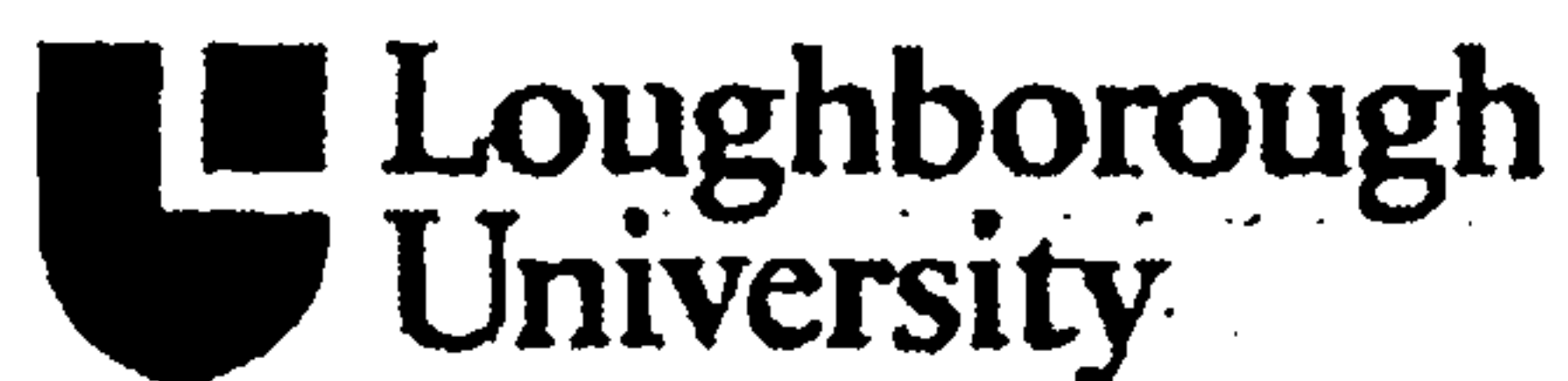
# **A Study of Overbank Flows in Non-Vegetated and Vegetated Floodplains in Compound Meandering Channels**

**by**

**Zulhilmi Ismail**

**A Doctoral Thesis**

**Submitted in partial fulfilment of the requirement for the award of  
Doctor of Philosophy of Loughborough University**



**March 2007**

**© by Zulhilmi Ismail, 2007**

---

## Abstract

Laboratory experiments concerning stage-discharge, flow resistance, bedforms, sediment transport and flow structures have been carried out in a meandering channel with simulated non-vegetated and vegetated floodplains for overbank flow. The effect of placing solid blocks in different arrangements as a model of rigid, unsubmerged floodplain vegetation on a floodplain adjacent to a meandering channel is considered. The aim was to investigate how density and arrangements of floodplain vegetation influence stage-discharge, flow resistance, sediment transport and flow behaviours. Stage-discharge curves, Manning's  $n$  and drag force  $F_D$  are determined over 165 test runs. The results from the laboratory model tests show that the placing of solid blocks along some part of the bend sections has a significant effect on stage-discharge characteristics. The change in stage-discharge by the blocks is compared using different arrangements, including the non-vegetated floodplains case. The experimental results show that the presence of energy losses due to momentum exchange between the main channel and the floodplain as well as the different densities of the blocks on a floodplain induce additional flow resistance to the main channel flow, particularly for shallow overbank flows. In general, the results show that the density and arrangement of blocks on the floodplains are very important for stage-discharge determination and, in some cases, for sediment transport rates, especially for a mobile main channel. Also, the correction parameter,  $\alpha$  is introduced in order to understand the effects of blocks and bedforms on the force balance equation. By applied the correction factor  $\alpha$ , a stage-discharge rating curve can be estimated when the  $\alpha$  value is calibrated well.

Telemac 2D and 3D were applied to predict mean velocity, secondary flow and turbulent kinetic energy. Telemac computations for non-vegetated and vegetated floodplain cases in a meandering channel generally give reasonably good predictions when compared with the measured data for both velocity and boundary shear stress in the main channel. Detailed analyses of the predicted flow variables were therefore carried out in order to understand mean flow mechanisms and secondary flow structures in compound meandering channels. The non-vegetated and two different cases of vegetated floodplain for different relative depths were considered. For the arrangement on a non-vegetated floodplain shows how the shearing of the main channel flow as the floodplain flow plunges into and over the main channel influences the mean and turbulent flow structures, particularly in the cross-over region. While applying vegetated floodplain along a cross-over section confirmed that the minimum/reduction shearing of the main channel flow by the floodplain flow plunging into and over the main channel is observed from the cross-sectional distributions of the streamwise velocity ( $U$ ), lateral velocity ( $V$ ), and secondary flow vectors. In addition to that, the vegetated floodplain along the apex bend region shows a small velocity gradient within the bend apex region. However, strong secondary flow in the cross-over section suggested that the flow interaction was quite similar to the non vegetation case in the cross-over section region.

**Keywords:** Stage-discharge, sediment transport, non-vegetated floodplain, vegetated floodplain, compound meandering channels, mean velocity, flow mechanisms, secondary flow and boundary shear stress.



## Acknowledgements

Praise to Allah who has made it possible for me to undertake this research work.

The author wishes to thank his supervisors, particularly Professor Koji Shiono, for their invaluable advice, constructive criticisms, stimulating discussions and valuable suggestions during the preparation of this thesis.

The author duly acknowledges the financial support of his employer, Universiti Teknologi Malaysia, which has enabled me to undertake this research and the Department of Civil and Building Engineering at Loughborough University for providing the research facilities without which this work would not have materialised.

Thanks to EDF France and HR Wallingford, UK for providing Telemac which has been of such importance for this research. The author is extremely grateful to Dr. J-M. Hervouet (EDF, France) and Dr. Kate Day from HR Wallingford for their support and advice on Telemac as well as Dr. Deepak Shukla for helping me in countless ways; particularly in introducing me to the basics of numerical modelling using Telemac.

The author is grateful to Dr. G. Sander (Director of Research) for ensuring this research went smoothly. I am also grateful to the other staff members of the department namely, Mick, Alex, Helen, Stevie and John for their assistance during the period of this research.

The author would also like to express his thanks to all his colleagues Zulkefli, Keyur, Syazli, and Xin for their advice and comments.

The author also wishes to thank his parents, parents-in-law, brothers and sisters for their continuous encouragement and moral support in so many ways. This study would not have been possible without the encouragement, patience, and overwhelming support of the author's wife, Ayu. Finally, the patience of the author's sons, Zafirul and Zarreq during the lengthy period of this research is especially acknowledged.

Last but not least, no words can be used to express my deepest gratitude to my parents for their encouragement and love, for which I will be forever indebted.



List of Contents

Section	Contents	Page
	Abstract	i
	Acknowledgements	ii
	List of Contents	iii
	List of Tables	vii
	List of Figures	ix
	List of Symbols	xix
Chapter 1: Introduction		
1.1	General	1
1.2	Scope and Objectives of the Research	4
1.3	Layout of the Thesis	5
Chapter 2: Literature Review		
2.1	Introduction	6
2.2	Research on Compound Channels	7
2.2.1	Research on Straight Compound Channels	8
2.2.2	Research on Meandering Compound Channels	10
2.2.2.1	Secondary Flow	13
2.2.2.2	Velocity Distribution	15
2.2.2.3	Boundary Shear Stress	19
2.3	Sediment Transport in Compound Meandering Channels	20
2.3.1	Sediment Transport with Vegetation	21
2.4	Flow Resistance in Compound Meandering Channels	22
2.5	Flow Resistance of Non-Rigid and Rigid Vegetation	23
2.5.1	The Case of Non-Rigid, Unsubmerged Vegetation on Floodplains	26
2.5.1.1	The Effect of Velocity and Depth on the Friction Factor	27
2.5.1.2	Friction Factor for Unsubmerged Flexible Vegetation	28

2.5.2	The Case of Rigid, Unsubmerged Vegetation	28
2.5.2.1	Resistance Due to Drag Forces	30
2.5.2.2	Finding the Friction Factor	30
2.5.2.3	Factors Affecting the Friction Factor	31
2.6	Computational Modelling	32
2.6.1	Grid Generation	37
2.6.2	Boundary Conditions	38
2.7	Chapter Summary	39

### **Chapter 3: Experimental Set-up and Procedures**

3.1	Introduction	41
3.2	The Loughborough Flume Facility Test Section	41
3.3	Laboratory Set-up	45
3.4	The Sediment Model	46
3.5	Model and Experimental Test Range	50
3.6	Mobile Bed Main Channel	53
3.7	Fixed Bed Main Channel	54
3.8	Measurement Procedures and Apparatus	55
3.8.1	Measurement of Flow Depths and Bedforms	55
3.8.2	Measurement of Sediment Transport	56
3.8.3	Measurement of Boundary Shear Stress	59
3.8.4	Measurement of Velocity	61
3.8.4.1	The Ventrino Velocimeter	64
3.8.4.1.1	Working Principle	64
3.8.4.1.2	Velocity Ranges	66
3.8.4.1.3	Operation Close to the Boundary	66
3.8.5	Small Tank	66
3.9	Experimental Procedure	69
3.10	Limitations of the Experimental Works	70
3.11	Simulation Works	71

## Chapter 4: Results of Stage-Discharge, Flow Resistance, Bedforms and Sediment Transport in Compound Meandering Channels

4.1	Introduction	75
4.2	Stage-Discharge Curves	81
4.3	Manning's $n$ Against Relative Depth	93
4.4	Force Balance over One Meander	99
4.4.1	Correction Parameter due to the Effect of Blocks ( $\alpha$ )	106
4.5	The Relationships Between the Blocks Density and Manning's $n$	116
4.6	Bedforms for the Mobile Bed Case	118
4.7	Sediment Transport for Overbank Flow in Compound Meandering Channels	122
4.7.1	Effect of Block Arrangement and Density on the Sediment Transport Rate	123
4.8	Discussion of Results	130

## Chapter 5: Results of Detailed Flow Structure in Compound Meandering Channels

5.1	Introduction	133
5.2	Governing Hydrodynamic Equations	134
5.3	Solution Algorithm	142
5.4	Mesh Generation	143
5.5	Initial and Boundary Conditions	144
5.6	Numerical Discretization and Solution Sequence	145
5.7	Description of Numerical Simulation	148
5.8	Comparisons and Validations of the Experiment Measurements	149
5.9	Flow Mechanism in a Compound Meandering Channels	166
5.9.1	Overbank Flow Non-Vegetated Floodplain: <i>Case L No Block</i>	166
5.9.1.1	Depth-averaged Velocity Vector Fields	166
5.9.1.2	3D Variable Velocities Field	167
5.9.1.2.1	Streamwise Velocity ( $U$ )	167
5.9.1.2.2	Lateral Velocity ( $V$ )	169
5.9.1.2.3	Vertical Velocity ( $W$ )	175



---

5.9.1.3	Secondary Flow Vectors	175
5.9.1.4	Turbulent Kinetic Energy	176
5.9.2	Overbank Flow with Vegetated Floodplain: <i>Case M Apex Block</i>	184
5.9.2.1	Depth-averaged Velocity Vector Fields	184
5.9.2.2	3D Variable Velocities Field	185
5.9.2.2.1	Streamwise Velocity ( $U$ )	185
5.9.2.2.2	Lateral Velocity ( $V$ )	186
5.9.2.2.3	Vertical Velocity ( $W$ )	187
5.9.2.3	Secondary Flow Vectors	195
5.9.3	Overbank Flow with Vegetated Floodplain: <i>Case N Cross-over Block</i>	199
5.9.3.1	Depth-Averaged Velocity Vector Fields	199
5.9.3.2	3D Variable Velocities Field	201
5.9.3.2.1	Streamwise Velocity ( $U$ )	201
5.9.3.2.2	Lateral Velocity ( $V$ )	204
5.9.3.2.3	Vertical Velocity ( $W$ )	204
5.9.3.3	Secondary Flow Vectors	209
5.10	Boundary Shear Stress Distribution	212
5.11	Sectional Averaged Discharges Distribution	217
5.12	Evaluation of Manning's $n$	220
5.13	Application of Projected Area Approach Velocity on Drag Force	221
5.14	Discussion of Results	223
<b>Chapter 6: Conclusions and Future Research Plans</b>		<b>227</b>
<b>References</b>		<b>234</b>

---

## List of Tables

3.1	Test flume geometrical parameters	44
3.2	Correction values for the water level along the flume	44
3.3	Model set-up consideration	46
3.4	Characteristics of the test bed material	48
3.5	Summary of Telemac simulation for a meandering channel	72
4.1	Summary of experimental data for <i>Case A No Block</i> with a rectangular, fixed-bed, main channel	75
4.2	Summary of experimental data for <i>Case B Apex Block</i> with a rectangular, fixed-bed, main channel	76
	(a) <i>Case B1</i> with higher density of blocks on floodplains	76
	(b) <i>Case B2</i> with middle density of blocks on floodplains	76
	(c) <i>Case B3</i> with lower density of blocks on floodplains	76
4.3	Summary of experimental data for <i>Case C Cross-over Block</i> with a rectangular, fixed-bed, main channel	76
	(a) <i>Case C1</i> with higher density of blocks on floodplains	76
	(b) <i>Case C2</i> with middle density of blocks on floodplains	77
	(c) <i>Case C3</i> with lower density of blocks on floodplains	77
4.4	Summary of experimental data for <i>Case D Combined Apex and Cross-over Block</i> with a rectangular, fixed-bed, main channel	77
	(a) <i>Case D1</i> with higher density of blocks on floodplains	77
	(b) <i>Case D2</i> with middle density of blocks on floodplains	77
	(c) <i>Case D3</i> with lower density of blocks on floodplains	78
4.5	Summary of experimental data for <i>Case E No Block</i> with a rectangular, mobile-bed, main channel	78
4.6	Summary of experimental data for <i>Case F Apex Block</i> with a rectangular, mobile-bed, main channel	78
	(a) <i>Case F1</i> with higher density of blocks on floodplains	78
	(b) <i>Case F2</i> with higher density of blocks on floodplains	78
	(c) <i>Case F3</i> with higher density of blocks on floodplains	79

---

4.7	Summary of experimental data for <i>Case G Cross-over Block</i> with a rectangular, mobile-bed, main channel	79
(a)	<i>Case G1</i> with higher density of blocks on floodplains	79
(b)	<i>Case G2</i> with higher density of blocks on floodplains	79
(c)	<i>Case G3</i> with higher density of blocks on floodplains	79
4.8	Summary of experimental data for <i>Case H Combined Apex and Cross-over Block</i> with a rectangular, mobile-bed, main channel	80
(a)	<i>Case H1</i> with higher density of blocks on floodplains	80
(b)	<i>Case H2</i> with higher density of blocks on floodplains	80
(c)	<i>Case H3</i> with higher density of blocks on floodplains	80
4.9	Summary of experimental data for <i>Case L No Block</i> with a trapezoidal, fixed- bed, main channel	80
4.10	Summary of experimental data for <i>Case M Apex Block</i> with a trapezoidal, fixed- bed, main channel	81
4.11	Summary of experimental data for <i>Case N Cross-over Block</i> with a trapezoidal, fixed- bed, main channel	81
5.1	Main summary of meshes for different simulation cases	144
5.2	Manning coefficient, $n$ for different simulation cases in Telemac 2D	145



## List of Figures

2.1	Photographic visualisation of the vortices present at the main channel and floodplain interface (Sellin, 1964)	8
2.2	Large-scale eddy structure (after Fukuoku and Fujita, 1989)	9
2.3	Illustration of secondary flows (a) Rectangular channel (b) Trapezoidal channel (after Shiono and Knight, 1989)	9
2.4	Mechanisms of overbank flow in a straight compound channel (after Shiono and Knight, 1991)	10
2.5	Flow mechanism in compound meandering channel (after Willets and Hardwick, 1993)	13
2.6	Illustration of the effects of (a) main channel aspect ratio on cross-over region mixing (b) main channel bank slope on mixing in cross-over region (after Ervine and Jasem, 1995)	14
2.7	Overall flow structure in meandering channel for overbank (a) Secondary flow generation mechanism (b) Contributions of flow mechanisms (turbulent shear, secondary flows and anisotropy of turbulence) towards the production of turbulence energy (after Shiono and Muto, 1998)	15
2.8	Illustration of floodplain flows resolved in the streamwise direction to show the effect of meander channel angle with the floodplain walls on the associated secondary flow structures (after Shiono and Muto, 1998)	17
2.9	The pattern of the flow visualisation of floodplain flow plunging into and over the main channel depends on the floodplain flow depth for different relative depths of 0.15, 0.2 and 0.25 (after Shiono and Muto, 1998)	18
2.10	Wake interference model predicts that the bulk drag coefficient, $\bar{C}_D$ , decreases with increasing array density $a/d$ , for both random (solid line) and staggered (dashed line) arrays. For the staggered arrays pitch is defined by $n$ = ratio of longitudinal to lateral row spacing, that is, $n = 1$ is a square staggered array (after Nepf, 1999)	24
2.11	Correlation of Darcy-Weisbach friction factor for four coniferous species with flow velocity (after Kouwen and Fathi, 2000)	25

2.12	Relationship between Manning's $n$ , mean velocity, MAA and depth of submergence model with foliage flow (a) Pine (b) Cedar (after Fathi and Kouwen, 1997)	26
2.13	Resistance characteristics of example floodplain (after Petryk and Bosmajian, 1975)	29
2.14	Comparison of (a) Depth-averaged velocity (b) Boundary shear stress for different turbulent models at the apex cross-over section (after Rameshwaran and Shiono, 2002)	35
3.1	Schematic layout of the flume (Not to scale)	43
3.2	Main channel cross-sections (a) Rectangular (m) (b) Trapezoidal (m)	43
3.3	(a) Flume cross-section (not to scale) (b) Details of meander geometry (m)	44
3.4	Grading curve of the uniform sand	47
3.5	Fall velocity of sand-sized particles (after Richardson and Davis, 1995)	48
3.6	Sediment particle movement over the bedforms	48
3.7	Shields diagram for critical condition of uniform sediment in water (after Melville and Surtherland, 1988)	49
3.8	Typical blocks to simulate roughness cause by vegetation on a floodplain	51
3.9	Planform of meandering experimental of arrangement of blocks on a floodplain bank:	52
	(a) <i>Case A No Block</i> (fixed-bed channel) and <i>Case E No Block</i> (mobile-bed channel) for rectangular channel cross-sections	52
	(b) <i>Case B Apex Block</i> and <i>Case F Apex Block</i> are rectangular channel cross-sections for fixed- and mobile-bed channels respectively	52
	(c) <i>Case C Cross-over Block</i> and <i>Case G Cross-over Block</i> are the rectangular channel cross-sections for fixed- and mobile-bed channels respectively	52
	(d) <i>Case D Combined Apex and Cross-over Block</i> and <i>Case H Combined Apex and Cross-over Block</i> are rectangular channel cross-sections for fixed- and mobile-bed channels respectively	52
	(e) <i>Case L No Block</i> trapezoidal fixed-bed channel cross-section	53
	(f) <i>Case M Apex block</i> trapezoidal fixed-bed channel cross-section	53
	(g) <i>Case N Cross-over Block</i> trapezoidal fixed-bed channel cross-section	53
3.10	Plywood board attaching to an aluminium frame with roller for screeded sand	54

3.11	Manual point gauge	55
3.12	Digital point gauge	56
3.13	Sediment collected at downstream of the flume	57
3.14	Transparent circular Perspex pipe to monitor sediment movement	58
3.15	Sediment catcher in diverted pipeline at upstream of the flume	58
3.16	Dry sediment weight against wet sediment weight	59
3.17	Vane indicator	60
3.18	Low pressure transducer	61
3.19	Plan of sign convention system for variable velocities and location details of the measurement sections S1, S4, S7, S10 and S12 for <i>Case L No Block</i>	62
3.20	Location details of the measurement sections S1, S4, S7, S10 and S12 in the main channel and sections FP7, FP9, FP11, FP13 and FP15 on the floodplain for <i>Case M Apex Block</i>	62
3.21	Location details of the measurement sections S1, S4, S7, S10 and S12 for <i>Case N Cross-over Block</i>	63
3.22	Velocity measurement grid for fixed-bed trapezoidal main channel case	63
3.23	The Vectrino naming convention	65
3.24	Vectrino downlooking probe	65
3.25	Small tank was modified to merge the acoustic receiver	67
3.26	Measurement results along the water depth using the small tank. Averaged velocities (a) and (b); Turbulent intensities (c) and (d); Reynolds stresses (e) and (f)	68
3.27	A thick plywood float was fixed in the stilling pool	70
3.28	Circulating heater tank	71
3.29	Plan of sign convention system for variable velocities and location details of the measurement sections S1 to S12 for <i>Case L No Block</i>	73
3.30	Location details of the measurement sections S1 to S12 in the main channel and sections FP7, FP9, FP11, FP13 and FP15 on the floodplain for <i>Case M Apex Block</i>	73
3.31	Location details of the measurement sections S1 to 12 for <i>Case N Cross-over Block</i>	74
4.1	Stage-discharge relationships for fixed bed channel <i>Case A No Block</i> and <i>Case B Apex Block</i>	85



---

4.2	Stage-discharge relationships for fixed bed channel <i>Case A No Block</i> and <i>Case C Cross-over Block</i>	85
4.3	Stage-discharge relationships for fixed bed channel <i>Case A No Block</i> and <i>Case D Combined Apex and Cross-over Block</i>	86
4.4	Comparison stage-discharge relationships for mobile bed channel <i>Case E No Block</i> and <i>Case F Apex Block</i>	86
4.5	Comparison stage-discharge relationships for mobile bed channel <i>Case E No Block</i> and <i>Case G Cross-over Block</i>	87
4.6	Comparison stage-discharge relationships for mobile bed channel <i>Case E No Block</i> and <i>Case H Combined Apex and Cross-over Block</i>	87
4.7	Stage-discharge relationships between fixed-bed and mobile-bed for <i>no block</i> and <i>cross-over block</i> cases	88
4.8	Variation of $Q^*$ with $Dr$ for different block arrangements for fixed bed cases (a) <i>Case B Apex Block</i> ; (b) <i>Case C Cross-over Block</i> and (c) <i>Case D Combined Apex and Cross-over Block</i>	90
4.9	Variation of $Q^*$ with $Dr$ for different block arrangements for mobile bed cases (a) <i>Case F Apex Block</i> ; (b) <i>Case G Cross-over Block</i> and (c) <i>Case H Combined Apex and Cross-over Block</i>	91
4.10	Percentage ratios of flow depth to flow depth at the bankful for the no block case against the ratios of discharge to discharge at bankful for the no block case (a) fixed bed channel (b) mobile bed channel	92
4.11	Stage-discharge curves of trapezoidal main channel cross-section for no block <i>L</i> , apex block <i>M</i> and cross-over block <i>N</i> cases	93
4.12	Manning's $n$ versus relative depth for fixed bed channel <i>Case A No Block</i> and <i>Case B Apex Block</i>	96
4.13	Manning's $n$ versus relative depth for fixed bed channel <i>Case A No Block</i> and <i>Case C Cross-over Block</i>	96
4.14	Manning's $n$ versus relative depth for fixed bed channel <i>Case A No Block</i> and <i>Case D Combined Apex and Cross-over Block</i>	97
4.15	Manning's $n$ relationships between fixed-bed and mobile-bed for different density of apex block cases <i>B</i> and <i>F</i> respectively	97
4.16	Manning's $n$ relationships between fixed-bed and mobile-bed for different density of cross-over block cases <i>C</i> and <i>G</i> respectively	98

---

4.17	Manning's $n$ relationships between fixed-bed and mobile-bed for different density of combined apex and cross-over block cases $D$ and $H$ respectively	98
4.18	Manning's $n$ relationship for trapezoidal main channel cross-section cases for no block $L$ , apex block $M$ and cross-over block $N$	99
4.19	Relative depth versus $F_D/w$ for fixed bed channel <i>Case B Apex Block</i>	103
4.20	Relative depth versus $F_D/w$ for fixed bed channel <i>Case C Cross-over Block</i>	104
4.21	Relative depth versus $F_D/w$ for fixed bed channel <i>Case D Combined Apex and Cross-over Block</i>	104
4.22	Relative depth versus $F_D/w$ for mobile bed channel <i>Case F Apex Block</i>	105
4.23	Relative depth versus $F_D/w$ for mobile bed channel <i>Case G Cross-over Block</i>	105
4.24	Relative depth versus $F_D/w$ for mobile bed channel <i>Case H Combined Apex and Cross-over Block</i>	106
4.25	$\log f - \log Re$ relationship for the non-vegetated fixed bed case	108
4.26	relationship between $\alpha$ and $Dr$ for fixed bed channel <i>Case B Apex Block</i>	111
4.27	The relationship between $\square$ and $Dr$ for fixed bed channel <i>Case C Cross-over Block</i>	111
4.28	The relationship between $\alpha$ and $Dr$ for fixed bed channel <i>Case D Combined Apex and Cross-over Block</i>	112
4.29	Ratios of each $\alpha$ value to $\alpha$ at the lowest number of blocks being considered against the ratios of the number of blocks to the lowest number of blocks being considered for each case	112
4.30	Ratios of bedform friction factor to boundary friction factor against $Dr$ for mobile bed channel <i>Case F Apex Block</i>	114
4.31	Ratios of bedform friction factor to boundary friction factor against $Dr$ for mobile bed channel <i>Case G Cross-over Block</i>	115
4.32	Ratios of bedform friction factor to boundary friction factor against $Dr$ for mobile bed channel <i>Case H Combined Apex and Cross-over Block</i>	115
4.33	The relationship between Manning's $n$ and the density of blocks for <i>Case B Apex Block</i>	117
4.34	The relationship between Manning's $n$ and the density of blocks for <i>Case C Cross-over Block</i>	117
4.35	The relationship between Manning's $n$ and the density of blocks for <i>Case D Combined Apex and Cross-over Block</i>	118

4.36	View of bedforms' morphology for <i>Case E No Block</i> (a) $Dr = 0.20$ (b) $Dr = 0.45$	120
4.37	View of bedforms' morphology for block 26 <i>Case F Apex Block</i> (a) $Dr = 0.20$ (b) $Dr = 0.45$	121
4.38	View of bedforms' morphology for block 30 <i>Case G Cross-over Block</i> (a) $Dr = 0.20$ (b) $Dr = 0.45$	121
4.39	View of bedforms' morphology for block 54 <i>Case H Combined Apex and Cross-over Block</i> (a) $Dr = 0.20$ (b) $Dr = 0.45$	122
4.40	Typical variation of sediment concentration for low and high concentration at $Q = 9.3 \text{ l/s}$ and $29.2 \text{ l/s}$ respectively	123
4.41	Discharge and sediment transport relationship for mobile-bed channel no block <i>E</i> and apex block <i>F</i> cases	127
4.42	Discharge and sediment transport relationship for mobile-bed channel no block <i>E</i> and cross-over block <i>G</i>	128
4.43	Discharge and sediment transport relationship for mobile-bed channel no block <i>E</i> and combined apex and cross-over block <i>H</i>	128
4.44	Normalised sediment rate relationships between <i>Case E No Block</i> and various densities of blocks for <i>Case F Apex Block</i>	129
4.45	Normalised sediment rate relationships between <i>Case E No Block</i> and various densities of blocks for <i>Case G Cross-over Block</i>	129
4.46	Normalised sediment rate relationships between <i>Case E No Block</i> and various densities of blocks for <i>Case H Combined Apex and Cross-over Block</i>	130
5.1	Elevation view of the three-dimensional mesh in the main channel for cases no block <i>L</i> , apex block <i>M</i> and cross-over <i>N</i> at the bend apex section (a) $Dr = 0.25$ (b) $Dr = 0.45$ [For details of meshes see <b>Table 5.1</b> ]	142
5.2	Plan view of two-dimensional base mesh for a half-meander wavelength (a) <i>Case L No Block</i> (b) <i>Case M Apex Block</i> and (c) <i>Case N Cross-over Block</i> [For details of meshes see <b>Table 5.1</b> ]	143
5.3	Streamwise velocity $U$ , normalised by $U_s$ for main channel in <i>Case L No Block</i> at $Dr = 0.45$ at sections S1, S4, S7, S10 and S12 (a) Measured (b) Predicted	150
5.4	Lateral velocity $V$ , normalised by $U_s$ for main channel in <i>Case L No Block</i> at $Dr = 0.45$ at sections S1, S4, S7, S10 and S12 (a) Measured (b) Predicted	151



5.5	Vertical velocity $W$ , normalised by $U_s$ for main channel in <i>Case L No Block</i> at $Dr = 0.45$ at sections S1, S4, S7, S10 and S12 (a) Measured (b) Predicted	152
5.6	Secondary flow vectors for main channel in <i>Case L No Block</i> at $Dr = 0.45$ at sections S1, S4, S7, S10 and S12 (a) Measured (b) Predicted	153
5.7	Streamwise velocity $U$ , normalised by $U_s$ for main channel in <i>Case M Apex Block</i> at $Dr = 0.45$ at sections S1, S4, S7, S10 and S12 (a) Measured (b) Predicted	154
5.8	Secondary flow vectors for main channel in <i>Case M Apex Block</i> at $Dr = 0.45$ at sections S1, S4, S7, S10 and S12 (a) Measured (b) Predicted	155
5.9	Streamwise velocity $U$ , normalised by $U_s$ for main channel in <i>Case N Cross-over Block</i> at $Dr = 0.45$ at sections S1, S4, S7, S10 and S12 (a) Measured (b) Predicted	156
5.10	Secondary flow vectors for main channel in <i>Case N Cross-over Block</i> at $Dr = 0.45$ at sections S1, S4, S7, S10 and S12 (a) Measured (b) Predicted	157
5.11	Comparison between measured and predicted of velocities in the floodplain for <i>Case M Apex Block</i> at $Dr = 0.45$ at sections FP7, FP9, FP11, FP13 and FP15	158
5.12	Measured and predicted boundary shear stress for main channel in <i>Case L No Block</i> at $Dr = 0.45$ at sections S1, S3, S5, S7, S9, S11 and S12	160
5.13	Measured and predicted boundary shear stress for main channel at section S1 for <i>Case M Apex Block</i> at $Dr = 0.45$	160
5.14	Measured and predicted boundary shear stress for main channel at section S1 for <i>Case N Cross-over Block</i> at $Dr = 0.45$	160
5.15	Measured and predicted lateral free-surface profile for main channel at section S1 at $Dr = 0.45$ (a) <i>Case L No Block</i> (b) <i>Case M Apex Block</i> and (c) <i>Case N Cross-over Block</i>	161
5.16	Predicted depth-averaged velocity for <i>Case L No Block</i> for different relative depth (a) $Dr = 0.25$ (b) $Dr = 0.45$	166
5.17	Predicted streamwise velocity $U$ , normalised by $U_s$ for main channel in <i>Case L No Block</i> at $Dr = 0.25$ at sections S1 to S12	167
5.18	Predicted streamwise velocity $U$ , normalised by $U_s$ for main channel in <i>Case L No Block</i> at $Dr = 0.45$ at sections S1 to S12	168
5.19	Predicted lateral velocity $V$ , normalised by $U_s$ for main channel in <i>Case L No Block</i> at $Dr = 0.25$ at sections S1 to S12	169

5.20	Predicted lateral velocity $V$ , normalised by $U_s$ for main channel in <i>Case L No Block</i> at $Dr = 0.45$ at sections S1 to S12	170
5.21	Predicted vertical velocity $W$ , normalised by $U_s$ for main channel in <i>Case L No Block</i> at $Dr = 0.25$ at sections S1 to S12	174
5.22	Predicted vertical velocity $W$ , normalised by $U_s$ for main channel in <i>Case L No Block</i> at $Dr = 0.45$ at sections S1 to S12	175
5.23	Predicted secondary flow vectors for main channel in <i>Case L No Block</i> at $Dr = 0.25$ at sections S1 to S12	176
5.24	Predicted secondary flow vectors for main channel in <i>Case L No Block</i> at $Dr = 0.45$ at sections S1 to S12	177
5.25	Predicted turbulent kinetic energy $TKE$ , normalised by $u'^2$ for main channel in <i>Case L No Block</i> at $Dr = 0.25$ at sections S1 to S12	178
5.26	Predicted turbulent kinetic energy $TKE$ , normalised by $u'^2$ for main channel in <i>Case L No Block</i> at $Dr = 0.45$ at sections S1 to S12	179
5.27	Predicted depth-averaged velocity for <i>Case M Apex Block</i> for different relative depth (a) $Dr = 0.25$ (b) $Dr = 0.45$	184
5.28	Predicted streamwise velocity $U$ , normalised by $U_s$ for main channel in <i>Case M Apex Block</i> at $Dr = 0.25$ at sections S1 to S12	185
5.29	Predicted streamwise velocity $U$ , normalised by $U_s$ for main channel in <i>Case M Apex Block</i> at $Dr = 0.45$ at sections S1 to S12	186
5.30	Predicted lateral velocity $V$ , normalised by $U_s$ for main channel in <i>Case M Apex Block</i> at $Dr = 0.25$ at sections S1 to S12	187
5.31	Predicted lateral velocity $V$ , normalised by $U_s$ for main channel in <i>Case M Apex Block</i> at $Dr = 0.45$ at sections S1 to S12	188
5.32	Predicted vertical velocity $W$ , normalised by $U_s$ for main channel in <i>Case M Apex Block</i> at $Dr = 0.25$ at sections S1 to S12	189
5.33	Predicted vertical velocity $W$ , normalised by $U_s$ for main channel in <i>Case M Apex Block</i> at $Dr = 0.45$ at sections S1 to S12	190
5.34	Predicted secondary flow vectors for main channel in <i>Case M Apex Block</i> at $Dr = 0.25$ at sections S1 to S12	193
5.35	Predicted secondary flow vectors for main channel in <i>Case M Apex Block</i> at $Dr = 0.45$ at sections S1 to S12	194
5.36	Predicted depth-averaged velocity for <i>Case N Cross-over Block</i> for different relative depth (a) $Dr = 0.25$ (b) $Dr = 0.45$	196



5.37	Predicted streamwise velocity $U$ , normalised by $U_s$ for main channel in <i>Case N Cross-over Block</i> at $Dr = 0.25$ at sections S1 to S12	198
5.38	Predicted streamwise velocity $U$ , normalised by $U_s$ for main channel in <i>Case N Cross-over Block</i> at $Dr = 0.45$ at sections S1 to S12	199
5.39	Predicted lateral velocity $V$ , normalised by $U_s$ for main channel in <i>Case N Cross-over Block</i> at $Dr = 0.25$ at sections S1 to S12	201
5.40	Predicted lateral velocity $V$ , normalised by $U_s$ for main channel in <i>Case N Cross-over Block</i> at $Dr = 0.45$ at sections S1 to S12	202
5.41	Predicted vertical velocity $W$ , normalised by $U_s$ for main channel in <i>Case N Cross-over Block</i> at $Dr = 0.25$ at sections S1 to S12	203
5.42	Predicted vertical velocity $W$ , normalised by $U_s$ for main channel in <i>Case N Cross-over Block</i> at $Dr = 0.45$ at sections S1 to S12	204
5.43	Predicted secondary flow vectors for main channel in <i>Case N Cross-over Block</i> at $Dr = 0.25$ at sections S1 to S12	206
5.44	Predicted secondary flow vectors for main channel in <i>Case N Cross-over Block</i> at $Dr = 0.45$ at sections S1 to S12	207
5.45	Predicted boundary shear stress for the main channel in <i>Case L No Block</i> for different relative depth, $Dr$ , at sections S1 to S12	210
5.46	Predicted boundary shear stress for the main channel in <i>Case M Apex Block</i> for different relative depth, $Dr$ , at sections S1 to S12	211
5.47	Predicted boundary shear stress for the main channel in <i>Case N Cross-over Block</i> for different relative depth, $Dr$ , at sections S1 to S12	212
5.48	Variation of cross-sectional discharge in the main channel for cases no block $L$ , apex block $M$ and cross-over block $N$ at $Dr = 0.25$	214
5.49	Variation of cross-sectional discharge in the main channel for cases no block $L$ , apex block $M$ and cross-over block $N$ at $Dr = 0.45$	214
5.50	Variation of cross-sectional discharge in the main channel for different relative depth (a) <i>Case L No Block</i> (b) <i>Case M Apex Block</i> and (c) <i>Case N Cross-over Block</i>	215
5.51	Comparison between simulation results of Manning's $n$ values and calculated values of Manning's $n$ for no block, apex block and cross-over block cases	216



- 5.52 Comparison between the average velocity,  $v$  and the projected area approach velocity,  $v_p$  on relative depth versus  $F_D/w$  for cases apex block  $M$  and cross-over block  $N$  respectively 218
- 5.53 Comparison between the average velocity,  $v$  and the projected area approach velocity,  $v_p$  on  $\alpha$  versus relative depth for cases apex block  $M$  and cross-over block  $N$  respectively 219

## List of Symbols

$A$	Cross-sectional area of the channel
$A_b$	Area of block in plan view
$A_p$	Projection of area
$b$	Rectangular main channel top width
$B$	Flume top width
$B(x, y)$	Bed elevation
$c$	Pollutant concentration
$c_f$	Friction factor
$C$	Chezy coefficient
$C_D$	Drag coefficient for the vegetation direction to the flow
$\bar{C}_D$	Bulk drag coefficient
$C_\mu$	Constant equal to 0.09
$d_{50}$	Median grain size or particle size for which 50 % of the sediment mixture is finer
$d_{84}$	Particle size for which 84 % of the sediment mixture is finer
$Dr$	Relative depth ( $H-h/H$ )
$D_m$	Vegetation width in the model
$D_p$	Vegetation width in the prototype
$f$	Darcy-Weisbach friction factor / Boundary friction factor
$f'$	Bedform friction factor
$F_D$	Drag force
$F_i$	Body force
$Fr$	Froude Number
$F_x$ and $F_y$	Body force in the $x$ and $y$ directions respectively
$g$	Gravitational acceleration
$h$	Main channel depth
$h_a$	Height of the predicted water depth of the section
$h_f$	Floodplain water depth
$H$	Total water depth
$i$ and $j$	Standard tensor
$k$	Turbulent kinetic energy

$k_s$	Grain size at the bottom
$l_m$	Length in the model
$l_p$	Length in the prototype
$L$	Length of the flume / Length of the channel reach considered
$L_c$	Curved channel length for one meander wavelength
$L_{co}$	Cross-over length
$L_w$	Meander wavelength
$L_{nw}$	Number of wavelength
$m$	Total volume
$M_w$	Cross-section volume
$M_b$	Total volume of blocks
$m_i$	Total number of predicted points ( $i$ ) over the depth of the main channel section
$MAA$	Momentum-absorbing area
$MBW$	Meander belt width
$n$	Manning's $n$
$n_v$	Velocity scale
$n_l$	Length scale
$n_{d50}$	Scale of sediment size
$N_b$	Number of blocks
$p$	Global pressure
$P$	Wetted perimeter of the channel
$q_b$	Sediment transport rate
$q_{bf}$	Sediment transport rate at bankful level
$Q$	Discharge
$Q_m$	Main channel sectional averaged discharge
$r_c$	Average bend radius of curvature
$R$	Hydraulic radius
$Re$	Reynolds number
$s$	Sinuosity of main channel ( $L_c/L_w$ )
$S_a$	Salinity
$S_o$	Energy slope / bed slope
$S_x$ and $S_y$	Depth-averaged source terms in the $x$ and $y$ directions



---

$S(x, y, t)$	Free surface elevation
$T$	Temperature
$t$	Time step
$\Delta t$	Time interval
$u_a(i)$	Velocity predicted at $(i)^{th}$ and $(I + 1)^{th}$ points respectively and at a height of $\Delta h_a$
$u_i$	Instantaneous velocity component in the $x_i$ direction
$U$	Mean velocity components in $x$ coordinate direction
$U_{cr}$	Average critical flow velocity
$U_{*cr}$	Critical shear velocity
$U_s$	Sectional averaged velocity
$v$	Mean velocity / average approach velocity
$v_f$	Floodplain velocity
$v_m$	Main channel velocity
$v_p$	Projected area approach velocity
$\nu_t$	Turbulent or eddy viscosity
$v_*$	Shear velocity
$\nu_i$	Velocity diffusivity
$V$	Mean velocity components in $y$ coordinate direction
$V_{den}$	Vegetation density
$w$	Weight component
$W$	Mean velocity components in $z$ coordinate direction
$\Delta W$	Dry sediment weight
$y$	Lateral distance
$z$	Vertical distance
$z_i$	Vertical coordinate of mesh nodes at $i^{th}$ horizontal level
$z_{*i}$	Value denotes the position of $i^{th}$ horizontal level
$Z$	Free-surface elevation
$Z_f$	Bottom elevation
$\alpha$	Correction parameter for the effect of blocks
$\lambda$	Wavelength of bedform
$\Delta$	Amplitude of bedform
$\theta$	Angle of meander bend arc

---

---

$\nu$	Kinematics viscosity of fluid
$\rho$	Density of fluid
$\rho_0$	Constant, average, reference fluid density
$\rho_s$	Density of sediment
$\tau$	Boundary shear force
$\tau_o$	Boundary Shear stress
$\tau_{ij}$	Viscous stresses for the laminar flows
$\tau_{bx}$ and $\tau_{by}$	Boundary shear stresses in the $x$ and $y$ directions respectively
$\mu$	Molecular viscosity of the fluid
$\sigma_g$	Geometric standard deviation
$\omega_s$	Fall Velocity
$\varepsilon$	Energy dissipation rate
$\delta_{ij}$	Kronecker delta function

# Chapter 1

## 1.0 Introduction

### 1.1 General

Rivers have fascinated engineers and scientists for many years, while providing water supply for domestic and industrial consumption, for irrigation, etc., as well as a means of transportation and recreation. However, the design and effective management of these systems requires a deep understanding of flow mechanics and sediment transport in rivers. A better understanding of river mechanics is also relevant for handling river management projects (involving e.g. shoreline protection, river restoration, land reclamation and transportation issues) in a more integrated fashion, taking into consideration ever-increasing environmental concerns.

Rivers are usually classified as straight, meandering and braiding (Leopold and Wolman, 1957) with meandering being by far the most common planform acquired by natural streams hence meandering rivers have received a great deal of attention. One of the environmentally attractive types is the two-stage channel. This consists of a deep main channel, which carries low discharge all the time flanked by one or two floodplains. When the flows in such sections exceed the main channel depth, the adjoining floodplains become inundated and carry part of the river flow. Due to different hydraulic conditions prevailing in the river and floodplain, the mean velocity in the main channel and that in the floodplain are different. Just above the bankful stage, the flow in the main channel exerts a pulling or accelerating force on the flow over the floodplains, which naturally generates a dragging or retarding force on the flow through the main channel. This leads to the transfer of momentum between the channel section and the floodplain. At the junction region between the main channel and that of the floodplain, Sellin (1964) indicated the presence of artificial banks made



of vortices, which acted as a medium for the transfer of momentum between the main channel and floodplain. At low depths over the floodplain, transfer of momentum takes place from the main channel flow to the floodplain leading to a decrease in the main channel velocity and discharge; meanwhile the floodplain components are increased. This process continues for certain depths of flow in the floodplain. When the depth of flow in the floodplain increases to reach the overall section mean velocity of the main channel of the compound section, there is no transfer of momentum between the main channel and floodplain. The accelerating force of the main channel water on the floodplain and the retarding force of the floodplain on the main channel each reach an average value of almost zero. Beyond this limiting depth of flow in the floodplain, the process of momentum transfer reverses and the section mean velocity in the floodplain at this stage becomes higher than that of the main channel. The assessment of flood discharge capacity associated with flood levels in compound river channels is uncertain. The flow patterns in such situations are complicated by interaction between flows in the main channel and the floodplains. In addition to this, the complexity of flow patterns may be increased due to variations of planform, such as meandering geometry, bed and bank materials, which may be fixed or erodible (mobile). Not surprisingly, therefore, there is as yet no commonly accepted standard method for predicting discharge capacity in two-stage meandering river channels (Lyness *et al.* 1998).

During the past decades, the conventional “flood control” ideology has evolved into a philosophy of “flood management”. An effective flood management program must consider environmental, recreational, and aesthetic issues in addition to flood control. Riparian vegetation has become an integral component of the flood channel. Vegetation stabilises stream banks, provides shade that prevents excessive water temperature fluctuations, supports wildlife and performs an essential role in nutrient cycling and water quality. In addition, vegetation is an important feature of many rivers, providing habitats for other organisms and enhancing amenity value for people. Emergent vegetation occurs commonly along the banks of rivers and artificial channels, both naturally and by design for erosion and habitat creation. The effect of such marginal vegetation on flow resistance has been investigated for straight channels but little is known of the effects for meandering channels under either inbank or overbank flow conditions (James and Myers, 2001).

In recent years, two-stage meandering channels have been intensively studied by Ervine and Jasem (1989), James and Wark (1992), Greenhill and Sellin (1993) and Rameshwaran and Willetts (1999) in order to develop an accurate prediction method for their conveyance capacity and to understand the mixing mechanism of the floodplain and main channel flows. Later on, James and Myers (2001) produced methods of estimating conveyance in two-stage meandering channels with marginal vegetation. They found that vegetation along the margins of the meandering channels has a significant effect on conveyance, whilst flow resistance is increased by the additional stem drag, but can also be decreased by the reduction of separation at tight bends. The combined effects can either increase or decrease conveyance. Understanding the impact of vegetation on flow conditions has become important in river restoration projects. Better knowledge of the impact of floodplain vegetation on flow conditions is needed. Vegetation may increase resistance to flow and cause higher water levels. Thus, determining the retardation in the channel and the floodplain is an important concern in order to enhance the knowledge of the physical processes involved between them, especially in two-stage meandering channels.

Estimating hydraulic characteristics in the channels and floodplains, in the case of rigid, unsubmerged vegetation is very difficult. Individual factors and their effects can be determined with acceptable accuracy, such as for a meandering channel with the presence of vegetation, by combining the factors to produce a single coefficient. In view of the need for further research on overbank flow in a meandering channel with the presence of vegetation, work will be carried out to fill the gaps to provide the required information. In order to calculate the stage-discharge relationship of a stream or river, it is necessary to accurately determine the flow resistance due to the channel bed and sides. Past research has made considerable progress predicting the roughness of a uniform channel based on both theoretical and experimental investigations. However, in order to determine the flow resistance associated with floodplains and overbank flow in a meandering channel, the effect of unsubmerged vegetation on the floodplains must be considered.

## 1.2 Scope and Objectives of the Research

The key purposes of the present research are to enhance our knowledge of the flow resistance caused by vegetation and to report the results of laboratory investigations into the physical processes involved in the flow structure, sediment transport and bedforms as well as to understand the flow characteristics and flow mechanisms in compound meandering channels with different arrangements of non-vegetated and vegetated floodplains. In this study both fixed bed and mobile bed conditions are examined, and uniform graded sand is used as the erodible bed material. Two separate sets of tests are carried out. In the first phase, a rectangular cross-section of the main channel is used. This enables the results of the present study and past studies to be compared. Concrete blocks are adopted as a physical model of vegetation. In the second phase, a trapezoidal main channel cross-section is modified in order to collect velocity measurements as well as numerical modelling with selected arrangements of non-vegetated and vegetated floodplains in compound meandering channels. The objectives of the present study are primarily as follows:

- (a) To investigate the stage-discharge, flow resistance, drag force and bedforms in the non-vegetated and vegetated floodplain in compound meandering channels.
- (b) To carry out the influence of using different arrangements and vegetation density on the floodplain resistance to sediment transport subjected to overbank flow conditions in meandering channels.
- (c) To carry out further detailed analyses of mean flow mechanisms and secondary flow structures by considering the experimental data as well as computational results.
- (d) To assess the capability of the computational model to reproduce the important flow characteristics, flow mechanisms and boundary shear stress associated with non-vegetated and vegetated floodplains in compound meandering channels with overbank flows.



### 1.3 Layout of the Thesis

This report consists of six chapters. **Chapter 2** contains a review of literature relevant to the topic of this thesis. This is divided into two parts. The first pertains to the characteristics of flow mechanisms and sediment transport for two-stage meandering channels. The second part covers topics concerning flow resistance, non-rigid and rigid unsubmerged vegetation cases, drag forces and friction factors. This chapter also includes the recent advances in numerical modelling specific to compound meandering channels.

**Chapter 3** describes the experimental setup of the Loughborough Flume Facility, and information concerning the experimental facility that was used in this research. A description of the methodology of the measurements is also given. A description of the location for all measurements will be explained. The experimental procedures adopted, including the method used to establish the uniform flow depths, are also provided. This chapter also outlines theoretical governing equations, Telemac modelling approaches and the meshing approach along with the details of simulations cases.

**Chapter 4** lists the results of the experimental tests. The discussion of the results is also part of this chapter. All the discussions on stage-discharge relationships, flow resistance, drag forces, bedforms and sediment transport are given.

**Chapter 5** presents computational results and the validation of the numerical model using the experimental data. This chapter also discusses the mean flow analysis based on the measured and predicted data, leading to a better understanding of mean flow mechanisms.

Finally, **Chapter 6** summarise the important findings from **Chapters 4** and **5** followed by future research plans. References of the texts quoted from the published papers are included in the last part of this thesis.

# Chapter 2

## 2.0 Literature Review

### 2.1 Introduction

In this chapter, previous research related to compound channel flows, the effects of vegetation on flow resistance and prediction methods for vegetation resistance and depth-average velocity at the laboratory scales are reviewed. A very important fact about the flow of any real fluid is the continuous dissipation of fluid energy as it moves through channel. Energy is dissipated, as the fluid has to do work to overcome the resistance imparted to the fluid by the boundaries and obstacles within the flow. This fact was noticed and described by Leonardo da Vinci who noticed the effect of the resistance on the velocity distribution. He said, "The water of straight rivers is the swifter the farther away it is from the walls, because of resistance" (Rouse, 1965). Indeed, as stated by Leopold and Langbein in 1966, "the striking geometric regularity of a winding river is no accident. Meanders appear to be the form in which a river does the least work in turning; hence they are the most probable form a river can take".

The energy losses contributing to flow resistance in meandering channels are substantially different in nature for inbank and overbank conditions, but in both cases the presence of vegetation on a floodplain can have a significant influence on overall channel resistance. Based on physical model with various model scales, previous investigations on flow resistance and energy loss induced by channel curvature for inbank and overbank flows have shown that the major sources of energy loss in channel bends are bed friction, increased bed friction resulting from secondary circulation, turbulence in eddies associated with flow separation at the apex section and local accelerations and expansion. Various empirical and theoretically-based

methods for accounting for the bend-related sources of resistance have been reviewed by James (1994).

It is necessary to briefly discuss the important factors affecting flow resistance. Flow resistance is affected by many factors. Among these factors are flow characteristics, which include the velocity, depth of flow and the degree of turbulence. The increase of velocity with intense turbulence causes very large losses of energy. The geometry of the section also plays an important role in energy losses. The losses are evidenced as instantaneous losses as in the case of non-uniformity in the geometry of the flow cross-section due to sudden pressure changes. This is important in this study because of the dense obstruction used in the flume to model vegetation.

## 2.2 Research on Compound Channels

Flow in river channels with floodplains, the so-called compound channel, has been an area of significant research since Sellin (1964) discovered the photographic evidence of the existence of vortices around the main channel and floodplain interface (see Figure 2.1). The seemingly straightforward estimation of the discharge capacity of such channels has proved to be difficult. In particular, the impact of this momentum interaction effect on the discharge capacity has been extensively investigated in the past. It has been found that the velocity difference between the typically slower moving floodplain and the faster moving main channel results in turbulent exchange which can dramatically reduce the overall discharge capacity of the channel. Past research also examines the different flow mechanisms that have been found to influence the flow and stage-discharge relationship of straight, skew and meandering channels. Ervine *et al.* (1993) and Rameshwaran (1997) listed the main influential basic factors for channels such as slope ( $S_o$ ), channel shape, boundary roughness, relative depth of the floodplain ( $Dr$ ), sinuosity ( $s$ ), aspect ratio, meander belt width relative to the floodplain width and system scale.



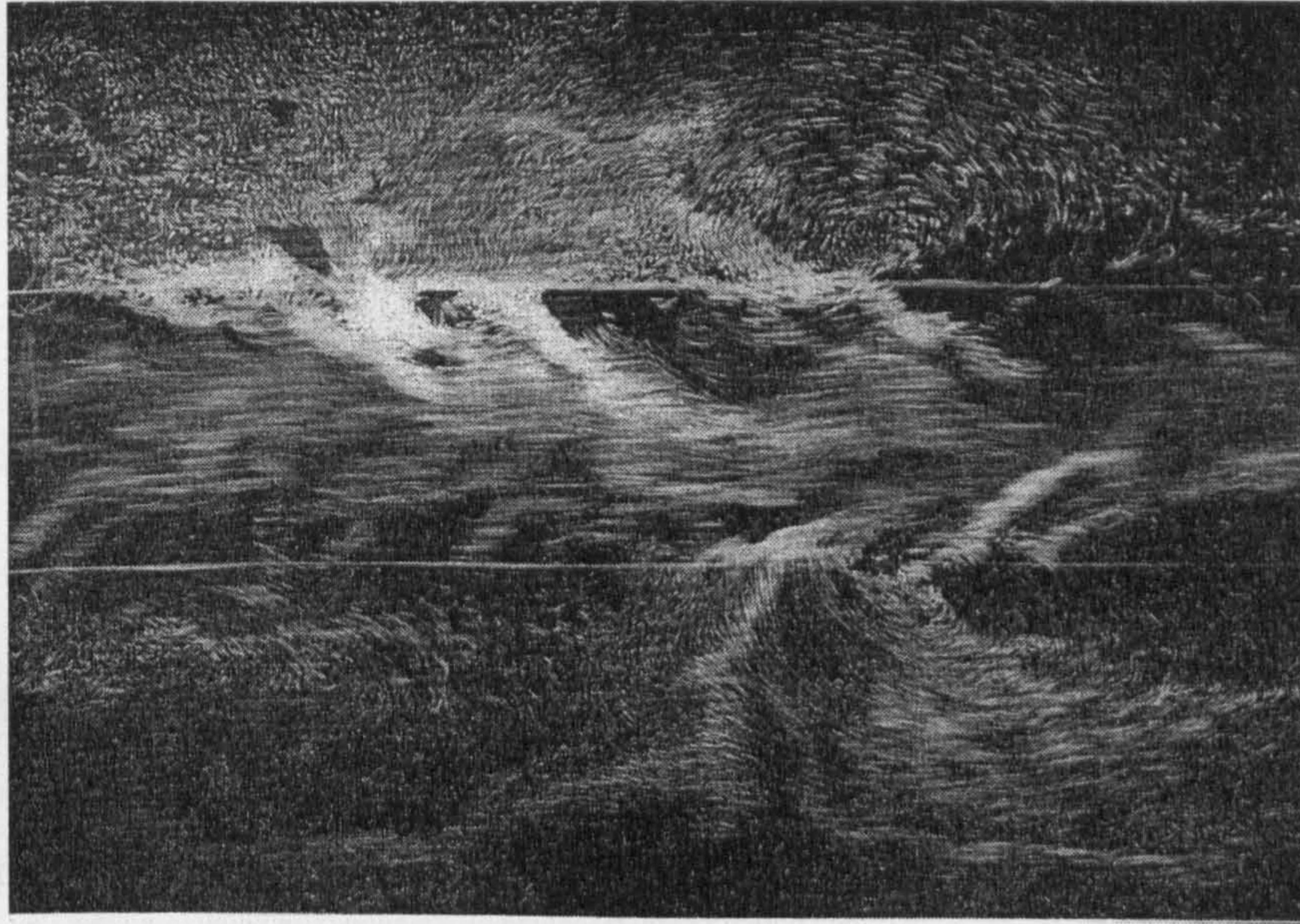


**Figure 2.1:** Photographic visualisation of the vortices present at the main channel and floodplain interface (Sellin, 1964)

### 2.2.1 Research on Straight Compound Channels

In the straight compound channels, one of the key elements was found to be the velocity difference between the main channel and the floodplain. The unique flow features such as momentum transfer, a transverse shearing layer and secondary flows are all clearly observed at the junction region. By using visualisation experiments, Fukuoka and Fujita (1989) showed the three-dimensional eddy structures of compound channel flows as illustrated in **Figure 2.2**. They described the flow transports upward from the bed with the large eddies occurring in the junction of the region. These large vortices or eddies converting high momentum fluid from the main channel onto the floodplain.



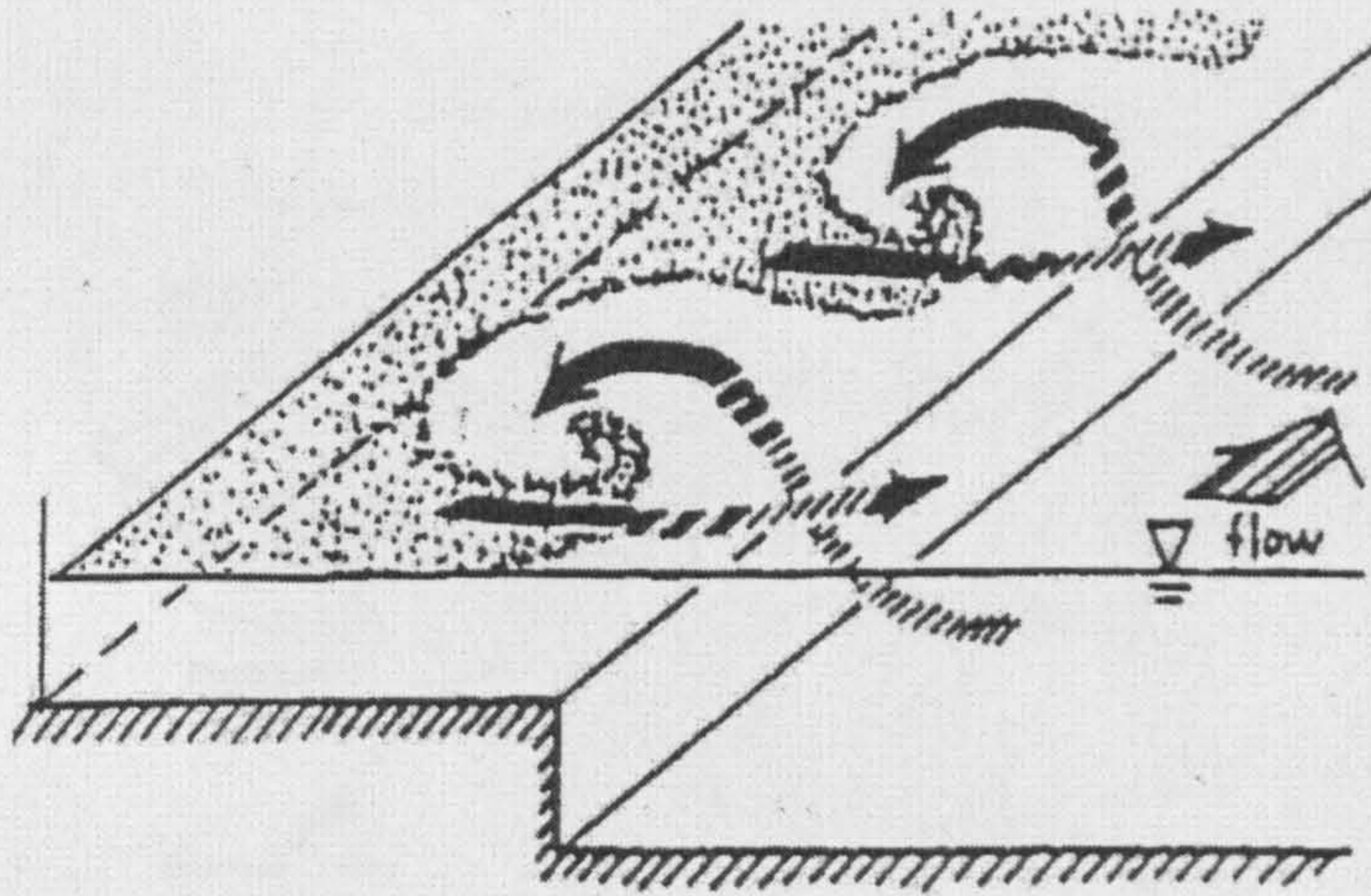
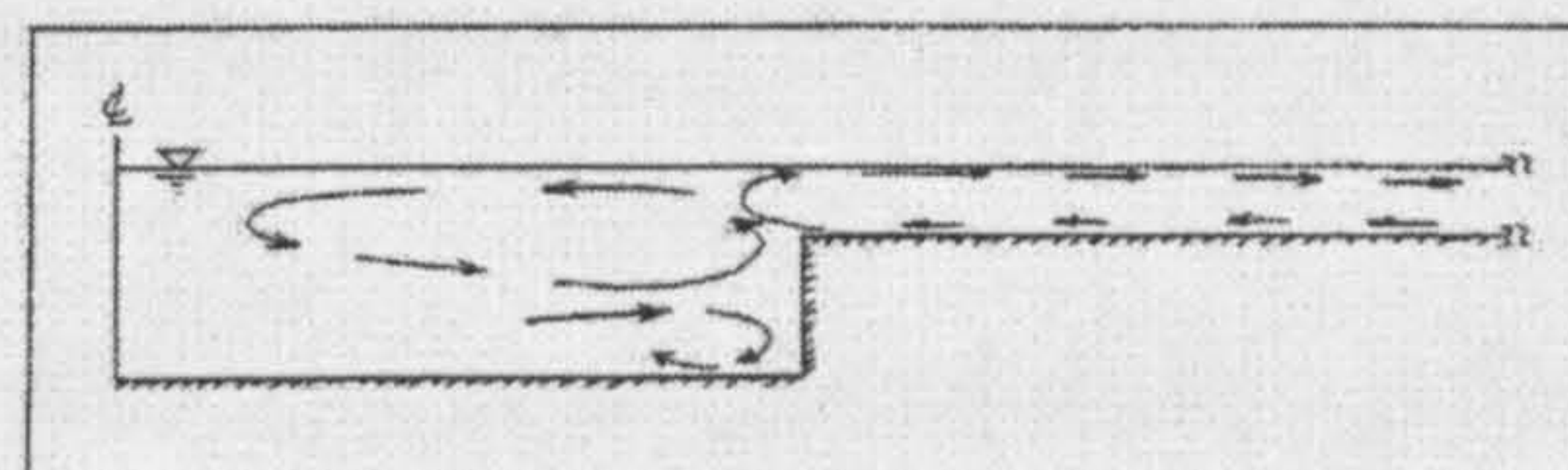
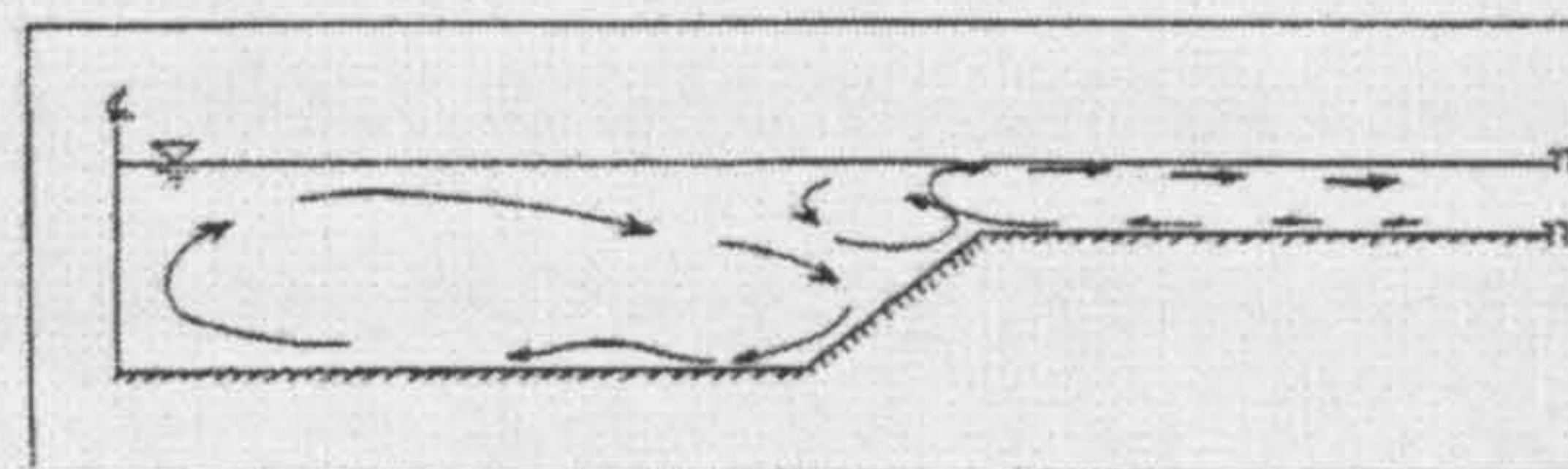


**Figure 2.2:** Large-scale eddy structure (after Fukuoku and Fujita, 1989)

The important hydraulic processes in a straight compound channel associated with overbank flow later on have been investigated including Shiono and Knight (1989, 1990), Tominaga and Nezu (1991) and Kiely and McKeogh (1993). Shiono and Knight (1989) and Tominaga and Nezu (1991) found two distinct main secondary flows or cells in the main channel/floodplain interface area with one large cell extending across the entire width of the floodplain. Shiono and Knight (1989) found that the shape of the channel influences the flow patterns of the secondary flow as shown in **Figure 2.3**. Kiely and McKeogh (1993) stated that secondary flows in the main channel and on the floodplain all act so that the water near the water surface moves away from the main channel/floodplain interface. **Figure 2.4** shows a conceptual model to illustrate secondary flow in a symmetrical compound channel with trapezoidal cross-section.



(a)



(b)

**Figure 2.3:** Illustration of secondary flows (a) Rectangular channel (b) Trapezoidal channel (after Shiono and Knight, 1989)



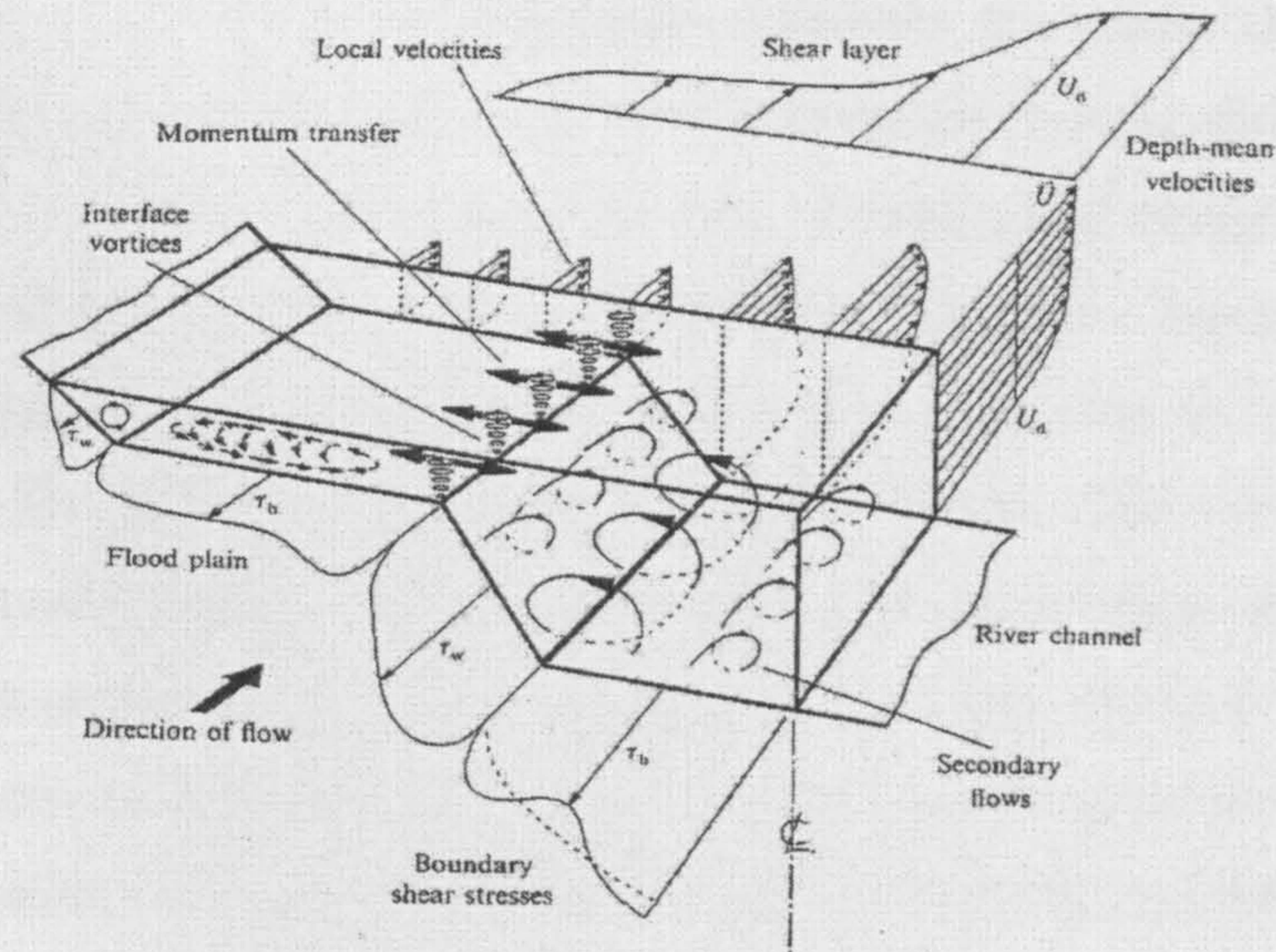


**Figure 2.4:** Mechanisms of overbank flow in a straight compound channel (after Shiono and Knight, 1991)

### 2.2.2 Research on Meandering Compound Channels

Compared with the understanding of flow mechanisms in the straight compound channels, the situation concerning meandering compound channels is still not well understood. The flow structure in these channels is highly three dimensional and extremely complicated, both for experimental development and computational models for the channel, since there is an insufficient understanding of the flow features. Several aspects of meandering flow such as velocity distribution, boundary shear stress, flow resistance, sediment transport and erosion/deposition patterns; have been the object of intensive experimental research in the past and present.

In recent years, research on flow mechanisms in meandering channels has been very active throughout the hydraulics field. Several researchers active in this field are Yen and Yen (1983), Ervine and Ellis (1987), Keily (1990), James and Wark (1992), Willets and Hardwick (1993), Sellin *et al.* (1993), Greenhill and Sellin (1993), Ervine *et al.* (1993), Sellin and Willetts (1996), Knight and Shiono (1996), Willetts and Rameshwaran (1996) and Muto and Shiono (1998), Patra and Kar (2001), Patra *et al.* (2004) and many others. The aims of these studies were to investigate flow mechanisms, mixing patterns, the behaviour and generation of secondary flow circulations, energy losses and finally the stage-discharge predictions.



Ervine and Ellis (1987) outlined the basic flow behaviour of compound meandering channels and investigated the shear interaction between the main channel and floodplain. In compound meandering channel flows, the main channel and floodplain flows are not parallel to each other as is in the case of compound straight channels. Ervine and Ellis (1987) stated that the horizontal interface at the bankful level is subjected to the co-flowing turbulent shear stress generated due to the velocity difference between the main channel and floodplain flows. The component of floodplain flow resolved ( $v_f \cos \theta$ , where  $\theta$  is bend angle at corresponding section) along the main channel direction is slow as compared to the main channel flow. They considered the apparent shear stress acting on the horizontal interface at the bankful proportional to the differential velocity between the main channel and the floodplain ( $v_m - v_f \cos \theta$ ).

The other component of floodplain flow ( $v_f \sin \theta$ ) enters into the main channel and leaves the main channel at the adjoining floodplain region. Due to this, the floodplain flow in the main channel is subjected to expansion and contraction losses as the floodplain flow enters and leaves the main channel respectively. Yen and Yen (1983) also demonstrated the expansion and contraction phenomenon that takes place when floodplain flow crosses over the main channel and re-enters the floodplain again.

James and Wark (1992) and Greenhill and Sellin *et al.* (1993) carried out a comprehensive study to investigate the behaviour of flow in compound meandering channels in the Science and Engineering Research Council Flood Channel Facility (SERC FCF) at HR Wallingford. They categorised the most influential factors in meandering channels with overbank flow as bed slope, channel shape, bed and floodplain roughness, relative flow depth of the floodplain, meander belt width, sinuosity and aspect ratio. In addition to this, James and Wark (1992) have identified the four most importance flow mechanisms in two-stage meandering channels as follows:

- (a) The longitudinal velocities in the main channel tend to follow the meandering main channel side walls while the floodplain velocities are generally in the valley direction. Hence, the floodplain flows pass over the main channel and induce a horizontal shear layer.

- (b) Water passes from the main channel onto the floodplain and back into the main channel in the following meander bend. Hence, the proportion of the discharge passed by the main channel and floodplain varies along a meander wavelength. These bulk exchanges of water between slow and fast moving regions of flow induce extra flow resistance.
- (c) The energy loss due to the secondary flows in the main channel is greater than for an equivalent simple channel and the secondary flows rotate in the opposite direction to that observed mostly in inbank flows.
- (d) Flows on the floodplain outside the meander belt are usually faster than those within the meander belt. It would appear that the extra flow resistance induced by the meandering main channel has a relatively small effect on the outer floodplain.

In 1993, Willets and Hardwick investigated the overbank flow in a meandering channel in a small-scale laboratory flume. They described the overbank flow structure as highly three-dimensional, with strong secondary currents, momentum exchanges between the main channel and floodplain and shear interaction on the horizontal interface region. These main features of the two-stage meandering with overbank flow are shown in **Figure 2.5**. The figure explains that the high velocity filament is shifting from the outer bank to the inner bank as the flow approaches the downstream apex. A vigorous exchange of water from the floodplain drives a large secondary flow in the main channel. Large secondary cells grow along the outer bank upstream of each bend apex and decay rapidly downstream of the bend apex. Floodplain flow plunging into the main channel and leaving the main channel created contraction and expansion exchange effects between the two regions of the channel.



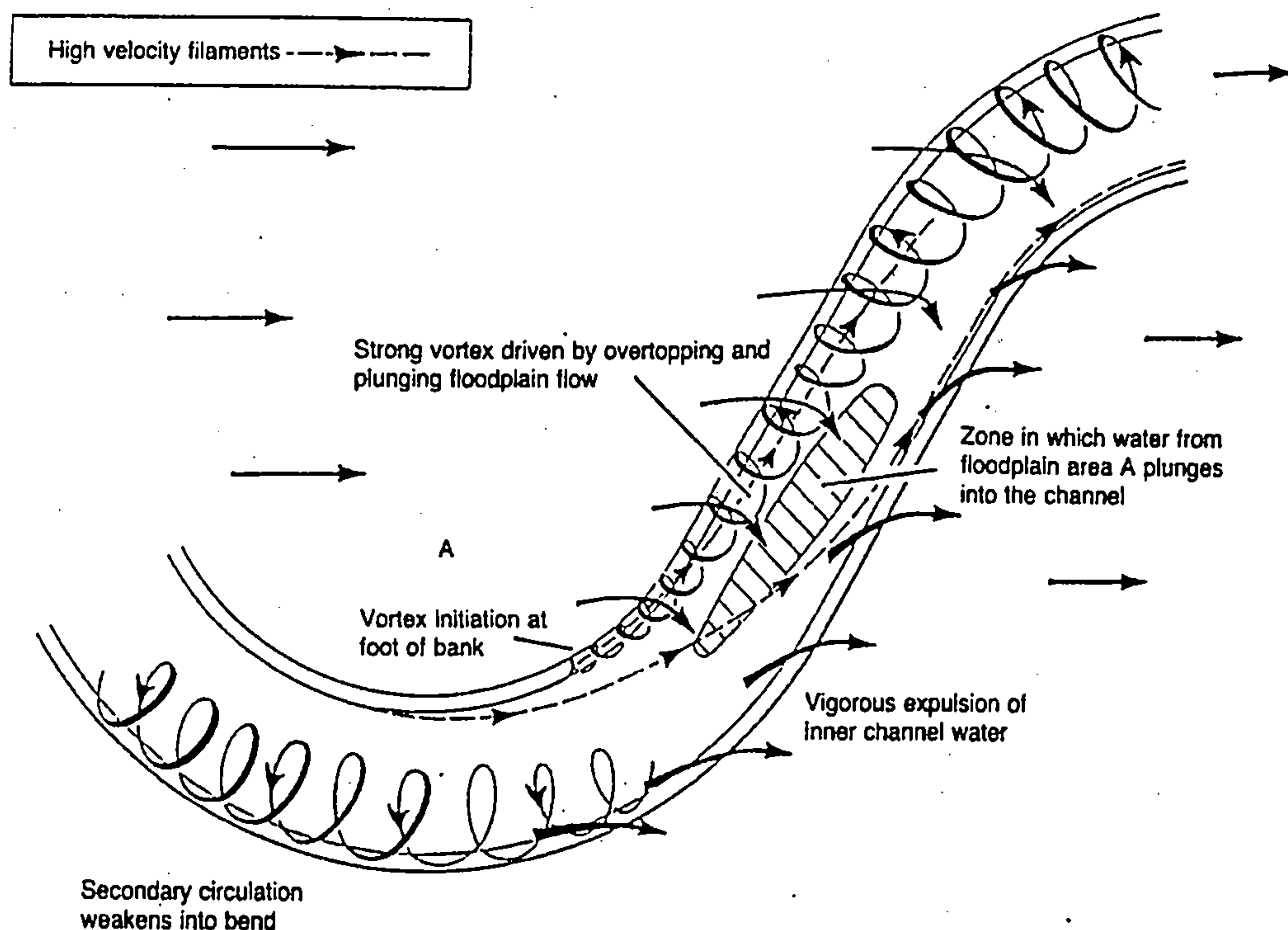


**Figure 2.5:** Flow mechanism in compound meandering channel (after Willetts and Hardwick, 1993)

#### 2.2.2.1 Secondary Flow

Bathurst *et al.* (1979) defined secondary flow as a flow normal to that in the longitudinal flow direction. It distorts the longitudinal velocity pattern and boundary shear stress distribution and is therefore important as it affects the flow resistance, sediment transport, bed and bank erosion and, in turn, influences the channel morphology. Previous researchers including Nezu and Rodi (1985), Tominaga *et al.* (1989), Shiono and Knight (1989, 1991), Tominaga and Nezu (1991), Willetts and Hardwick (1993), Ervine and Jasem (1995) and Muto and Shiono (1998) have investigated experimentally the secondary flows in compound channels. They found that the secondary flow could be classified into two kinds. The first kind is driven by turbulence and the second one is driven by the geometry of the channel. The turbulence and geometry form of the secondary flows has a significant effect on the boundary shear stress distribution in the fluid system.

By using a dye injection technique, Willetts and Hardwick (1993) demonstrated that the flow structures in a main channel with a trapezoidal cross-section are different from those observed in channels with a natural cross-section. Based on their



experiments on the skewed compound channels, Ervine and Jasem (1995) illustrated the effect of the main channel aspect ratio and the channel bank side slope on the patterns of secondary flow circulations. This is shown in Figure 2.6.

Muto and Shiono (1998) studied the three-dimensional flow structures in meandering channels with overbank flow based on velocity measurement using a two-component Laser Doppler Anemometer (LDA). They stated that the development of secondary flow for overbank flow structures is controlled by the flow interaction in the cross-over section as shown in Figure 2.7. In addition, the flow interaction between the two layers also creates the shearing effect and the maximum shearing effect in overbank flow occurs at a relative depth of around 0.05. So, it can be noted that the secondary flow is a dominant factor influencing a compound meandering channel. By advecting flow, the secondary flow redistributes velocity and boundary shear stress and then enhances the mixing and transport process and is highly responsible for the bank erosion process.

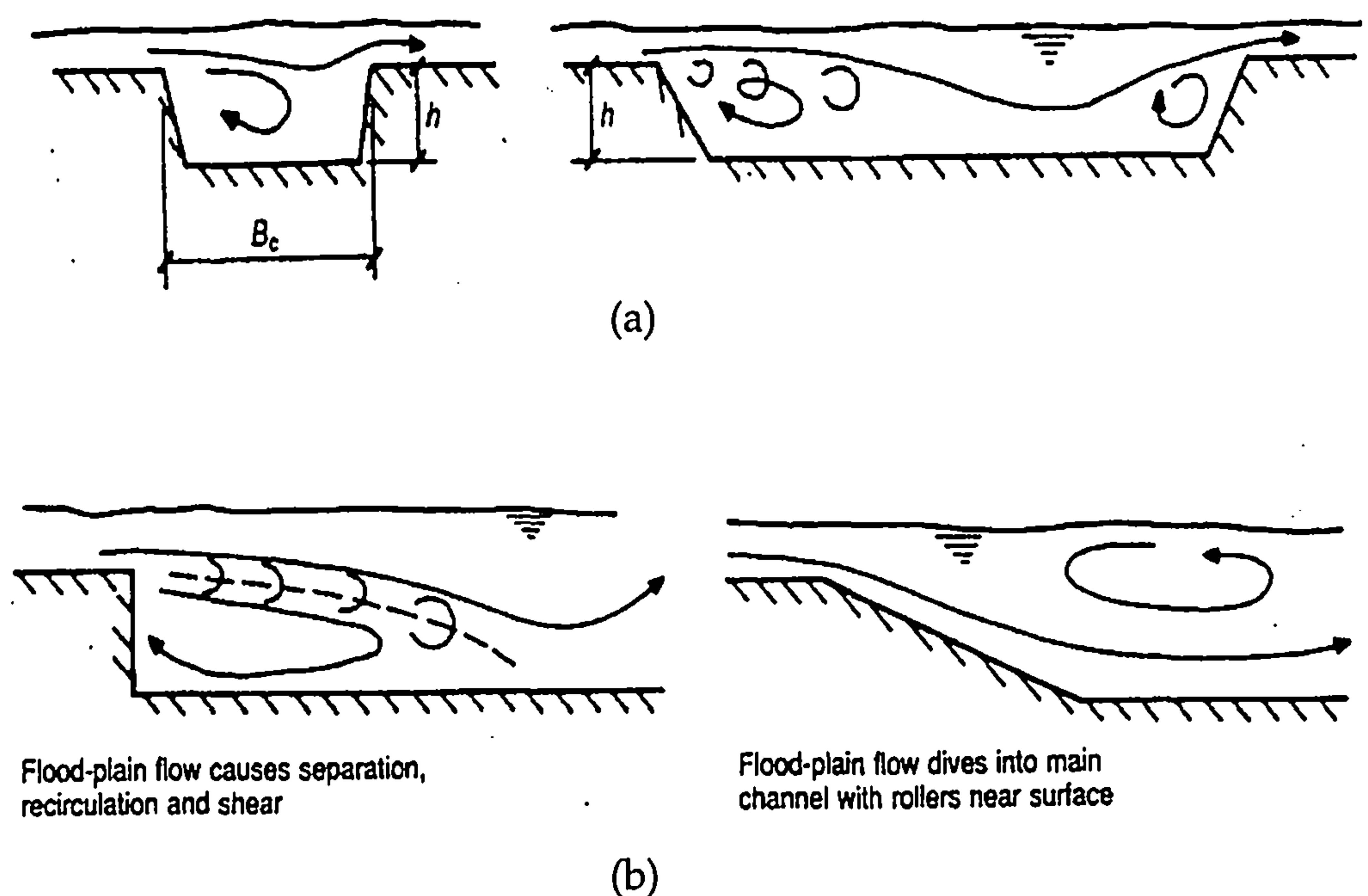


**Figure 2.6:** Illustration of the effects of (a) main channel aspect ratio on cross-over region mixing (b) main channel bank slope on mixing in cross-over region (after Ervine and Jasem, 1995)



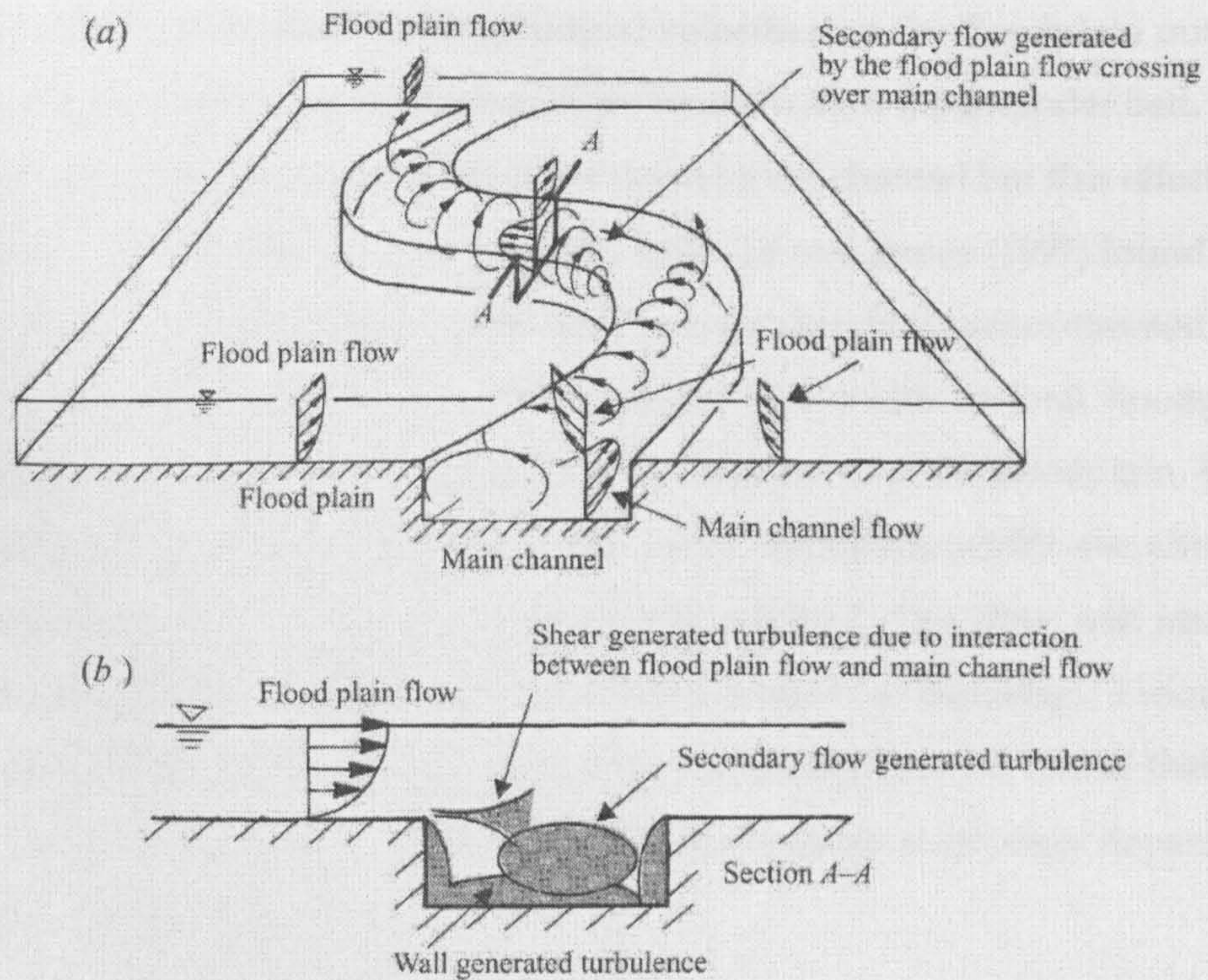


**Figure 2.7:** Overall flow structure in meandering channel for overbank (a) Secondary flow generation mechanism (b) Contributions of flow mechanisms (turbulent shear, secondary flows and anisotropy of turbulence) towards the production of turbulence energy (after Shiono and Muto, 1998)

### 2.2.2.2 Velocity Distribution

Velocity measurements for compound meandering channels have been conducted by Toebe and Sooke (1967), McKeogh and Kiely (1989), James and Wark (1992), Shiono and Muto (1993), Shiono *et al.* (1993), Liu and James (1997), Muto and Shiono (1998), Lyness *et al.* (1998), and Liriono *et al.* (2001). Toebe and Sooke (1967) observed that the vectors of the horizontal resultant velocity have a divergence pattern, indicating strong interaction of vertical flow components. McKeogh and Kiely (1989) found that the primary velocity vectors on the floodplain were essentially parallel to the valley slope direction, whereas the primary velocity flow in the main channel tends to follow along the course of the meandering channel wall direction during high overbank flow. Shiono *et al.* (1993) also reported a similar observation, hence the velocity differential between the floodplain flows and main channel flow created a lateral shear layer horizontally between these two regions. Furthermore, they suggested that, for the discharge assessment, it is best to use a horizontal division method at the shear layer interface between the main channel and floodplain.



James and Wark (1992) described the longitudinal velocities on the floodplain outside the meander belt as usually being faster than those found within the meander belt. This is due to an extra flow resistance induced by the meandering channel but this effect has less significance for the flow beyond the meander belt. Liu and James (1997) found that accounting only for frictional losses outside the meander belt overestimated the conveyance of the section, nevertheless, the meander belt width to total floodplain width ratio affects the interaction between the main channel and the floodplain. With the smaller meander belt width in relation to the overall floodplain width, the effect of the meandering channel on the overall discharge is reduced. The flow will also be affected by obstructions on the floodplain, such as vegetation or buildings. Liriono *et al.* (2001) investigated the effect of obstructions on the floodplain and found that the magnitude of the effect on water level due to such obstructions is strongly dependent upon the location of the obstructions.

In 1993, Shiono and Muto measured the three-components of instantaneous velocity using a two-component Laser Doppler Anemometer in a trapezoidal cross-section meandering channel with straight floodplain wall for inbank and shallow overbank flow cases at  $Dr = 0.15$ . In the case of overbank flows, a strong gradient of streamwise velocity in the vertical direction was observed at the start of the cross-over region. This was due to the plunging of the floodplain flows into and over the main channel, which ultimately triggers the generation of the secondary flow circulations. Since the experimental data was available only at seven different cross-sections along the meander, the exact point from which the secondary flow circulations started to be generated was not investigated. Based on the measured lateral and vertical shear stresses, they confirmed the large momentum exchange taking place in the region of strong interaction (the cross-over region) between the main channel and the floodplain flows. Later on, experimental work carried out by Muto and Shiono (1998) showed that in overbank flow the maximum velocity filament in the main channel occurred near the inner bank at the upstream apex section and moved progressively across the outer bank as it approached the downstream apex. Muto and Shiono (1998) also observed in overbank flow that the gradient of the streamwise velocity becomes larger in the cross-over region due to a strong interaction between the main channel and floodplain flow. Shiono and Muto (1998) reported that this large interfacial shear stress induced at around the bankfull level, especially in the cross-over region and was found to be



larger than the bed shear stress. They further stated that the strong shear layer generated by the floodplain flow crossing over the main channel flow is controlled by the angle between the meandering channel and the floodplain wall together with the depth of the water. The floodplain flow can be resolved into two components with an angle,  $\theta$ , where this angle is the angle of the floodplain flow entering the meander channel. The floodplain flow components resolved along the streamwise main channel flow direction is shown in Figure 2.8. They observed that this floodplain angle at the bankfull level in the cross-over region agreed with the angle of the meandering channel. Thus they concluded that the angle of meandering channel is one of the main parameters generating velocity differences, or shear at the bankfull level.

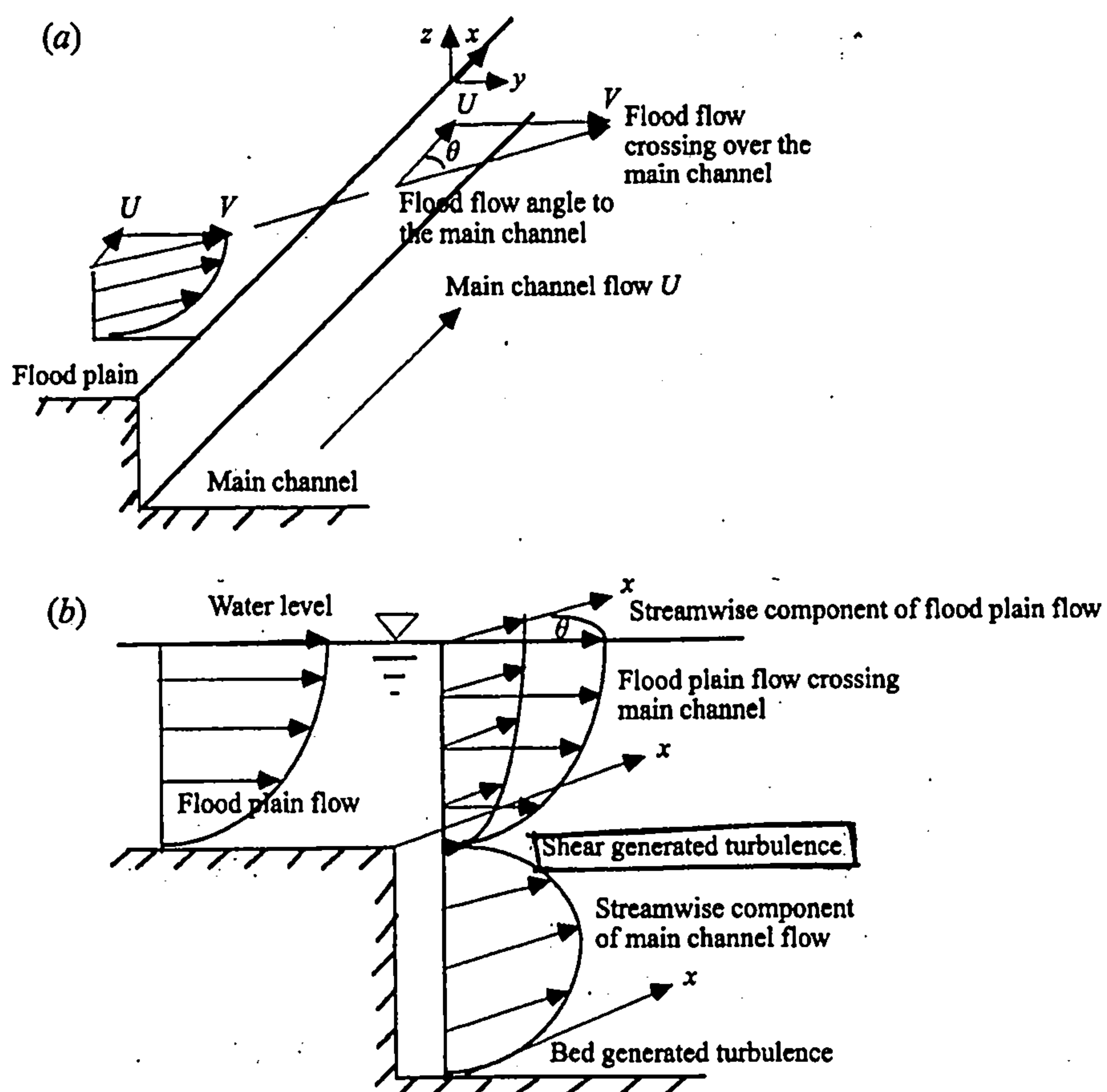
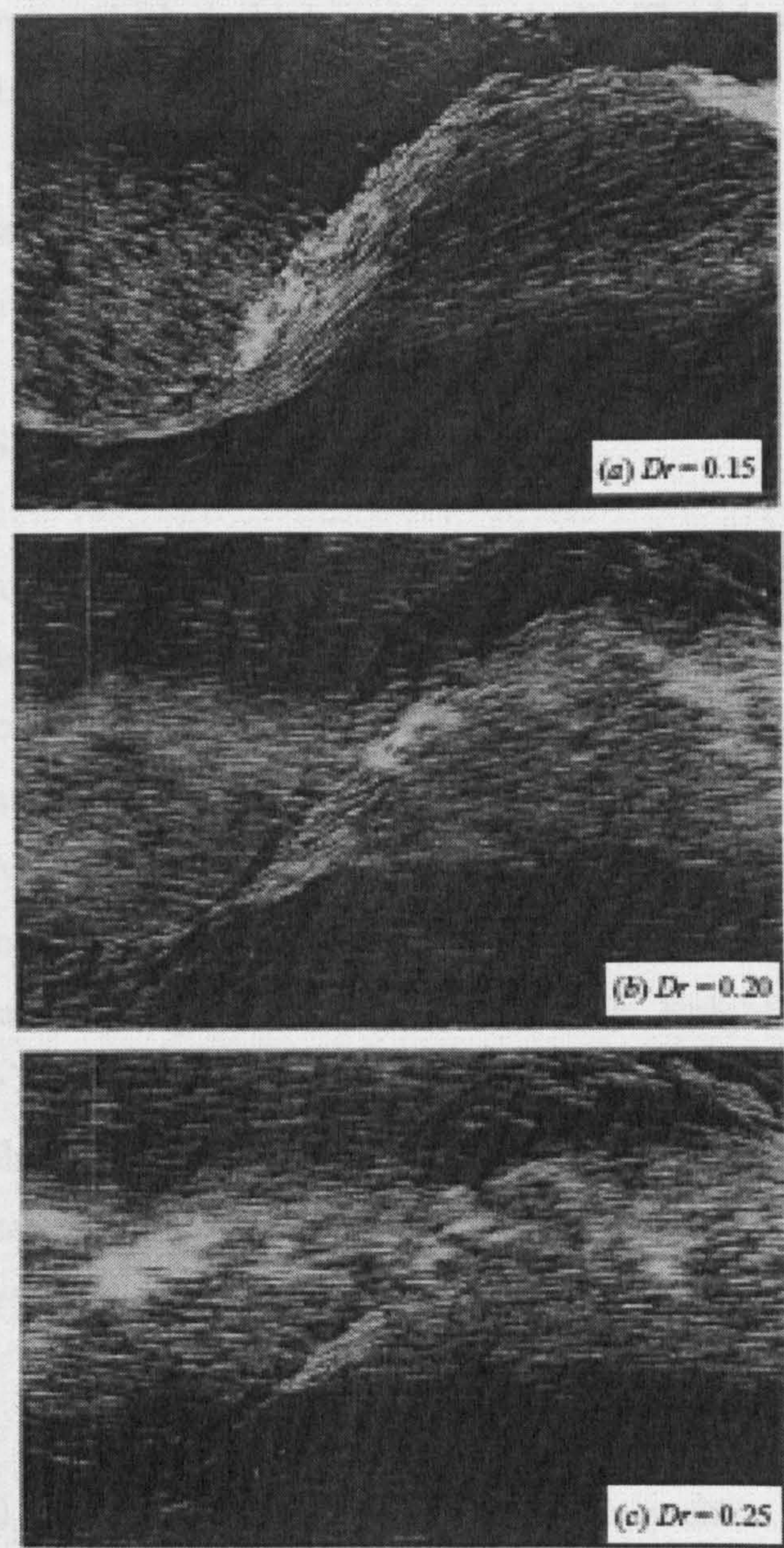


Figure 2.8 Illustration of floodplain flows resolved in the streamwise direction to show the effect of meander channel angle with the floodplain walls on the associated secondary flow structures (after Shiono and Muto, 1998)



The pattern of floodplain flow plunging into the main channel varies with the floodplain flow depth. This is shown in **Figure 2.9**. The figure shows the flow visualisation for different relative depths as conducted by Shiono and Muto (1998). For shallower floodplain depth, the main channel flow is still seen to be dominant and as the floodplain flow depth increases the floodplain flow dominates the main channel flow direction above the bankfull level (see  $Dr = 0.25$  in **Figure 2.9**).



**Figure 2.9** The pattern of the flow visualisation of floodplain flow plunging into and over the main channel depends on the floodplain flow depth for different relative depths of 0.15, 0.2 and 0.25 (after Shiono and Muto, 1998)



Lyness *et al.* (1998) examined the hydraulic characteristics of overbank flows in a meandering mobile bed compound channel at the UK Flood Channel Facility (FCF). They carried out the experiment both for rough and smooth floodplains with a mobile bed channel using uniformly graded sediment. Their results found that for overbank flow with relative depth,  $Dr$  greater than 0.2, the average floodplain flow in the valley direction is greater than the main channel average flow velocity. Floodplain roughness progressively increased to single channel Manning's  $n$  and Darcy-Weisbach by up to 100 % and 300 % respectively in high overbank depth. The Manning's  $n$  value in the mobile-bed main channel is generally greater than the floodplain Manning's  $n$  for both rough and smooth cases. At high relative depth,  $Dr$  greater than 0.4, the main channel and floodplain Manning's  $n$  values are identical, reflecting that the flow resistance is becoming more uniform in high overbank flows.

#### 2.2.2.3 Boundary Shear Stress

The boundary shear stress is an important parameter commonly used to measure flow competence, predict sediment transport rates and discharge conveyance in both immobile and mobile boundary channels in fluvial hydraulics. In general, the distribution of boundary shear stress along the wetted perimeter of a channel is governed by many factors such as the geometry of the cross-section, longitudinal variation in planform geometry, lateral and longitudinal boundary roughness and sediment concentration (Knight *et al.* 1994). Previously, Knight *et al.* (1992) reported that the secondary cells, sinuosity and cross-sectional geometry have a considerable influence on the value of the boundary shear stress for meandering channels. However, in a meandering channel with overbank flow condition, the estimation of the boundary shear stress on the channel bed becomes more difficult due to the complexity of the flow mechanisms.

Knight *et al.* (1992) studied the distribution of boundary shear stress in meandering channels with sinuosities of 1.374 and 2.042 under inbank and overbank flow conditions. The main channel had a fixed bed with a smooth boundary on the floodplain. Boundary shear stress throughout the whole wavelength was measured by means of a Preston tube. This comprehensive study revealed that the magnitude of the boundary shear stress reduced significantly in the cross-over region and it is inversely



proportional to the sinuosity of the meander channel as the water depth increased. In both cases, the highest value of shear stress is observed near the bend apex and the sectional average boundary shear stress in the main channel below bankful level varies with both longitudinal position and stage. They found two important boundary shear stress features on the floodplain. Firstly, the flow on the floodplain area is mainly two-dimensional giving rise to nearly uniform values for the shear stress in the valley slope direction and secondly, the magnitude of the shear stress increases dramatically on the outside edge of the main channel at the outer bend. Similarly, Lorena (1992) found that large values of the boundary shear stress normally occur at the floodplain area near the cross-over region where the lower main channel flow is ejected onto the adjacent floodplain.

According to Shiono *et al.* (1999) the magnitude of the boundary shear stress depends on the velocity gradient close to the bed and consequently on the pattern of the primary isovels. The highest magnitudes of shear stress occur in the regions of downwelling where the isovels are compressed and the region where the primary velocity is relatively high. The uniformity of boundary shear stress at bends is influenced by the strength of the secondary flow and Reynolds number. They also pointed out that the magnitude of the normalized boundary shear stress becomes smaller as the depth of the water increases. The variation of the boundary shear stress distribution is significant where the secondary flow cells exist in the main channel.

### **2.3 Sediment Transport in Compound Meandering Channels**

In general, the sediment transport processes in a river channel is governed by a number of factors. These factors can be classified into three categories, namely the characteristics of the sediment properties, characteristics of the fluid and the characteristics of the channel. In the overbank flow condition, additional factors may arise resulting from complex overbank flow characteristics which are not fully understood.

Willems and Rameshwaran (1996) reported that the primary velocities at the bend apex are distributed differently in overbank and inbank flow in a meandering channel corresponding to the relocation of the secondary flow in the main channel. The

strongest part of the current relocates from the area near the outer bank for inbank flows and towards the inner bank for overbank flows. Since boundary shear stress is primarily influenced by the flow velocity, the sediment transport could be most active in areas where the maximum velocity occurred.

In overbank flow, O'Sullivan (1999) observed that sediment transport rate in the inbank flow increases with the flow depth and reaches a maximum at the bankfull depth and suddenly drops when the flow starts to inundate the floodplain. Rameshwaran *et al.* (1999), Shiono *et al.* (2001) and Chan (2003) reported that a significant reduction of sediment transport rate occurs in the shallow overbank flow. They explained that such a reduction is affected by the increase in flow resistance induced by the existing bedforms and momentum exchanges. This subsequently leads to the reduction in main channel velocity and boundary shear stress.

### **2.3.1 Sediment Transport with Vegetation**

It is common knowledge that the presence of vegetation in a channel or floodplain will affect the sediment transport and the scour or erosion of the channel bottom and sides. Vegetation will certainly reinforce and strengthen the soil surfaces through the development of root systems. The effective soil boundary is then more resistant to soil movement and erosion. Vegetation can also impede the movement of the contact portion of the bed load (Vanoni, 1977), and stabilise bedforms.

Another common belief is that the presence of vegetation increases flow resistance, which results in the reduction of flow velocity and increased depth. The reduced velocity will then reduce the sediment transport of the channel and reduce the forces necessary to cause scour and erosion. Li and Shen (1973) have developed a theory to explain how the retarding flow rate is the result of the drag forces on tall vegetation, and developed the methodology to predict the reduction of sediment load. Their investigations were based on cylinders as a model of vegetation and relied on their assumption of uniformly distributed bed shear. The development of their theory was based on a horizontal, two-dimensional flow field around multiple cylinders. Tests of actual vegetation were not available for their study and two-dimensional analysis precluded the consideration of the vertical velocity components. The blockage

produced by vegetation or trees could produce vertical velocity components that would then create flow vortices and local scour. Local scour immediately upstream of bridge piers is a classical example of this type of phenomenon.

## 2.4 Flow Resistance in Compound Meandering Channels

Flow resistance is affected by many factors. Among these factors are flow characteristics, which include the velocity, depth of flow and the degree of turbulence. The increase of velocity and intense turbulence causes very large losses of energy. The geometry of the section also plays an important role in energy losses. The losses are evidenced as instantaneous losses as in the case of non-uniformity in the geometry of the flow cross-section due to sudden pressure changes. This is important in this study because of the dense obstruction used in the flume to model vegetation.

The extensive researches on flow resistance in meandering compound channels with fixed and mobile beds and rough and smooth floodplains were carried out in FCF, HR Wallingford. In conjunction with this, the flow resistances in compound meandering channels have been subjected to recent investigations such as those by Rameshwaren (1997), Myers *et al.* (1999), O'Sullivan (1999), Myers *et al.* (2000) and Knight and Brown (2001).

Numerous explanations have been advanced to account for the additional resistance to flow in a meandering channel in terms of geometric and flow variables including those by Toebe and Sooke (1967) and Chang (1984). According to Chan (2003), The Soil Conservation Service (SCS) presented a method for estimating flow resistance in considering meander losses in term of sinuosity ( $s$ ) by adjusting the basic Manning's  $n$  equation.

Rameshwaren (1997) investigated the flow behaviours in overbank flow and suggested that the non-bed friction losses increase with the increase of depths at low overbank flow and non-bed losses decrease with depth in high overbank flow. Myers *et al.* (1999) found that flow resistance in the meandering compound channels is significantly more complex than for simple channels. The fixed-bed main channel flow is greatly influenced by the floodplain roughness due to high momentum exchange between the



main channel and floodplain flows. However, in a mobile bed, the main channel resistance is independent of floodplain roughness at low overbank flow. Lyness *et al.* (1998) and O'Sullivan (1999) investigated the effect of the main channel sinuosity on flow resistance. They concluded that the flow resistance in the main channel increases with the increase of sinuosity by a factor of approximately 1.5 at low overbank depths. Thus, flow in the main channel slows down in high sinuosity channels, which substantially reduces the amount of discharge in the meandering channel.

Myers *et al.* (2000) demonstrated that the flow resistance values for meandering channels at high overbank depths are half greater than those for the straight channel with similarly roughened floodplains. This indicates that there is an additional source of flow resistance occurring in meandering channels. This additional source of the flow resistance during overbank flow is due to the meander bend loss as describe by Ervine *et al.* (1993). However, in their small-scale laboratory tests, Toebe and Sookey (1967) found that energy losses in a meandering channel were up to 2.5 times greater than those for a uniform channel of identical width, hydraulic radius and discharge.

## **2.5 Flow Resistance of Non-Rigid and Rigid Vegetation**

Flow resistance problems are usually classified into submerged vegetation flow and unsubmerged vegetation flow. Most efforts to study vegetal resistance have concentrated on studying submerged and rigid roughness. There is only a small amount of available field data, other than overall roughness coefficients, representing limited flow conditions. Most laboratory studies have been conducted using artificial roughness. Investigations concerning flow resistance with vegetation have been conducted by Li and Shen (1973), Petryk and Bosmajian (1975), Fathi and Kouwen (1997), Nepf (1999), Wu *et al.* (1999), Kouwen and Fathi, (2000) and Jarvela (2002). Recently, however, some investigations have been performed using actual plants (Kouwen and Fathi, 2000 and Jarvela, 2002).

Li and Shen (1973) studied the effect of tall, unsubmerged vegetation on flow resistance by investigating the wake caused by various cylinder set-ups. Experimental results indicated that different patterns or groupings of cylinders significantly affected flow rates. For unsubmerged vegetation they extended their method to calculate the drag



coefficient for a single plant in a group and further the friction factor for the vegetation. The governing equation for the friction factor utilised readily measurable physical properties in addition to the drag coefficients for longitudinal and lateral distances between the plants and also the plant diameter. Drag coefficient was determined through an iterative process including empirical relationships, which were formulated from experiments on rigid cylinders.

Nepf (1999) conducted experiments using a cylinder-based model of vegetation resistance by including the dependence of the bulk drag coefficient,  $\bar{C}_D$ , on the vegetation density for  $Re > 200$ . This model was confirmed by a study of the drag, turbulence and diffusion in flow through emergent vegetation. The experimental results show that the turbulence intensity is principally dependent on the vegetative drag and that for vegetative densities as small as 1 %, the bed-drag and bed shear production are negligible compared to their vegetation counterparts as shown in **Figure 2.10**. In addition, the fraction of mean energy partitioned to turbulence depends on the on the morphology and flexibility of the stems and stem Reynolds number.

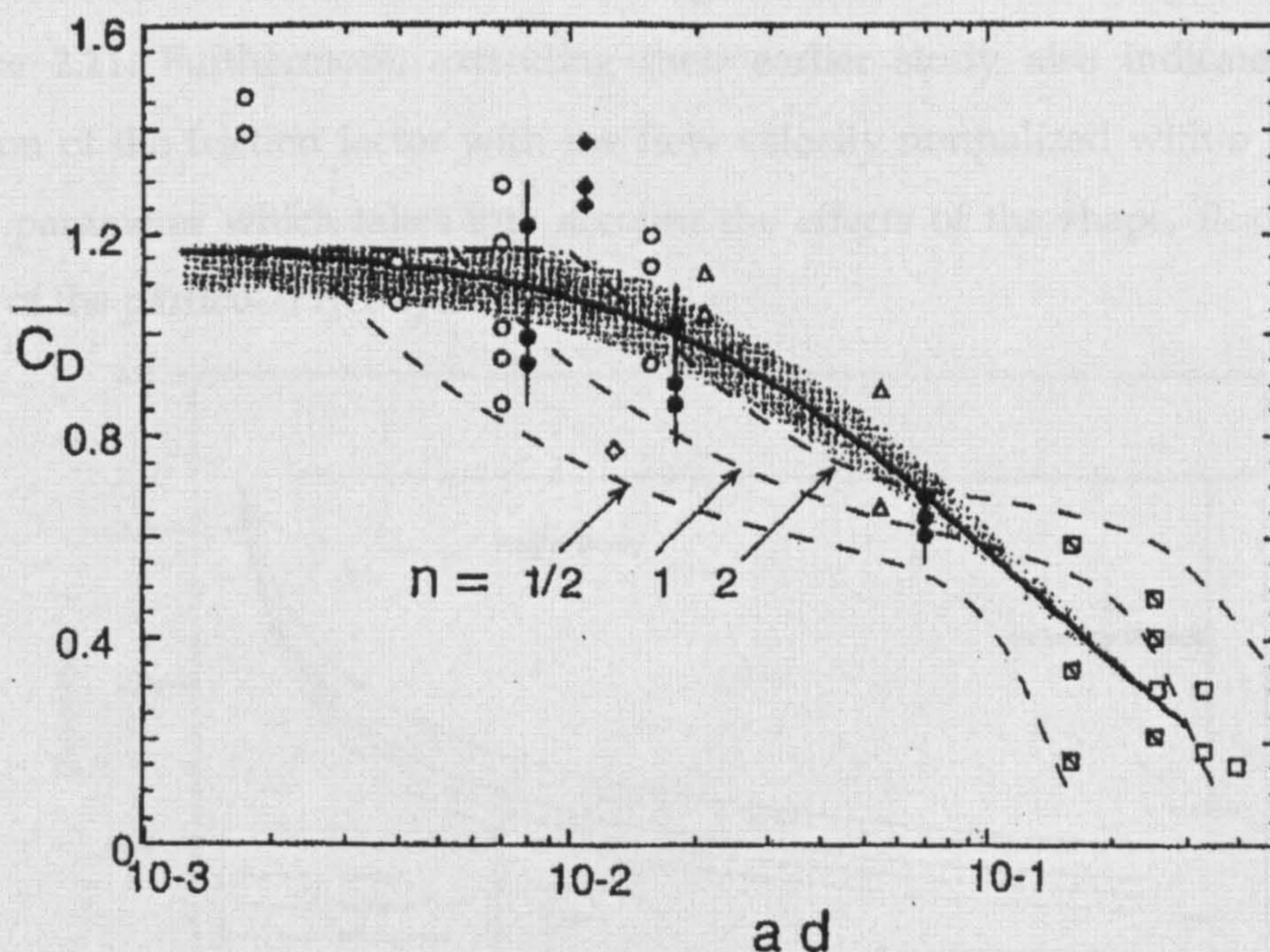


**Figure 2.10:** Wake interference model predicts that the bulk drag coefficient,  $\bar{C}_D$ , decreases with increasing array density  $a d$ , for both random (solid line) and staggered (dashed line) arrays. For the staggered arrays pitch is defined by  $n$  = ratio of longitudinal to lateral row spacing, that is,  $n = 1$  is a square staggered array (after Nepf, 1999)



Any analytical method for estimating the contribution of vegetation to the total flow resistance must consider the drag force exerted by the vegetation on the flow. The flow velocity through vegetation is reduced as a result of the momentum from the fluid to the vegetation which occurs in response to the drag force. Wu *et al.* (1999) and Jarvela (2002) conducted experiments on simulated vegetation under uniform flow conditions in a straight channel and proposed a simplified model to estimate the vegetal drag coefficient for submerged and non-submerged vegetation. They showed that the magnitude of the drag force exerted by a single vegetation element is a function of the frontal area of the element projected onto a plane perpendicular to the flow direction. In hydraulic calculations, it is convenient to use an expression for the drag force exerted in a control volume. The sum of the areas of the individual plant elements in the direction of flow for a control volume is the vegetation density.

In the next section the extensive work of Fathi and Kouwen (1997) and Kouwen and Fathi (2000) will be reviewed. Their results were achieved by using coniferous tree saplings and branches in flume experiments and showed that the friction factor varied greatly with mean flow velocity due to the bending of the vegetation and with flow depth as a result of an increase in the submerged momentum-absorbing area as shown in Figure 2.11. Furthermore, extending their earlier study also indicated a good correlation of the friction factor with the flow velocity normalized with a vegetation index, a parameter which takes into account the effects of the shape, flexibility and biomass of the particular tree species.

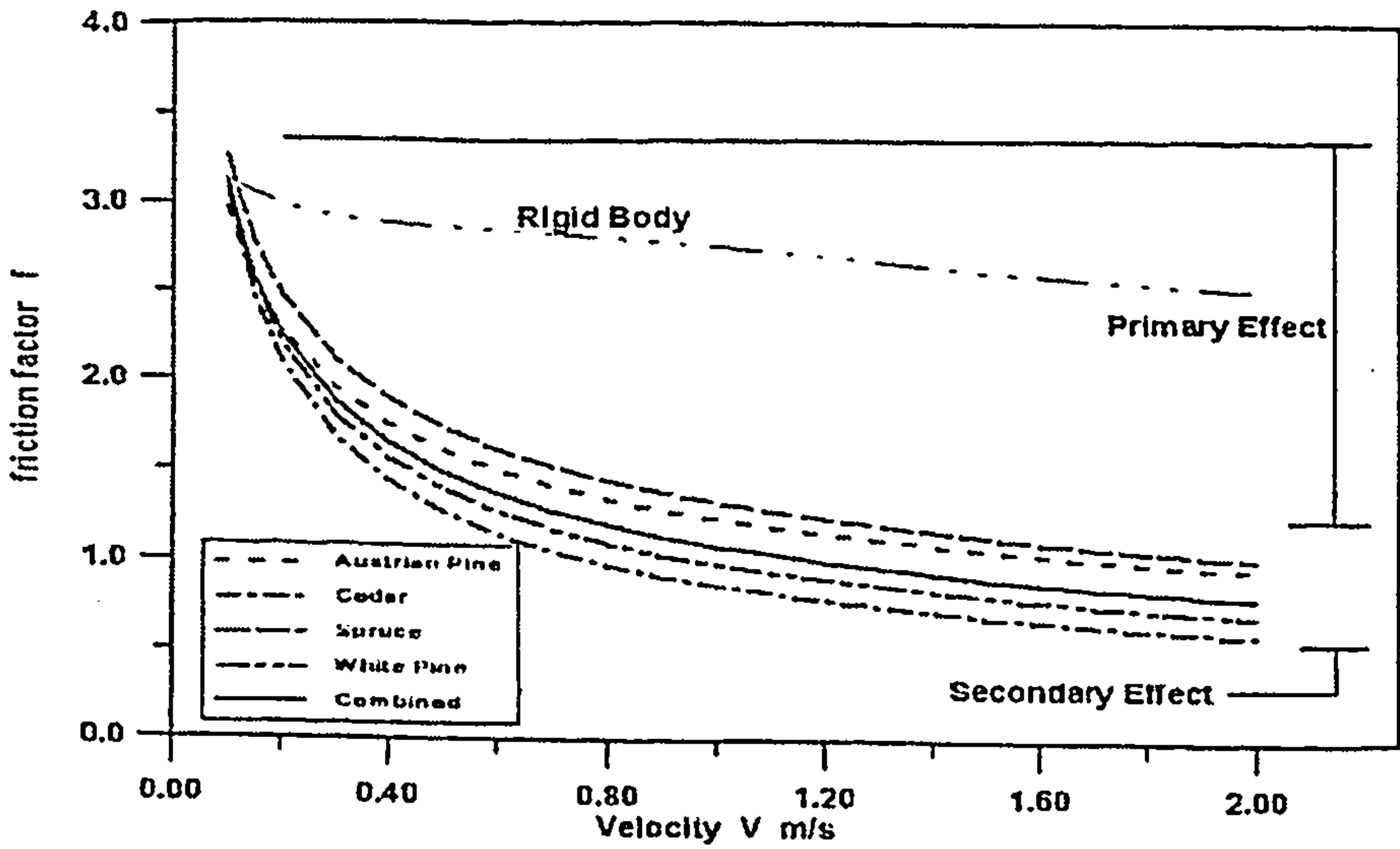


Figure 2.11: Correlation of Darcy-Weisbach friction factor for four coniferous species with flow velocity (after Kouwen and Fathi, 2000)



### 2.5.1 The Case of Non-Rigid, Unsubmerged Vegetation on Floodplains

Fathi and Kouwen (1997) studied the case of non-rigid, unsubmerged, vegetation roughness on floodplains. They studied the effect of different values of velocity and depth of flow on the friction factor value. They also proposed a model to calculate the Manning's  $n$  or Darcy-Weisbach  $f$  friction factors for unsubmerged flexible vegetation in the vegetated zone of river cross-sections. They concluded that the Manning's  $n$  vary greatly with the mean channel flow velocity due to the bending of vegetation and with flow depth as a result of the increase of the submerged momentum-absorbing area as shown in Figure 2.12. They also developed a dimensional analysis approach to obtain a relationship between roughness conditions and flow conditions. The following section will review their work in this area.

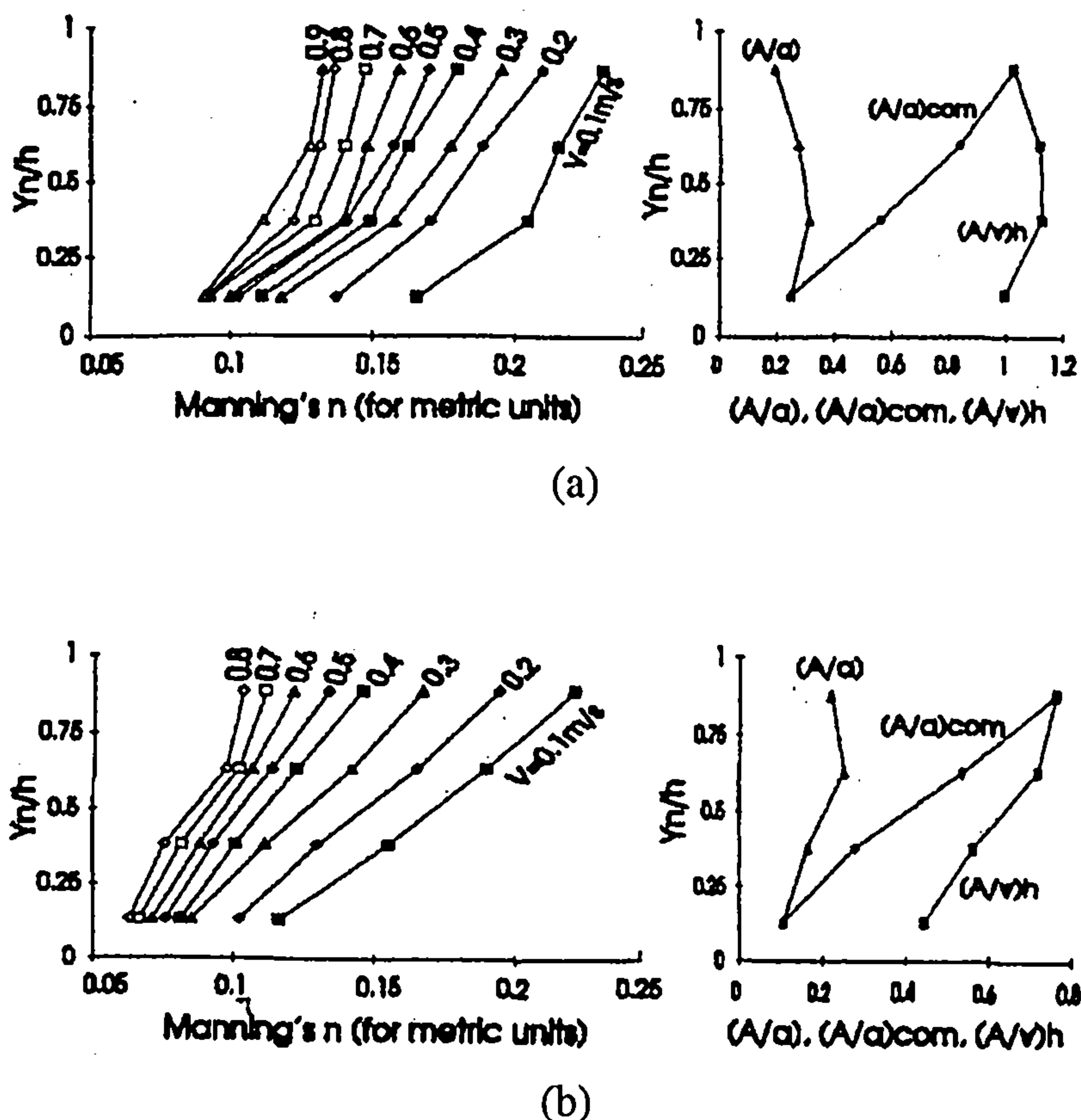


Figure 2.12: Relationship between Manning's  $n$ , mean velocity, MAA and depth of submergence model with foliage flow (a) Pine (b) Cedar (after Fathi and Kouwen, 1997)



### 2.5.1.1 The Effect of Velocity and Depth on the Friction Factor

Fathi and Kouwen (1997) studied the effect that the depth of flow can have on the resistance to flow. Their primary concern was that there might be an extreme variation of roughness with depth of flow due to the large increase in the momentum-absorbing area (MAA) in the unsubmerged vegetation as the depth of flow is increased. This fact might lead to a conclusion that all the available roughness equations, which are based on the relative roughness approach, would have a weak applicability in these circumstances. They were also concerned with the fact that the non-rigid vegetation on floodplains is usually assumed to behave as rigid roughness which can lead to large errors in the relationships between velocity and drag force. They developed a dimensional analysis approach that was supported by experimental results. The purpose of this approach was to obtain a relationship between roughness conditions in non-rigid vegetation flow, which includes the density and flexural rigidity of trees, and the flow condition, which includes velocity and depth of flow for floodplains and vegetation zones of natural waterways.

In their results, they found that a linear relationship appeared to exist between drag force and velocity. For a rigid roughness, the drag is expected to increase linearly with the square of the velocity. The difference can be explained by the deflection of the plant foliage area and the reduction of the drag coefficient  $C_D$  with the increase of the flow velocity. They concluded that if a linear increase of the momentum-absorbing area with the depth of flow can be assumed.

The Manning's  $n$  value increases proportionally to the square root of the flow depth and is inversely proportional to the mean velocity. They concluded also that, regardless of tree species or foliage shape and distribution, the variation of the Manning's  $n$  with depth is due merely to the increase of the submerged momentum-absorbing area with the depth of flow, thus the density of vegetation is always a dominant parameter for the unsubmerged condition.



### 2.5.1.2 Friction Factor for Unsubmerged Flexible Vegetation

Kouwen and Fathi (2000) proposed a model to calculate the Darcy-Weisbach friction factor  $f$  and Manning's  $n$  for unsubmerged, flexible vegetation in the vegetated zones of a river cross-section. The model accounts for the effect of velocity, depth of flow and type of vegetation with readily defined and measurable parameters of flow and vegetation. The proposal was to help an engineer select proper values for Manning's  $n$  for a particular condition of flow and vegetation and to give information on how the resistance might change with velocity and depth.

Their experimental results showed large variations of Manning's  $n$  with velocity, depth of flow, vegetative stiffness and density. The approach they used depended on the approach by Fathi and Kouwen (1997). In this approach it was assumed that the dominant parameters for estimating the resistance parameter for flow through unsubmerged isolated plants in a canopy are  $C_D$ , which is the average drag coefficient based on the total frontal area of biomass, the flow properties and the vegetative properties. The flow properties considered are the average channel velocity, the density of the fluid, the fluid viscosity, the gravitational constant and the flow depth. The vegetative properties considered are the total upstream exposed area of submerged biomass, the flexural rigidity of the plant, the average canopy height and the characteristic length that represents the spacing or density of plant in a canopy. It was assumed that the bed shear stress is negligible compared to the total plant drag and that the plant stem and foliage are uniformly distributed. In their analysis, they developed a general mathematical model for estimating the friction factor  $f$  in flexible, unsubmerged vegetation. An important conclusion made by Kouwen and Fathi is that the variation of the Manning's  $n$  with the depth of flow is only due to the increase of submerged MAA with flow depth. The density of vegetation is always a dominant parameter for the unsubmerged condition.

### 2.5.2 The Case of Rigid, Unsubmerged Vegetation

Usually the larger vegetation, such as shrubs and trees, are found in the floodplains adjacent to the main channel. This type of vegetation is a major influence on flow depth and resistance during situations such as overbank flooding. Li and Shen (1973) studied



the effect of tall, unsubmerged vegetation on flow resistance by investigating the wake caused by various cylinder set-ups. Experimental results indicated that different patterns or groupings of cylinders significantly affected flow rates. Since the larger types of vegetation constitute much of the resistance within floodplains, Petryk and Bosmajian (1975) proposed a method to calculate flow resistance based on the drag forces created by the larger plants. They derived an equation for Manning's  $n$  by summing the pressure force, gravitational force, shear force and the drag force in the longitudinal direction and the resulting computed vegetation distribution is shown in Figure 2.13.

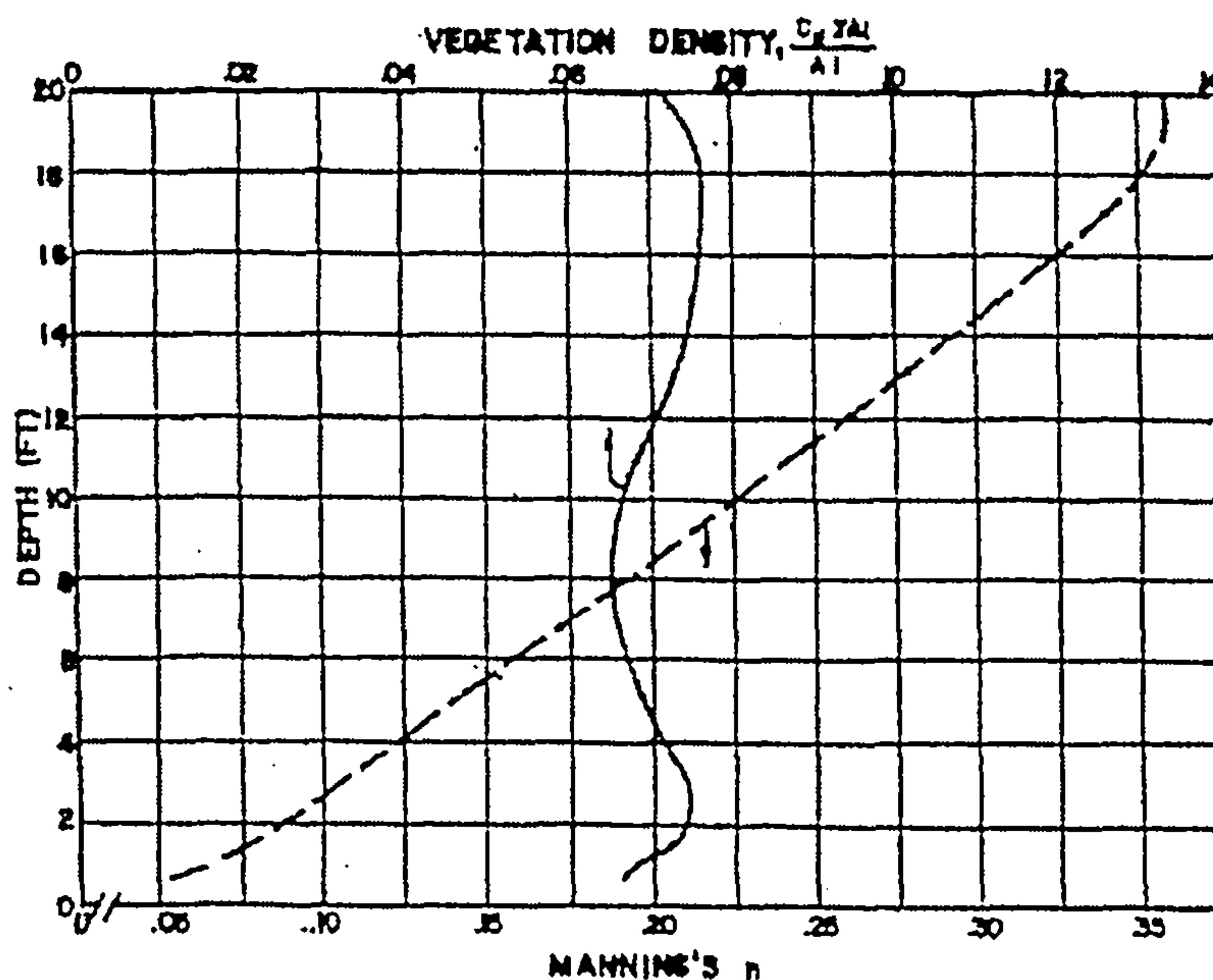


Figure 2.13: Resistance characteristics of example floodplain (after Petryk and Bosmajian, 1975)

There are several limitations on Petryk and Bosmajian's equation. The channel velocity must be small enough to prevent bending or distortion of the shape of the vegetation and large variations in velocity cannot occur across the channel. Vegetation must also be distributed relatively uniformly in the lateral direction. Finally, the flow depth must be less than or equal to the maximum vegetation height. During flooding, the velocities over the floodplains can be relatively high and large degrees of bending and distortion of vegetation will occur. Vegetation can also vary widely across a floodplain and flood depths often submerge vegetation. However, when tree trunks dominate sections of a floodplain, this method can be used for predicting the total roughness coefficient.



Kedlec (1990) published one of the works on blockage and drag forces due to plants. His work focuses on determining the energy slope for wetland types of plants, especially grassy types of plants, and on wetland flows that are laminar to transitional in terms of Reynold's number. Since his study was limited to fairly low velocities, his analysis was based on the flow blockage of rigid plant stems and a small range of shallow flow depths. He did acknowledge that the determination of Manning's  $n$  would require flow data for different depths and would be quite difficult. Kedlec proposed that flow resistance could be based on the summation of drag forces from individual plants, which is the basis for the theoretical development in this study.

#### 2.5.2.1 Resistance Due to Drag Forces

In order to be able to find the drag force on a body immersed in fluid, detailed information about the shear stress and pressure distribution on the body is needed. This is very difficult to accomplish, which is why the dimensionless drag coefficient,  $C_D$ , is used as an alternative. The values of  $C_D$  are found by means of a simplified analysis, numerical techniques, or an appropriate experiment.

According to dimensional analysis arguments, the flow characteristics should depend on various dimensional parameters. The most important parameters of these are the Reynolds number ( $Re$ ) and Froude number ( $Fr$ ). The importance of the Froude number increases for flow with a free surface (Chow, 1959). At high Reynolds numbers, form drag predominates and  $C_D$  become independent of  $Re$ . The drag becomes due almost entirely to the pressure distribution around the body (Bruce *et al.* 1994). This observation is also evident from bridge pier studies. According to Henderson (1966), the resistance to flow of normal bridge pier shapes is such that the drag coefficient is over unity. This implies that form drag is a substantial part of the total drag so that the Reynolds number will be relatively unimportant.

#### 2.5.2.2 Finding the Friction Factor

Fathi and Kouwen (1997) studied the effect that the depth of flow can have on the resistance of flow. Their primary concern was that there might be an extreme variation of roughness with depth of flow due to the large increase in the momentum-absorbing



area in the non-submerged vegetation as depth of flow is increased. This fact might lead to a conclusion that all the available roughness equations, which are based on the relative roughness approach, would be weakly applicable in this situation. They were also concerned with the fact that the non-rigid vegetation on floodplains is usually assumed to behave as a rigid roughness which can lead to large errors in the relationships between velocity and drag force.

Fathi and Kouwen later on studied the effect of velocity and depth of flow on the friction factor. They used several equations that relate the drag force absorbed by vegetation to the boundary shear stress, the drag coefficient and flow properties.

### 2.5.2.3 Factors Affecting the Friction Factor

In fluid mechanics, it is normal to plot experimental data in a dimensionless format. In this study, the friction factor that will be studied primarily is Manning's  $n$ . It is not correct to think of the channel and floodplain as having the same value of Manning's  $n$  all the time, especially when discussing the case of vegetation roughness, which will be changing in height and density throughout the year. Thus, Manning's  $n$  is expected to be a function of several factors.

The most important fluid property affecting flow resistance is the viscosity of the water. Its role, as explained by Cruise *et al.* (2003), is through the determination of the internal shear or deformation of the flow on the micro-scale level. Viscosity is introduced in fluid mechanics as a parameter in the Reynolds number. It is known that for the case where the projection element of the bed roughness breaks through the laminar sub layer they will dominate the flow behaviour. The flow will then be fully rough and the resistance will be due to form drag on the projections. According to Henderson (1966), the resistance coefficient is independent of the Reynolds number in this case. It is reasonable then to assume that the same would be true for the case of rigid non-submerged flow where the effect of form drag is much more significant and the flow is fully rough. The concept that at high Reynolds numbers, the drag force is dependent upon inertia effects only, was also advanced by Gerhart and Gross (1985).

The flow conditions that are expected to have the most effect on the friction factor are the velocity and depth. In their study on non-submerged non-rigid vegetation, Fathi and Kouwen (1997) concluded that the Darcy-Weisbach friction factor  $f$  and the Manning's  $n$  vary greatly with the increase of flow depth because of an increase of the submerged momentum-absorbing area. For the case of the flow past rigid objects in an open channel, the friction factor will decrease with the increase of velocity as a result of changing conditions around the object.

The density of vegetation is always a dominant parameter for the non-submerged condition. Also, it was mentioned by Chow (1959) that the Manning's  $n$  for bridge piers depends on their size, shape, number and distribution, which are all terms of the density of the obstruction to flow. The density of vegetation is a very important factor affecting the friction coefficient. It can be represented by several terms, the distance between the obstructions in the direction of the flow, the distance between the obstructions in the perpendicular direction to flow, and the diameter/width of the tree/obstruction. The flow depth  $H$  will have an effect on the surface area of the obstructions facing the flow. It will be expected that the friction factor would increase as diameter/width of the tree/obstruction and  $H$  increase and would decrease as they decrease.

## 2.6 Computational Modelling

The development of computational models applicable to flows in compound meandering channels is still in its infancy. The problems that modellers encounter include grid calculation and the estimation of various factors which are supposed to be effective in determining flow behaviour. With respect to the grid system, curvilinear systems or element schemes can meet the requirement for irregular geometries.

As discussed in the previous sections, the behaviour, extent and strength of momentum exchange between the fast and slow fluids in the shallow shear layer are important in the compound channel flows. The momentum exchange; bed generated turbulence; secondary flow circulations and sudden expansion and contraction of the floodplain flows are some of the peculiar characteristics of the compound straight and meandering channels. The three-dimensional (3D) Reynolds-Averaged Navier-Stokes



(*RANS*) and continuity equations describe turbulent free-surface flows that have a practical interest being commonly encountered in water and environmental engineering problems. Solving the full set of three-dimensional equations requires considerable time and computing resources. For the sake of simplicity and computational economy, appropriate assumptions and approximations are often made to simplify the 3D *RANS* equations. Depending on these assumptions, numerical models and their modelling approaches are broadly classified as area-averaged (1D) models, quasi-2D models or the lateral distribution methods, depth-averaged (2D) models, quasi-3D models and full three-dimensional (3D) models. Several researchers active in this field are Djordjevic (1993), Bousmar and Zech (1999) and Bousmar (2002), Shiono and Knight (1991) and Ervine *et al.* (2000), Samuels (1985), Hervouet and Van Haren (1996) and Ye and McCorquodale (1997), Falconer and Lin (1997) and Casulli and Stelling (1998), Jankowski (1998), Ye and McCorquodale (1998) and Lin and Fleming (2003).

The accuracy of the predictions using the above models depends on the accuracy of the equations themselves, the numerical schemes and their solvers. With the advent of powerful computing resources, 3D computational models are now being increasingly used to study compound channel flows. Numerical modelling of compound open channels is a vast research area and numerous numerical models that solve the depth-averaged and three-dimensional *RANS* equations have been developed, tested and applied in the study of a variety of flow problems.

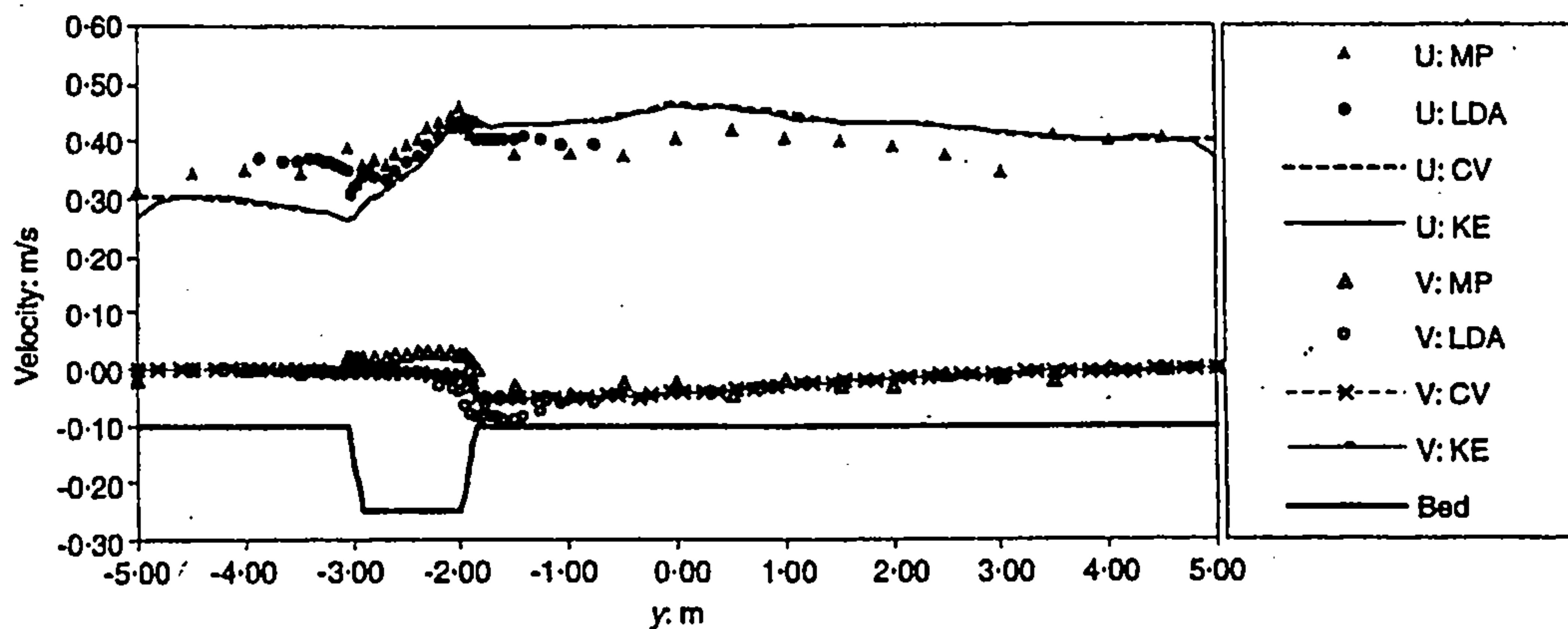
Shiono and Knight (1991), Ervine *et al.* (2000) carried out the quasi-2D models or the lateral distribution methods (LDM) are particularly useful when only the transverse distribution of the primary flow velocity and bed shear stress is of interest. The LDM is based on the streamwise component of the depth-averaged Navier-Stokes equation. Assuming the flow to be uniform, the equation reduces to a single ordinary differential equation.

According to Ye and McCorquodale (1997), two-dimensional or depth-averaged models are frequently applied to study free-surface problems because of their computational efficiency and reasonable accuracy. These models are generally valid when the width-to-depth ratio is large and the vertical accelerations are not significant.

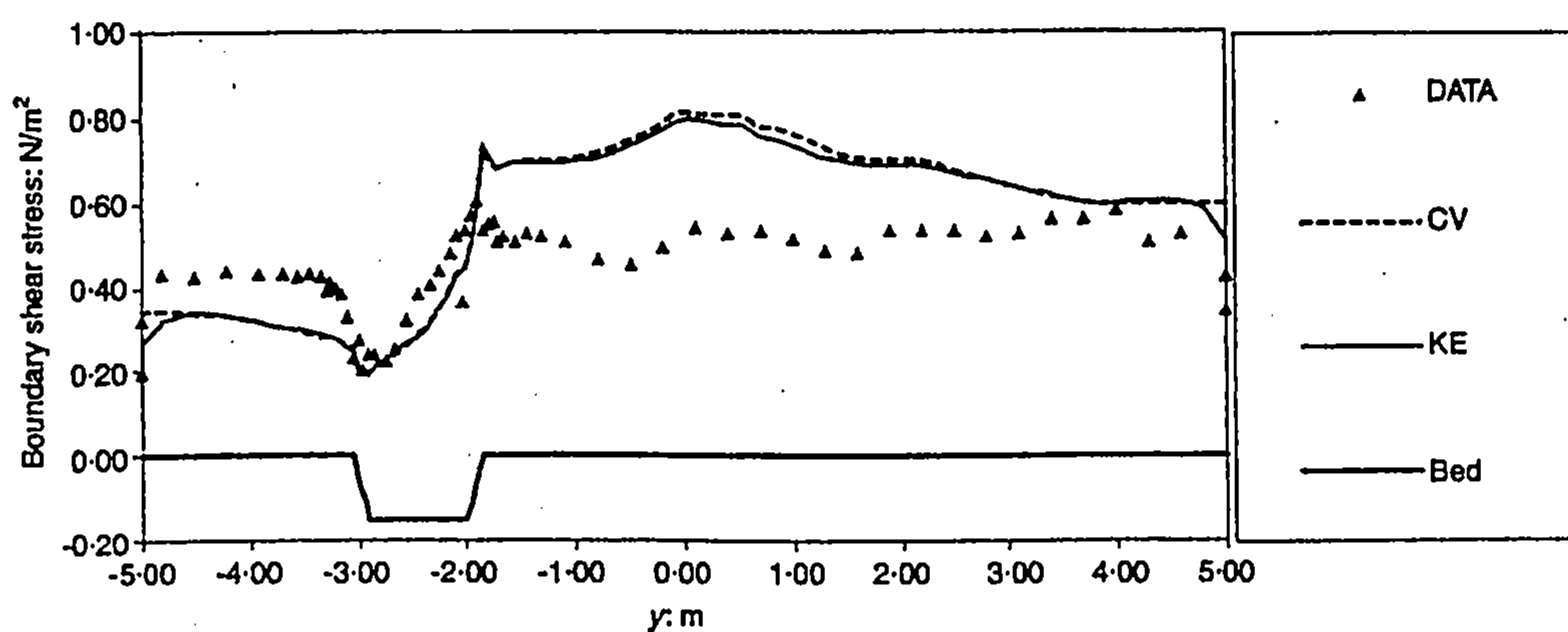
In 1985, Samuels applied a depth-averaged finite element model to a meandering two-stage channel and compared the numerical results with the experimental data of Toebe and Sooke (1967), giving an acceptable correlation for discharge. Later on, Stein and Rouve (1989) and Rouve and Schroder (1992) also developed a two-dimensional depth-averaged numerical model and compared the results with the experimental data. They found that the constant eddy viscosity model also gives a reasonable prediction for the water level across the cross-section compared with the  $k-\epsilon$  model. However, both the models gave significant deviations of depth-averaged velocity with respect to the data. Ye and McCorquodale (1997) developed a two-dimensional depth-averaged model of turbulent flows in a boundary fitted curvilinear coordinate system.

Later on, Rameshwaran and Shiono (2002) used Telemac2D (Hervouet and Van Haren, 1996) to predict the depth-averaged velocity and bed shear stress in a compound meandering channel with a natural cross-section. They reported calibrating the Manning's coefficient to achieve a uniform flow condition that was 18 % higher than the skin friction of the bed material. The velocity and bed shear stress were predicted reasonably well in the main channel using both the constant eddy viscosity and  $k-\epsilon$  turbulence model as shown in Figure 2.14. Recently, Rameshwaran and Shiono (2003) extended this study further and carried out depth-averaged modelling of a compound meandering channel with different main channel cross-sections and relative depths. They found that the flow predictions were similar when using the standard  $k-\epsilon$  model and eddy viscosity for all the flow cases. Based on the calibrated Manning's coefficient, Rameshwaran and Shiono (2003) carried out sensitivity analysis with regard to the different advection schemes offered within the framework of Telemac2D. They suggested using the streamline upwind Petrov-Galerkin FEM method (Brooks and Hughes, 1982) for the advection of velocity and water depth. Wilson *et al.* (2002) used Telemac2D to compare the constant eddy viscosity model, Elder model (Fischer *et al.*, 1979) and  $k-\epsilon$  turbulence model in predicting the stage-discharge curves for inbank and overbank flows through reach scale straight and meandering channels. They found that for moderate and high overbank conditions all the three turbulence models gave similar predictions whereas for inbank and low overbank flows, the Elder model and  $k-\epsilon$  model performed better than the constant eddy viscosity model.





(a)



(b)

Figure 2.14: Comparison of (a) Depth-averaged velocity (b) Boundary shear stress for different turbulent models at the apex cross-over section (after Rameshwaran and Shiono, 2002)

Numerous attempts have been made to simulate the flows in compound channels using three-dimensional (3D) numerical models. Many of these studies concentrated on compound straight channels only including Naot *et al.* (1993), Cokljat and Younis (1995), Sofialidis and Prinos (1998), and Rameshwaran and Naden (2003). Most of these studies involved the development and testing of higher order turbulence models to predict the secondary flows in compound straight channels. In 1993, Naot *et al.* applied an algebraic stress model developed by Naot and Rodi (1982) for the flow in an asymmetric compound channel that was studied experimentally by Tominaga and Nezu (1991). They obtained good agreement for relative depths of 0.75 and 0.5; but the calculations for a relative depth of 0.25 revealed the necessity for a low Reynolds number modification to their model in conjunction with the fine grid in the shallow floodplain. Cokljat and Younis (1995) applied a full Reynolds stress transport model of turbulence, based on the one developed by Launder *et al.* (1975), for computing the

flow in an asymmetric compound channel system with a rectangular main channel (Tominaga and Nezu, 1991) and in a symmetric trapezoidal compound channel (Yuen and Knight, 1990). However, the relative depths used were also high (0.35 - 0.50) and hence performance of the model for conditions of shallow floodplains was not evaluated. Later on, Sofialidis and Prinos (1998) used a low Reynolds Number, non-linear  $k-\varepsilon$  model to predict the flow in compound open channels for low relative depths and found an improvement in the results as compared to the linear  $k-\varepsilon$  model. Recently, Rameshwaran and Naden (2003) used general-purpose finite-volume code to simulate the flow in a compound straight channel (FCF geometry) for inbank and overbank flow cases using a standard  $k-\varepsilon$  turbulence model. The calibration of roughness height ( $k_s$ ) was carried out to make the flow uniform. They stated that the calibrated  $k_s$  value varied with the relative depth of the flow. The three-dimensional model was found to perform relatively better for inbank and high overbank flow in channels with a large aspect ratio (width/depth  $\geq 10$ ).

According to Launder and Spalding (1974), many researchers have often used a standard  $k-\varepsilon$  turbulence model based on the isotropic eddy viscosity assumption to study the flows in laboratory scale compound meandering channels. However, in 1995, Cokljat and Younis said that all of these studies showed the  $k-\varepsilon$  turbulence model to be deficient in predicting flows of complex turbulent shear layers such as compound straight and meandering channel flows. Continuation to this, Ye and McCorquodale (1998) applied a 3D free-surface hydrodynamic model to simulate the flow through the curved channels of Hicks (1985) and Chang (1971). The modified  $k-\varepsilon$  turbulence model was used to account for the anisotropic effect caused by the streamlined curvature, free-surface and solid walls. Recently, Shao *et al.* (2003) used several algebraic stress models, including non-linear  $k-\varepsilon$  models, to simulate the secondary currents in helically coiled channels using curvilinear coordinates.

A recent research trend shows the increasing use of commercially available, general-purpose, computational fluid dynamics (CFD) codes to study compound channels including Morvan *et al.* (2002), Wilson *et al.* (2002), Rameshwaran and Naden (2003, 2004a; b), Wilson *et al.* (2003a; b), and Wilson *et al.* (2004). According to Olsen (2003), the CFD started to be applied to hydraulic engineering flow problems from 1990. Three-dimensional computational fluid dynamics (CFD) models have since been



increasingly used to predict compound channel flows and to assess the suitability of a range of turbulence models for simulating flow structures, particularly those generated by the main channel-floodplain interactions (Nicholas and McLelland, 2004). Some of CFD codes, which are being increasingly adopted and used to study the compound channel flows include CFX, Phoenix, Fluent, Hydro-3D and Telemac3D (Hervouet and Van Haren, 1996, and Jankowski, 1998)

Morvan *et al.* (2002) used standard CFD techniques (CFX-finite volume) to simulate the flow in compound meandering channels using a simple  $k-\varepsilon$  turbulence model and the simplified anisotropic Reynolds stress model (RSM) of Launder *et al.* (1975). A 30% increase in computational time for the RSM model as compared to the  $k-\varepsilon$  model was observed, with little difference between the predicted velocity fields. Morvan *et al.* (2002) stated that the proper problem discretization (choice of numerical schemes and meshing approach) is much more important than the use of a complex turbulence model. Rameshwaran and Naden (2004a; b) used general-purpose CFD code for the free-surface flow predictions in compound meandering channels (FCF geometry). They used a standard  $k-\varepsilon$  turbulence model with a free-surface treatment and found that the code was able to predict the free-surface behaviour as observed in the experiments. The  $k-\varepsilon$  model was found to be unable to predict the observed secondary flow circulations and the need was felt for the more sophisticated turbulence model to improve the predictions.

### 2.6.1 Grid Generation

According to Jordan and Spaulding (1993), a grid generation is an integral part of solving complex computational fluid dynamics problems. Grid generation strongly affects the accuracy of numerical simulation. Computational processes for numerical system solutions require powerful discretization methods based on the use of appropriate grids. These consist of a discrete set of points representing the geometry of the definition domain (Conti *et al.* 2004). The domain discretization is often difficult for natural rivers due to the irregular and variable shape of cross-sections, which prevent the use of an orthogonal coordinate system. One of the greater tasks for engineers is to search for an adaptable grid system, which efficiently makes use of geographical

information such as shorelines and the bed topography whilst at the same time achieving higher quality numerical results (Yu *et al.*, 1997).

Sinha (1997) stated that a general approach to the discretization of domains with complex geometry is the generation of a boundary-fitted coordinate system by the solution of elliptic partial differential equations known as the finite difference of finite volume methods. The ability of finite difference of finite volume methods to model natural river flows in such a formulation depends on the adequacy of the numerical grid (Sinha, 1997). According to Khamayseh *et al.* (1999), grids are required to satisfy some properties like smoothness and boundary orthogonality, which affects the solution accuracy. Non-orthogonal boundary-fitted grids can be generated to model complex river using a variety of techniques such as the difference methods or the algebraic methods (Sinha, 1997).

### 2.6.2 Boundary Conditions

Implementing boundary conditions for a finite volume requires that the flux at the boundaries is physically correct. These boundary conditions are the free-surface, bed surface, extent of domain and inflow characteristics (Ferguson *et al.* 2003). The free-surface is defined as a plane of symmetry, which implies that the normal velocity and the normal gradient of all variables are zero at the plane of symmetry (Ferguson *et al.* 2003). However, the free-surface may be depressed or super elevated, for example in the separation zone and near the apex of an open channel junction flow (Rhoads, 1996). This surely influences the flow field. Although it is necessary to identify the relationship between free-surface geometry and the flow field, it is quite difficult to collect actual free-surface elevation data for large-scale natural channels. One of the methods of tracing the free-surface geometry in numerical models is to use the porosity correction concept (Biron *et al.* 2002).

Bed surfaces are treated by assuming that they are in the wall region and that the standard law of the wall applies (Wu *et al.* 2000). In this procedure, a roughness height is adopted. It is usually estimated from the grain size of the bed particles (Ferguson *et al.* 2003). Bed and bank roughness are often parameterised using the Launder and Spalding (1974) non-equilibrium version of the law of the wall for the layers of cells



touching the rough boundaries (Dargahi, 2004). The extent of the domain is described by the riverbed and the water edges, which must remain fixed (Dargahi, 2004). The inlet conditions require the values of the velocity and turbulence properties at the furthest upstream cross-section (Lane *et al.* 1999, and Dargahi, 2004). A good knowledge of the upstream boundary specification is required in 3D models, particularly in terms of inflow data, and difficulties in such specifications may provide fundamental limitations in the predictive ability of a model (Lane *et al.* 1999).

## 2.7 Chapter Summary

This chapter demonstrates that the overall flow mechanism in the compound meandering channel is a lot more complex than that for straight channels. The dominant flow characteristics in the meandering channel with overbank flow can be simplified into several categories, such as momentum transfer, secondary flow, horizontal and vertical shear effects and the flow expansion and contraction at the cross-over section. As demonstrated by previous researchers, these mechanisms affect the distribution of the flow. Furthermore, when the river is in flood they increase the flow in the floodplain and reduce it in the main channel. But in the case of the present study, the situation is different because of the major roughness elements caused by the vegetation. The vegetation model covers a significant part of the floodplain edge such as at the apex of the bend and the cross-over section and, of course, the relative roughness will be 100 % of the flow depth.

The sources of energy loss in the main channel are friction loss caused by friction on the bed and sidewall, secondary currents, turbulent shear between the main channel and floodplain flows and flow separation induced by the channel bend. Within the meander belt on the floodplain region, the three sources of energy loss are bed friction and expansion and contraction losses in between the floodplain and the main channel flow. However, the energy loss within the meander belt will be totally changed due to the arrangement of the vegetated floodplain in a compound meandering channel, which will affect the sources of energy loss in the main channel and floodplain. Beyond the meander belt region, the energy loss still remains similar, which is mainly due to the bed friction only.

Sediment places a load into open channel flows with or without mobile beds and especially with bedforms that are poorly understood. For flows with mobile beds, including bedforms, there are relatively few experimental studies that include the variables under consideration. An important finding from Fathi and Kouwen (1997) is that the variation of the Manning's  $n$  constant with depth of flow is only due to the increase of submerged momentum-absorbing area (MAA) with flow depth. The density of vegetation is always a dominant parameter for the non-submerged condition.

The combination of these energy losses could result in the erroneous estimation of discharge conveyance for higher flow depths (overbank flow). Although numerous findings on the flow effects have been discussed in the earlier sections, it is clear that not every aspect, especially the presence of vegetation in a compound meandering channel flow, has been investigated. Substantial research is still required to better understand the flow mechanisms in order to ensure a more accurate prediction of discharge conveyance, particularly that related to the presence of vegetation.

Research on compound meandering channels is dominated by both experimental and numerical studies. This thesis uses computational modelling to address one of the objectives towards establishing a clear and improved understanding of the secondary flow structures in compound meandering channels. Telemac (Hervouet, 2000) is the suite of computer codes dedicated to the numerical simulation of free-surface flows developed by the Laboratoire National d'Hydraulique, Electricite de France (EDF). In the United Kingdom, the Telemac codes are distributed by Hydraulic Research (HR) Wallingford, UK. The detailed presentation of the solution algorithm and numerical issues concerning Telemac would be very exhaustive and is therefore beyond the scope of this thesis.



# Chapter 3

## 3.0 Experimental Set-up and Procedures

### 3.1 Introduction

The principle purpose of this study is to investigate the characteristics of flow, flow resistance and sediment transport behaviours as well as to assess the capability of the computational model in reproducing the important flow characteristics, flow mechanisms and boundary shear stress associated with non-vegetated and vegetated floodplains in compound meandering channels with overbank flows. It is therefore essential to collect a sufficient amount of data to establish the influence of vegetation arrangements with different densities on the stage-discharge relationship, sediment transport rate and flow resistance in meandering channels.

All the experiments reported here were conducted at the Loughborough University Flume Facility. The details of the experimental set-up, instruments used, laboratory experiments, and the experimental procedure are described in this chapter.

### 3.2 The Loughborough Flume Facility Test Section

The experiments pertaining to the study were performed in a recirculating flume measuring 13 m in length, 2.4 m in width and 0.3 m in depth with a fixed longitudinal gradient of 1/500. It is approximately one quarter of the size of the flume at the Flood Channel Facility at HR Wallingford and its features are described herein.

The flume is built on a number of rigid steel structures to support its weight, achieve maximum stability and maintain its longitudinal gradient. It was constructed to include tanks, sumps and pipeworks. Both sidewalls of the flume were built using

glass to ease visibility during the setting-up of the instruments used. Flow circulation was facilitated by two pumps recycling water from two storage reservoirs, namely the sediment reservoir and the main reservoir. The two pumps were capable of delivering a total discharge rate of around 30 litres per second. One pump carried the flow from the water reservoir back into the flume by a pipe installed along one side of the flume. A pump was calibrated in the laboratory before installation and was capable of delivering the maximum discharge of about 23.2 litres per second. A special sediment pump was used to convey a mixture of sediment and water from the sediment reservoir through a pipe system back to the inlet. The maximum pump capacity was around 6.8 litres per second and the flow was measured by a 3100 Maxflo flow meter, which was calibrated by the manufacturer. The minimum flow rate used to ensure smooth sediment recirculation was 2.0 l/s. A thick plywood float was put in the stilling pool to reduce the water disturbance caused by turbulence and the wavy surface at the entry to the channel. The water surface slope and flow depth in the flume were controlled by three tailgates with hand-held adjustment at the end of the flume. This permitted control of the working uniform flow. Figure 3.1 shows a schematic layout of the flume, which forms the main test apparatus for the study.

The flume included a meandering channel and floodplain. The floodplain was formed from 150 mm thick Styrofoam and finished with artificial grass. Two types of main channel cross-sections have been constructed and modified in this study: one rectangular and the other trapezoidal. The rectangular main channel had a base width of 0.4 m, a depth of 0.04 m and bankside slope ( $S_0$ ) of 90°. It was later changed to the trapezoidal main channel cross-section 0.38 m wide, 0.04 m deep and with a bankside slope ( $S_0$ ) of 45° as shown in Figure 3.2. Both main channel cross-sections were linked to the same floodplain, which was 2.4 m wide with vertical sidewalls constructed from glass and Perspex. The main channel planform comprised three and a half identical meander wavelengths over a total length of 11.9 m. Each meander bend consisted of a 120° circular arc with a centre radius of curvature of 0.765 m and successive bends were connected with 0.75 m cross-over length straight sections. The resulting sinuosity (the ratio of the distance along the channel between corresponding points on successive bends to the straight-line distance between these points) was 1.384. This basic geometry was selected to match the configurations used in the compound channel study carried out in the Flood Channel Facility (FCF) at HR Wallingford.



Figure 3.3 shows the plan details of geometry for the flume and main channel and the detail parameters are shown in Table 1.

The post-construction surveys showed the longitudinal floodplain slope to be 0.002. To make sure that the flume was set up to the required longitudinal slope, a topographical levelling survey was carried out using a standard land surveying technique. One survey station was fixed on the ground as the base station between the inlet and outlet of the flume. The levels were measured at several chainage stations on the main channel and floodplains. These were located in the centreline of each wavelength unit. Some of the data were taken from a movable aluminium bridge, so the effect of the bridge sag under the weight of a fully laden instrument carriage was assessed at points along the bridge where the measurements were taken. As the bridge was rested on rails, it was found that the sagging effect was not significant for the water slope measurement but the effect of the level of the rails relative to the horizontal plane was substantial. Consequently, the correction values were applied to water slope measurement locations according to all levels surveyed along both rails as shown in Table 3.2.

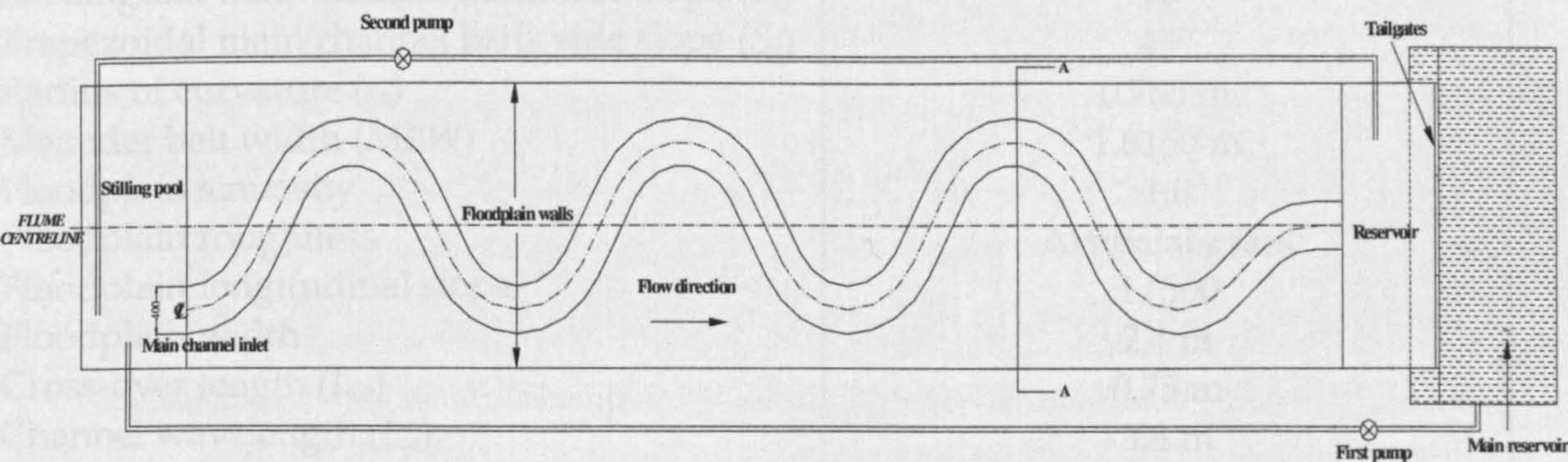


Figure 3.1: Schematic layout of the flume (Not to scale)

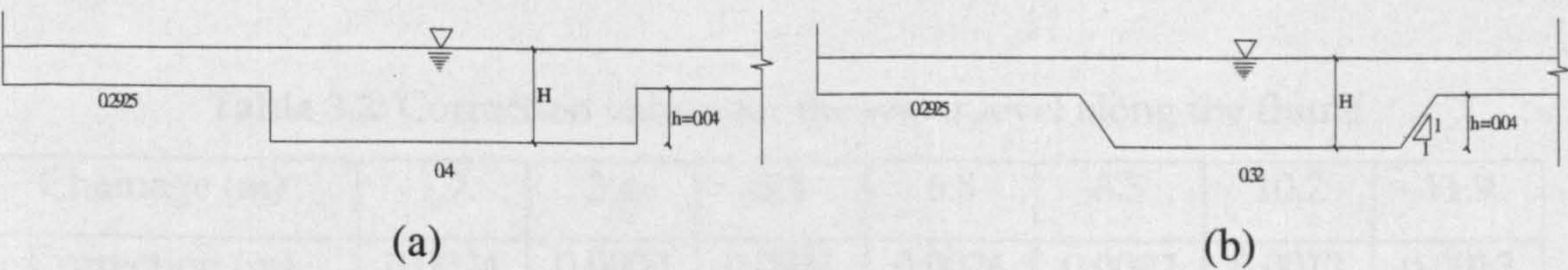


Figure 3.2: Main channel cross-sections (a) Rectangular (m) (b) Trapezoidal (m)



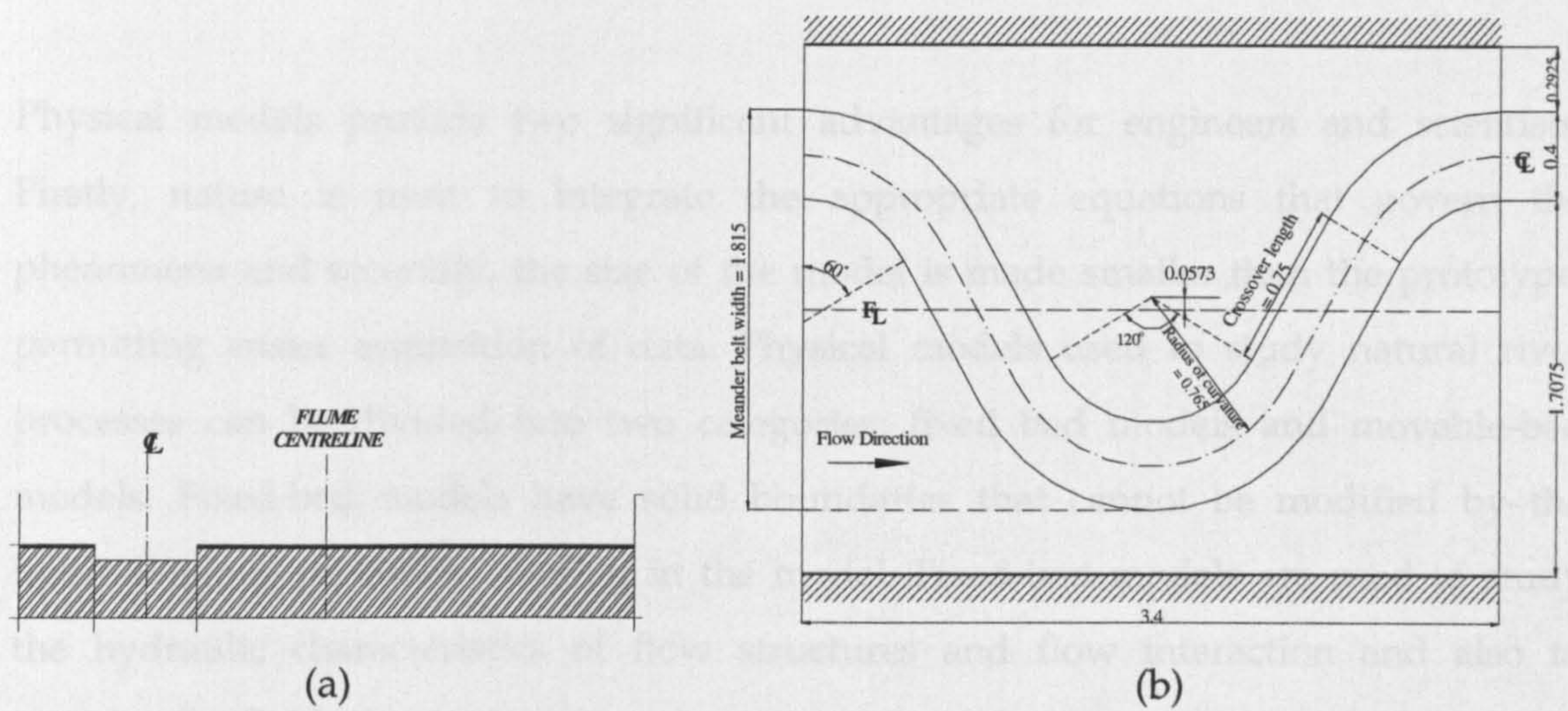


Figure 3.3: (a) Flume cross-section (not to scale); (b) Details of meander geometry (m)

Table 3.1: Test flume geometrical parameters

Main channel sinuosity ( $s$ )	1.384 ( $60^\circ$ )
Rectangular main channel top width	0.4 m
Trapezoidal main channel top width	0.38 m
Rectangular main channel bank side slope ( $S_o$ )	$90^\circ$
Trapezoidal main channel bank side slope ( $S_o$ )	$45^\circ$
Radius of curvature ( $r_c$ )	0.765 m
Meander belt width (MBW)	1.8150 m
Floodplain sinuosity	1.0
Floodplain roughness	Artificial grass
Floodplain longitudinal slope	1/500
Floodplain width	2.4 m
Cross-over length ( $L_{co}$ )	0.75 m
Channel wavelength ( $L_w$ )	3.4 m
Total length of the flume ( $L$ )	12 m
Number of wavelength ( $L_{nw}$ )	3.5 m

Table 3.2: Correction values for the water level along the flume

Chainage (m)	1.7	3.4	5.1	6.8	8.5	10.2	11.9
Correction (m)	0.0034	0.0009	0.0031	0.0026	0.0007	0.0013	0.0013



### 3.3 Laboratory Set-up

Physical models provide two significant advantages for engineers and scientists. Firstly, nature is used to integrate the appropriate equations that govern the phenomena and secondly, the size of the model is made smaller than the prototype, permitting easier acquisition of data. Physical models used to study natural river processes can be divided into two categories; fixed bed models and movable-bed models. Fixed-bed models have solid boundaries that cannot be modified by the hydrodynamic processes ongoing in the model. Fixed-bed models are used to study the hydraulic characteristics of flow structures and flow interaction and also to examine the fluid kinematics.

For the movable-bed model, all or part of the model bed is composed of granular material that can be transported by hydrodynamic forces imposed by currents. There are several problems concerning the similitude of physical parameters to most proposed scaling models. The prototype-to-model ratio of the fluid density could be manipulated by the selection of a different model fluid rather than water.

Sediment grain size diameter is another model variable that needs to be manipulated properly. If the selected scaling criteria require that grain size be scaled in proportion to the geometric length scale, there is a possibility that non-cohesive prototype sediments may be scaled to grain diameters that would put the sediment into the cohesive sediment range (grain diameter  $< 0.8$  mm) in the model. If this were to happen, different fundamental sediment transport processes would occur in the model, and the model would not be a dynamic representation of the prototype. Noda (1972) recommended using sand with a mean diameter of not less than 0.1 mm as the model sediment.

Another technique for meeting similitude criteria is to select a model sediment having both different size and different density rather than the prototype sediment. This would greatly simplify the engineer's task except for two problems. First, there is not an abundant supply of inexpensive materials of all sizes, shapes and densities available for modelling purposes. Second, the successful technique of lightweight bed materials

for unidirectional flow models does not appear to be successful under unsteady flow conditions or when the sediment is migrated onto the dry beach (Kamphuis 1985).

In the present study, the experimental works were carried out under both fixed bed and movable bed conditions. A physical model scale of 1:15 was used. The references to establish the physical model and scaling factors such as Hughes (1993) and Dalrymple (1985) were used. A summary of length scale  $n_l$ , velocity scale  $n_v$  and the scale of sediment size  $n_{d50}$  is shown in Table 3.3.

Table 3.3: Model set-up consideration

Prototype	Model
Length $n_l = l_p/l_m$ Channel length, $L_p = 243.3$ m Channel width, $L_p = 6$ m Vegetation width, $D_p = 0.9$ m	1:15 Channel length, $L_m = 16.22$ m Channel width, $L_m = 0.4$ m Block width, $D_m = 0.06$ m
Velocity $n_v = (n_l)^{1/2}$ Range 0.45 – 1.26 m/s	1:4.5 Range 100 – 280 mm/s
Sediment size $n_{d50} = (n_l)^{1/4}$ $d_{50} = 0.98$ mm	1:1.15 $d_{50} = 0.855$ mm

### 3.4 The Sediment Model

The test section was composed of uniformly graded sand. The result of the sieve analysis on the selected sand is shown in Figure 3.4. A measure of the uniformity of the sand can be obtained by estimating the geometric standard deviation,  $\sigma_g$ , defined as follows:

$$\sigma_g = \left( \frac{d_{84}}{d_{50}} \right) \quad (3.1)$$

in which,

$d_{84}$  = particle size for which 84% of the sediment mixture is finer

$d_{50}$  = median grain size or particle size for which 50% of the sediment mixture is finer



Referring to Figure 3.4, the average values of  $d_{84}$  and  $d_{50}$ , are obtained as 1.05 mm and 0.855 mm, respectively. Therefore, using Equation (3.1),  $\sigma_g$  was found to be 1.23. In order to obtain the fall velocity of bed material based on the  $d_{50}$ , the diagram shown in Figure 3.5 can be used to obtain a plot of median grain size,  $d_{50}$  against fall velocity,  $\omega_s$  for a water temperature of 20° C. Table 3.4 shows the characteristics of the bed sediment used for the test section. The main reason for the choice of uniform graded sand was to minimise the influence of the “sheltering” and “hiding” effects. As bedforms propagate downstream, sediment moves from the crest of the bedforms to the trough. In the trough, the sediment is sheltered and overlaid by the advancing grains from the upstream bedforms. A schematic sketch of bedload transport mechanisms over the bedforms was produced referring to a video clip captured by the underwater camera as shown in Figure 3.6.

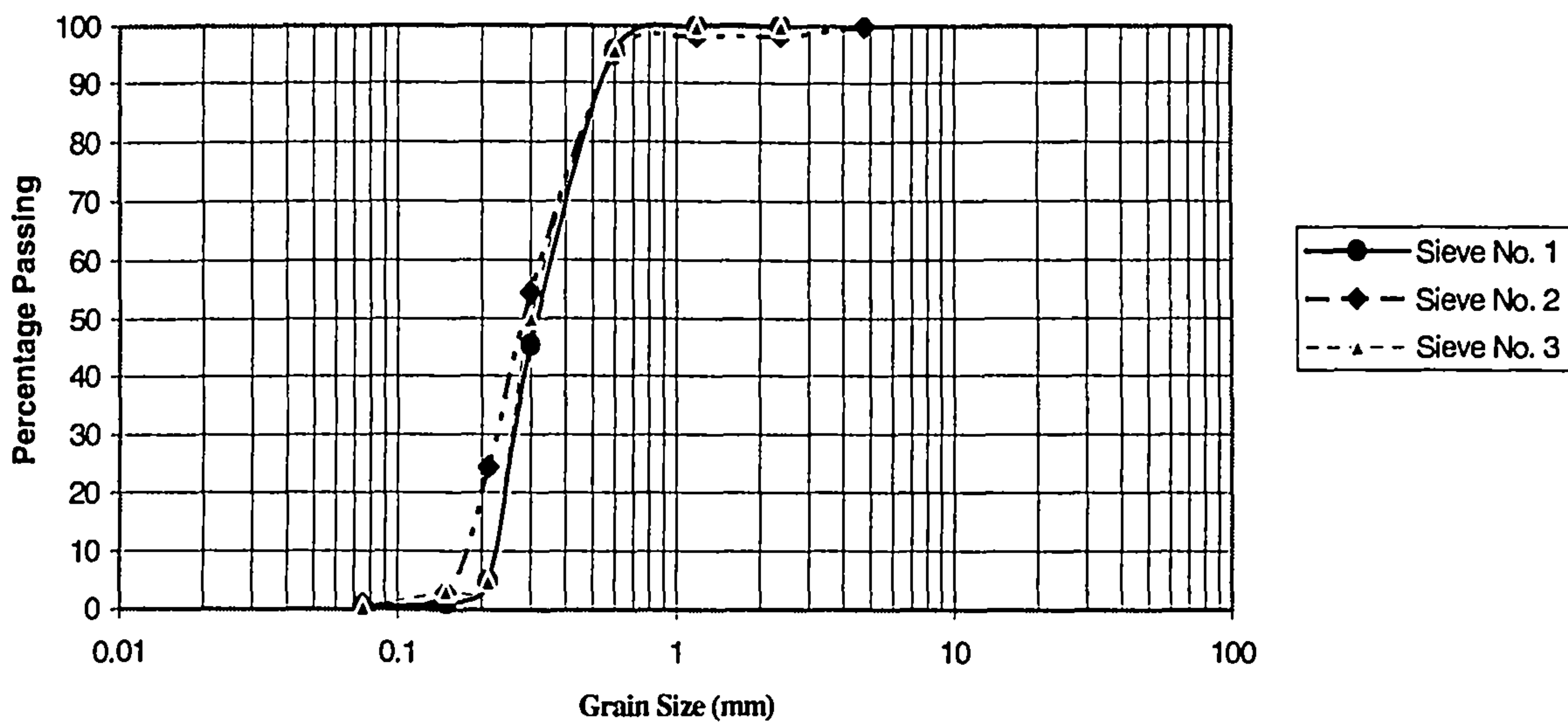


Figure 3.4: Grading curve of the uniform sand



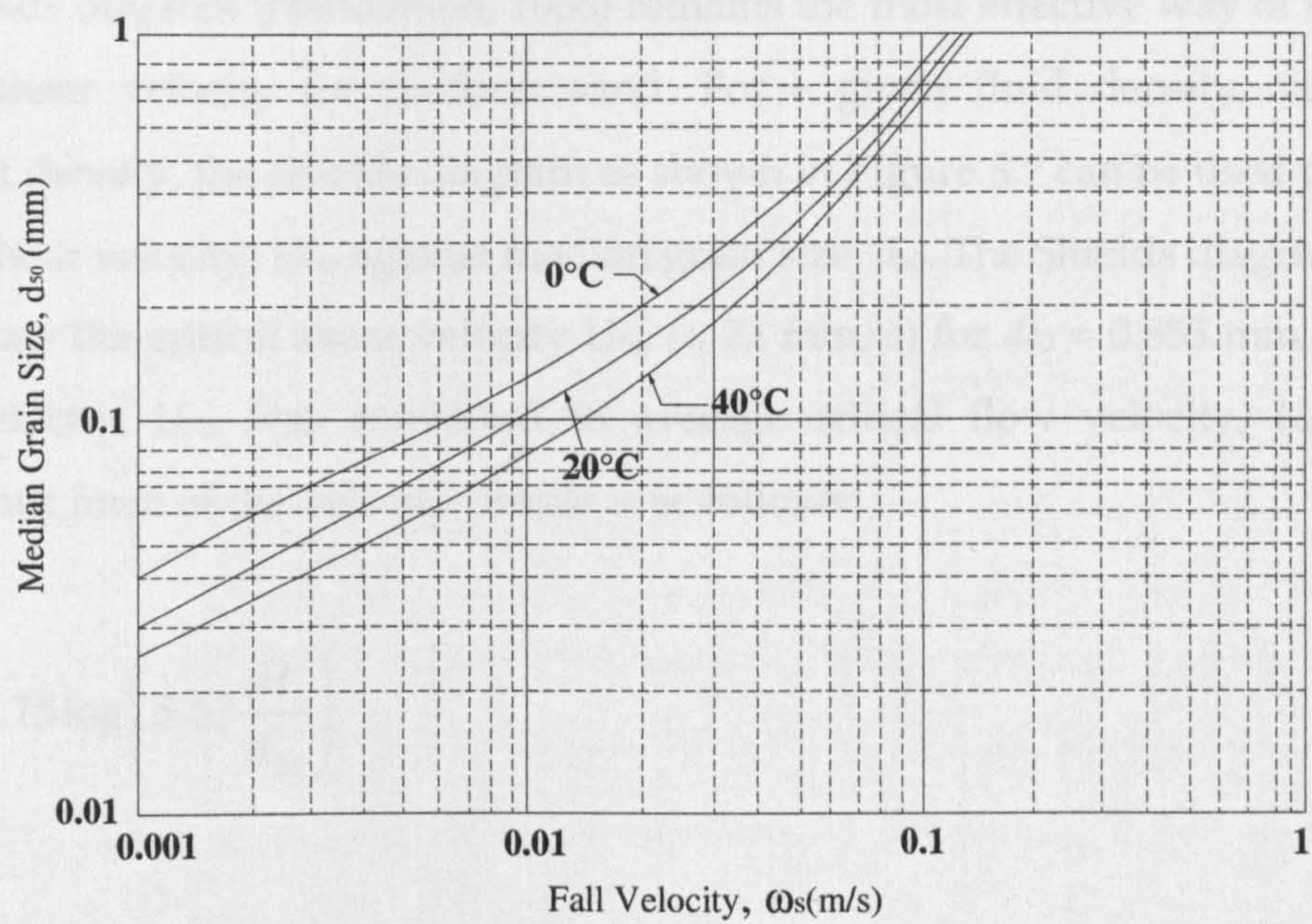


Figure 3.5: Fall velocity of sand-sized particles (after Richardson and Davis, 1995)

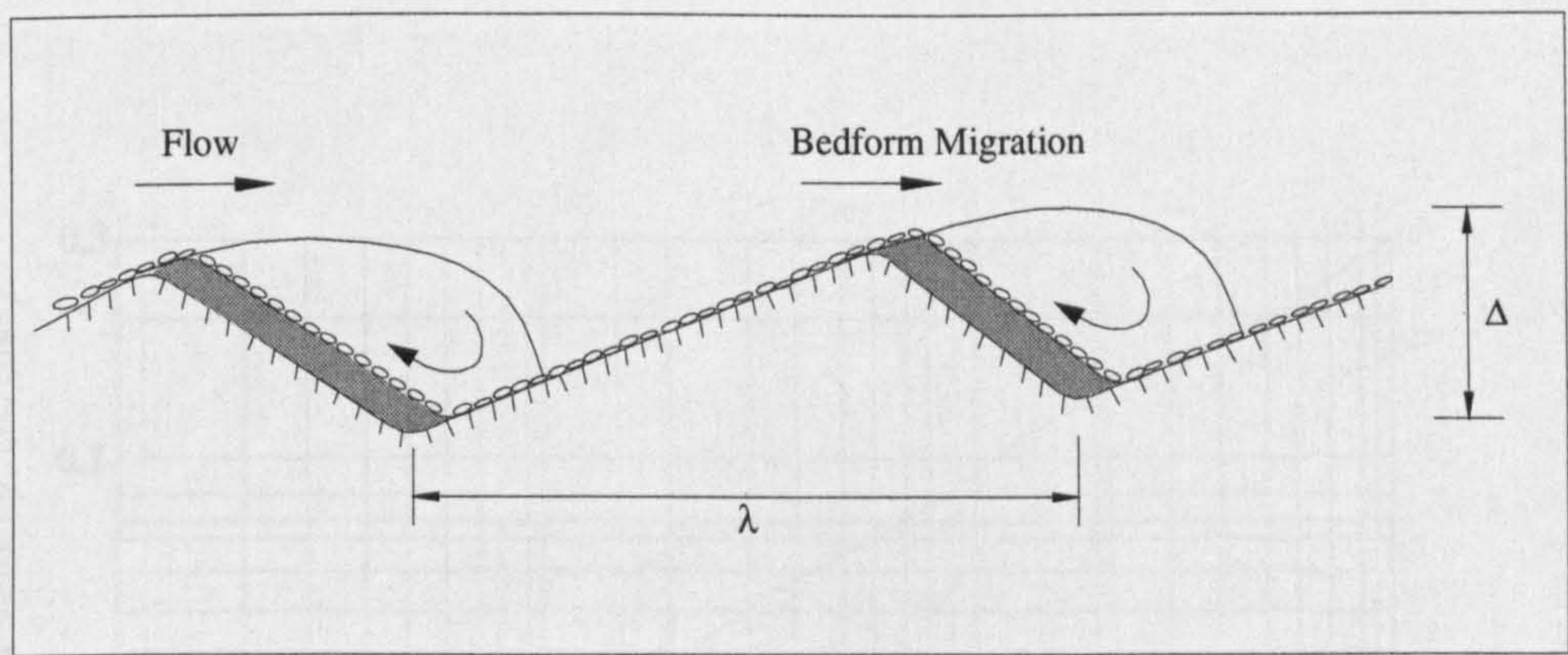


Figure 3.6: Sediment particle movement over the bedforms

Table 3.4: Characteristics of the test bed material

Properties	Value
Median grain size ( $d_{50}$ )	0.855 mm
Sediment density ( $\rho_s$ )	2669 kg/m <sup>3</sup>
Geometric standard deviation ( $\sigma_g$ )	1.23
Fall Velocity ( $\omega_s$ )	105 mm/s



The Shields diagram (Henderson, 1966) remains the most effective way of determining critical shear velocity for uniform sand. For a given fluid density, viscosity and sediment density, the Shields diagram as shown in Figure 3.7 can be used to obtain the critical shear velocity,  $U_{*cr}$  against median grain size,  $d_{50}$ . The Shields diagram was used to calculate the critical shear velocity  $U_{*cr}$  ( $= 22 \text{ mm/s}$ ) for  $d_{50} = 0.855 \text{ mm}$ . The critical shear velocity,  $U_{*cr}$  was converted to average critical flow velocity,  $U_{cr}$  using the logarithmic form of the velocity profile is as follows:

$$\frac{U_{cr}}{U_{*cr}} = 5.75 \log \left( 5.53 \frac{H}{d_{50}} \right) \quad (3.2)$$

in which;

$U_{cr}$  = average critical flow velocity

$U_{*cr}$  = critical shear velocity

$H$  = flow depth

$d_{50}$  = median grain size

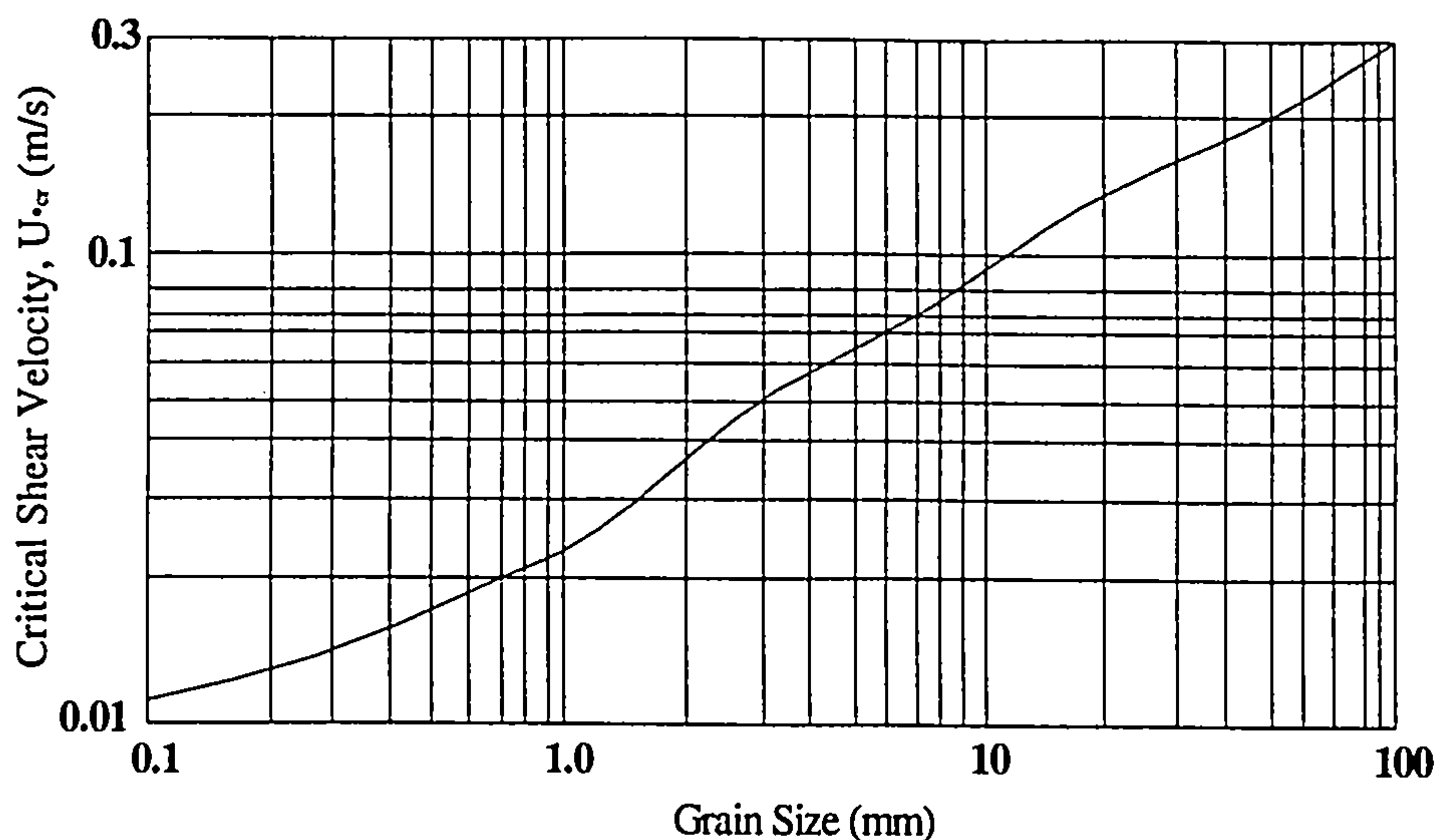


Figure 3.7: Shields diagram for critical condition of uniform sediment in water (after Melville and Surtherland, 1988)



### 3.5 Model and Experimental Test Range

The experimental investigation was carried out using rectangular blocks, one of which had the dimensions of 0.06 m wide, 0.06 m long and 0.1 m height to simulate the roughness caused by vegetation as shown in Figure 3.8. The aims of adopting the blocks were to examine the influence of vegetation on sediment transport behaviour and the change of flow mechanisms in the main channel during overbank flow. Although this may not represent the true scenario of shape and scale to the real situation, it was generally hoped that the block roughness and arrangement would create a logical step forward to model such flow. For all the meandering channel configurations described previously, measurements were carried out with four main arrangements of blocks at the edge of the main channel/floodplain as shown in Figures 3.9(a) to (k) with different densities as follows:

- (1) *Case A No Block* (A – rectangular fixed bed channel) – No continuous hedges of blocks along both sides of the meandering channel.
- (2) *Case B Apex Block* (B1, B2 and B3 - rectangular fixed bed channel) - Continuous hedges of blocks along the outer side of the meandering channel but no hedges along the inner side of the meandering channel.
- (3) *Case C Cross-over Block* (C1, C2 and C3 – rectangular fixed bed channel) - Continuous hedges of blocks along the inner side of the meandering channel but no hedges along the outer side of the meandering channel.
- (4) *Case D Combined Apex and Cross-over Block* (D1, D2 and D3 - rectangular fixed bed channel) - Continuous hedges of blocks along both edges of the meandering channel.
- (5) *Case E No Block* (rectangular mobile bed channel) - No continuous hedges of blocks along both sides of the meandering channel.
- (6) *Case F Apex Block* (F1, F2 and F3 - rectangular mobile bed channel) - Continuous hedges of blocks along the outer side of the meandering channel but no hedges along the inner side of the meandering channel.
- (7) *Case G Cross-over Block* (G1, G2 and G3 – rectangular mobile bed channel) - Continuous hedges of blocks along the inner side of the meandering channel but no hedges along the outer side of the meandering channel.



- (8) *Case H Combined Apex and Cross-over Block (H1, H2 and H3 - rectangular mobile bed channel)* - Continuous hedges of blocks along both edges of the meandering channel.
- (9) *Case L No Block* (trapezoidal fixed bed channel) - No continuous hedges of blocks along both sides of the meandering channel.
- (10) *Case M Apex Block* (trapezoidal fixed bed channel) - Continuous hedges of blocks along the outer side of the meandering channel but no hedges along the inner side of the meandering channel.
- (11) *Case N Cross-over Blocks* (trapezoidal fixed bed channel) - Continuous hedges of blocks along one of the inner side of the meandering channel but no hedges along the outer side of the meandering channel.

The blocks were placed in line with the meandering channel. The different densities were created by reducing the number of blocks at  $5^\circ$  intervals starting from the apex of the section. The higher density had one block at every  $5^\circ$ ,  $10^\circ$  for a middle density and followed by the lowest density of one for every  $20^\circ$  for meander bend, which consisted of a  $120^\circ$  circular arc. In *Case C Cross-over Block* and *Case D Combined Apex and Cross-over Block* the different densities at the cross-over length are continued with similar spacings with different densities considered.

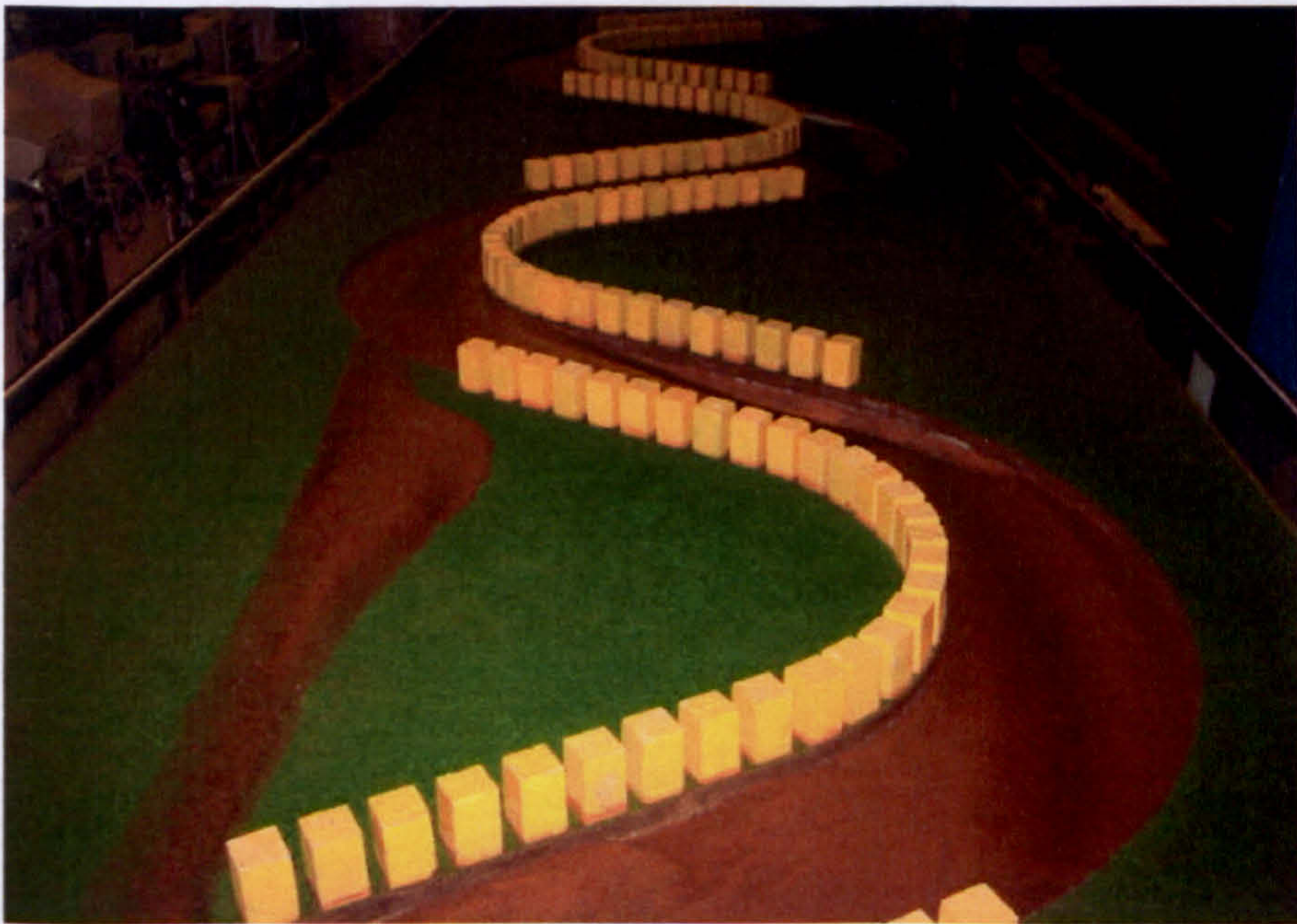
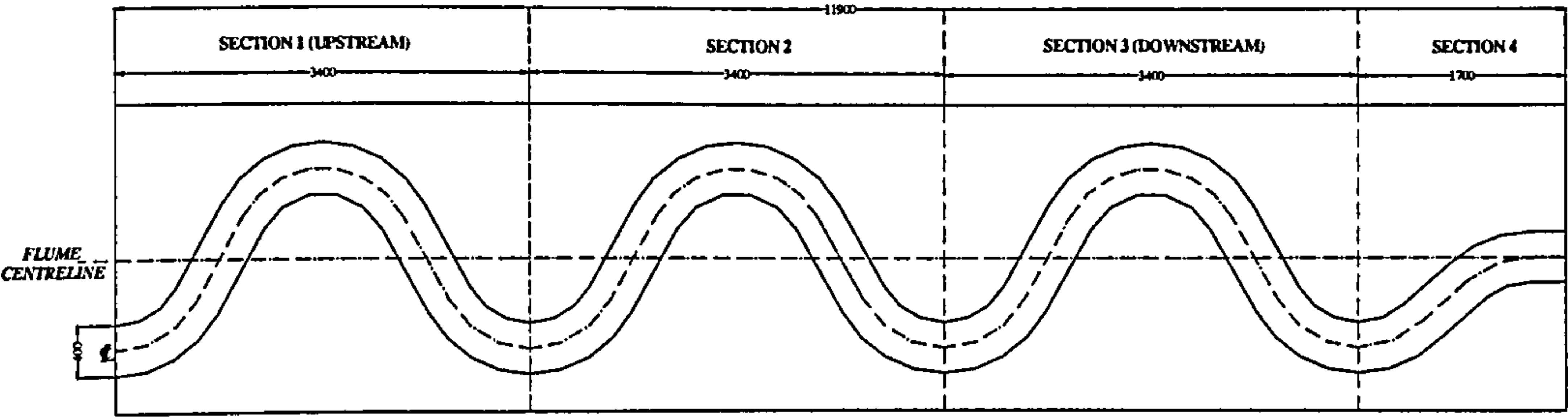
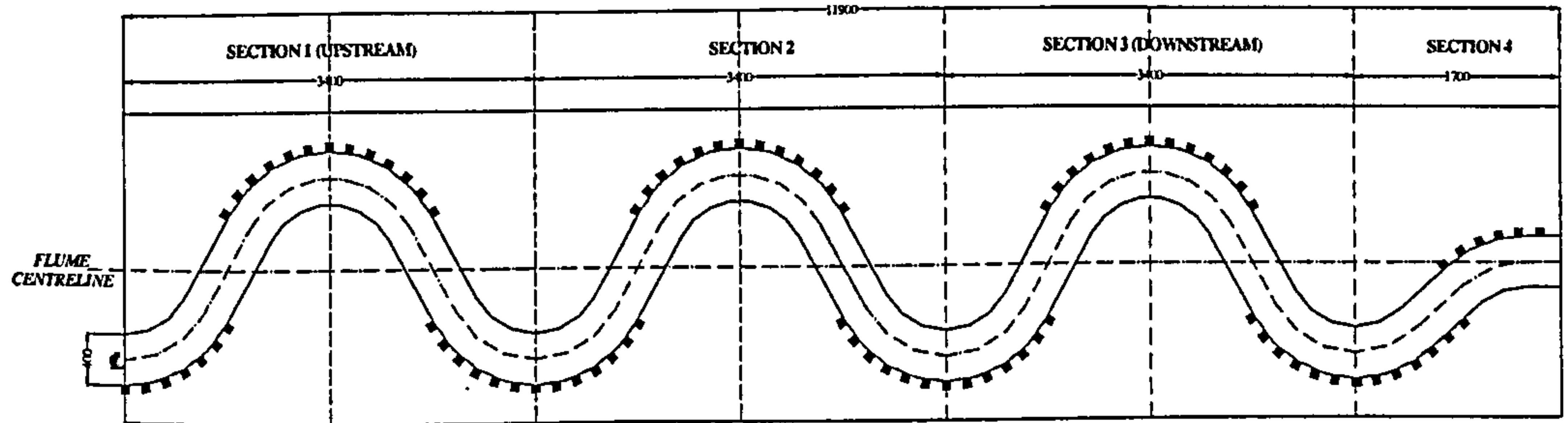


Figure 3.8: Typical blocks to simulate roughness cause by blocks on a floodplain

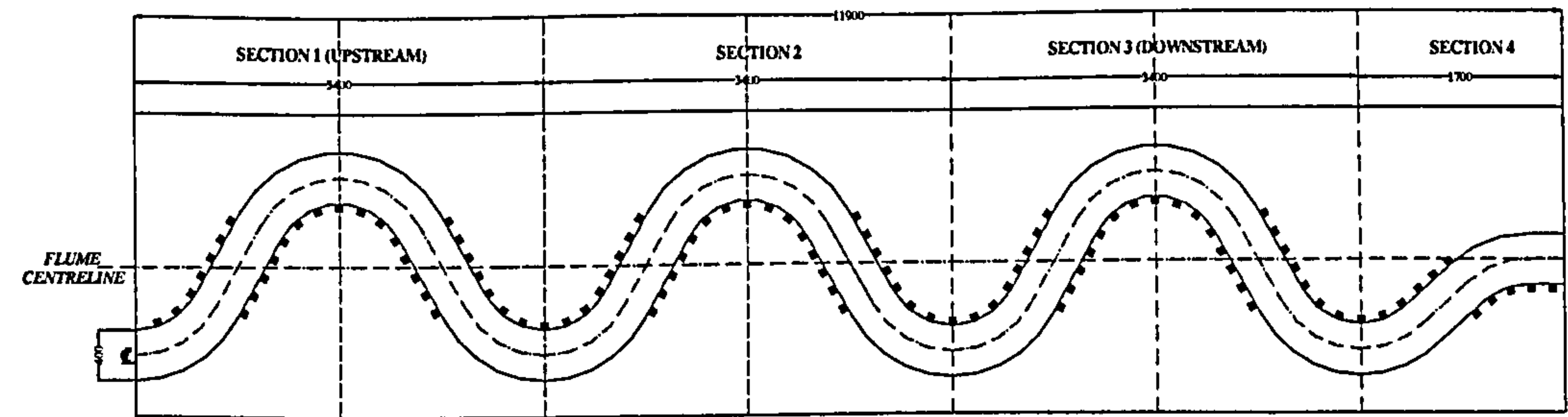




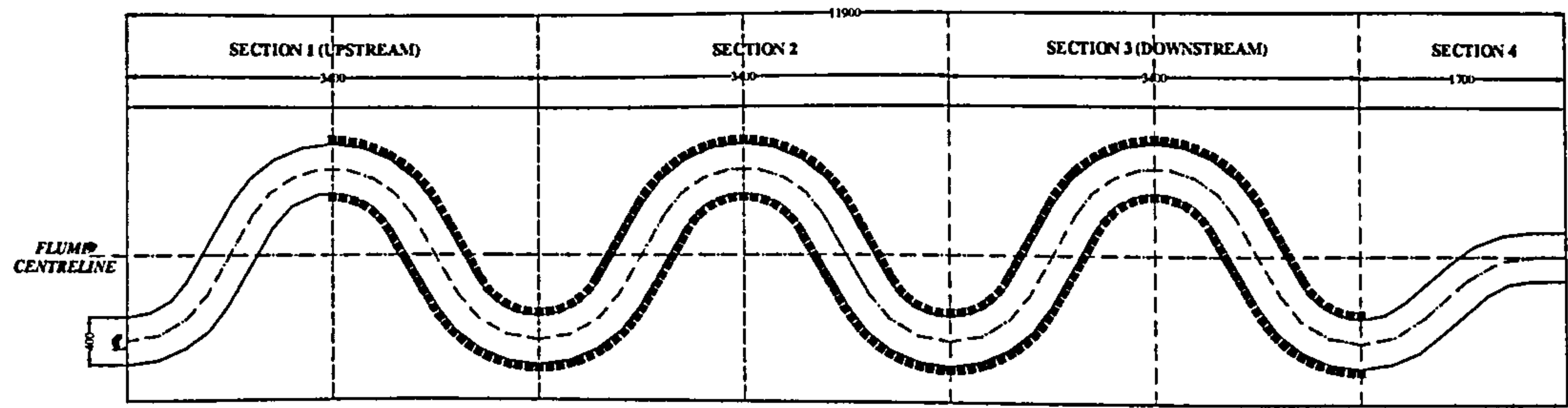
(a) *Case A No Block* (fixed-bed channel) and *Case E No Block* (mobile-bed channel) for rectangular channel cross-sections



(b) *Case B Apex Blocks* and *Case F Apex Block* are rectangular channel cross-sections for fixed- and mobile-bed channels respectively

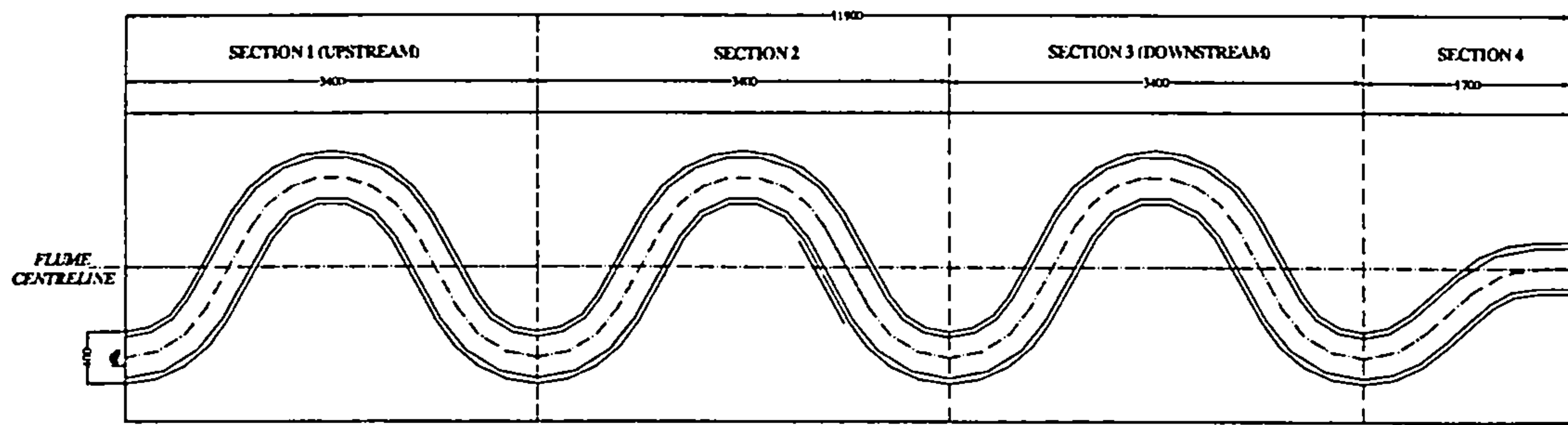


(c) *Case C Cross-over Block* and *Case G Cross-over Block* are the rectangular channel cross-sections for fixed- and mobile-bed channels respectively

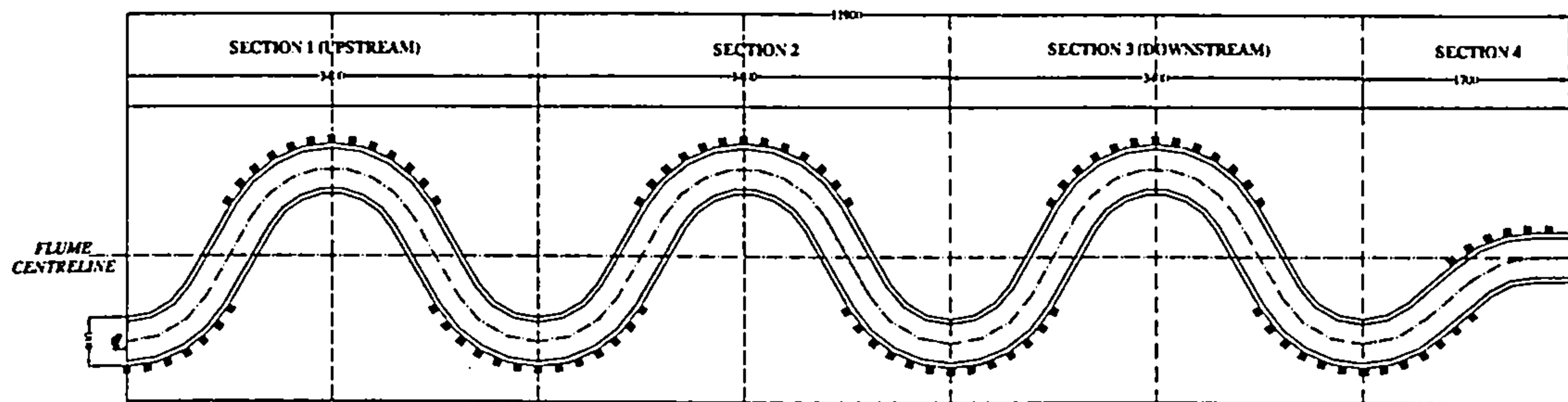


(d) *Case D Combined Apex and Cross-over Block* and *Case H Combined Apex and Cross-over Block* are rectangular channel cross-sections for fixed- and mobile-bed channels respectively

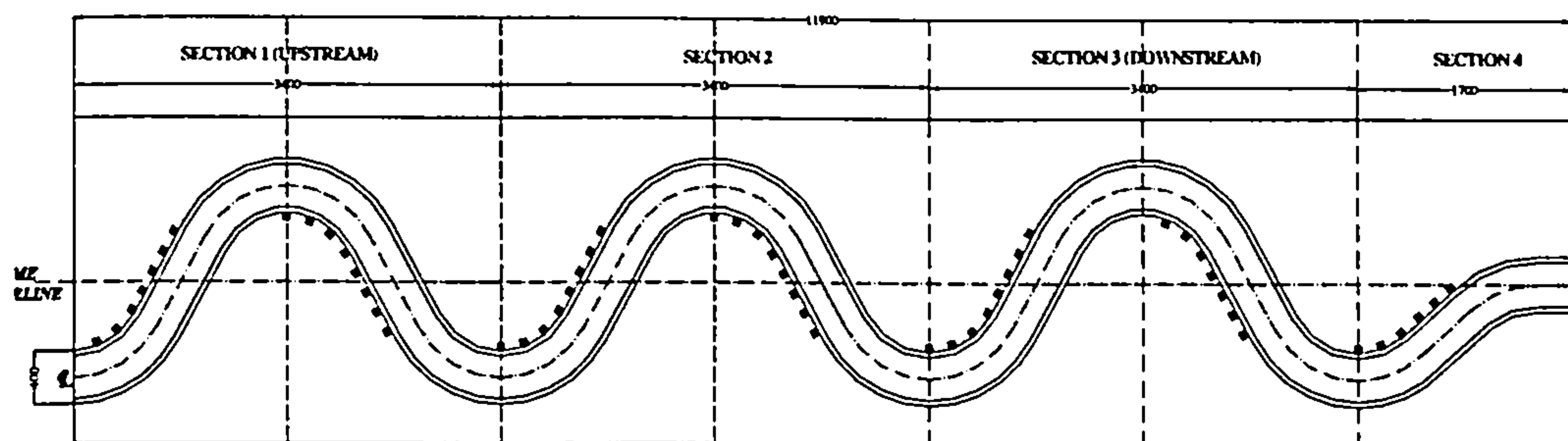




(e) *Case L No Block* trapezoidal fixed-bed channel cross-section



(f) *Case M Apex block* trapezoidal fixed-bed channel cross-section



(g) *Case N Cross-over Block* trapezoidal fixed-bed channel cross-section

**Figure 3.9: Planform of meandering experimental of arrangement of blocks on a floodplain bank (m)**

### 3.6 Mobile Bed Main Channel

The main channel was filled with uniform sand with a mean size diameter of 0.855 mm. In the present study with overbank flow, the depth of the screeded sand bed was 40 mm below the bankful level, which gives an aspect ratio of 10. This geometry was appropriate to investigate sediment transport and flow characteristics at higher flows. Furthermore, this aspect ratio is more realistic because the aspect ratio is within the range 10 to 15 that is commonly found in natural rivers (Sellin *et al.* 1993).



Screeding was carried out with a plywood board that was cut into the dimensions of the inner channel and positioned so that a constant screeded depth is maintained for the entire length of the channel. This board was attached to an aluminium frame with a roller as shown in Figure 3.10. The screeded sand was initially allowed to settle by running a shallow flow over the bed. Once the water had drained away and the sand had compacted naturally, then the screeding procedure was repeated to top up the sand to the required level.



**Figure 3.10:** Plywood board attaching to an aluminium frame with roller for screeded sand

### 3.7 Fixed Bed Main Channel

The fixed bed main channel was formed by screeding the sand at a depth of 40 mm below the bankful level which gives an aspect ratio of 10. The screeded bed was consolidated naturally by running a shallow flow over it and allowed to settle. The resulting flat surface was stabilised using a 'freezing' technique using Rugby Ordinary Portland cement to prevent further evolution. Experience suggested that cements from other brands took a considerable time to harden and were too influenced by the room temperature and humidity. The cemented crust surface was fairly smooth along the meander channel and water was sprinkled on the cement regularly during the cement 'curing' process to keep it moist. Both rectangular and trapezoidal main channels are termed as flat bed channels, the type which will be used in this study.



### 3.8 Measurement Procedures and Apparatus

#### 3.8.1 Measurement of Flow Depths and Bedforms

The flow depth and bedforms were measured using both a pointer gauge operated manually and digitally with an accuracy of  $\pm 0.1$  mm. These measurements were taken from a bridge across the flume. This manual and digital pointer gauge is shown in **Figures 3.11** and **3.12** respectively. In order to obtain reliable mean readings of water surface and bedforms, several readings were taken at each apex section on the floodplain along the flume.

For each phase of the overbank flow experiment, the flow was usually set to run for more than three days in order to develop typical bedforms. The flow rate was then increased gradually to the higher flow depth. On completion of the sediment transport rate measurement, the water was then drained slowly out of the channel. To avoid damaging the bedforms, several concrete blocks were placed at the outlet of the channel to prevent the water from draining away too rapidly.

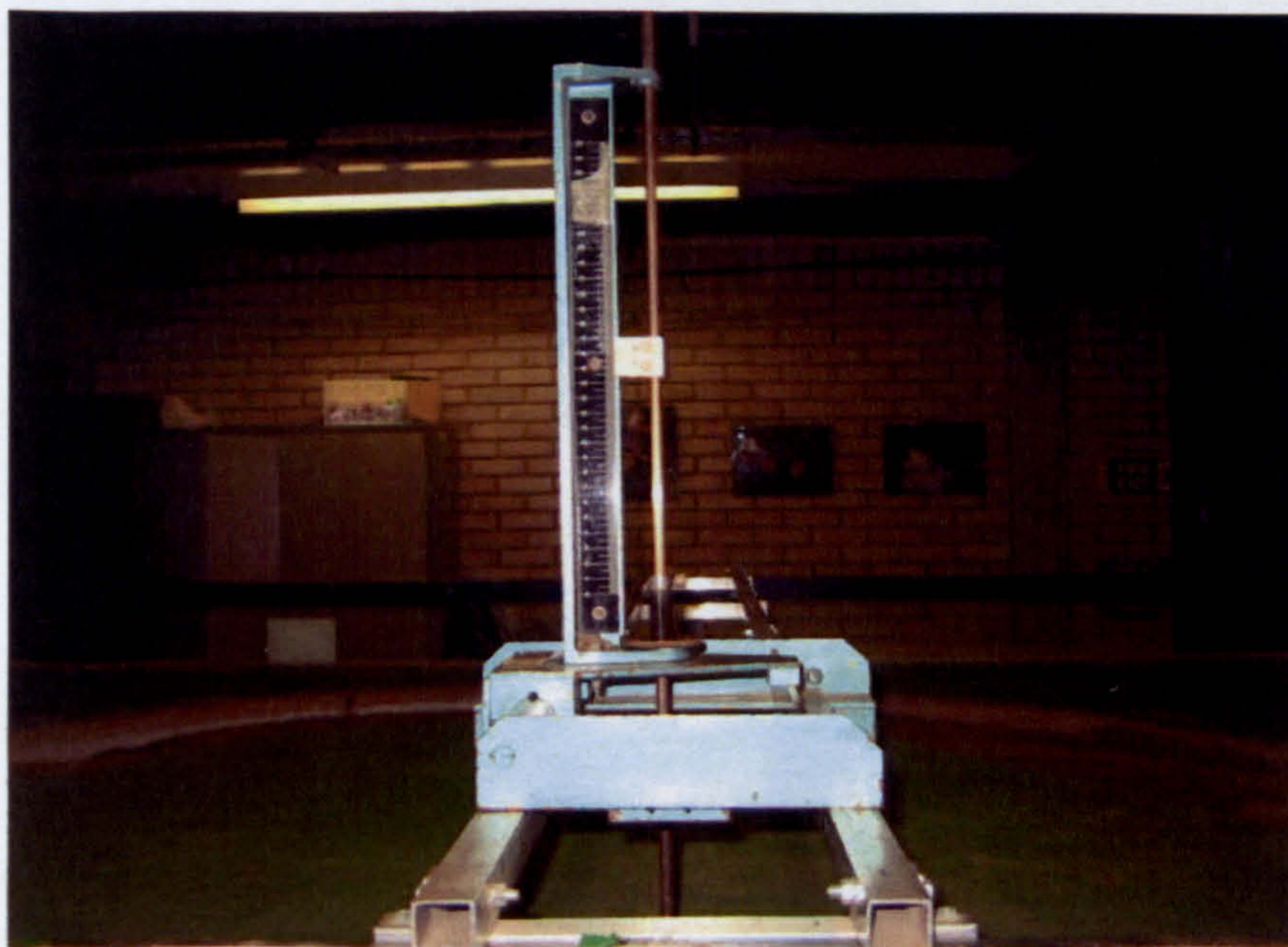


**Figure 3.11:** Manual point gauge



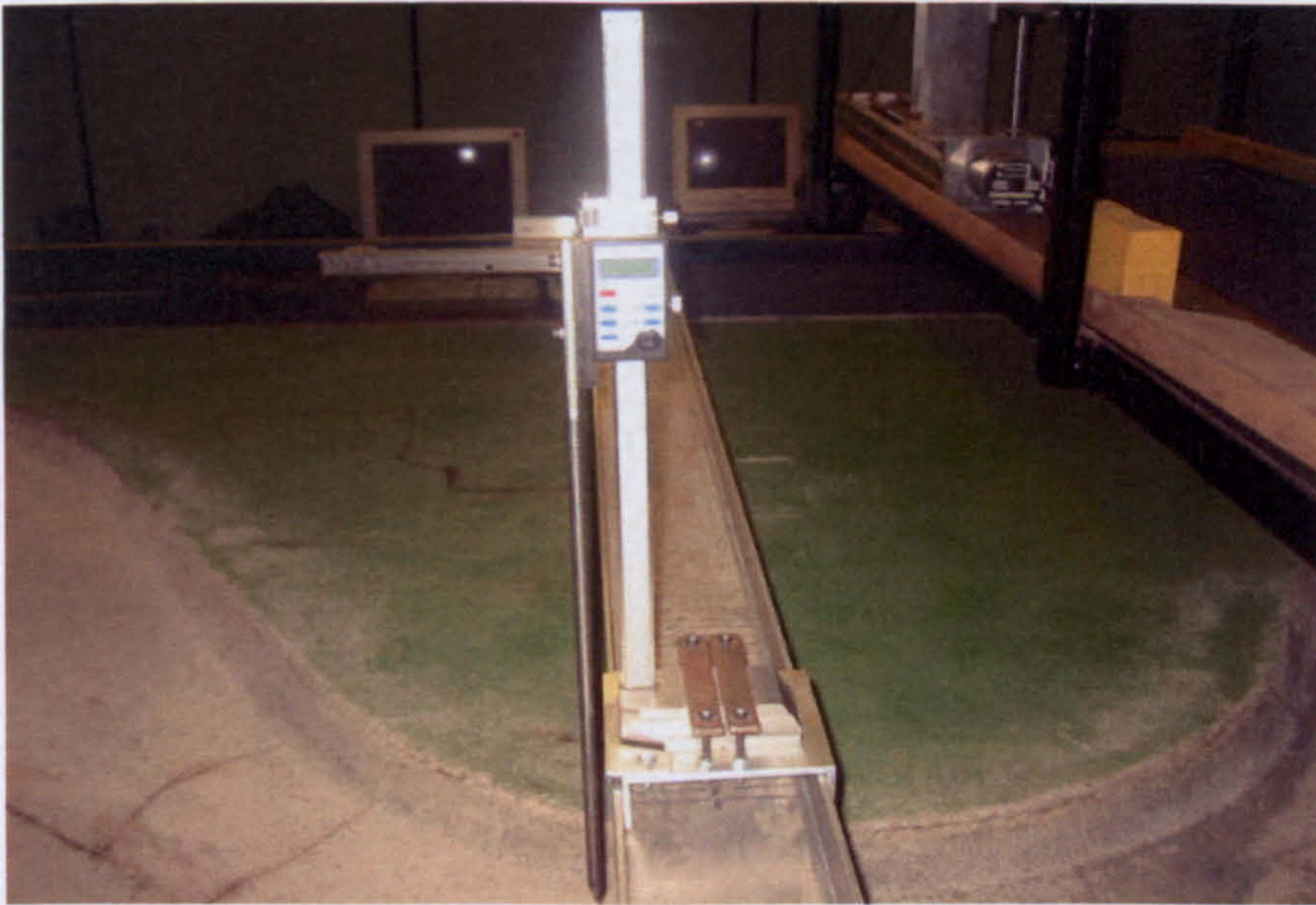


Figure 3.12: Digital point gauge

### 3.8.2 Measurement of Sediment Transport

After achieving uniform flow and equilibrium bedforms status, the sediment transport rate was measured manually using a sieve catcher. A sediment collector as shown in Figure 3.13 was placed at the downstream end of the channel to receive sediment which was then carried back to the entrance through a circulation pipeline with a sediment recycling pump. A transparent circular Perspex pipe of length 60 cm was installed in the circulation pipeline in order to monitor the sediment transport load as shown in Figure 3.14.

At the end of the circulation pipeline, a sieve catcher was used to retain the sediments as shown in Figure 3.15. Collected sediment was weighed in its wet condition, otherwise a sufficiently long period of time could have been required to allow excess water to drain from the catcher. Weighing the sediment in this manner eliminates the difficulties associated with the rapid drying of large quantities of sediment. Therefore, the investigation was carried out to determine a correction factor to convert the wet weight for wetted sediment to the equivalent mass of dry sediment. As a result, a correction factor for converting the weight of wetted sediment to the equivalent mass of dry sediment was found to be 0.82 as shown in Figure 3.16. Cassells (1998) suggested that a correction factor between 0.80 and 0.85 is reasonable for non-cohesive sediments.



In the case of the mobile bed channel, the sediment transport rate was determined by collecting sediment discharge at 15 to 30 minutes interval over a period of 6 hours. The transport rate was calculated by dividing the dry sediment's weight by the time interval as follows:

$$q_b = \frac{\Delta W}{\Delta t} \quad (3.3)$$

where,

$\Delta W$  = dry sediment weight

$\Delta t$  = time interval

The mean transport rate was calculated by taking the average of the transport rates over the whole collection period. A conversion factor was applied to each of the collected sediments in order to determine the equivalent mass of sediment in the dry condition. The mean sediment transport rates for mobile bed channel *E*, *F*, *G* and *H* cases will be seen in Tables 4.5 to 4.8 in Chapter 4.

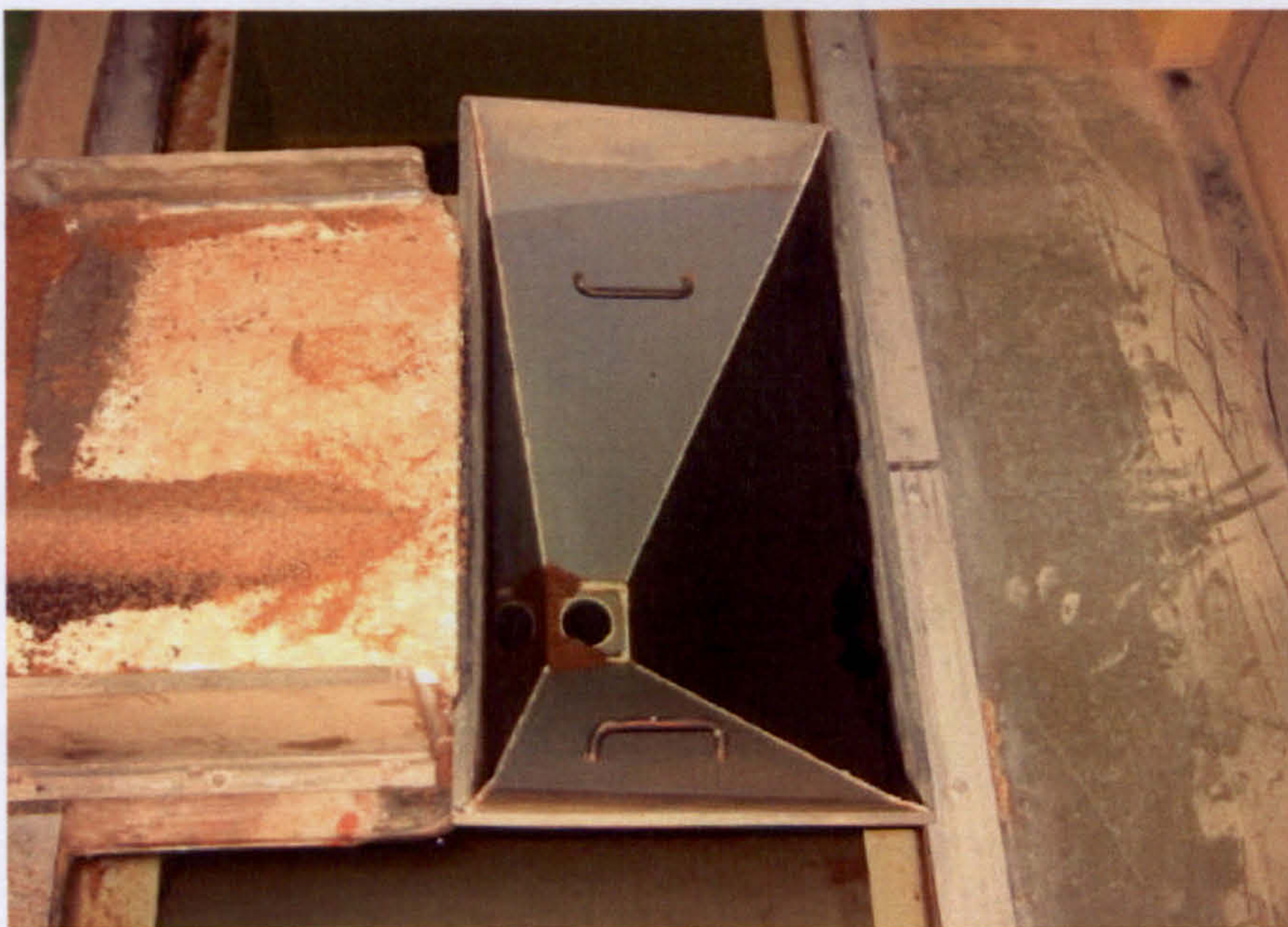


**Figure 3.13:** Sediment collected at downstream of the flume





**Figure 3.14:** Transparent circular Perspex pipe to monitor sediment movement

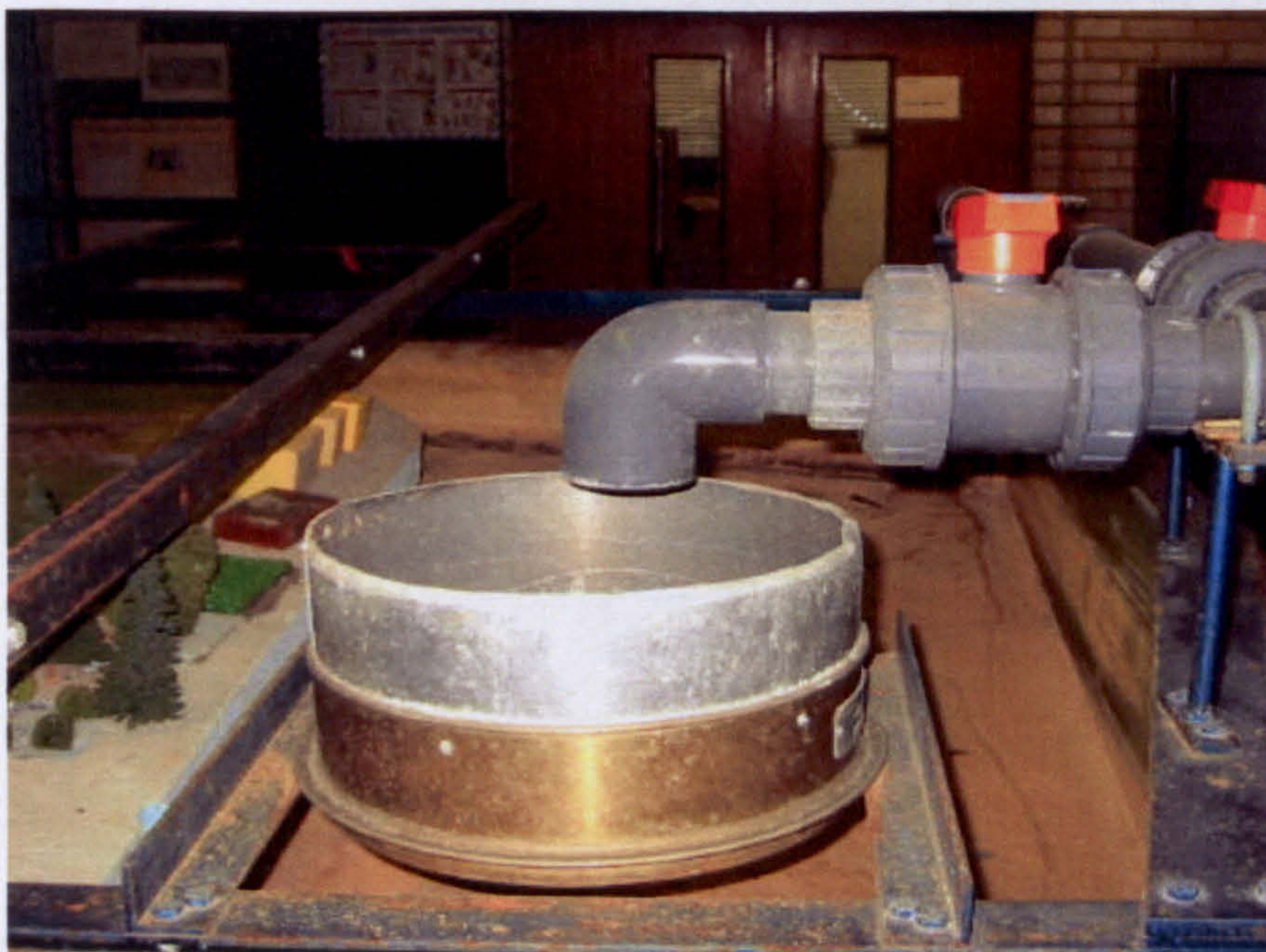


**Figure 3.15:** Sediment catcher in diverted pipeline at the upstream of the flume



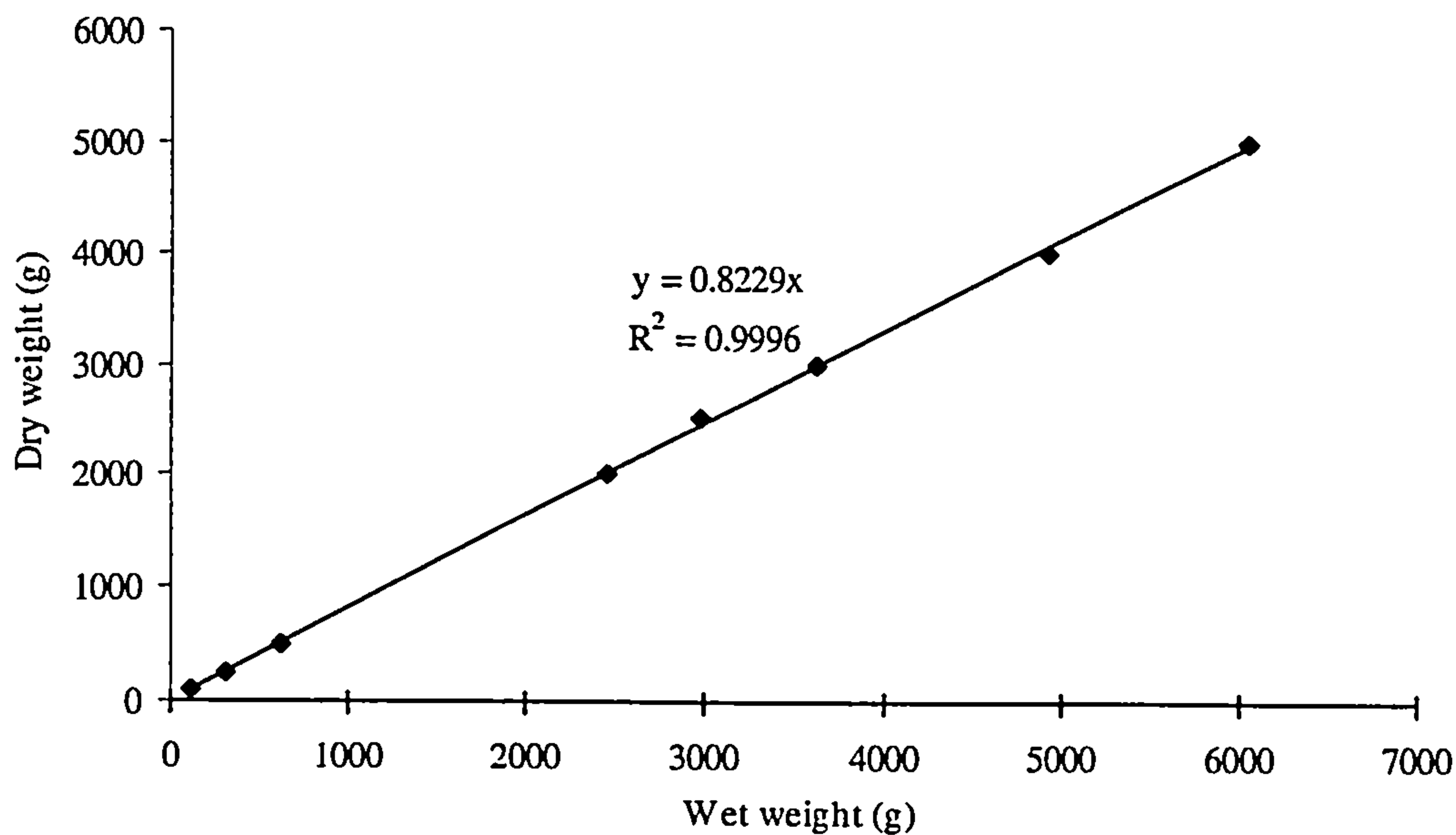


Figure 3.16: Dry sediment weight against wet sediment weight

### 3.8.3 Measurement of Boundary Shear Stress

Boundary shear stresses were measured using a Preston tube across the main channel bed. The Preston tube has an inner diameter of 2.72 mm, thus satisfying the size limitation recommended by Preston (1954). It was used together with a low pressure differential transducer range  $\pm 5.0$  mbar. One of the limiting criteria as recommended by Preston is that a minimum water depth must be five times greater than the outer diameter of the Preston tube for open channel measurements. The boundary shear stress in the main channel was measured at every 10 mm vertically on the sidewall and 20 mm laterally on the channel bed.

The data acquisition began with measuring the static pressure in a stable beaker filled with clean water. Due to the meandering channel, the flow angles were recorded for each measurement point using a vane indicator as shown in Figure 3.17. Then, the Preston tube was placed onto the measurement position and oriented according to the angle measured earlier, facing the flow direction. The whole operation was carried out manually in the fixed bed main channel only. The measured static-dynamic pressure



from the tube was transmitted to a pressure transducer, where it produced an analog signal in millivolts. Each of the data acquired consisted of 1,000 readings per minute and this large dataset provided an accurate mean value. Al-Romaih (1995) reported that for 900 readings per minute, the mean value was practically constant by the fortieth second of the sampling time. An analog to digital converter card was installed inside a standard Pentium computer to convert the analog signal to a digital signal from which shear stress values were calculated using a programme based on Patel's (1965) calibration curve for a smooth boundary.

A pressure differential transducer was a part of the apparatus used in the boundary shear stress measurement as shown in **Figure 3.18**. The transducer was capable of measuring pressures in a scale range of 0 to 5 mbar and was powered by a 220-volt direct current. The diaphragm of the transducer was made of a Beryllium Copper alloy for maximum flexibility and sensitivity, with an adjustable response time of 10 ms to 2 s.



**Figure 3.17:** Vane indicator



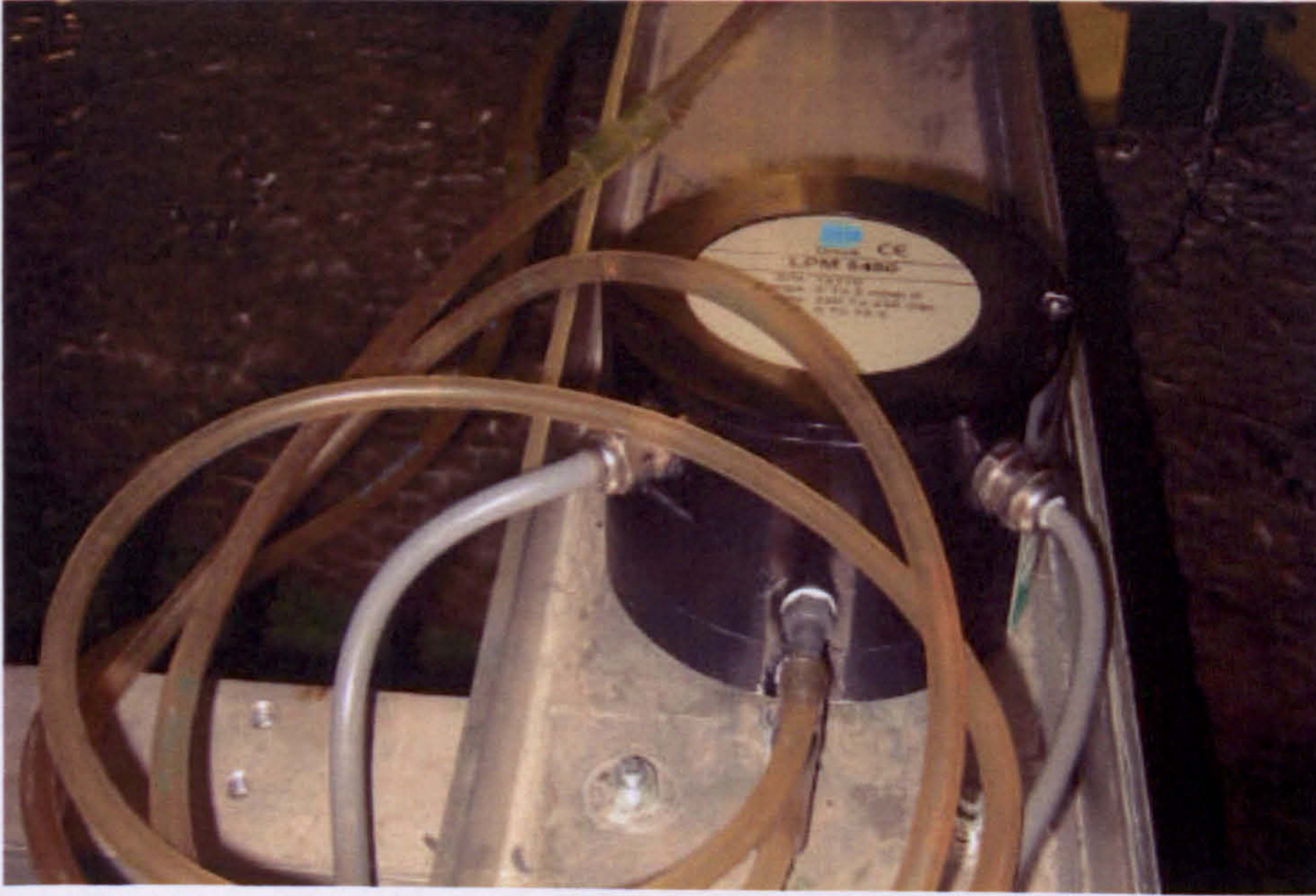


**Figure 3.18:** Low pressure transducer

#### 3.8.4 Measurement of Velocity

The detailed description of the velocity measurement collected at the Loughborough Flume will be described herein. The main channel is 0.04 m deep and trapezoidal in cross-section with a top width of 0.4 m and 45 degree side bank slopes. Further details on the geometry and flow parameters specific to the meandering channel can be found in the previous section. The measurements at the velocity components were undertaken under the steady and uniform flow conditions. For the three cases namely *Case L No Block*, *Case M Apex Block* and *Case N Cross-over Block*, velocity measurements were carried out using a three-component Vectrino Velocimeter at the selected main channel apex section/cross-sections for each case. The details of the locations for the velocity measurement for each case are shown in **Figures 3.19 to 3.21**.



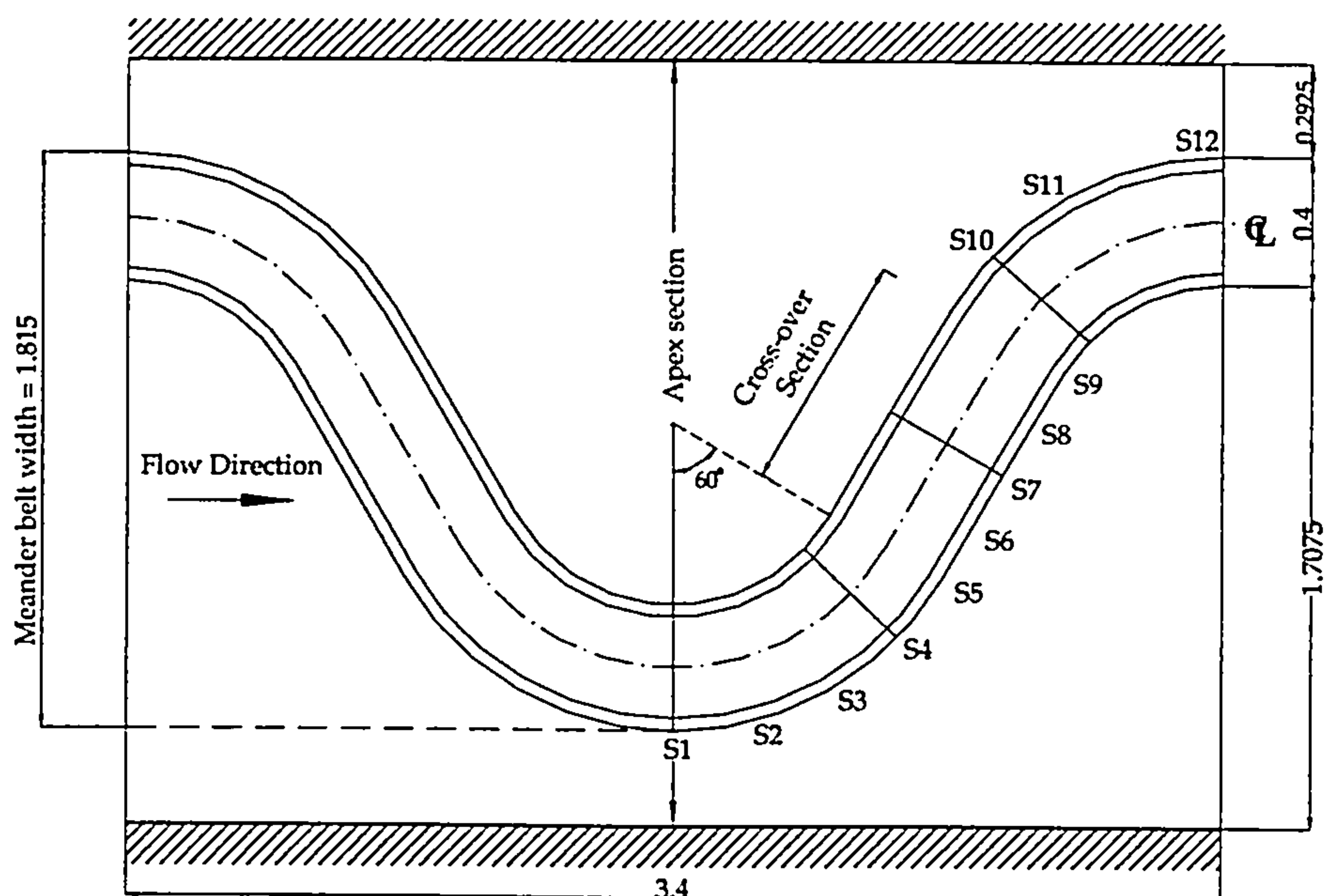


Figure 3.19: Plan of sign convention system for variable velocities and location details of the measurement sections S1, S4, S7, S10 and S12 for Case L No Block

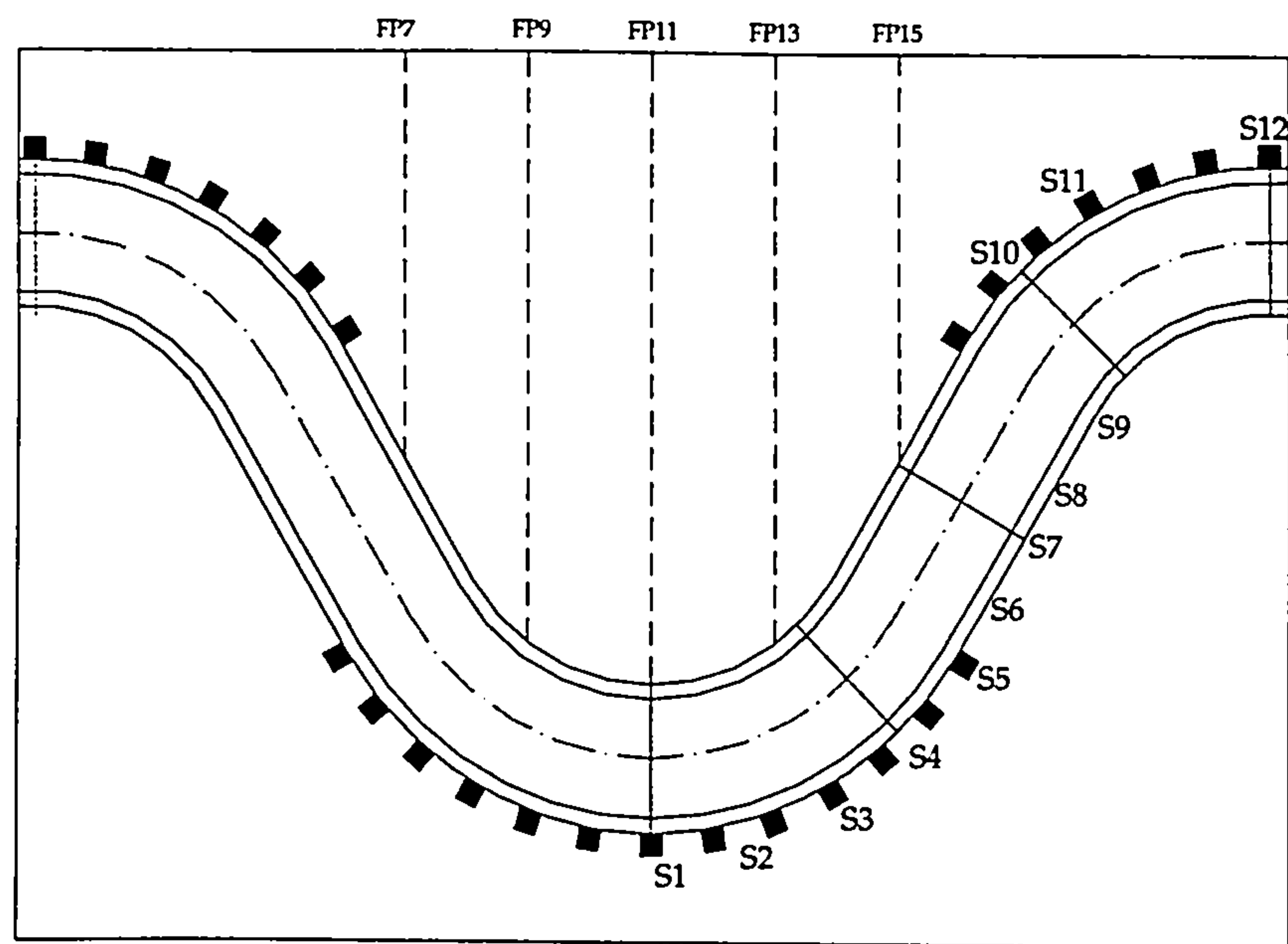
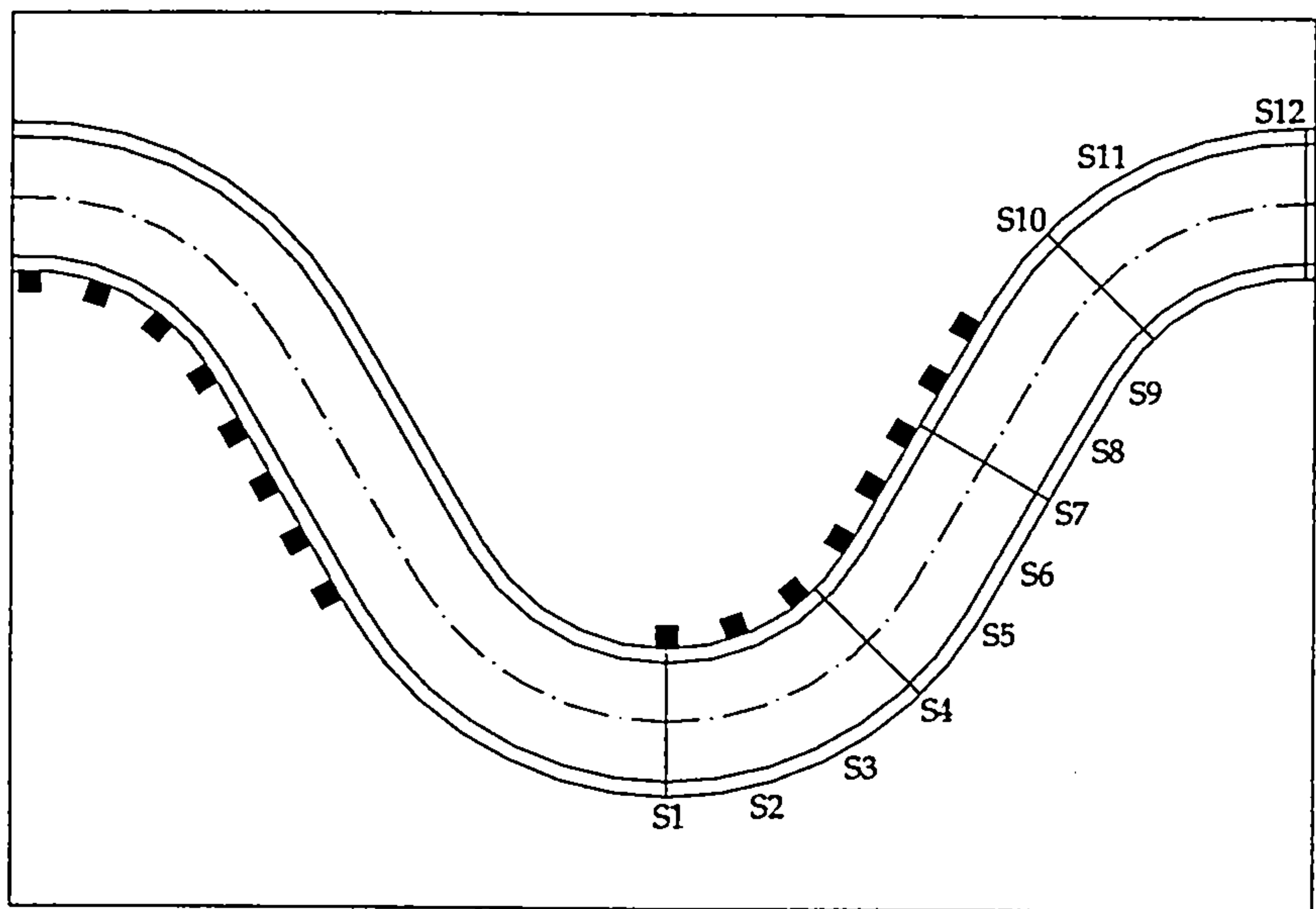


Figure 3.20: Location details of the measurement sections S1, S4, S7, S10 and S12 in the main channel and sections FP7, FP9, FP11, FP13 and FP15 on the floodplain for Case M Apex Block





**Figure 3.21:** Location details of the measurement sections S1, S4, S7, S10 and S12 for *Case N Cross-over Block*

The main channel and floodplain velocities were recorded in a reach of half of the wavelength in the channel. Velocities for all experiments were taken at five cross-sections. It should be noted that the velocity measurements were carried out on the floodplain to see the decay of the effect of wake flow only for *Case M Apex Block*. That is why only in the *Case M Apex Block* was the velocity on the floodplain measured. All these sections were selected because of the distinctive features of the flow structures. The measurement grid pattern at each cross-section is shown in Figure 3.22. The disturbance of noise signals reflected from the channel bed restricted the velocity that could be measured to at least 5 mm above the bottom of the channel bed in the main channel and floodplain. The grid had a spacing of 1 cm in height and 2 cm in width.

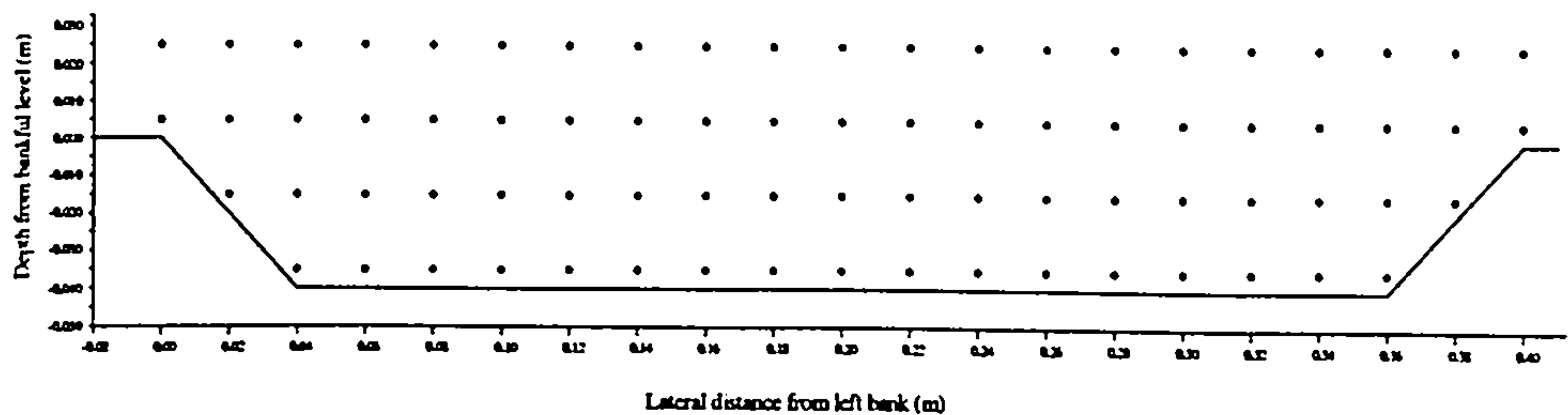


**Figure 3.22:** Velocity measurement grid for fixed-bed trapezoidal main channel case



#### 3.8.4.1 The Vectrino Velocimeter

The Vectrino Velocimeter was developed by Nortek AS. It has been designed for simplicity and versatility. It is a three-dimensional (3D) velocity sensor, originally developed and tested for use in physical model facilities. The use of the Vectrino Velocimeter is becoming popular because of some of its advantages in flow measurement.

The Vectrino is used to measure the three-dimensional velocity components  $u$ ,  $v$ , and  $w$  in the  $x$ ,  $y$ , and  $z$  directions respectively. The Vectrino is a high-resolution acoustic velocimeter used to measure 3D water velocity in a wide variety of situations from the laboratory to the ocean. The instrument is simple to use and the performance compares favourably with laser Doppler systems costing many times more. The basic measurement technology is coherent Doppler processing, which is characterized by accurate data with no appreciable zero offset. The standard Vectrino allows data collection rates up to 25 Hz, and with the optional Vectrino + firmware a collection rate of 200 Hz can be achieved (User Guide, 2004).

##### 3.8.4.1.1 Working Principle

The Vectrino Velocimeter is connected to a notebook computer, and used for the measurement of 3D velocity components. It transmits acoustic pulses into the water that are scattered by the particles present in the water. A pulse is transmitted from the central transducer, and the Doppler shift caused by the reflections from particles suspended in the water, is picked up by the 4 receivers. Data is collected using the Vectrino software supplied by the company. This raw data can then be converted using the Vectrino data conversion program and then imported using a special processing software package provided by Vectrino for velocity analysis.

The naming convention and working principle of the Vectrino are shown in Figure 3.23. There are four types of Vectrino probes known as the 3D downlooking probe, the 3D uplooking probe, the 3D side looking probe and the 2D sidelooking probe. Among these four types of probes, only the 3D downlooking probe was employed for this study. The Vectrino downlooking probe used in the present study is shown in Figure



3.24. The receiving arm on the 3D downlooking probe points in the direction of the x-axis and the value for the velocity  $v_x$  in the software refers to the velocity along this axis.

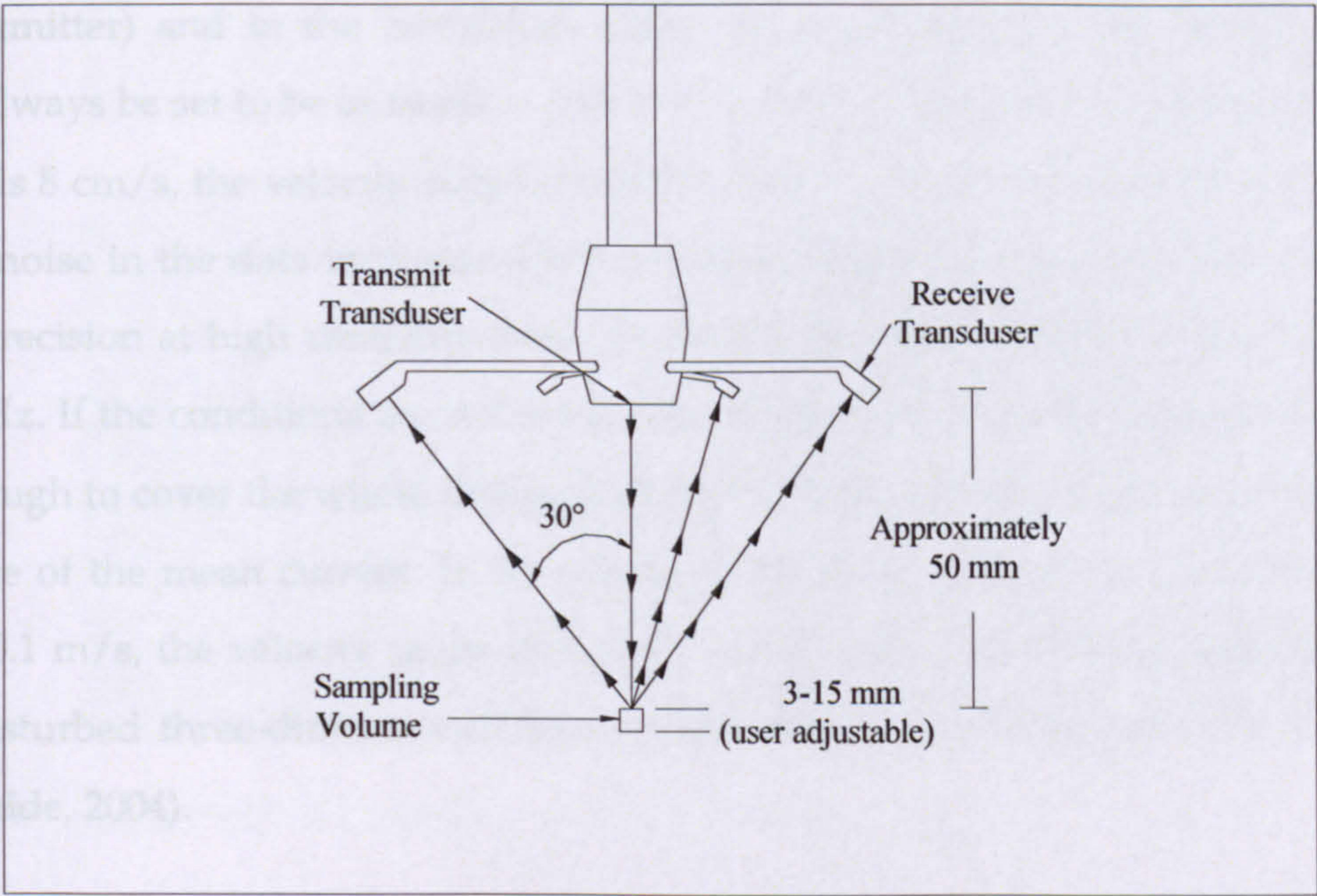


Figure 3.23: The Vectrino naming convention

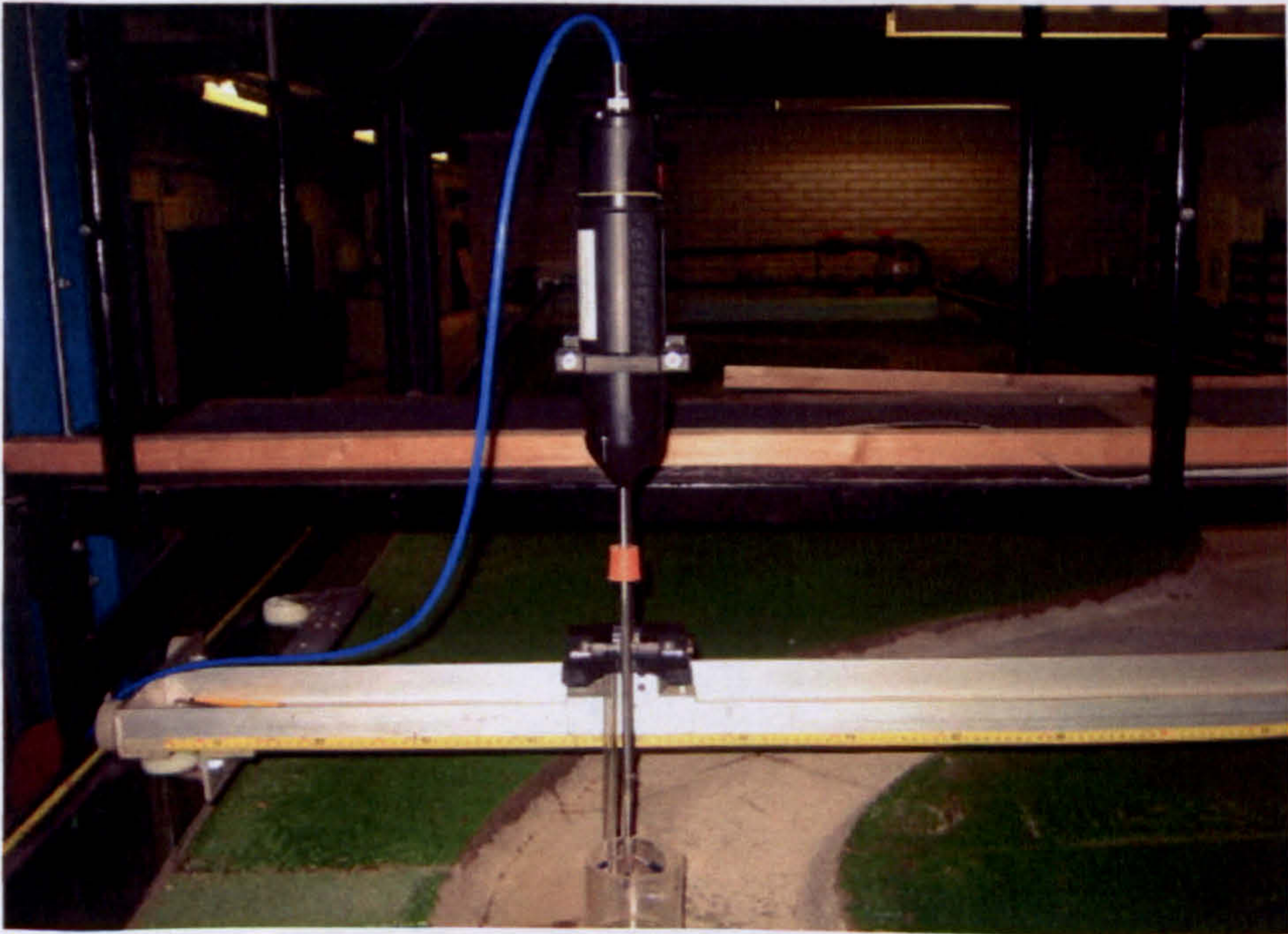


Figure 3.24: Vectrino downlooking probe



#### 3.8.4.1.2 Velocity Ranges

The velocity range is to be set before starting the data collection. The range is a nominal value and the exact maximum velocity is different along the vertical axis (i.e., towards the transmitter) and in the horizontal plane. As a general rule, the velocity range should always be set to be as small as possible. If, for example, the maximum expected velocity is 8 cm/s, the velocity range should be set to  $\pm 10$  cm/s. The reason for this is that the noise in the data increases with increasing velocity range and hence causes a loss of precision at high sampling rates. In the present study, the sampling rate used was 25 Hz. If the conditions are not known in advance, the velocity range must be set high enough to cover the whole deployment period. The velocity range must cover the full range of the mean current. If, for example, the mean currents are expected to be around 0.1 m/s, the velocity range should be set to 1 m/s. The Vectrino can measure the undisturbed three-dimensional flow components at a velocity range of  $\pm 4$  m/s (User Guide, 2004).

#### 3.8.4.1.3 Operation Close to the Boundary

The middle of the sampling volume is positioned approximately 0.05 m below the transmit transducer located at the centre of the probe and hence the Vectrino measures the undisturbed flow. The distance to the boundary shown on the computer display is the distance from the middle of the sampling volume to the nearest boundary. The sampling volume is of finite extent and the minimum distance to the boundary that still permits data collection is 3 to 15 mm (User Guide, 2004). Some initial experimentation is required because the exact limit depends on both the conditions of the boundary as well as the exact software configuration.

#### 3.8.5 Small Tank

When dealing with the measurement of velocity on the floodplain especially for shallower flow depth by using Vectrino Velocimeter down-looking probe, the velocity near the water surface cannot be measured directly due to the limitation of a 5 cm distance between the transmitter and the sampling point. To overcome this, a special small cylindrical tank of 8.4 cm diameter, as shown in Figure 3.25, was designed and



placed on the water surface to measure the velocities below the water surface. This is the first application of using Vectrino Velocimeter with a 3-D down-looking probe to measure velocity near the water surface.

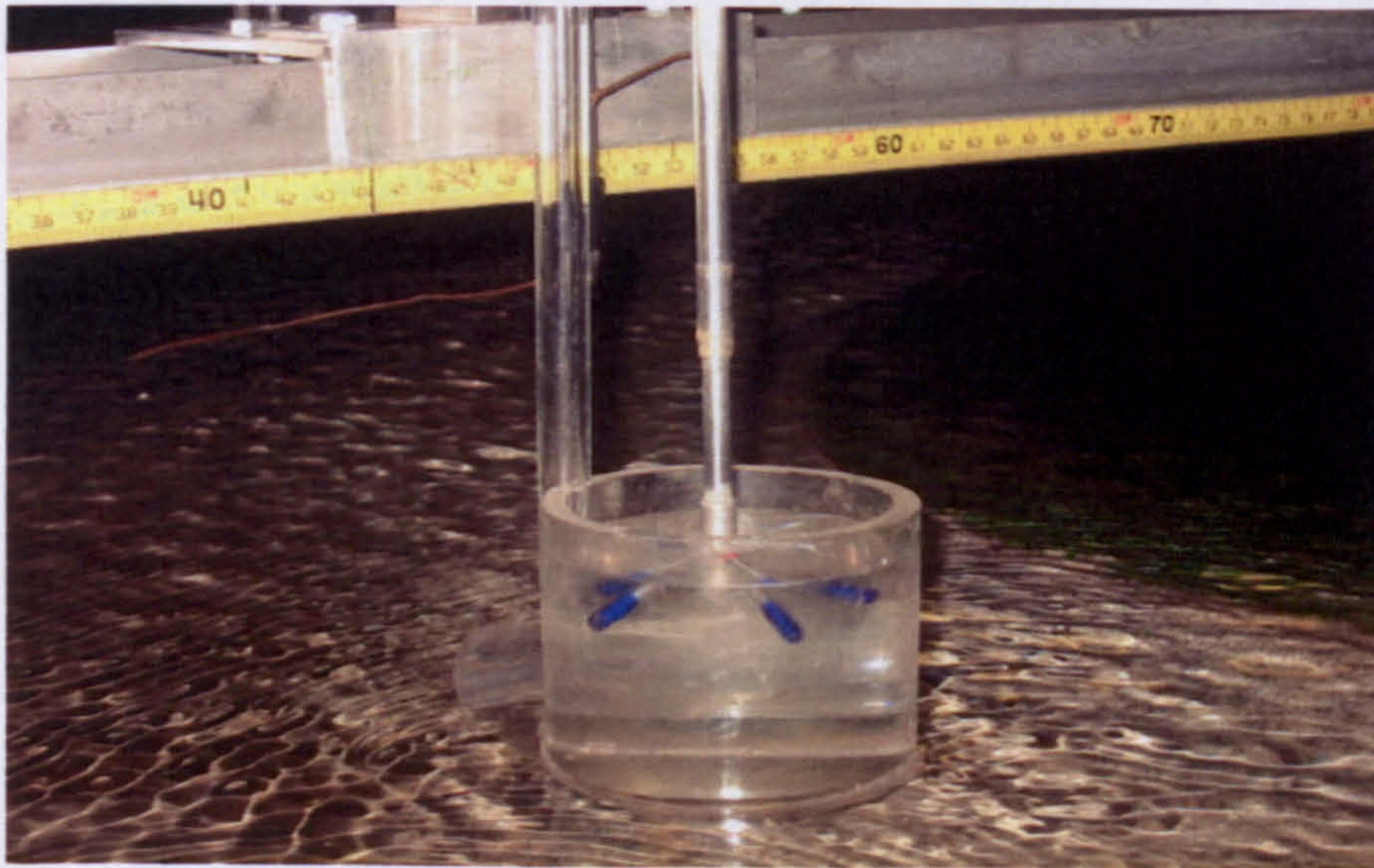


**Figure 3.25:** Small tank was modified to merge the acoustic receiver

The cylindrical tank was made out of Perspex with a depth of 6 mm. Several transparent materials were tried to seal the tank bottom. No signal was detected by Vectrino Velocimeter when a Perspex plate with a depth of 6 mm and thick plastic film were used. This might indicate that most of the acoustic energy from the transmit sensor or (and) from the receiver sensors was absorbed by the thick materials. A thin film was proved to be the best material for making the tank bottom. The thin film was stuck to the Perspex wall with superglue. To avoid the sudden water level jump near the small tank and to minimize the flow disturbance around the tank, the film extended about 2 cm in the front and back of the flow direction to make a smooth flow.

The height of the small tank was set as 8 cm, which was 3 cm larger than the minimum distance between the sampling point and the transmitter head. The main purpose of setting this height was to ensure that the sensor head was submerged during the measurements. Moreover, the tank on the water surface cannot be too large because a large tank would pose holding difficulties. The capability of using the small tank to measure the velocities near the water surface was investigated in the large compound channel. Some representative test results are presented in Figures 3.32 (a) to (f). The water depth in the main channel was 20 cm. Velocities at  $z = 0$  to 15 cm were measured



with Vectrino in the channel directly and velocities at  $z = 16$  to  $20$  cm were measured with Vectrino in the tank on the water surface.

In Figure 3.26(a), the velocity  $U$  profile was not continuous at  $z = 17$  cm which might be caused by the boundary interference. Lane *et al* (1998) studied the boundary interference and identified the zone where the noise might mask the velocity signal. Velocities decreased quickly between  $z = 190$  and  $z = 200$  mm and this is because a boundary layer had developed below the water tank. In Figures 3.26(c) and (d), the turbulence intensities decreased gradually as the distances from the channel bottom increased to  $150$  mm. Higher turbulence intensities  $u'^2$  and  $w'^2$  occurred around  $z = 17$  cm which corresponded to the sharp changes of velocity  $U$  and  $W$  in this zone. In Figures 3.26(e) and (f), higher Reynolds stresses were also related to the velocity profiles. These results indicate that the small water tank can be used to measure velocity near the water surface, except in the zones which are  $0$  to  $1$  cm and around  $3$  cm below the water surface.

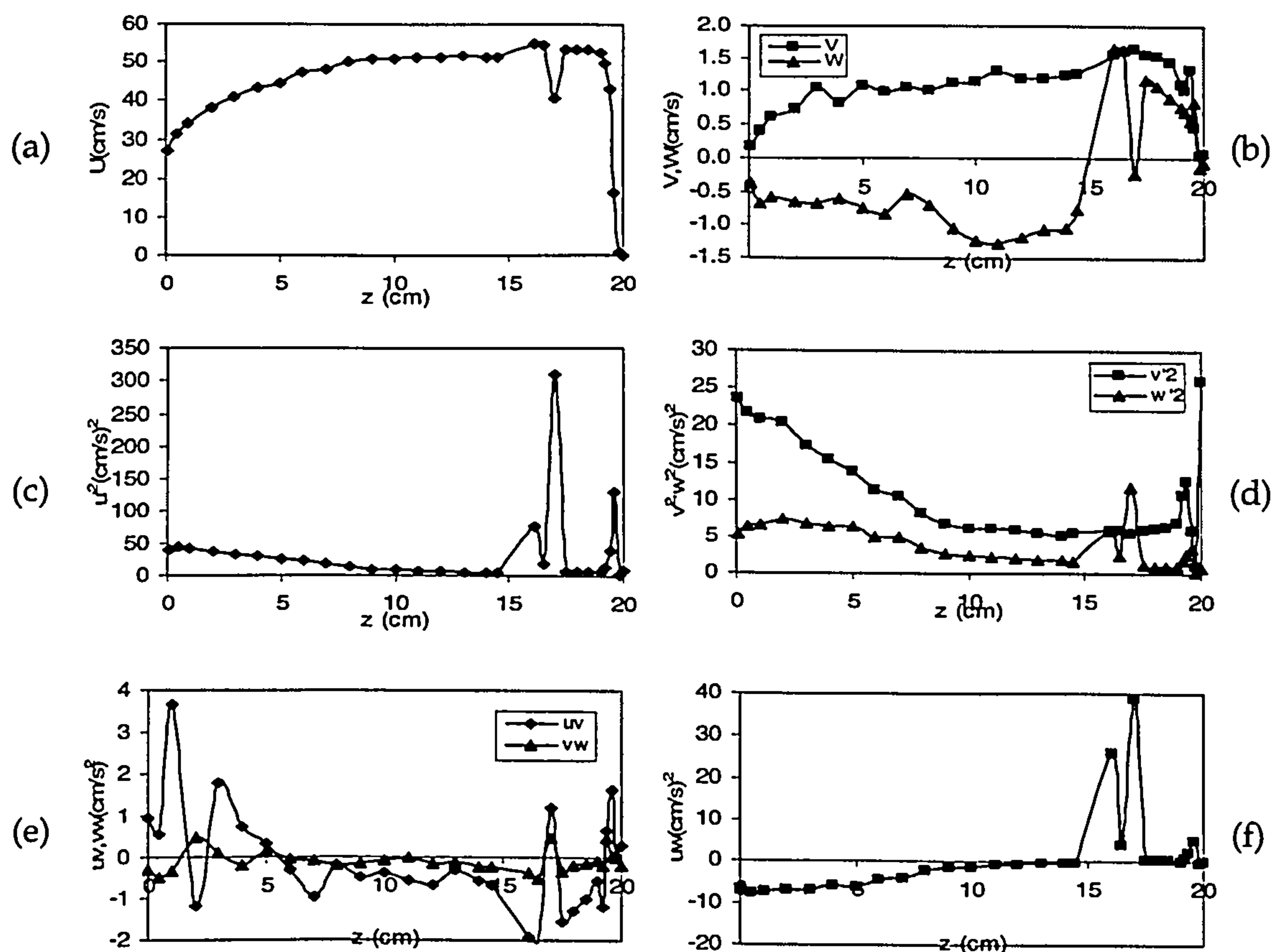


Figure 3.26: Measurement results along the water depth using the small tank. Averaged velocities (a) and (b); Turbulent intensities (c) and (d); Reynolds stresses (e) and (f)



### 3.9 Experimental Procedure

The preliminary objectives of the experiment for this study was to supply data representing the relation between the flow resistance, flow characteristics and sediment transport behaviours with different densities of the blocks, and to model the vegetation on a floodplain. The data were collected for several scenarios of block configurations and discharge values.

Experiments involving eleven block arrangement cases have been carried out under both fixed and mobile bed main channel cross-sections. Eight cases were carried out for the rectangular main channel cross-section with the remaining three cases being carried out for the trapezoidal main channel cross-section.

For stage-discharge readings in the case of fixed bed channel, the water was left running for approximately 2 to 3 hours to establish the uniform flow then stage-discharge readings were taken. In the case of the mobile bed channel, water surface readings were taken at an interval of 60 minutes. The tailgate was adjusted to achieve a water surface slope within  $\pm 2\%$  of the valley slope. After uniform flow was obtained, the flow was left to run continuously for more than 12 hours and the water surface level evaluation was checked regularly until equilibrium bedforms had developed. At higher flow depth, it was quite difficult to ensure that the flow was uniform due to fluctuations of the water level. Additionally, the development of bedforms varied dramatically with time; taking sometimes more than five days.

For sediment transport measurement, sediment transport rates were recorded continuously for a sampling duration of six hours. The sampling was every thirty minutes. In each sampling, the weight of the catcher and wet sediments were measured instantaneously by a micro-milligram weighing scale with an accuracy of up to  $\pm 0.001$  gram. The weighed sediments were placed carefully back into the channel at the inlet with minimum disturbance to the flow. The self-weights of the wetted catchers were measured at the end of the experiment to determine the true weight of the sediment.



### 3.10 Limitations of the Experimental Work

There exist some limitations in the laboratory study which should be noted. These limitations are summarised below:

- (a) In the stilling pool of the flume, there was severe turbulence of the incoming flow. A thick plywood float fixed in the stilling pool temporarily solved the fluctuations of the water surface caused by this turbulence. It was also used to ensure unidirectional flow in the flume and prevent fluctuations of water. (see Figure 3.27).
- (b) The velocity measurement cannot be taken place due to shallow water on the floodplain because the sampling volume is positioned approximately 0.05 m below the transmit transducer located at the centre of the probe. To overcome this problem, a small circular tank was adopted as an index-matching tank in order to measure the velocity on the floodplain at a particular depth as shown in Figure 3.25 (see Section 3.8.5).
- (c) In the cold winter season there is leaking underneath the flume due to the shrink of material. In order to overcome the problem, a water heater tank as shown in Figure 3.28 was used to circulate hot water into the main reservoir in order to maintain a water temperature of around 20° C.

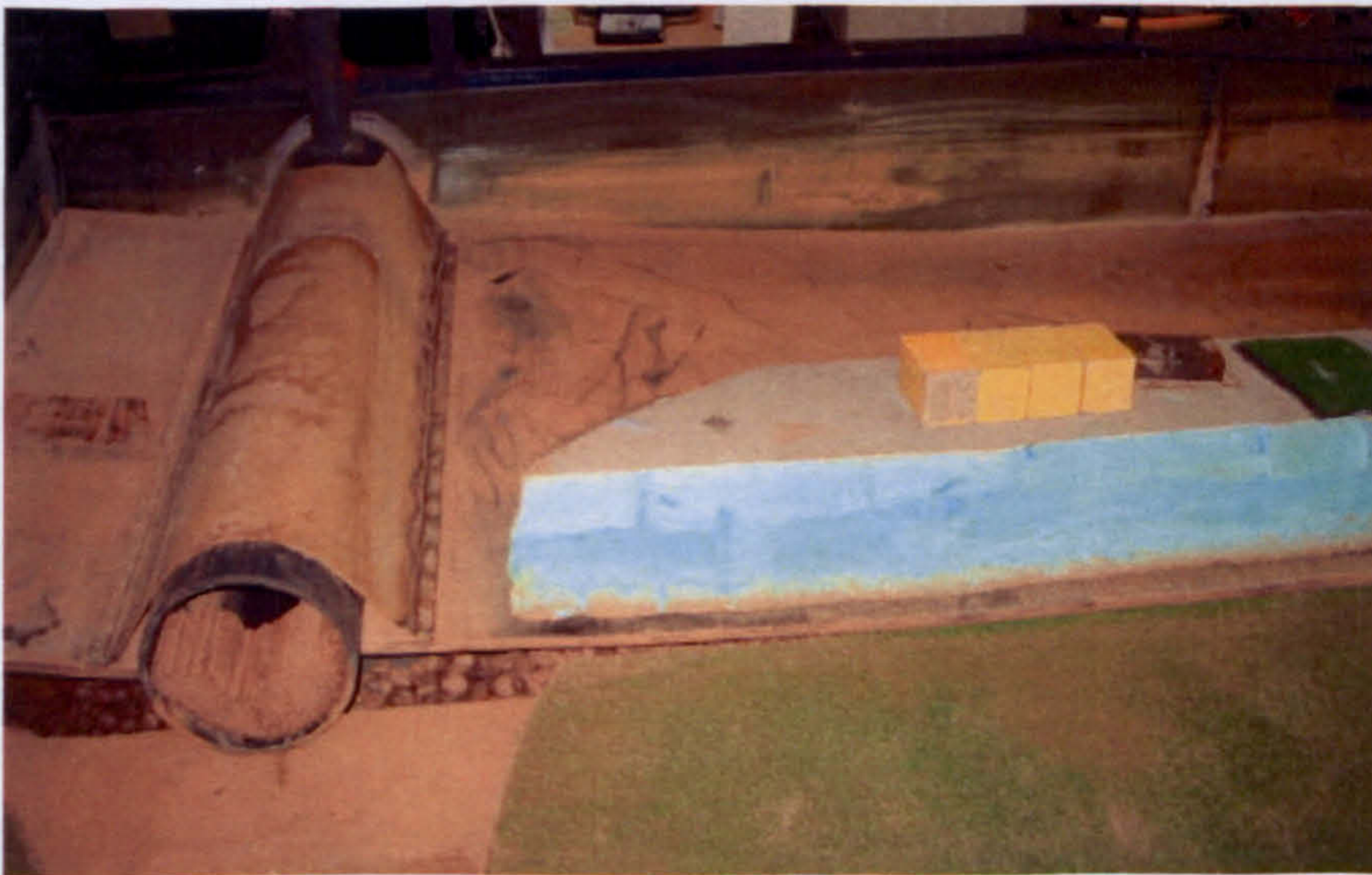


Figure 3.27: A thick plywood float was fixed in the stilling pool





Figure 3.28: Circulating heater tank

### 3.11 Simulation Works

The following sections concentrate mainly on the issues concerning the details of the computational predictions for the different simulation cases. The Telemac modelling system is one of the well-established, hydraulics modelling packages, which was developed by the Institute of Mechanics of Hanoi (IOM) and the National Hydraulics Laboratory of Electricite de France (LNHE - EDF) in the 1960's. According to Hervouet (2000), Telemac is the standard computational fluid dynamics (CFD) tool, which was used in this study to solve the two- and three-dimensional Reynolds-averaged Navier-Stokes (RANS) and continuity equations. The details on the finite-element unstructured meshes, initial and boundary conditions, numerical schemes and, finally, the solution approach are presented in the latter part of this next section.

The numerical simulations of the compound meandering channel flows have been carried out for the three different cases each with different block arrangements with different relative depths. The Loughborough Flume is considered as a small-scale model (10.2 m long and 2.4 m wide) of a compound meandering channel. The simulations were carried out for the Loughborough Flume with the relative depths of 0.25 and 0.45. The range of relative depths was selected so as to study the gradual development of the overbank flows for these flume geometries. Thus, in all three different simulations were carried out. Table 3.5 details the nomenclature of the test cases and their preliminary classifications.

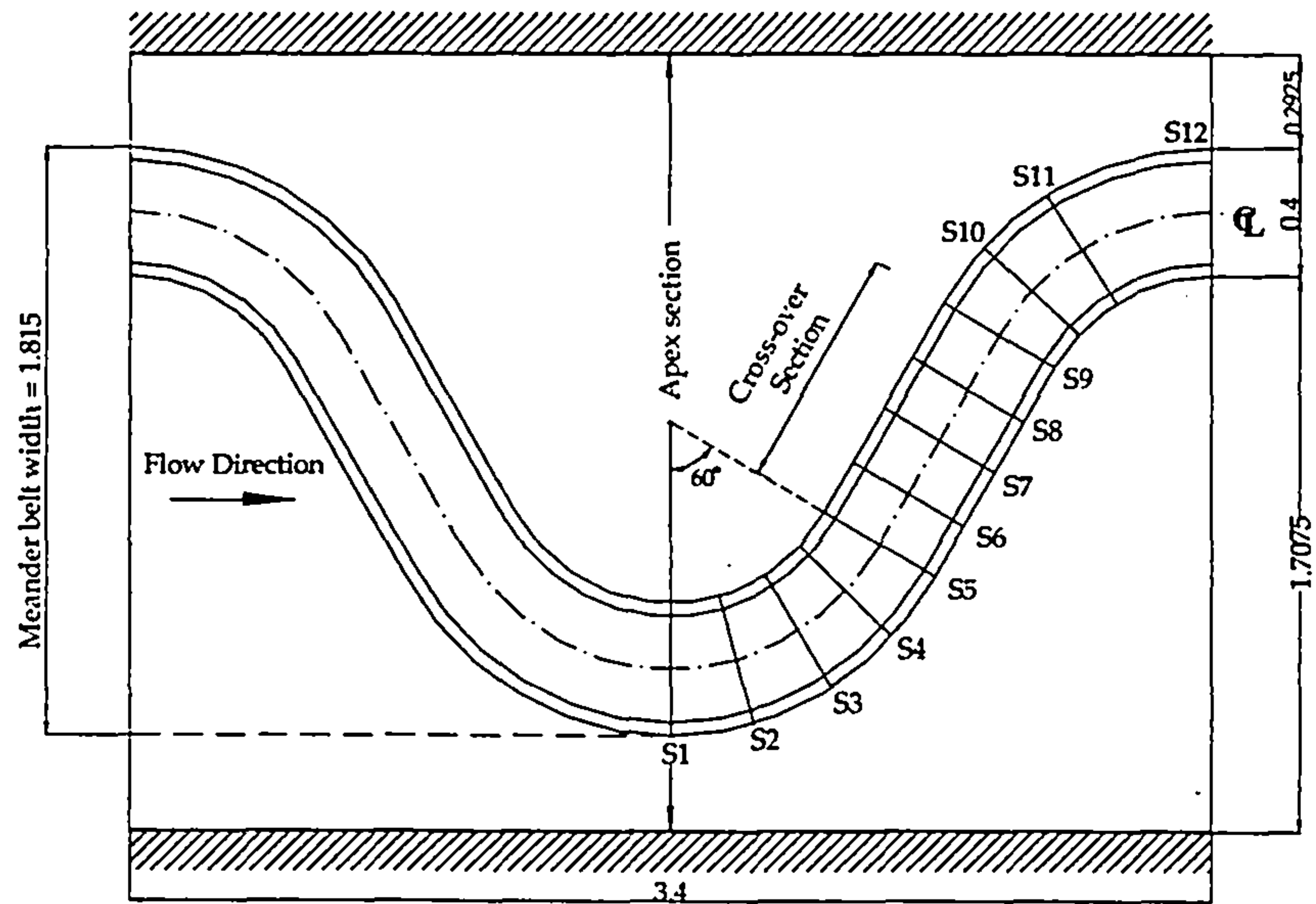


Table 3.5: Summary of Telemac simulation for a meandering channel

Case	Software System	Roughness Element	$Q$ (m <sup>3</sup> /s)	$H$ (m)	$Dr$
<i>Case L</i> <i>No Block</i>	Telemac 2D	No block	0.00522	0.05335	0.25
	Telemac 2D	No block	0.026525	0.07275	0.45
	Telemac 3D	No block	0.00522	0.05335	0.25
	Telemac 3D	No block	0.026525	0.07275	0.45
<i>Case M</i> <i>Apex Block</i>	Telemac 2D	<i>Apex Block</i>	0.00490	0.05335	0.25
	Telemac 2D	<i>Apex Block</i>	0.01900	0.07275	0.45
	Telemac 3D	<i>Apex Block</i>	0.00490	0.05335	0.25
	Telemac 3D	<i>Apex Block</i>	0.01900	0.07275	0.45
<i>Case N</i> <i>Cross-over Block</i>	Telemac 2D	<i>Cross-over Block</i>	0.00540	0.05335	0.25
	Telemac 2D	<i>Cross-over Block</i>	0.02100	0.07275	0.45
	Telemac 3D	<i>Cross-over Block</i>	0.00540	0.05335	0.25
	Telemac 3D	<i>Cross-over Block</i>	0.02100	0.07275	0.45

The 3D velocity consists of three components of velocity namely the streamwise velocity ( $U$ ), the lateral velocity ( $V$ ) and the vertical velocity ( $W$ ). These components were plotted to show the magnitude of each component in the main channel. For the no block  $L$ , apex block  $M$  and cross-over block  $N$  cases, the velocities ( $U$ ,  $V$  and  $W$ ) were predicted at 12 different main channel cross-sections (namely, sections S1 to S12). For *Case M Apex Block* only, the velocities at 5 different floodplain cross-sections (namely FP7, FP9, FP11, FP13 and FP15) along the meander were predicted in order to see how the decay of velocity on the floodplain was affected by the blocks. Figure 3.29 shows the detailed plan view of the compound meandering channel including the cross-sections. It is noted that the flow variables were plotted, as looking from the upstream end (eye at the upstream). The plan views for cases apex block  $M$  and cross-over block  $N$  are shown in Figures 3.30 and 3.31 respectively. In order to understand the flow behaviour along the half-meander wavelength, sections S1 to S12 are used as the benchmark sections for all the flow cases considered here. Thus, the isolines of the flow variables at sections S1 to S12 for different flow cases were plotted. All contour plots were confined to the main channel section only. For comparison and the validation of the computational results with the experimental data for the different flow cases, the detailed descriptions of the velocity measurements collected at the Loughborough Flume were undertaken at selected cross-sections (see Section 3.8.4). In all cases, velocity and turbulence measurements were carried out using a three-component Vectrino Velocimeter as described previously.





**Figure 3.29: Plan of sign convention system for variable velocities and location details of the measurement sections S1 to S12 for *Case L No Block***

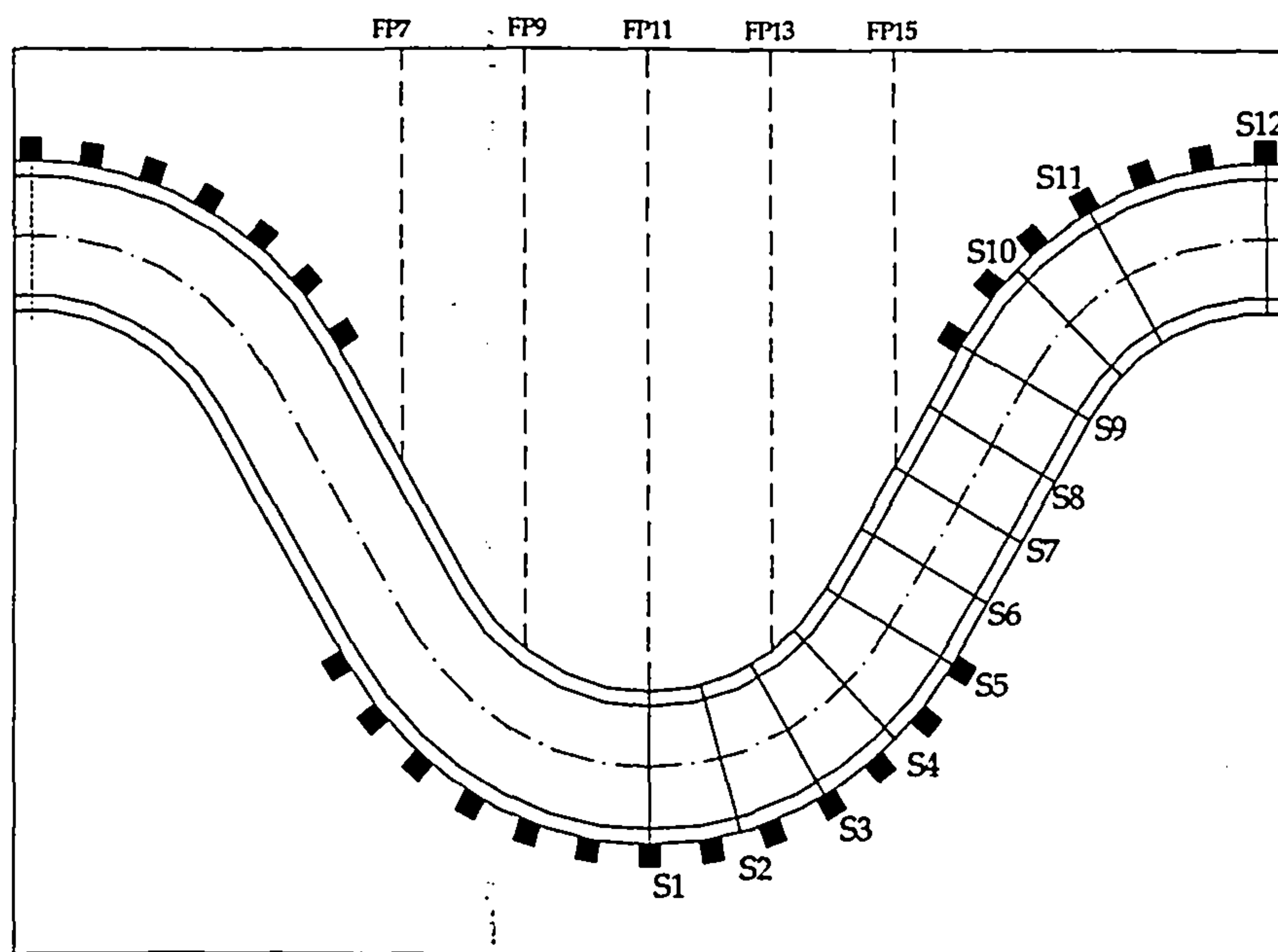


**Figure 3.30: Location details of the measurement sections S1 to S12 in the main channel and sections FP7, FP9, FP11, FP13 and FP15 on the floodplain for *Case M Apex Block***



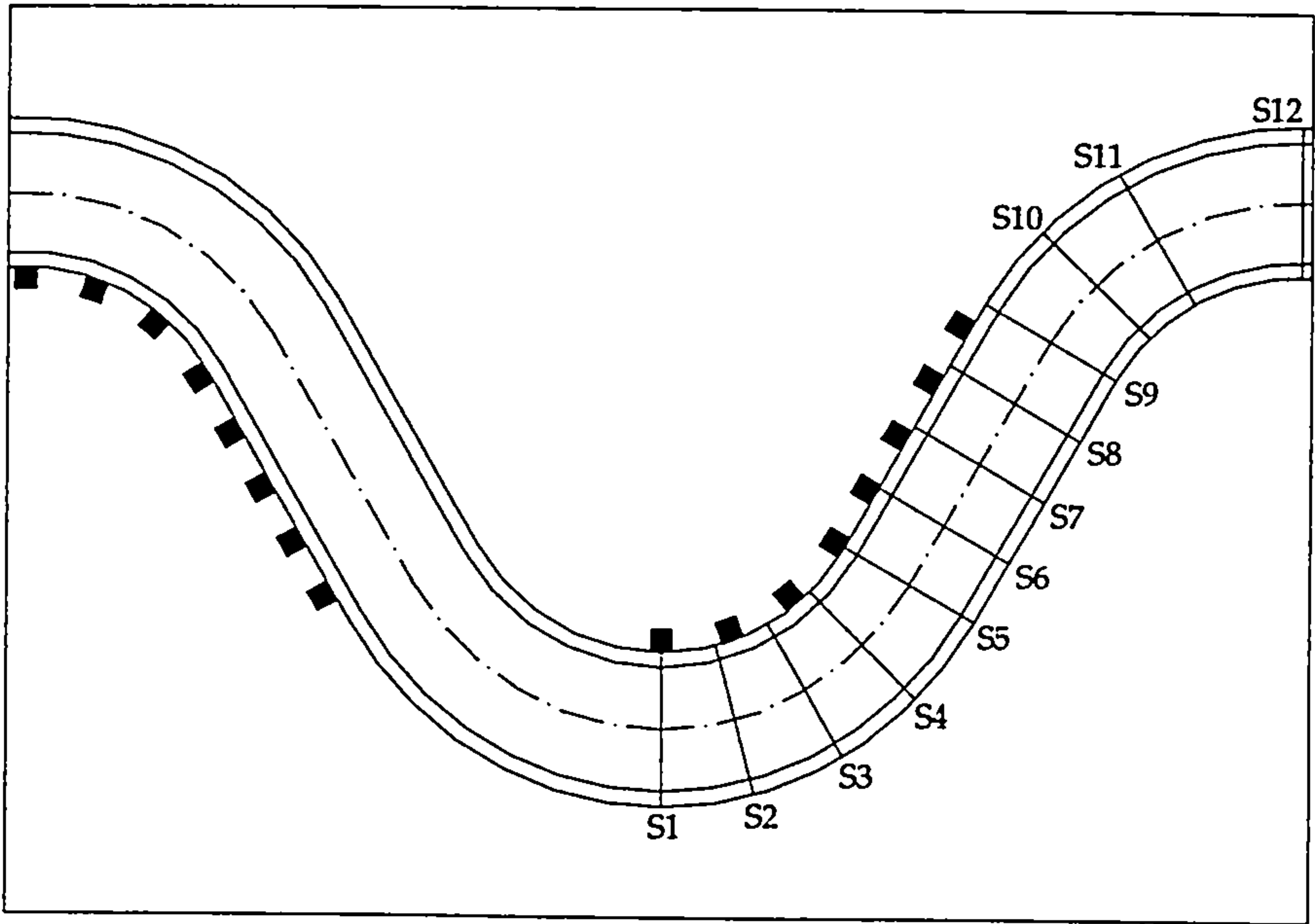


**Figure 3.31:** Location details of the measurement sections S1 to 12 for *Case N Cross-over Block*



# Chapter 4

## 4.0 Results of Stage-Discharge, Flow Resistance, Bedforms and Sediment Transport in Compound Meandering Channels

### 4.1 Introduction

The aims of this chapter are to investigate the stage-discharge, flow resistance, drag force and bedforms in the non-vegetated and vegetated floodplain in compound meandering channels as well as to carry out the influence of using different arrangements and vegetation density on the floodplain resistance to sediment transport subjected to overbank flow conditions in meandering channels. This chapter presents the results of the experiments undertaken in order to investigate the stage-discharge, the resistance to flow, bedforms and sediment transport behaviours through rigid unsubmerged blocks. Stage-discharge curves of the fixed and mobile beds for both rectangular and trapezoidal cross-sections are compared. Manning's n friction factor and sediment transport are also discussed and related results are shown for eleven main arrangements of the blocks for both fixed and mobile-bed channels. A total of one hundred and sixty five tests were carried out in this phase of the experimental program. The details of flow condition and block arrangements can be found on Tables 4.1 to 4.11.

Table 4.1: Summary of experimental data for *Case A No Block* with a rectangular fixed-bed channel

Test No.	Flow Type	Q (m <sup>3</sup> /s)	H (m)	A (m <sup>2</sup> )	P (m)	R (m)	v (m/s)	Dr	Manning's n
A.1	Overbank	0.0051	0.0534	0.0480	2.5067	0.0192	0.1058	0.25	0.0303
A.2	Overbank	0.0086	0.0600	0.0639	2.5199	0.0254	0.1347	0.33	0.0287
A.3	Overbank	0.0117	0.0640	0.0735	2.5279	0.0291	0.1596	0.37	0.0265
A.4	Overbank	0.0149	0.0678	0.0826	2.5355	0.0326	0.1798	0.41	0.0254
A.5	Overbank	0.0180	0.0705	0.0892	2.5410	0.0351	0.2017	0.43	0.0238
A.6	Overbank	0.0203	0.0726	0.0941	2.5451	0.0370	0.2161	0.45	0.0230
A.7	Overbank	0.0227	0.0747	0.0993	2.5494	0.0389	0.2285	0.46	0.0225
A.8	Overbank	0.0294	0.0787	0.1089	2.5574	0.0426	0.2703	0.49	0.0202



Table 4.2: Summary of experimental data for Case B Apex Block with a rectangular fixed-bed channel

(a) Case B1 with higher density of blocks on floodplains

Test No.	Q (m³/s)	H (m)	A (m²)	v (m/s)	A <sub>p</sub> (m²)	V <sub>den</sub>	F <sub>D</sub> (N)	Dr	Manning's n
B1.1	0.0051	0.0588	0.0612	0.0833	0.2502	0.6355	0.67	0.32	0.0450
B1.2	0.0093	0.0651	0.0762	0.1216	0.3330	0.6797	1.33	0.39	0.0356
B1.3	0.0127	0.0712	0.0908	0.1403	0.4137	0.7087	2.08	0.44	0.0346
B1.4	0.0165	0.0759	0.1021	0.1619	0.4764	0.7255	2.95	0.47	0.0323
B1.5	0.0204	0.0805	0.1132	0.1805	0.5381	0.7388	4.11	0.50	0.0310
B1.6	0.0240	0.0865	0.1276	0.1881	0.6175	0.7525	5.53	0.54	0.0321
B1.7	0.0298	0.0945	0.1469	0.2027	0.7244	0.7667	8.12	0.58	0.0326

(b) Case B2 with middle density of blocks on floodplains

Test No.	Q (m³/s)	H (m)	A (m²)	v (m/s)	A <sub>p</sub> (m²)	V <sub>den</sub>	F <sub>D</sub> (N)	Dr	Manning's n
B2.1	0.0062	0.0566	0.0558	0.1107	0.1147	0.3192	0.32	0.29	0.0319
B2.2	0.0094	0.0622	0.0692	0.1356	0.1532	0.3440	0.57	0.36	0.0300
B2.3	0.0131	0.0686	0.0845	0.1554	0.1973	0.3627	0.96	0.42	0.0298
B2.4	0.0156	0.0722	0.0934	0.1676	0.2226	0.3707	1.22	0.45	0.0295
B2.5	0.0188	0.0762	0.1029	0.1825	0.2500	0.3778	1.53	0.48	0.0288
B2.6	0.0234	0.0818	0.1162	0.2016	0.2884	0.3858	1.85	0.51	0.0282
B2.7	0.0305	0.0890	0.1336	0.2280	0.3384	0.3938	2.53	0.55	0.0273

(c) Case B3 with lower density of blocks on floodplains

Test No.	Q (m³/s)	H (m)	A (m²)	v (m/s)	A <sub>p</sub> (m²)	V <sub>den</sub>	F <sub>D</sub> (N)	Dr	Manning's n
B3.1	0.0055	0.0538	0.0490	0.1117	0.0511	0.1622	0.19	0.26	0.0290
B3.2	0.0093	0.0611	0.0666	0.1398	0.0784	0.1830	0.36	0.35	0.0284
B3.3	0.0125	0.0672	0.0813	0.1540	0.1011	0.1935	0.59	0.40	0.0293
B3.4	0.0156	0.0715	0.0916	0.1708	0.1171	0.1988	0.90	0.44	0.0285
B3.5	0.0188	0.0749	0.0998	0.1882	0.1298	0.2023	1.05	0.47	0.0274
B3.6	0.0227	0.0797	0.1114	0.2037	0.1478	0.2063	1.28	0.50	0.0272
B3.7	0.0297	0.0859	0.1261	0.2356	0.1707	0.2103	1.79	0.53	0.0254

Table 4.3: Summary of experimental data for Case C Cross-over Block with a rectangular fixed-bed channel

(a) Case C1 with higher density of blocks on floodplains

Test No.	Q (m³/s)	H (m)	A (m²)	v (m/s)	A <sub>p</sub> (m²)	V <sub>den</sub>	F <sub>D</sub> (N)	Dr	Manning's n
C1.1	0.0058	0.0527	0.0466	0.1243	0.2010	0.6663	0.82	0.24	0.0252
C1.2	0.0087	0.0602	0.0645	0.1351	0.3186	0.7631	1.53	0.34	0.0287
C1.3	0.0128	0.0666	0.0799	0.1606	0.4203	0.8119	2.84	0.40	0.0278
C1.4	0.0156	0.0719	0.0925	0.1691	0.5031	0.8396	3.78	0.44	0.0290
C1.5	0.0192	0.0757	0.1016	0.1887	0.5628	0.8553	5.26	0.47	0.0276
C1.6	0.0231	0.0793	0.1102	0.2093	0.6198	0.8679	7.13	0.50	0.0263
C1.7	0.0295	0.0846	0.1303	0.2266	0.7046	0.8833	10.64	0.53	0.0246



(b) Case C2 with middle density of blocks on floodplains

Test No.	$Q$ (m <sup>3</sup> /s)	$H$ (m)	$A$ (m <sup>2</sup> )	$v$ (m/s)	$A_p$ (m <sup>2</sup> )	$V_{den}$	$F_D$ (N)	$Dr$	Manning's $n$
C2.1	0.0055	0.0528	0.0467	0.1173	0.1039	0.3393	0.37	0.24	0.0268
C2.2	0.0090	0.0606	0.0653	0.1377	0.1670	0.3898	0.82	0.34	0.0285
C2.3	0.0125	0.0665	0.0796	0.1572	0.2153	0.4125	1.38	0.40	0.0283
C2.4	0.0156	0.0714	0.0915	0.1711	0.2553	0.4259	1.94	0.44	0.0285
C2.5	0.0191	0.0754	0.1010	0.1890	0.2876	0.4344	2.66	0.47	0.0275
C2.6	0.0231	0.0799	0.1118	0.2065	0.3240	0.4423	3.58	0.50	0.0269
C2.7	0.0298	0.0865	0.1275	0.2335	0.3774	0.4515	5.34	0.54	0.0258

(c) Case C3 with lower density of blocks on floodplains

Test No.	$Q$ (m <sup>3</sup> /s)	$H$ (m)	$A$ (m <sup>2</sup> )	$v$ (m/s)	$A_p$ (m <sup>2</sup> )	$V_{den}$	$F_D$ (N)	$Dr$	Manning's $n$
C3.1	0.0055	0.0530	0.0473	0.1158	0.0534	0.1822	0.20	0.25	0.0274
C3.2	0.0087	0.0597	0.0633	0.1371	0.0808	0.2058	0.42	0.33	0.0280
C3.3	0.0125	0.0662	0.0788	0.1589	0.1072	0.2194	0.74	0.40	0.0278
C3.4	0.0156	0.0706	0.0894	0.1750	0.1254	0.2261	1.05	0.43	0.0274
C3.5	0.0192	0.0747	0.0992	0.1933	0.1420	0.2309	1.45	0.46	0.0266
C3.6	0.0227	0.0788	0.1090	0.2081	0.1589	0.2349	1.88	0.49	0.0262
C3.7	0.0290	0.0849	0.1238	0.2339	0.1841	0.2397	2.76	0.53	0.0253

Table 4.4: Summary of experimental data for Case D Combined Apex and Cross-over Block with a rectangular fixed-bed channel

(a) Case D1 with higher density of blocks on floodplains

Test No.	$Q$ (m <sup>3</sup> /s)	$H$ (m)	$A$ (m <sup>2</sup> )	$v$ (m/s)	$A_p$ (m <sup>2</sup> )	$V_{den}$	$F_D$ (N)	$Dr$	Manning's $n$
D1.1	0.0055	0.0559	0.0541	0.1011	0.3280	1.3092	1.23	0.28	0.0342
D1.2	0.0092	0.0673	0.0814	0.1124	0.5626	1.4931	2.61	0.41	0.0402
D1.3	0.0117	0.0770	0.1048	0.1120	0.7634	1.5746	3.52	0.48	0.0475
D1.4	0.0156	0.0909	0.1381	0.1133	1.0504	1.6431	4.95	0.56	0.0561
D1.5	0.0196	0.0998	0.1596	0.1225	1.2350	1.6721	6.81	0.60	0.0568
D1.6	0.0235	0.1099	0.1837	0.1282	1.4425	1.6966	8.70	0.64	0.0593
D1.7	0.0302	0.1212	0.2108	0.1431	1.6759	1.7174	12.60	0.67	0.0579

(b) Case D2 with middle density of blocks on floodplains

Test No.	$Q$ (m <sup>3</sup> /s)	$H$ (m)	$A$ (m <sup>2</sup> )	$v$ (m/s)	$A_p$ (m <sup>2</sup> )	$V_{den}$	$F_D$ (N)	$Dr$	Manning's $n$
D2.1	0.0058	0.0556	0.0534	0.1084	0.1608	0.6508	0.69	0.28	0.0317
D2.2	0.0088	0.0648	0.0755	0.1160	0.2559	0.7323	1.27	0.38	0.0371
D2.3	0.0125	0.0743	0.0983	0.1273	0.3541	0.7780	2.11	0.46	0.0401
D2.4	0.0156	0.0815	0.1155	0.1355	0.4279	0.8005	2.88	0.51	0.0418
D2.5	0.0188	0.0869	0.1285	0.1461	0.4838	0.8135	3.79	0.54	0.0415
D2.6	0.0231	0.0965	0.1515	0.1523	0.5827	0.8311	4.97	0.59	0.0442
D2.7	0.0297	0.1069	0.1764	0.1681	0.6901	0.8450	7.16	0.63	0.0441



(c) Case D3 with lower density of blocks on floodplains

Test No.	$Q$ (m <sup>3</sup> /s)	$H$ (m)	$A$ (m <sup>2</sup> )	$v$ (m/s)	$A_p$ (m <sup>2</sup> )	$V_{den}$	$F_D$ (N)	$Dr$	Manning's $n$
D3.1	0.0059	0.0547	0.0514	0.1142	0.0794	0.3317	0.38	0.27	0.0293
D3.2	0.0095	0.0633	0.0718	0.1328	0.1254	0.3745	0.81	0.37	0.0314
D3.3	0.0125	0.0684	0.0841	0.1488	0.1529	0.3902	1.24	0.42	0.0310
D3.4	0.0161	0.0741	0.0977	0.1649	0.1835	0.4029	1.82	0.46	0.0309
D3.5	0.0197	0.0803	0.1126	0.1750	0.2170	0.4134	2.42	0.50	0.0318
D3.6	0.0231	0.0857	0.1257	0.1836	0.2463	0.4205	3.03	0.53	0.0326
D3.7	0.0290	0.0946	0.1470	0.1970	0.2942	0.4294	4.16	0.58	0.0335

Table 4.5: Summary of experimental data for Case E No Block with a rectangular mobile-bed channel

Test No.	Flow Type	$Q$ (m <sup>3</sup> /s)	$H$ (m)	$Dr$	$v$ (m/s)	$q_b$ (g/s)	$q_b/q_{bf}$	Manning's $n$
E1.1	Bankful	0.0036	0.0479	0.16	0.1019	0.00782	1.00000	0.0255
E1.2	Overbank	0.0063	0.0589	0.32	0.1029	0.00426	0.54438	0.0365
E1.3	Overbank	0.0095	0.0657	0.39	0.1219	0.00074	0.09467	0.0359
E1.4	Overbank	0.0126	0.0704	0.43	0.1416	0.00056	0.07101	0.0338
E1.5	Overbank	0.0173	0.0748	0.47	0.1735	0.00065	0.08284	0.0297
E1.6	Overbank	0.0208	0.0780	0.49	0.1939	0.00403	0.51479	0.0279
E1.7	Overbank	0.0251	0.0805	0.50	0.2218	0.01486	1.89941	0.0252
E1.8	Overbank	0.0296	0.0818	0.51	0.2545	0.05333	6.81657	0.0223

Table 4.6: Summary of experimental data for Case F Apex Block with a rectangular mobile-bed channel

(a) Case F1 with higher density of blocks on floodplains

Test No.	$Q$ (m <sup>3</sup> /s)	$H$ (m)	$Dr$	$v$ (m/s)	$A_p$ (m <sup>2</sup> )	$V_{den}$	$F_D$ (N)	$q_b$ (g/s)	$q_b/q_{bf}$	Manning's $n$
F1.1	0.0063	0.0601	0.33	0.0973	0.0643	0.6464	0.67	0.00069	0.08876	0.0399
F1.2	0.0095	0.0685	0.42	0.1121	0.0844	0.6973	1.26	0.00065	0.08282	0.0412
F1.3	0.0125	0.0750	0.47	0.1253	0.0999	0.7226	1.93	0.00065	0.08282	0.0412
F1.4	0.0156	0.0837	0.52	0.1294	0.1209	0.7465	2.57	0.00190	0.24258	0.0450
F1.5	0.0196	0.0930	0.57	0.1366	0.1432	0.7642	3.47	0.00190	0.24258	0.0476
F1.6	0.0227	0.1008	0.60	0.1401	0.1619	0.7753	4.19	0.00500	0.63905	0.0501
F1.7	0.0294	0.1091	0.63	0.1620	0.1817	0.7846	6.36	0.01843	2.35503	0.0466

(b) Case F2 with higher density of blocks on floodplains

Test No.	$Q$ (m <sup>3</sup> /s)	$H$ (m)	$Dr$	$v$ (m/s)	$A_p$ (m <sup>2</sup> )	$V_{den}$	$F_D$ (N)	$q_b$ (g/s)	$q_b/q_{bf}$	Manning's $n$
F2.1	0.0067	0.0613	0.35	0.0999	0.1468	0.3406	0.39	0.00069	0.08876	0.0399
F2.2	0.0094	0.0671	0.40	0.1157	0.1873	0.3591	0.66	0.00065	0.08282	0.0390
F2.3	0.0126	0.0724	0.45	0.1342	0.2238	0.3711	1.07	0.00065	0.08282	0.0369
F2.4	0.0160	0.0797	0.50	0.1438	0.2744	0.3831	1.50	0.00190	0.24258	0.0385
F2.5	0.0187	0.0841	0.52	0.1537	0.3042	0.3886	1.90	0.00190	0.24258	0.0381
F2.6	0.0228	0.0930	0.57	0.1595	0.3658	0.3974	2.46	0.00530	0.67740	0.0407
F2.7	0.0294	0.1034	0.61	0.1752	0.4377	0.4048	3.55	0.02361	3.01775	0.0411



(c) Case F3 with higher density of blocks on floodplains

Test No.	Q (m³/s)	H (m)	Dr	v (m/s)	A <sub>p</sub> (m²)	V <sub>den</sub>	F <sub>D</sub> (N)	q <sub>b</sub> (g/s)	q <sub>b</sub> /q <sub>bf</sub>	Manning's n
F3.1	0.0067	0.0610	0.34	0.1009	0.0780	0.1828	0.21	0.00069	0.08876	0.0392
F3.2	0.0094	0.0673	0.41	0.1150	0.1016	0.1936	0.36	0.00065	0.08282	0.0393
F3.3	0.0126	0.0728	0.45	0.1328	0.1220	0.2002	0.57	0.00065	0.08282	0.0375
F3.4	0.0160	0.0766	0.48	0.1540	0.1362	0.2038	0.85	0.00190	0.24258	0.0344
F3.5	0.0187	0.0819	0.51	0.1604	0.1559	0.2079	1.06	0.00190	0.24258	0.0355
F3.6	0.0228	0.0897	0.55	0.1686	0.1850	0.2124	1.39	0.01000	1.27811	0.0372
F3.7	0.0298	0.0988	0.60	0.1898	0.2187	0.2164	2.08	0.08481	10.84024	0.0363

Table 4.7: Summary of experimental data for Case G Cross-over Block with a rectangular mobile-bed channel

(a) Case G1 with higher density of blocks on floodplains

Test No.	Q (m³/s)	H (m)	Dr	v (m/s)	A <sub>p</sub> (m²)	V <sub>den</sub>	F <sub>D</sub> (N)	q <sub>b</sub> (g/s)	q <sub>b</sub> /q <sub>bf</sub>	Manning's n
G1.1	0.0058	0.0573	0.30	0.1008	0.2725	0.7324	0.73	0.01907	2.43786	0.0357
G1.2	0.0087	0.0656	0.39	0.1199	0.4042	0.8055	1.34	0.00620	0.79294	0.0389
G1.3	0.0128	0.0750	0.47	0.1284	0.5521	0.8527	2.39	0.00065	0.08282	0.0402
G1.4	0.0156	0.0832	0.52	0.1335	0.6814	0.8794	3.06	0.00190	0.24258	0.0443
G1.5	0.0192	0.0924	0.57	0.1329	0.8277	0.9007	3.96	0.00727	0.92906	0.0478
G1.6	0.0231	0.0982	0.59	0.1483	0.9183	0.9109	5.30	0.02400	3.06746	0.0462
G1.7	0.0295	0.1056	0.62	0.1702	1.0360	0.9216	7.88	0.05200	6.64615	0.0431

(b) Case G2 with higher density of blocks on floodplains

Test No.	Q (m³/s)	H (m)	Dr	v (m/s)	A <sub>p</sub> (m²)	V <sub>den</sub>	F <sub>D</sub> (N)	q <sub>b</sub> (g/s)	q <sub>b</sub> /q <sub>bf</sub>	Manning's n
G2.1	0.0063	0.0601	0.33	0.0984	0.1632	0.3877	0.41	0.00333	0.42599	0.0394
G2.2	0.0095	0.0641	0.38	0.1280	0.1958	0.4044	0.83	0.00232	0.29588	0.0332
G2.3	0.0126	0.0696	0.43	0.1446	0.2403	0.4213	1.30	0.00120	0.15388	0.0326
G2.4	0.0165	0.0761	0.47	0.1607	0.2931	0.4357	1.96	0.00116	0.14788	0.0327
G2.5	0.0204	0.0815	0.51	0.1764	0.3371	0.4448	2.72	0.00218	0.27812	0.0321
G2.6	0.0239	0.0884	0.55	0.1811	0.3928	0.4537	3.34	0.00273	0.34905	0.0341
G2.7	0.0298	0.0992	0.60	0.1884	0.4807	0.4640	4.42	0.01236	1.57987	0.0367

(c) Case G3 with higher density of blocks on floodplains

Test No.	Q (m³/s)	H (m)	Dr	v (m/s)	A <sub>p</sub> (m²)	V <sub>den</sub>	F <sub>D</sub> (N)	q <sub>b</sub> (g/s)	q <sub>b</sub> /q <sub>bf</sub>	Manning's n
G3.1	0.006322	0.0617	0.35	0.0927	0.0891	0.2107	0.21	0.00370	0.47341	0.0433
G3.2	0.009458	0.0649	0.38	0.1245	0.1023	0.2173	0.44	0.00079	0.10059	0.0346
G3.3	0.012586	0.0702	0.43	0.1419	0.1241	0.2256	0.69	0.00181	0.23083	0.0336
G3.4	0.016397	0.0763	0.48	0.1588	0.1490	0.2327	1.03	0.00144	0.18341	0.0331
G3.5	0.020508	0.0830	0.52	0.1718	0.1765	0.2384	1.43	0.00162	0.20705	0.0336
G3.6	0.025102	0.0891	0.55	0.1872	0.2016	0.2425	1.94	0.00208	0.26623	0.0332
G3.7	0.029775	0.0986	0.59	0.1900	0.2402	0.2472	2.38	0.00500	0.63905	0.0361



Table 4.8: Summary of experimental data for *Case H Combined Apex and Cross-over Blocks* with a rectangular mobile-bed channel

(a) *Case H1* with higher density of blocks on floodplains

Test No.	$Q$ (m <sup>3</sup> /s)	$H$ (m)	Dr	$v$ (m/s)	$A_p$ (m <sup>2</sup> )	$V_{den}$	$F_D$ (N)	$q_b$ (g/s)	$q_b/q_{bf}$	Manning's n
H1.1	0.0067	0.0644	0.38	0.0898	0.2675	1.4594	1.49	0.00125	0.15976	0.0475
H1.2	0.0106	0.0807	0.50	0.0935	0.3786	1.5969	2.70	0.00069	0.08876	0.0599
H1.3	0.0126	0.0888	0.55	0.0946	0.4644	1.6349	3.31	0.00060	0.07692	0.0655
H1.4	0.0157	0.0986	0.59	0.1003	0.5803	1.6686	4.47	0.00051	0.06509	0.0685
H1.5	0.0187	0.1097	0.64	0.1020	0.7037	1.6962	5.50	0.00069	0.08876	0.0744
H1.6	0.0220	0.1175	0.66	0.1088	0.8073	1.7111	6.96	0.00065	0.08284	0.0741
H1.7	0.0294	0.1294	0.69	0.1278	0.9172	1.7294	11.06	0.00106	0.13609	0.0685

(b) *Case H2* with higher density of blocks on floodplains

Test No.	$Q$ (m <sup>3</sup> /s)	$H$ (m)	Dr	$v$ (m/s)	$A_p$ (m <sup>2</sup> )	$V_{den}$	$F_D$ (N)	$q_b$ (g/s)	$q_b/q_{bf}$	Manning's n
H2.1	0.0071	0.0616	0.35	0.1044	0.2230	0.7101	0.89	0.00256	0.32663	0.0385
H2.2	0.0106	0.0710	0.44	0.1176	0.3199	0.7647	1.63	0.00069	0.08876	0.0411
H2.3	0.0126	0.0773	0.48	0.1193	0.3849	0.7883	2.01	0.00065	0.08284	0.0448
H2.4	0.0157	0.0896	0.55	0.1164	0.5117	0.8191	2.55	0.00060	0.07692	0.0537
H2.5	0.0187	0.0977	0.59	0.1210	0.5959	0.8330	3.21	0.00060	0.07692	0.0564
H2.6	0.0220	0.1075	0.63	0.1234	0.6968	0.8457	3.90	0.00216	0.27669	0.0604
H2.7	0.0294	0.1189	0.66	0.1435	0.8140	0.8568	6.15	0.00774	0.98935	0.0568

(c) *Case H3* with higher density of blocks on floodplains

Test No.	$Q$ (m <sup>3</sup> /s)	$H$ (m)	Dr	$v$ (m/s)	$A_p$ (m <sup>2</sup> )	$V_{den}$	$F_D$ (N)	$q_b$ (g/s)	$q_b/q_{bf}$	Manning's n
H3.1	0.0071	0.0629	0.36	0.0999	0.1232	0.3731	0.45	0.00269	0.34438	0.0413
H3.2	0.0106	0.0711	0.44	0.1173	0.1676	0.3968	0.84	0.00069	0.08876	0.0413
H3.3	0.0126	0.0748	0.47	0.1265	0.1875	0.4043	1.09	0.00069	0.08876	0.0407
H3.4	0.0157	0.0837	0.52	0.1300	0.2354	0.4180	1.45	0.00051	0.06509	0.0448
H3.5	0.0187	0.0888	0.55	0.1405	0.2630	0.4239	1.89	0.00056	0.07101	0.0442
H3.6	0.0220	0.0971	0.59	0.1436	0.3078	0.4314	2.31	0.00360	0.46036	0.0472
H3.7	0.0294	0.1066	0.62	0.1675	0.3588	0.4380	3.67	0.01297	1.65799	0.0442

Table 4.9: Summary of experimental data for *Case L No Block* with a trapezoidal fixed-bed channel

Test No.	Flow Type	$Q$ (m <sup>3</sup> /s)	$H$ (m)	$A$ (m <sup>2</sup> )	$P$ (m)	$R$ (m)	$v$ (m/s)	Dr	Manning's n
L.1	Overbank	0.0047	0.05072	0.0401	2.5344	0.0158	0.1179	0.21	0.0244
L.2	Overbank	0.0069	0.05581	0.0523	2.5446	0.0206	0.1311	0.28	0.0260
L.3	Overbank	0.0110	0.06050	0.0636	2.5540	0.0249	0.1725	0.34	0.0225
L.4	Overbank	0.0156	0.06481	0.0739	2.5626	0.0289	0.2116	0.38	0.0202
L.5	Overbank	0.0188	0.06759	0.0806	2.5682	0.0314	0.2328	0.41	0.0194
L.6	Overbank	0.0231	0.07002	0.0864	2.5730	0.0336	0.2669	0.43	0.0177
L.7	Overbank	0.0302	0.07441	0.0970	2.5818	0.0376	0.3115	0.46	0.0163



**Table 4.10:** Summary of experimental data for *Case M Apex Block* with a trapezoidal fixed-bed channel

Test No.	Flow Type	$Q$ (m <sup>3</sup> /s)	$H$ (m)	$A$ (m <sup>2</sup> )	$P$ (m)	$R$ (m)	$v$ (m/s)	Dr	Manning's n
M.1	Overbank	0.0046	0.0508	0.0404	2.5346	0.0159	0.1145	0.21	0.0247
M.2	Overbank	0.0071	0.0568	0.0547	2.5466	0.0215	0.1301	0.30	0.0266
M.3	Overbank	0.0113	0.0621	0.0675	2.5572	0.0264	0.1675	0.36	0.0237
M.4	Overbank	0.0160	0.0688	0.0834	2.5705	0.0325	0.1921	0.42	0.0237
M.5	Overbank	0.0196	0.0743	0.0966	2.5815	0.0374	0.2024	0.46	0.0247
M.6	Overbank	0.0227	0.0778	0.1052	2.5886	0.0406	0.2157	0.49	0.0245
M.7	Overbank	0.0257	0.0804	0.1114	2.5938	0.0429	0.2310	0.50	0.0237
M.8	Overbank	0.0305	0.0850	0.1225	2.6031	0.0471	0.2486	0.53	0.0235

**Table 4.11:** Summary of experimental data for *Case N Cross-over Block* with a trapezoidal fixed-bed channel

Test No.	Flow Type	$Q$ (m <sup>3</sup> /s)	$H$ (m)	$A$ (m <sup>2</sup> )	$P$ (m)	$R$ (m)	$v$ (m/s)	Dr	Manning's n
N.1	Overbank	0.0047	0.0507	0.0400	2.5344	0.0158	0.1168	0.21	0.0241
N.2	Overbank	0.0071	0.0566	0.0542	2.5462	0.0213	0.1306	0.29	0.0263
N.3	Overbank	0.0110	0.0611	0.0651	2.5552	0.0255	0.1685	0.35	0.0230
N.4	Overbank	0.0156	0.0660	0.0768	2.5650	0.0299	0.2031	0.39	0.0212
N.5	Overbank	0.0185	0.0698	0.0859	2.5726	0.0334	0.2153	0.43	0.0215
N.6	Overbank	0.0210	0.0728	0.0931	2.5786	0.0361	0.2255	0.45	0.0217
N.7	Overbank	0.0249	0.0756	0.0998	2.5842	0.0386	0.2494	0.47	0.0205
N.8	Overbank	0.0305	0.0789	0.1078	2.5908	0.0416	0.2826	0.49	0.0190

4.2 Stage-Discharge Curves

Accurate estimation of the relationship between the stage and discharge for rivers or floodplains, which are called the stage-discharge curves or rating curves, is very important. Stage-discharge curves are usually found by collecting data from gauges along rivers. These stage-discharge curves are critical for flood forecasting because they convert discharge at a certain point into stage values for issuing public forecasts. Stage-discharge curves need to be updated periodically due to changes in the beds of rivers and floodplains. These changes may be major, such as the case when the vegetation size and density varies significantly. In some events, the forecast flow or stage is beyond the uppermost values on the rating curve for that location. For these cases, the stage-discharge curve must be extended. The ability to find the relation between the discharge of the channel or floodplain and the depth of flow for given roughness conditions can help the forecasters to predict the stage-discharge values that are not included within the stage-discharge curves. This information can make it possible to update the stage-discharge values when the roughness characteristics of the



floodplain change. In this section, stage-discharge curves were plotted for eleven different cases (see Figures 4.1 to 4.10) in order to investigate the magnitude of the resistance to the flow and to pinpoint the factors and parameters influencing and controlling the flow. The effect of each arrangement and density of blocks on the stage-discharge curve was investigated. Figure 4.1 shows the relationship of discharge versus depth ( $H$ ) for *Case A No Block* and *Case B Apex Block*. It is clearly seen from the plots that the depth increases almost linearly with an increase in flow depth in all cases. For the Apex block *B1* case with 50 blocks for the highest density, the flow depth was found to be higher compared to apex block *Case B2* with 26 blocks, apex block *Case B3* with 14 blocks and without blocks. This indicates that, for this arrangement, a lower density of blocks conveyed water with greater efficiency as compared to higher densities.

For instance, in *Case A No Block* it is apparent that the stage-discharge curve gradually increases until the flow reaches a certain depth, and the stage-discharge curve tends approximately to a single, open-channel, stage-discharge curve. This is due to the influence of the main channel flow that is significantly reduced as the flow on the floodplain becomes dominant. At the beginning of the overbank flow it can be seen that stage-discharge curves for cases no block *A*, apex blocks *B2* and *B3* are approximately similar up to a discharge of about  $0.0085 \text{ m}^3/\text{s}$ . However, above this point the difference in stage between *Case A No Block* and the others increases as discharge increases. This indicates that the effect of blocks on flow is not significant up to a discharge of about  $0.0085 \text{ m}^3/\text{s}$ , and after this discharge, the effect of block becomes significant. This might be due to the arrangement with no blocks at the cross-over section in which slow moving floodplain flow interacts with the main-channel flow, which generates momentum exchange between the floodplain and the main channel and thus results in a reduction of flow in the main channel. These results also show the higher stages with the greater densities (see Figure 4.3). However, in *Case C Cross-over Block*, the results for the stage-discharge curves show very small discrepancies, as a result the different densities of blocks are insignificant (see Figure 4.2). In addition, at low overbank flow it can be seen that stage-discharge curves for cases no block *A*, cross-over blocks *C1*, *C2* and *C3* are crossing each other at a discharge of around  $0.0085 \text{ m}^3/\text{s}$  and at a flow depth of 60 mm. The reason is the lower momentum transfer from the floodplain to the main channel due to the continuous



blocks along the cross-over section compared to that for *Case A No Block*. In *Case D Combined Apex and Cross-over Block* (see Figure 4.3), it can be clearly seen that the stage becomes higher at the same discharge when the block density increases. As the block density increases until there are no gaps between the blocks, the block walls along the meandering channel effectively divide the main channel and the floodplain. From this figure, discharge becomes smaller than that with blocks. However, in the case of a straight compound channel, discharge becomes larger than that with walls along the floodplains, (division method). Hence, a simple division method is likely to substantially underestimate the discharge for the compound meandering channel.

Figures 4.4 to 4.6 show the stage-discharge curves for the mobile bed cases of three different arrangements of blocks on the floodplain banks. These results clearly depict the impact of the arrangements on the stage-discharge curve. The higher disparity of stages for the mobile bed cases are clearly seen for the higher density of blocks, especially for *Case H Combined Apex and Cross-over Block* with mobile bed compared to the other cases from the fixed bed results.

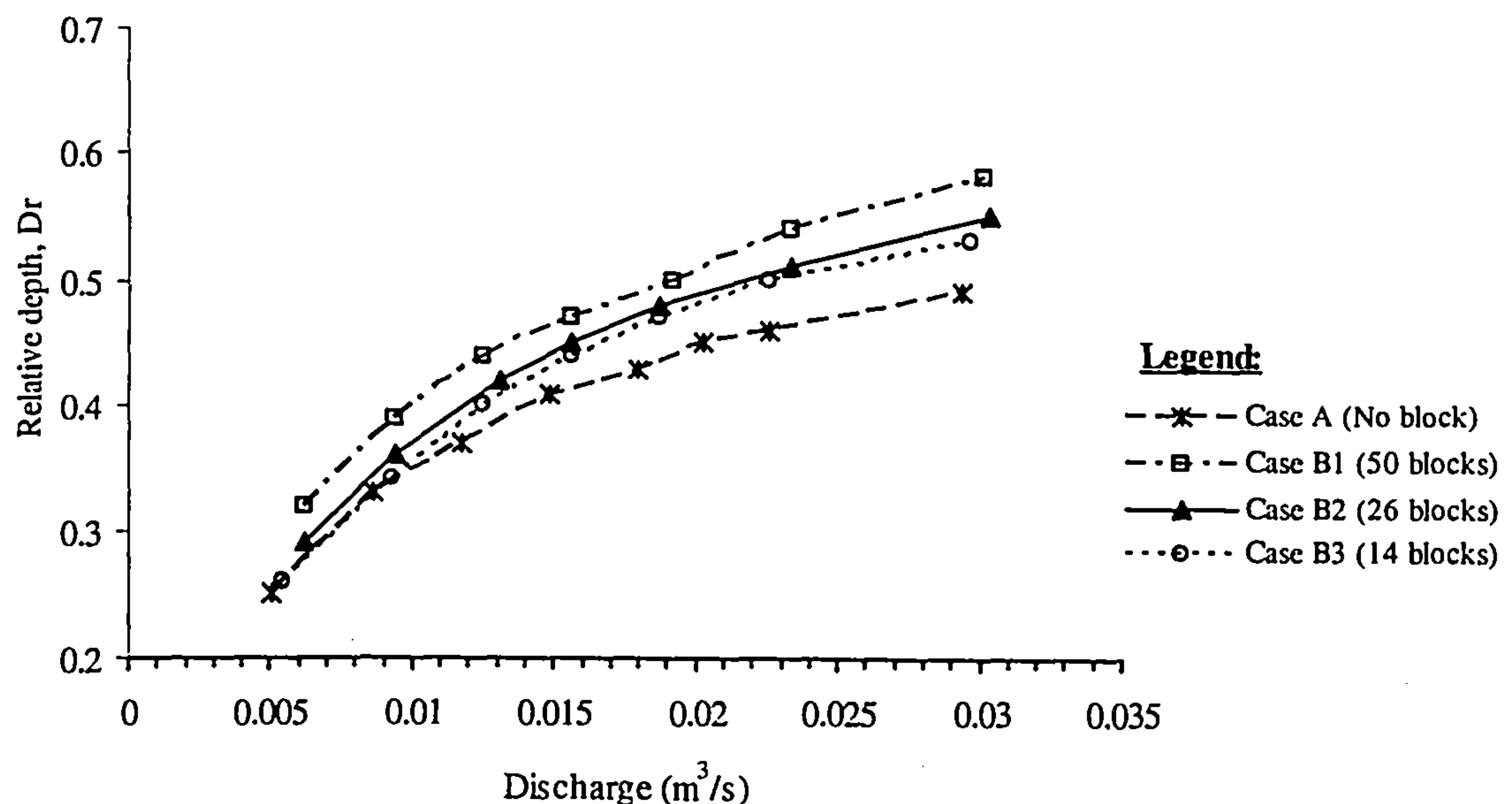


**Figure 4.1:** Stage-discharge relationships for fixed bed channel *Case A No Block* and *Case B Apex Block*



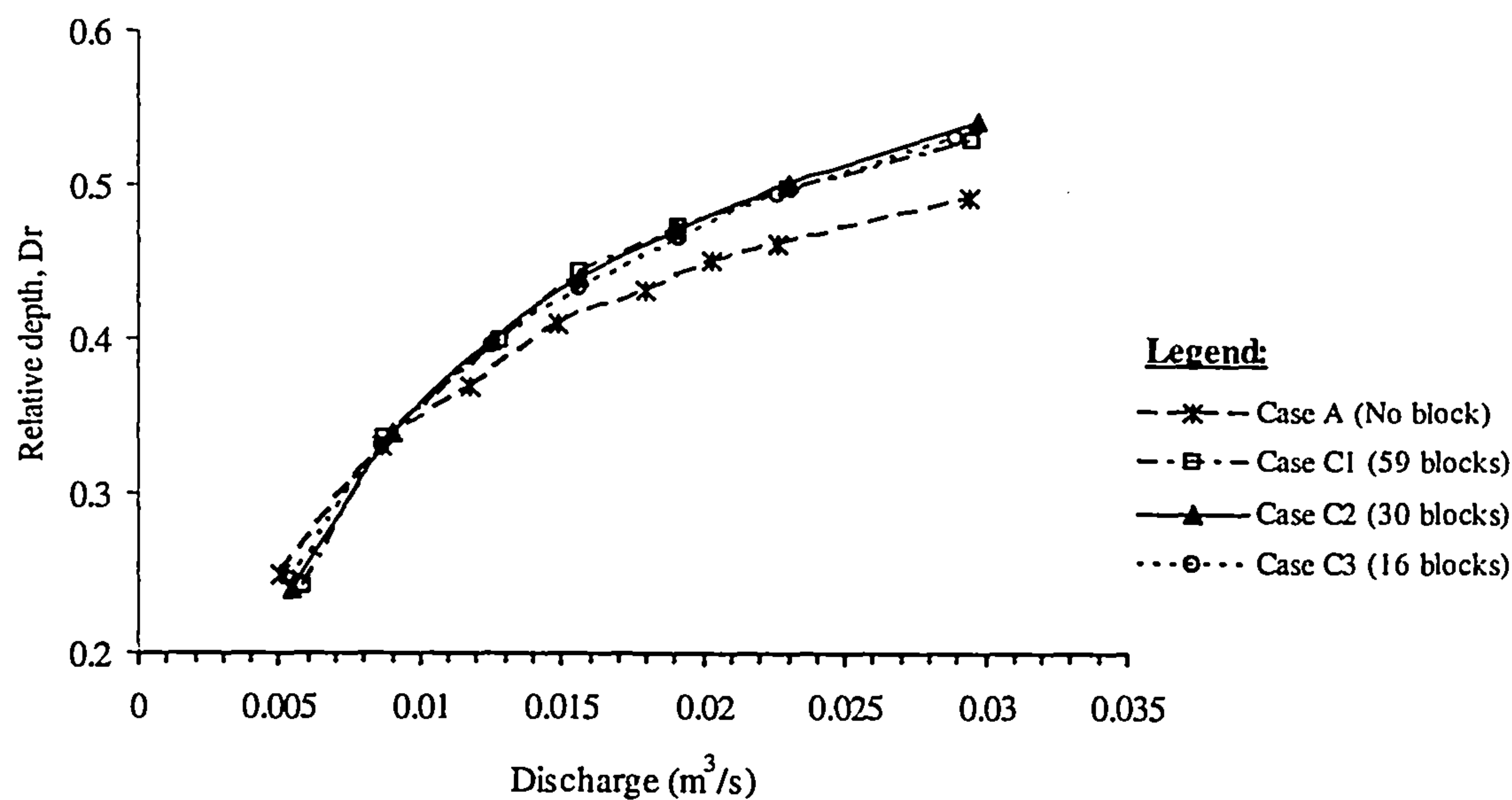


Figure 4.2: Stage-discharge relationships for fixed bed channel *Case A No Block* and *Case C Cross-over Block*

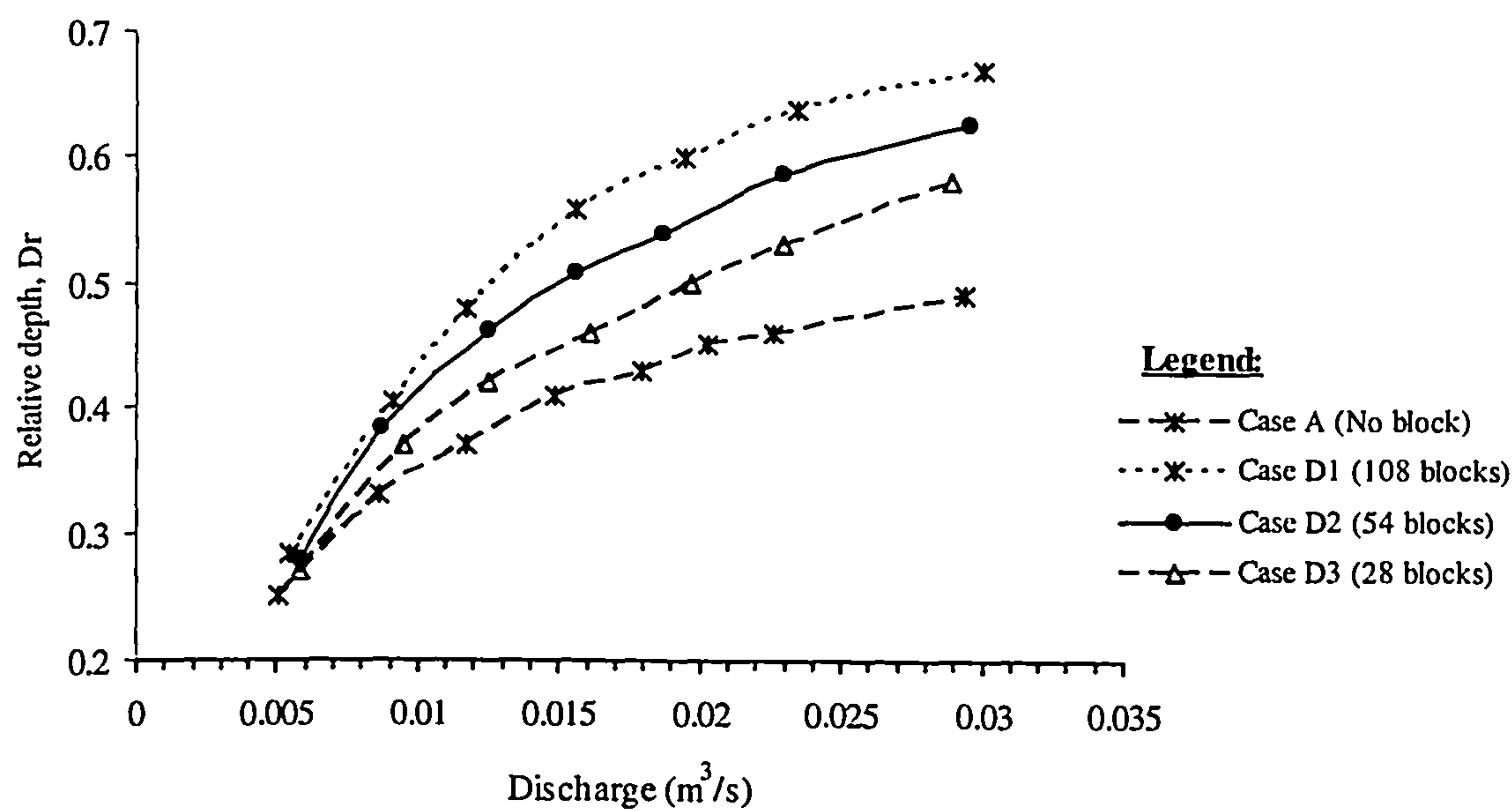


Figure 4.3: Stage-discharge relationships for fixed bed channel *Case A No Block* and *Case D Combined Apex and Cross-over Block*



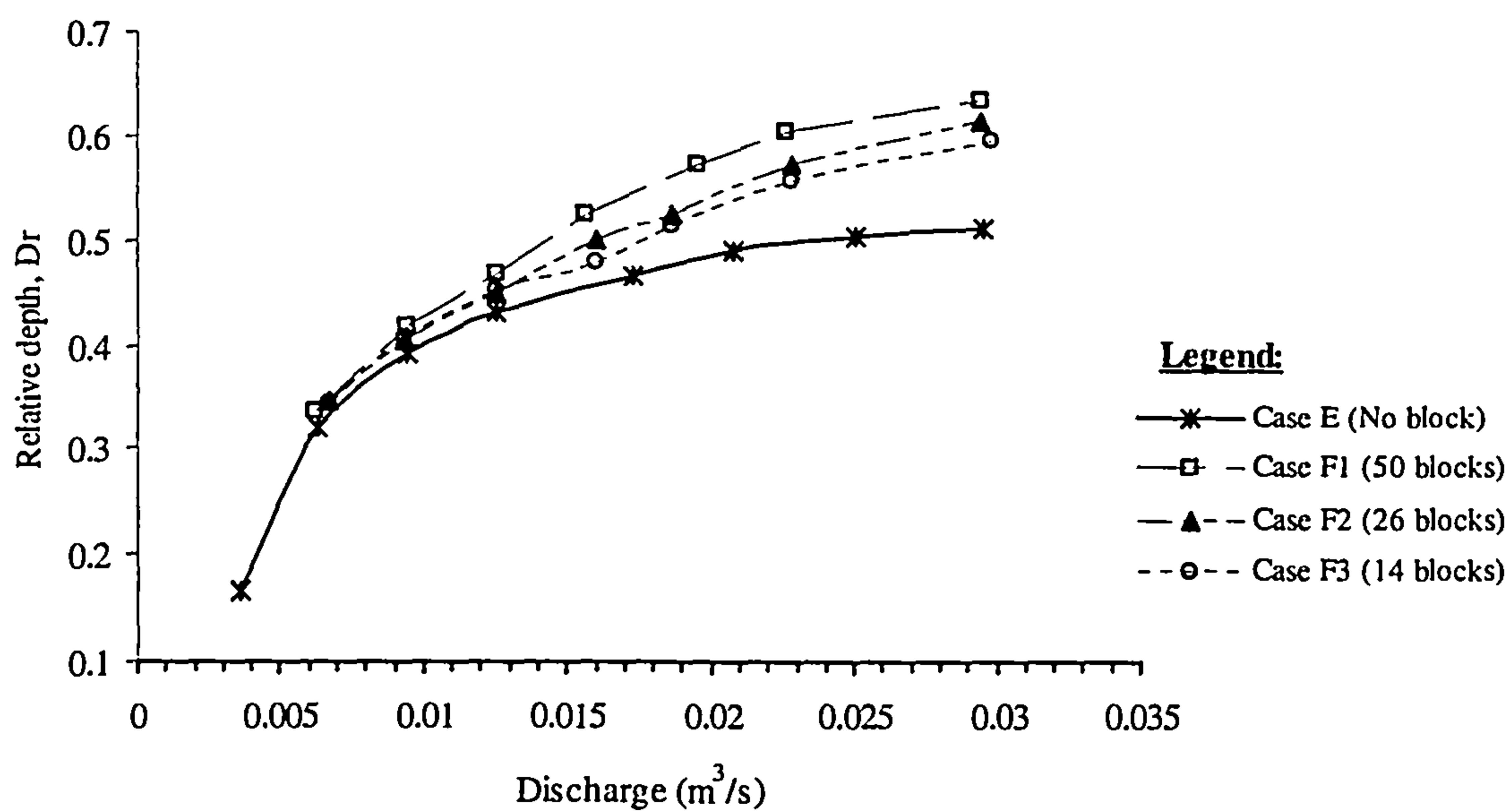


Figure 4.4: Comparison stage-discharge relationships for mobile bed channel Case E No Block and Case F Apex Block

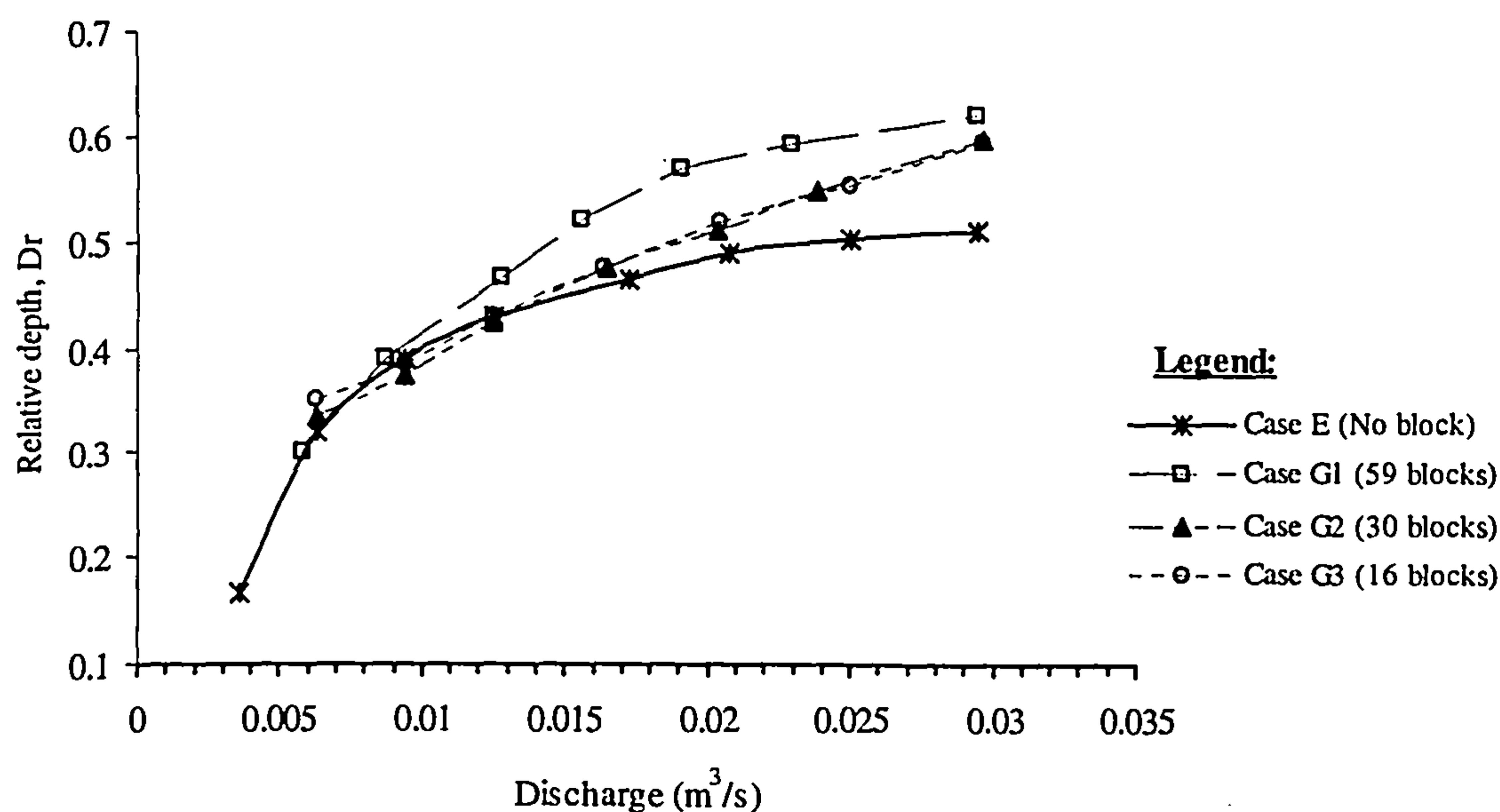
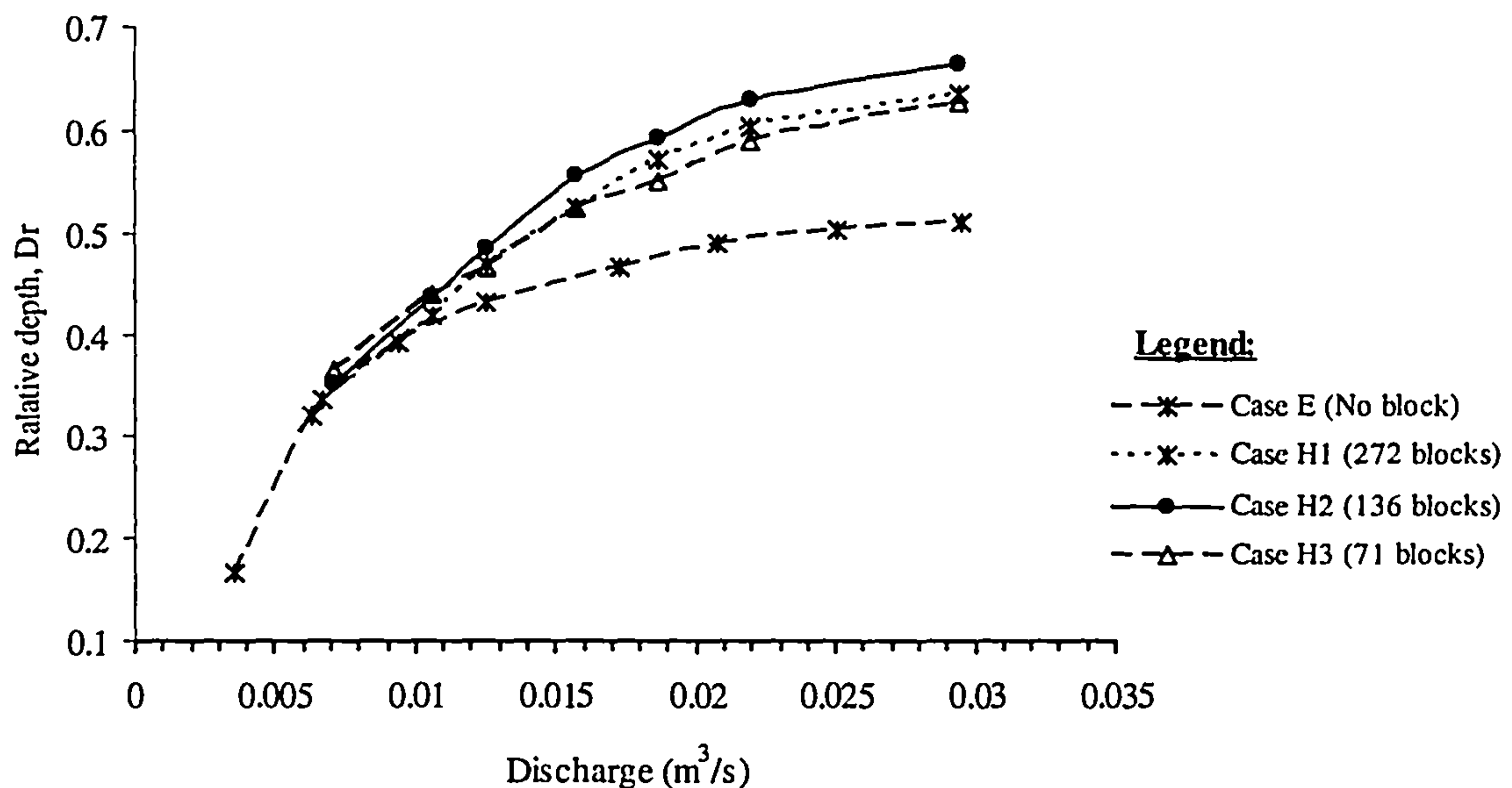


Figure 4.5: Comparison stage-discharge relationships for mobile bed channel Case E No Block and Case G Cross-over Block





**Figure 4.6:** Comparison stage-discharge relationships for mobile bed channel *Case E No Block* and *Case H Combined Apex and Cross-over Block*

Figure 4.7 also shows the comparison of the stage-discharge curves between the mobile bed channel and fixed bed channel with the different arrangements and densities of blocks. The figure shows that the rate of divergence between the fixed bed and mobile bed for different densities of blocks on the floodplain increases as the discharge increases (typically see the *C Cross-over Block* with fixed bed and *G Cross-over Block* with mobile bed cases). For the same density of blocks on the floodplains, the difference between cases *C Cross-over Block* with fixed bed and *G Cross-over Block* with mobile bed is smaller for shallow depths, which indicates an increase in friction due to mobile bedforms at greater water depths. However, the stage-discharge curves between the mobile bed channel for *Case E No Block* with mobile bed and the cross-over block with fixed bed channel for *Case C1* are very similar for  $0.016 < Q < 0.025$ . For  $0.016 > Q$ , the depth is higher for *Case E No Block* than for cross-over block *Case C1* and for  $Q > 0.025$ , smaller for *Case E No Block* with mobile bed than cross-over block *Case C1*. This indicates that the overall friction is larger for the mobile bed case at the shallow floodplain depth, which means that the effect of bedforms on the friction is dominant. In the middle water-depth region, the effects of bedform and blocks on the friction are the same, but above this region, the effect of the blocks dominates the friction, since the drag force caused by the blocks becomes larger as water depth increases.



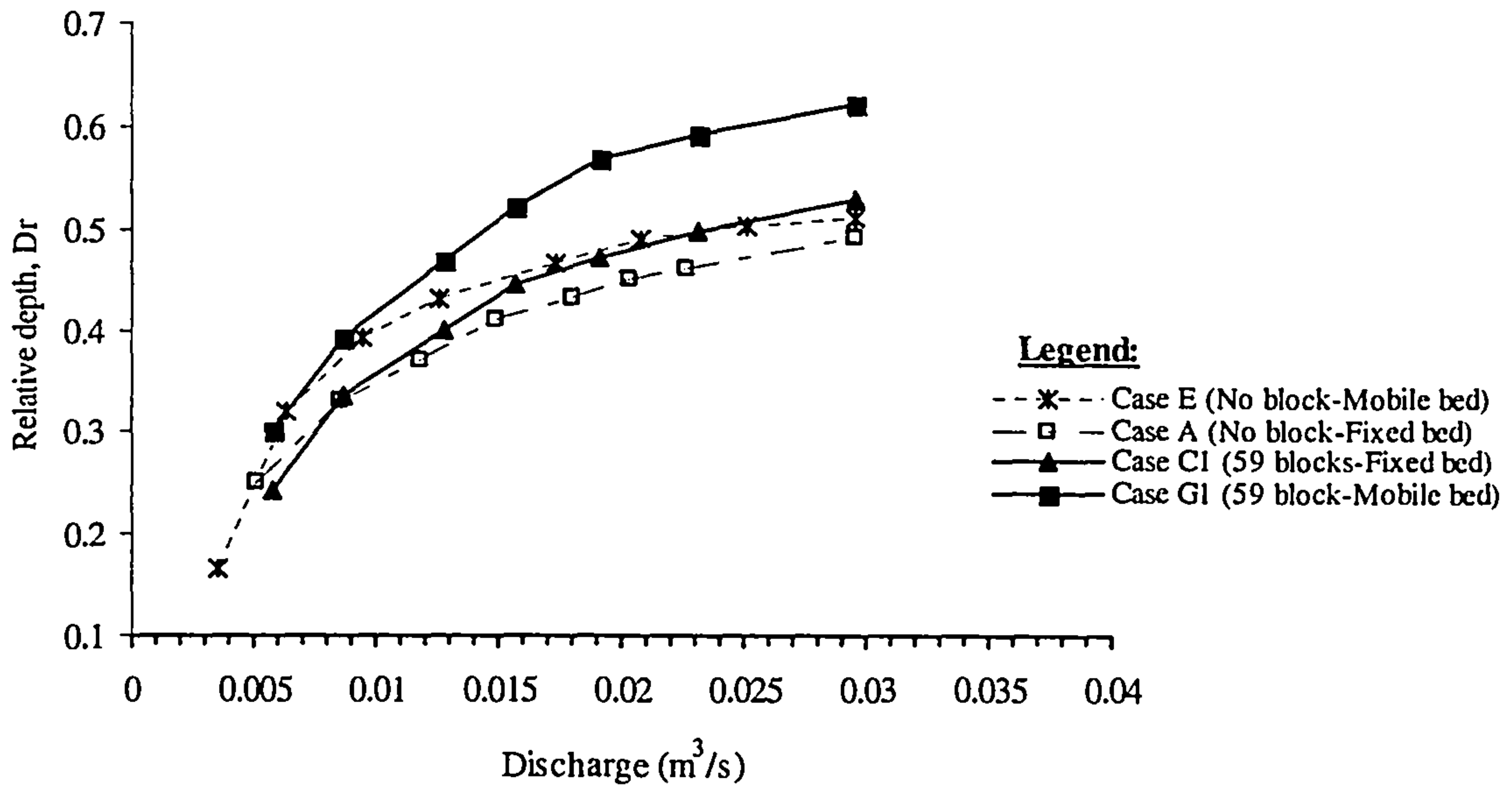


Figure 4.7: Stage-discharge relationships between fixed-bed and mobile-bed for *no block* and *cross-over block* cases

The non-dimensional discharge ( $Q^*$ ), the ratio of the discharge to channel characteristics was used to see the effects for each arrangement affecting conveyance in meandering two-stage channel flows. This approach based on uniform flow where the gravity acceleration and bed friction must be balance, so the non dimensional discharge is given by;

$$Q^* = \frac{Q}{A \sqrt{\frac{V_w}{P} g \sin \theta}} \quad (4.1)$$

Where,

$Q$  = Discharge considered

$A$  = Average cross-sectional area

$P$  = Wetted area of channel

$V_w$  = Total volume of water in the flume

The energy losses other than the bed friction will be reflected in the non-dimensional discharge  $Q^*$ . A value of  $Q^*$  higher means bed frictional losses are dominant. As  $Q^*$  decreases, this implies that non-bed friction losses are increasing as a proportion of



total losses. Such losses in meandering two-stage channels include planform-bend losses, expansion-contraction losses and other interaction losses (Ervine *et al.* 1993). The influence of each arrangement of block on the non-dimensional discharge  $Q^*$  is discussed in this section. The results are presented as  $Q^*$  against relative depth,  $Dr$ . For *Case B Apex Block* with different densities, Figure 4.8(a) indicates that the value of  $Q^*$  increases with relative flow depth,  $Dr$ . In other work, the influence of non-bed friction losses declines as the relative flow depth increases. For *Case A No Block*,  $Q^*$  value are higher at the larger relative flow depths and the losses induced by bed friction higher of total energy losses at a relative depth of 0.48. This implies that for higher relative depths, most of the energy losses are due to bed friction rather than block friction and additional non-bed friction losses.

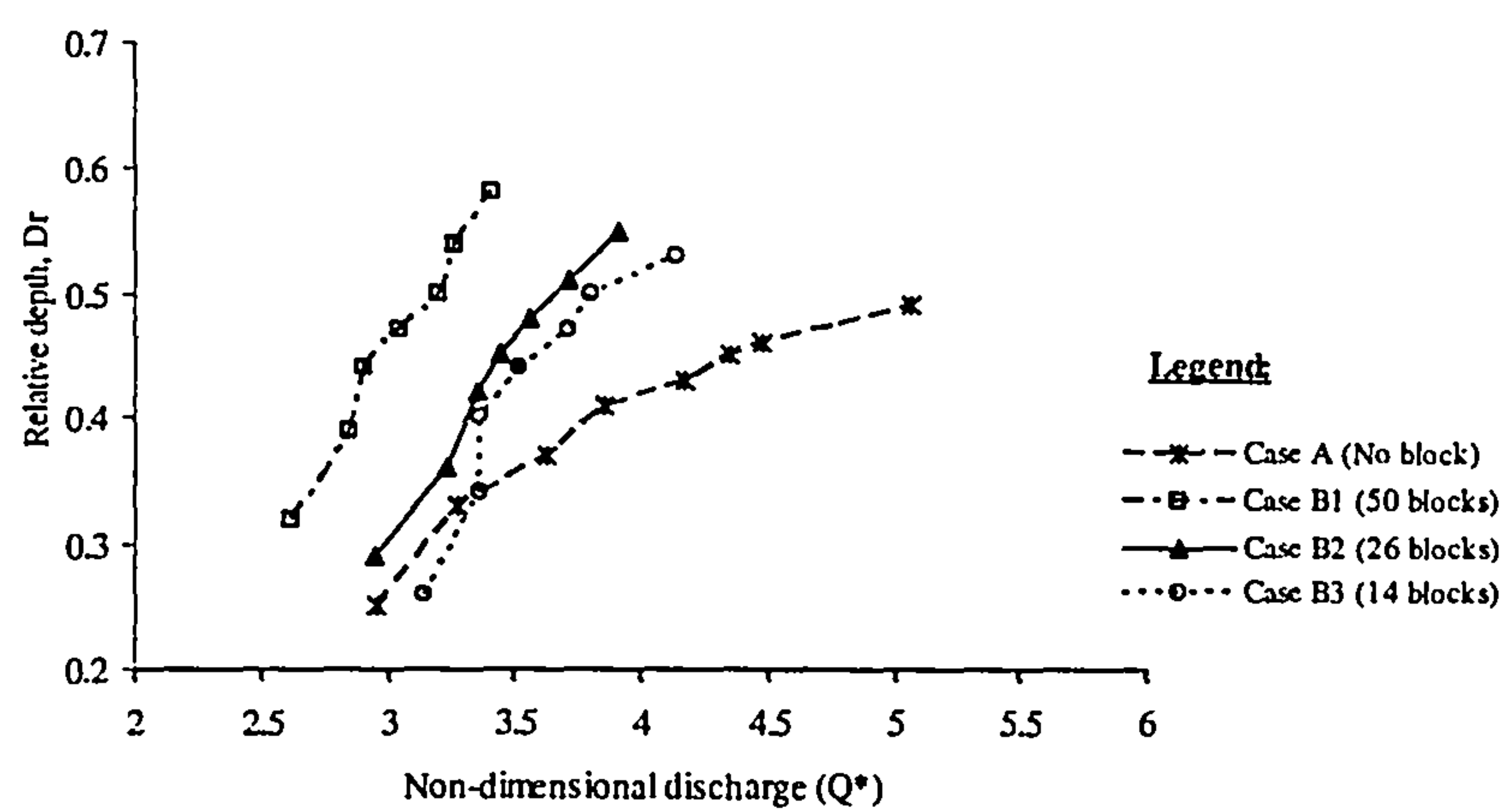
Considering the  $Q^*$  values for *Case C Cross-over Block* for three densities of blocks as shown in Figure 4.8(b) shows the quite similar  $Q^*$  varying between 3.5 and 4 in which there exist three regions:  $Q^*$  decreases to  $Dr = 0.35$ , remains relatively constant till  $Dr = 0.45$  and then starts to increase. However, the  $Q^*$  values for all combined apex and cross-over block *D* cases show a similar variation but different in magnitude for different densities of blocks. In this arrangement, the increased density of blocks gives small  $Q^*$  values as shown in Figure 4.8(c). Figure 4.9(a) show the comparison between mobile-bed for cases no block *E* and apex block *F* respectively. The values of  $Q^*$  vary for mobile bed case for different densities of blocks. For 50 block case, the  $Q^*$  decreases from the bankful to  $Dr = 0.42$ , then remaining a constant at small depth and then decreases to  $Dr = 0.6$  and then increases. However, 26 and 14 block cases show the decrease and increase of  $Q^*$  within ranges 2.3 – 3.3 over the flow depths. Figure 4.9(b) shows the  $Q^*$  for *Case C Cross-over Block* for mobile bed,  $Q^*$  varies and the values are smaller. The values of  $Q^*$  ranges from 2 to 3.5, which is 30% or more smaller than the fixed bed case. This suggests that bedforms give such magnitude contributing the total flow resistance. The 59 block case shows totally different behaviour of sediment transport rate from the others and the values are significantly smaller as the relative water depth increases. This implies that bedforms change drastically. In the 16 and 30 block cases there are also three regions of the  $Q^*$  behaviour: increasing to  $Dr = 0.37$ , remaining a constant to  $Dr = 0.5$  and then decreasing. However in the 59 block case, the  $Q^*$  decreases from the bankful to  $Dr = 0.55$  and then increases. For 108, 54 and 28 block cases in *Case H Combined Apex and Cross-over Block* for mobile bed case show that the  $Q^*$



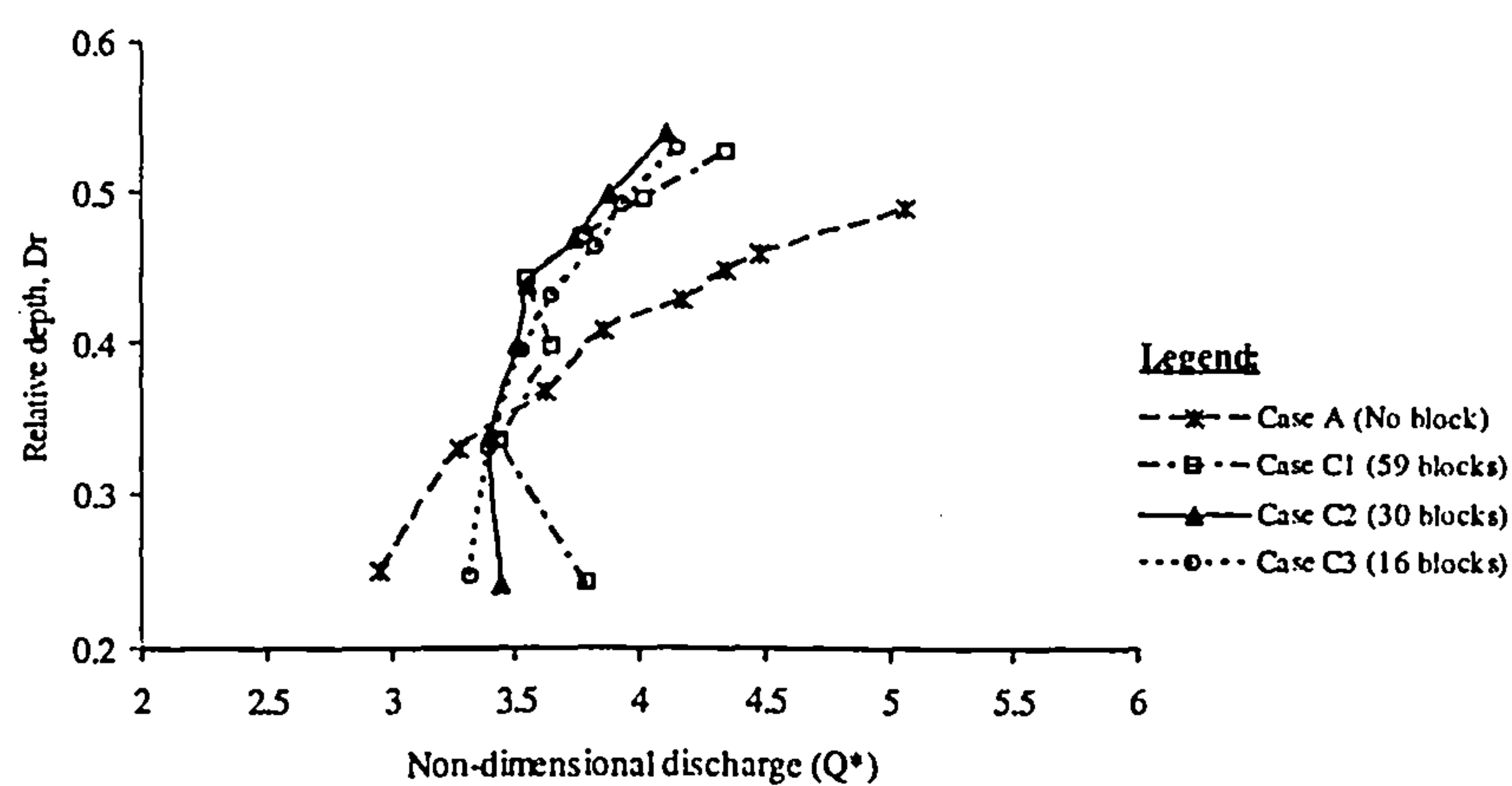
decreases from the bankful to  $Dr = 0.6$  and then increases shown in Figure 4.9(c). The variations of the  $Q^*$  with relative depth for the mobile bed cases follow a similar trend to those for the fixed bed case. The  $Q^*$  value for mobile bed is approximately 20% smaller than that for the fixed bed case. When the ratios of  $Q^*$  to  $Q^*$  at bankful level for no block case were plotted against ratios of flow depth to flow at the bankful for no block case, the results show that there are not quite clearly depict the percentage of flow depth for each case. In order to see the percentage of water level changes for each case, the plot of flow depth to flow depth at the bankful for the no block case against the ratios of discharge to discharge at bankful for the no block case is used.

Figures 4.10(a) and (b) show that the percentage ratios of flow depth to flow depth at bankful for the no block case against the ratios of discharge to discharge at bankful for the no block case for a fixed bed and mobile bed respectively. The results for different ratios of discharge to discharge at bankful and different cases have been compared for different densities of blocks. It is clearly seen that the combined apex block and cross-over block for both fixed and mobile channels has a significant effect as expected. For a fixed bed channel, the ratio for higher densities of blocks is up to 55 % of the flow depth, for middle block density 35 % and for the lower block density the ratio is up to 20 % for maximum discharge. However for a mobile bed channel, the values are 58 %, 45 % and 30 % of flow depth for higher, middle and lower densities of block. In the case of the apex block, the average percentages of flow depth for fixed bed and mobile bed channels are 15% and 25% respectively for the higher discharge under consideration. The cross-over block for different densities results in the smallest increase in the percentage of flow with an average of 5 % for the fixed bed case. However, some disparity in the results in the percentage of flow for a mobile bed with middle and lower densities of blocks give an average of 20% compared to around 28% for the higher density of blocks at the higher discharge ratio. The results clearly depict that the magnitude of the percentage of flow depths of a vegetated floodplain depends strongly on the location of the vegetation arrangement since the combined apex and crossover blocks for higher densities shows a higher impact on the water levels. Care should be taken when planning the development of vegetation on floodplains to ensure that vegetation is located in areas likely to have minimal impact on water levels.

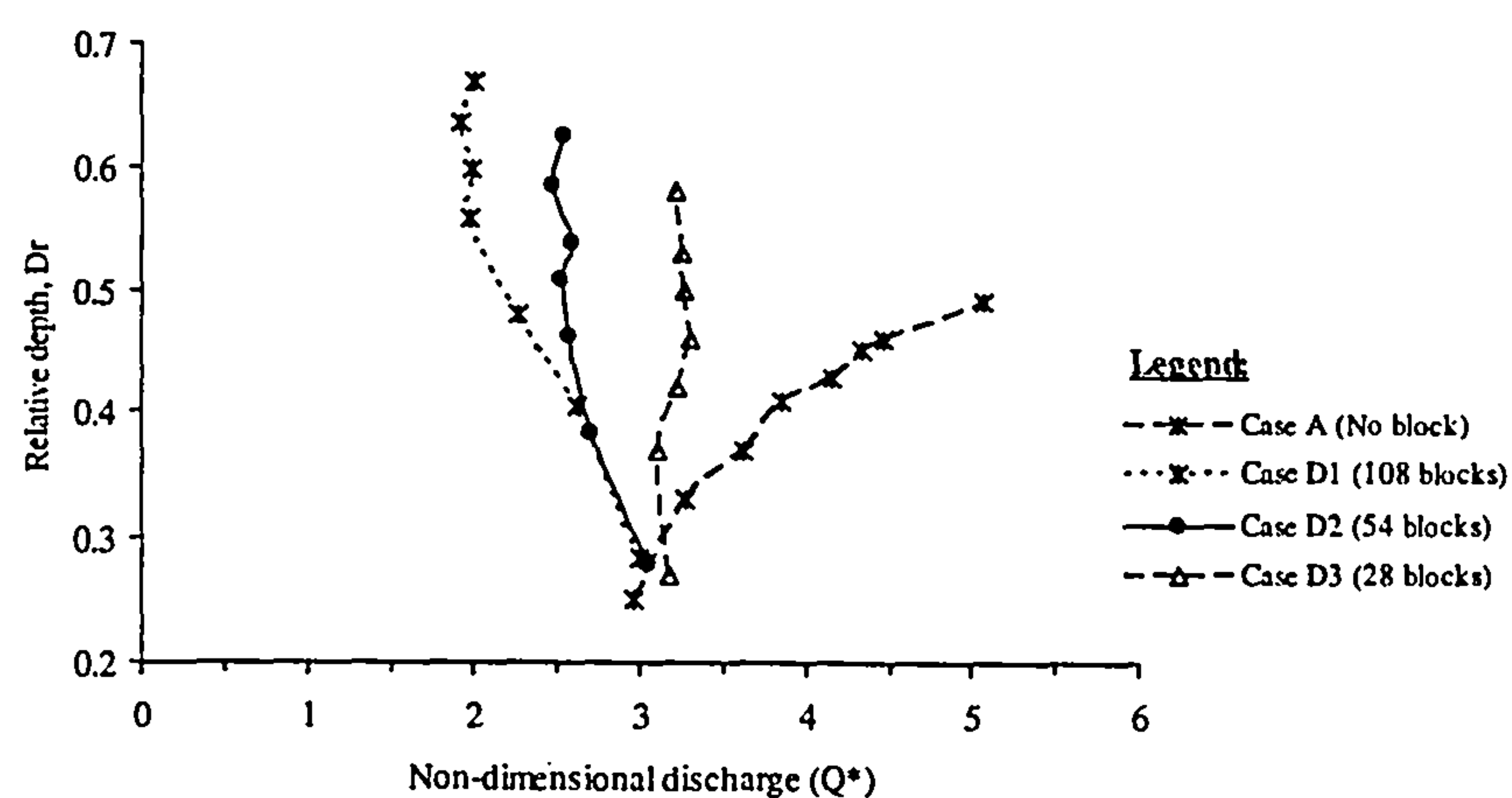




(a)



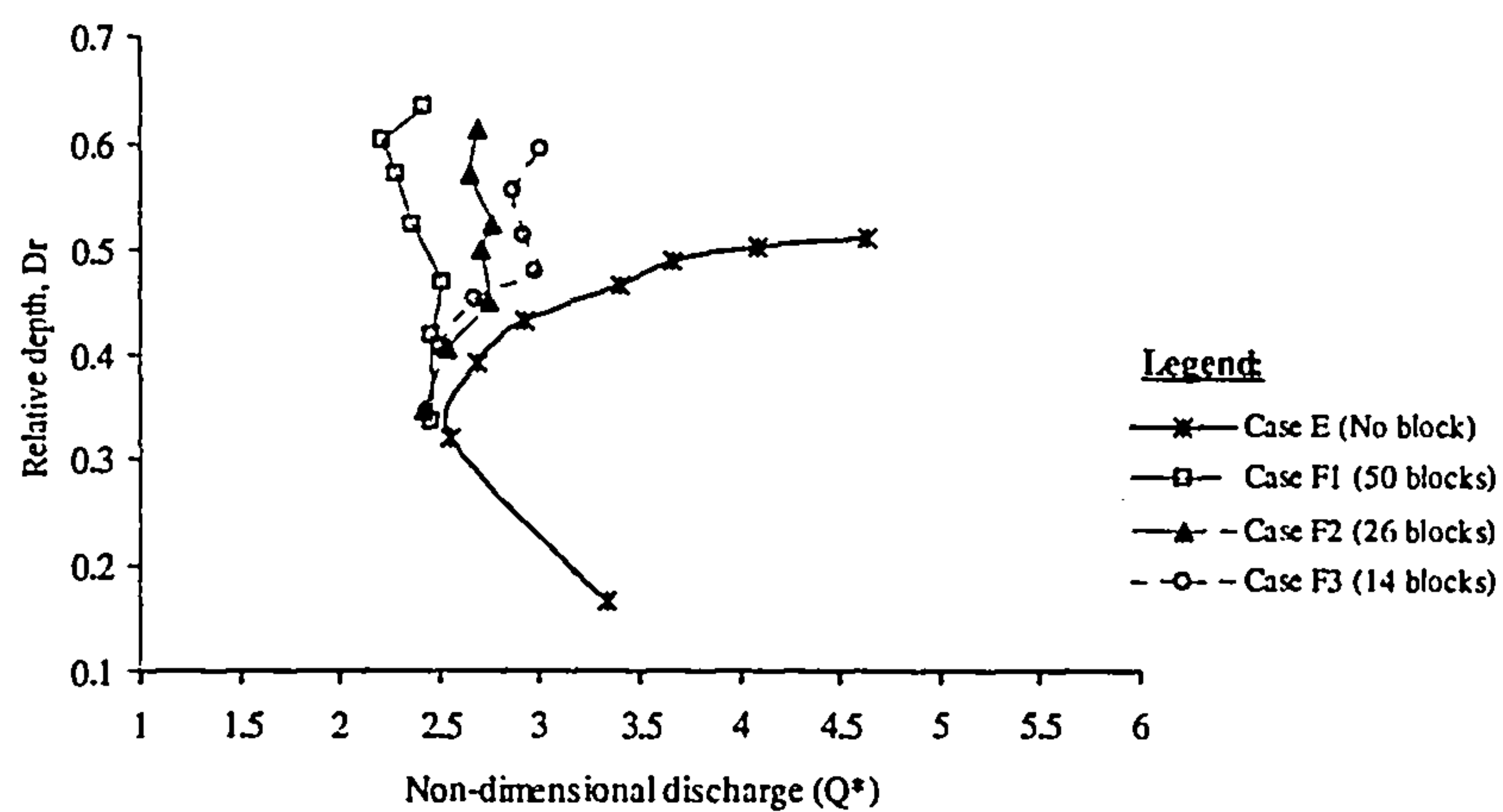
(b)



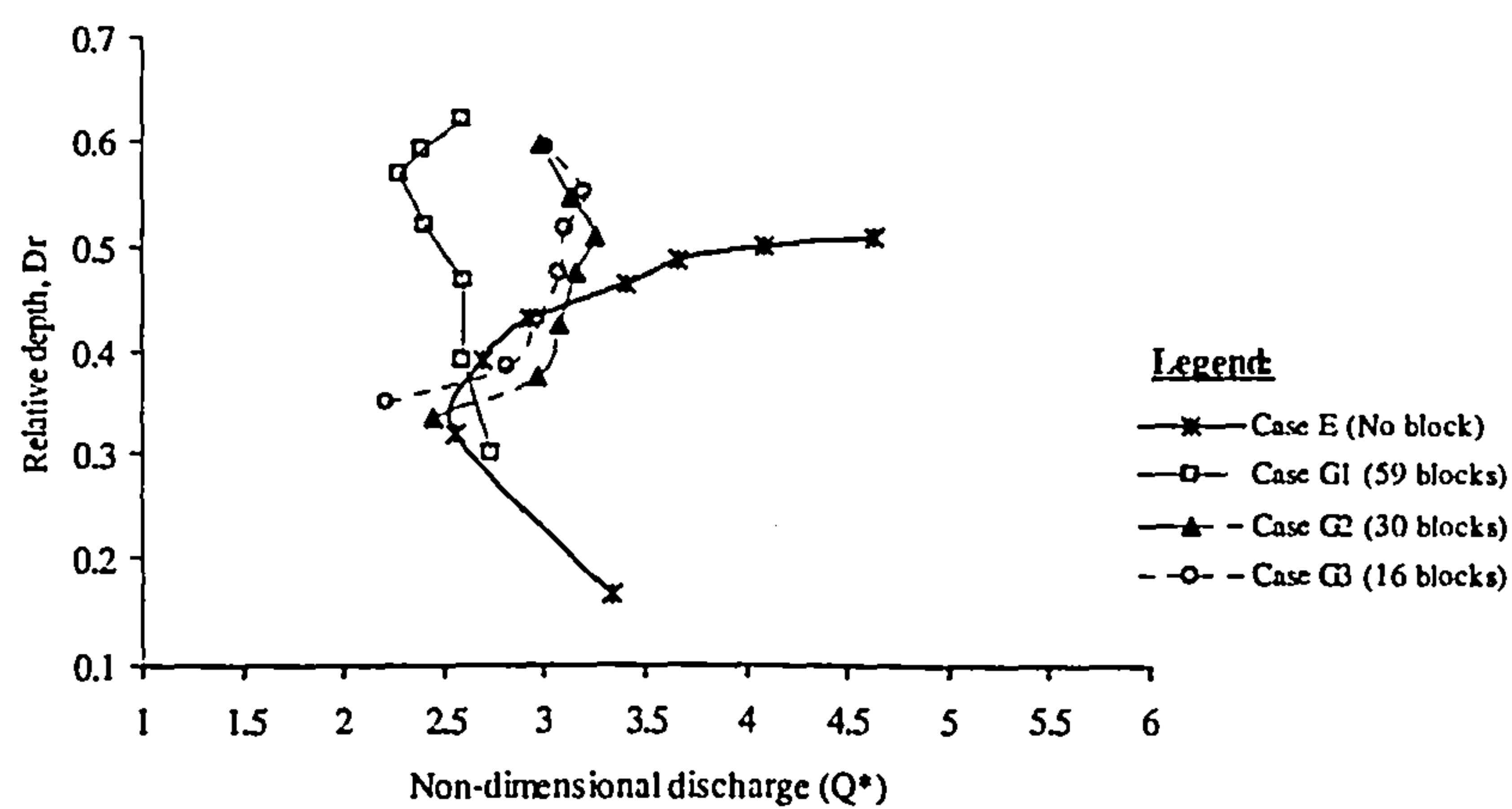
(c)

Figure 4.8: Variation of  $Q^*$  with  $Dr$  for different block arrangements for fixed bed cases (a) Case B Apex Block; (b) Case C Cross-over Block and (c) Case D Combined Apex and Cross-over Block

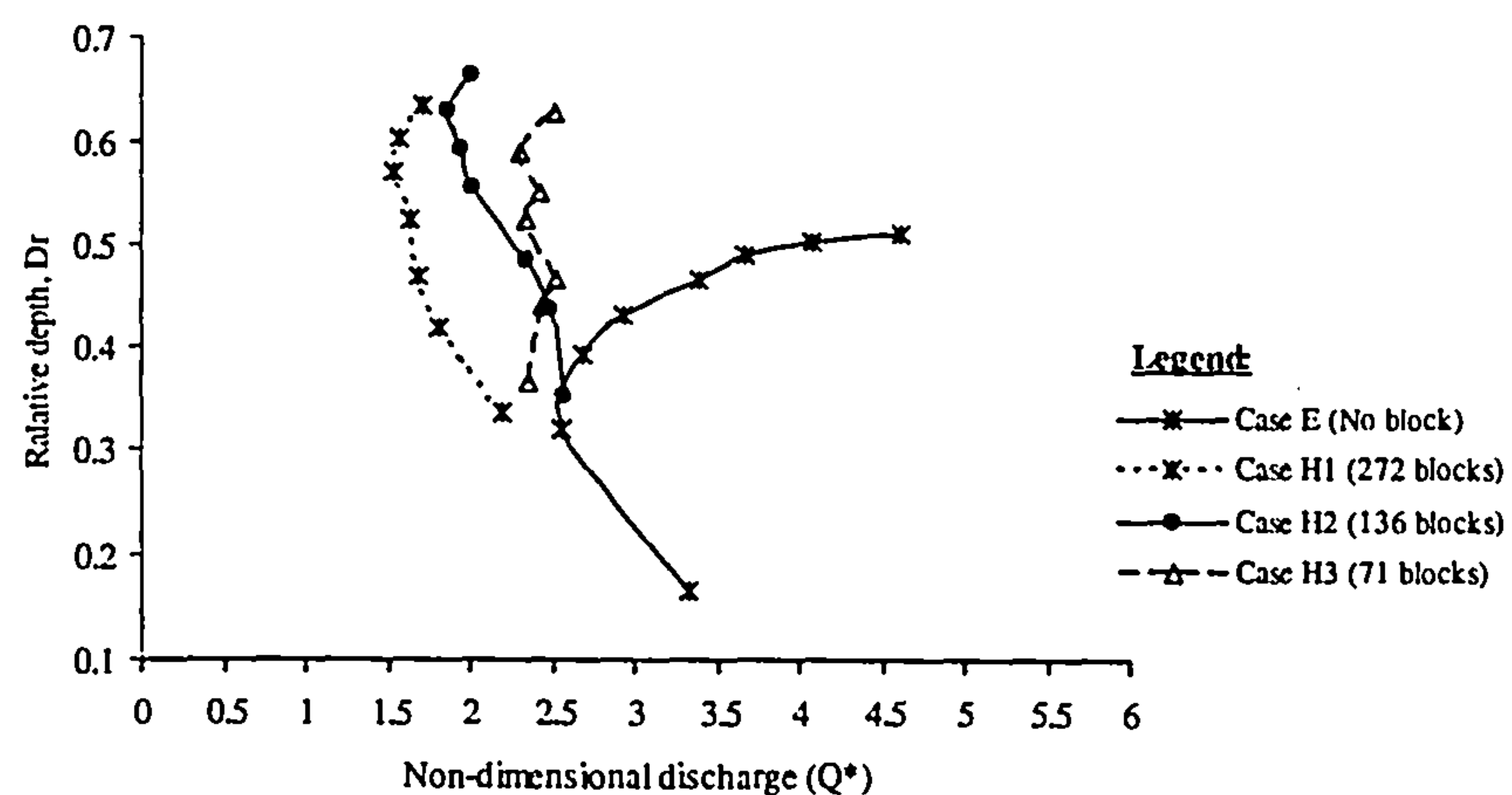




(a)



(b)



(c)

Figure 4.9: Variation of  $Q^*$  with  $Dr$  for different block arrangements for mobile bed cases (a) Case F Apex Block; (b) Case G Cross-over Block and (c) Case H Combined Apex and Cross-over Block



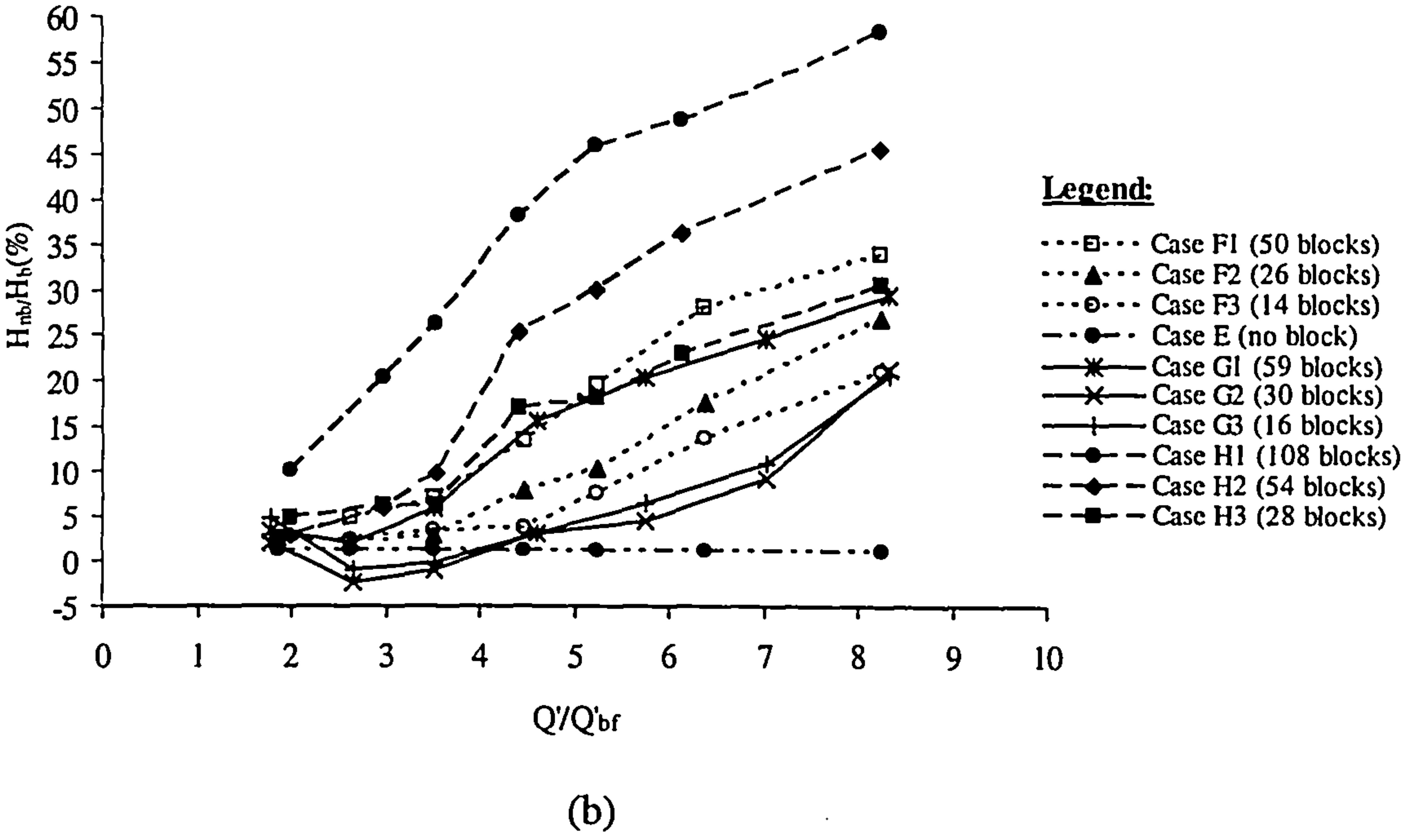
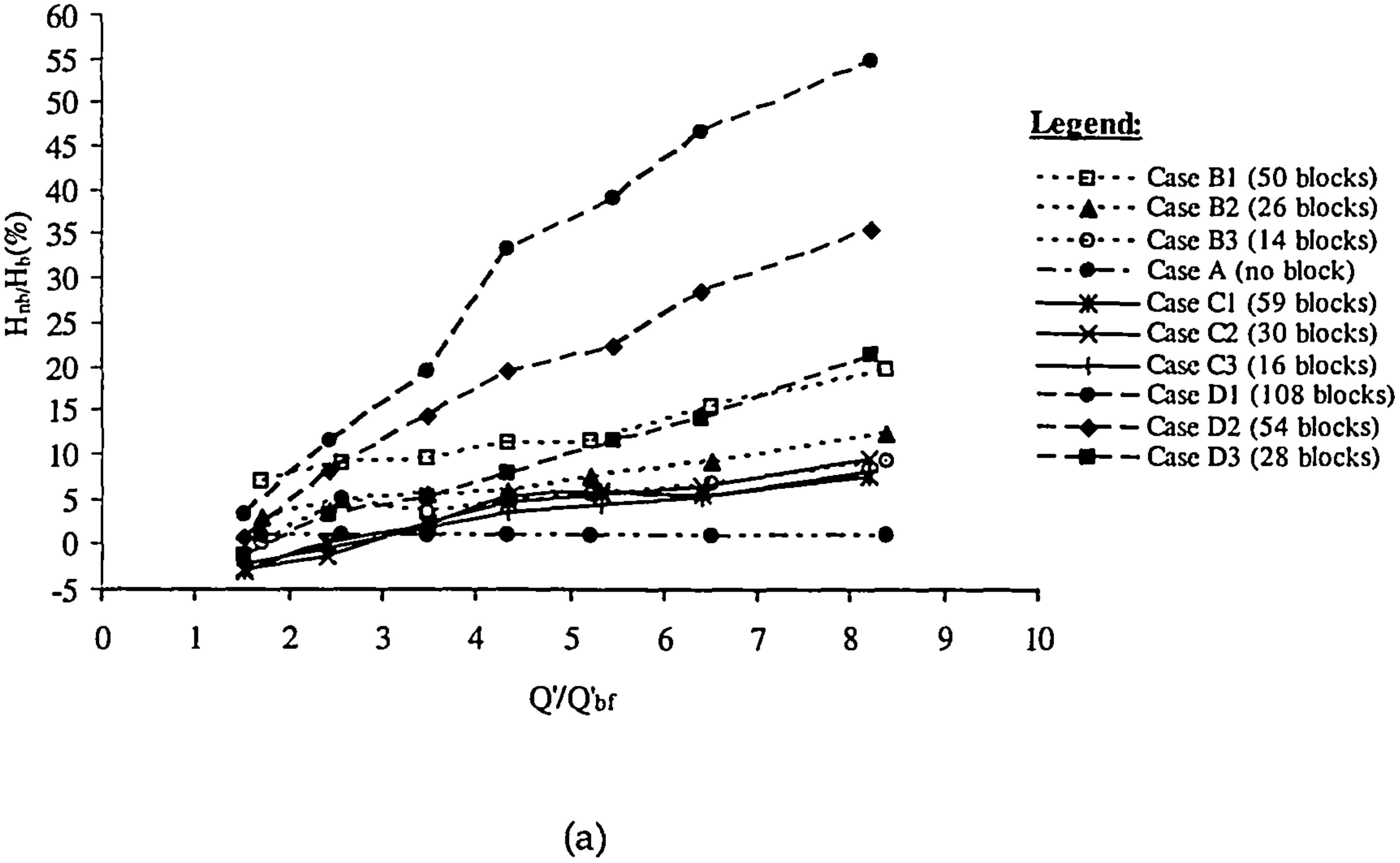


Figure 4.10: Percentage ratios of flow depth to flow depth at the bankful for the no block case against the ratios of discharge to discharge at bankful for the no block case (a) fixed bed channel (b) mobile bed channel



Figure 4.11 shows the stage-discharge curves for a trapezoidal main channel cross-section with three different cases. From the figure, it is clear that the pattern is similar to those of the rectangular main channel cross-section for no block *A*, apex block *B1* and cross-over block *C1* cases with higher density of blocks. However, the magnitude of the depth is lower for each case.

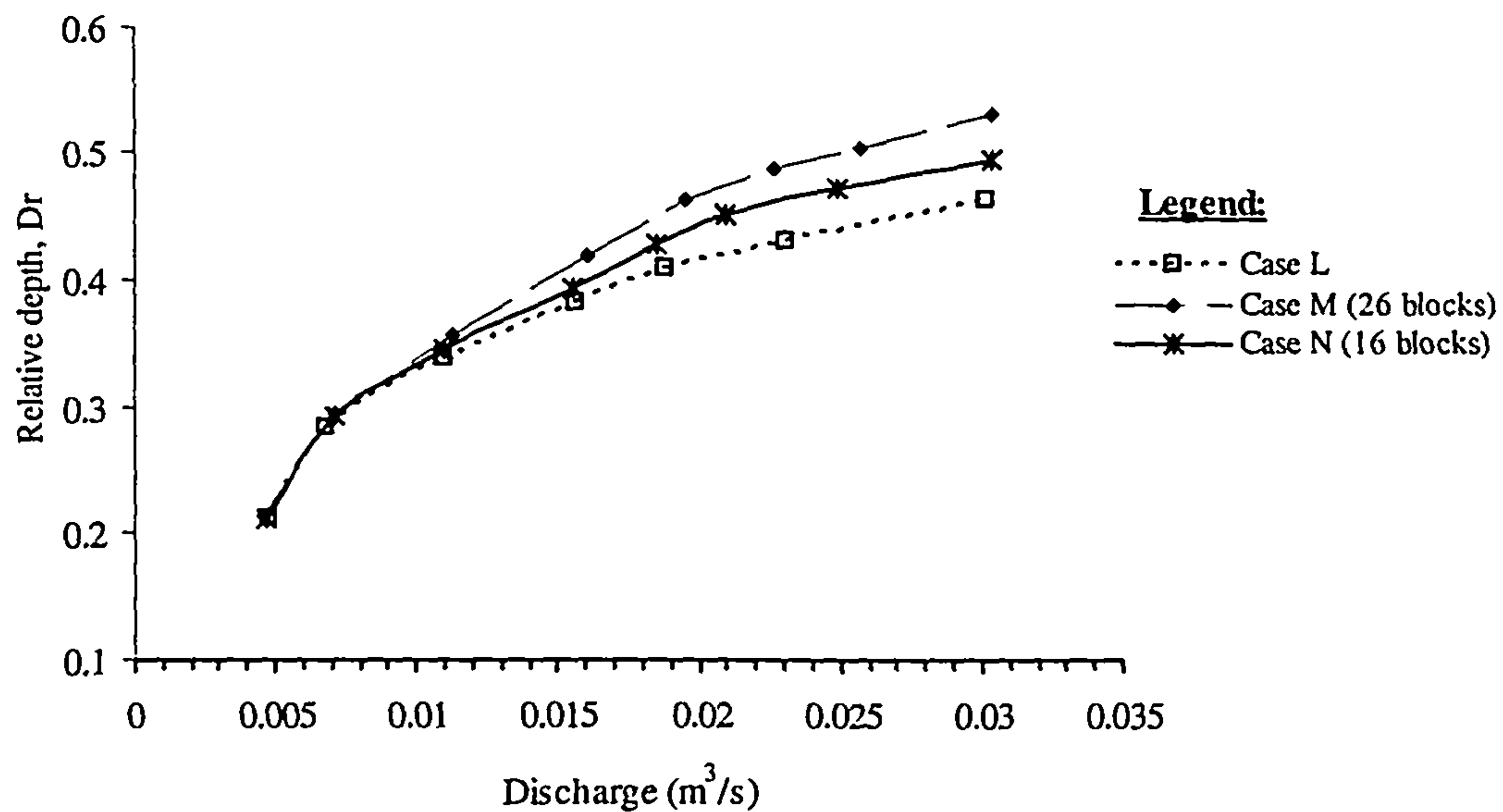


Figure 4.11: Stage-discharge curves of trapezoidal main channel cross-section for no block *L*, apex block *M* and cross-over block *N* cases

### 4.3 Manning's *n* Against Relative Depth

The study of resistance in the flow is very important. Much effort has been expended by many researchers to develop means and formulae to calculate the relationship between different flow characteristics and the channel characteristics. The aim of this section was to relate the depth of flow to the resistance coefficients for different arrangements in the vegetated floodplain case. This is important in this study because of the distribution density of the obstructions used in the floodplain edges to model vegetation. In this section, the most widely used formula for the calculation of velocity is Manning's *n* equation. For this study, it is very important to have a good understanding of Manning's *n* equation in order to understand the effects caused by the presence of vegetation. This equation has proved most reliable in practice, although



it is applicable only in the fully rough zone. Henderson (1966) pointed out that Manning's  $n$  is suitable for all fully rough flows and transition flows.

The single channel Manning's  $n$  was calculated for each overbank discharge using Equation (4.2) below and the variation of the single channel Manning's  $n$  with depth is shown in Figures 4.12 to 4.16.

$$n = \frac{AR^{\frac{2}{3}}S_o^{\frac{1}{2}}}{Q} \quad (4.2)$$

Considering the Manning's  $n$  values for *Case B Apex Block* with three different densities, from Figure 4.12, the Manning's  $n$  for *Case A No Block* is seen to decrease as  $Dr$  increases. There is also a similar trend for apex block cases *B1*, *B2* and *B3*. The Manning's  $n$  values for the apex block *Case B1* with the higher density are higher than those for the apex block *B2* and *B3* cases. This indicates an increase in drag force as block density increases. The Manning's  $n$  for apex block *B1* is approximately 20% greater than those for apex block cases *B2* and *B3*. The Manning's  $n$  values for all combined apex and cross-over block *D* cases show a similar variation but different in magnitude for different densities of blocks. In this arrangement, the increased density of blocks gives large Manning's  $n$  values as shown in Figure 4.14. However in *Case C Cross-over Block* for three densities of blocks as shown in Figure 4.13 shows the quite similar Manning's  $n$  varying between 0.025 and 0.0285 in which there exist three regions: Manning's  $n$  increases to  $Dr = 0.35$ , remains relatively constant till  $Dr = 0.45$  and then starts to decreases.

Figure 4.15 show the comparison between fixed- bed and mobile-bed for cases apex block *B* and *F* respectively. The values of Manning's  $n$  vary for mobile bed case for different densities of blocks. For 50 block case, the Manning's  $n$  increases from the bankful to  $Dr = 0.42$ , then remaining a constant at small depth and then increases to  $Dr = 0.6$  and then decreases. However, 26 and 14 block cases show the increase and decrease of Manning's  $n$  within ranges 0.035 – 0.045 over the flow depths.



Figure 4.16 shows the Manning's  $n$  for *Case C Cross-over Block*. For fixed bed case, the Manning's  $n$  increases up to  $Dr = 0.45$  and then decreases. For mobile bed, Manning's  $n$  varies more than that in the fixed bed case and the values are higher. Manning's  $n$  ranges from 0.0315 to 0.049, which is 30% or more larger than the fixed bed case. This suggests that bedforms give such magnitude contributing the total flow resistance. The 59 block case shows totally different behaviour of sediment transport rate from the others and the values are significantly larger as the relative water depth increases. This implies that bedforms change drastically. In the 16 and 30 block cases there are also three regions of the Manning's  $n$  behaviour: decreasing to  $Dr = 0.37$ , remaining a constant to  $Dr = 0.5$  and then increasing. However in the 59 block case, the Manning's  $n$  increases from the bankful to  $Dr = 0.55$  and then decreases. For mobile bed 108, 54 and 28 block cases in *Case H Combined Apex and Cross-over Block* show that the Manning's  $n$  increases from the bankful to  $Dr = 0.6$  and then decreases shown in Figure 4.17. The variations of the Manning's  $n$  with relative depth for the mobile bed cases follow a similar trend to those for the fixed bed case. The Manning's  $n$  value for mobile bed is approximately 20% higher than that for the fixed bed case.

Manning's  $n$  for trapezoidal cross-sections in the meandering channel is also investigated, and  $n$  values are plotted against relative depth in Figure 4.18. The variation of Manning's  $n$  shows a wide range of values from less than 0.02 for the trapezoidal cross-section to around 0.03 for the rectangular cross-section. This is a simplification as far as a comparison with the main channel cross-section for a fixed bed is concerned; however, it is presented as the best basis of comparison between the cross-sections of different roughness characteristics.



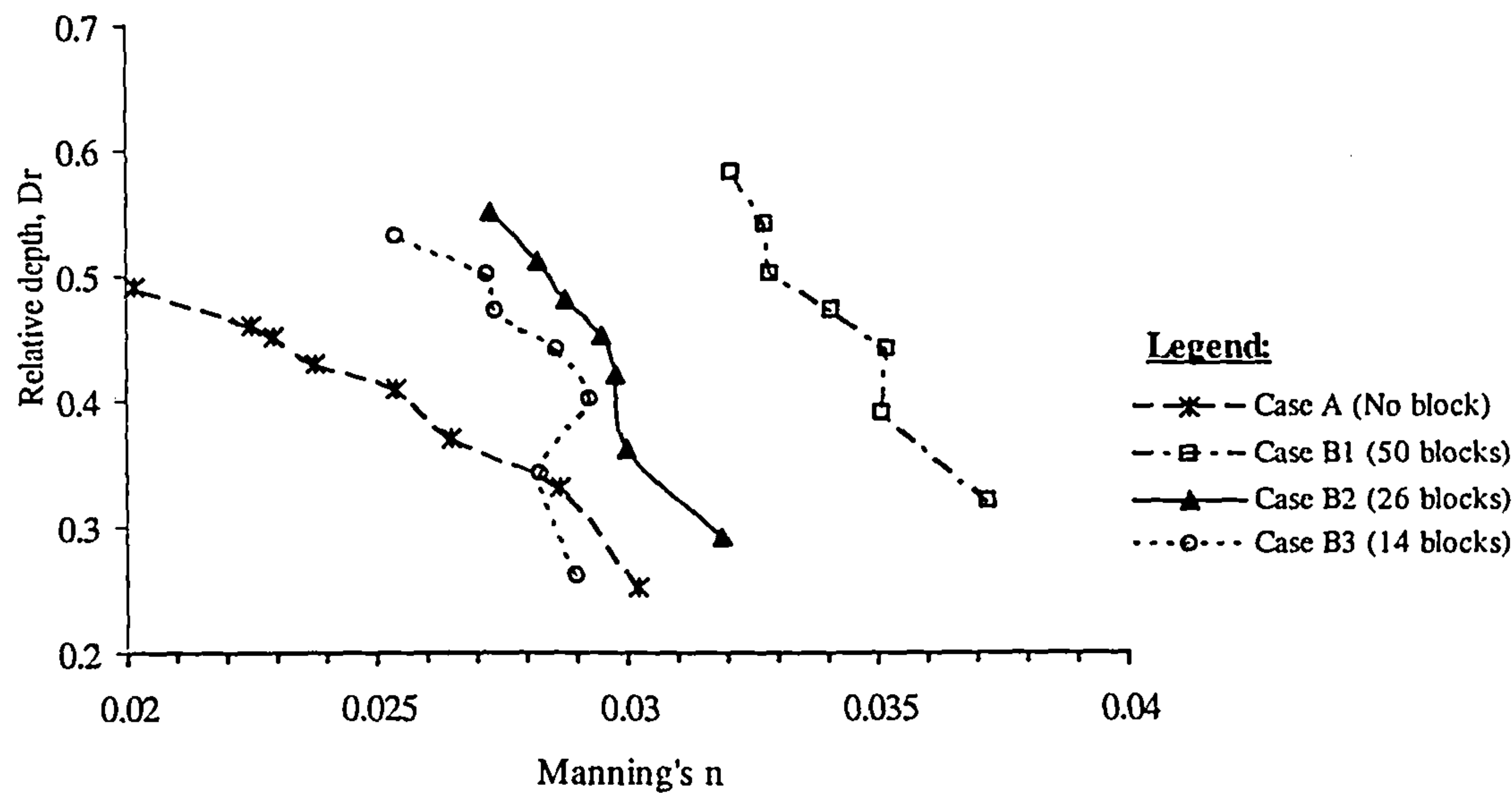


Figure 4.12: Manning's  $n$  versus relative depth for fixed bed channel *Case A No Block* and *Case B Apex Block*

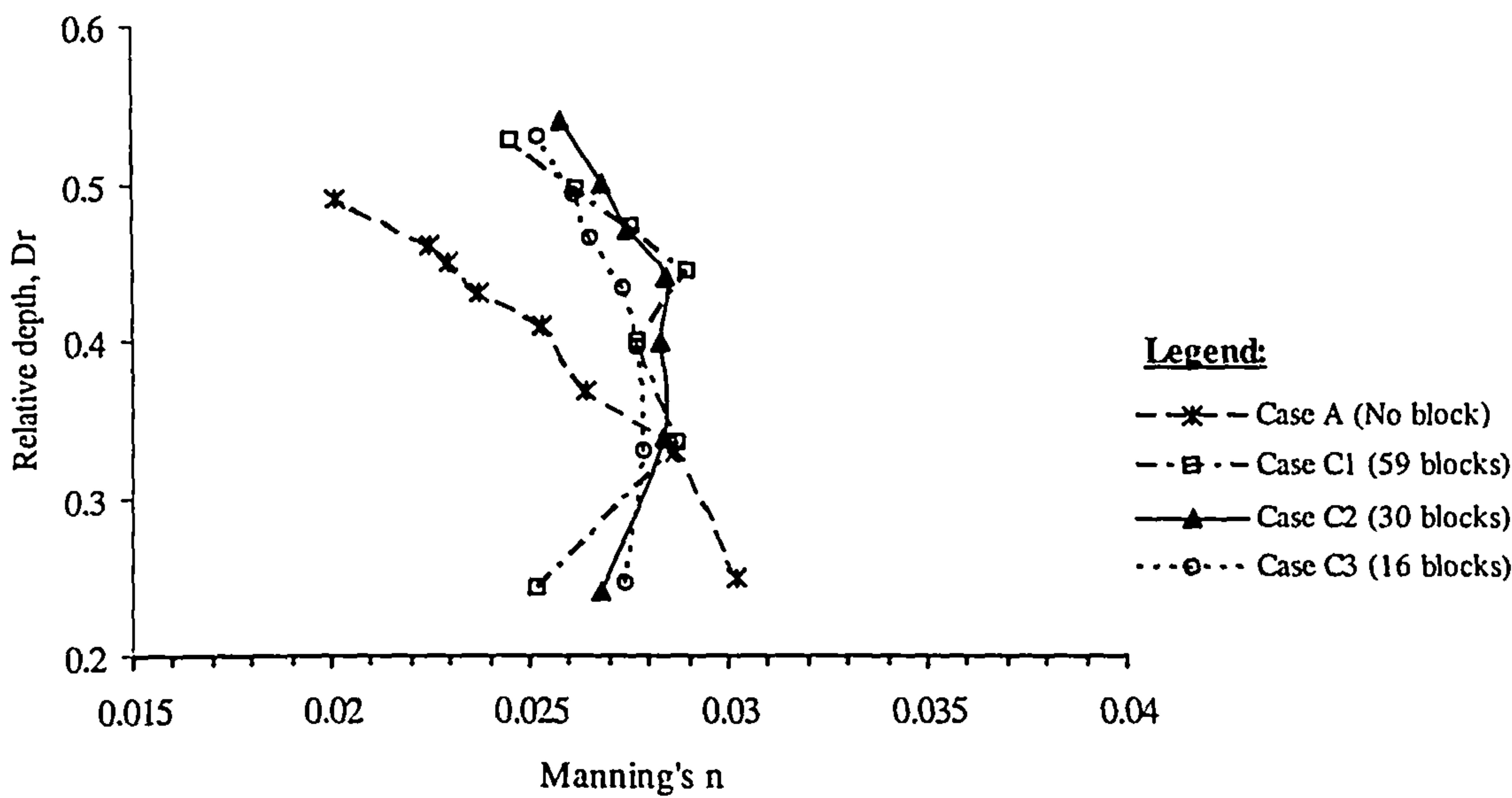


Figure 4.13: Manning's  $n$  versus relative depth for fixed bed channel *Case A No Block* and *Case C Cross-over Block*



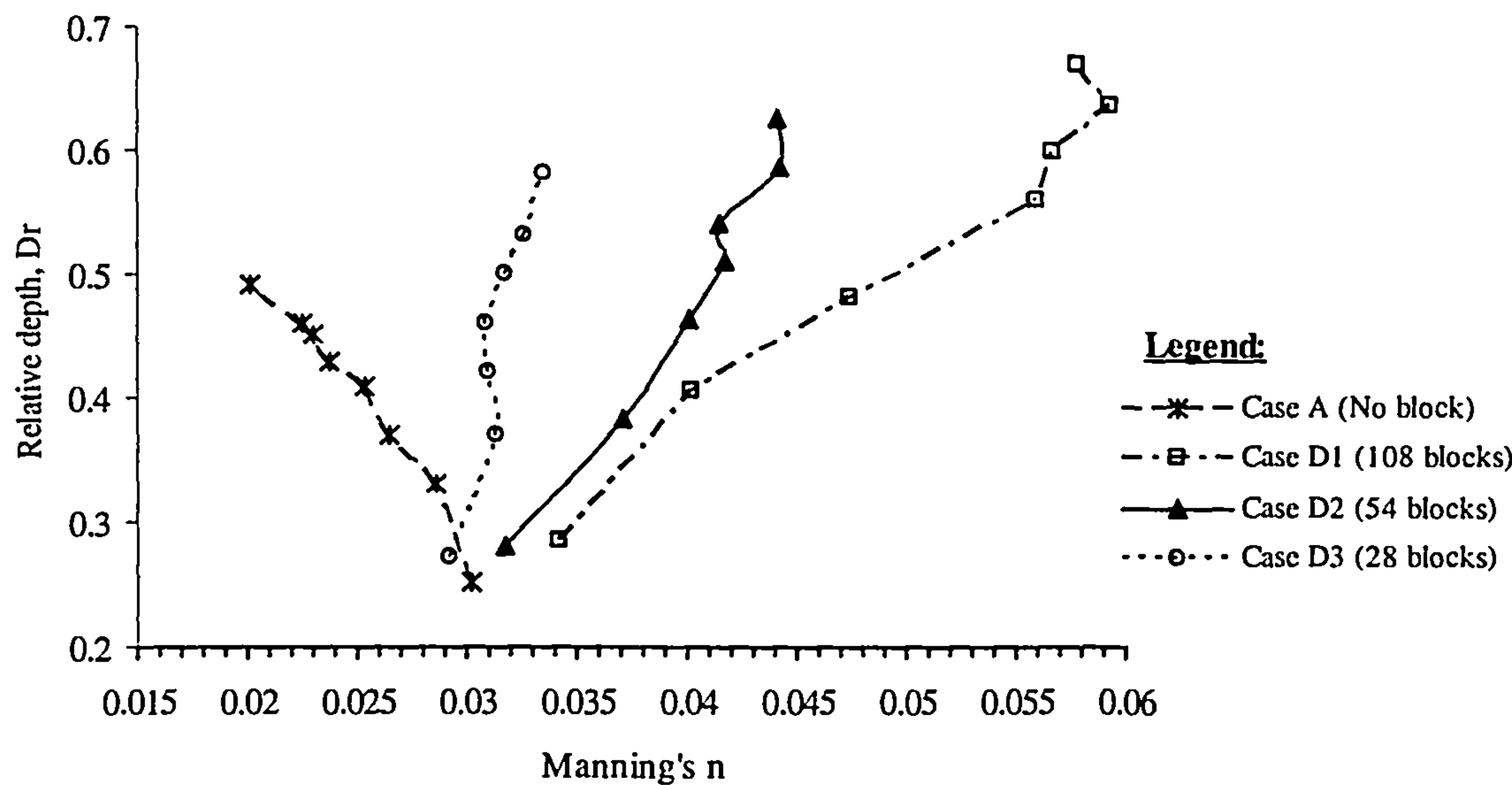


Figure 4.14: Manning's  $n$  versus relative depth for fixed bed channel Case A No Block and Case D Combined Apex and Cross-over Block

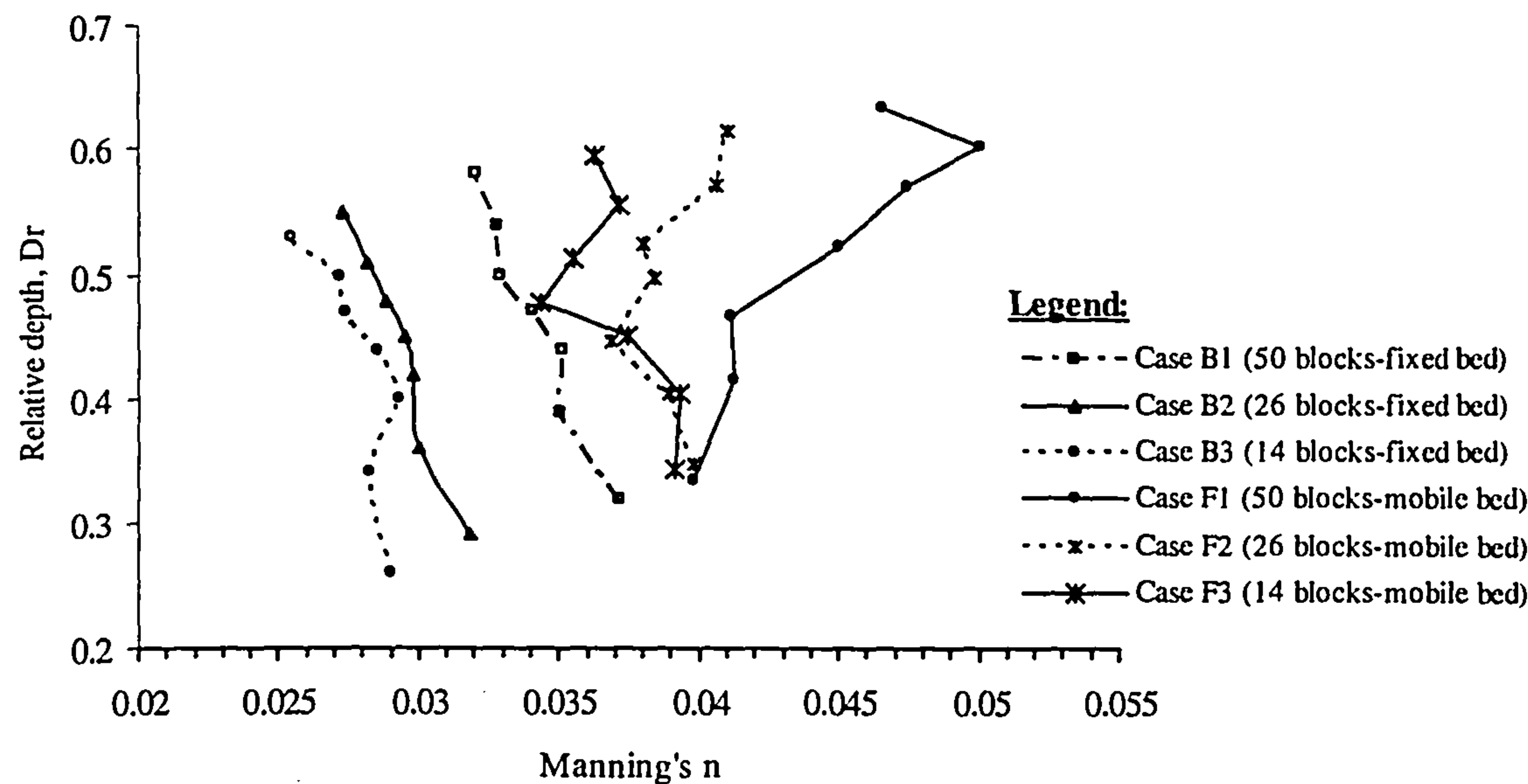


Figure 4.15: Manning's  $n$  relationships between fixed-bed and mobile-bed for different density of apex block cases B and F respectively



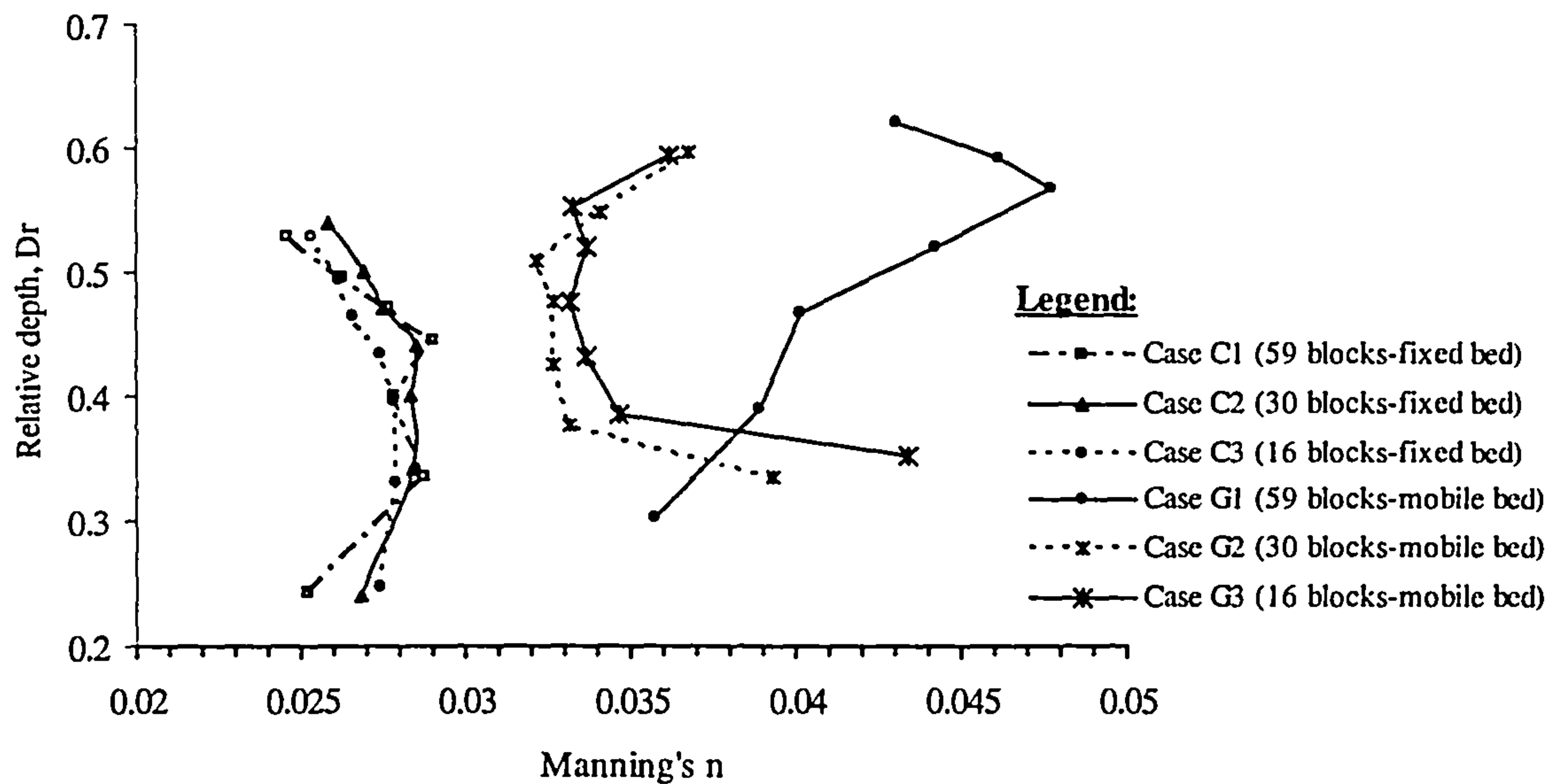


Figure 4.16: Manning's  $n$  relationships between fixed-bed and mobile-bed for different density of cross-over block cases C and G respectively

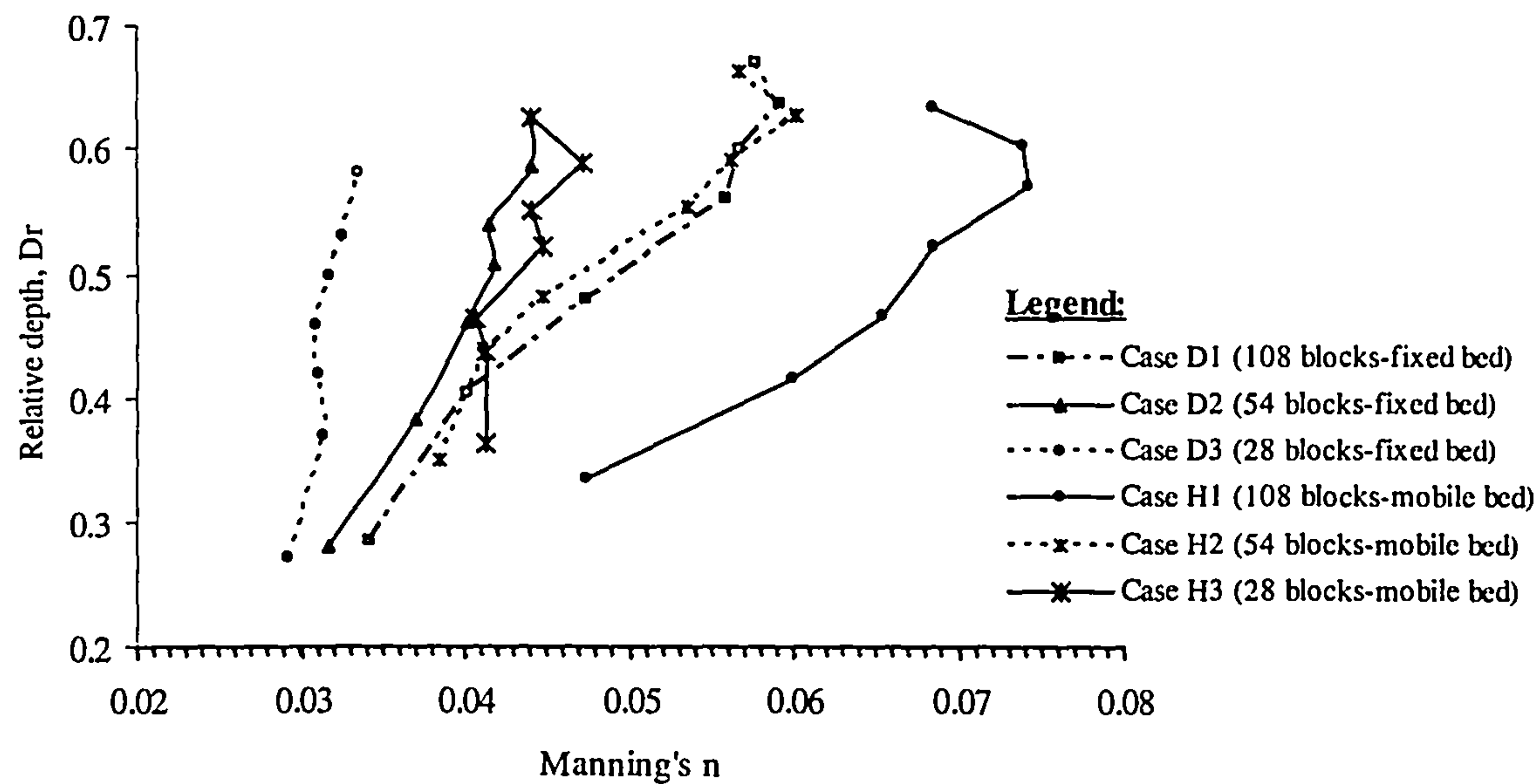
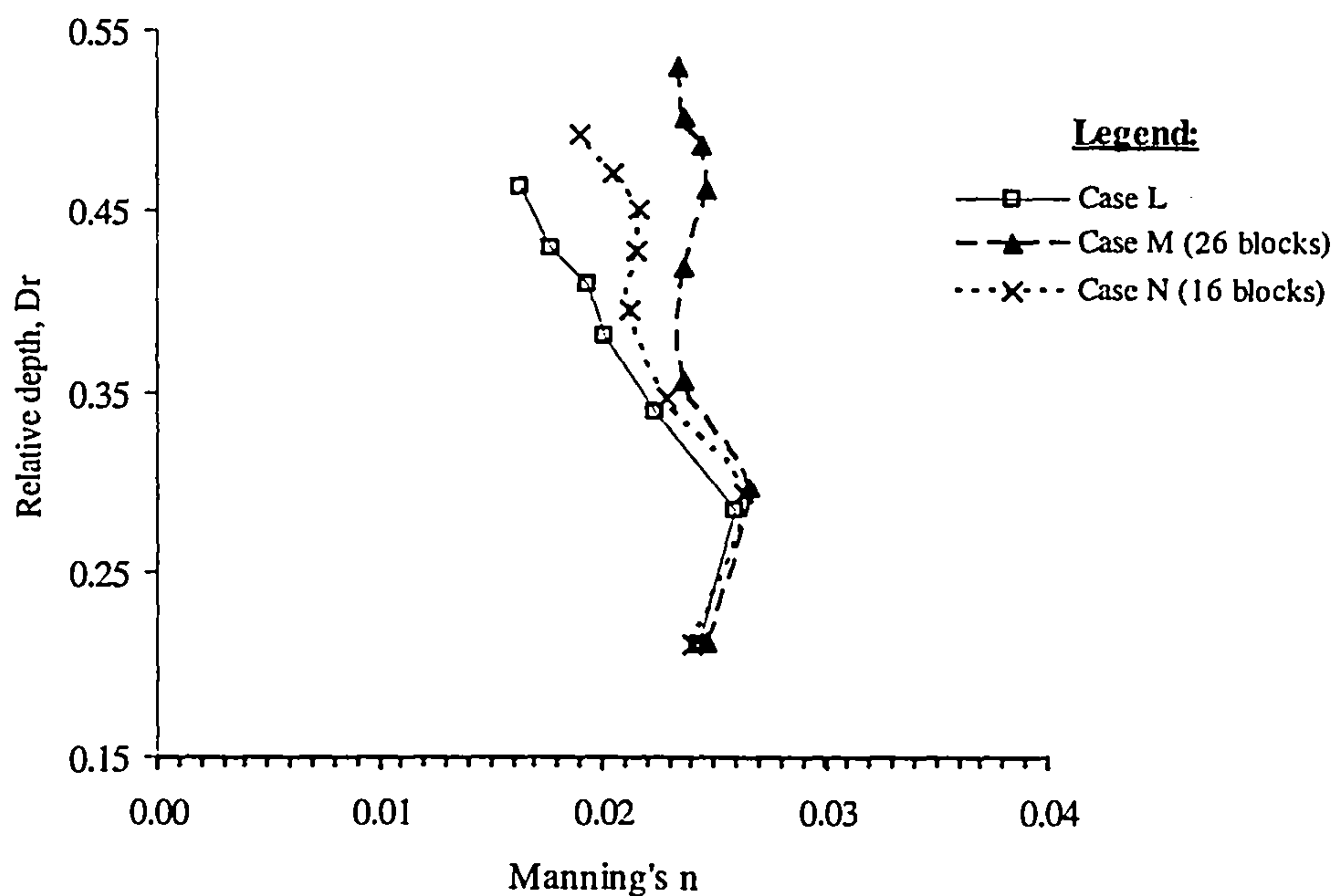


Figure 4.17: Manning's  $n$  relationships between fixed-bed and mobile-bed for different density of combined apex and cross-over block cases D and H respectively





**Figure 4.18:** Manning's  $n$  relationship for trapezoidal main channel cross-section cases for no block L, apex block M and cross-over block N

#### 4.4 Force Balance over One Meander

The equation of motion for free-surface steady flow can be derived by summing the retarding shear force at the boundary against the propulsive force acting in the direction of flow. The net force of the summation is not zero because the flow is accelerating. The propulsive force for free-surface flow is supplied by the component of the weight of the flowing fluid at the direction of flow (Henderson, 1966). For the original case of flow resistance where the dominant effect is due to the roughness elements of the bed, the resistance is maximised near the bed and the boundaries of the channel. But in the case of this study, the situation is different. The major roughness elements are the vegetation (blocks). The floodplain vegetation covers a significant part of the floodplain edge and the relative roughness will be higher of the flow depth. This is why the form drag is considered to be a major factor affecting the flow resistance. This means that for calculating the friction factor, the factors that need to be mainly considered are those that affect the form drag. Furthermore, in this section, by considering forces over one meander for quasi-uniform flow, all the forces within the



control volume have to be balanced. These include: the gravitational force due to the weight component, boundary shear force and drag forces due to blocks over one meander. The force balance can be expressed as:

$$w = \tau + F_D \quad (4.3)$$

where,

$w$  = weight component of the flowing fluid

$\tau$  = boundary shear force

$F_D$  = drag forces

The weight component in the flow direction is

$$w = \rho g m S_o \quad (4.4)$$

where,

$\rho$  = density of fluid

$g$  = gravitational acceleration

$m$  = total volume

$S_o$  = valley slope

For cross-section volume,  $m_w$  defined as,

$$m_w = B(H - h)L_w + bhL_w s \quad (4.5)$$

where,

$B$  = flume top width

$H$  = total water depth

$h$  = main channel depth

$L_w$  = meander wavelength

$s$  = sinuosity of main channel

The cross sectional area given as,



$$A = B(H - h) + bh \quad (4.6)$$

So volume,

$$m_w = AL_w \left[ 1 + (s-1) \frac{bh}{A} \right] \quad (4.7)$$

The total volume of blocks:

$$m_b = N_b (H - h) A_b \quad (4.8)$$

where,

$N_b$  = number of block

$A_b$  = area of block in plan view

So, the total volume is

$$m = m_w - m_b \quad (4.9)$$

$$m = AL_w \left[ 1 + (s-1) \frac{bh}{A} \right] - N_b (H - h) A_b \quad (4.10)$$

By substituting Equation (4.10) into Equation (4.4), this will lead to the following weight component as,

$$w = \rho g S_o \left[ AL_w \left( 1 + (s-1) \frac{bh}{A} \right) - N_b (H - h) A_b \right] \quad (4.11)$$

Boundary shear force can be given by boundary shear stress x area. Area of boundary is

$$\text{Cross-sectional area} = B \times L_w + 2(H - h)L_w + 2hsL_w \quad (4.12)$$



Recalling that the wetted parameter,  $P = B + 2(H - h) + 2h$  then Equation (4.12), then

$$\text{Cross-sectional area} = L_w P \left[ 1 + \frac{2h(s-1)}{P} \right] \quad (4.13)$$

Total block area is

$$\text{Block areas} = N_b \times A_b \quad (4.14)$$

So, the area of boundary = cross-sectional area – block area:

$$\text{Area of boundary} = L_w P \left[ 1 + \frac{2(s-1)}{P} - \frac{N_b A_b}{L_w P} \right] \quad (4.15)$$

Hence boundary shear force is boundary shear stress,  $\tau_o$  x area of boundary:

$$\tau = \tau_o L_w P \left[ 1 + \frac{2(s-1)}{P} - \frac{N_b A_b}{L_w P} \right] \quad (4.16)$$

and finally the drag force equation is

$$F_D = \frac{\rho C_D A_p v^2}{2} \quad (4.17)$$

where,

$\rho$  = water density

$C_D$  = the drag coefficient for the block ( $C_D = 1.85$  used in this study)

$v$  = the average approach velocity (sectional averaged velocity used in this study)

$A_p$  = projected area of the block in the streamwise direction

The projected area  $A_p$  is defined as the area of all blocks facing the flow = (number of blocks considered) x (flow depth) x (average width of the block). So, the force balance equation can be expressed as:



$$\rho g S_o A L_w \left[ 1 + (s-1) \frac{bh}{A} - \frac{N_b (H-h) A_b}{A L_w} \right] = \tau_o L_w P \left[ 1 + \frac{2h(s-1)}{P} - \frac{N_b A_b}{L_w P} \right] + \frac{\rho C_D A_p v^2}{2} \quad (4.18)$$

Typical plots of  $F_D/w$  with relative depth,  $Dr$  for all the cases of block arrangement and density are shown in Figures 4.19 to 4.24. As expected, according to Equation (4.18), the  $F_D/w$  value shown in Figures 4.19 to 4.24 varies almost parabolic with increase in relative depth. It is noticed that  $F_D/w$  is greater than 1.0 in *Case C Cross-over Block*, but should not exceed 1.0. The reason why the value of  $F_D/w$  is more than 1.0 may be due to the use of the average velocity instead of the approaching velocity to the projected area. As density of blocks increases,  $F_D/w$  increases for all the cases. This is again the use of averaged velocity rather than approaching velocity to the projected area, since the approaching velocity in the projected area decreases as the density increases. For the mobile bed cases, a trend of  $F_D/w$  with respect to  $Dr$  is not quite parabolic. This could be reflected by evolution of bedforms when water depth changes.

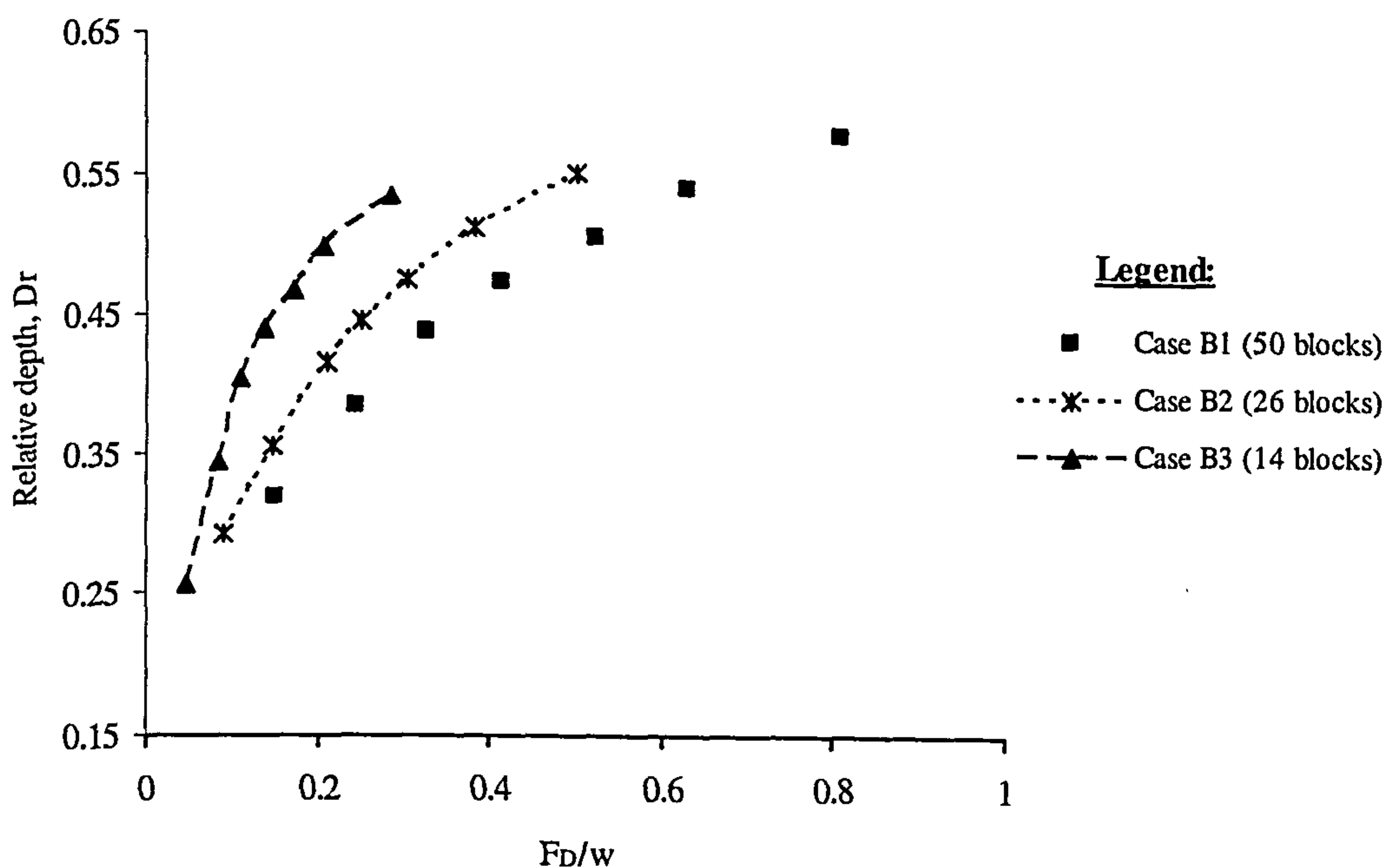


Figure 4.19: Relative depth versus  $F_D/w$  for fixed bed channel *Case B Apex Block*



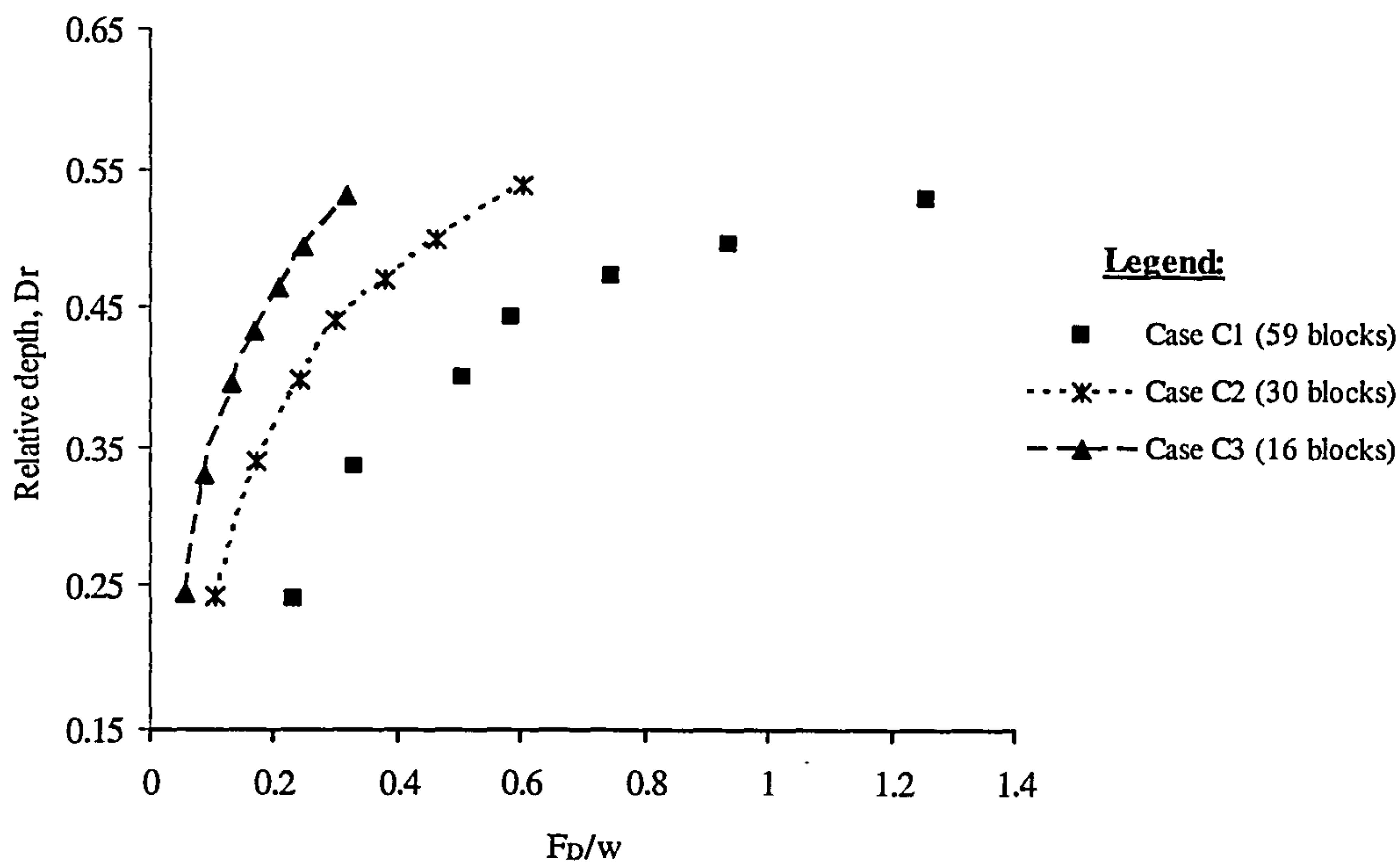


Figure 4.20: Relative depth versus  $F_D/w$  for fixed bed channel Case C Cross-over Block

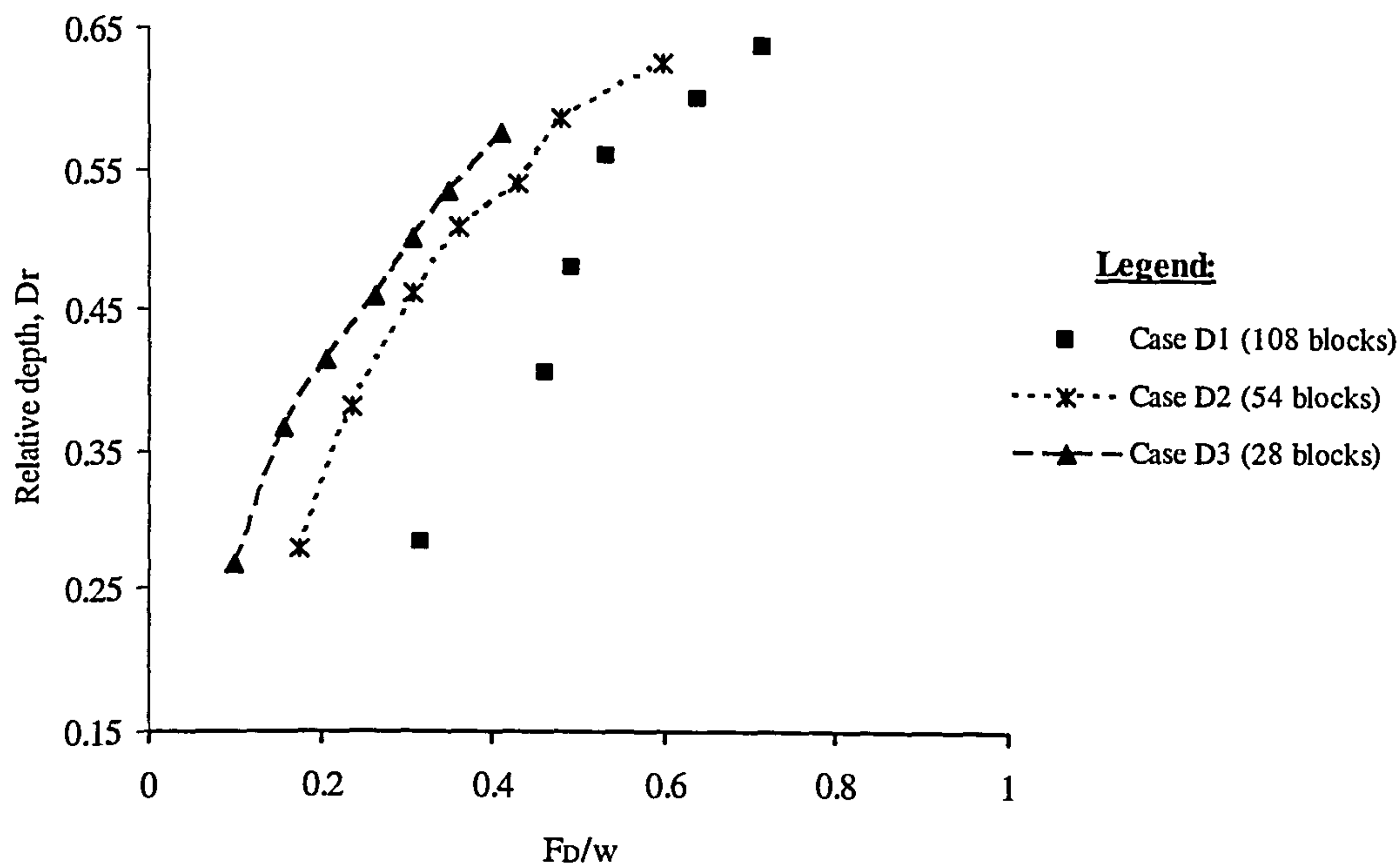


Figure 4.21: Relative depth versus  $F_D/w$  for fixed bed channel Case D Combined Apex and Cross-over Block



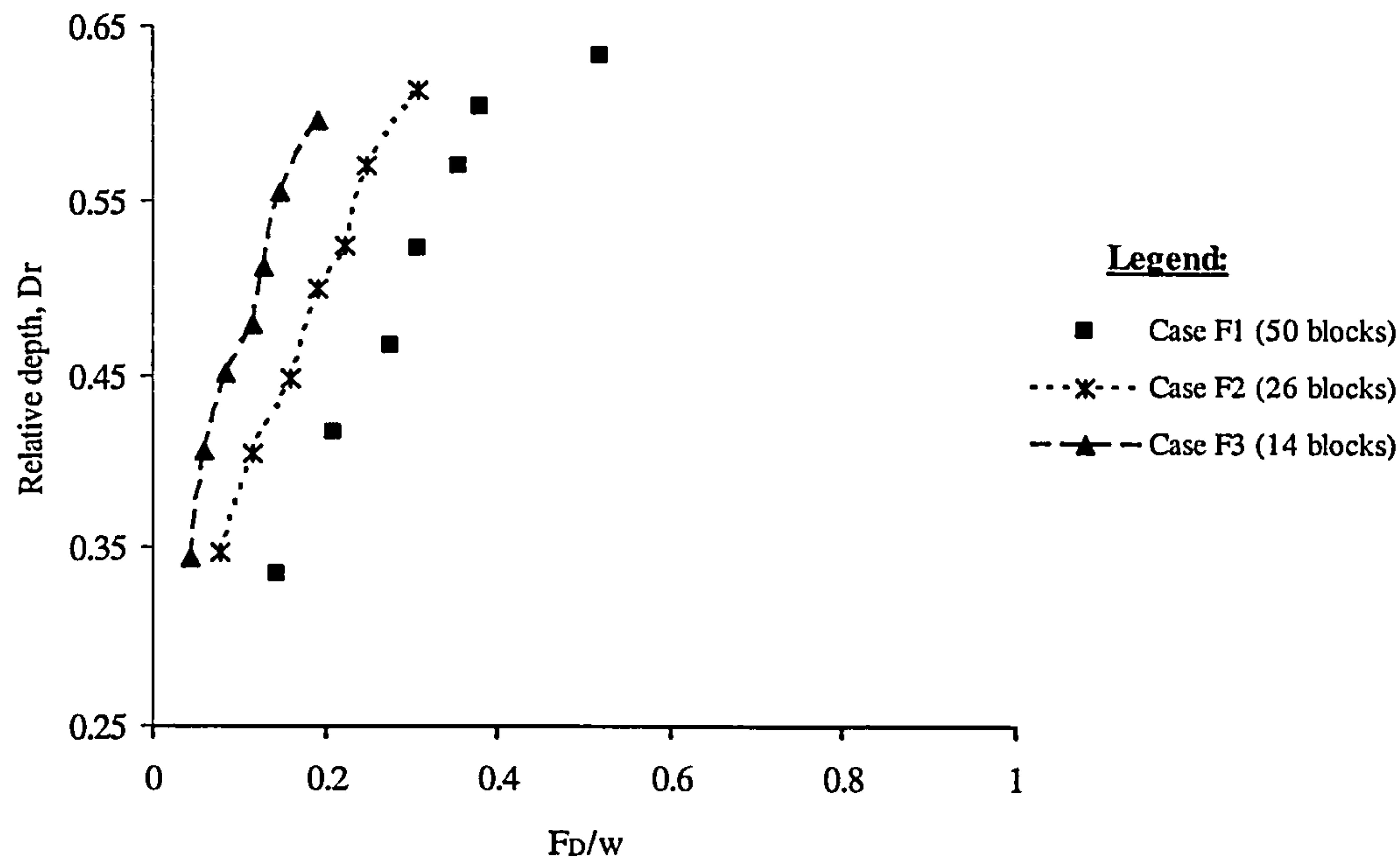


Figure 4.22: Relative depth versus  $F_D/w$  for mobile bed channel *Case F Apex Block*

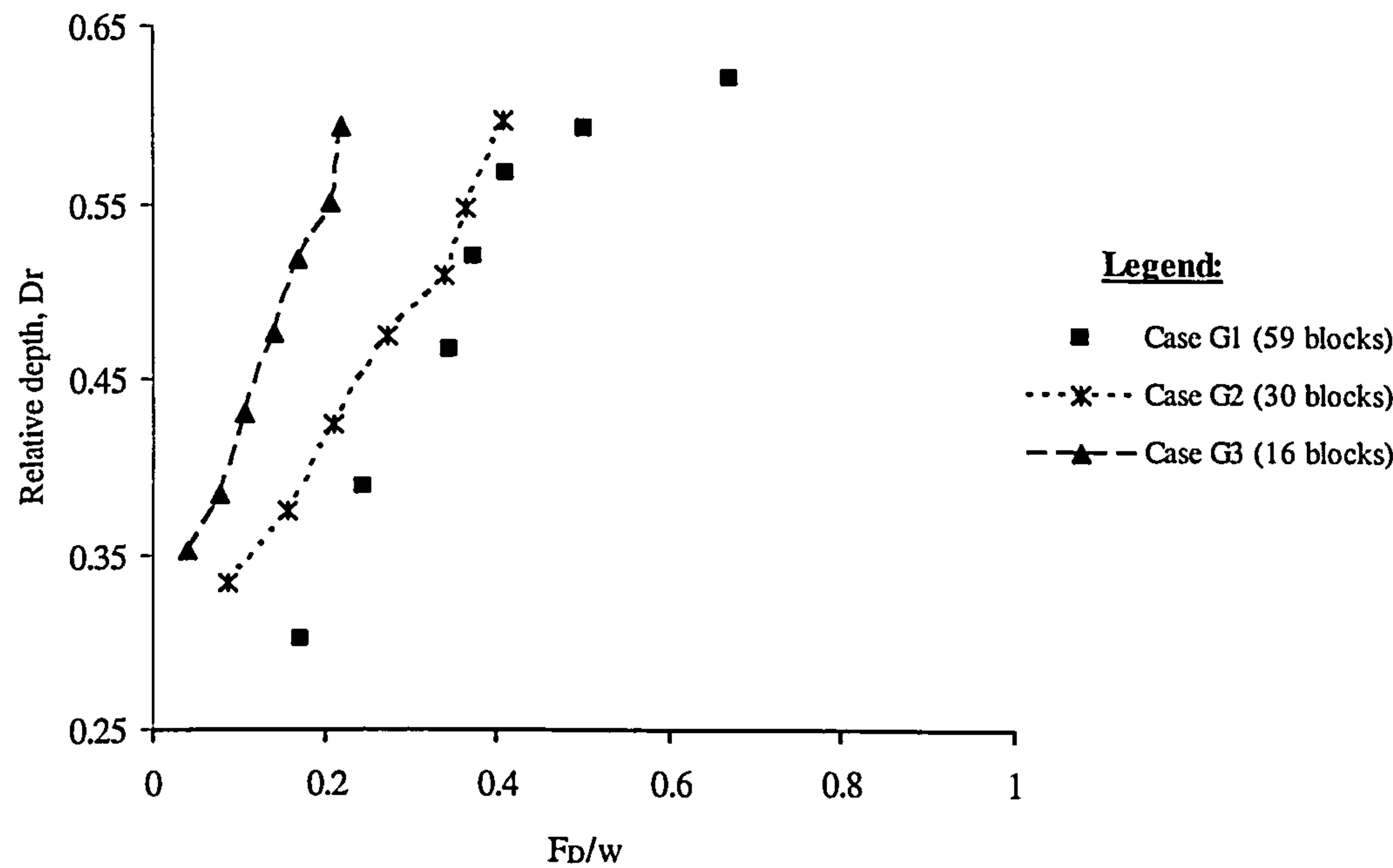
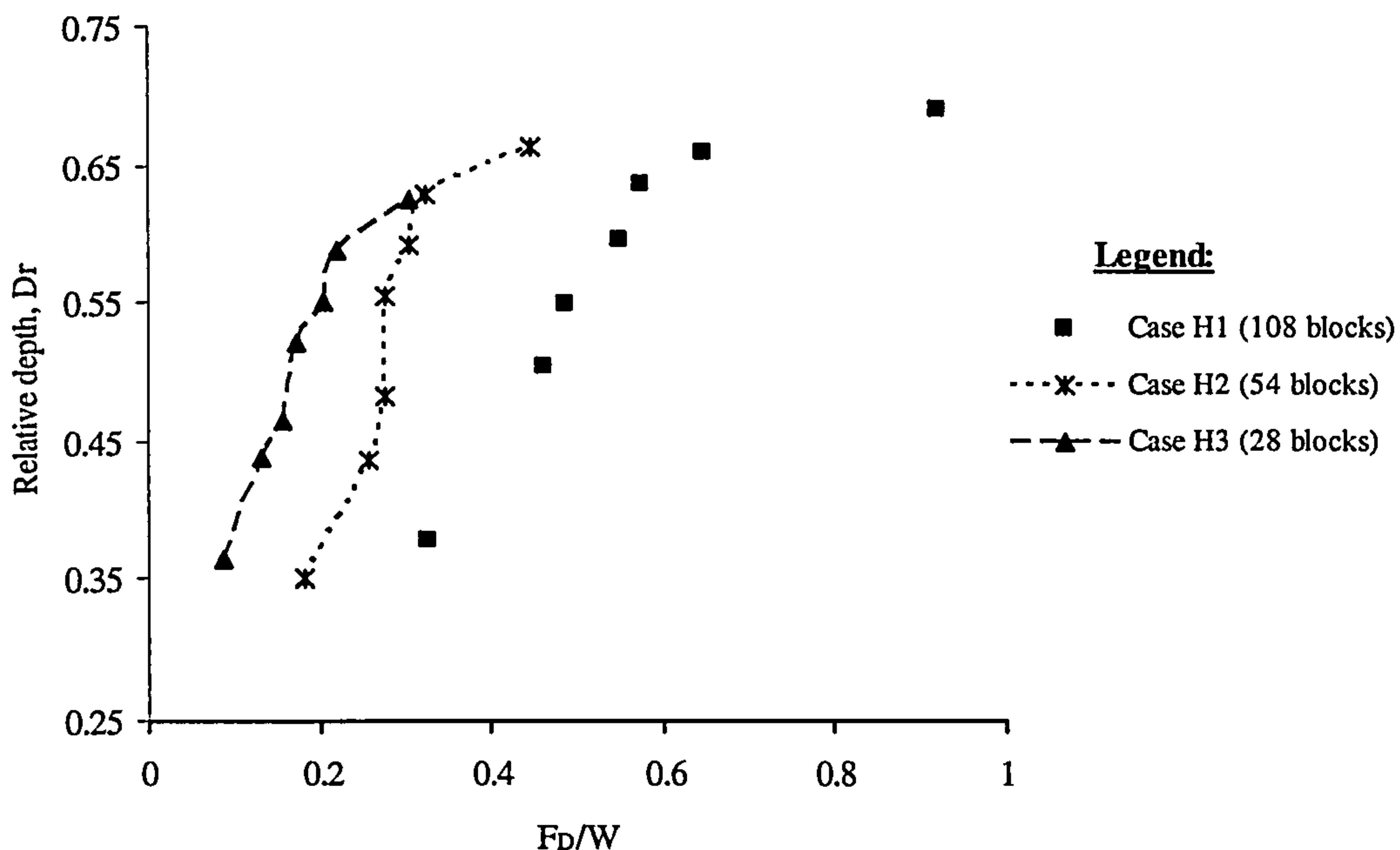


Figure 4.23: Relative depth versus  $F_D/w$  for mobile bed channel *Case G Cross-over Block*





**Figure 4.24:** Relative depth versus  $F_D/w$  for mobile bed channel *Case H Combined Apex and Cross-over Block*

#### 4.4.1 Correction Parameter for the Effect of Blocks ( $\alpha$ )

The ratio,  $F_D/w$  showed that the resistance to flow at high block densities and high relative depth is dominated by drag forces exerted on individual parts of the vegetation field. In this case,  $v$  was the section mean velocity (average velocity) not the approach velocity, as a result, the ratios for some cases are greater than 1.0, which shows that from Equation (4.18), the boundary shear force is negative. This should not happen in physics. The cause of this can be investigated by introducing  $v_p = \alpha w$  and the Darcy-Weisbach friction factor for the non-vegetation case. Recalling that the force balance Equation (4.18) in the previous section was in the following form:

$$\rho g S_o A L_w \left[ 1 + (s-1) \frac{bh}{A} - \frac{N_b (H-h) A_b}{A L_w} \right] = \tau_o L_w P \left[ 1 + \frac{2h(s-1)}{P} - \frac{N_b A_b}{L_w P} \right] + \frac{\rho C_D A_p v_p^2}{2} \quad (4.19)$$

where  $v_p$  = approaching velocity



The Darcy-Weisbach friction factor  $f$  is defined as,

$$\tau_o = \frac{\rho f v^2}{8} \quad (4.20)$$

where  $\tau_o$  = mean boundary shear stress

By substituting Equation (4.20) to Equation (4.19), the following equation can be obtained:

$$\rho g S_o A L_w \left[ 1 + (s-1) \frac{bh}{A} - \frac{N_b (H-h) A_b}{A L_w} \right] = \frac{\rho f}{8} v^2 L_w P \left[ 1 + \frac{2h(s-1)}{P} - \frac{N_b A_b}{L_w P} \right] + \frac{\rho C_D A_p \alpha^2 v^2}{2} \quad (4.21)$$

For the fixed bed case with no blocks, Equation (4.21) becomes,

$$\rho g S_o A L_w \left[ 1 + (s-1) \frac{bh}{A} \right] = \frac{\rho f}{8} v^2 L_w P \left[ 1 + \frac{2h(s-1)}{P} \right] \quad (4.22)$$

When the stage-discharge for the no block case is known, the friction factor  $f$  can be estimated, hence  $f$  can be related with Reynolds number,  $Re$ , as for a Moody diagram ( $f - Re$ ). Applying this  $f - Re$  in block cases to Equation (4.21),  $\alpha$  can be estimated. It should be noted that this  $\alpha$  contains the main effect of  $v_p/v$ , and also some effects of the drag coefficient,  $C_D$ , and the interaction of block wakes with the main channel flow. The following steps are used to estimate  $\alpha$ :

(a) Find the relationship  $f - Re$  from the data for the non-vegetated fixed bed case using

$$f = \frac{8 \rho S_o A L_w \left[ 1 + (s-1) \frac{bh}{A} \right]}{\rho v^2 L_w P \left[ 1 + \frac{2h(s-1)}{P} \right]} \quad (4.23)$$

and the Reynolds number,  $Re$  as,



$$Re = \frac{4vR}{\nu} \quad (4.24)$$

where,

$v$  = average flow velocity

$R$  = hydraulic radius

$\nu$  = kinematic viscosity

(b) Use a fitted curve for  $f - Re$  as shown in Figure 4.25. The fitted  $f - Re$  relationship was

$$\log f = -0.3456 \log Re^2 + 2.3061 \log Re - 4.2569 \quad (4.25)$$

where,

$f$  = bed friction for the non-vegetated fixed bed case

$Re$  = Reynolds number for the non-vegetated fixed bed case

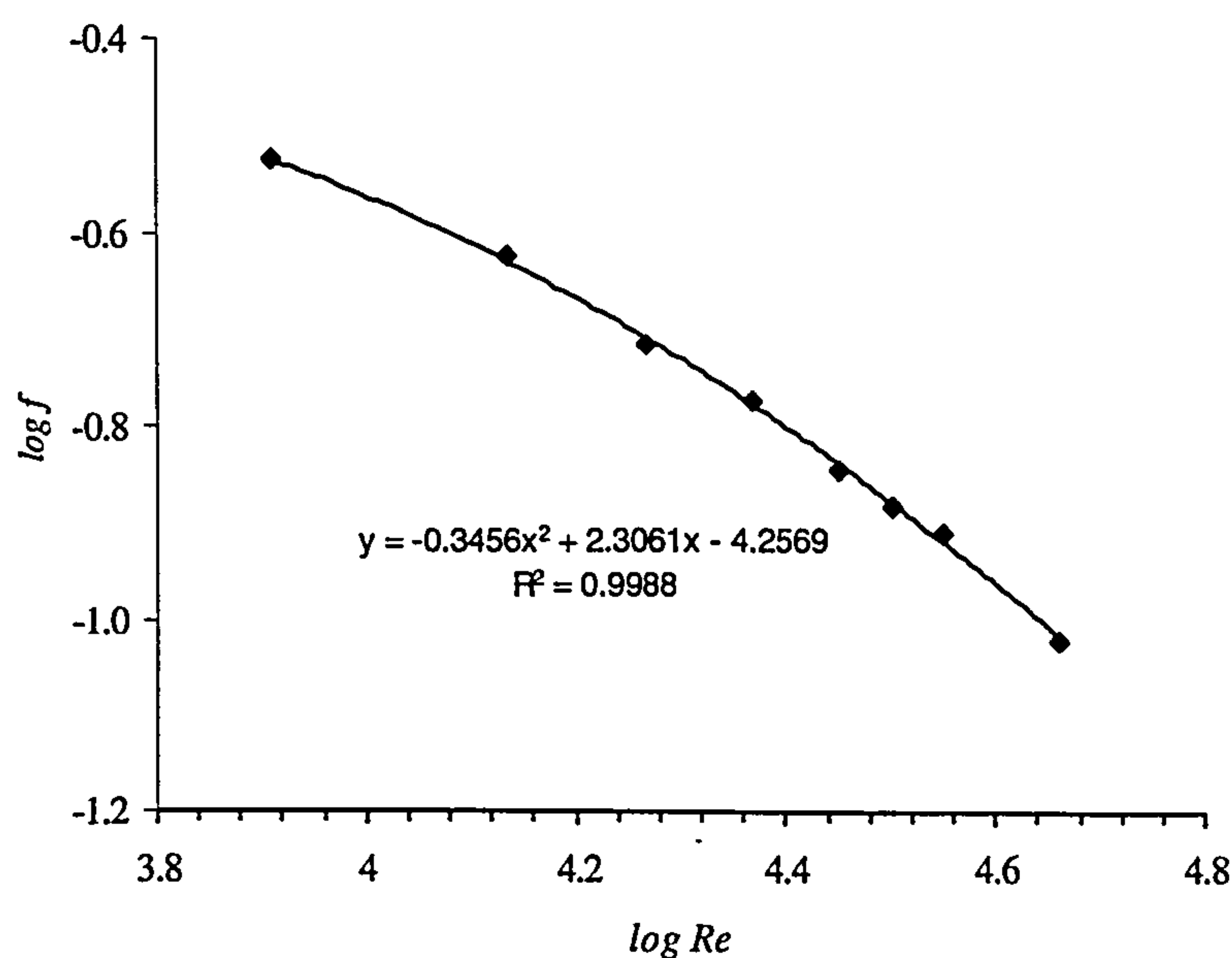


**Figure 4.25:**  $\log f - \log Re$  relationship for the non-vegetated fixed bed case

(c) Use Equation (4.25), and  $Re$  for block cases to estimate  $f$  and then substitute  $f$  and  $v$  in Equation (4.21) and finally estimate  $\alpha$ .

(d) Plot  $\alpha$  against water depth to understand the variation of  $\alpha$ .



The  $\alpha$  -  $Dr$  variations are shown in Figures 4.26 to 4.28. Figure 4.26 shows that the  $\alpha$  coefficient increases as the relative depth increases to  $Dr = 0.4$ , then it decreases for the 50 block case but not for the 14 and 26 block cases where  $\alpha$  decreases over the flow depths. It is noticed that the value of  $\alpha$  is greater than 1.0 in most of depths. This means that the approach velocity,  $v_p$  is greater than average velocity  $v$  or other additional friction occurs.

Figure 4.27 clearly shows that all block cases have a similar pattern where  $\alpha$  increases as the relative depth increases to  $Dr = 0.45$ . This shows that,  $\alpha = v_p/v$ , floodplain velocity,  $v_f (\approx v_p)$  is very small as compared to mean velocity while the floodplain water depth is small. As water depth on the floodplain increases,  $v_f$  also increases so as  $v_p$ , hence  $\alpha$  approaches 1.0. In lower water depth region, the main channel velocity is therefore predominant. However, when  $Dr > 0.45$ , the 16 block case shows that  $\alpha$  remains constant at around 1.0 but not for the 30 and 59 block cases which show that  $\alpha$  decreases as the relative depth increases. The coefficient,  $\alpha$  is less than 1.0 and decreases as water depth increases from  $Dr = 0.45$ . This means that the difference between the mean velocity and the approach velocity becomes larger as water depth increases. The blocks were placed over the cross-over section, the floodplain flow from the main channel, as seen in Shiono and Muto (1998), would be prevented by blocks, hence the velocity on the floodplain behind the blocks is much smaller than no block case. This may be one of the reason for  $\alpha < 1.0$  as water depth increases. The flow interaction in the cross-over section of the main channel due to the floodplain flow entering is also less as compared to no block case, hence the main channel flow is more, as a results, mean velocity possibly increases while the main channel is predominant, hence  $v_p/v$  is getting smaller. The gap between the cases for higher overbank flow shows that  $\alpha$  values significantly reduce when the number of blocks increases, indicating that the approaching velocity is smaller as compared to the average velocity. For *Case D Combined Apex and Cross-over Block*, the  $\alpha$  coefficient increases as the relative depth increases to  $Dr = 0.38$  for the 28 and 54 block cases, then it gradually decreases but the 108 block case clearly shows that  $\alpha$  increases over the flow depth as shown in Figure 4.28. This result apparently shows that  $\alpha$  is higher than 1.0, which implies that the additional friction exists since the approach velocity is blocked by the blocks. This is due to the effect of the changes of drag coefficient,  $C_D$ , the effective projected area,



$A_p$ , and wake interaction with main channel flow interference of wakes of blocks, because the gap between blocks is not wide enough.

Figure 4.29 shows the variation ratios of each mean  $\alpha$  value to  $\alpha$  at the lowest number of blocks against the ratios of the number of blocks to the lowest number of blocks. The results of the best-fit line are presented for three different vegetated floodplain, fixed-bed cases respectively and the equations are given below:

For Case B Apex Block:

$$\frac{\alpha N_b}{\alpha N_{14}} = -0.0786 \left( \frac{N_b}{N_{14}} \right) \quad (4.26)$$

For Case C Cross-over Block:

$$\frac{\alpha N_b}{\alpha N_{16}} = -0.1707 \left( \frac{N_b}{N_{16}} \right) \quad (4.27)$$

For Case D Combined Apex and Cross-over Block:

$$\frac{\alpha N_b}{\alpha N_{28}} = -0.0122 \left( \frac{N_b}{N_{28}} \right) \quad (4.28)$$

This is important because Equation (4.21) with these Equations (4.26) to (4.28) for the fixed bed case shows that, by knowing the geometry, water depth and  $\alpha$ , the discharge can be worked out by using a successive approximations method or the Newton-Raphson Method for solving non-linear equations. Obviously, the  $f - Re$  relationship could be different for different roughnesses of the floodplain and main channel.



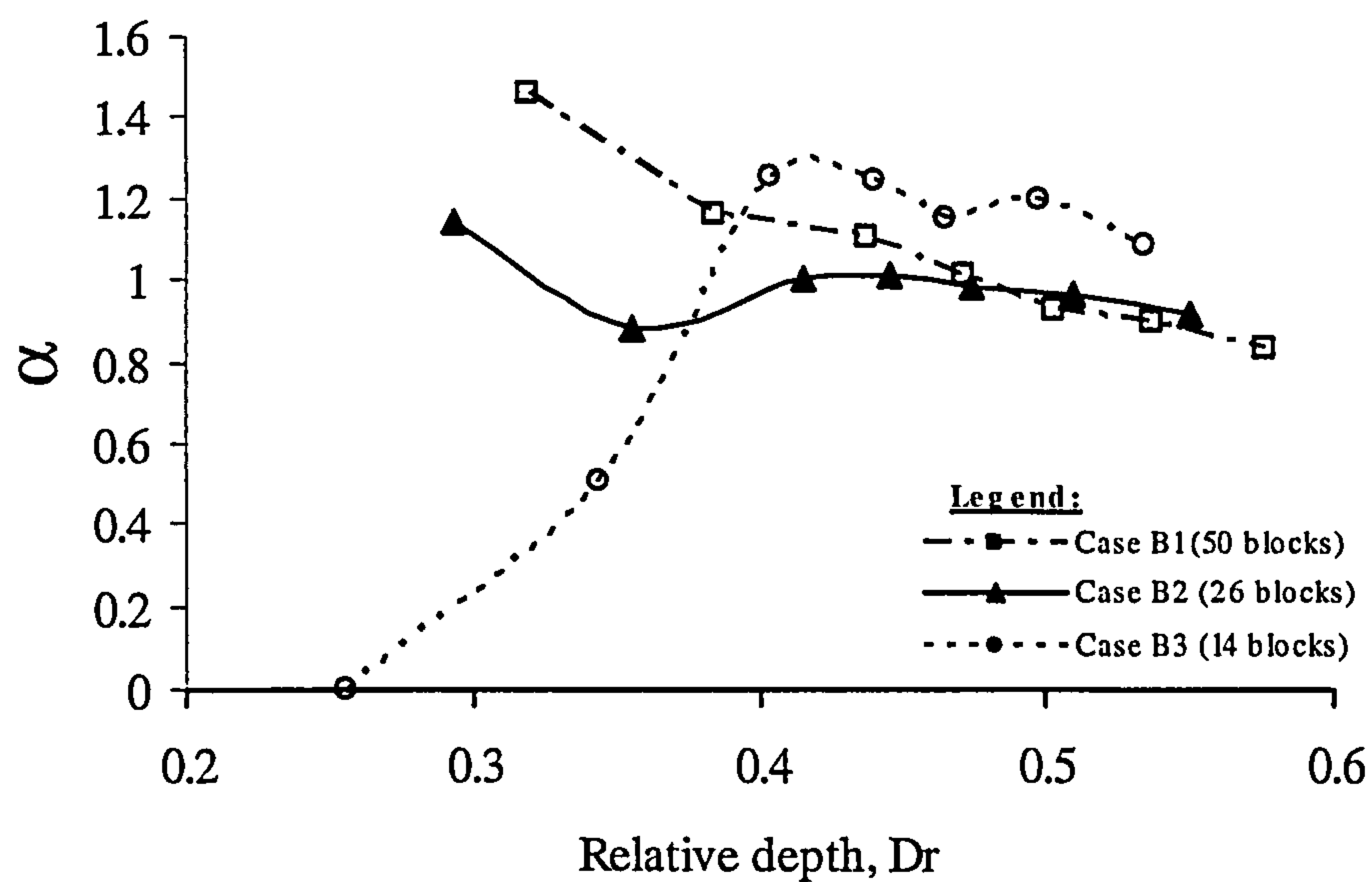


Figure 4.26: The relationship between  $\alpha$  and  $D_r$  for fixed bed channel *Case B Apex Block*

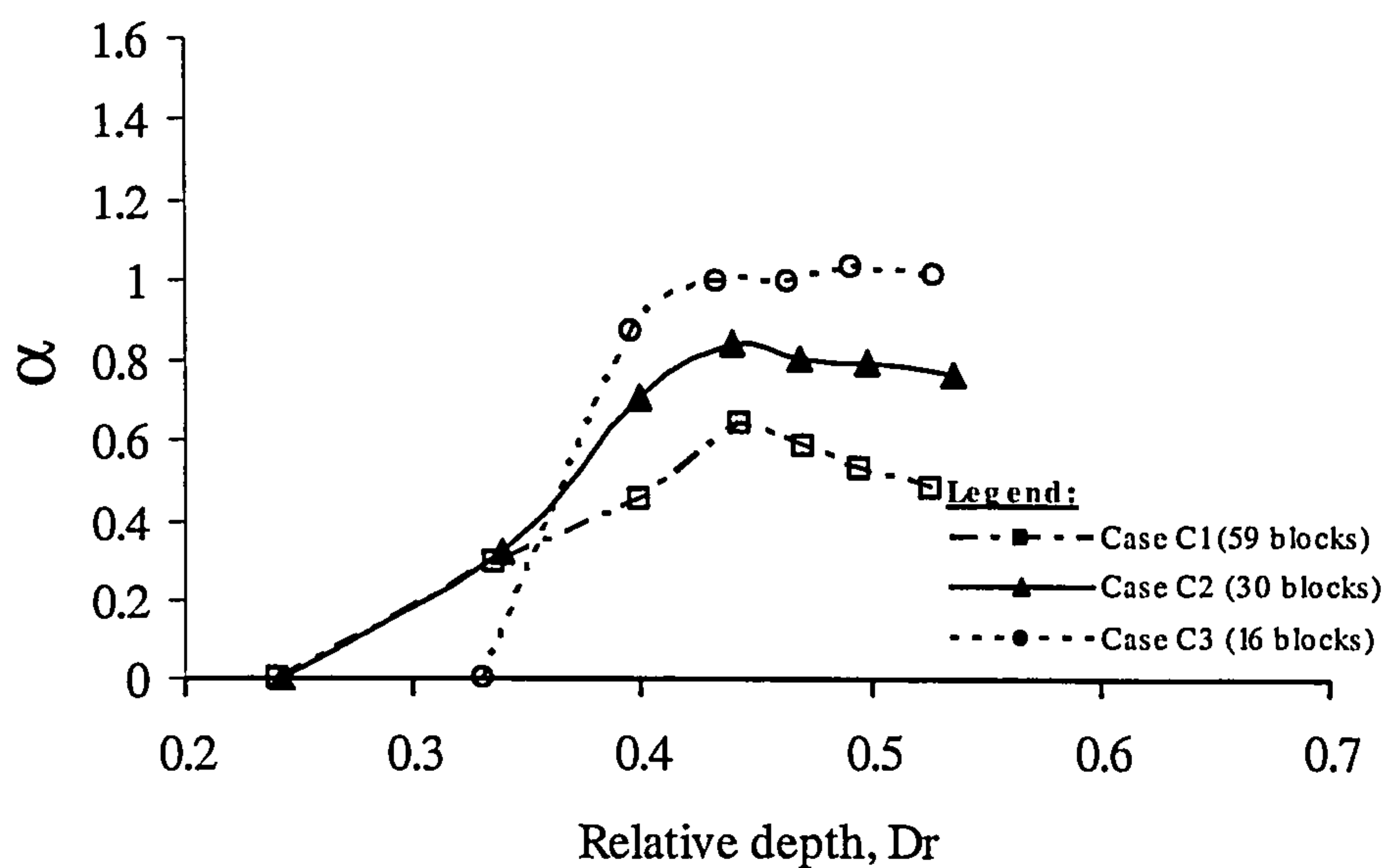


Figure 4.27: The relationship between  $\alpha$  and  $D_r$  for fixed bed channel *Case C Cross-over Block*



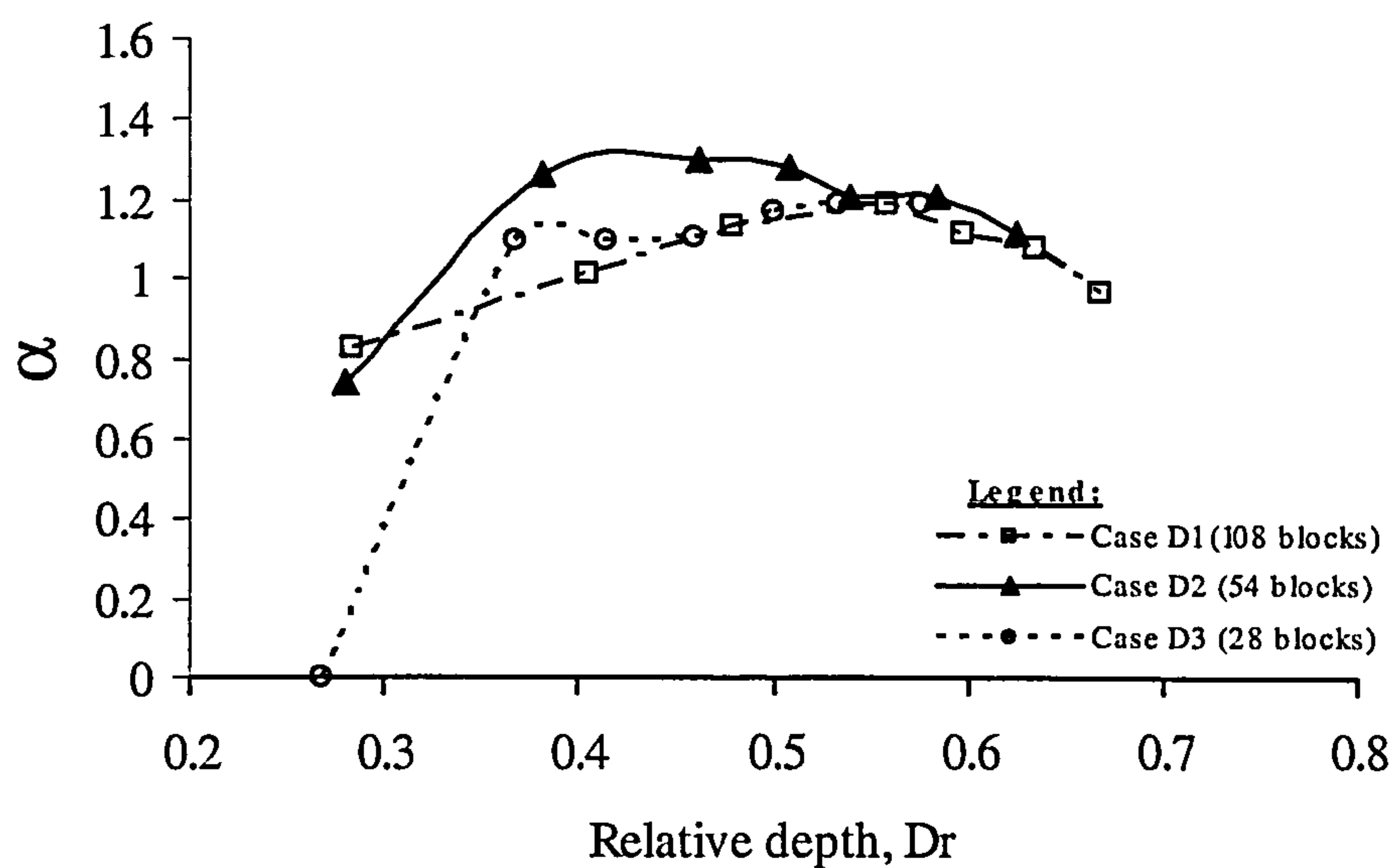


Figure 4.28: The relationship between  $\alpha$  and  $Dr$  for fixed bed channel Case D Combined Apex and Cross-over Block

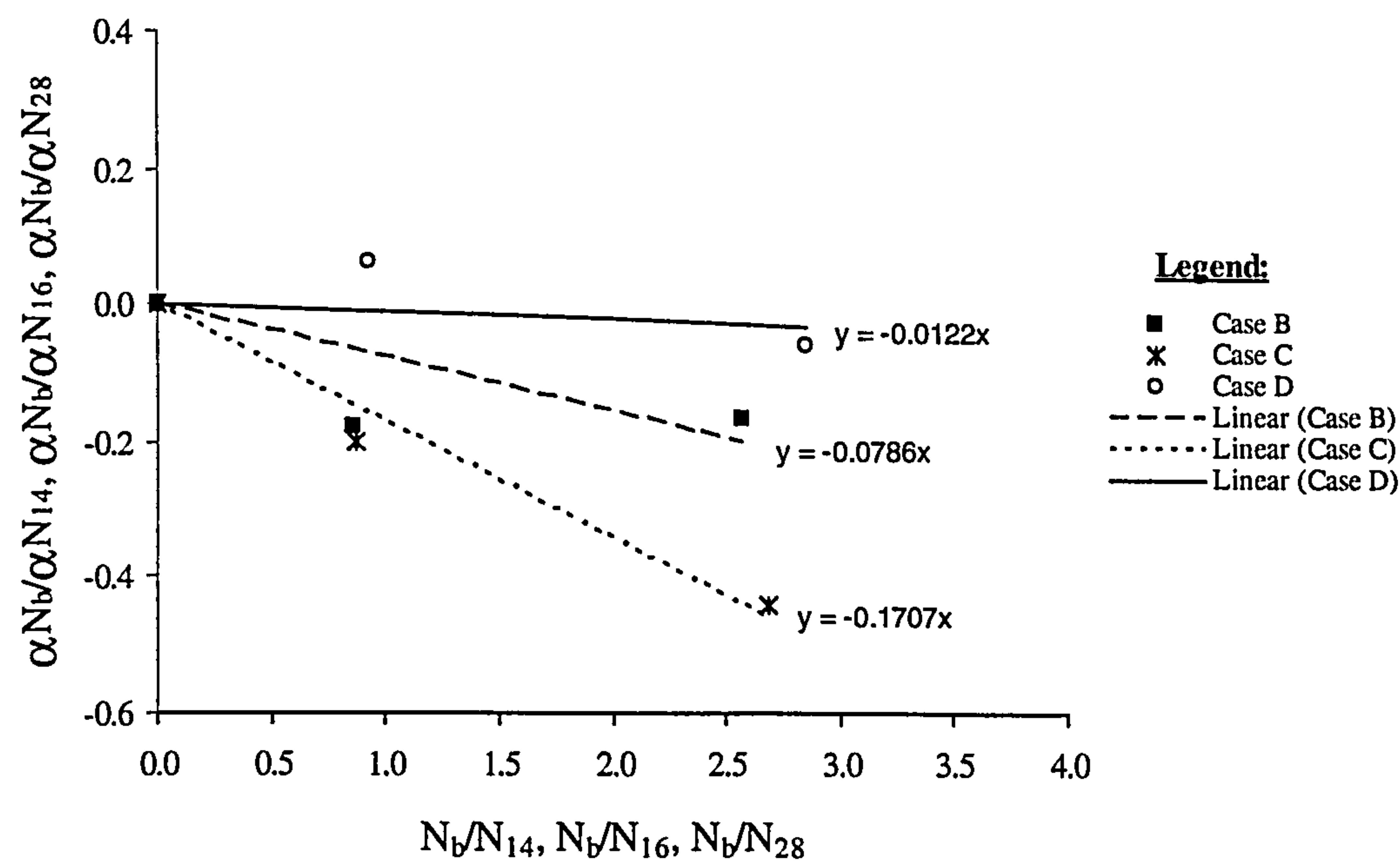


Figure 4.29: Ratios of each  $\alpha$  value to  $\alpha$  at the lowest number of blocks being considered against the ratios of the number of blocks to the lowest number of blocks being considered for each case



In the mobile bed case, the total boundary friction factor is the sum of the boundary friction factor and the additional bedform friction factor in the main channel. It seems that adding the two friction factors in this manner is technically wrong, however in normal engineering practice, the main channel flow resistance is commonly calculated in the divided approach. The attempt to estimate the total friction factor was made assuming that the variations of the bedform friction factor within the main channel are significant between the fixed bed and mobile bed cases. The total friction factor in the mobile bed case should be the sum of the boundary friction factor with the fixed bed in the whole meandering compound channel and additional bedform friction factor within the main channel as,

$$\rho g S_o A L_w \left[ 1 + (s-1) \frac{bh}{A} - \frac{N_b (H-h) A_b}{A L_w} \right] = \frac{\rho f}{8} v^2 L_w P \left[ 1 + \frac{2h(s-1)}{P} - \frac{N_b A_b}{L_w P} \right] + \frac{\rho f'}{8} v_m^2 P L_w s b + \frac{\rho C_D A_p v^2}{2} \quad (4.29)$$

where,

$f$  = boundary friction factor

$f'$  = bedform friction factor

$v_m$  = main channel velocity

and for bedform friction factor,  $f'$  is:

$$f' = \frac{8 \rho S_o A L_w \left[ 1 + (s-1) \frac{bh}{A} - \frac{N_b (H-h) A_b}{A L_w} \right] - \frac{\rho f}{8} v^2 L_w P \left[ 1 + \frac{2h(s-1)}{P} - \frac{N_b A}{L_w P} \right] - \frac{\rho C_D A_p \alpha^2 v^2}{2}}{\rho v_m^2 L_w P s b} \quad (4.30)$$

In the mobile bed case, the bedform friction factor can be calculated using Equation (4.30) after having fitted an equation for  $\alpha$  in the fixed bed case. However  $v_m^2$  is not known, in this case,  $v_m = v$  was used to estimate  $f$ . As the main channel flow is dominated in the shallower floodplain water depth, the main channel velocity is nearly the mean velocity on the other hand, in deeper floodplain water depth, the floodplain flow is dominated, and the main channel velocity is depressed by the flow crossing over the main channel, hence  $v > v_m$  as a result,  $f'$  is expected to be smaller than true value. Figures 4.30 to 4.32 show the plots of the ratio of bedform friction factor to boundary friction factor against the relative depth. In general, it is clearly seen from the



figures that the ratio of bedform friction factor to boundary friction factor increases as the relative depth increases, which implies that the bedform friction factor indeed increases at the higher overbank flow.

Figure 4.30 shows that the bedform friction factor contributes 40 % of the boundary friction factor at the shallower depth and more than 80 % at higher overbank for *Case F Apex Block*. For *Case G Cross-over Block*, the bedform friction factor is shown to vary and depend on the number of blocks as shown in Figure 4.31. Cross-over block *Case G2*, the 30 block case, has 10 % bedform friction factor of the boundary friction factor at the shallow overbank flow on the other hand, the 59 and 16 block cases, have around 30 %. However, in *Case H Combined Apex and Cross-over Block*, as shown in Figure 4.32, the bedform friction factor for higher overbank flow is seen to be much than the other cases, which is up to 300 % for the 108 block case compared to 220 % and 150 % for the 54 and 28 block cases respectively. In general, all cases show higher percentages of bedform friction factor as the number of blocks increases. Also, it is clearly seen that the bedform friction factor values are smaller for *Case G Cross-over Block* than for *Case F Apex Block* and *Case H Combined Apex and Cross-over Block*. This indicates a good agreement with the reduction of channel average velocity and boundary shear stress in the main channel, which will be discussed in detail in Chapter 5.

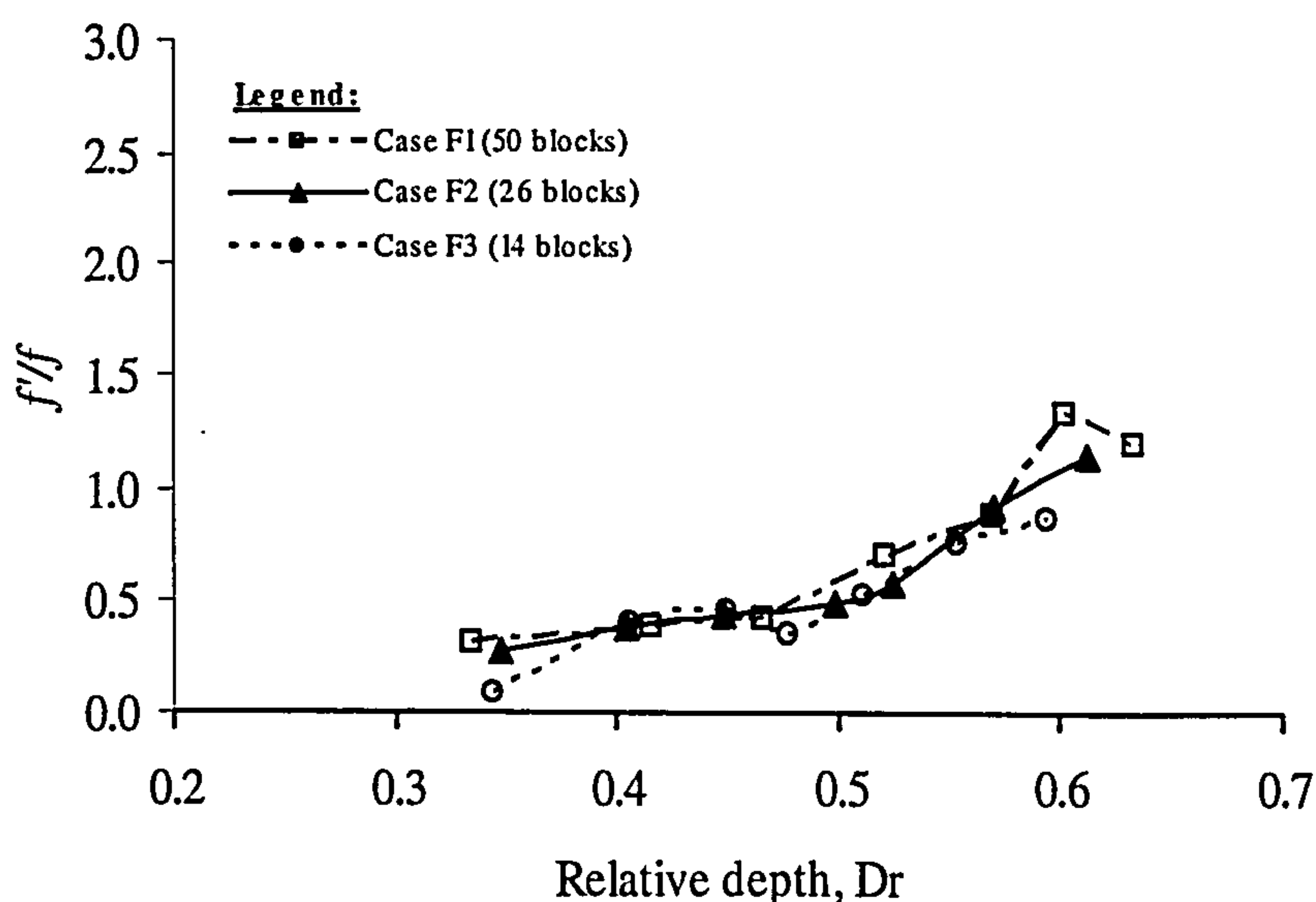


Figure 4.30: Ratios of bedform friction factor to boundary friction factor against  $D_r$  for mobile bed channel *Case F Apex Block*



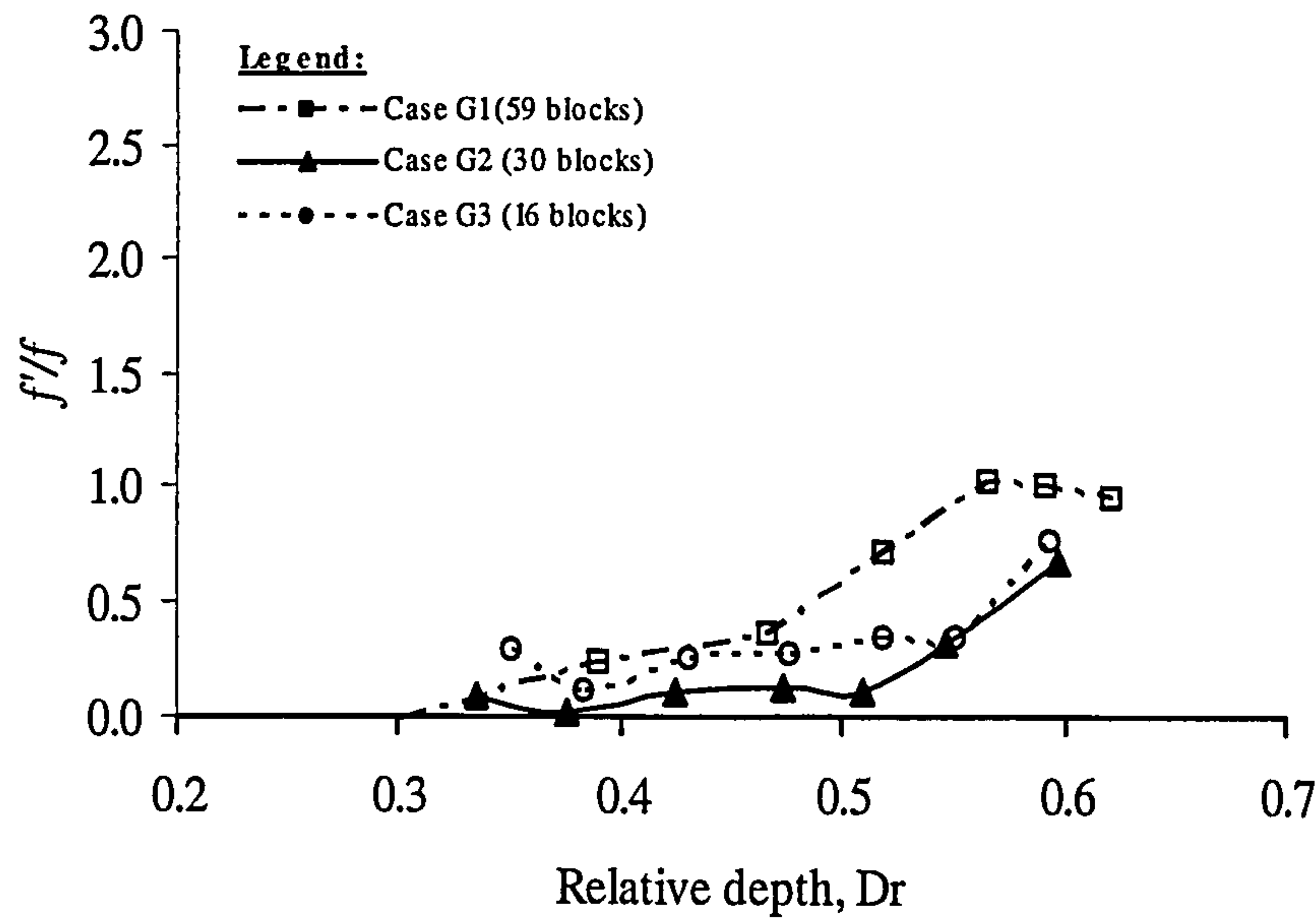


Figure 4.31: Ratios of bedform friction factor to boundary friction factor against  $Dr$  for mobile bed channel *Case G Cross-over Block*

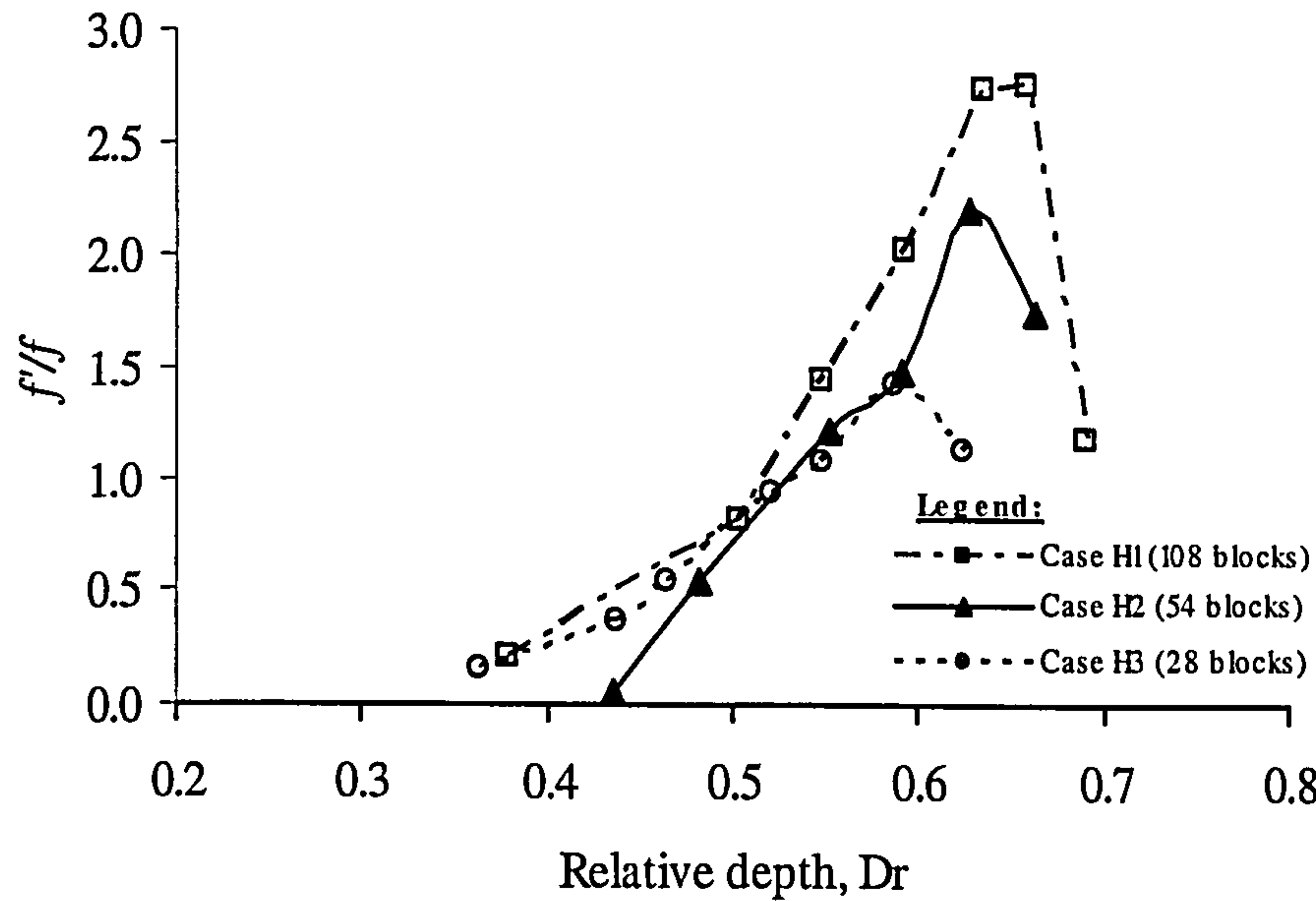


Figure 4.32: Ratios of bedform friction factor to boundary friction factor against  $Dr$  for mobile bed channel *Case H Combined Apex and Cross-over Block*



#### 4.5 The Relationships Between the Blocks Density and Manning's n

In this study block density or vegetation density ( $V_{den}$ ) is an effective quantitative expression representing the block area per unit length of channel per unit area of flow. It has been used by Pertryk and Bosmajian (1975) and James *et al.* (2001) in the form:

$$V_{den} = \frac{C_D \sum A_p}{AL} \quad (4.31)$$

where,

$C_D$  = block drag coefficient

$A_p$  = projected area of block in the flow direction

$A$  = total cross-sectional area of flow

$L$  = length of channel reach considered

In order to investigate the effect of block density parameters on values of the Manning's n, several comparisons were made between the Manning's n values of different block densities by plotting Manning's n versus each arrangement as shown in Figures 4.33 to 4.35 for fixed bed case only. Figure 4.33 shows the increase in Manning's n when the number of the blocks increases from 14 blocks to 26 blocks and from 26 blocks to 50 blocks for *Case B Apex Block*. Figures 4.34 and 4.35 also show that the change in Manning's n due to the change in the projected area of the blocks increases as the density of the blocks increases. It is very obvious that the value of Manning's n increases when the projected area becomes larger and the density of the vegetation is higher, as in *Case D Combined Apex and Cross-over Block*.

It was expected that the major factor affecting Manning's n would be the density of the blocks. As was mentioned in the literature review, the drag coefficient is assumed to be related to Manning's n, it is therefore very relevant to use  $A_p/AL$  for the analysis. The ratio  $C_D A_p/AL$  will be a good indication of how the intensity of the momentum of flow is absorbed by the blocks. In other words, it indicates that using  $V_{den}$  is a good representation of the density of the areas absorbing the momentum of the flow.



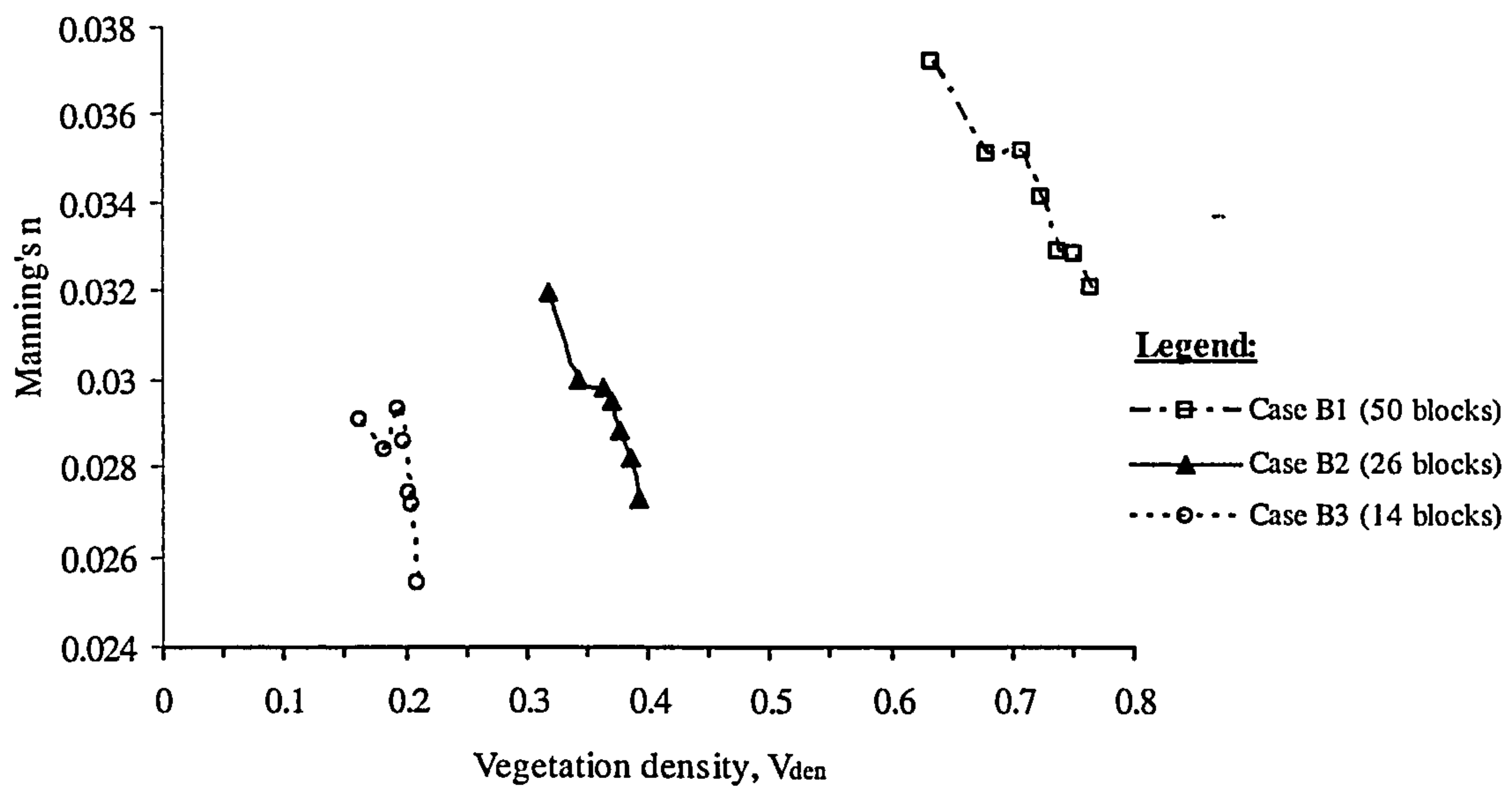


Figure 4.33: The relationship between Manning's  $n$  and the density of blocks for *Case B Apex Block*

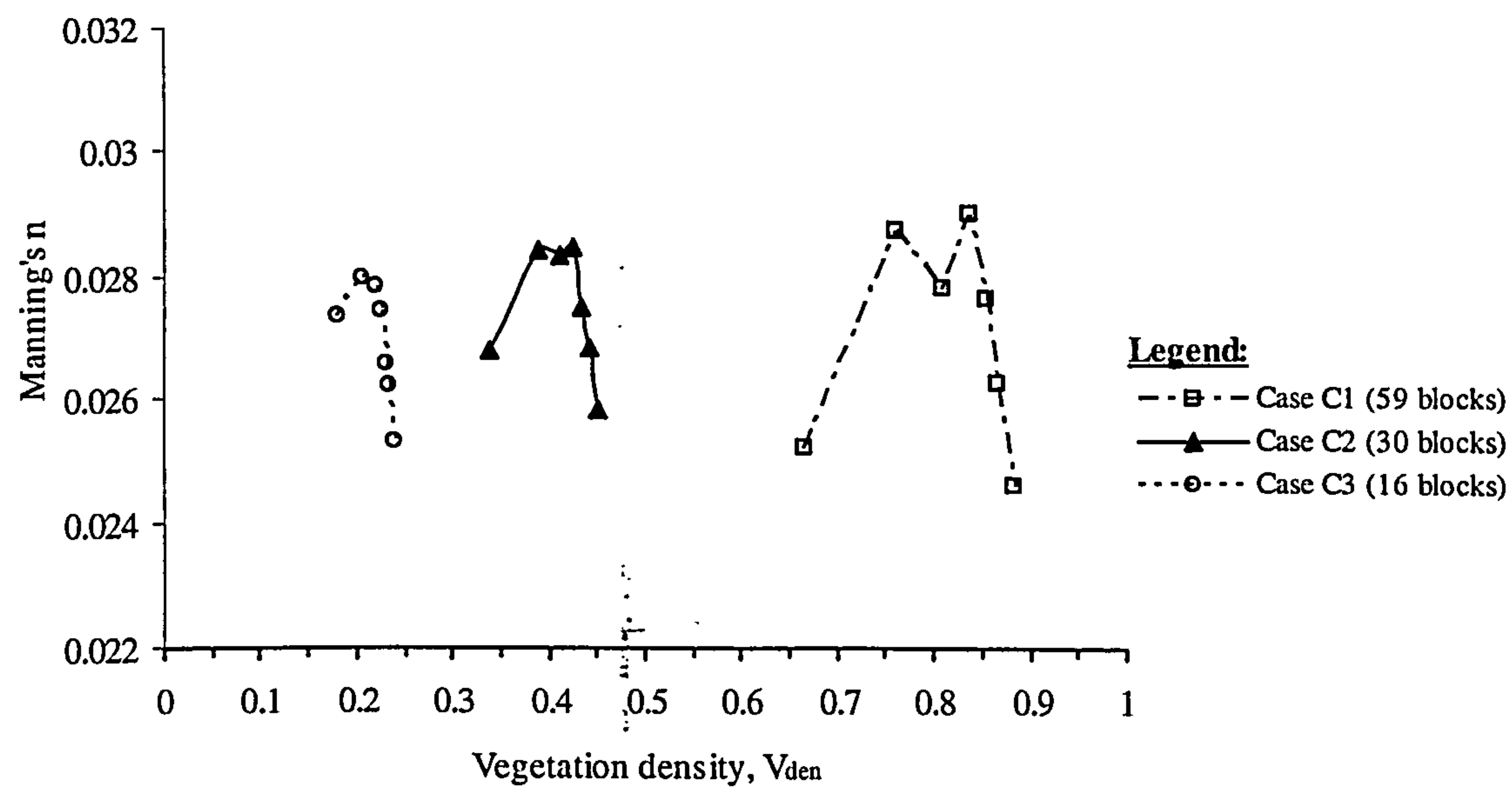


Figure 4.34: The relationship between Manning's  $n$  and the density of blocks for *Case C Cross-over Block*



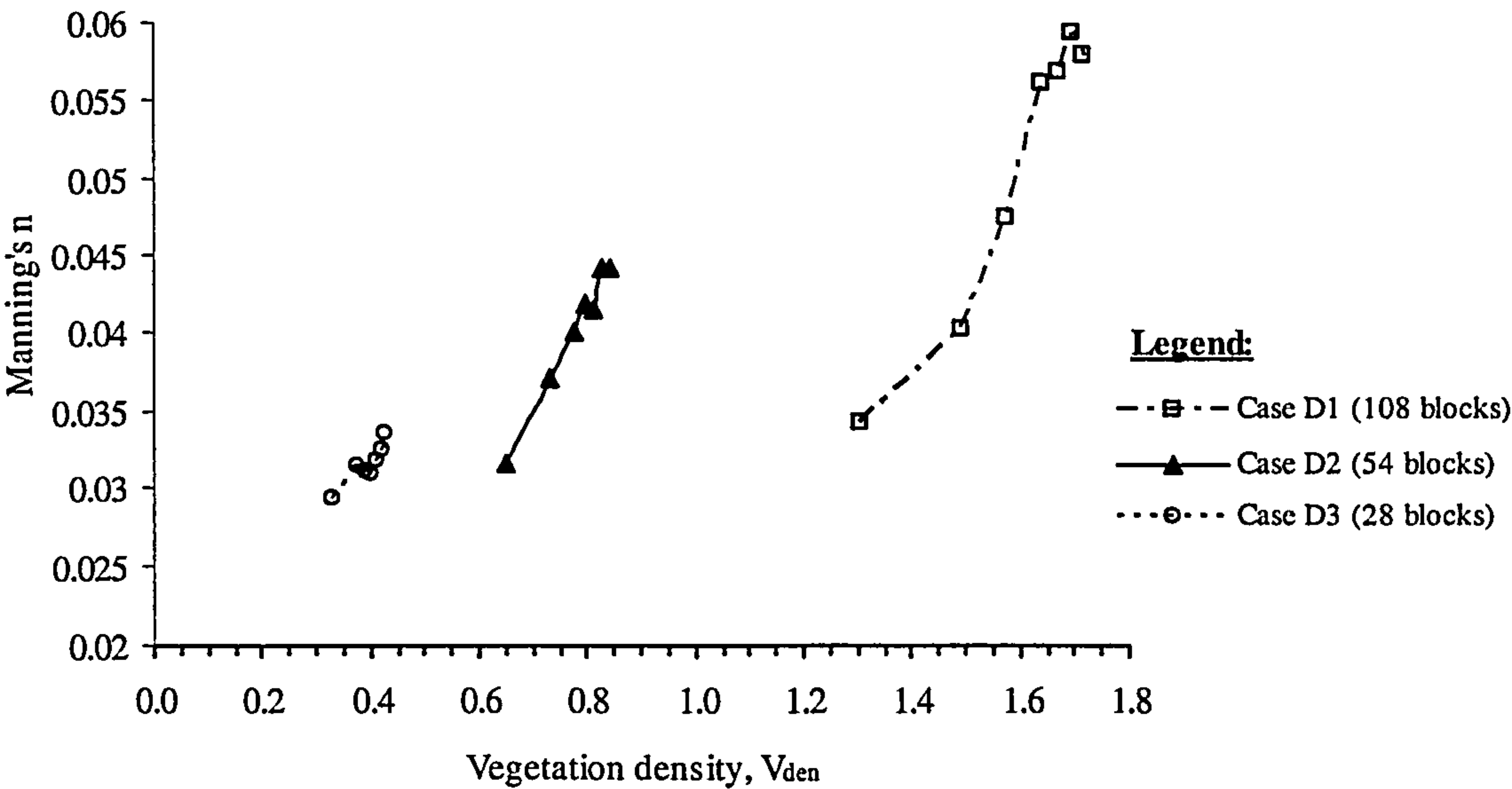


Figure 4.35: The relationship between Manning’s  $n$  and the density of blocks for *Case D Combined Apex and Cross-over Block*

4.6 Bedforms for the Mobile Bed Case

In this section, the bedform morphology is observed with the purpose of visualising and understanding the flow phenomena happening behind the blocks. All experiments were carried out using a constant flow rate and runs were allowed to continue until the bed reached a state of dynamic equilibrium. Typical bedforms were observed in four series of experiments for two relative depths, namely, *Case E No Block*, *Case F Apex Block*, *Case G Cross-over Block* and *Case H Combined Apex and Cross-over Block* as shown in Figures 4.36, 4.37, 4.38 and 4.39 respectively. The water is flowing from the right hand side (upstream) to the left hand side (downstream) shown by an arrow.

Figure 4.36 shows a series of bedforms for *Case E No Block*. The bedforms at the lower relative depth,  $Dr = 0.2$  exhibit a typical bedform profile as normally expected for shallow water depths which is that the deeper section appears along the outside of the bend and the shallow section appears on the inside of the bend. At  $Dr = 0.45$  for higher flow depths distinctive sand bars with a series of ridges are formed. It is clear that the ridges are created by the secondary flows. At the cross-over section the ridges extend



directly across the channel from the upstream to the downstream bank. The ridges originating further downstream from the cross-over section continue down the bend apex. Similar bedforms have been observed by Rameshwaran *et al.* (1999).

In *Case F Apex Block* for 26 block case, as shown in Figure 4.37, at  $Dr = 20$ , small dunes are formed in the cross-over section, due to the arrangement of blocks on the floodplain. At  $Dr = 0.45$ , the sand bars appear, a scouring region occurs at the inner apex bank immediately after the cross-over section, the largest deposition occurs at the centre of the apex bend and several scourings are formed behind the blocks at the outer side of the apex bend.

For 30 blocks *Case G Cross-over Block*, as shown in Figure 4.38, at  $Dr = 0.2$ , the bed topography with several scourings is formed behind the blocks at the cross-over section. This is due to the vortices generated by blocks like wake flow. At  $Dr = 0.45$  the higher flow-depths show that the bed is covered with irregular bedforms consisting of ripples along the cross-over section. It was observed that sediment was carried away from the main channel at the centre of the apex section and deposited onto the floodplain downstream due to the strong “cross-over” flow at the apex section. The strong “cross-over” flow is caused by blocking flow in the meander belt with blocks along the inner side.

The bedforms at  $Dr = 0.20$  and  $Dr = 0.45$  for 54 blocks *Case H Combined Apex and Cross-over Block* are shown in Figure 4.39. At  $Dr = 0.20$  the bedforms are fairly similar to those generated in *Case E No Block* but the bedforms indicate that scouring clearly occurs behind each block along the cross-over section. The deposition of sediment occurs at the inner side of the apex bend with the bedform at the cross-over section again showing a number of scourings, which indicates that the flow interaction between the floodplain flow and the main channel flow helps to generate the vortices. At  $Dr = 0.45$  distinctive bedforms due to scouring are formed at the cross-over section and extend across the channel whilst deposition of sediment occurs at the outer side of the apex bend.

Looking at bedforms' morphology, it what is happening behind the blocks can be imagined, although it cannot be seen in the fixed bed experiment.



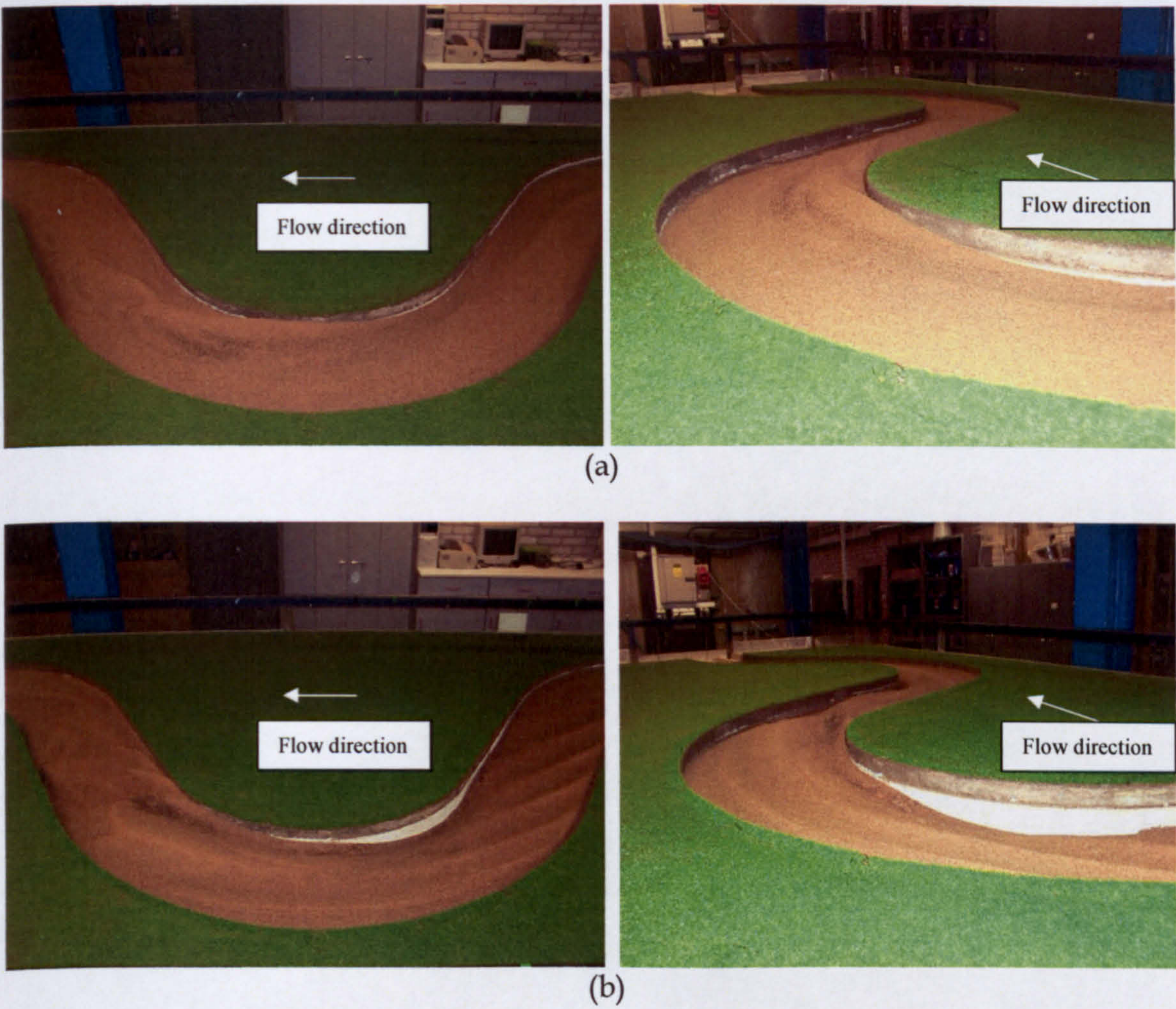
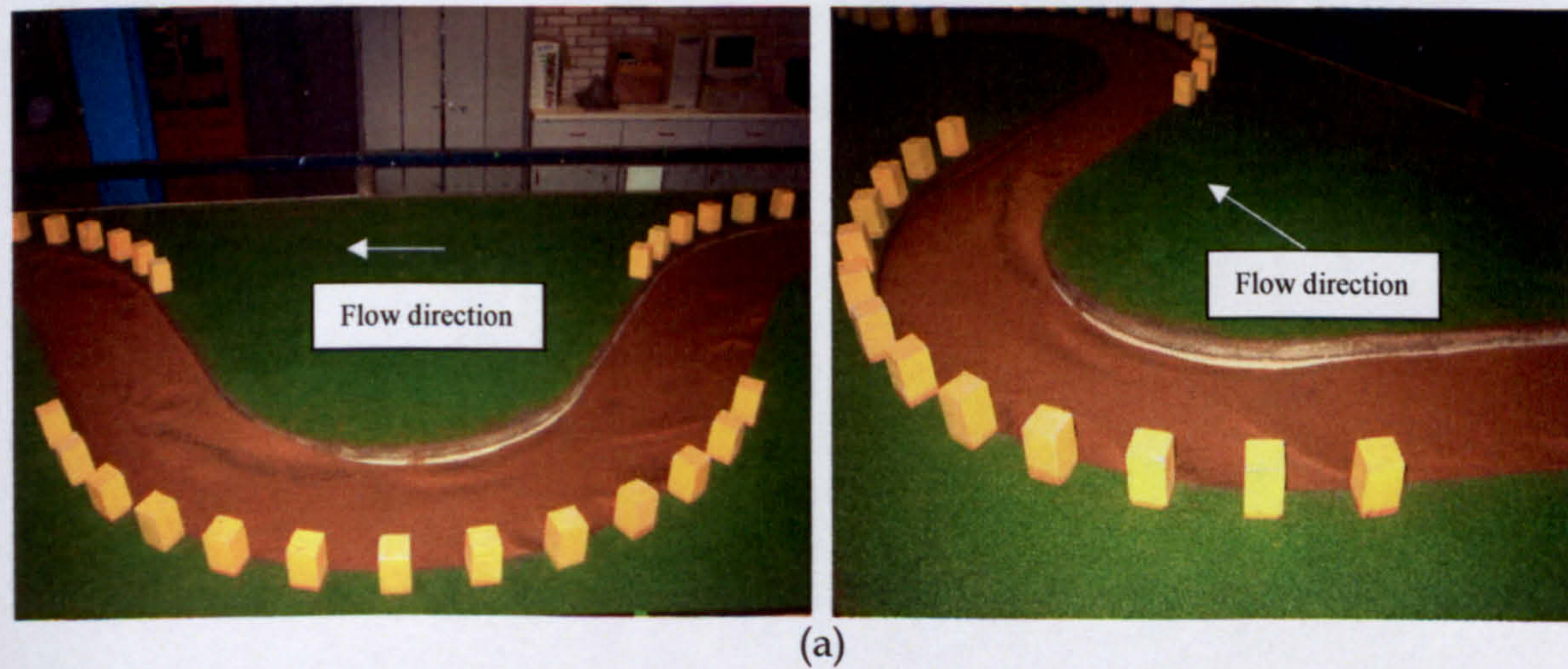


Figure 4.36: View of bedforms' morphology for *Case E No Block* (a)  $Dr = 0.20$  (b)  $Dr = 0.45$





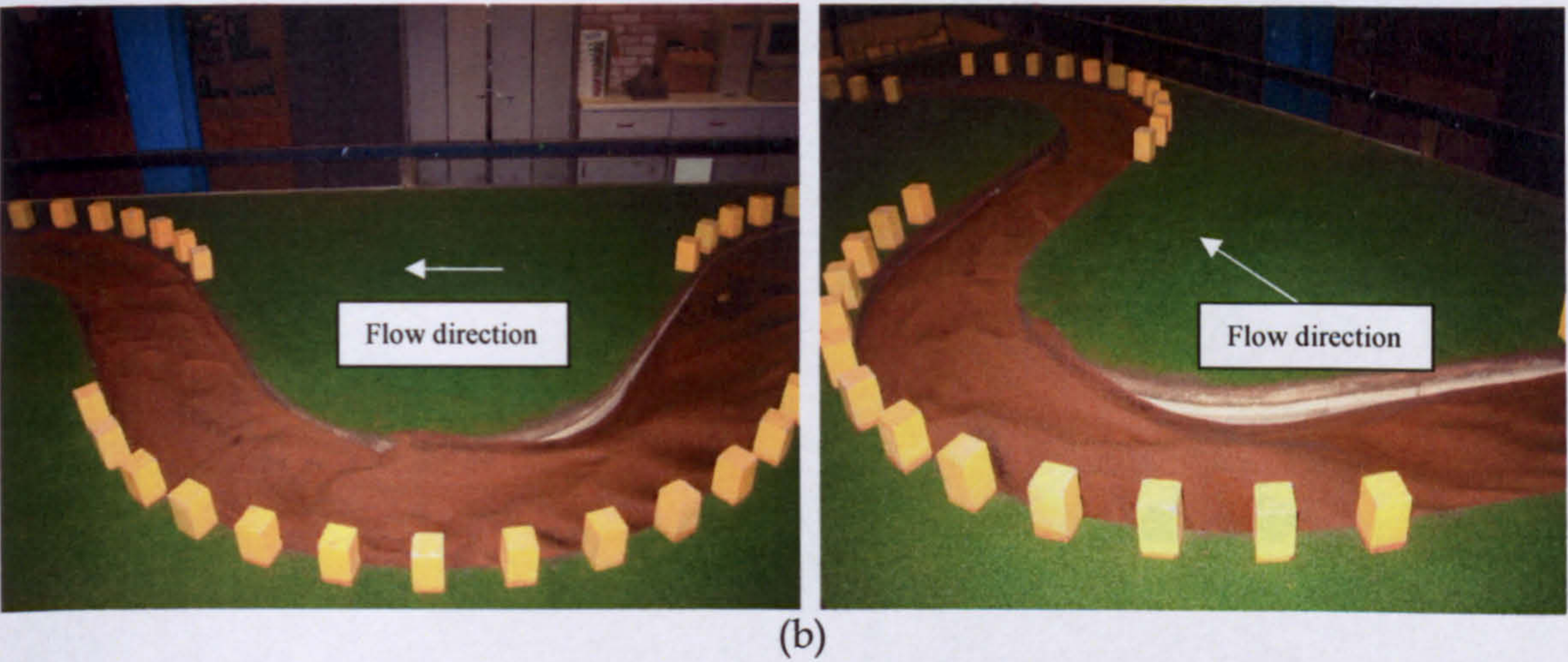


Figure 4.37: View of bedforms' morphology for block 26 *Case F Apex Block* (a)  $Dr = 0.20$  (b)  $Dr = 0.45$

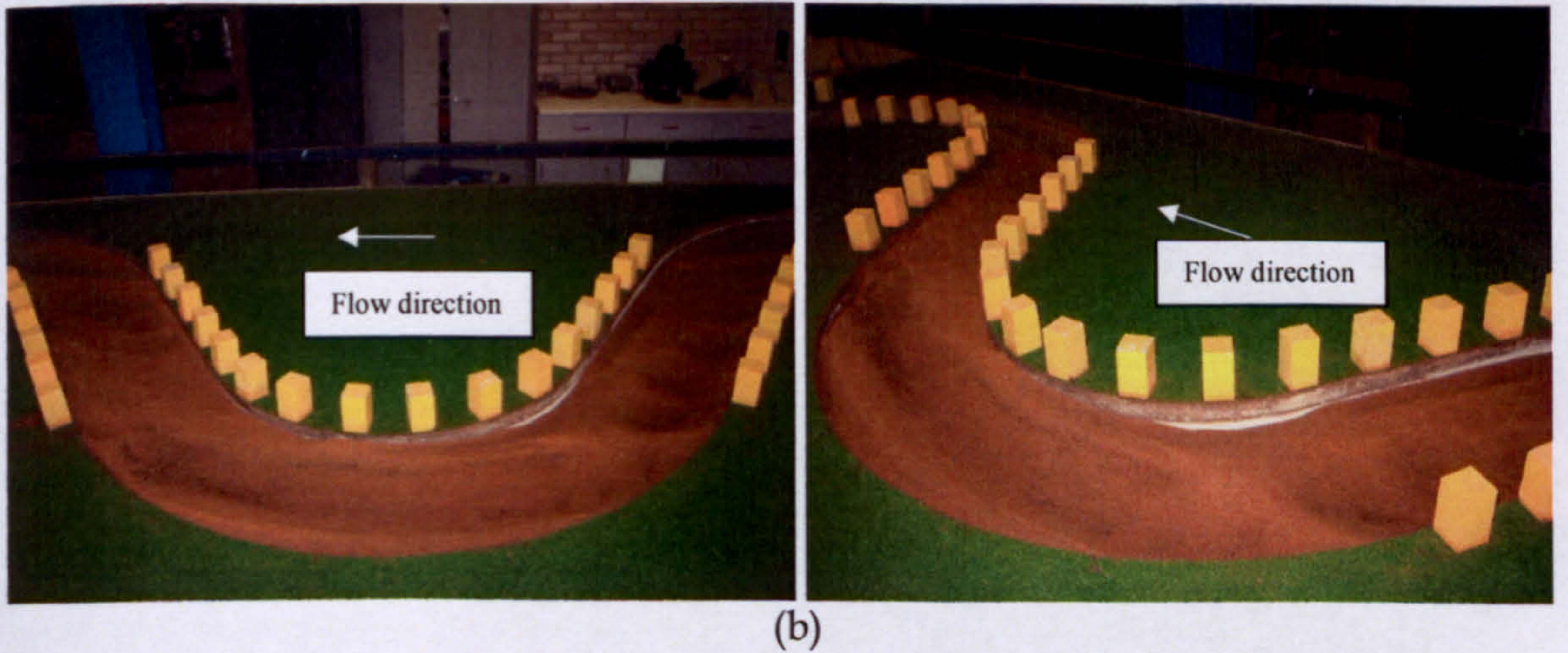
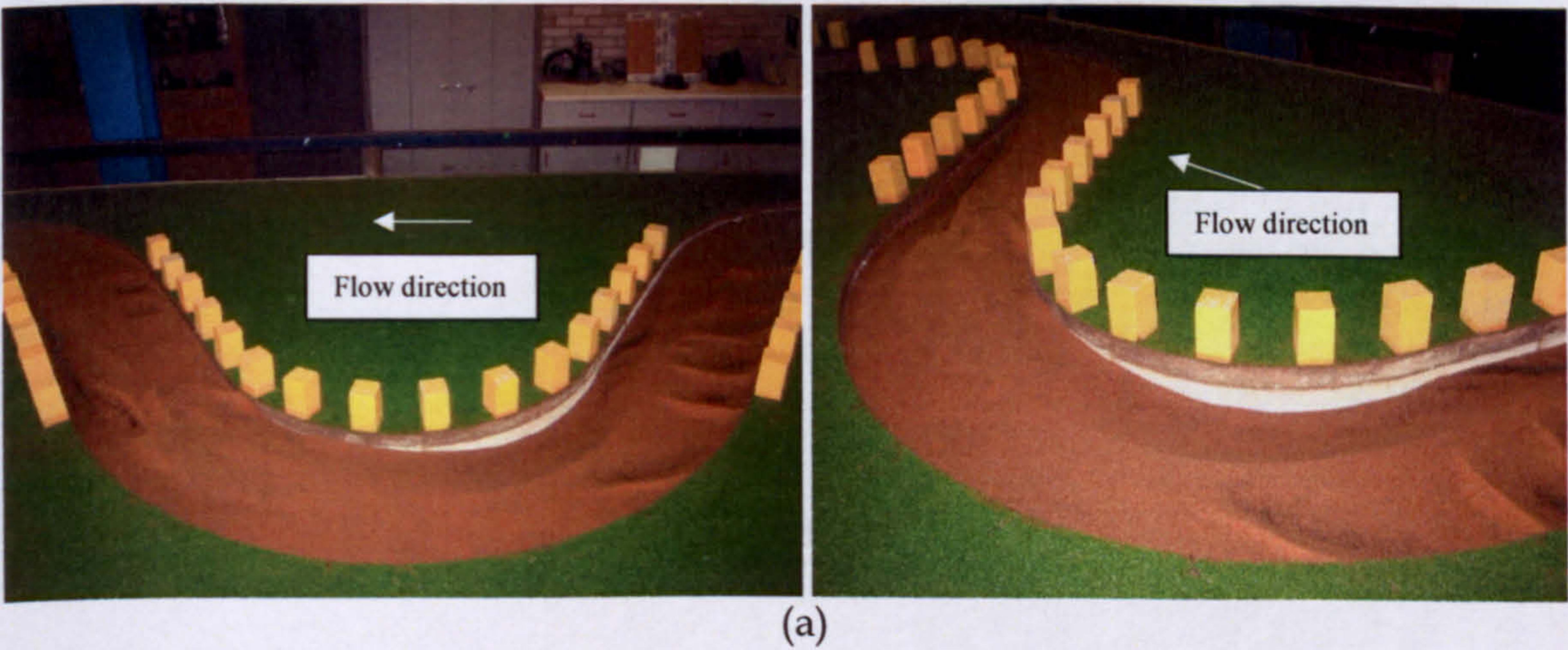
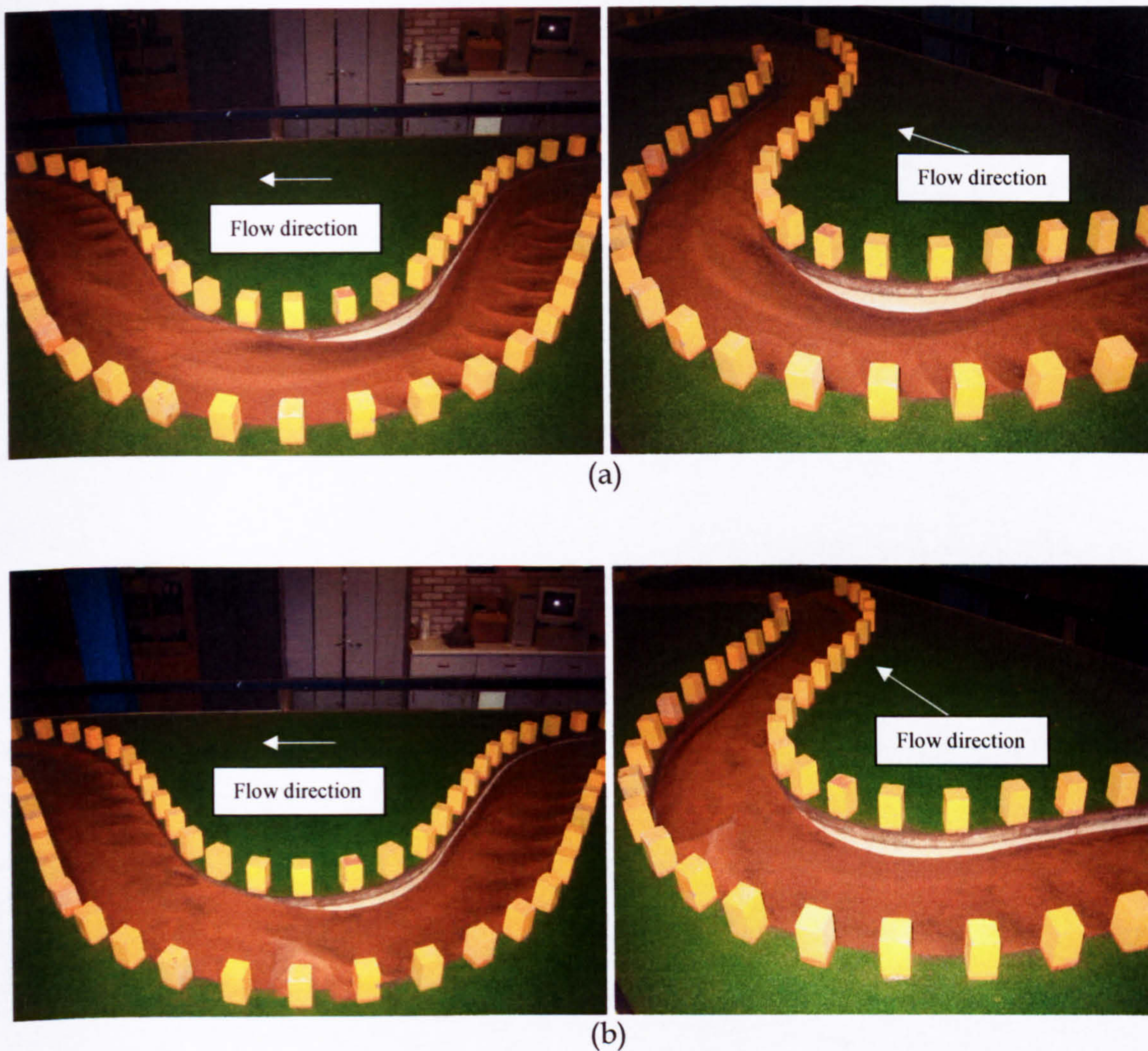


Figure 4.38: View of bedforms' morphology for block 30 *Case G Cross-over Block* (a)  $Dr = 0.20$  (b)  $Dr = 0.45$





**Figure 4.39:** View of bedforms' morphology for block 54 *Case H Combined Apex and Cross-over Block* (a)  $Dr = 0.20$  (b)  $Dr = 0.45$

#### 4.7 Sediment Transport for Overbank Flow in Compound Meandering Channels

The aim of this section is to investigate the influence of using different arrangements and vegetation density on the floodplain resistance to sediment transport subjected to an overbank flow condition in the small-scale meandering channel. This is important because, despite field measurements being the most reliable form of estimating sediment transport in a river, they suffer from two great limitations: 1) the ability to obtain data at all times and at the location of interest is nearly impossible (Hodkinson and Furguson, 1998), and 2) measurements can be expensive and difficult to make at



the high flow stage (higher overbank). These factors serve as a great disadvantage in using field measurements for studying complex meandering rivers effectively. In this study, laboratory physical methods have been used as the preferred alternative to field measurements in order to understand the sediment transport behaviour with the presence of vegetation. Figure 4.40 shows a typical variation of sediment concentration with time for the low flow and high flow discharges. It shows fluctuations arising from the change in bed elevation caused by the bedforms and dune mitigation rate. In most cases, the overall bed load transport rates were fluctuating, against the mean value. This indicates that the sediment transport was maintained reasonably well in the equilibrium condition.

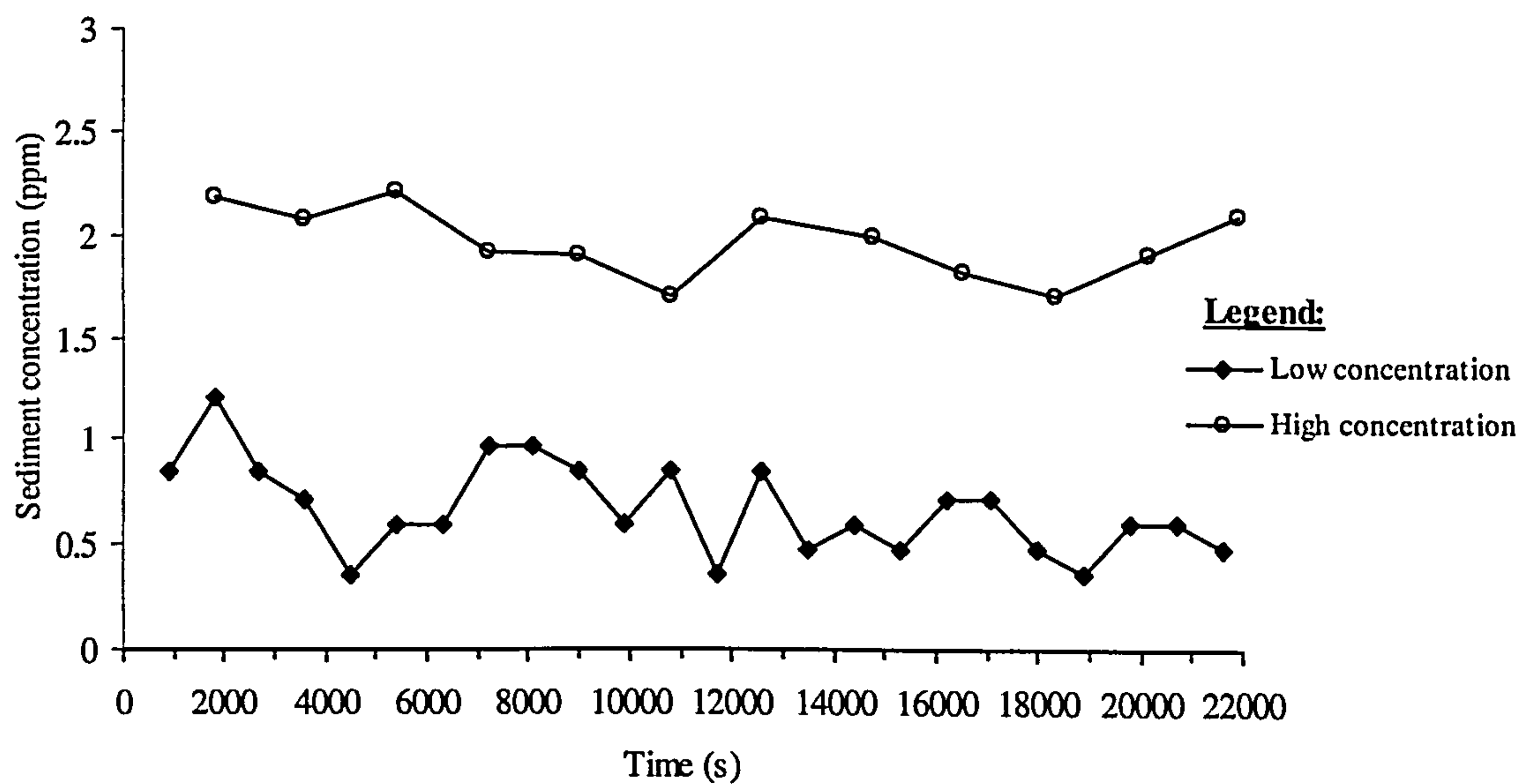


Figure 4.40: Typical variation of sediment concentration for low and high concentration at  $Q = 9.3 \text{ l/s}$  and  $29.2 \text{ l/s}$  respectively

#### 4.7.1 Effect of Block Arrangement and Density on the Sediment Transport Rate

Figures 4.41 to 4.43 show the sediment transport rate and the discharge relationship for mobile-bed channels for three different block arrangements. Each case shows a different trend, which means that a different substantial reduction in sediment load occurs during the early stage of overbank flow. Figure 4.41 shows the relationship between sediment transport rate and discharge for *Case E No Block* and *Case F Apex Block*. Sediment transport rate is seen to be very small at the early stage of overbank



flow within the range of discharge around  $0.0065 - 0.019 \text{ m}^3/\text{s}$ . However, as flow depth increases and the discharge reaches  $0.020 \text{ m}^3/\text{s}$  the sediment transport rate for all cases starts to increase. Looking at the sediment transport rates for the blocks cases, it is noticed that the sediment transport rate is smaller in magnitude for apex block cases *F1* and *F2* for higher and middle densities of blocks compared to apex block *Case F3* with a lower density of block and *Case E No Block*. This might be caused by interactions with the floodplain, which can be divided into two depth regimes. The interaction over cross-over is strong for shallower floodplain depth; hence there is a reduction of velocity, mainly at the cross-over section. For the deeper water case, floodplain flow accelerates the main channel flow, but where the blocks are more densely arranged, the slower velocity along the blocks into the main channel may partially reduce the velocity in the main channel. In this case, the velocity through the blocks becomes faster as their density decreases; hence there is an acceleration of the main channel flow caused by the floodplain flow along the blocks.

Figure 4.42 shows that sediment transport rates for *Case E No Block* and *Case G Cross-over Block* have a very similar trend in the early stage of overbank flow. When the flow depth increases, the sediment transport rate decreases dramatically in the range of discharge of about  $0.01 - 0.02 \text{ m}^3/\text{s}$ . For these overbank depths, the sediment load detained in the sediment catcher was minimum but bedform features were generated during the early stage of overbank flow. After a certain depth, the sediment transport rate starts to increase. The reason for the decrease in the sediment transport rate during the shallow overbank flow is due to the sudden reduction of velocity in the main channel owing to the momentum exchange between the floodplain and the main channel flows. The relatively slow floodplain flow generates a shearing effect as it is entering over the main channel. This “retarding effect” is created by the blocks, resulting in a substantial reduction in velocity in the main channel. The reduction of the main channel velocity therefore causes the decreases in sediment load during the early stage of overbank flow in the compound meandering channel.

Figure 4.42 also shows sediment transport rates for no block and three different densities considered behave a very similar trend in such way that it starts to decrease to minimum then increase at higher relative depth. Looking at sediment transport rates for all the block cases, it is also noticed that as block density increases, the range



of discharge for which the sediment transport rates remain minimum becomes narrower, but no block case is different. The sediment transport rate is directly related to the velocity in the main channel and, therefore, the reduction of the sediment transport rate means a reduction of velocity.

Rameshwaran *et al.* (1999) gave the reason for the decrease in the sediment transport rate in a meandering compound channel. Relative slow floodplain flow, compared with the meandering channel flow, enters the main channel in the cross-over section, which reduces velocity in the main channel by momentum transfer due to interfacial turbulence at the bankful level. This interfacial turbulence also interacts with the bed and develops irregular bedforms, which has been observed by Shiono *et al.* (2001) meaning an increase in flow resistance in the main channel occurs, which results in a substantial reduction of the velocity in the main channel.

With this in mind, the reason why the range of discharge for minimum sediment transport rate becomes smaller as the block density increases will be explained below. When block density increases, the gaps between blocks is getting narrower and narrower, meaning that flow through the gaps from floodplain becomes lesser and lesser, hence lesser and lesser interaction between the floodplain and main channel flows in the cross-over section, as a result, the velocity in the main channel in higher density block case does not decrease as much as that for lesser density block case. In addition, the velocity just outside of the blocks also becomes faster in the higher density block case at the same flow since flow becomes smaller in the blocked area of the meander belt, and consequently the velocity becomes faster quickly around the bend apex. Thus the overall main channel flow becomes faster as block density increases. Therefore as flow rate increases, velocity in the main channel increases hence sediment transport rate quickly increases.

It is apparent from Figure 4.43 that the sediment transport rate at the early stage for combined apex and cross-over block *Case H1* (highest density of blocks) followed the trend of *Case F Apex Block*. However, the combined apex and cross-over block *H2* and *H3* cases (lower density of blocks) show a quite similar trend to the no block *E* and cross-over block *G* cases in which, as flow depth increases, the sediment transport rate slightly decreases in the range of discharge of about 0.007 - 0.022 m<sup>3</sup>/s. However, as



flow depth increases and the discharge reaches  $0.018 \text{ m}^3/\text{s}$ , the sediment transport rates start to increase for the combined apex and cross-over block *H2* and *H3* cases but not for *Case H1*. In common sense, as density of blocks increases, the channel appear to resemble those of a single meandering channel, hence sediment transport rate suppose to be increases as depth of flow increases. However this is contradicting with the above result and the reasons why the sediment transport rates remain smaller over the flow depths can be clearly explained in previous section shows that the higher percentages of bedform friction factor as the number of blocks increases (see Figure 4.32).

A series of the experimental data incorporating the various floodplain block densities in *Case F Apex Block* and *Case G Cross-over Block* are plotted (see Figures 4.41 and 4.42). *Case F Apex Block* show that the sediment transport rate is smaller in magnitude for the apex blocks *F1* and *F2* cases for higher and middle densities of blocks compared to *Case F3* with the lower density of blocks and *Case E No Block*. However, the sediment transport rate is smaller in magnitude for the combined apex and cross-over block *G2* and *G3* cases for the middle and lowest densities of blocks compared to *Case G1* for a higher density of block and *Case E No Block*, as seen in Figure 4.42. The threshold of the transport rate with respect to the water depth is also affected by the density of blocks on the floodplains. It might be suggested that the block density could induce additional flow resistance, which, in turn, increases the shear interaction that causes flow reduction in the main channel flow. The reduction of flow in the main channel subsequently leads to substantial sediment rate reduction as well as delaying the threshold of the transport rate.

For the purpose of rendering suitable data for comparison, the sediment transport rate was further transformed into a non-dimensional form known as the normalised sediment transport rate. Each transport rate ( $q_b$ ) was normalised by the transport rate at bankful level ( $q_{bf}$ ). The normalised sediment transport rates with relative depth are presented in Figures 4.44 to 4.46. Figure 4.44 noticed that the reduction in sediment rate for *Case E No Block* is around  $Dr = 0.43$ , but there are no reductions in sediment transport rate in this data range for all the apex block *F* cases. However, the reduction in the cross-over block *G1*, *G2* and *G3* cases extends to a slightly higher relative depth of around  $Dr = 0.48$  as shown in Figure 4.45 but not in *Case H Combined Apex and Cross-over Block* as shown in Figure 4.46 where the reduction in sediment transport rate only



can be seen for combined apex and cross-over block *H2* and *H3* cases. The difference of the relative depth between no block *E*, apex block *F* and cross-over block *G* cases suggests that the boundary shear stress remains small even for greater water depths when the blocks are on the floodplain. The effect of the blocks in the apex block *F* and cross-over block *G* arrangements indirectly implies that the sediment transport rate is significantly influenced by the arrangement of blocks on the floodplain.

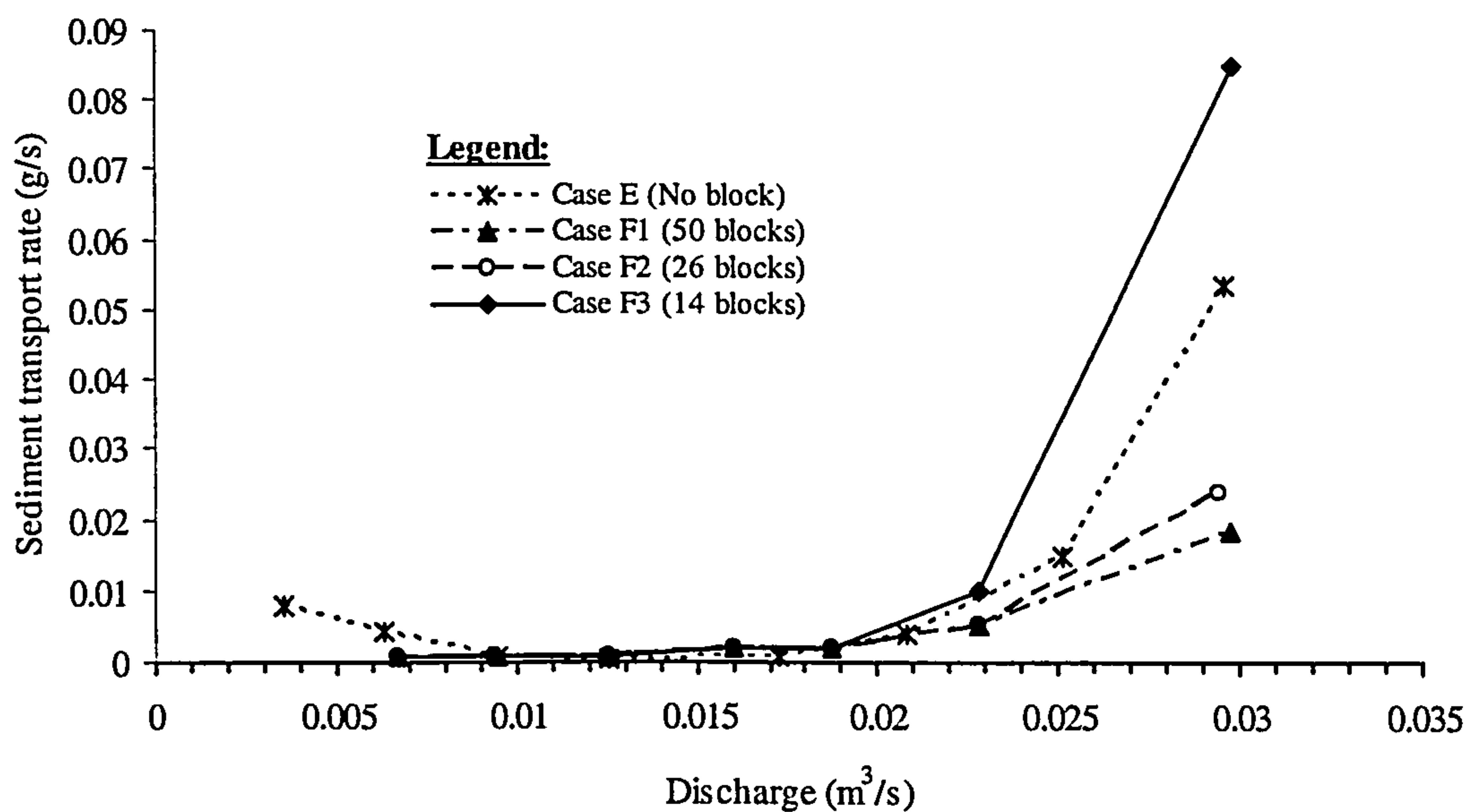


Figure 4.41: Discharge and sediment transport relationship for mobile-bed channel no block *E* and apex block *F* cases



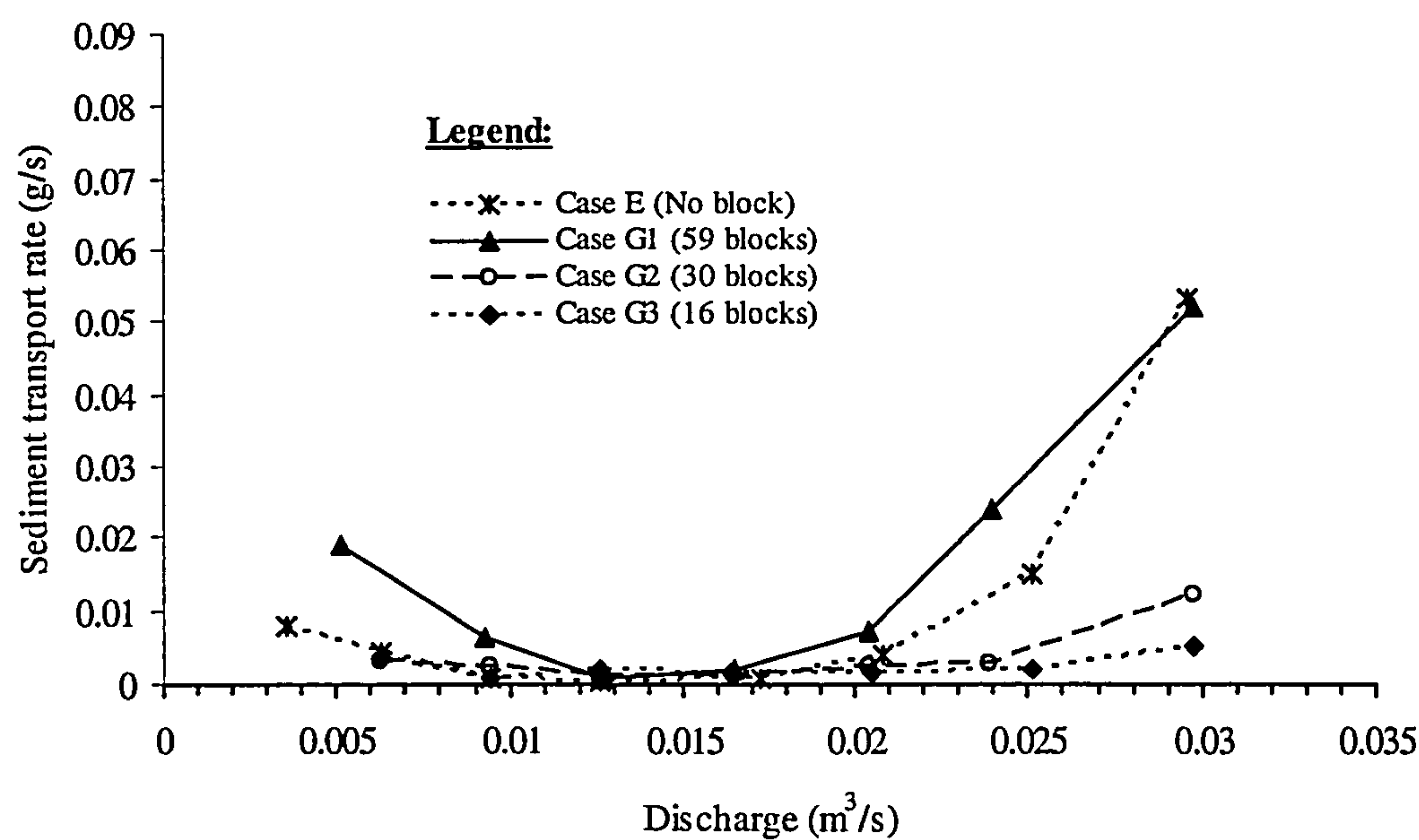


Figure 4.42: Discharge and sediment transport relationship for mobile-bed channel no block *E* and cross-over block *G*

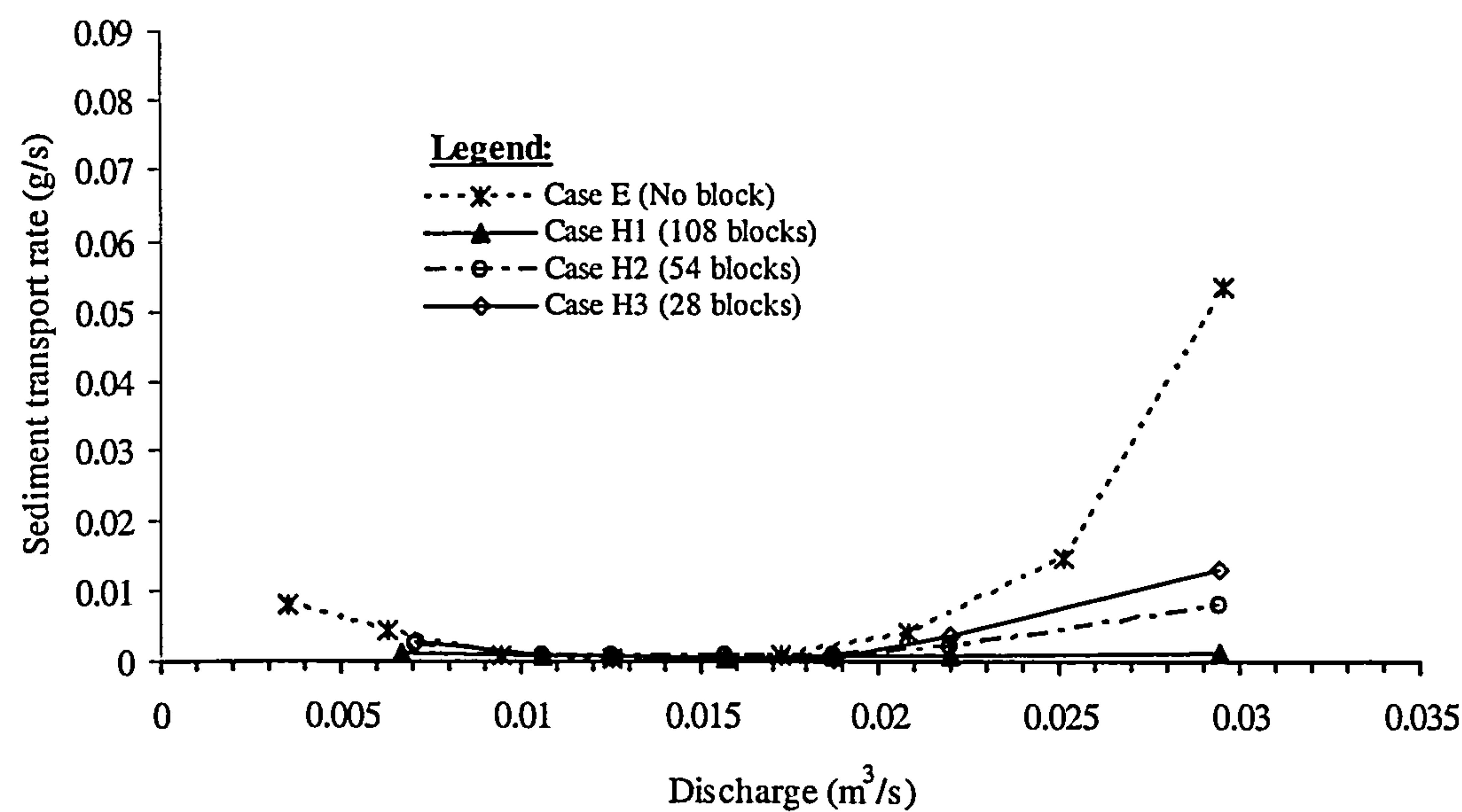


Figure 4.43: Discharge and sediment transport relationship for mobile-bed channel no block *E* and combined apex and cross-over block *H*



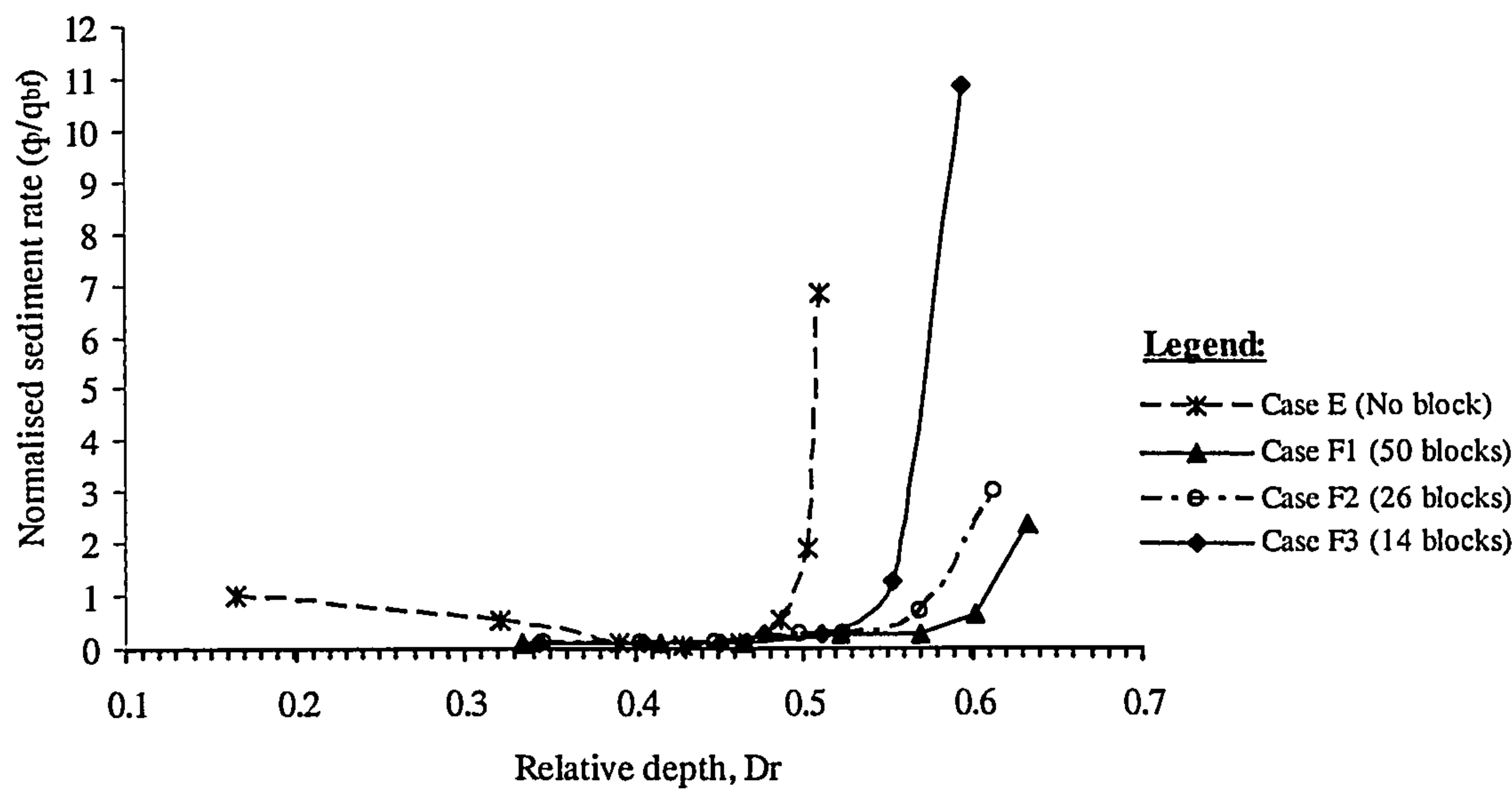


Figure 4.44: Normalised sediment rate relationships between *Case E No Block* and various densities of blocks for *Case F Apex Block*

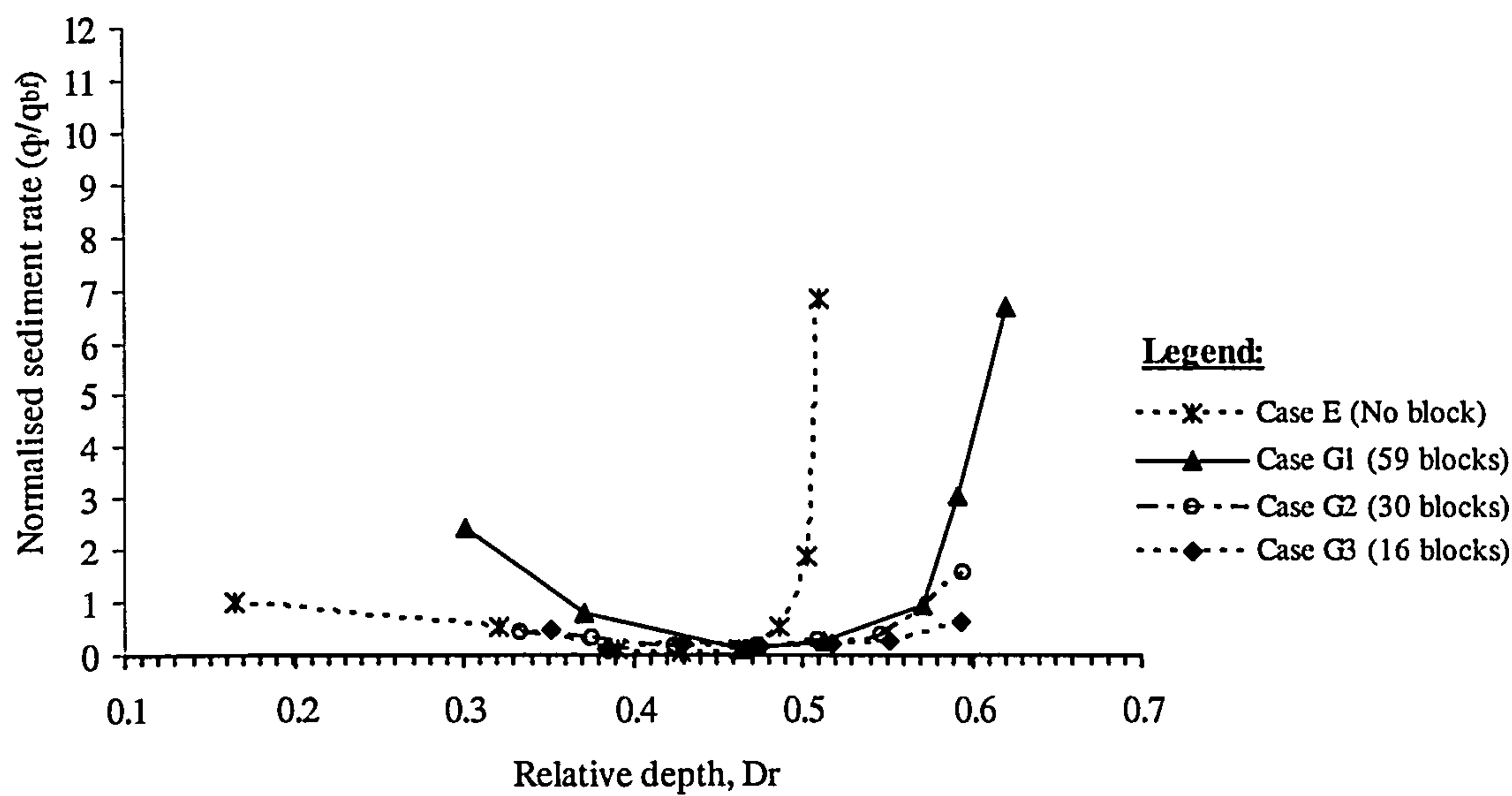
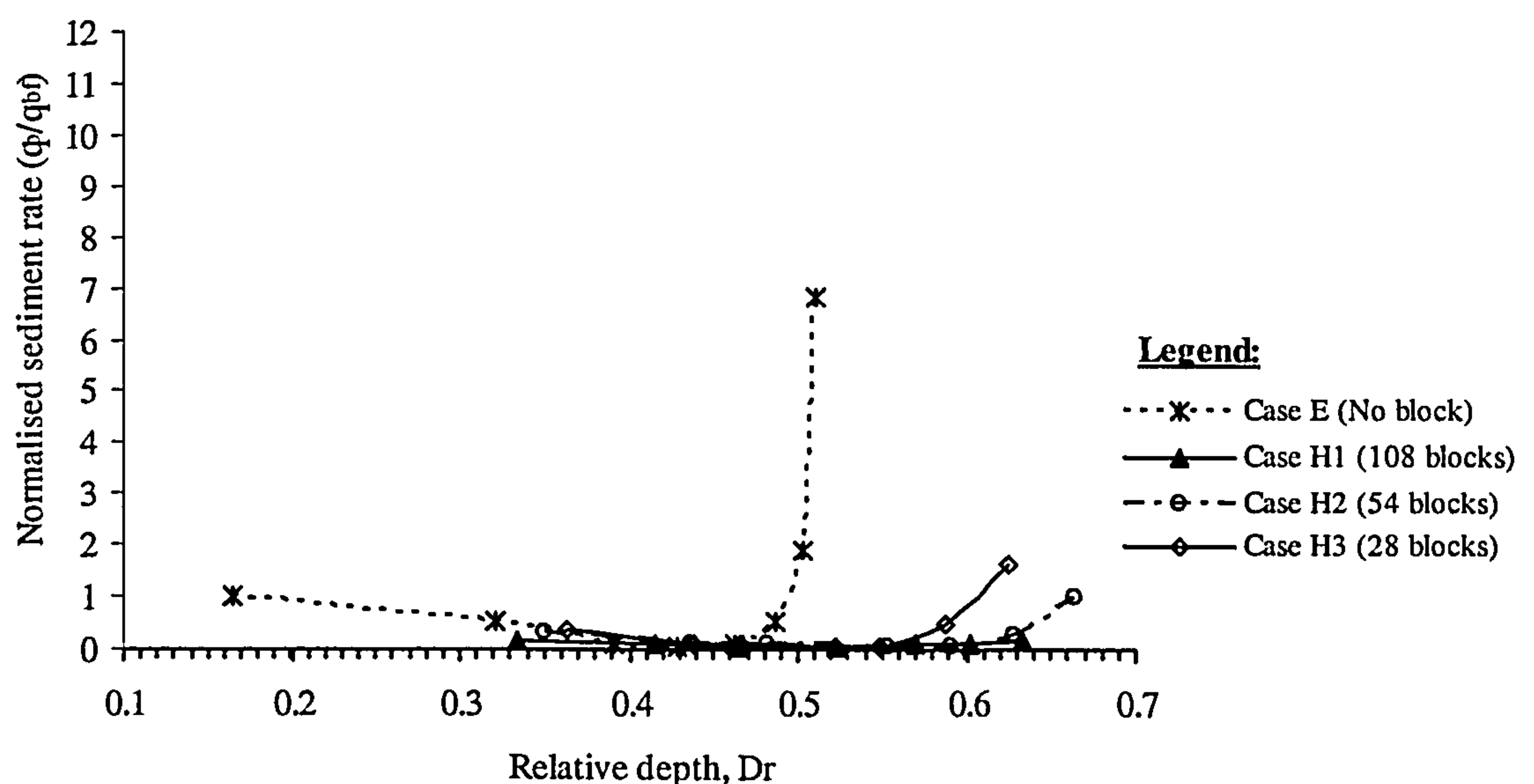


Figure 4.45: Normalised sediment rate relationships between *Case E No Block* and various densities of blocks for *Case G Cross-over Block*





**Figure 4.46:** Normalised sediment rate relationships between *Case E No Block* and various densities of blocks for *Case H Combined Apex and Cross-over Block*

#### 4.8 Discussion of Results

The results show important differences between flow in the non-vegetated and vegetated floodplain cases in the meandering channel. The experimental results show that the fixed bed channels have better efficiency in conveying flow when compared to the mobile bed channels, but the efficiency depends on the arrangement and density of vegetation/blocks. In the case of the low density of blocks the channel conveys water with greater efficiency than when compared to the cases with a higher density of vegetation. The conveyance efficiency in the low density of *Case D Combined Apex and Cross-over Block* is up to 25 % more than the higher density, and the efficiency is lower at the higher stage for the higher block density. Accurate assessment of the discharge capacity in the non-vegetated and vegetated floodplains is important due to the essential in controlling floods and designing artificial waterways. The three dimensional nature of the flow due to bends in the main channel is further enhanced due to the interaction between the main channel flow and the floodplain flow when flow becomes overbanks.



All the values of Manning's  $n$  were found to be within the accepted range of Manning's  $n$  as reported by Chow (1959). The use of the single channel Manning  $n$ , in which the channel is treated as a single unit with some appropriate averaging for the friction coefficient, produces satisfactory results for overbank flow depths. *Case D Combined Apex and Cross-over Block* for higher density shows that the Manning's  $n$  value was generally greater than the Manning's  $n$  for both rough apex block  $B$  and cross-over block  $C$  arrangements of blocks, but for higher overbank at relative depth, with a  $Dr$  approximately = 0.4, the Manning's  $n$  values tend to follow their trend. The results also show that the Manning's  $n$  for this study of rigid unsubmerged vegetation is directly proportional to the depth of flow. Recall that it was given by Fathi and Kouwen (1997) that the Manning's  $n$  increases proportionally with the square root of the flow depth, the results emphasize this. For mobile bed case, Manning's  $n$  varies more than that in the fixed bed case and the value is higher. This suggests that bedforms give such magnitude contributing the total flow resistance and the overall Manning's  $n$  value for mobile bed is approximately 20 % higher than that for fixed bed case.

The force balance over one meander for various block cases has been investigated by considering forces over one meander for quasi-uniform flow. It is noticed that  $F_D/w$  is greater than 1.0 in *Case C Cross-over Block*, however, it should not exceed 1.0 in physics. One of the reasons may be due to the use of the average velocity instead of the approach velocity in the projected area. For the mobile bed cases, the trend of  $F_D/w$  with respect to  $Dr$  is not quite parabolic. This could reflect the evolution of bedforms as the water depth changes. According to this, a correction parameter for the effect of blocks,  $\alpha$ , ( $v_p = \alpha w$ ) was introduced and also investigated to show the variation for each case. Correction coefficient  $\alpha$  is the parameter used to take into account the effect of the blocks. In the case of mobile bed floodplain vegetated show the bedform friction factor for higher overbank flow is seen to be higher at up to 300 % for rough floodplain case. In general, all cases show higher percentages of bedform friction factor as the number of blocks increases with agrees with Lyness *et al.* (1998).

The observation of the bedforms changes shows that, for the case with no block  $E$  for higher flow depth, ripples were seen in the main channel. This indicates that the flow resistance becomes more homogeneous at the high overbank flow depth. However, when the changes of floodplain topography with different arrangements of blocks



were setup, the results show that those arrangements of blocks give a significant variation of bedform patterns in the main channel, and then were influenced by sediment movement in the main channel. In general, the amount of sediment load migrating along the main channel is increased as discharge and flow depth increases.

For mobile-bed cases, the sediment transport rate for *Case G Cross-over Block* gives better efficiency for conveying water when compared to the other cases. In general, a low sediment transport rate is seen for *Case G Cross-over Block* instead of for cases apex block *F* and combined apex and cross-over block *H* when comparing the effectiveness by placing the blocks between both arrangements. *Case F Apex Block* shows that the lowest density of block along the apex bend section has an impact on higher sediment transport rates and *Case H Combined Apex and Cross-over Block* show that the flow interaction in the main channel not well understood. Also, it was found that in *Case G Cross-over Block*, the blocks generate local vortices, which accelerate bed erosion from the cross-over section to the apex in the main channel. In most tested cases, a significant reduction of the sediment transport rate occurs at early overbank flow and the sediment rate increases again after a certain overbank depth. The reduction of sediment transport rate in shallow overbank flow is due to the sudden reduction of velocity in the main channel owing to the momentum exchange between the floodplain and main channel flows. It was found that the arrangement and the density of blocks on the floodplains also affect the threshold of the sediment transport rate during overbank flow.

In summary, an arrangement of blocks along the bank of the floodplain of a meandering channel can have a significant effect on conveyance for the overbank flow condition. The total resistance is increased by the additional blocks. So, it can be noted that the magnitude of the effect on stage/water level by obstructing the floodplain depends strongly on the location of the model blocks within the meander belt. The experimental results also show that the cases cross-over block *C* and *G* for fixed- and mobile-bed channels are more efficient in conveying flow when compared to the other arrangements of blocks on floodplains, but the efficiency depends on the arrangement and density of the blocks. Hence, this result is useful for any planning and managing of vegetation on floodplains to ensure that vegetation is located in areas or arrangements that have a minimal impact on stage, sediment transport rate and erosion.



# Chapter 5

## 5.0 Results of Detailed Flow Structure in Compound Meandering Channels

### 5.1 Introduction

The aims of this chapter are firstly to carry out further detailed analyses of mean flow mechanisms and secondary flow structures by considering the experimental data as well as computational results and secondly, to assess the capability of the computational model to reproduce the important flow characteristics, flow mechanisms and boundary shear stress associated with non-vegetated and vegetated floodplains in compound meandering channels with overbank flows. As we know that banks and floodplains of many natural rivers and streams are vegetated with trees and shrubs, it is reasonable to suppose that this vegetation affects the flow and boundary shear stress and consequently influences the pattern of erosion and deposition. Understanding the effects of floodplain vegetation on the main channel flow and boundary shear stress is essential for extending the knowledge of sediment transport rates. The boundary shear stress in the neighbourhood of the toe of a bank determines the sediment transport field, which in turn controls lateral erosion. An accurate understanding of the main channel flow and boundary shear stress are therefore required in order to quantify the effects of the factors that control the main channel flow.

The flow structures for overbank flows in compound meandering channels have been clarified quite clearly from the forgoing observations. It should be noticed that the flow shows rather different behaviour between when the flooding depth is relatively shallow ( $D_r = 0.15$ ) and when it is deep ( $D_r = 0.5$ ). The difference can be summarised as the shift of the dominant flow from the lower layer to the upper layer. This suggests



that different approaches in engineering applications for compound meandering channel flows may be necessary as the flooding depth varies.

These unique and important structures of the compound meandering channel flow are internal ones, which means that they cannot be observed directly on the water surface. It is, however, this internal structure that determines the entire flow behaviour and the resultant response of the channel system. It can therefore be said that, despite the difficulties, measurements for the secondary flow and the turbulence of the internal flow behaviour are necessary using both computational and experimental approaches.

In the previous chapter, the stage-discharge, flow resistance, bedforms and sediment transport rate in compound meandering channels have been discussed in detail for both the non-vegetated and vegetated floodplain cases. In order to determine whether a particular discharge or velocity can create sufficient sediment transport to remove fine sediment, accurate estimates of bed shear stress are very important since the pattern of the bed shear stress distribution is dependent on the distribution of the flow structure. Continuing from the above, this chapter will show and describe very detailed velocity variables in order to show the internal flow structure along a meandering channel. One of the objectives of this study is to assess the capability of the computational model to produce the important flow characteristics and flow mechanisms as well as the boundary shear stress associated with non-vegetated and vegetated floodplains in compound meandering channels with overbank flows. From the results in Chapter 4, an arrangement of blocks along the meandering bank of floodplain can have a significant effect on the conveyance of flow as well as on the reduction in the sediment transport rate for the overbank flow condition. This might suggest ways of planting trees for bank protection, erosion control etc.

## 5.2 Governing Hydrodynamic Equations

2D Saint-Venant equations are derived from the Navier-Stokes equations by taking the vertical average under following assumptions and approximations. Firstly, the vertical acceleration caused by the pressure is assumed to balance gravity and the hydrostatic pressure assumption can be expressed as:



$$-\frac{1}{\rho} \frac{\partial p}{\partial z} - g = 0 \quad (5.1)$$

where  $p(x,y,z) = -\rho g z + \text{constant}$

The vertical velocity is then neglected in the Saint-Venant equations and the vertical accelerations and shear stress can be assumed to be zero. Secondly, it is assumed that there will be no transfer of water either through the bottom or from the free-surface. Finally, the rule of Leibnitz is mainly used for the derivation of the Saint-Venant equations which is expressed as follows:

$$\frac{\partial}{\partial x} \int_{Z_f}^Z F dz = \int_{Z_f}^Z \frac{\partial F}{\partial x} dz + F(x, y, Z) \frac{\partial Z}{\partial x} - F(x, y, Z_f) \frac{\partial Z_f}{\partial x} \quad (5.2)$$

where,

$Z$  = free-surface elevation

$Z_f$  = bottom elevation

$H$  = water depth is defined as  $Z - Z_f$

Under constant density and hydrostatic pressure, the Navier-Stokes equations can be averaged vertically by integrating from the bottom to the free-surface. The two components of depth-averaged velocities  $u$  and  $v$  are defined as:

$$u = \frac{1}{h} \int_{Z_f}^Z U_1 dz \text{ and } v = \frac{1}{h} \int_{Z_f}^Z U_2 dz \quad (5.3)$$

Using the Leibnitz rule and impermeability condition, the continuity and momentum equation for 2D shallow flow can be given as follows:

$$\frac{\partial h}{\partial t} + \text{div}(h\bar{u}) = 0 \quad (5.4)$$

$$\frac{\partial h}{\partial t} + \text{div}(uhu) = -gh \frac{\partial Z}{\partial x} + hS_x + \text{div}(hv, gradu) \quad (5.5)$$



$$\frac{\partial h}{\partial t} + \text{div}(uhv) = -gh \frac{\partial Z}{\partial x} + hS_y + \text{div}(hv_t \text{grad}v) \quad (5.6)$$

where,

$S_x$  and  $S_y$  = depth-averaged source terms in the  $x$  and  $y$  directions

$v_t$  = velocity diffusivity

For 2D bed friction modelling, the bed friction is usually given by:

$$\tau = \frac{1}{2} \rho c_f |u| \bar{u} \quad (5.7)$$

where,

$\tau$  = bed shear stress

$\rho$  = water density

$c_f$  = friction factor

The friction factor  $c_f$  is rarely used and it is usually replaced by the Chezy coefficient  $C$  or Manning coefficient  $n$ . The Chezy coefficient is expressed by,

$$C = \sqrt{\frac{2g}{c_f}} \quad (5.8)$$

or Nikuradse's Law as:

$$c = 7.83 \log \left( 12 \frac{h}{k_s} \right) \quad (5.9)$$

or Manning's  $n$ ,

$$c_f = \frac{2gn^2}{h^{\frac{1}{3}}} \quad (5.10)$$



where,

$h$  = water depth

$k_s$  = grain size at the bottom

According to Rameshwaran and Shiono (2003), when determining the Manning coefficient,  $c_f$  as expressed by Equation (5.10) is used. Thus the bed shear stress can then be determined by:

$$\tau_{bx} = \rho g \frac{n^2}{h^{\frac{1}{3}}} u \sqrt{u^2 + v^2} \quad (5.11)$$

$$\tau_{by} = \rho g \frac{n^2}{h^{\frac{1}{3}}} v \sqrt{u^2 + v^2} \quad (5.12)$$

where  $\tau_{bx}$  and  $\tau_{by}$  = boundary shear stresses in the  $x$  and  $y$  directions

When looking at the three dimensional situation, Newton's second law of motion together with Newton's law of viscosity and the mass conservation equation form the basis of the general governing equations describing fluid flows. Newton's Second Law of Motion states that the time rate of change of momentum of a fluid particle equals the sum of the external forces on the particle, whereas the mass of the fluid is conserved according to the law of mass conservation. Newton's law of viscosity relates the viscous stresses appearing in the momentum equations to the local deformation rate (or the strain rate). These three fundamental principles, when put together, take the form of partial differential equations, commonly and collectively referred to as the Navier-Stokes equations. Many standard texts are available on the detailed derivation of the three-dimensional Navier-Stokes equations, such as Rodi (1993) and Ferziger and Peric (1996). The three-dimensional continuity and momentum equations for unsteady, incompressible and viscous flows can be written in the following form:

$$\frac{\partial \rho}{\partial t} + \frac{\partial (\rho u_i)}{\partial x_i} = 0 \quad (5.13)$$



$$\frac{\partial(\rho u_i)}{\partial t} + \frac{\partial(\rho u_i u_j)}{\partial x_j} = -\frac{\partial p}{\partial x_i} + \frac{\partial \tau_{ij}}{\partial x_j} + \rho F_i \quad (5.14)$$

where,

$i$  and  $j$  = standard tensor

$u_i$  ( $i = 1, 2, 3$ ) = instantaneous velocity component in the  $x_i$  direction

$F_i$  = body force

$\rho$  = fluid density

$p$  = pressure

$\tau_{ij}$  = viscous stresses for the laminar flows

Further approximation and assumptions are required so that the above set of equations represents the flows of practical interest. Most of the flows encountered in hydrodynamic problems can be treated as incompressible. The density variations due to the temperature, salinity etc., are then taken into consideration through the equation of state. Assuming the fluid obeys Newton's law of viscosity and that the viscosity is constant throughout the flow, the Equations (5.13) and (5.14) take the following forms:

$$\frac{\partial u_i}{\partial x_i} = 0 \quad (5.15)$$

$$\frac{\partial u_i}{\partial t} + \frac{\partial(u_i u_j)}{\partial x_j} = -\frac{1}{\rho} \frac{\partial p}{\partial x_i} + \frac{1}{\rho} \frac{\partial}{\partial x_j} \left[ \mu \left( \frac{\partial u_i}{\partial x_j} + \frac{\partial u_j}{\partial x_i} \right) \right] + F_i \quad (5.16)$$

where,

$\mu$  = molecular viscosity of the fluid

$F_i$  = body force

The above equations are the instantaneous continuity and Navier-Stokes equations and describe flows which are incompressible and laminar. Since an estimate of the time-averaged variables is of more engineering use, the instantaneous continuity and momentum equations need to be time-averaged. For this, the statistical approach as first suggested by Osborne Reynolds (Rodi, 1993) is usually used. Since Osborne Reynolds first suggested the approach, the time averaging of instantaneous Navier-



Stokes equations is also known as Reynolds averaging and the resulting equations are termed as Reynolds-averaged Navier-Stokes (RANS) equations. Thus, in a statistically steady flow, the flow variables can be written as the sum of a time-averaged (mean) value (e.g.  $U$ ) and fluctuation about the mean value (e.g.  $u'$ ) can be represented as:

$$u = U + u' ; v = V + v' ; w = W + w' ; p = P + p' \quad (5.17)$$

If the mean quantities in the above equations are defined as in Rodi (1993) then

$$U = \frac{1}{t_0} \int_t^{t+t_0} u \, dt ; P = \frac{1}{t_0} \int_t^{t+t_0} p \, dt \quad (5.18)$$

Incorporating Equations (5.17) and (5.18) in the instantaneous continuity and Navier-Stokes Equations (5.15) and (5.16) leads to the following equations,

$$\frac{\partial U_i}{\partial x_i} = 0 \quad (5.19)$$

$$\frac{\partial U_i}{\partial t} + \frac{\partial (U_i U_j)}{\partial x_j} = -\frac{1}{\rho} \frac{\partial P}{\partial x_i} + \frac{\mu}{\rho} \frac{\partial}{\partial x_j} \left( \frac{\partial U_i}{\partial x_j} + \frac{\partial U_j}{\partial x_i} \right) + \frac{\partial}{\partial x_j} \left( -\overline{u'_i u'_j} \right) + F_i \quad (5.20)$$

Equations (5.19) and (5.20) are the three-dimensional Reynolds-averaged continuity and Navier-Stokes equation (RANS) for turbulent flows. Due to the non-linearity involved in the original instantaneous momentum equations, the time-averaging process resulted in unknown correlations between the fluctuating velocities, such as  $-\overline{u'v'}$ . These correlations when multiplied by the density  $\rho$  represent the transport of momentum due to the fluctuating or turbulent motion (Rodi 1993). Thus  $-\rho \overline{u'v'}$  is the transport of  $u$  momentum in the direction of  $v$  and it acts as a stress on the fluid. Thus there are six such additional stress terms appearing in the mean momentum equations, three are the normal stress terms whilst the remaining three are the shear stress terms. Since these stresses appeared due to the Reynolds averaging of the momentum equations, they are referred to as Reynolds stresses. Due to these additional stress terms, the system of equations is no longer closed, and requires an empirical approximation, usually in the form of a relationship between the Reynolds stresses and the mean flow variables. To predict the behaviour of particular turbulent flows, the



above equations need to be solved numerically using appropriate initial and boundary conditions. The outcome of the numerical simulation will be a complete description of how the flow varies in space and time.

Analogous to using Newton's law of viscosity to approximate the viscous stress in the laminar flows, the Boussinesq eddy viscosity concept is used for this study to approximate the turbulent shear stresses. The turbulent Reynolds stresses  $-\overline{u_i u_j}$  are modelled as in Rodi (1993),

$$\tau_{ij} = -\rho \overline{u_i u_j} = \mu_t \frac{\partial}{\partial x_j} \left( \frac{\partial U_i}{\partial x_j} + \frac{\partial U_j}{\partial x_i} \right) - \frac{2}{3} k \delta_{ij} \quad (5.21)$$

where,

$k$  = turbulent kinetic energy

$\delta_{ij}$  = Kronecker delta function

$\nu_t$  = turbulent or eddy viscosity

The value of  $\nu_t$  varies with time and space and is calculated using an appropriate turbulence model. In this study, the widely used standard  $k$ - $\epsilon$  turbulence model (Rodi, 1993) is used for calculating eddy viscosity  $\nu_t$ . The eddy viscosity is related to turbulent kinetic energy,  $k$ , and the energy dissipation rate,  $\epsilon$ , through the Kolmogorov-Prandtl relationship as follows:

$$\nu_t = C_\mu \frac{k^2}{\epsilon} \quad (5.22)$$

where  $C_\mu$  = a constant equal to 0.09

The following transport equations are solved for  $k$  and  $\epsilon$ ,

$$\frac{\partial k}{\partial t} + U_i \frac{\partial k}{\partial x_i} = \frac{\partial}{\partial x_i} \left( \frac{\nu_t}{\sigma_k} \frac{\partial k}{\partial x_i} \right) + P - \epsilon \quad (5.23)$$

$$\frac{\partial \epsilon}{\partial t} + U_i \frac{\partial \epsilon}{\partial x_i} = \frac{\partial}{\partial x_i} \left( \frac{\nu_t}{\sigma_\epsilon} \frac{\partial \epsilon}{\partial x_i} \right) + (C_{1\epsilon} P - C_{2\epsilon} \epsilon) \frac{\epsilon}{k} \quad (5.24)$$



where,

$$P = \nu_t \left( \frac{\partial U_i}{\partial x_j} + \frac{\partial U_j}{\partial x_i} \right) \frac{\partial U_i}{\partial x_j} = \text{the production rate of turbulent kinetic energy } k$$

The standard values of the model coefficients are used:  $C_\mu = 0.09$ ,  $C_{1\varepsilon} = 1.44$ ,  $C_{2\varepsilon} = 1.92$ ,  $\sigma_k = 1.0$  and  $\sigma_\varepsilon = 1.3$  (Rodi, 1993). The kinematic boundary condition and the conservative free-surface equations are the most widely used equations for the free-surface tracking. For the computations reported in this thesis, the conservative free-surface equation was used to calculate the free-surface position. The conservative free-surface equation is obtained by integrating the continuity equation over the depth from the bottom  $z = -B(x, y)$  to the free-surface  $z = S(x, y, t)$  and using the kinematic boundary condition and impermeability condition at the bottom and is written as (Jankowski, 1998):

$$\frac{\partial S}{\partial t} + \frac{\partial}{\partial x} \int_{-B}^S U dz + \frac{\partial}{\partial y} \int_{-B}^S V dz = 0 \quad (5.25)$$

where,

$S(x, y, t)$  = free surface elevation

$B(x, y)$  = bed elevation

$U$  and  $V$  = mean velocity components in  $x$  and  $y$  coordinate directions respectively

$t$  = time step

The main advantage of the conservative equation is that it includes the proper impermeability boundary conditions at the bottom and the free-surface. This automatically satisfies the mass conservation criteria.

The three-dimensional Reynolds-averaged continuity and Navier-Stokes equations (RANS) (Equations (5.19) and (5.20)) together with the transport equation for  $k$  and  $\varepsilon$  (Equations (5.23) and (5.24)) and the free-surface Equation (5.25) are solved using finite element techniques and the non-hydrostatic pressure code of Telemac3D [Version 5.4] (Janin *et al.* 1997, and Hervouet, 2000). The following section introduces Telemac3D code and its solution algorithm.



### 5.3 Solution Algorithm

The Telemac modelling system is one of the well-established hydraulics modelling packages developed by the Institute of Mechanics of Hanoi (IOM) and the National Hydraulics Laboratory of Electricite de France (LNHE – EDF) in the 1960's. For the detailed description readers are referred to Hervouet and Van Haren (1996) for Telemac2D; Janin *et al.* (1997) for the hydrostatic pressure code of Telemac3D and Jankowski (1998) for the non-hydrostatic pressure code of Telemac3D. Within the already existing framework of Telemac3D hydrostatic pressure code, Jankowski (1998) implemented the non-hydrostatic solution algorithm. The information on the solution algorithms of hydrostatic and non-hydrostatic pressure codes of Telemac3D, described by Jankowski (1998) and Hervouet and Van Haren (1996) are used and briefly discussed in the following section.

The hydrodynamic equations considered as a basis for the development of the non-hydrostatic code of Telemac3D were as follows,

$$\nabla \cdot \mathbf{U} = 0 \quad (5.26)$$

$$\frac{\partial U}{\partial t} + \mathbf{U} \cdot \nabla U = -\frac{1}{\rho_0} \frac{\partial P}{\partial x} + \nabla \cdot (\nu_t \nabla U) + F_x \quad (5.27)$$

$$\frac{\partial V}{\partial t} + \mathbf{U} \cdot \nabla V = -\frac{1}{\rho_0} \frac{\partial P}{\partial y} + \nabla \cdot (\nu_t \nabla V) + F_y \quad (5.28)$$

$$\frac{\partial W}{\partial t} + \mathbf{U} \cdot \nabla W = -\frac{1}{\rho_0} \frac{\partial P}{\partial z} - \frac{\rho}{\rho_0} g + \nabla \cdot (\nu_t \nabla W) \quad (5.29)$$

$$\rho = \rho(T, s_a, c) \quad (5.30)$$

where,

$\rho$  = fluid density (variable, local density)

$\rho_0$  = constant, average, reference fluid density

$\nu_t$  = turbulent eddy viscosity



$g$  = acceleration due to gravity

$T$  = temperature

$S_a$  = salinity

$c$  = pollutant concentration

## 5.4 Mesh Generation

According to Spitaleri and Micacchi (1998), grid generation is one of the most crucial and time consuming tasks when solving partial 2D and 3D differential equations in a complex-shaped domain such as the geometry of a natural river. The adaptive mesh generator called MATISSE provided within the framework of Telemac3D was used to generate the finite element unstructured triangular mesh. Telemac uses a two-dimensional (2D) mesh as a base mesh to construct the full three-dimensional (3D) mesh. The 2D mesh is an unstructured triangular mesh based on Delaunay Triangulation. The 3D mesh is obtained by duplicating the 2D base mesh on a number of horizontal planes along the vertical direction. Due to the duplicating of the triangular element over the vertical, the 3D mesh consists of prismatic elements with 6 nodes. According to Jankowski (1998), the  $x$  and  $y$  coordinates of the 3D mesh nodes remain the same as those of the base mesh whereas the  $z$ -coordinate of the 3D mesh nodes is defined as:

$$z_i = B(x, y) + z_{*i}(S(x, y, t) - B(x, y)), \quad z_{*i} \in [0, 1] \quad (5.31)$$

where,

$z_i$  = vertical coordinate of mesh nodes at  $i^{th}$  horizontal level

$z_{*i}$  = value denotes the position of  $i^{th}$  horizontal level ( $z_{*i} = 0$  defines the bottom and  $z_{*i} = 1$  denotes the free-surface)

Duplicating the 2D base mesh over the constant number of horizontal planes along the vertical sometimes poses severe discretization problems, particularly when the geometry of the flow domain is complicated as in compound meandering channels. The main disadvantage of using such a meshing structure is that, with the constant number of horizontal mesh levels, the deeper region of the flow domain is always under-discretized and the shallower region is always over-discretized (Jankowski, 1998). Thus, in the case of compound meandering channels, the floodplain region is



over-discretized and the main channel is under-discretized as also pointed out by Morvan (2001). Ideally, a higher numbers of horizontal levels are required in the main channel and fewer on the floodplain. The details of the 2D and 3D meshes and the number of horizontal levels used for the different flow cases are summarised in Table 5.1.

Table 5.1: Main summary of meshes for different simulation cases

Case	2D mesh (Triangular element)		3D mesh (Prismatic element)		No. of Horizontal planes
	Total nodes	Total elements	Total nodes	Total elements	
Case L No Block	22612	44573	63756	113520	12
Case M Apex Block	8137	15676	39024	67199	12
Case N Cross-over Block	8070	15576	64788	114741	12

For all cases, the 2D base mesh was built over the three and half-meander wavelengths respectively. Using the limited length of meander wavelength for the numerical simulations means that extra attention was required to ensure that the flow was developed. To ensure that the flow was developed, the lateral profile of the horizontal velocities and free-surface elevations were compared at different sections along the whole length of the domain. The mass balance was checked at every apex section of the meander bend.

For cases apex block M and cross-over block N, the 2D base mesh was duplicated over the 12 horizontal levels along the vertical to satisfy the  $Y^+$  criteria, which is to make sure that the first horizontal level above the channel bottom lies in a logarithmic velocity region. Figures 5.1(a) and (b) show the elevation view of the 3D mesh in the main channel at the bend apex for two different flow cases in Telemac 3D while Figures 5.2(a) to (c) show the plan view of the 2D base mesh (half-meander only) for all the cases.

5.5 Initial and Boundary Conditions

For any free-surface flow simulation, the computational domain is bounded by open boundaries like inlet and outlet, lateral sidewalls, bottom and free-surface. The



boundary conditions are to be specified along these boundaries. In Telemac3D most of the boundary conditions are set internally by default, which can, however, be modified via FORTRAN subroutines.

As an initial condition, the water surface profile was set parallel to the bed to match the uniform flow profile. The unknown velocity field was set to zero. The numerical simulations were carried out by using steady-state boundary conditions, with constant flow rate prescribed at the inlet and fixed water depth at the outlet end.

5.6 Numerical Discretization and Solution Sequence

The computational simulations were started with the initial conditions as discussed above. The boundary conditions as discussed earlier were applied. As already explained, the Telemac3D is based on a decoupled algorithm based on the fractional step (operator splitting) techniques, in which the governing equations are split into fractional steps and treated using appropriate numerical schemes (Jankowski, 1998).

The simulations were carried out for the steady uniform flow conditions. In order to ensure that the flow is uniform, the free-surface profile outside the meander-belt region and the lateral free-surface at the bend apex section were compared with the experimental free-surface profiles. In Telemac 2D the only way to achieve uniform flow without changing the experimental flow conditions is by changing either the Manning coefficient or the eddy viscosity. According to Spooner and Shiono (2003), the eddy viscosity does not significantly affect depth-averaged velocity distribution, therefore the Manning coefficient was adjusted. With the different arrangement of floodplain roughness and using the constant eddy viscosity, the calibrated Manning coefficients for uniform flow were obtained and are list in Table 5.2.

Table 5.2: Manning coefficient, n for different simulation cases in Telemac 2D

Case	Manning's n	
	Dr = 0.25	Dr = 0.45
Case L No Block	0.01125	0.01175
Case M Apex Block	0.01145	0.01190
Case N Cross-over Block	0.01100	0.01120



The steady state of the numerical simulation is judged based on mass conservation. Since a finite element is associated with mass conservation problems, the mass conservation was checked at different measurement cross-sections of the channel, which ensures that the flow is fully developed. This also justified the use of only three and half-meander wavelength meshes. The computations were assumed to converge when the mass is balanced to within 1 % and the absolute increment values of all the computed variables between the two time steps at all the nodes were below  $10^{-4}$ .

By having applied the selected arrangements of blocks on the floodplain in the previous chapter, such as cases no block *L*, apex block *M* and cross-over block *N*, comparisons of the velocity variables and boundary shear stress are made with different floodplain block arrangements and relative depths. These flows are also compared to flows for a basic meandering channel without floodplain vegetation. This chapter also presents the comparisons and the validation of the computational results with the experimental data for the different flow cases. In this chapter, finite element codes, Telemac2D and 3D, were used to present all the results. Numerical models, particularly 3D models, have been shown to predict the flow field reasonably accurately in natural rivers (Ferguson *et al.* 2003).

From this point of view, detailed computation of the variation of the flooding depth gradually from  $Dr = 0.15$  to  $0.50$  is necessary. In this present study, for a small-scale model category of meandering channel, the computations were carried out under shallow overbank flow ( $Dr = 0.25$ ) and higher overbank flow ( $Dr = 0.45$ ) conditions. For this thesis, the experimental measurements yielded little data for the  $Dr = 0.45$  condition because of the time restrictions involved in the research programme.

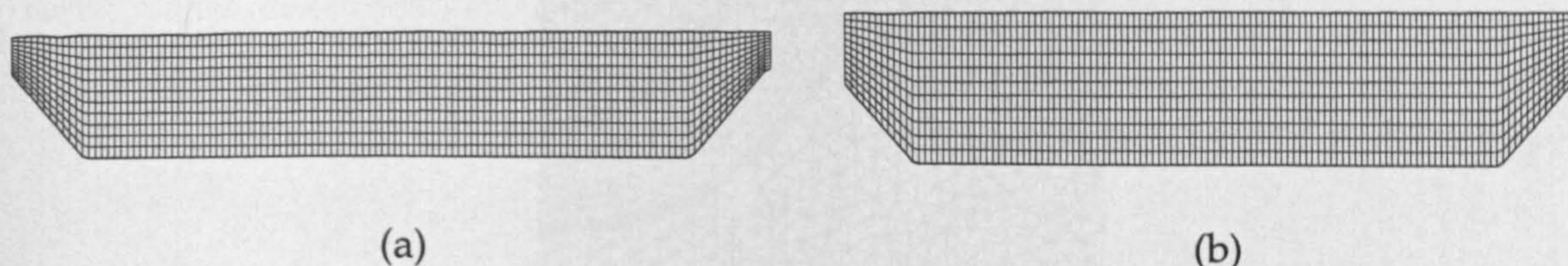
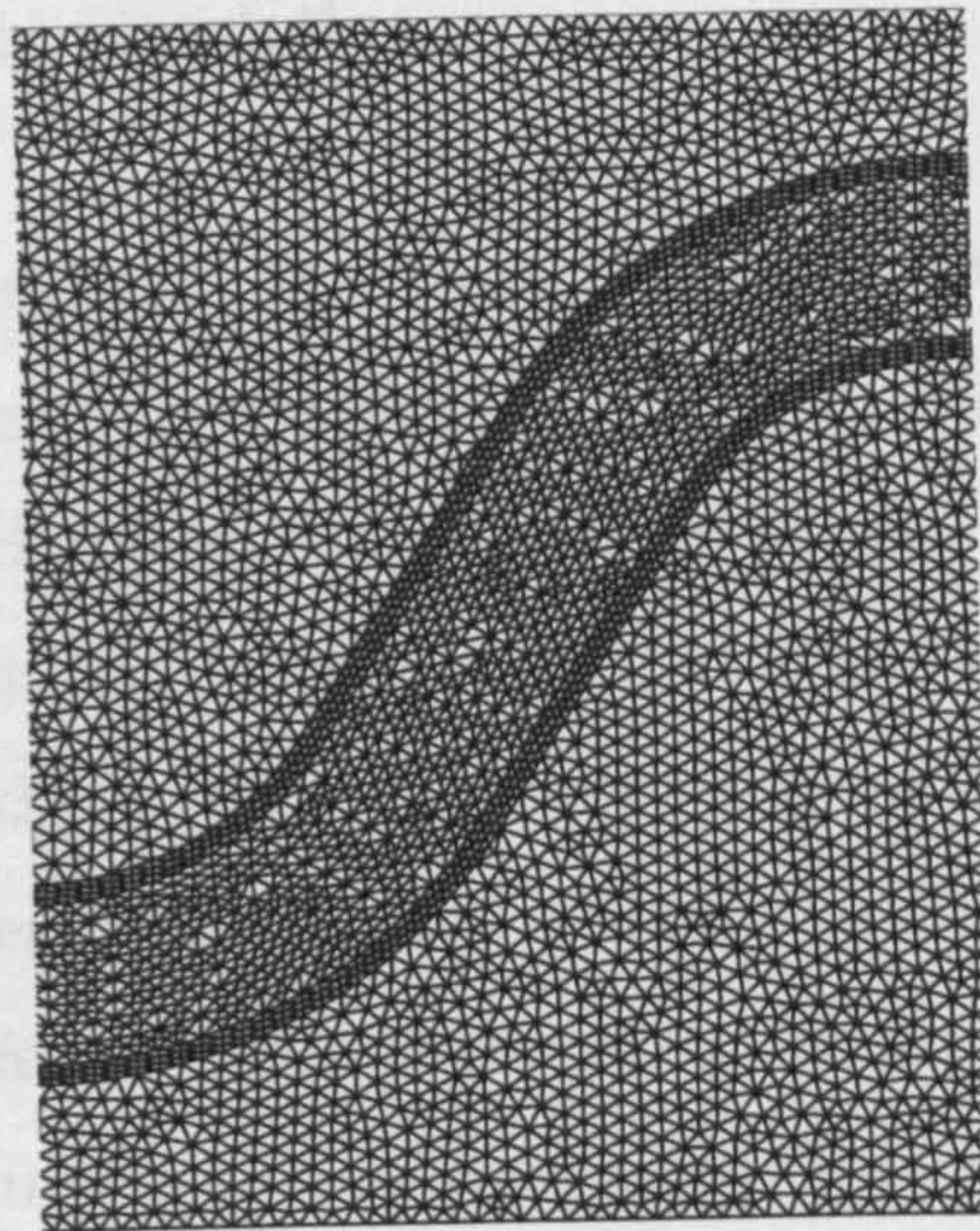
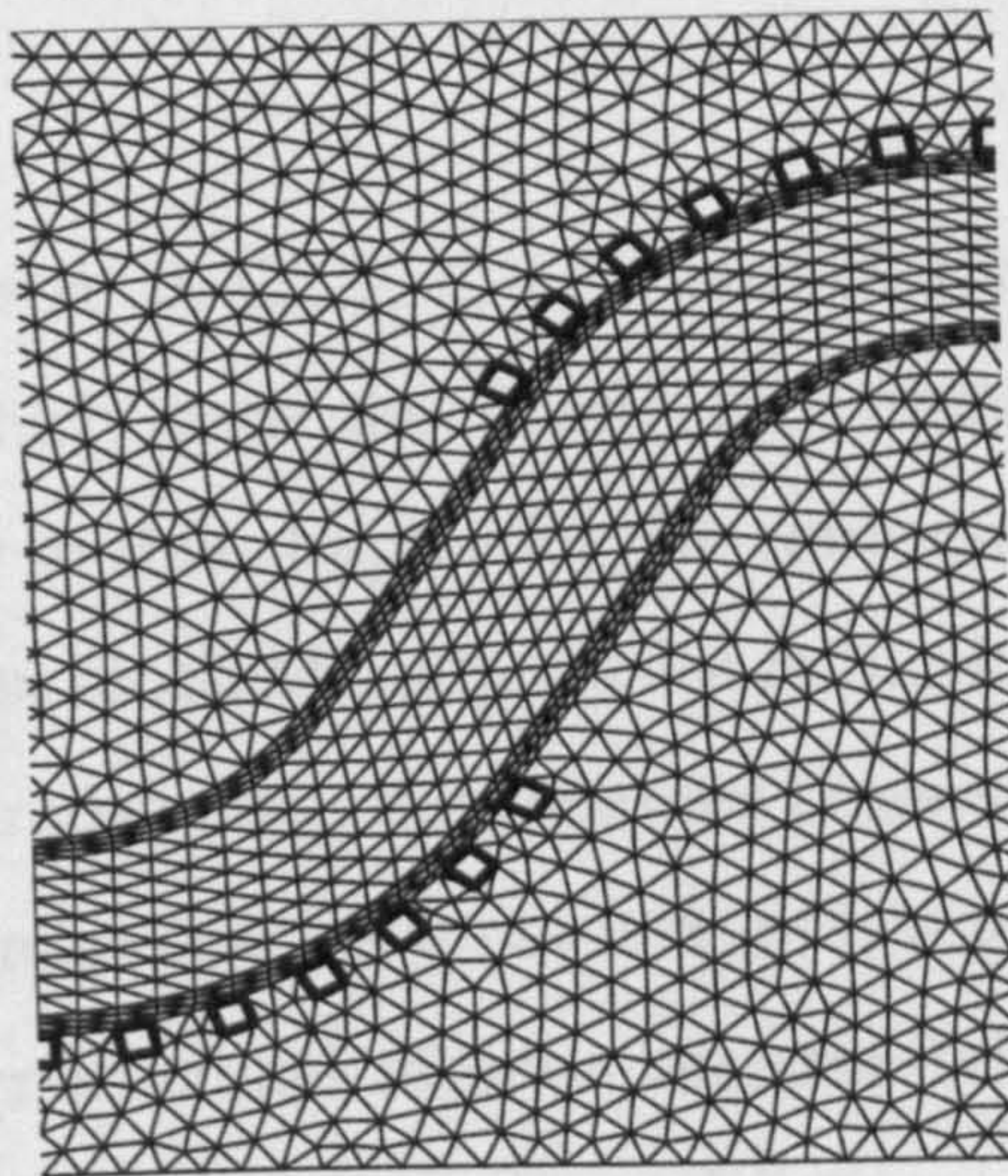


**Figure 5.1:** Elevation view of the three-dimensional mesh in the main channel for cases no block *L*, apex block *M* and cross-over *N* at the bend apex section (a)  $Dr = 0.25$  (b)  $Dr = 0.45$  [For details of meshes see Table 5.1]

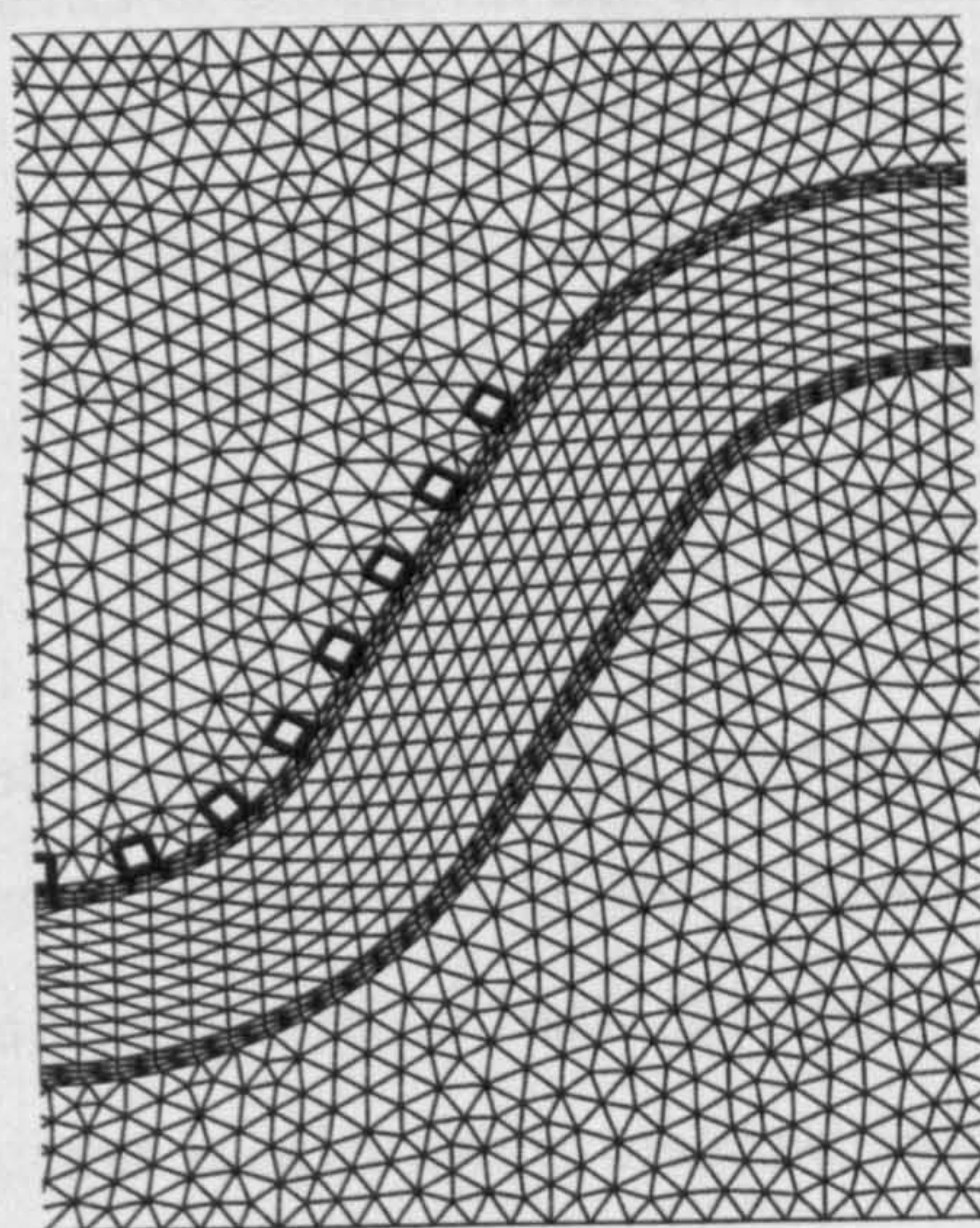




(a)



(b)



(c)

**Figure 5.2:** Plan view of two-dimensional base mesh for a half-meander wavelength (a) Case L No Block (b) Case M Apex Block and (c) Case N Cross-over Block [For details of meshes see Table 5.1]



## 5.7 Description of Numerical Simulation

A description of flow variables, secondary flow vectors, turbulent kinetic energy and boundary shear stress in the main channel is helpful in understanding the important flow characteristics and mechanisms associated with the compound meandering channel with overbank flows. The simulations and experiments conducted in the present study will be divided into two parts. The first looks into the flow characteristics in the meandering compound channel with overbank flows. In the second part, studies on the effect of floodplain vegetation with different arrangements of meandering compound channels will be conducted. For clarity, the simulations are thus categorised as cases no block *L*, apex block *M* and cross-over *N* as described in Chapter 3.

In Chapter 4, results of cases *A*, *B*, *C*, *D*, *E*, *F*, *G* and *H* involve a rectangular main channel cross-section for which both the fixed- and mobile-bed cases have been discussed in detail. However in this chapter for the computational model, only three cases namely no block *L*, apex block *M* and cross-over block *N* will be discussed and have been modified to use a trapezoidal main channel cross-section. The change from a rectangular to a trapezoidal main channel cross-section is due to the need for the slope of the main channel in order to create meshes because Telemac used in simulation could not handle vertical wall of the main channel in compound channel. By having applied the selected arrangements of blocks on the floodplain in the previous chapter, such as cases no block *L*, apex block *M* and cross-over block *N*, to a 45-degree slope of the main channel cross-section, comparisons of the velocity variables and boundary shear stress are made with different floodplain block arrangements and relative depths.

The problem arises with mesh generation for the boundary condition file for blocks along both sides at the cross-over section (*Case N Cross-over Block*). In order to overcome this problem of producing similar basic flow structures in the main channel along the cross-over section, the blocks were inserted downstream only along the cross-over section which reduced the number of blocks to 16 instead of 30 for one meander wavelength but the basic concept is still similar to *Case C Cross-over Block* for



rectangular main channel, only reduction in number of block at one side at the cross-over section (see Figures 3.9(c) and (g)).

The simulations reported in this thesis were run under two different Telemac versions. *Case L No Block* for 2D and 3D were run under Telemac version V5P4 and cases *M* and *N* were simulated under Telemac version V5P5. In this study, the Turbulent Kinetic Energy (*TKE*) or  $k-\varepsilon$  model has been used for *Case L No Block*. However, when applied to the other block cases the program kept crashing just after the initial few iterations under all advection schemes such as Method of Characteristics (*MCH*), Streamline Upwind Petrov-Galerkin (*SUPG*) and Multidimensional Upwind Residual Distribution (*MURD*). In order to overcome this problem Telemac V5P5 was applied for apex block *M* and cross-over block *N* cases and run under the Smagorinsky Model by using the *MCH* advection scheme.

For the *Case L No Block* on floodplain, the study attempts firstly to generate basic flow characteristics and mechanisms followed by cases apex block *M* and cross-over block *N* with vegetated floodplains. In all cases, 2D and 3D simulations have been applied to carry out the flow behaviours. The axis normalisation is explained here. The lateral and horizontal axis represents the lateral distance ( $y$ ) normalised by the channel depth at the bankfull level ( $h$ ), taking the left end of the channel bottom width as the origin. The vertical axis represents the vertical distance ( $z$ ) also normalised by the channel depth ( $h$ ), which is taken from the channel bottom. The mean velocities ( $U$ ,  $V$  and  $W$ ) were normalised by the sectional averaged velocity ( $U_s = Q/A$ ), where  $Q$  is the measured discharge and  $A$  is the cross-sectional area at the bend apex. The *TKE* were normalised by the shear velocity squared ( $u^*{}^2$ ) where  $u^* = \sqrt{gRS_o}$ . The governing *RANS* and continuity equations were solved in the Cartesian coordinate system.

## 5.8 Comparisons and Validations of the Experiment Measurements

This section presents a comparison of the computational results with the experimental data for the higher flow case only. A particular attention is paid to the assessment of the numerical model's ability to reproduce the important mean flow characteristics observed from the measurement data. The experiment was undertaken to measure



velocities for the selected simulated velocities in Sections 5.9.1, 5.9.2 and 5.9.3 for *Case L No Block*, *Case M Apex Block* and *Case N Cross-over Block* respectively at  $Dr = 0.45$ .

Figures 5.3(a), 5.4(a) and 5.5(a) show the cross-sectional distribution of the measured streamwise, lateral and vertical velocities from selected sections S1, S4, S7, S10 and S12 respectively for *Case L No Block*. When comparing the predicted streamwise velocity as shown in Figure 5.3(b) shows that the measured streamwise velocity is well agreement at the apex region, sections S1 and S4. For cross-over section S7, the streamwise velocity is not agreement near the inner side of the main channel near the bankful level. The streamwise velocity contours are quite well agreement at the region for the bend sections S10 and S12.

By comparing the cross-sectional distributions of the measured and predicted lateral velocities as shown in Figure 5.4 along the half-meander for *Case L No Block* the overall lateral velocity distribution is consistently well agreement for all the sections (S1, S4, S7, S10 and S12). Figures 5.5(a) and (b) show the measured and predicted vertical velocities respectively. It can be seen that the computational results show that the vertical velocity has been fairly well agreement, especially at section S4.

Figure 5.6 shows the measured and predicted secondary flow vectors for *Case L No Block* at sections S1, S4, S7, S10 and S12 respectively. At section S1, which is the apex section, a single dominant anticlockwise circulation cell occupying almost the whole of the main channel area was both measured and predicted. Following this, the circulation cell was measured for sections S4, S7, S10 and S12 respectively, and agreement with the predicted secondary flow vectors was obtained. The strengths and the magnitudes of the secondary flow vectors are well agreement, which is consistent with the quite good predictions of  $V$  and  $W$ . In general, the measured secondary flow seems to be in good agreement when compared to the predicted one.

For cases apex block *M* and cross-over block *N*, only the measured and predicted streamwise velocity contours and secondary flow vectors were compared due to the fact that  $V$  and  $W$  contribute to the secondary flow vector plotted. For *Case M Apex Block*, Figures 5.7(a) and (b) show the respective measured and predicted streamwise velocities for *Case M Apex Block*. It can be noticed that the streamwise velocity contours



are not well agreement in the region of the bend sections S1 and S4. However, the rest of the sections S7, S10 and S12 show that the streamwise velocity contours are well agreement at the cross-over section and downstream bend region respectively. When looking at the measured and predicted values of the secondary flow vectors for *Case M Apex Block* as shown in Figure 5.8, it can be seen that there are two anticlockwise circulation cells at section S1. At section S4, a small clockwise circulation cell is seen near the inner side of the main channel which indicates a very good agreement between the measured and predicted secondary flow at the apex bend region for the block case. Similar good agreement for the downstream apex region sections, S10 and S12, are seen, however, at the cross-over section, S7, the secondary flow vectors are not agreement with a small clockwise circulation cell being seen rather than the measured secondary flow vectors which indicate a large clockwise circulation below the bankful level for almost the whole of main channel area. In general the overall secondary flow vectors were well agreement in the block *Case M Apex Block*.

Figure 5.9 shows the measured and predicted streamwise velocity contours for *Case N Cross-over Block* for the selected sections. The figure shows that there are complex flow behaviours that are quite difficult to understand. Section S1 shows that the streamwise velocity is not agrees near the surface and at the outer side of the main channel. At section S4 shows that the streamwise velocity is well agreement at the inner side and at the central part of the main channel, however not at the outer side of the main channel. At the cross-over section, S7, it was noticed that the streamwise velocity is well agreement at the inner side of the main channel (left side) but not at the outer side of the main channel (right side). At the downstream apex region it can be seen that for section S10 the streamwise velocity is well agreement, however not at section S12. Figure 5.10 shows the measured and predicted secondary vectors for *Case N Cross-over Block*. At the apex bend, section S1 shows that two circulation cells are both measured and predicted. At section S4, where a small magnitude of secondary flow is seen near the inner side of the main channel, there is a close similarity with the predicted secondary flow for block *Case N Cross-over Block*. Similar high levels of agreement for cross-over section S7 and the downstream apex region, sections S10 and S12, also exist.

The profiles of the measured and predicted depth-averaged velocity along the floodplain for *Case M Apex Block* are shown in Figure 5.11. The origin of x axis is at the



floodplain wall. At sections FP7 to FP15, the decay of flow on the floodplain can be clearly seen. The minimum velocity starts a negative velocity, which means, reverse flow due to wakes of the blocks, at section FP7 and then becomes a positive value, increasing after section FP9. This indicates that the effect of wakes due to the blocks is decaying along the floodplain. The overall patterns between the measured and predicted depth-averaged velocity are almost identical, even behind the blocks. The predicted streamwise velocity for sections FP7, FP9 and FP11 are slightly higher, especially for both left and right floodplains. However, as the flow moves towards sections FP13 and FP15, the streamwise velocity is well agreement at the middle (behind the blocks) but not on the left and right sides at section FP13 and at the right side at section FP15. In general, local velocities on the floodplain behind the blocks are reasonably well agreement, but slightly higher in predicted streamwise velocity on both left and right sides of the floodplain.

The distribution of boundary shear stresses on the wetted perimeter over the main channel were measured and predicted for only selected sections in three different cases known as *Case L No Block*, *Case M Apex Block* and *Case N Cross-over Block* respectively. The measured and predicted boundary shear stresses were compared for a high relative depth,  $Dr = 0.45$ , only. For *Case L No Block*, the boundary shear stresses were plotted at sections S1, S3, S5, S7, S9, S11 and S12 over the half wavelength and are shown in Figure 5.12, however for cases M and N, the boundary shear stresses were plotted at section S1, the bend apex, only and are shown in Figures 5.13 and 5.14. In general, Figures 5.12, 5.13 and 5.14 show the measured and predicted boundary shear stresses for cases no block L, apex block M and cross-over block N respectively.

The measured and predicted boundary shear stresses for *Case L No Block* at  $Dr = 0.45$  are shown in Figure 5.12. The boundary shear stress is very well agreement at the inner side of the main channel apex section at sections S1, S3 and S5. At the cross-over section S7, the boundary shear stress is shown to be higher for predicted boundary shear stress at the inner side but well agreement at the outer side of the main channel. At sections S9, S11 and S12, the boundary shear stress on both the side walls is well agreement. The boundary shear stress predicted by Shukla (2006) is also in quite good agreement, however, Rameshwaran and Naden (2004a) did not predict the boundary shear stress very well. Both used the data from the FCF and different models. Figures



5.13 and 5.14 show the predicted and measured boundary shear stress at the bend apex, section S1, only for *Case M Apex Block* and *Case N Cross-over Block* respectively. For *Case M Apex Block*, the boundary shear stresses on both the side walls are well agreement whereas, in *Case N Cross-over Block*, the boundary shear stress at the inner side to the mid point of the main channel bottom is good agreement but not at the outer side of the main channel. Overall, the measurements of boundary shear stresses are reasonably in agreement with the predictions. It was expected from the good agreement between the measured and predicted velocities that the measured boundary shear stress would also be in good agreement with the predicted stress. However, the measured boundary shear stress is somewhat lower at several cross-sections at the inner side of the main channel for *Case L No Block*. This could suggest errors in the boundary shear stress measurement using the Preston tube in this region due to the complex flow structure and a non-logarithmic velocity profile at the point where the Preston tube was placed.

The free-surface profile was only measured for a higher relative depth,  $Dr = 0.45$ , at the apex section for each case. Figure 5.15 show the comparison of the measured and predicted lateral free-surface profiles for each case. Reasonably good agreement between the measured and predicted free surface is observed in the main channel for the three cases but, overall, the free-surface elevation is somewhat not well agreement on the floodplain.

There are some differences between the measured and predicted isovels near the boundary for velocity plotted. This is caused by plotting the isovels of using software, not using zero value at the boundary for the measured data, but using zero value for the predicted data. In general, the computation using Telemac 3D used to predict the velocity for the case of overbank flow for a meandering channel with both non-vegetated and vegetated floodplains is in very good agreement with the measured data in the main channel. Hence, Telemac 3D result can be used to explain flow mechanisms along meandering channel in detail.



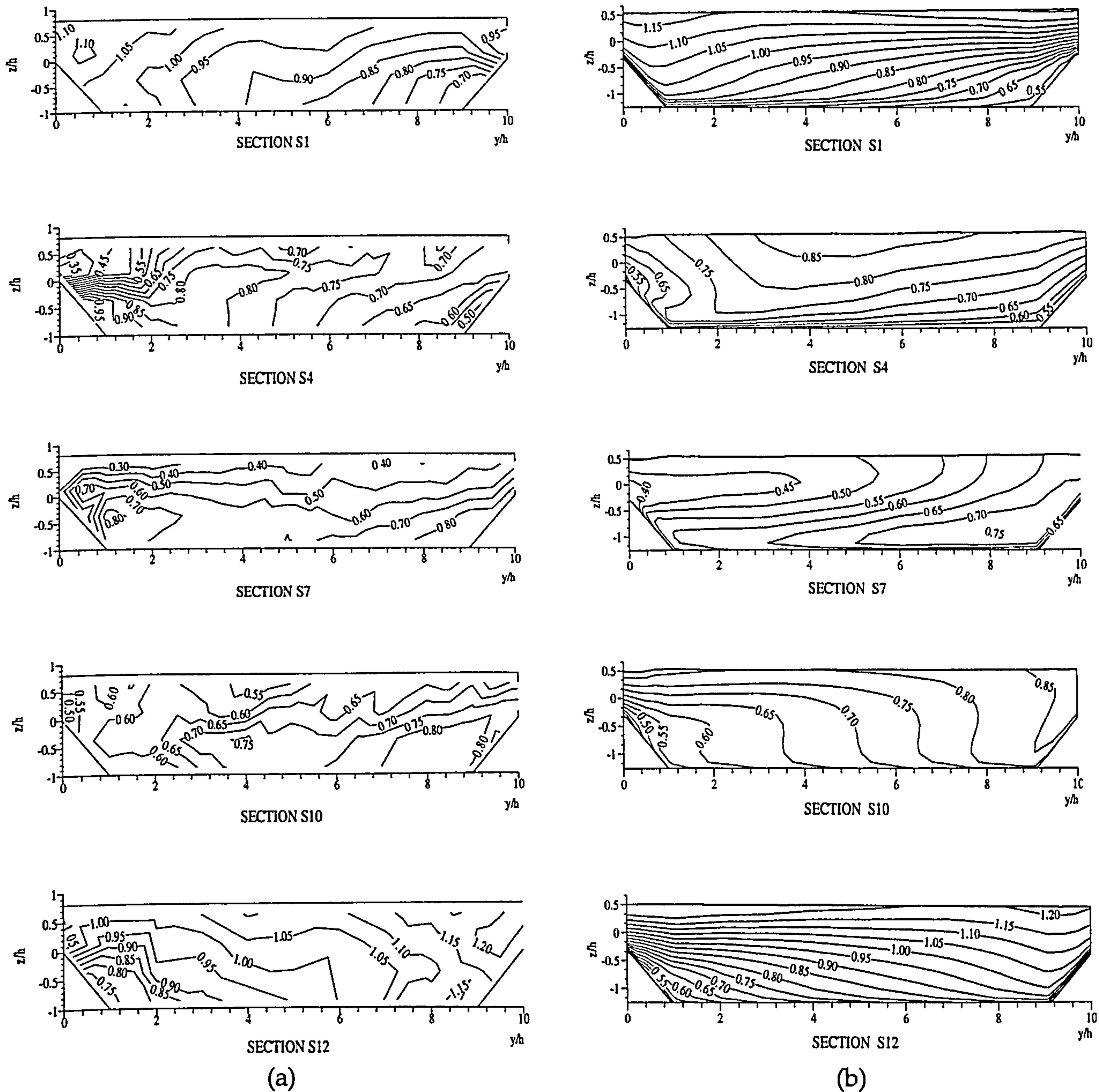


**Figure 5.3:** Streamwise velocity  $U$ , normalised by  $U_s$  for main channel in *Case L No Block* at  $Dr = 0.45$  at sections S1, S4, S7, S10 and S12 (a) Measured (b) Predicted



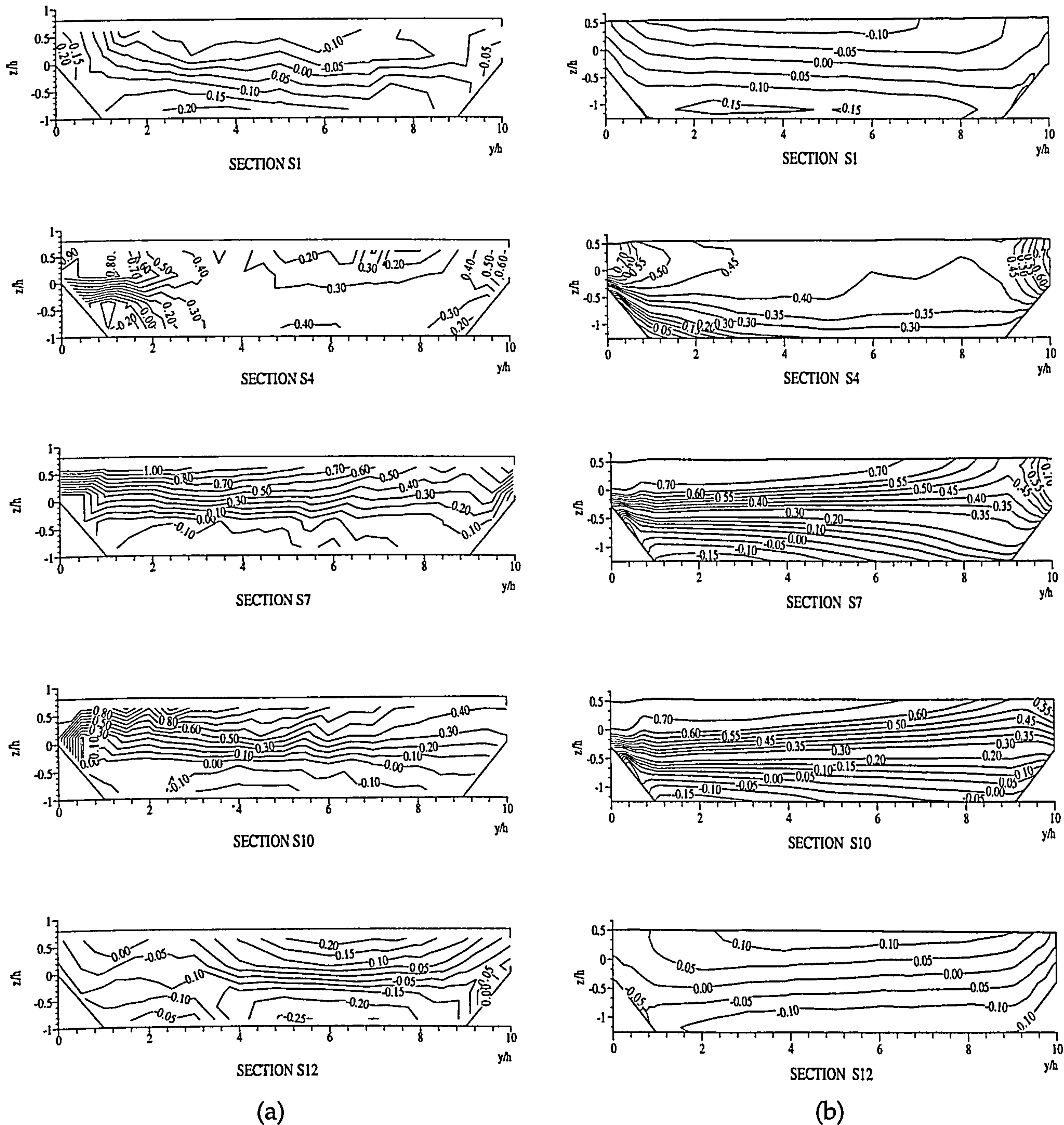


**Figure 5.4:** Lateral velocity  $V$ , normalised by  $U_s$  for main channel in *Case L No Block* at  $Dr = 0.45$  at sections S1, S4, S7, S10 and S12 (a) Measured (b) Predicted



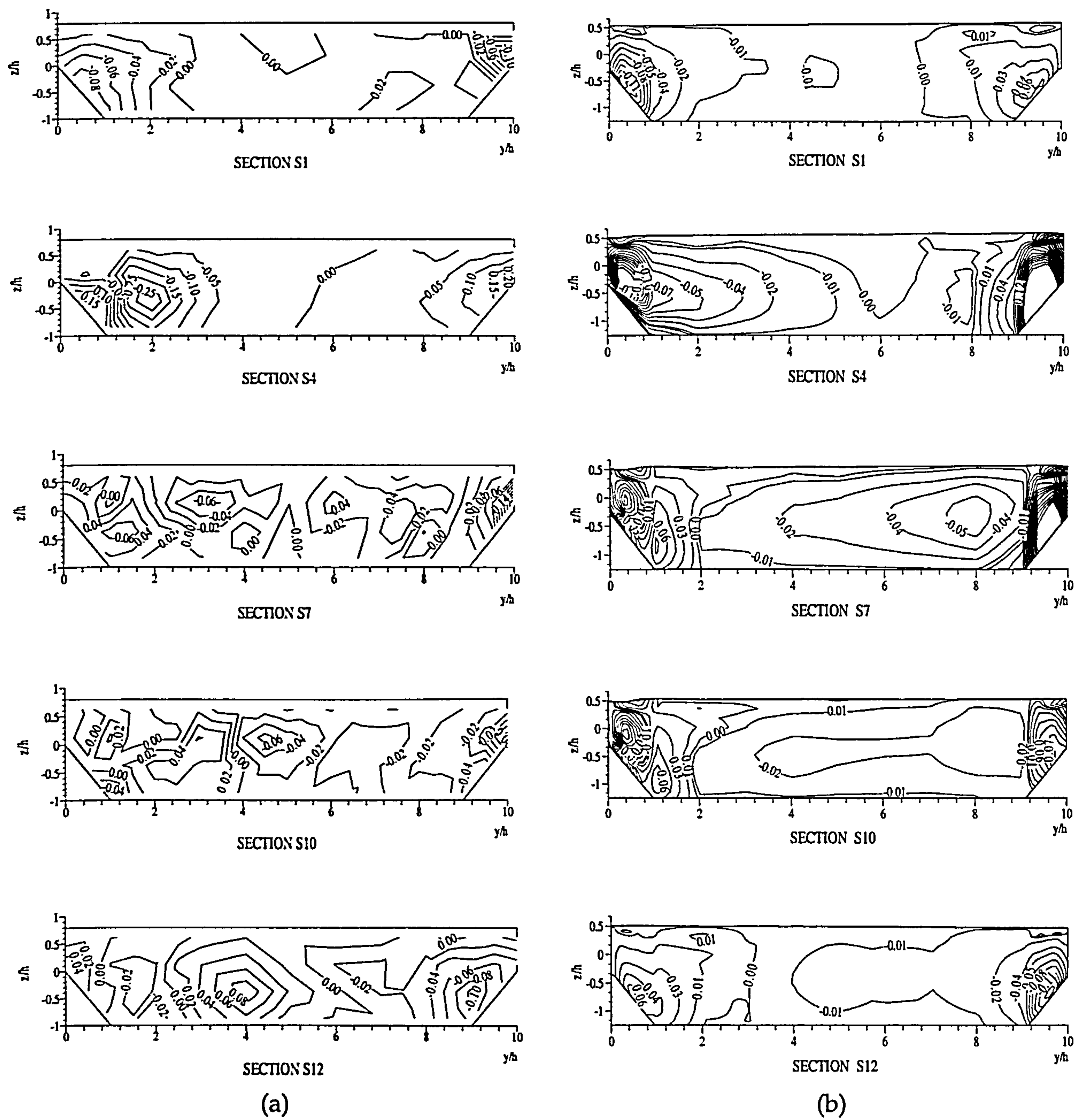


Figure 5.5: Vertical velocity  $W$ , normalised by  $U_s$  for main channel in *Case L No Block* at  $Dr = 0.45$  at sections S1, S4, S7, S10 and S12 (a) Measured (b) Predicted



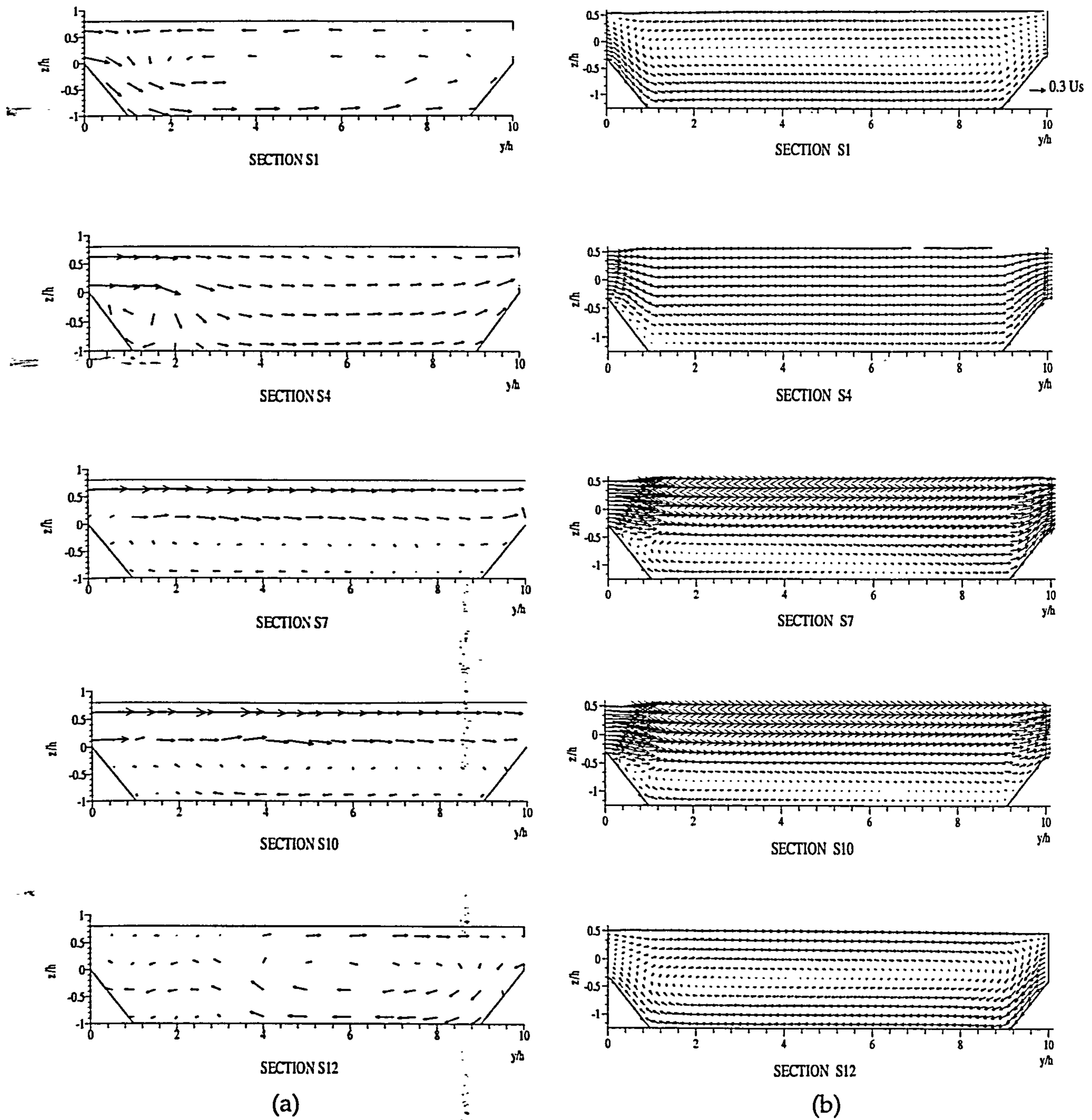


Figure 5.6: Secondary flow vectors for main channel in *Case L No Block* at  $Dr = 0.45$  at sections S1, S4, S7, S10 and S12 (a) Measured (b) Predicted



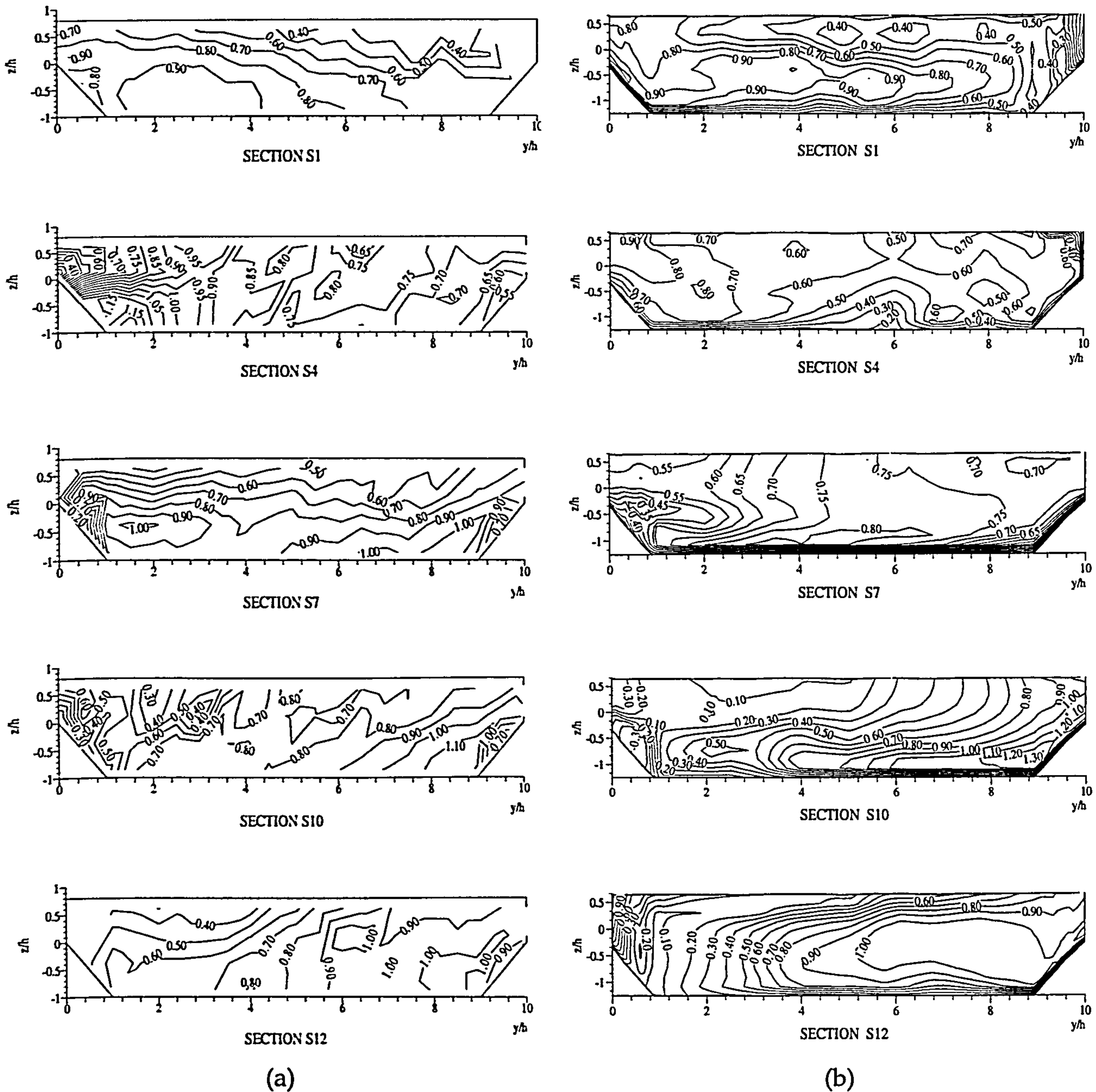


Figure 5.7: Streamwise velocity  $U$ , normalised by  $U_s$  for main channel in Case M Apex Block at  $Dr = 0.45$  at sections S1, S4, S7, S10 and S12 (a) Measured (b) Predicted



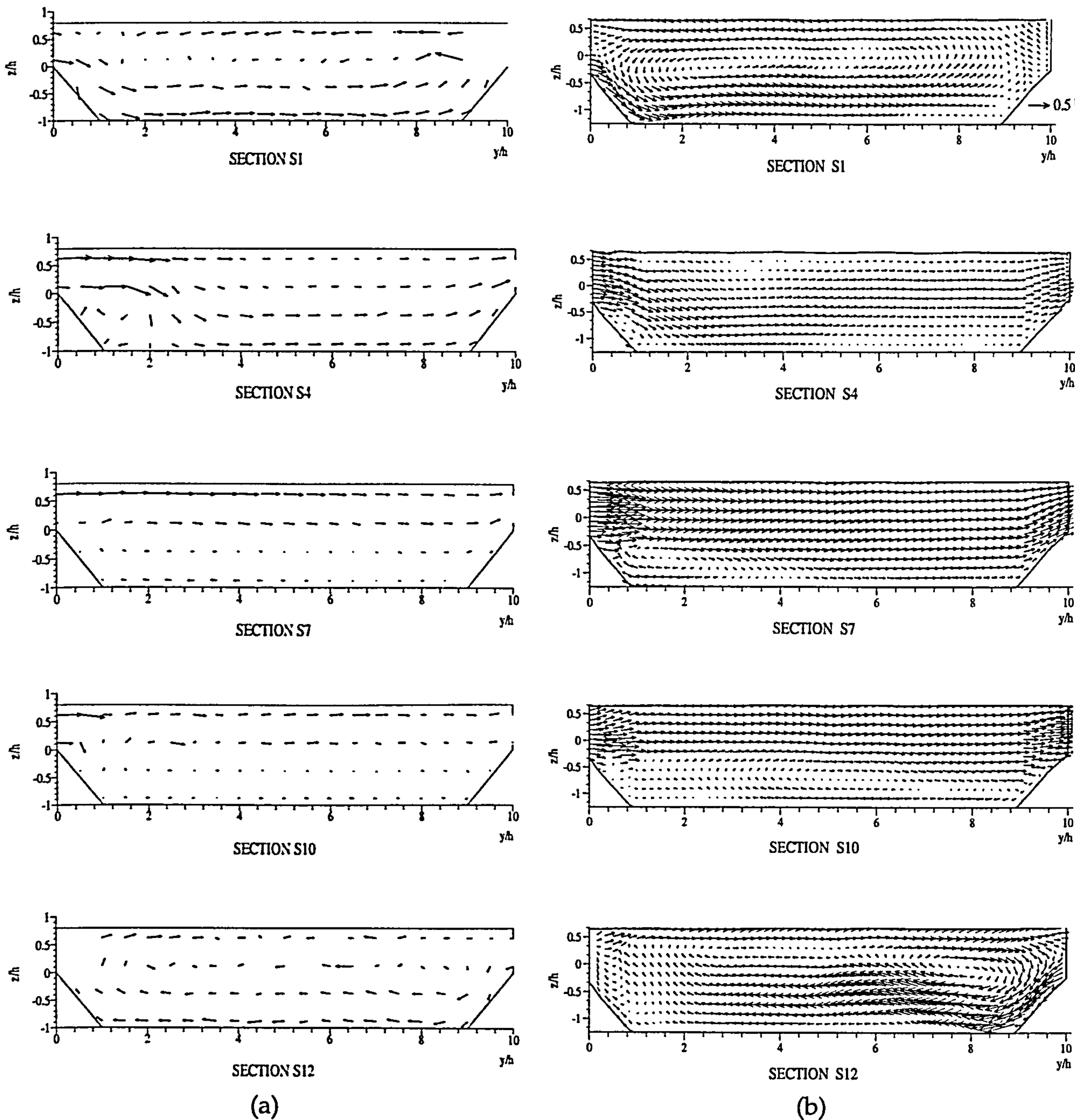


Figure 5.8: Secondary flow vectors for main channel in *Case M Apex Block* at  $Dr = 0.45$  at sections S1, S4, S7, S10 and S12 (a) Measured (b) Predicted



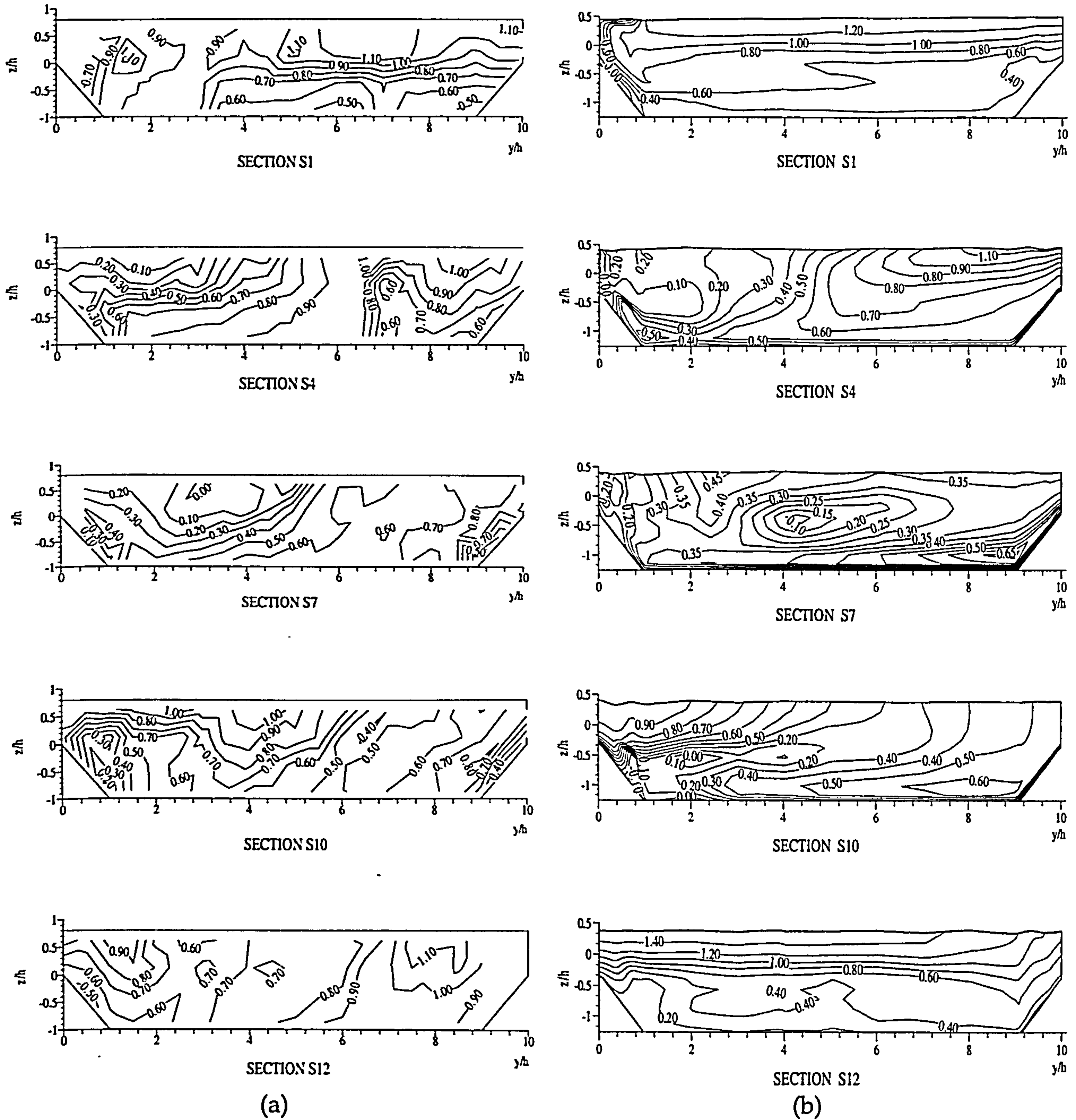


Figure 5.9: Streamwise velocity  $U$ , normalised by  $U_s$  for main channel in Case N Cross-over Block at  $Dr = 0.45$  at sections S1, S4, S7, S10 and S12 (a) Measured (b) Predicted



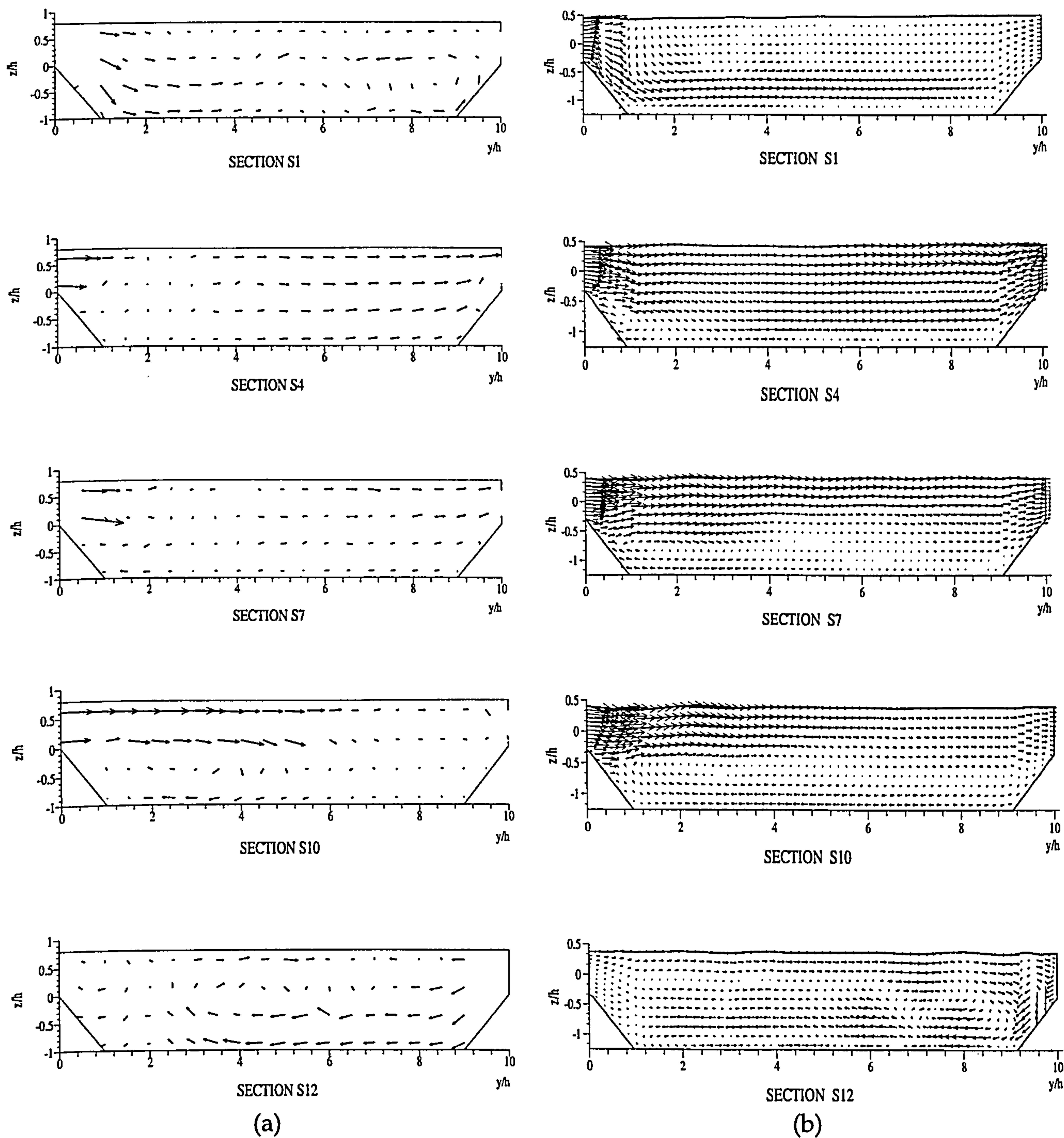


Figure 5.10: Secondary flow vectors for main channel in *Case N Cross-over Block* at  $Dr = 0.45$  at sections S1, S4, S7, S10 and S12 (a) Measured (b) Predicted



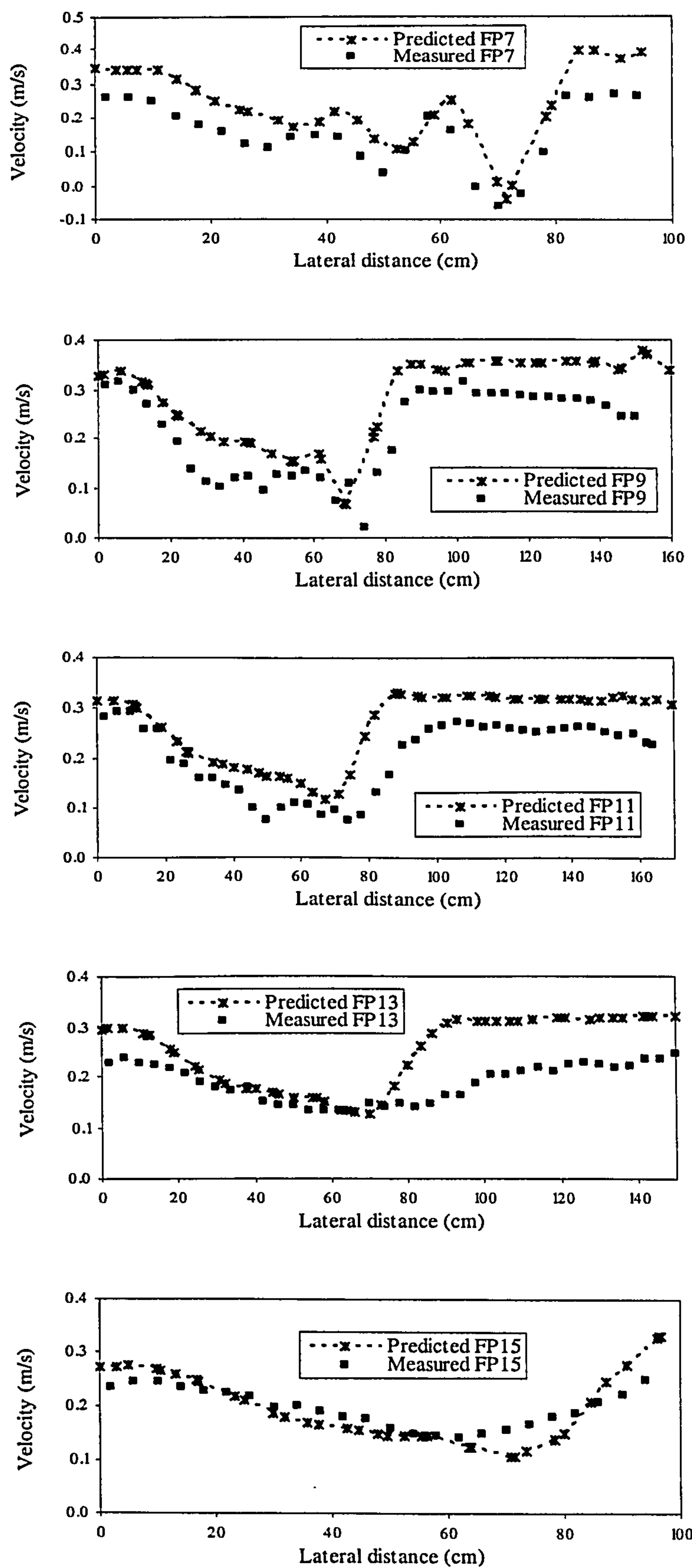
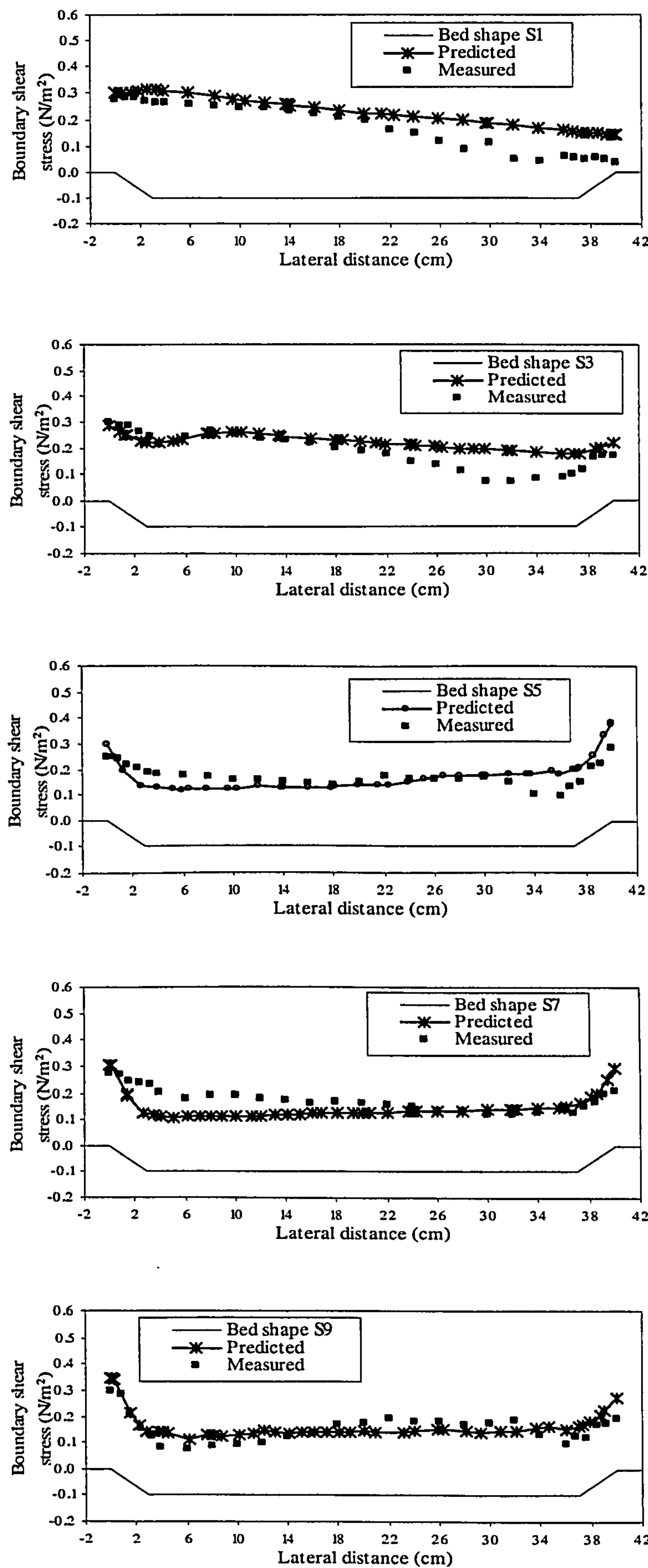


Figure 5.11: Comparison between measured and predicted of velocities in the floodplain for *Case M Apex Block* at  $Dr = 0.45$  at sections FP7, FP9, FP11, FP13 and FP15







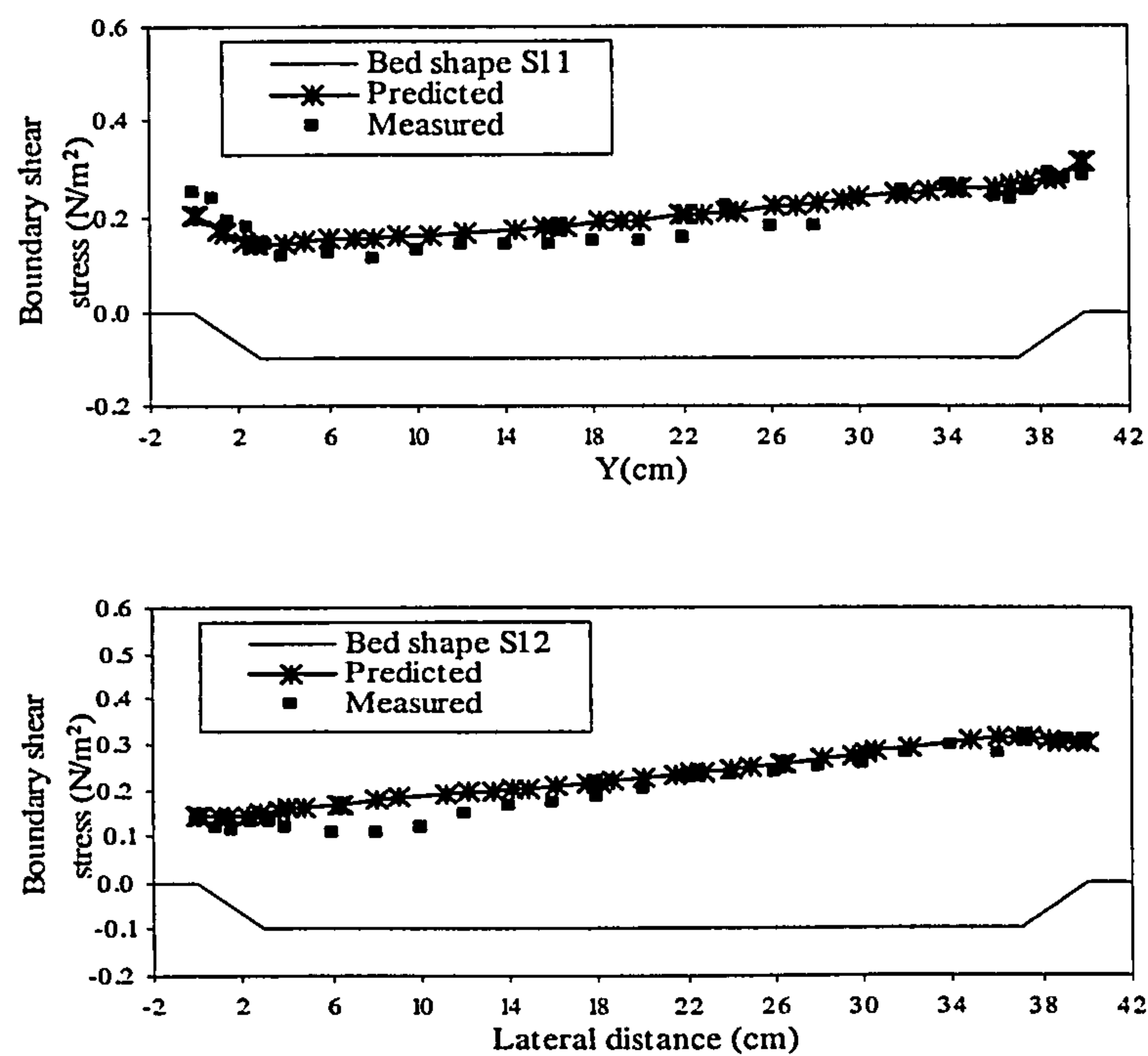


Figure 5.12: Measured and predicted boundary shear stress for main channel in *Case L No Block* at  $Dr = 0.45$  at sections S1, S3, S5, S7, S9, S11 and S12

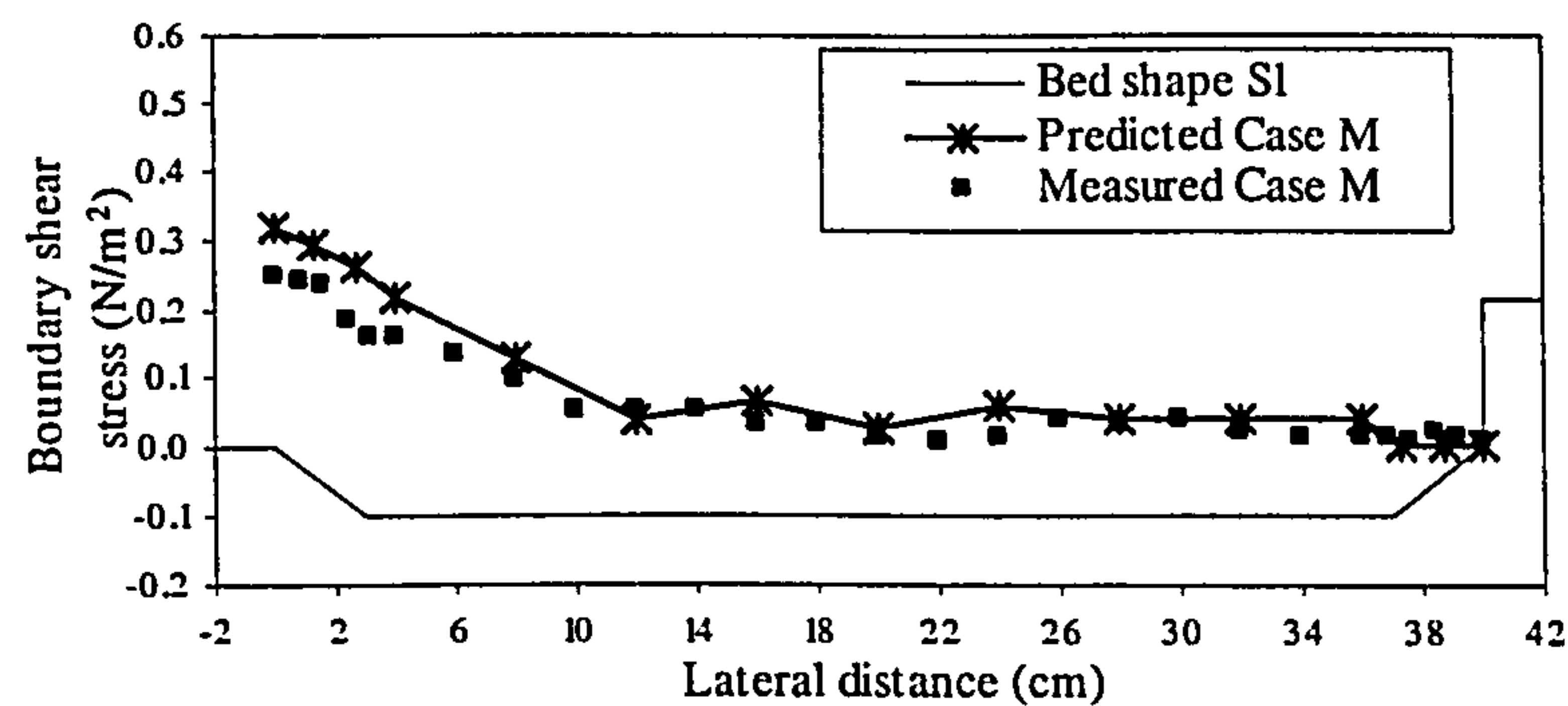


Figure 5.13: Measured and predicted boundary shear stress for main channel at section S1 for *Case M Apex Block* at  $Dr = 0.45$

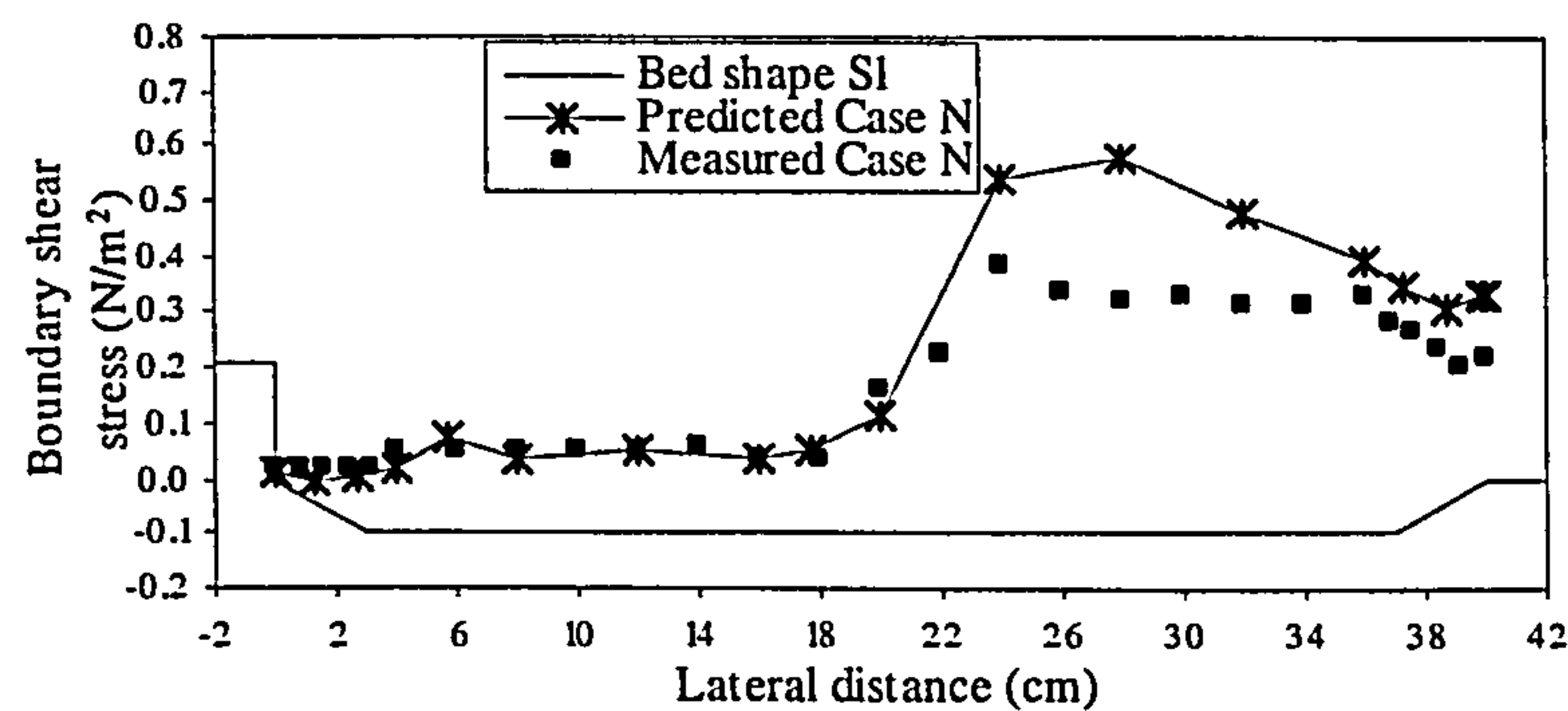
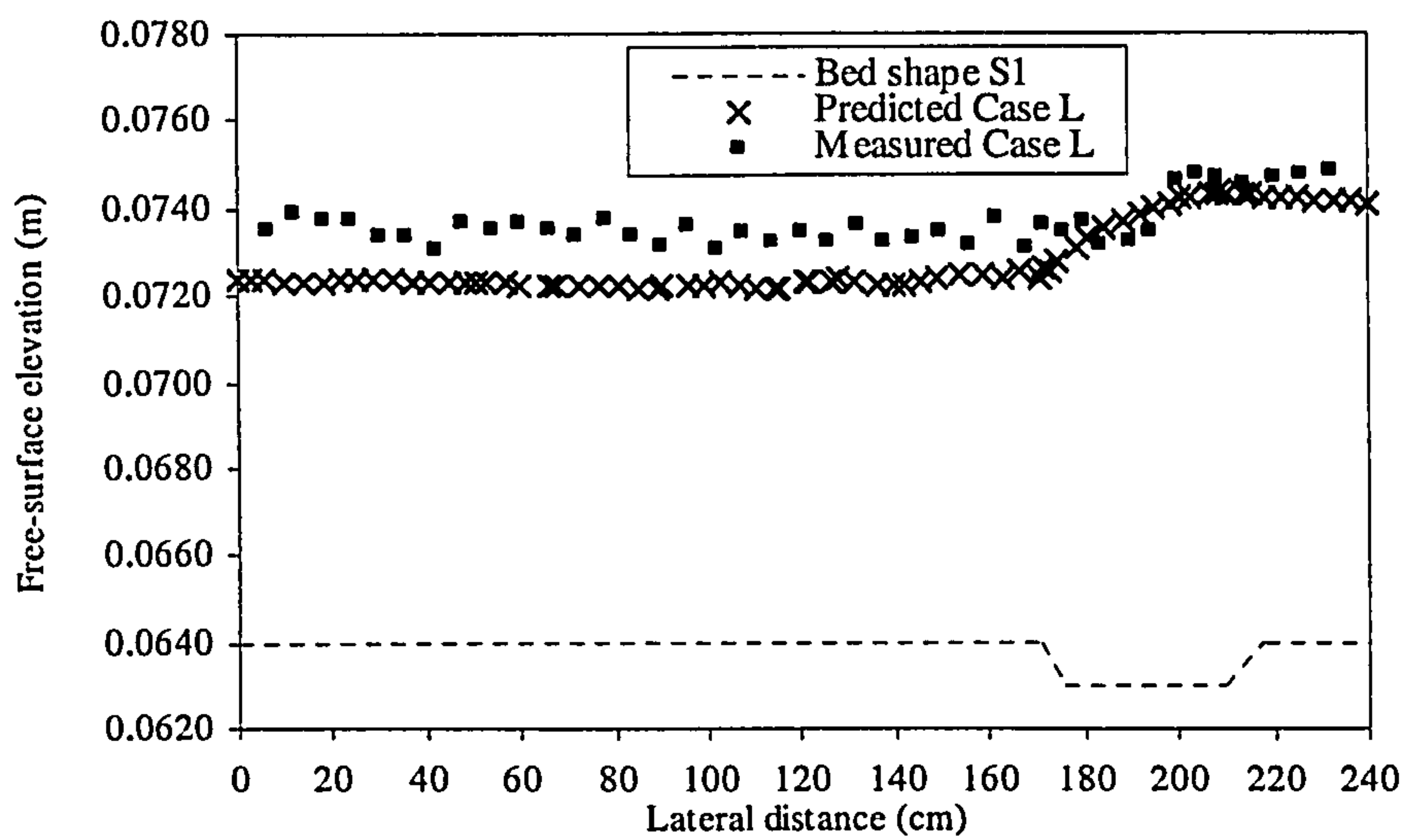
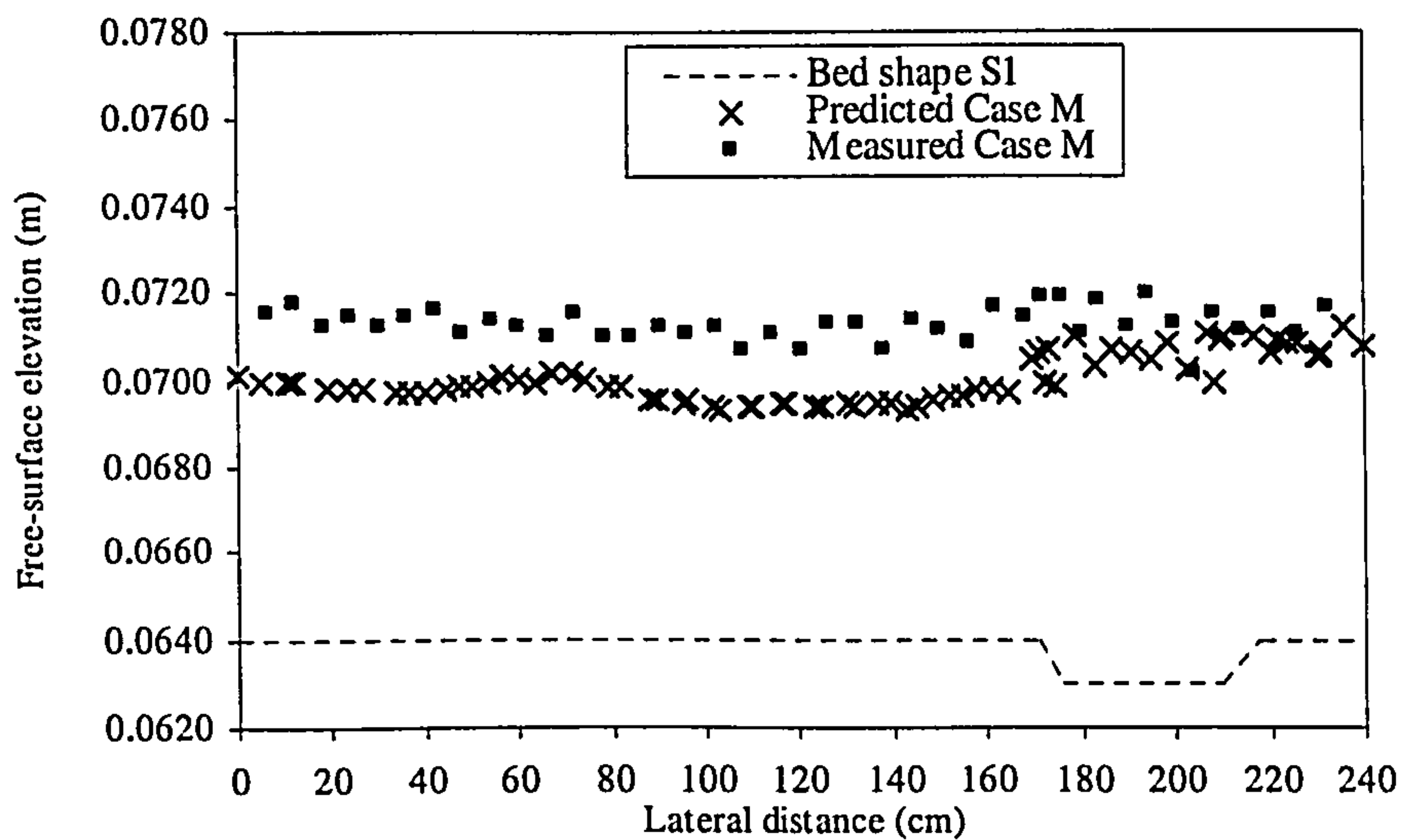


Figure 5.14: Measured and predicted boundary shear stress for main channel at section S1 for *Case N Cross-over Block* at  $Dr = 0.45$

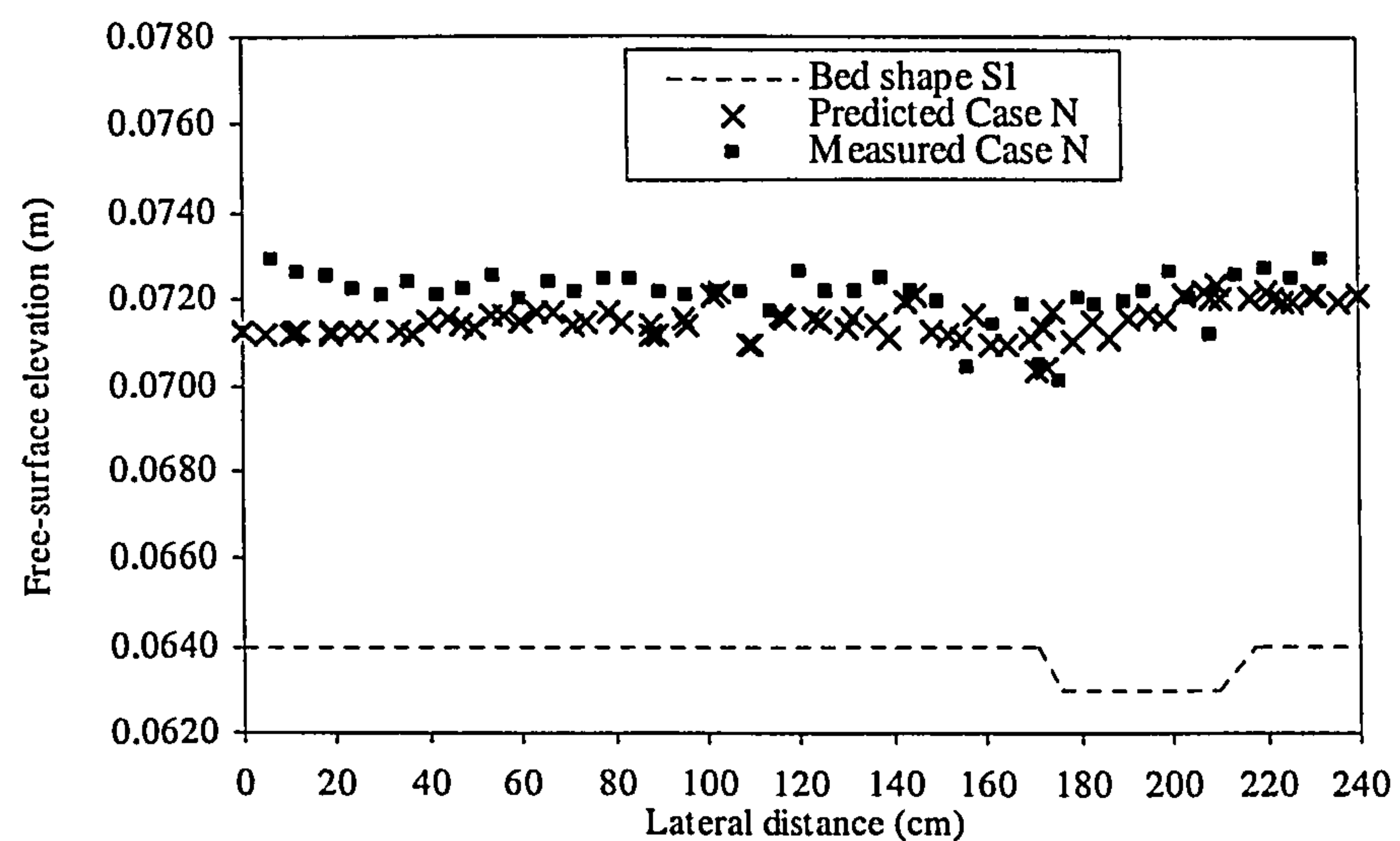




(a)



(b)



(c)

**Figure 5.15:** Measured and predicted lateral free-surface profile for main channel at section S1 at  $Dr = 0.45$  (a) Case L No Block (b) Case M Apex Block and (c) Case N Cross-over Block



## 5.9 Flow Mechanism in a Compound Meandering Channel

In this section, the flow structures of *Case L No Block* on the floodplain were simulated for 0.25 and 0.45 relative depths. For the velocity vector fields herein, the depth-averaged velocity was calculated over the depth of the main channel and floodplain. In order to present a better picture of the flow distribution, the vector field has been superimposed over the velocity distribution to demonstrate a better understanding between the flow in the main channel and floodplain. The 2D and 3D Reynolds-averaged Navier-Stokes (RANS) and continuity equations were solved in the Cartesian coordinate system to predict the flow in compound meandering channels for different model scales and relative depths ( $Dr$ ) as mentioned above. This sub-chapter describes detailed results for main channel cross-sections consisting of flow velocities ( $U$ ,  $V$  and  $W$ ), secondary flow vectors and turbulent kinetic energy ( $TKE$ ).

### 5.9.1 Overbank Flow without Floodplain Vegetation: *Case L No Block*

#### 5.9.1.1 Depth-averaged Velocity Vector Fields

Figures 5.16(a) and (b) show the results for the distribution of depth-averaged velocities along one meander wavelength for  $Dr = 0.25$  and  $Dr = 0.45$  respectively. Shallow overbank flow of  $Dr = 0.25$  shows that the maximum velocity filament in the main channel occurs relatively near to the inner bank sidewall at the upstream apex bed and moves progressively to the outer bank as it approaches the downstream bend apex. However, a substantial reduction of the velocity at the cross-over section occurred near to the inner bank of the channel. It can also be seen that the cross-over flow effect gradually reduces as the flow moves further away from the inner bank of the main channel. The magnitude of the floodplain flow is generally higher on the downstream of the main channel compared to the upstream and this varies at different locations. However, on the floodplain flow vectors are more consistent in magnitude at the outer meander belt region and are mostly parallel in the valley direction, whilst within the meander belt region the flow diverts towards the inside of the channel.

At the higher overbank flow,  $Dr = 0.45$ , the main channel flow deviates at an angle away from the meander streamline direction due to the strong floodplain flow, which



predominantly follows the direction of the valley. This feature will cause the retardation of the flow within the meander belt, being slower than the outer side. On the other hand, from the middle part of the cross-over section, the velocity distribution becomes more uniform and its primary direction is streamwise. This is due to the flow structure in the main channel being significantly changed from the exit of the bend to the cross-over region. At the bend apex, it is also clear that the flow along the inner bank is faster than along the outer bank.

#### 5.9.1.2 3D Variable Velocities Field

The previous depth-averaged flow vectors do not show internal flow structures along a meandering channel; hence this section shows clearly the details of the velocity distribution for a better understanding of the velocity distribution in the main channel. The streamwise velocity ( $U$ ), lateral velocity ( $V$ ) and vertical velocity ( $W$ ) were plotted using a contour format to show the magnitude of each component along the main channel.

##### 5.9.1.2.1 Streamwise Velocity

Figures 5.17 and 5.18 show contour lines of predicted streamwise velocities normalised by the sectional averaged velocity at  $Dr = 0.25$  and  $Dr = 0.45$  respectively at sections S1 to S12.

Figure 5.17 shows the cross-sectional distributions of the predicted streamwise velocity ( $U$ ) for  $Dr = 0.25$ . At all main channel cross-sections the velocity is positive. At the bend apex section S1, maximum streamwise velocity is observed to be  $1.15U_s$  near the inner side of main channel. Minimum streamwise velocity is found to be  $0.65U_s$  near the bottom closer to the outer side of the main channel. It can be seen from Figure 5.16(a) that the main channel and floodplain flow directions are parallel to each other, thus the flow interaction due to floodplain flow entering into the main channel is not significant at this section. At sections S2 and S3, the maximum streamwise velocities are reduced to the magnitudes of about  $1.10U_s$  and  $1.05U_s$  at the inner side of the main channels respectively and start to shift towards the outer side of the main channel for both sections. Maximum streamwise velocity is below the free-surface after section S8. From



section S3, at the edge of the floodplain in the inner bank region, the velocity starts to decrease along the meandering channel until section S9 and then starts to increase. At section S5, lower magnitudes of velocity around  $0.4U_s$  are observed at the inner bankful level of the main channel, which extends laterally as the flow moves downstream to section S9. This is due to the shearing of the main channel flow at the inner bankful level by the floodplain flow plunging into the main channel. The streamwise velocity below the bankful level is higher than the velocity above the bankful level. Due to this, the horizontal shear layer at around the bankful level, particularly in the cross-over region sections S5 to S9, is generated. With regard to the streamwise velocity, another important flow behaviour observed is the formation of the faster flow region at the inner side of the bend apex section. Faster flow crosses the cross-over region and again occupies the inner side of the next bend apex section, S12. Thus the flow in the meander bend follows the shortest path of travel. The almost mirror images of the predicted streamwise velocity distributions are attained at the consecutive bend apex sections (S1 and S12). This eventually implies that the predicted flow is fully developed.

**Figure 5.18** shows the cross-sectional distributions of the predicted streamwise velocity ( $U$ ) for  $Dr = 0.45$ . The distribution profile and the behaviour of the streamwise velocity for the higher relative depth are more or less similar to the shallower relative depth case. Particularly at the bend apexes, the streamwise velocity distributions for both depths are very similar. Maximum streamwise velocity was observed to be  $1.15U_s$  near the inner side of the main channel. Minimum streamwise velocity was found to be  $0.55U_s$  near the bottom closer to the outer side of main channel. However, distinct differences in the streamwise velocity distributions at the cross-over region between the two flow depths are observed in terms of the streamwise velocity vertical gradients. The gradients of the streamwise velocity at the inner bankful level for this flow case in the cross-over region are not larger than those for  $Dr = 0.25$ .

The lower layer (below bank) flow follows the streamwise direction, whereas the direction of the upper layer flow depends on the relative depths. As flow depth increases, the floodplain flow increases while the flow in the main channel shows relatively small increases, thus the difference in velocity between the main channel and the streamwise component of the floodplain flow is getting smaller as the depth



increases. When the difference is zero, the interactions between the main channel and the floodplain flows would be relatively less significant.

#### 5.9.1.2.2 Lateral Velocity

Figures 5.19 and 5.20 show contour lines of predicted lateral velocity normalised by the sectional averaged velocity at  $Dr = 0.25$  and  $Dr = 0.45$  respectively.

At sections S1 and S2, from Figure 5.19, the magnitudes of the lateral velocity are very small and the averages of around  $0.1U_s$  and  $0.2U_s$  respectively. The small magnitudes of lateral velocities are also seen at sections S3 and S4. As discussed earlier, at the apex section, since the main channel and floodplain flows are parallel to each other, the influence of the interaction between the two flows is less significant at the bend apex. However, from section S5 to section S9 the magnitude above the bankful level at the inner side of the main channel increases. The maximum lateral velocity is  $0.7U_s$  at the inner bankful level of the main channel from section S4 to section S9, along the cross-over section, which is larger than the streamwise velocity; its influence area corresponds to the front. As the flow moves downstream to section S11, the magnitude above the bankful level starts to decrease to become weak at the front. Thus the figure clearly shows that the floodplain flow particularly becomes a strong influence in the cross-over region. As will be discussed in a later section, the secondary flow circulations in compound meandering channels are mainly generated due to the floodplain flow plunging the main channel flow at the bankful level in the cross-over region. For the  $Dr = 0.45$ , Figure 5.20, show that the magnitude and distribution profiles of the lateral velocity are similar to those at the shallow relative depth.



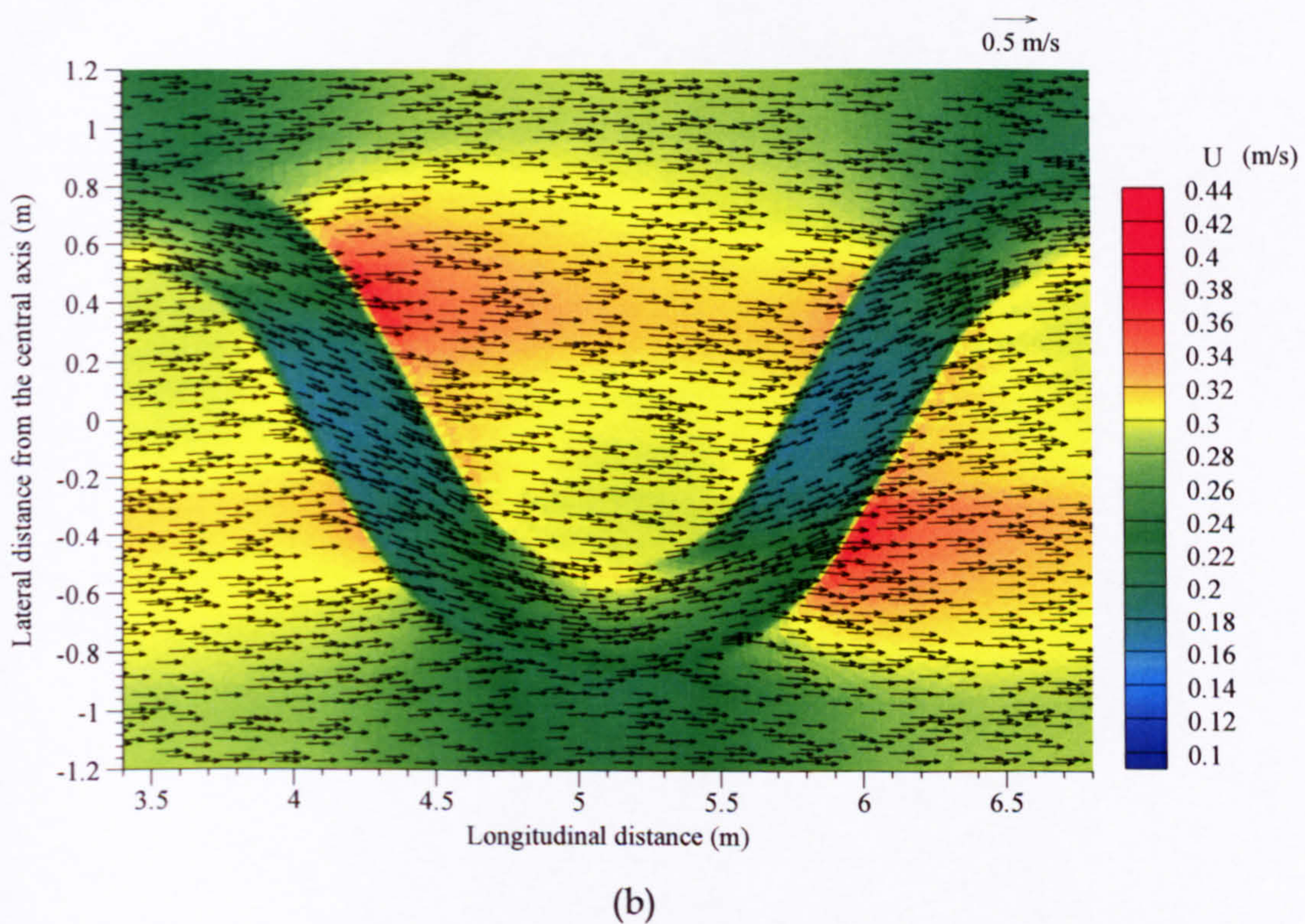
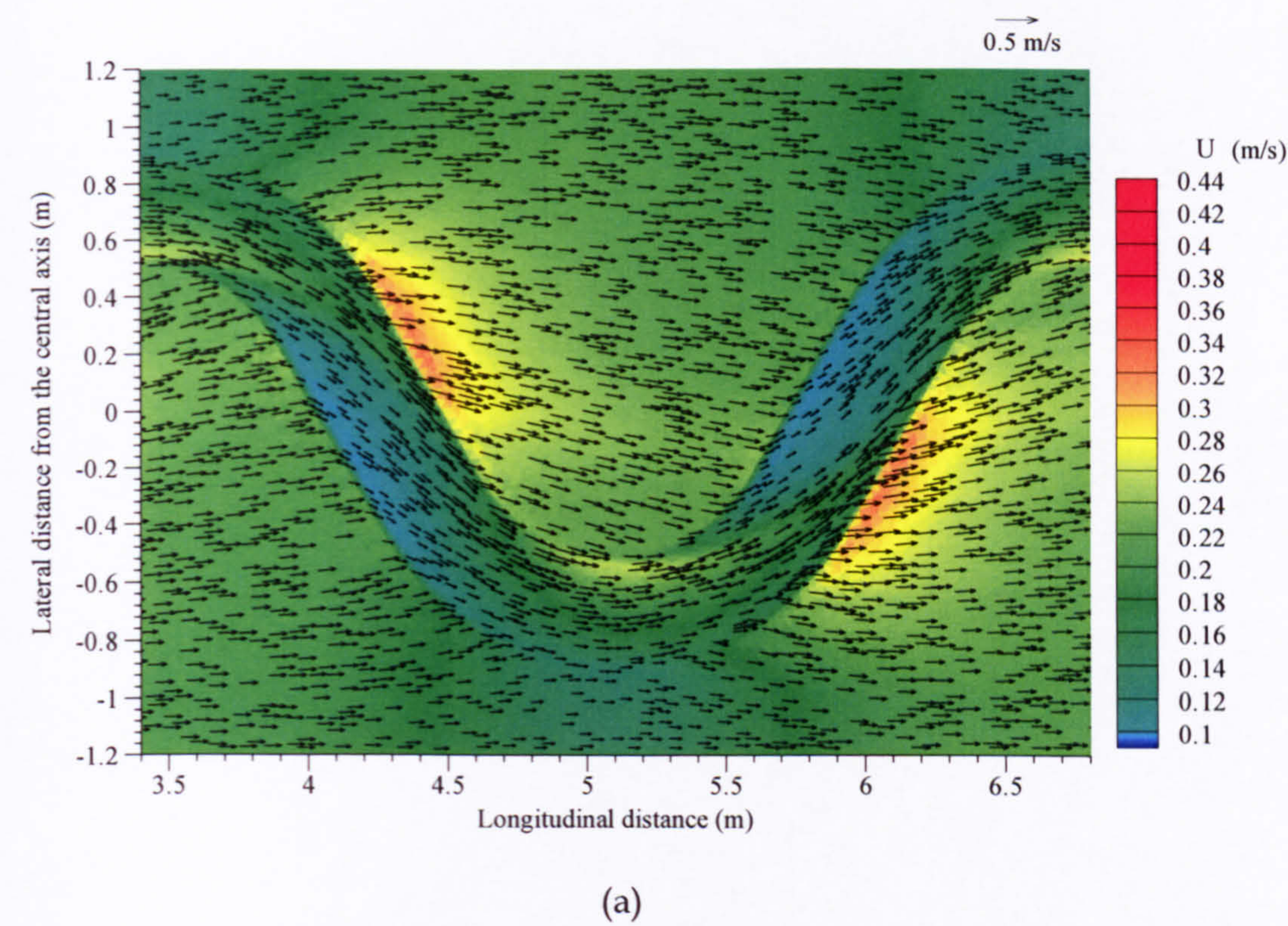


**Figure 5.16:** Predicted depth-averaged velocity for *Case L No Block* for different relative depth (a)  $Dr = 0.25$  (b)  $Dr = 0.45$



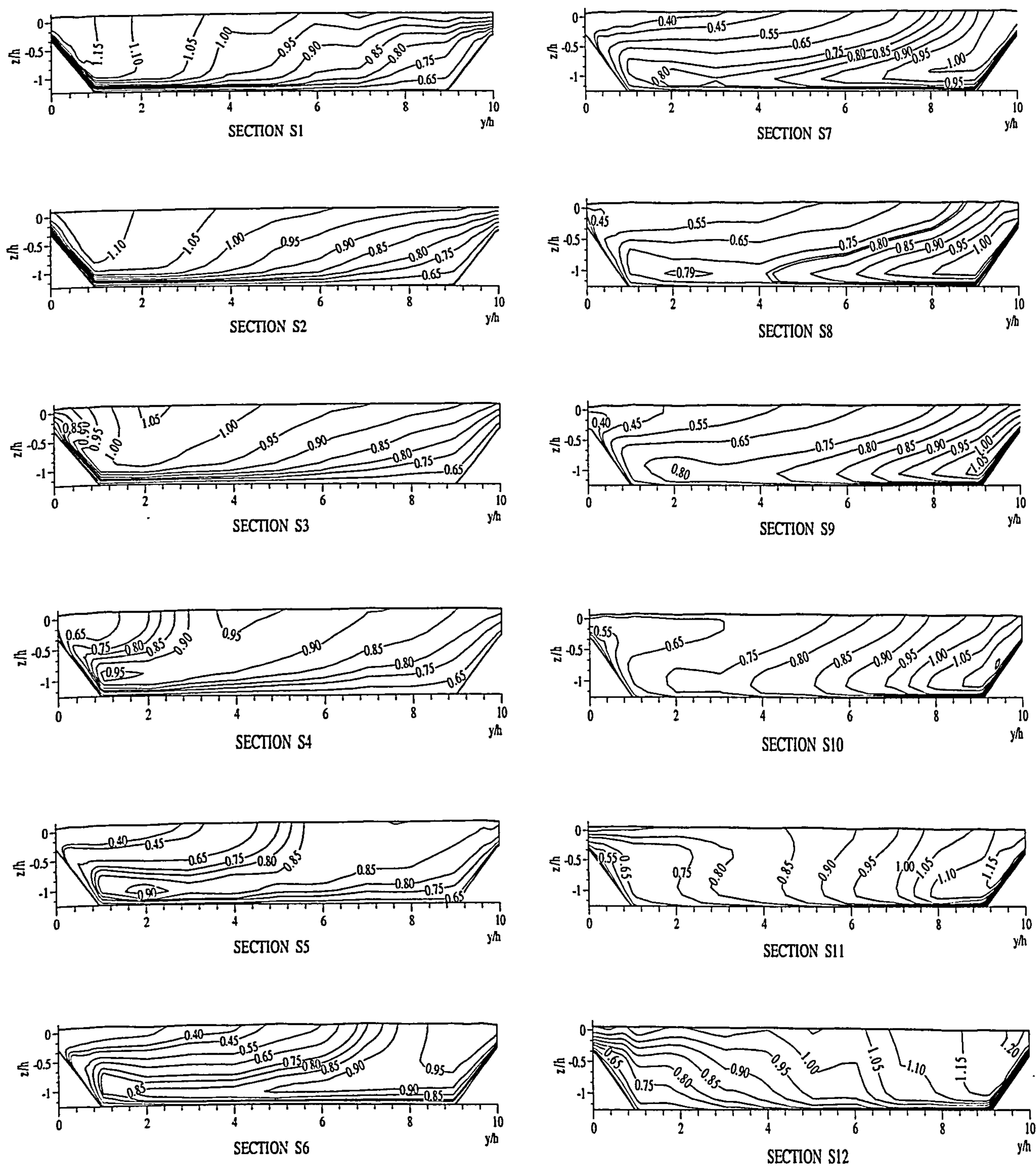
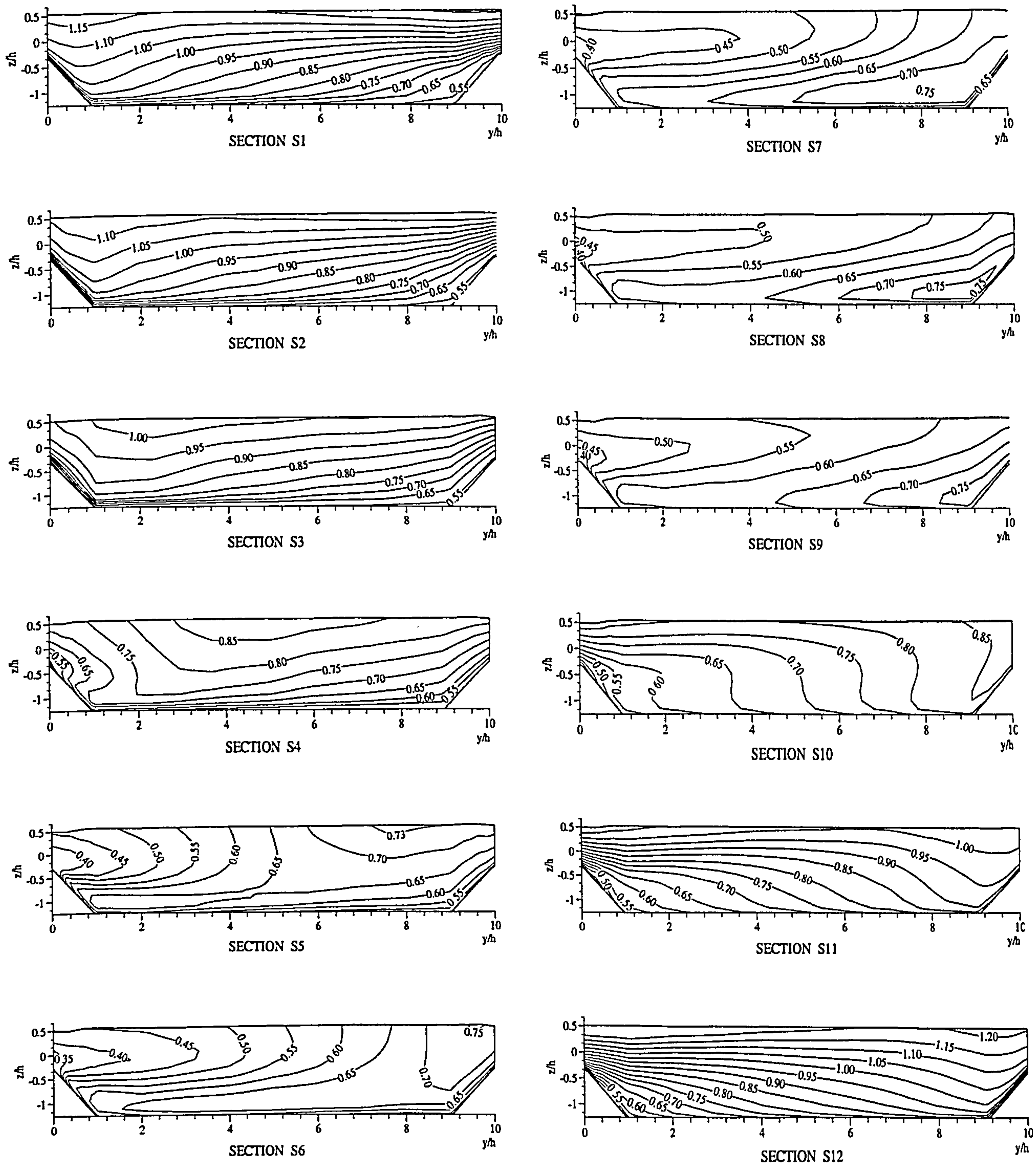


Figure 5.17: Predicted streamwise velocity  $U$ , normalised by  $U_s$  for main channel in Case L No Block at  $Dr = 0.25$  at sections S1 to S12





**Figure 5.18:** Predicted streamwise velocity  $U$ , normalised by  $U_s$  for main channel in *Case L No Block* at  $Dr = 0.45$  at sections S1 to S12



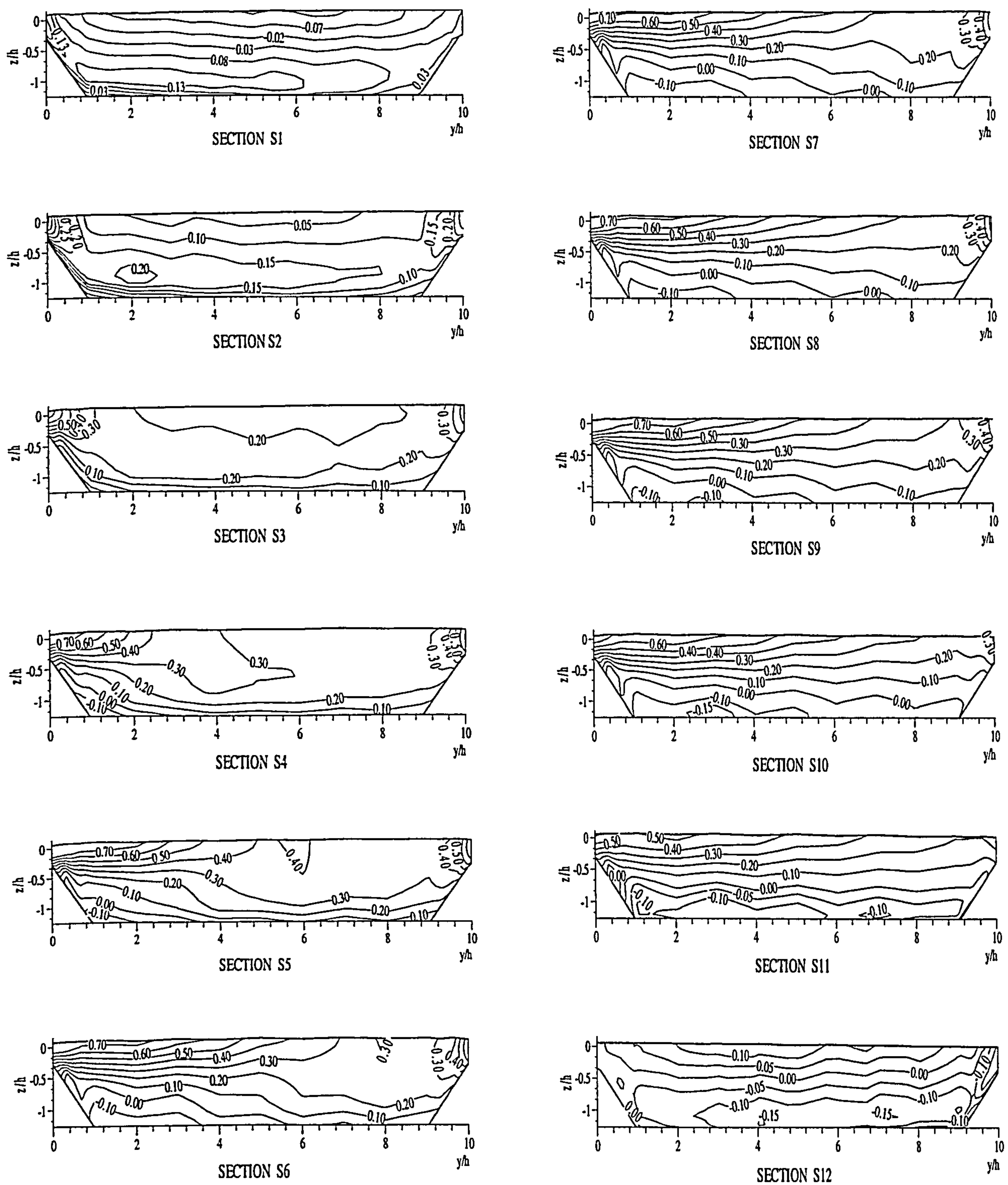


**Figure 5.19:** Predicted lateral velocity  $V$ , normalised by  $U_s$  for main channel in *Case L No Block* at  $Dr = 0.25$  at sections S1 to S12



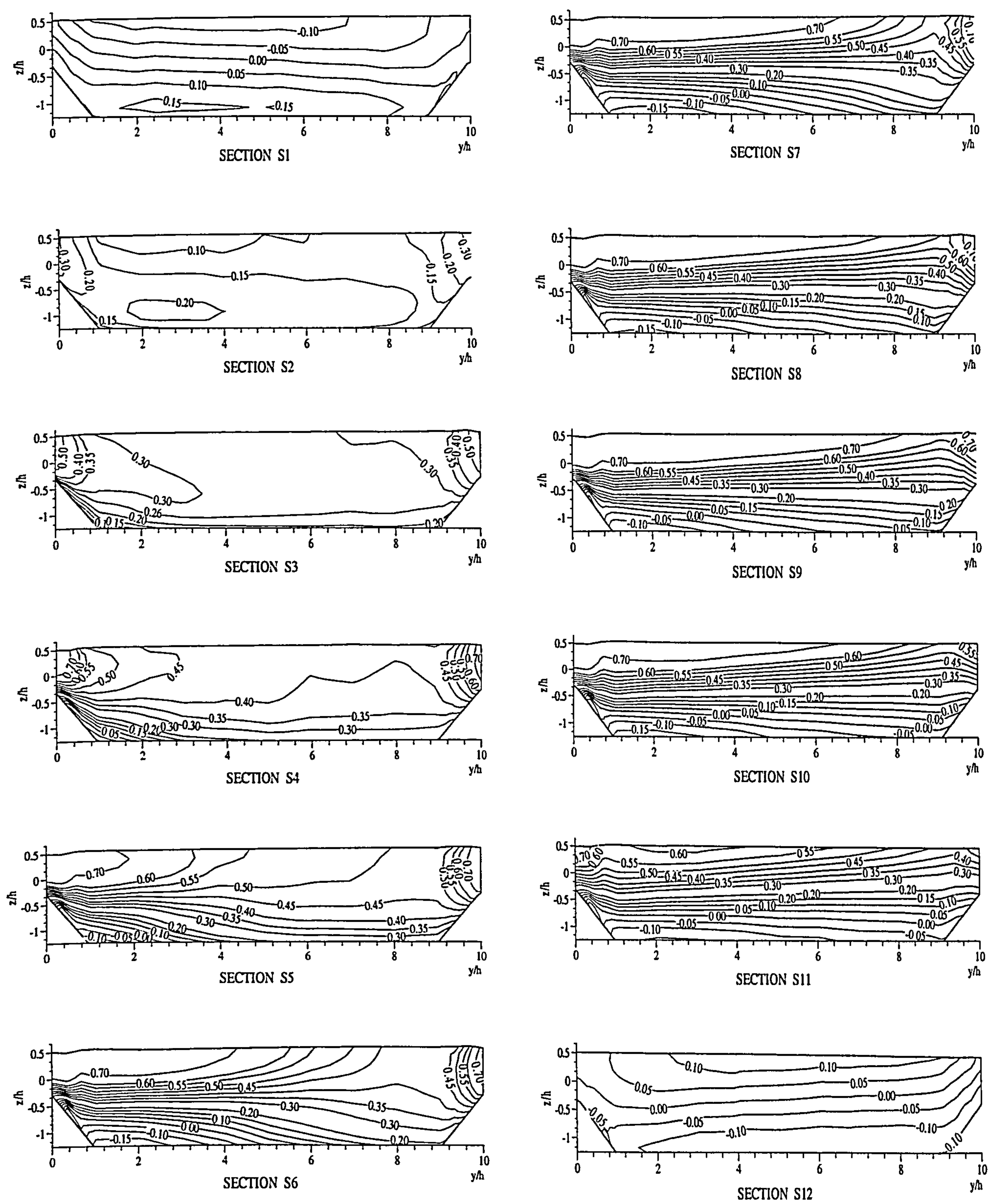


Figure 5.20: Predicted lateral velocity  $V$ , normalised by  $U_s$  for main channel in Case L No Block at  $Dr = 0.45$  at sections S1 to S12



### 5.9.1.2.3 Vertical Velocity

It is not customary to study the distribution of the vertical velocity. However, for the completeness of this chapter, the vertical velocity distributions are included for all the cases at sections S1 to S12 and discussed very briefly. Figure 5.21 shows the cross-sectional distribution of the predicted vertical velocity for  $Dr = 0.25$ . At the apex section S1, the vertical velocity is less than  $0.01U_s$  for most of the area except the left side area where it is  $0.03U_s$ . These are substantially smaller than the other components. Negative velocities are seen close to the inner bankful main channel and positive velocities are observed close to the outer bankful main channel at sections S1, S2 and S3. Maximum negative velocity is  $-0.15U_s$  at section S2. This indicates that higher downflow occurs close to the inner bankful main channel. On the other hand, flow is always in the upward direction close to the outer bankful main channel with a positive velocity of as much as  $0.1U_s$ , which indicates that the flow is escaping from the main channel onto the floodplain. At sections S3 to S9 there are even larger positive vertical velocities at the main channel sidewalls thus enhancing the main channel flow escaping onto the floodplain. Maximum vertical velocity was found to be  $0.2U_s$  at section S5. Figure 5.22 for  $Dr = 0.45$  shows similar profiles of vertical velocity to those for  $Dr = 0.25$ , but the larger positive gradients of vertical velocity near both the main channel sidewalls are observed in the cross-over region.

### 5.9.1.3 Secondary Flow Vectors

In order to examine the secondary flow structure in more detail, as described before, the resultant velocities of the two components,  $V$  and  $W$ , and their distribution were plotted as a vector in Figures 5.23 and 5.24 for  $Dr = 0.25$  and  $Dr = 0.45$  respectively.

Figure 5.23 shows the predicted secondary vectors for  $Dr = 0.25$  at sections S1 to S12. At section S1, which is the apex section, a single dominant anticlockwise circulation cell, which occupies almost the whole main channel area, can be seen. As the flow moves downstream to section S3, the anticlockwise cell seen at section S1 disappears completely. However, the new clockwise circulation cell is seen near the inner side (left side) of the main channel. Thus it is evident that this new circulation cell originates from somewhere between section S1 and section S3. The generation of this new



circulation cell at section S3 coincides well with the shearing of the main channel flow by the floodplain flow plunging into the main channel as clearly seen from the streamwise velocity and the lateral velocity profile at the same section. The large gradient of the streamwise velocity and higher positive magnitude of the lateral velocity at around the bankful level near the inner side of the main channel confirms the impingement of the floodplain flow into the main channel (see Figures 5.17 and 5.19 for the predicted  $U$  and  $V$  profile). At section S5 which is the start of the cross-over region, the magnitude of the floodplain flow entering the main channel increases due to which the circulation cell seen at section S3, gains strength and size and travels towards the outer side of the main channel. This cell occupies most of the main channel inbank area at section S7, which is at the mid point of the cross-over region. The pattern of circulation remains almost the same at section S9 as it was at section S7. This suggests that the same magnitude of the floodplain flow entering the main channel maintains the same secondary flow along the cross-over region. At section S11, the magnitude of the secondary vectors at the bankful level near the inner side of the main channel is being reduced as expected. The secondary flow circulation pattern at section S12 is similar to that in section S1 except with the opposite sense of rotation. In general, the pattern and the behaviour of the secondary flow vectors for  $Dr = 0.45$  are very much similar to those for  $Dr = 0.25$ , as seen from Figure 5.24.

#### 5.9.1.4 Turbulent Kinetic Energy (TKE)

Turbulent Kinetic Energy ( $TKE$ ) was calculated with three components of turbulence intensities at each measurement point, i.e.  $TKE = 1/2(u'^2 + v'^2 + w'^2)$ . The results are shown in Figures 4.25 and 4.26 and the  $TKE$  is normalised by  $u^{*2}$  as defined before.

Figure 4.25 shows the isolines of the predicted  $TKE$  for *Case L* for  $Dr = 0.25$  at the sections S1 to S12. At section S1, the distribution pattern of the predicted  $TKE$  corresponds to the predicted single dominant anticlockwise secondary circulation cell. At section S1, the predicted maximum magnitude of  $TKE$  is around  $1.8u^{*2}$  at the centre of the main channel not near the boundary, which means smaller bed-generated turbulence than that at the centre. At sections S2 and S3, the distribution pattern remains similar to the previous section S1 but the  $TKE$  magnitude at the centre of the circular pattern decreases to about  $1.3u^{*2}$  and  $0.9u^{*2}$  respectively. At section S4, the



maximum *TKE* core is shifted laterally towards the outer side of the main channel with the maximum magnitude of *TKE* being around  $1.2u^2$ . At section S5, the maximum *TKE* core with the magnitude of  $1.2u^2$  occurs near the inner side of the main channel. Thus, a new zone of high *TKE* at around the bankful level near the inner side of the main channel occurs. This high turbulence zone at the inner bankful level of section S5 is formed due to the shear interaction between the main channel and the floodplain flows. As the flow travels further downstream to sections S6 and S7, the high *TKE* zone develops further and extends laterally towards the right side of the main channel. The maximum magnitudes of *TKE* at section S6 and S7 are found to be around  $2.6u^2$  and  $3.4u^2$  respectively and still growing due to the interaction of floodplain. At sections S8 and S9, these high turbulence regions travel little further towards the inner side (right side) of the main channel with a maximum *TKE* of around  $4.5u^2$  and  $3u^2$  respectively. Thus the pattern of the *TKE* follows the profile or behaviour of the secondary flow circulations. At sections S10 and S11, the magnitude of *TKE* decreases further. At section S12, the pattern and magnitude of *TKE* is the mirror image of that at section S1.

Figure 4.26 shows the isolines of the predicted *TKE* at sections S1 to S12 with a higher water depth of  $Dr = 0.45$ . As compared to the shallow flow depth of  $Dr = 0.25$ , the overall magnitude of *TKE* for  $Dr = 0.45$  is higher. For this case, the distribution pattern remains fairly similar to that for  $Dr = 0.25$ . The predicted maximum magnitude of *TKE* increases from  $1.6u^2$ ,  $2.4u^2$ ,  $3.4u^2$  and  $3.6u^2$  at sections 6, 7, 8 and 9 respectively. The rest of the maximum magnitudes of the *TKE* range from  $3.4u^2$ ,  $3.2u^2$ ,  $2.2u^2$ ,  $2.0u^2$ ,  $1.6u^2$ ,  $1.2u^2$ ,  $0.9u^2$ ,  $0.14u^2$  at sections S10, S11, S1, S2, S3, S4, S5 and S12, respectively, clearly indicating that the turbulence generated by shear is decaying after section S10.



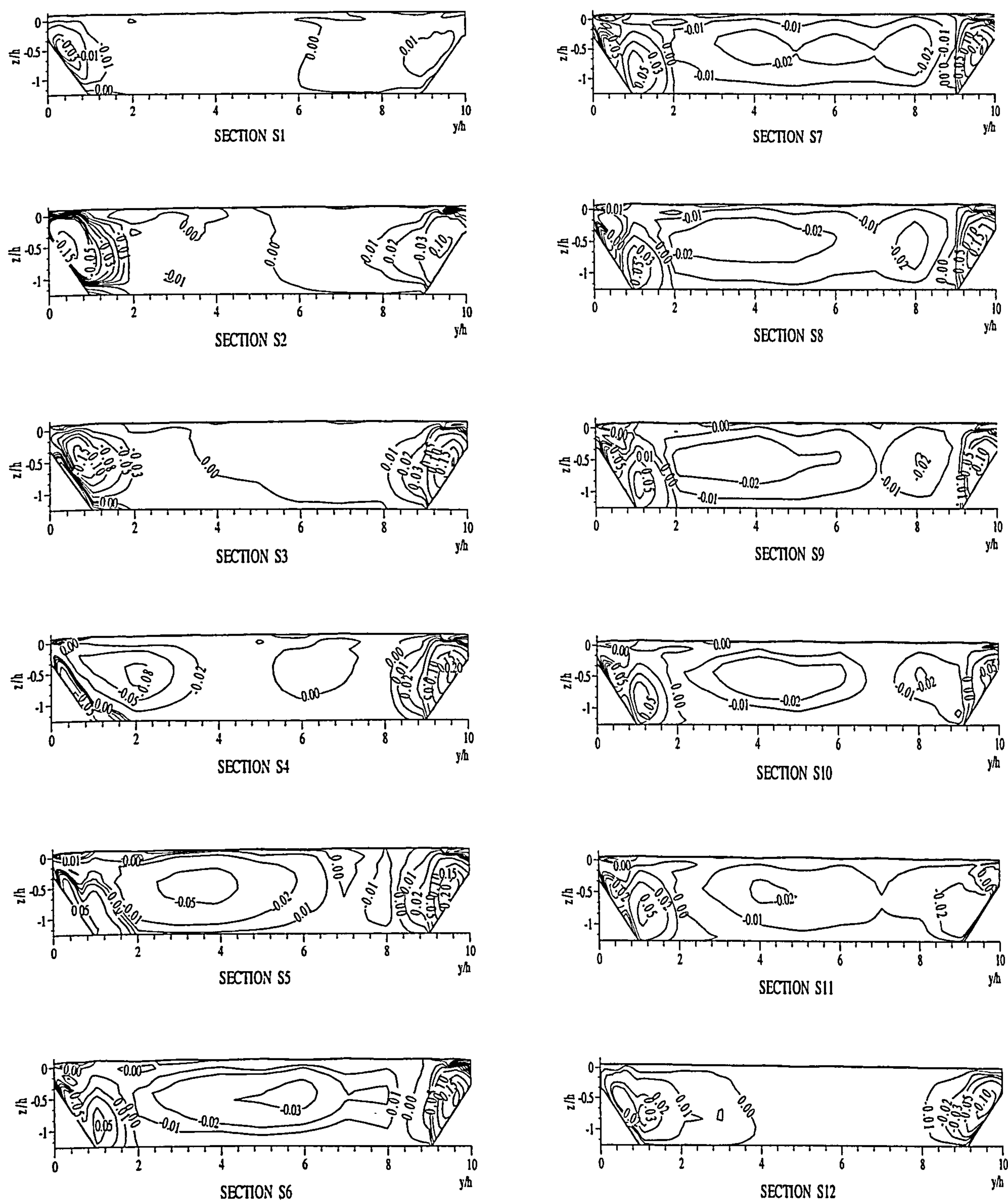


**Figure 5.21:** Predicted vertical velocity  $W$ , normalised by  $U_s$  for main channel in *Case L No Block* at  $Dr = 0.25$  at sections S1 to S12



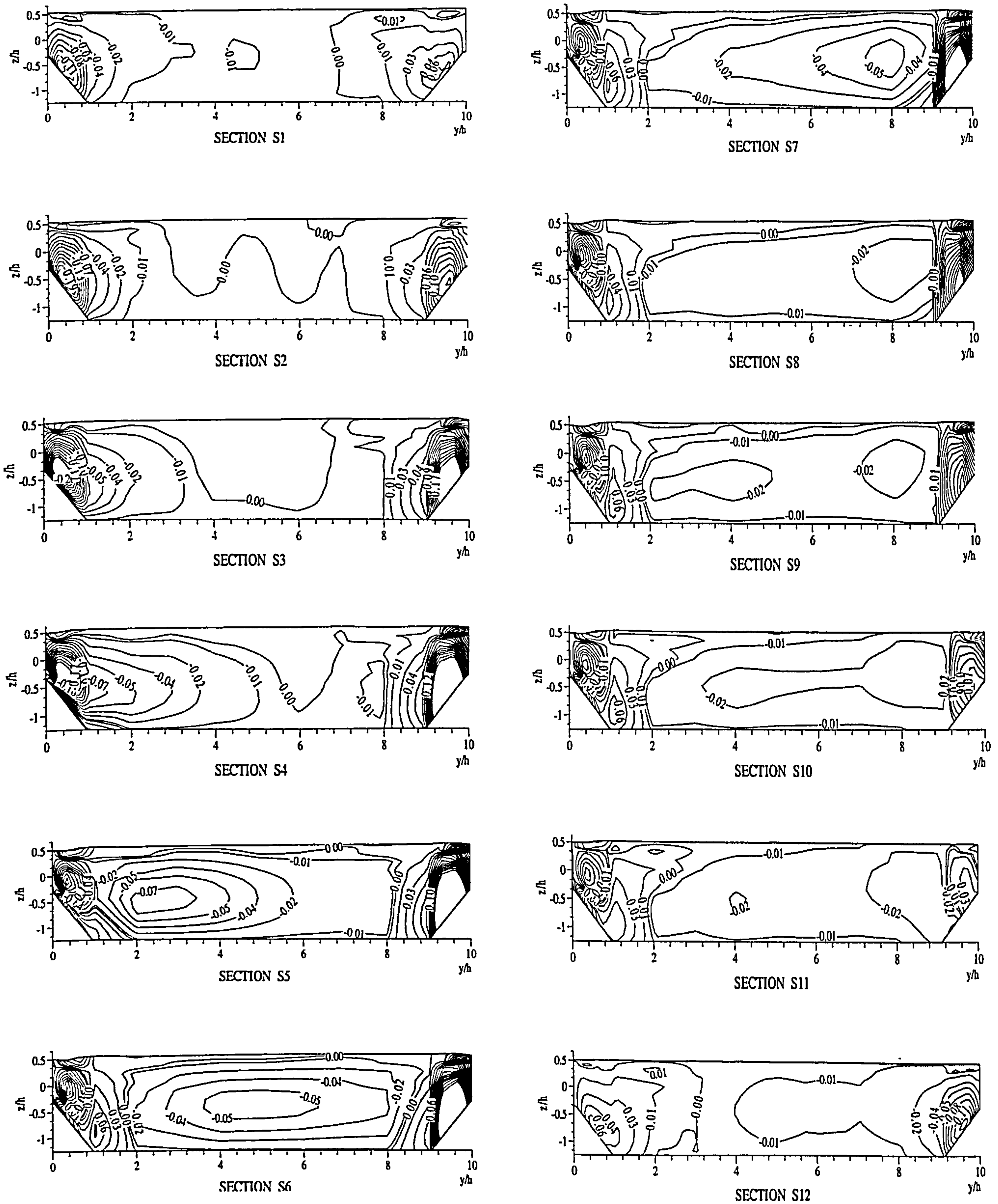


**Figure 5.22:** Predicted vertical velocity  $W$ , normalised by  $U_s$  for main channel in *Case L No Block* at  $Dr = 0.45$  at sections S1 to S12



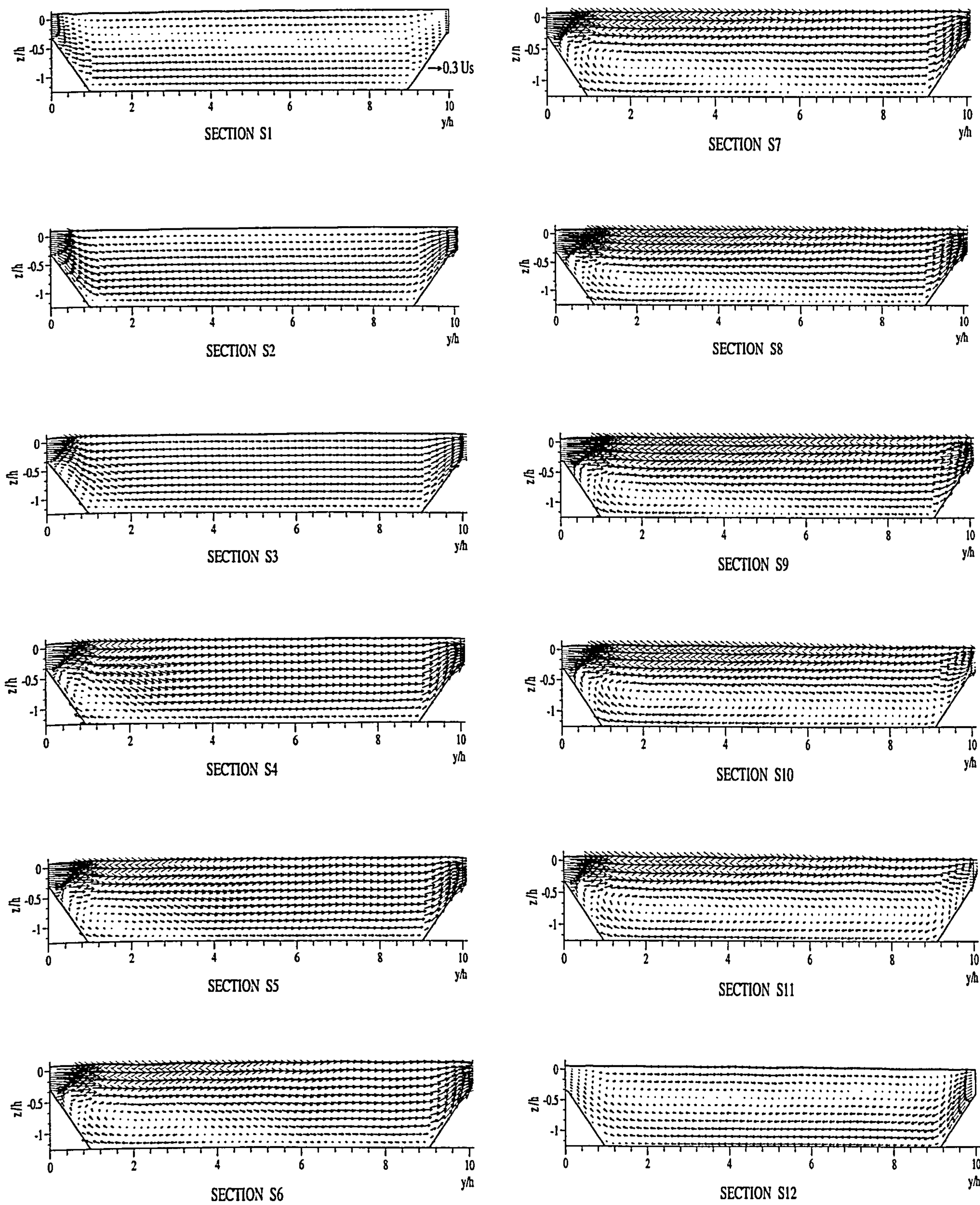


Figure 5.23: Predicted secondary flow vectors for main channel in *Case L No Block* at  $Dr = 0.25$  at sections S1 to S12



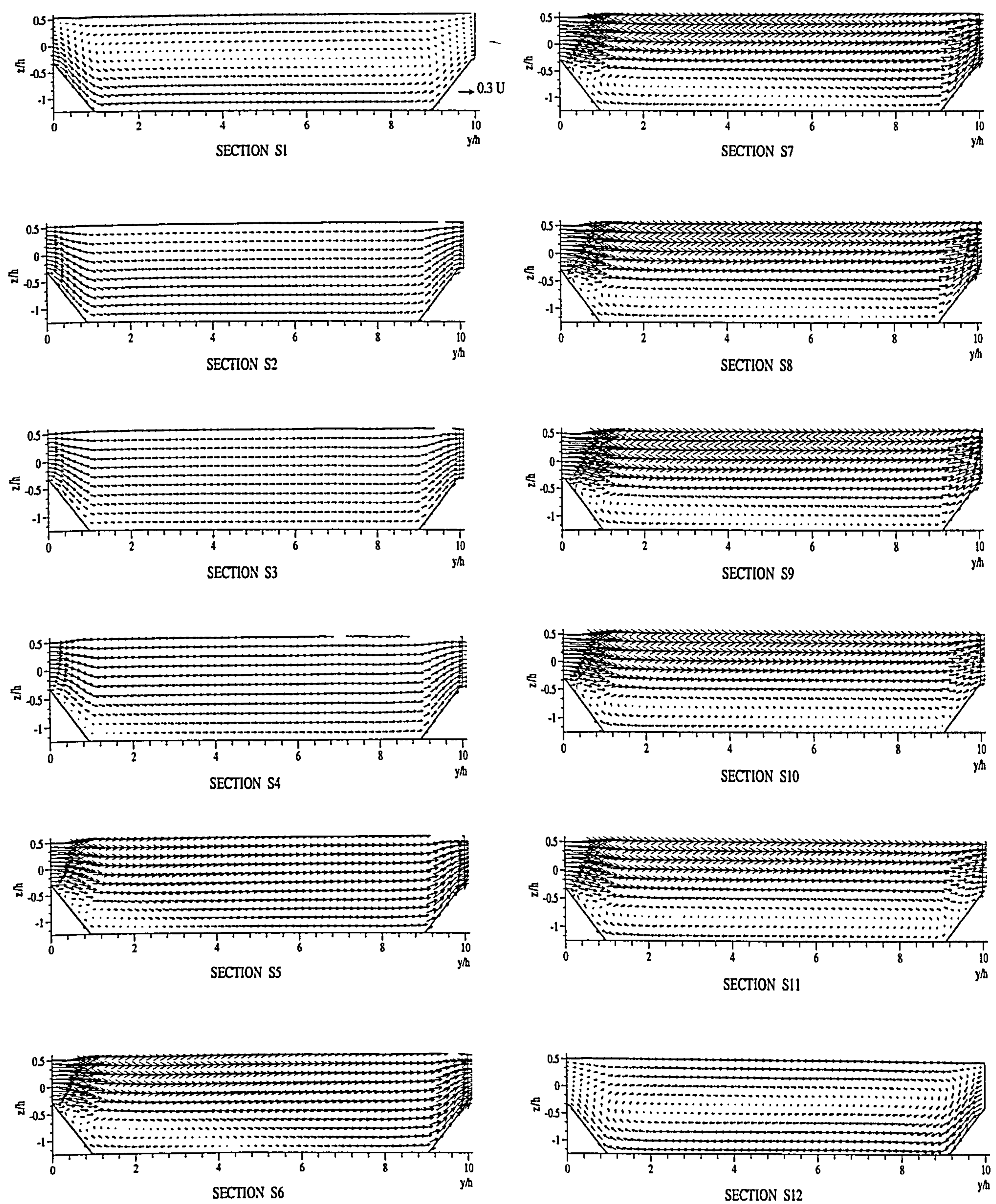


Figure 5.24: Predicted secondary flow vectors for main channel in *Case L No Block* at  $Dr = 0.45$  at sections S1 to S12



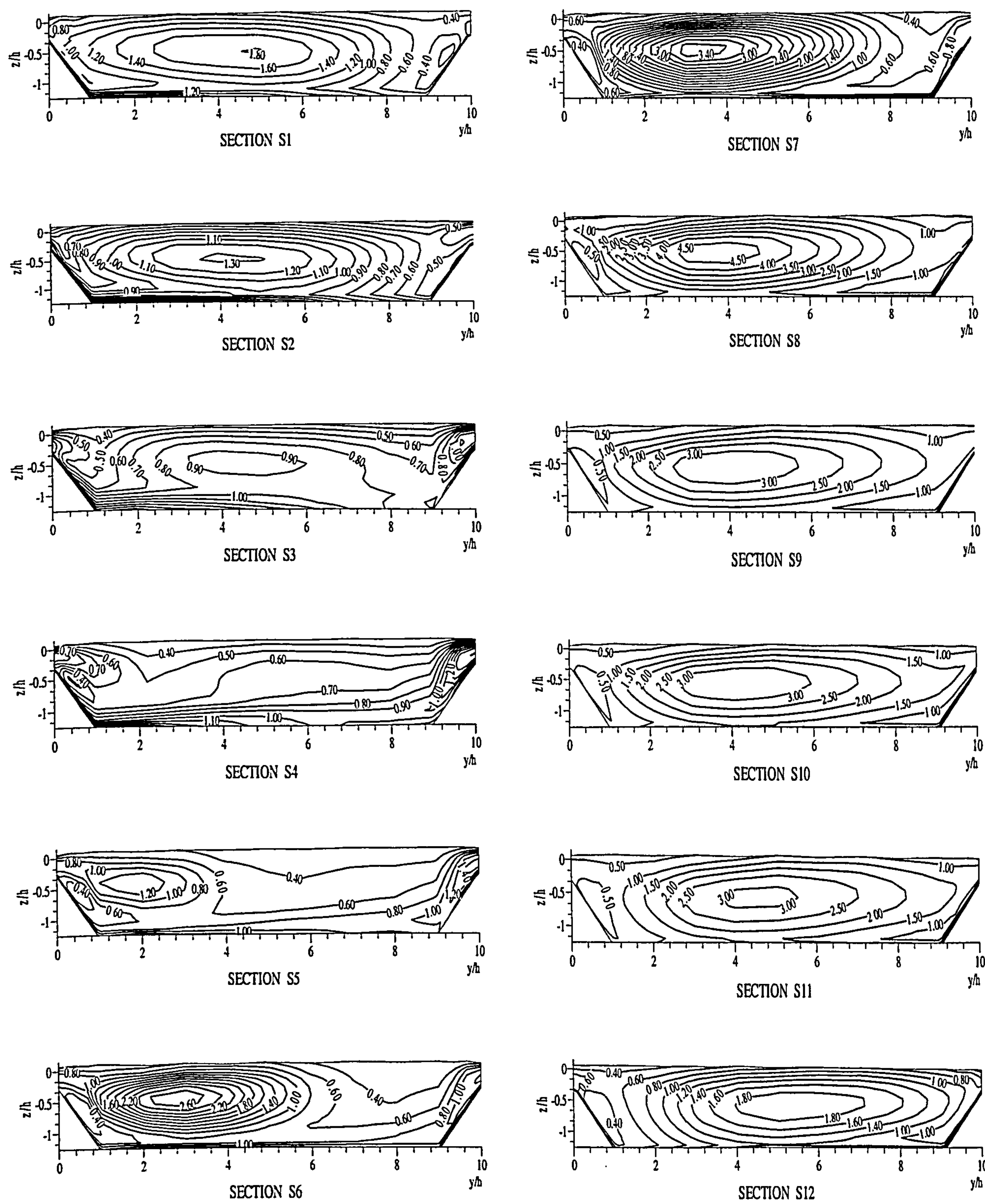


Figure 5.25: Predicted turbulent kinetic energy  $TKE$ , normalised by  $u^2$  for main channel in Case L No Block at  $Dr = 0.25$  at sections S1 to S12



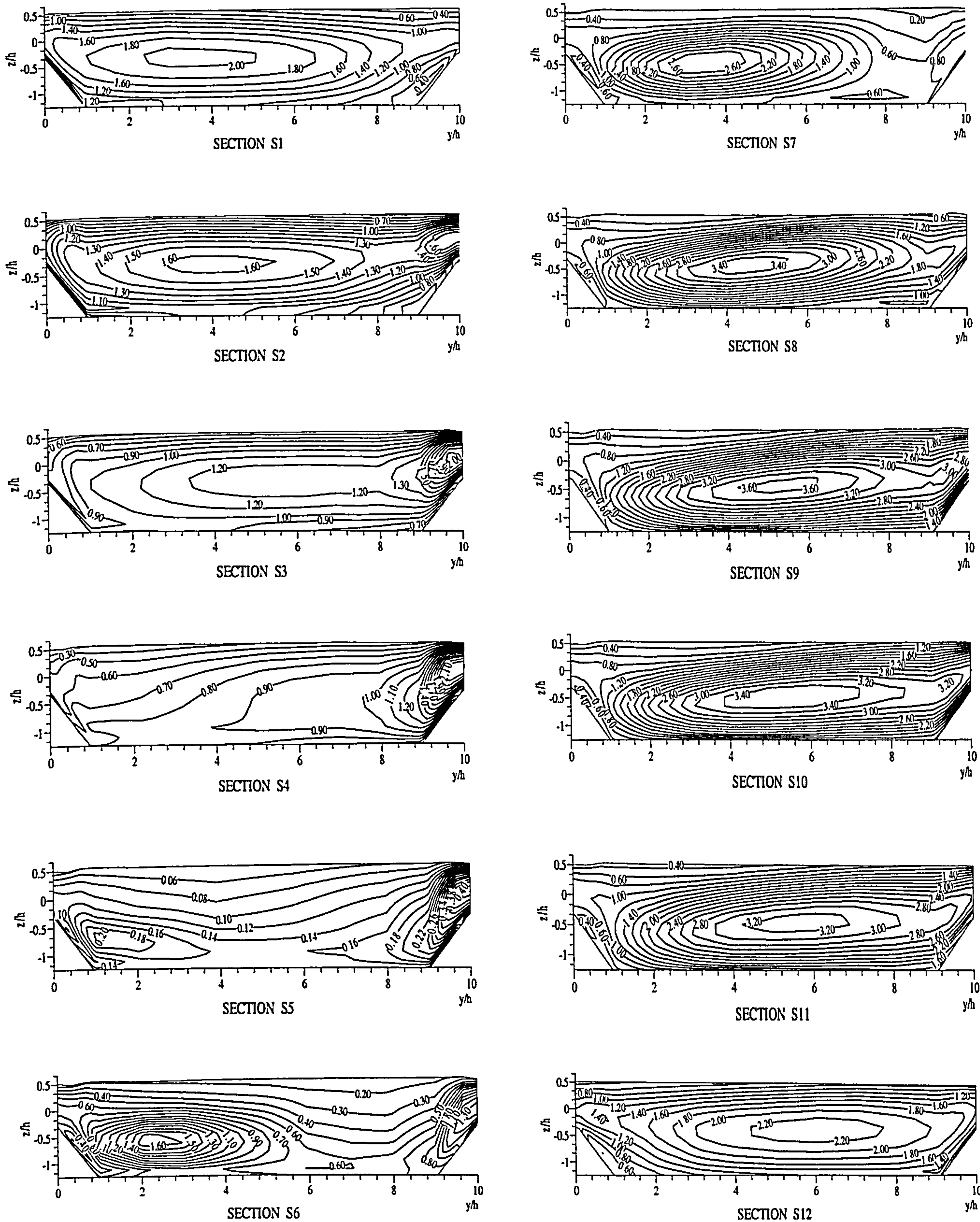


Figure 5.26: Predicted turbulent kinetic energy  $TKE$ , normalised by  $u^2$  for main channel in Case L No Block at  $Dr = 0.45$  at sections S1 to S12



### 5.9.2 Overbank Flow with Vegetated Floodplain: *Case M Apex Block*

This section will explain the case of overbank flow with a vegetated floodplain along the outer side of the apex bend along with the details of what happens in the main channel cross-section over a half meander wavelength. This is very important because in Chapter 4 it was shown that a similar arrangement of vegetations (blocks) would contribute to the higher stage-discharge curve. However, a reduction in the sediment transport rate when compared to *Case L No Block* (with no block) was caused. This subsection will discuss the 2D depth-average velocity vector field in one meander, 3D variable velocities field in the main channel and the secondary flow vector. For this case, a Smagorinsky model was used to simulate the 2D and 3D flow distribution due to the  $k-\epsilon$  model crashing after a few seconds.

#### 5.9.2.1 Depth-averaged Velocity Vector Fields

This column will show the velocity vector fields for both main channel and floodplain which were predicted for the streamwise and lateral velocity components. These were plotted on a plan view of the channel in order to provide an overall picture of the flow structure.

Figures 5.27(a) and (b) show the results for the depth-averaged velocity vector distribution for the vegetated floodplain (*Case M Apex Block*) along one meander wavelength for  $Dr = 0.25$  and  $Dr = 0.45$  respectively. Both flow depths show similar flow patterns and velocity distributions but differ in their magnitude. From the results shown, it can be seen that the main channel and floodplain flow structures are significantly different from those described for the floodplain without vegetation, *Case L No Block*. In general, it is apparent that the overall velocity in *Case L No Block* is greater than for the floodplain vegetation *Case M Apex Block*. Due to the continuous blocks along the outer side of the apex, the figure shows that the small velocity filament in the main channel occurs relatively near the outer bank sidewall along the apex bend and that many vortices also occur behind the blocks both in the main channel and floodplain. This reflects the increase of the flow resistance resulting in a substantial reduction in the depth-averaged velocity within the main channel. This reduction in main channel velocity seems highly likely to affect the boundary shear



stress and, furthermore, contribute in causing a reduction in the sediment transport rate as described in Chapter 4 (see Figure 4.38) with a similar arrangement of blocks. A substantial reduction of the velocity also occurs near the inner bank of the channel at the cross-over section. It can be also seen that the cross-over flow gradually increases as the flow moves further from the inner bank of the main channel. The magnitude of the floodplain flow is generally higher at the middle section compared to behind the apex section because the flow is blocked by the blocks.

### 5.9.2.2 3D Variable Velocities Field

Having understood the general flow distribution from the depth-averaged velocities as described above, this section will go on to explain the details of the internal flow structure that determines the entire flow behaviour over a half-meander wavelength for sections S1 to S12 as described in Chapter 3. Previous depth-averaged velocity flow vectors do not show the internal flow structures along a meandering channel; hence this section shows clearly the details of the velocity distribution to achieve a better understanding of the velocity distribution in the main channel.

#### 5.9.2.2.1 Streamwise Velocity ( $U$ )

Figures 5.28 and 5.29 show the contour lines of the predicted streamwise velocities normalised by the sectional averaged velocity at  $Dr = 0.25$  and  $Dr = 0.45$  respectively for sections S1 to S12.

Figure 5.28 shows the cross-sectional distributions of the predicted streamwise velocity ( $U$ ) for  $Dr = 0.25$ . The streamwise velocity varies in terms of magnitude from one cross-section to another across the full width of the channel. Due to the continuous blocks along the outer (right) side of main channel, sections S1 to S5 show that the maximum streamwise velocity occurs near the centre part of the main channel and close to the outer (right) bank in the cross-over sections S6 to S9. At the bend apex section S1, the maximum streamwise velocity in terms of magnitude is  $0.9U_s$  whilst at the central part of the main channel and minimum streamwise velocity is  $0.4U_s$  close to the outer side of the main channel. The maximum streamwise velocities reduce slightly to around  $0.8U_s$  and  $0.75U_s$  at sections S2 and S3 respectively at the central part of the main



channel. At section S6, the flow behaviour starts to resemble *Case L No Block* but the magnitude of the streamwise velocity is lower. Magnitudes of velocity of around  $0.3U_s$  are seen at the inner bankful level of the main channel, which extends laterally as the flow moves downstream to section S9. This is due to there being no blocks at the cross-over section. Also the shearing of the main channel flow in the inner side at the bankful level due to the floodplain flow plunging into the main channel can also be seen as in *Case L No Block*. The streamwise velocity below the bankful level is higher than the velocity above the bankful level. At sections S10 and S11, negative velocities which is flowing upstream, can be seen close to the outer side (left side) of the main channel and positive velocities occur at the central part and inner (right) side of the main channel. Maximum negative velocities are around  $-0.4U_s$  and  $-2.0U_s$  respectively at sections S10 and S11. From Figure 5.27 and the above, the vortices occurring behind the blocks generate the complex internal flow structure.

Figure 5.29 shows the cross-sectional distributions of the predicted streamwise velocity ( $U$ ) for  $Dr = 0.45$ . The distribution profile and the behaviour of the streamwise velocity for the higher relative depth are more or less similar to the shallower relative depth case. Particularly at the bend apexes, the streamwise velocity distributions for both the depths are very similar. In general, it is observed that the overall magnitudes of the streamwise velocity predicted at both flow depths for *Case M Apex Block* are smaller than those for *Case L No Block*. Of course, the greatest difference in magnitudes of velocity and flow structures appears to be in the bend section due to the existence of blocks that exert extra flow resistance within the main channel. However, at the cross-over section the streamwise velocity shows generally similar flow patterns and structures to *Case L No Block*.

#### 5.9.2.2.2 Lateral Velocity ( $V$ )

Figures 5.30 and 5.31 show contour lines of predicted lateral velocity normalised by the sectional averaged velocity at  $Dr = 0.25$  and  $Dr = 0.45$  respectively.

At section S1, as shown in Figure 5.30, the positive lateral velocity covers most of the main channel and the negative lateral velocity is close to the upper central part of the main channel. The maximum positive velocity was observed to be  $0.3U_s$  with a



minimum negative velocity of  $-0.3U_s$ , which is much larger than that in *Case L No Block*. At sections S2, S3 and S4, the negative velocities were found in the upper inner region of the main channel. However, at the beginning of cross-over section S5 the negative velocity starts to occur in the inner region of the main channel bed and move towards the central part of the main channel as flow goes downstream to section S9. Positive velocities are observed in the upper inner region of the main channel. The maximum lateral velocity from the floodplain increases as the flow travels downstream from sections S3 to S7. The maximum magnitude ranges from  $0.6U_s$ ,  $0.7U_s$ ,  $0.8U_s$ , and  $0.9U_s$  at sections S3, S4, S5 and S7 respectively, which is slightly higher than those in *Case L No Block*. The magnitude decreases from section S8 to section S10. As flow moves downstream to sections S9, S10 and S11, the lateral velocity from the floodplain varies considerably due to the blocks at the edge of the floodplain and the overall velocity also decreases. Figure 5.31 shows that the overall trend of the lateral velocity below the bankful level is similar to that at  $Dr = 0.25$ , flow behaviours at  $y/h = 0$ , from sections S8 to S12 are quite different since as the water depth increases, the block wakes occupied a larger area than for the shallower depths. The gaps between the blocks may not be big enough to avoid wake-interaction due to the blocks.

#### 5.9.2.2.3 Vertical Velocity (W)

Figure 5.32 shows the cross-sectional distribution of the predicted vertical velocity at section S1 for  $Dr = 0.25$ . At the apex section, vertical velocity is very small compared to the other components in most of the area except for the left side. The negative velocity can be seen close to the inner bankful main channel at sections S1, S2 and S3. Maximum negative velocity is  $-0.24U_s$  at sections S3 and S4. This indicates that higher downflow occurs close to the inner bankful main channel. However, at sections S5 to S9 in the cross-over region, a large gradient of the vertical velocity can be seen near both sides of the main channel bank. Figure 5.33 for  $Dr = 0.45$  shows similar magnitude and profile of the vertical velocity to those for  $Dr = 0.25$ . The large gradient of the vertical velocity can be seen at the outer side of the bank in the main channel at section S7 in the cross-over region, with flow escaping onto the floodplain and plunging into the main channel.



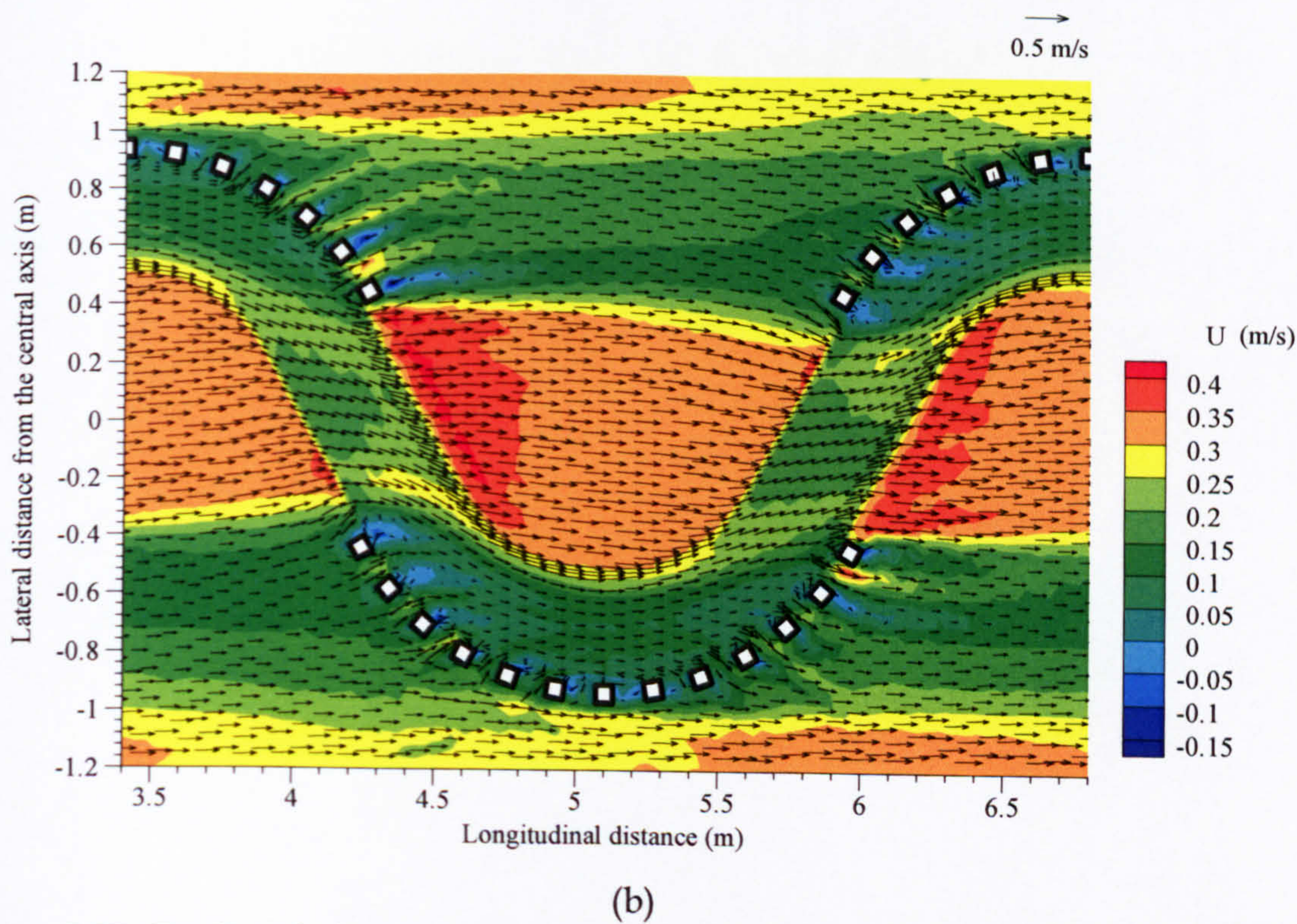
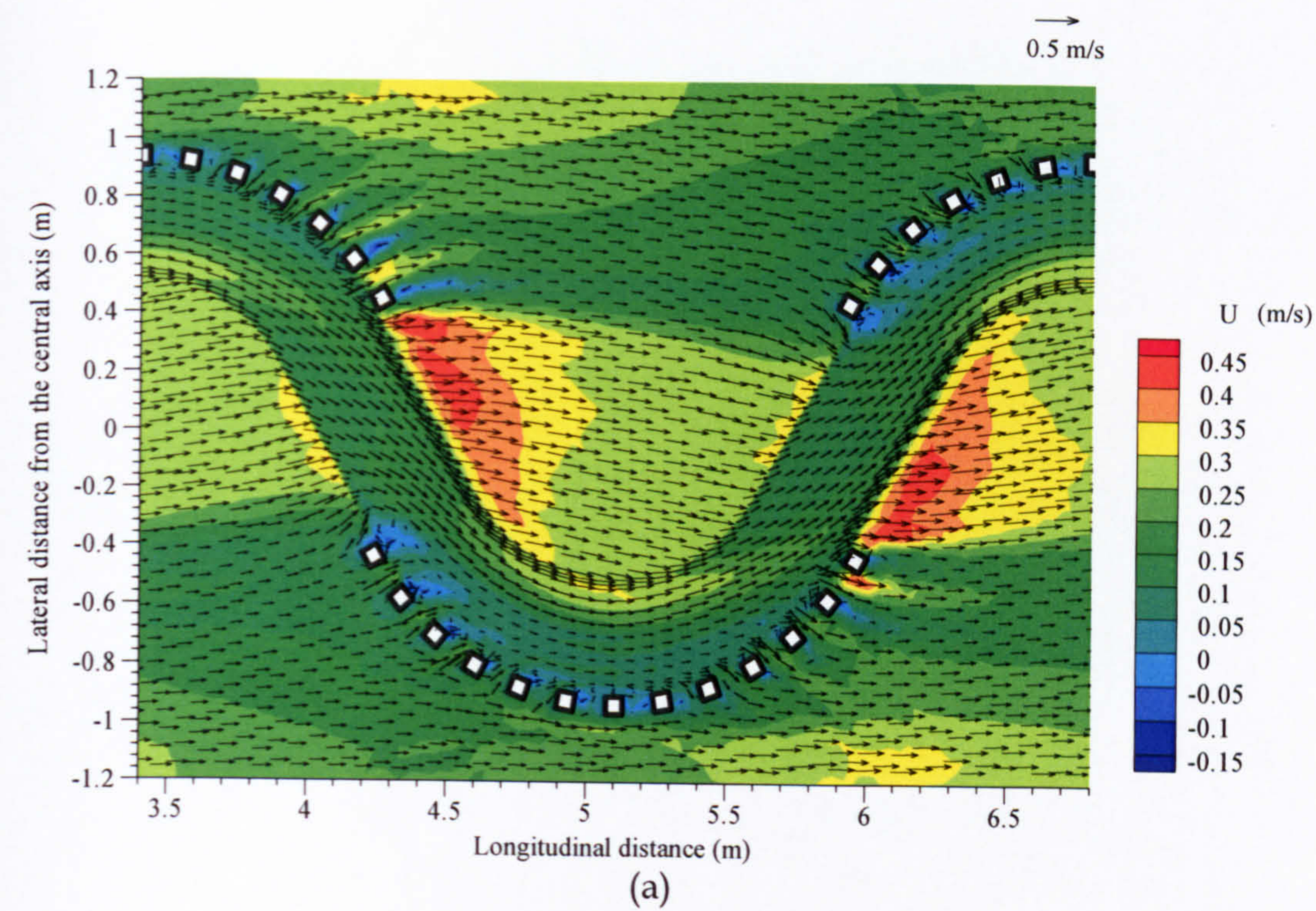


**Figure 5.27:** Predicted depth-averaged velocity for *Case M Apex Block* for different relative depth (a)  $Dr = 0.25$  (b)  $Dr = 0.45$



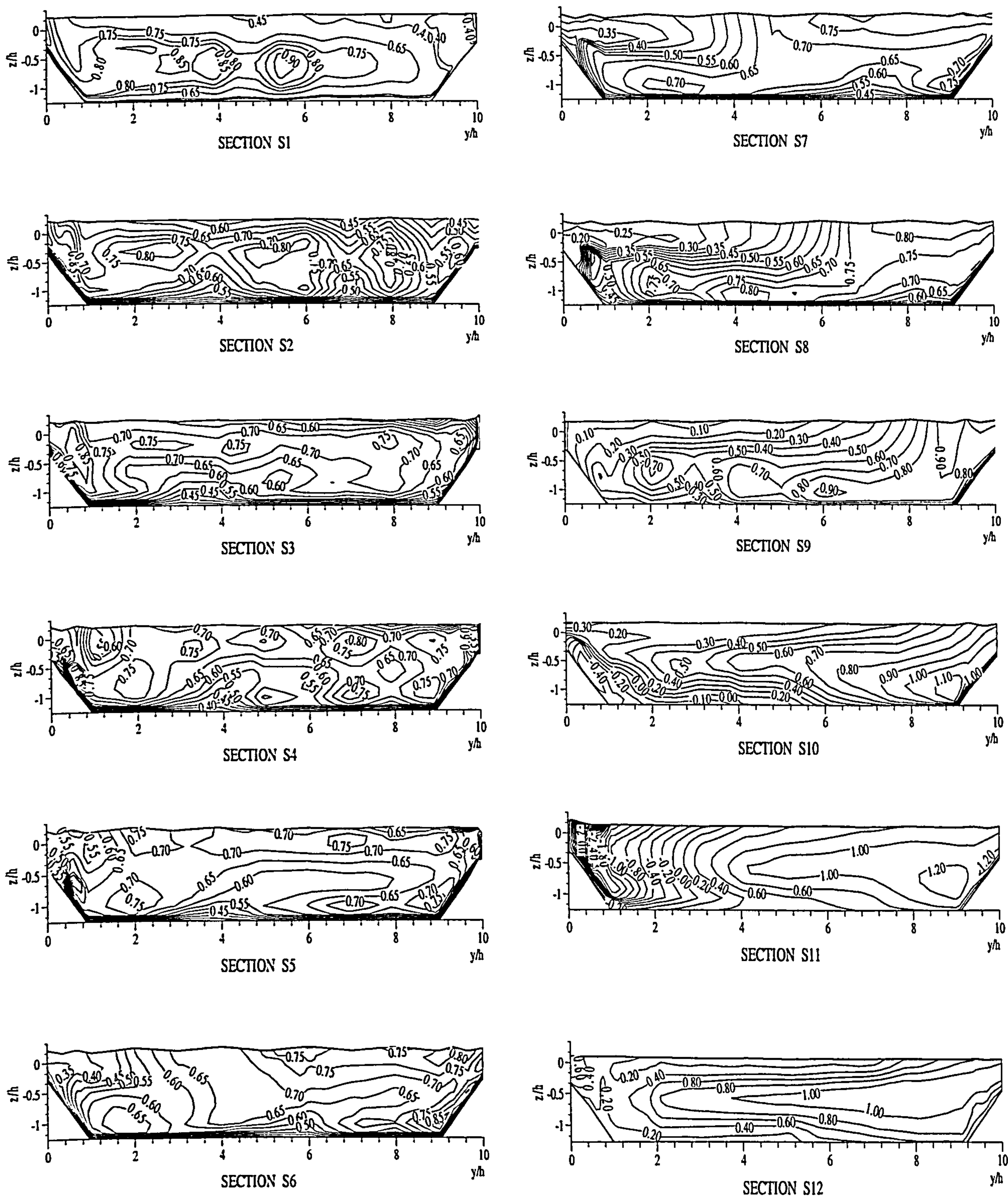
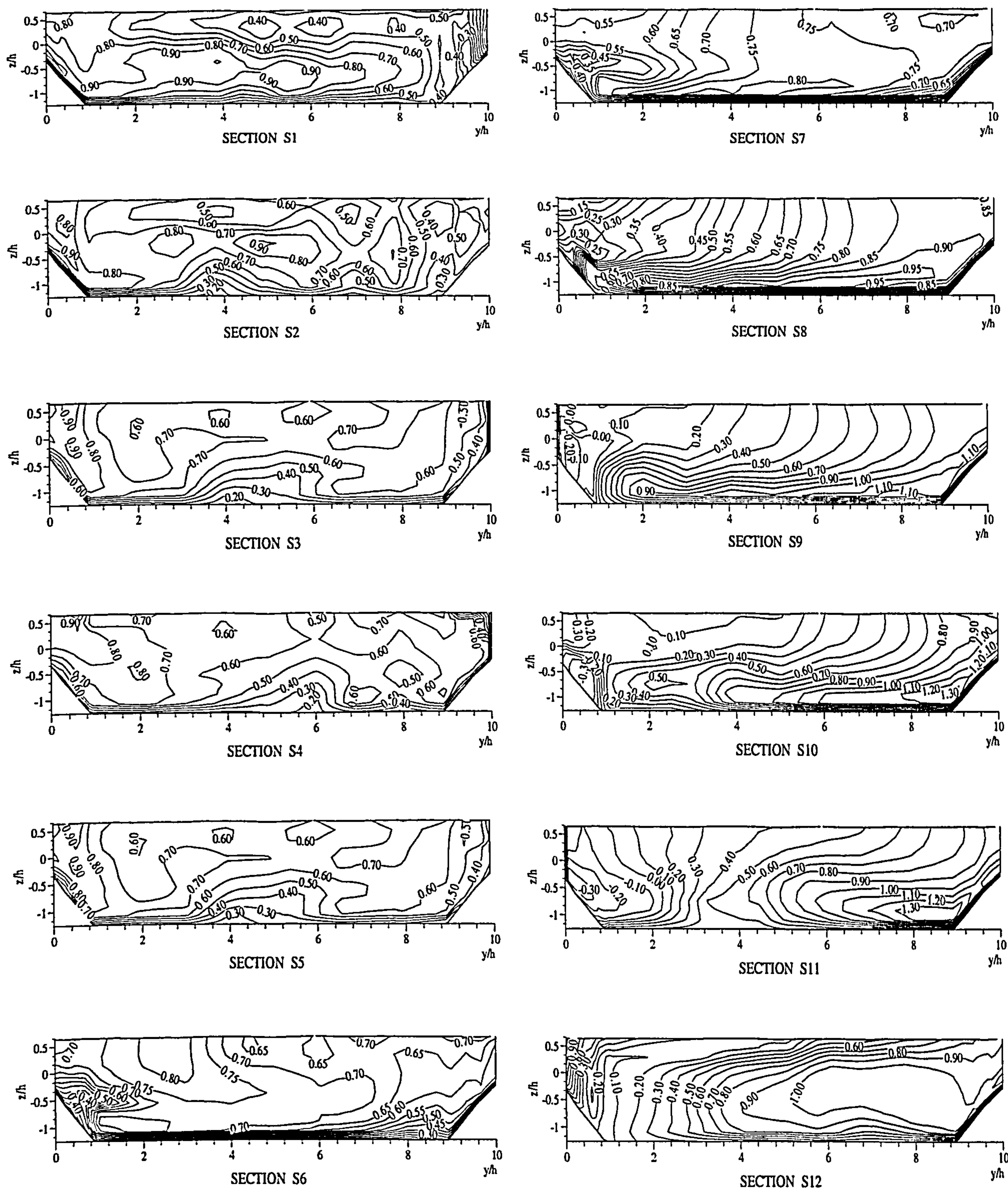


Figure 5.28: Predicted streamwise velocity  $U$ , normalised by  $U_s$  for main channel in Case 1. Apex Block at  $Dr = 0.25$  at sections S1 to S12





**Figure 5.29:** Predicted streamwise velocity  $U$ , normalised by  $U_s$  for main channel in *Case M Apex Block* at  $Dr = 0.45$  at sections S1 to S12



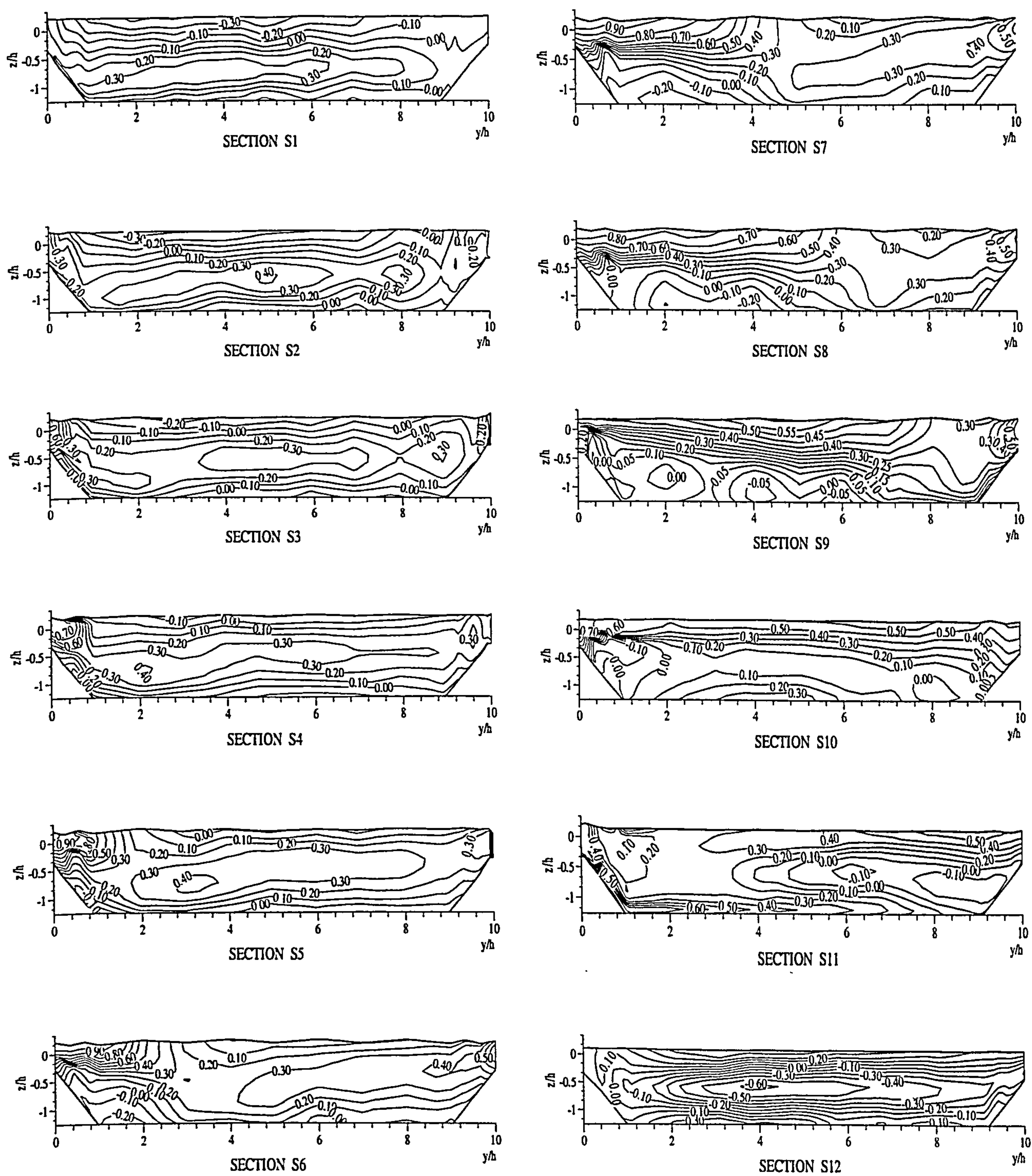
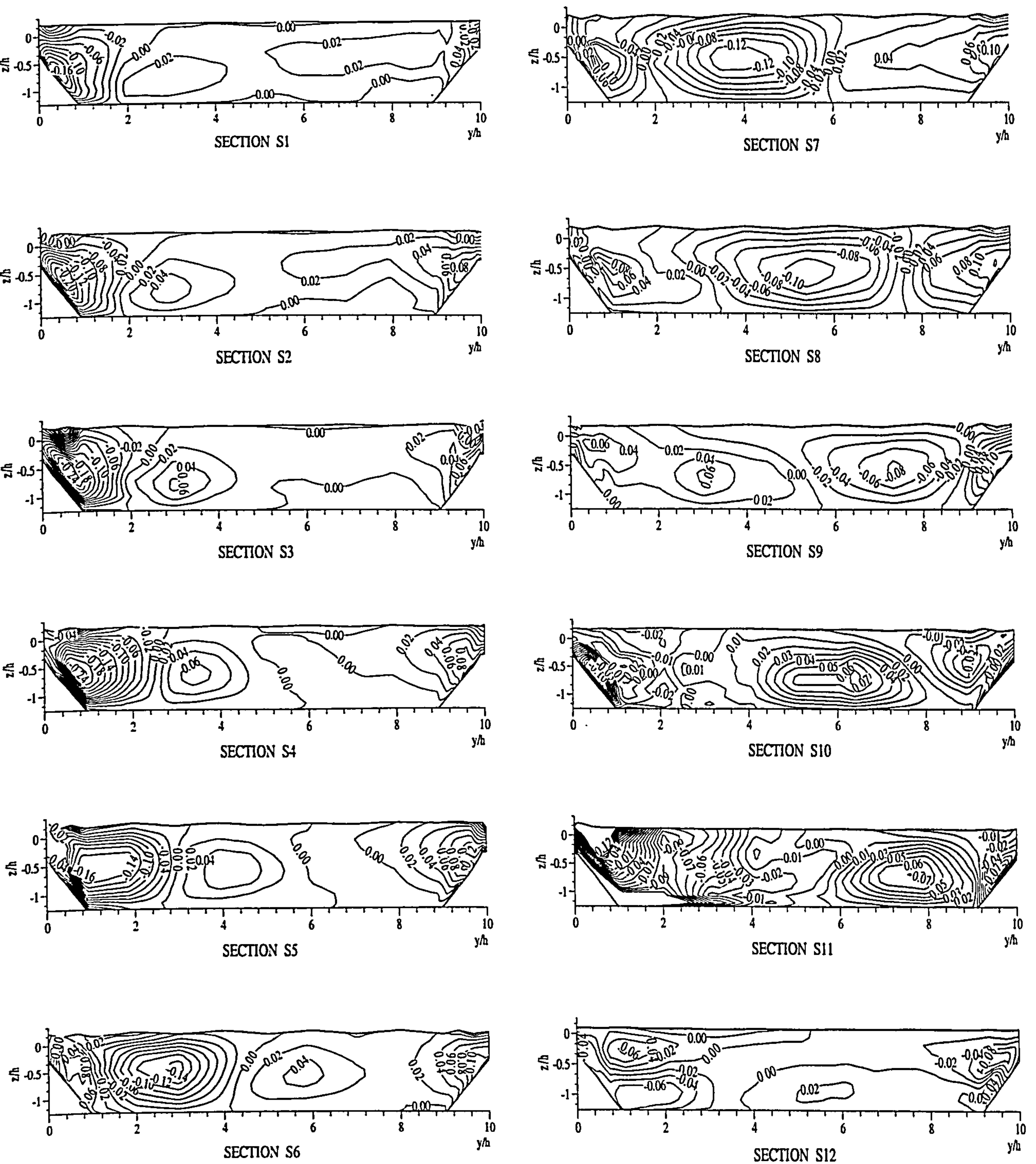


Figure 5.30: Predicted lateral velocity  $V$ , normalised by  $U_s$  for main channel in Case M Apex Block at  $Dr = 0.25$  at sections S1 to S12









**Figure 5.32:** Predicted vertical velocity  $W$ , normalised by  $U_s$  for main channel in *Case M Apex Block* at  $Dr = 0.25$  at sections S1 to S12







### 5.9.2.3 Secondary Flow Vectors

The secondary flow generation associated with different flow depths is shown in 2D vector form. Figure 5.34 shows the predicted secondary vectors for  $Dr = 0.25$  at sections S1 to S12. At section S1, which is the apex section, a clear, single, dominant, anticlockwise circulation cell is predicted, which occupies almost the whole of the upper main channel area. As the flow moves downstream to sections S3 and S4, the anti-clockwise cell observed at sections S1 and S2 appears above the bankful level. However, at section S4, the new clockwise circulation cell is seen near the inner side (left side) of the main channel. Thus it is proven that this new circulation cell originates somewhere between the sections S3 and S4 but the magnitude of the new clockwise circulation cell is smaller than that in *Case L No Block*, because the blocks reduce the shearing effect of the main channel flow caused by the floodplain flow plunging into the main channel. At the cross-over region, sections S5 to S8, the magnitude of the floodplain flow entering the main channel increases due to which the circulation cell seen at section S4, gains strength and size and it travels towards the central part of the main channel. This cell occupies half of the main channel inbank area at section S8, which is at the mid point of the cross-over region. However, the pattern of circulation changes at section S9 where an anti-clockwise secondary flow cell seems to appear on the inner side of the main channel and a complementary clockwise secondary flow cell appears at the central part of the main channel and moves towards the outer side of the main channel at section S10. At section S11, the lateral velocity is progressively moving toward the outside bank of the main channel, although it appears that a clear pattern for the magnitude of the secondary flow cell can be observed within the bankful main channel with small scale vortices appearing towards the inner side. The secondary flow cell circulation pattern at section S12 is different to that in section S1 with two dominant circulation cells being observed. The flow pattern is complicated by the emergence of two secondary flow cells.

In general, the pattern and the behaviour of the secondary flow vectors for  $Dr = 0.45$  are quite different from  $Dr = 0.25$ , as seen in Figure 5.35. Reviewing the apex section, S12, three circulation cells are seen with one anticlockwise circulation occurring at the outer left side of the main channel and two clockwise circulations being seen at the



central part of the main channel above the bankful level and at the inner (right) side of the main channel.

From the look of the secondary flow vectors for *Case M Apex Block*, the flow mechanism is quite complex when compared to *Case L No Block* with an unvegetated floodplain. The main difference with the secondary flow structure for *Case M Apex Block* is the number of secondary flow cells appearing in the main channel at the apex region. As expected, the main factor that could significantly affect the complex flow mechanism is the placement of the blocks along the meander belt. Looking at the apex bend S1, in *Case M Apex Block*, there exist two dominant anticlockwise cells in the main channel for higher overbank flow compared to *Case L No Block* where only one dominant anticlockwise cell is seen. These cells appear in a quite different location for shallow relative depth in *Case M Apex Block* where one anticlockwise cell is seen above the bankful level and one clockwise cell is seen near the bed at the outer side of the main channel. When the flow moves from sections S2 to S5, this multiple secondary cell is totally different from the structure for section S1 with a different location for *Case M Apex Block*. However, a new, small, single, circulation cell appears at section S3 and increase in strength of secondary flow up to section S8 at the cross-over section for *Case M Apex Block*. It is expected that, judging from the differences of secondary flow cells and structure, the interaction mechanism of the vortices within the apex region is due to the blocks placed along this section. Instead of large vortices interacting within the main channel, the shearing of the main channel flow by the floodplain plunging into the main channel is also seen from sections S3 to S5.



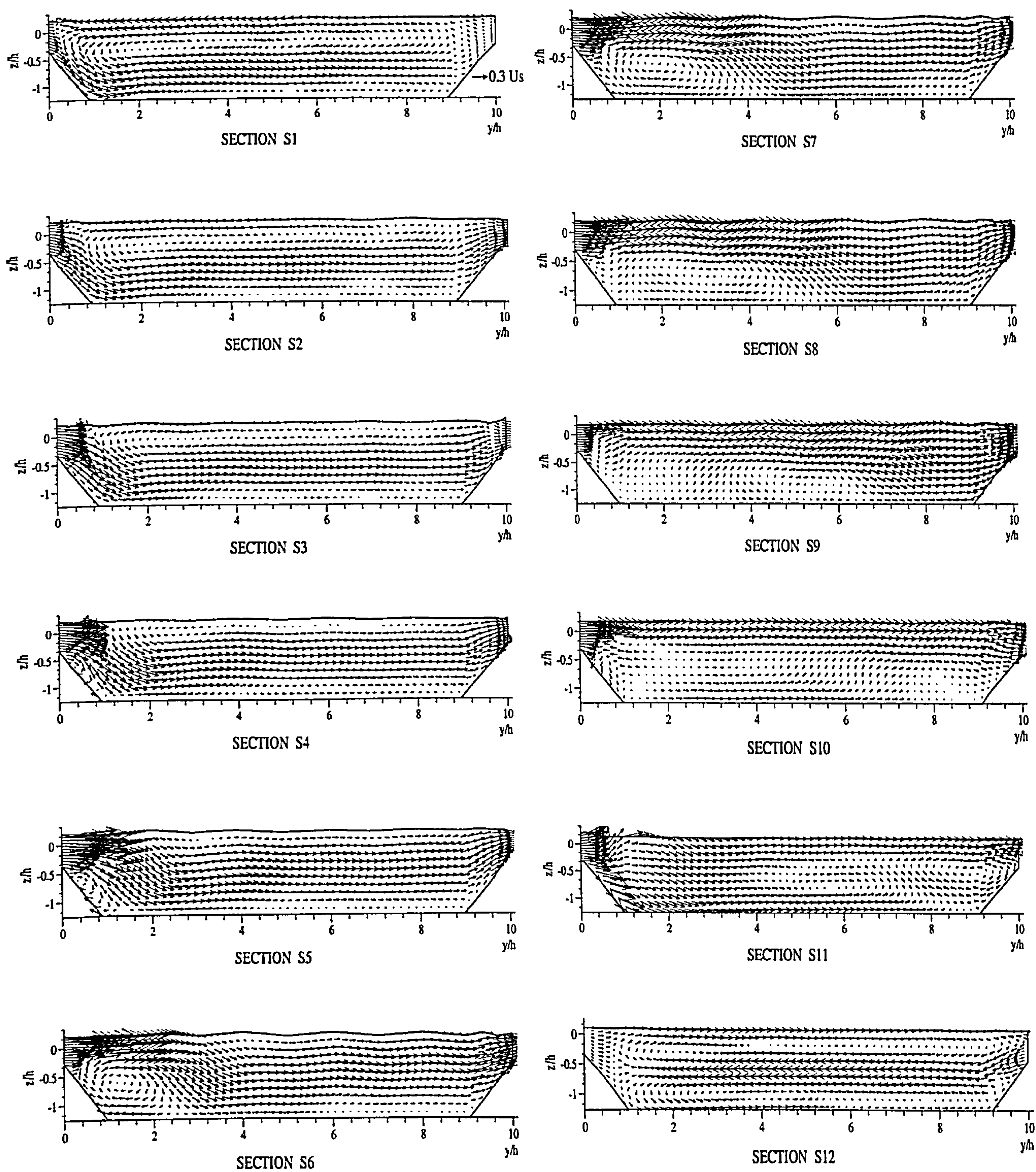


Figure 5.34: Predicted secondary flow vectors for main channel in *Case M Apex Block* at  $Dr = 0.25$  at sections S1 to S12



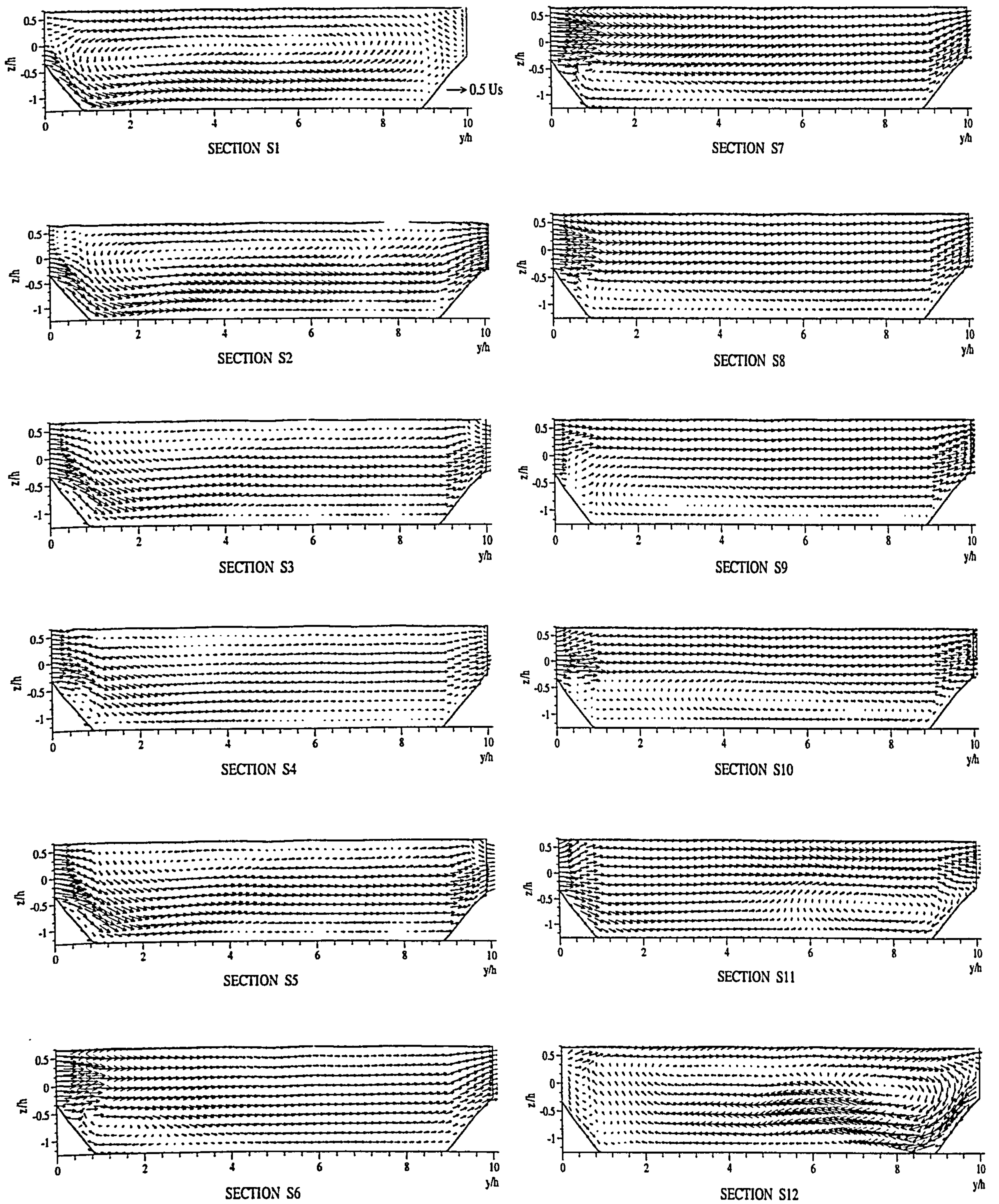


Figure 5.35: Predicted secondary flow vectors for main channel in *Case M Apex Block* at  $Dr = 0.45$  at sections S1 to S12



### 5.9.3 Overbank Flow with Vegetated Floodplain: *Case N Cross-over Block*

From this section, the case of overbank flow with a vegetated floodplain along the cross-over section is examined due to the interesting results in Chapter 4. Despite the block arrangement, *Case N Cross-over Block* is quite different from *Case C* but it still generates a similar basic flow structure in the cross-over section. The reasons why blocks were placed on only one side of the cross-over section have been explained before. The arrangement of blocks along the cross-over section is very important to show the internal flow behaviour because in Chapter 4 it was shown that firstly, the arrangement of blocks along the cross-over section causes small differences in the stage-discharge curves compared to the other cases for a rectangular fixed-bed main channel. Secondly, this arrangement conveys water with greater efficiency as compared to the other cases. For these reasons, the simulation has been set-up and run to see the internal flow behaviour, especially in the main channel cross-section over a half-meander belt. These sub-sections also explain the 2D depth-averaged velocity vector field, 3D variable velocities field and secondary flow vectors.

#### 5.9.3.1 Depth-averaged Velocity Vector Fields

Figures 5.36(a) and (b) show the results of vectors of depth-averaged velocities along one meander wavelength for  $Dr = 0.25$  and  $Dr = 0.45$  respectively. Both the shallow and higher overbank flows show that the maximum velocity filament in the main channel occurs relatively near the outer bank sidewall at the upstream apex bed and continues to move steadily to the outer bank as it approaches the downstream bend apex. However, along the cross-over section many vortices occur near the inner bank of the main channel behind the blocks. However, the main channel flow predominantly follows the main channel direction at the outer bank of the main channel. At the end of the blocks in the cross-over section, interestingly, there are large vortices. These are produced by the interaction of the blocks and the floodplain flow because of the faster velocity from the floodplain being naturally concentrated due to the blocks at the end of the cross-over. This vortex may cause a deep scour or erosion of the main channel as seen in Figure 4.35. The floodplain flow field shows for  $Dr = 0.45$ , that the floodplain flow is generally higher at the outer meander belt region than for  $Dr = 0.25$  and mostly



parallel to the valley direction. However, within the meander belt region both depths show that a small velocity filament diverts towards the inside of the channel.

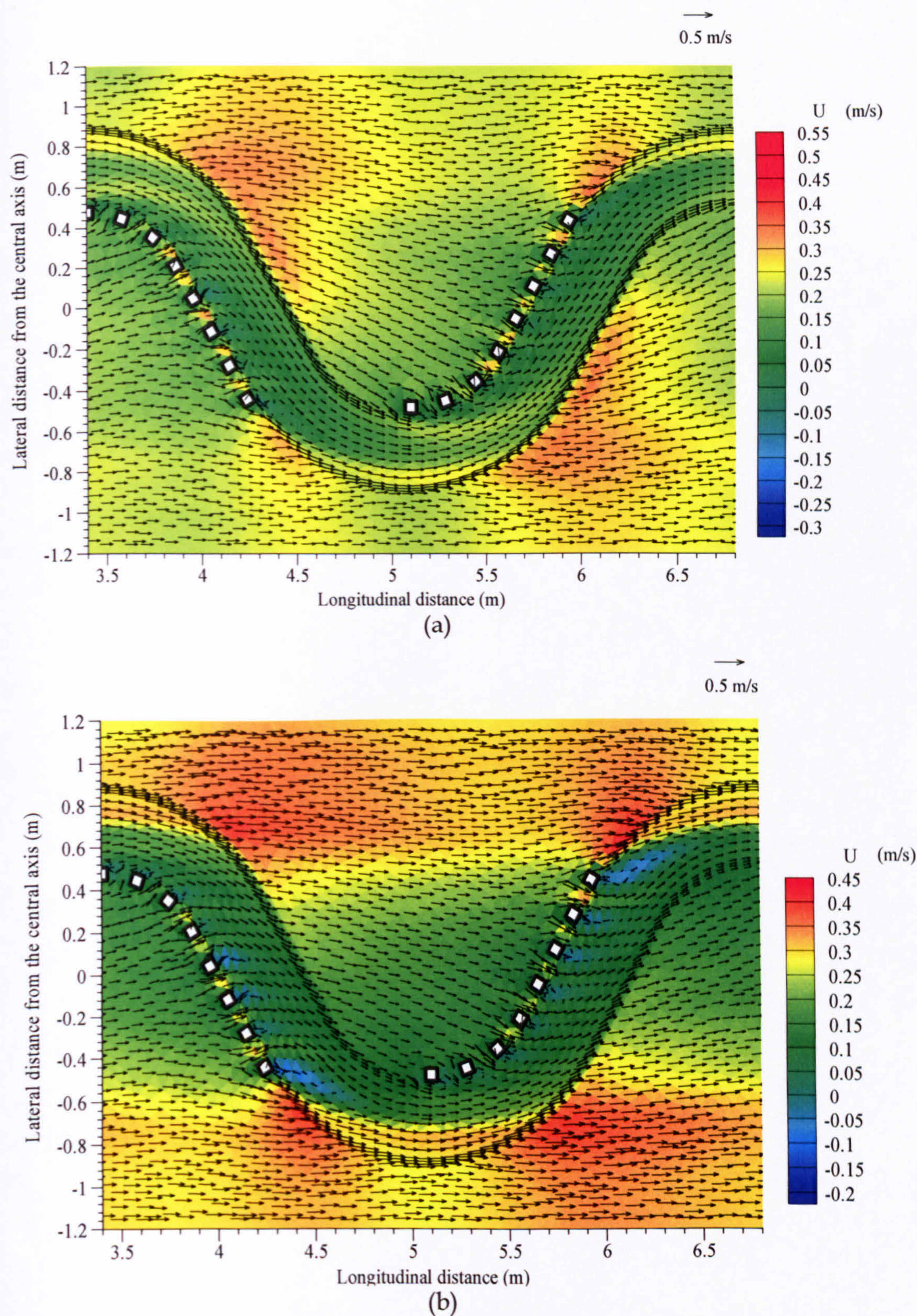


**Figure 5.36:** Predicted layered depth-averaged velocity for Case N Cross-over Block for different relative depth (a)  $Dr = 0.25$  (b)  $Dr = 0.45$



### 5.9.3.2 3D Variable Velocities Field

#### 5.9.3.2.1 Streamwise Velocity ( $U$ )

In *Case N Cross-over Block*, Figures 5.37 and 5.38 show the 3D distributions of the predicted streamwise velocity ( $U$ ) for  $Dr = 0.25$  and  $Dr = 0.45$ . For the lower flow depth, as shown in Figure 5.37, velocities are positive in all cross-sections. At the bend sections S1, S2 and S3, maximum streamwise velocity is about  $1.0U_s$  near the surface and minimum streamwise velocity is  $0.4U_s$  near the bottom, which is closer to the outer side of the main channel. At section S4, the streamwise velocity starts to separate with the fastest occurring in the outer side of the main channel and the slowest streamwise velocity being observed at the inner side of the main channel. At the cross-over sections S5 to S9, the streamwise velocities decrease slightly at the inner side and high at the outer side of the main channel. At sections S11 and S12, it should be highlighted that the higher vortices start from these sections because the floodplain flow interacts with the blocks. It can be seen that the maximum streamwise velocities of about  $1.0U_s$  and  $1.2U_s$  occur at the outer (left) sides of the main channel near the surface and that the lower streamwise velocities of about  $0.1U_s$  and  $0.3U_s$  are found at the outer (left) side of the main channel near the bed for sections S11 and S12 respectively. This is a quite distinct feature in the upper layer and lower layer, which is totally different from those in cases *L* and *M*.

Figure 5.38 shows the cross-sectional distributions of the predicted streamwise velocity ( $U$ ) for  $Dr = 0.45$ . The distribution profile and the behaviour of the streamwise velocity are higher. Particularly at the bend section, the average maximum streamwise velocity is  $1.2U_s$  above the bankful level of the main channel. In the cross-over region, most of the maximum streamwise velocity is seen at the outer (right) side. At the cross-over sections S5 to S7, the velocity at  $y/h = 0$ , (left hand side) is almost zero, which is totally different from those in cases *L* and *M*, thus substantial reductions in shearing due to the floodplain flow plunging onto the main channel. Therefore the shear interaction between the floodplain flow and the main channel flow is significantly less taken place. However, there are distinct velocity difference between the upper layer and lower layer in the inner side of the main channel (i.e. slower flow in the upper layer and faster flow in the lower layer) even the large relative depth. This means that the flow in



the lower layer is retardant, rather than acceleration by the upper layer flow in cases no block  $L$  and apex block  $M$ . At the cross-over section (sections S6 to S9), the minimum shearing of the main channel flow by the floodplain flow plunging into and over the main channel can be seen due to blocking the floodplain flow entering the main channel by the blocks.

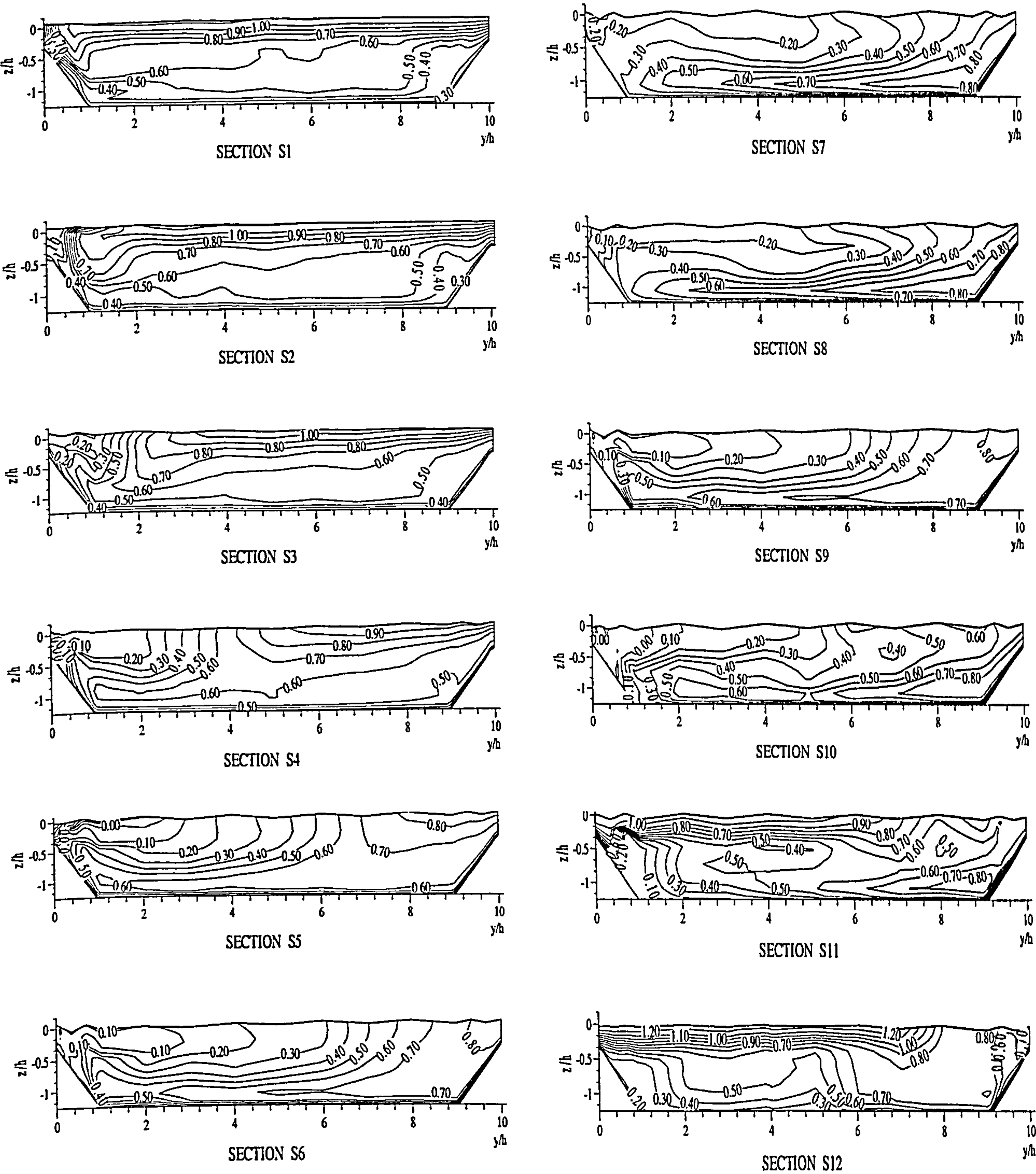


Figure 5.37: Predicted streamwise velocity  $U$ , normalised by  $U_s$  for main channel in Case N Cross-over Block at  $Dr = 0.25$  at sections S1 to S12



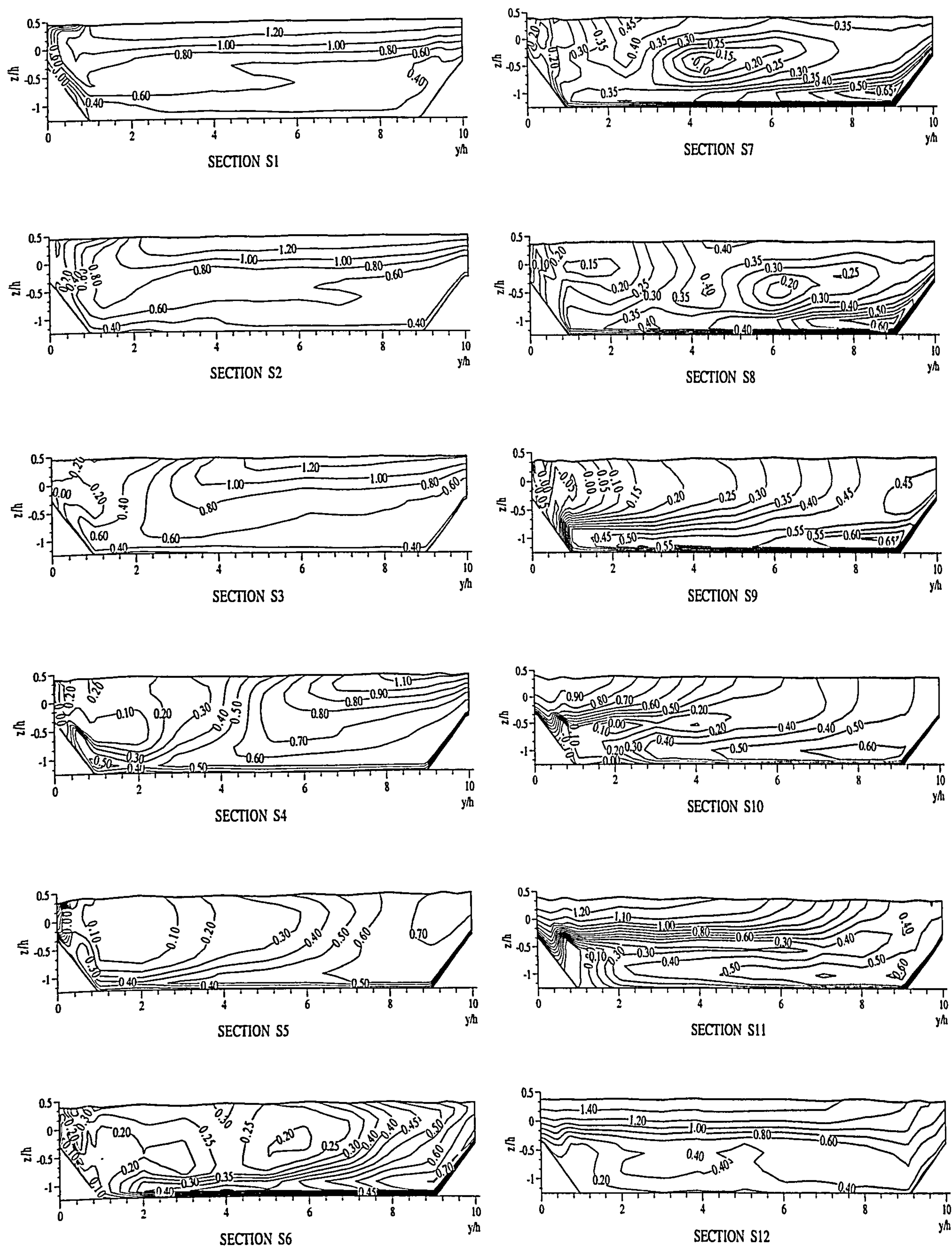


Figure 5.38: Predicted streamwise velocity  $U$ , normalised by  $U_s$  for main channel in Case N Cross-over Block at  $Dr = 0.45$  at sections S1 to S12



### 5.9.3.2.2 Lateral Velocity ( $V$ )

The lateral velocity shown in Figures 5.39 and 5.40 has a quite complicated pattern of flow but there is a noticeable pattern of higher lateral velocities at the inner side of the main channel and relatively slower velocities near the bed of the bend apex section S1. Maximum positive lateral velocity is observed to be  $0.3U_s$  and the minimum negative lateral velocity is observed to be  $-0.1U_s$ . The positive velocities increase gradually at the inner side of the main channel around  $0.35U_s$ ,  $0.5U_s$  and  $0.6U_s$  at sections S2, S3 and S4 respectively. However, at the beginning of cross-over section, S5, a higher velocity starts to occur at the outer side above the bankful level of the main channel up to section S6 showing that the main channel flow escaping onto the floodplain. The complicated flows can be seen in sections S7, S8 and S9 where higher positive lateral velocities are observed at most parts of the main channel and negative lateral velocities are observed near the bed. As the flow moves downstream to sections S10 to S12, the negative magnitudes of the lateral velocity in the main channel are seen, meaning that the flow is moving from the outer side towards the inner side of the main channel within the range  $-0.15U_s$  to  $-0.2U_s$ . For  $Dr = 0.45$ , Figure 5.40, show that the magnitude and distribution profiles of the lateral velocity are similar to those for shallow relative depth but the magnitude of the lateral velocity is higher.

### 5.9.3.2.3 Vertical Velocity

Figure 5.41 shows the cross-sectional distribution of the predicted vertical velocity at section S1 for  $Dr = 0.25$ . Negative velocities are observed close to the inner bankful main channel and positive velocities are observed close to the outer bankful main channel at sections S1, S2 and S3. Maximum negative vertical velocity is observed to be  $-0.12U_s$  at section S2. Negative vertical velocities also are observed at sections S6 and S7 at the outer side of the main channel at the cross-over section. This indicates that downflow occurs close to the inner bankful main channel at the apex section and at the outer side at the bankful level at the mid point of the cross-over section. However, at sections S10 to S12, positive vertical velocities were found near both sides of the main channel sidewalls and negative vertical velocities are found at the central part of the main channel. Figure 5.42 for  $Dr = 0.45$  shows a similar pattern of vertical velocity to that for  $Dr = 0.25$ .



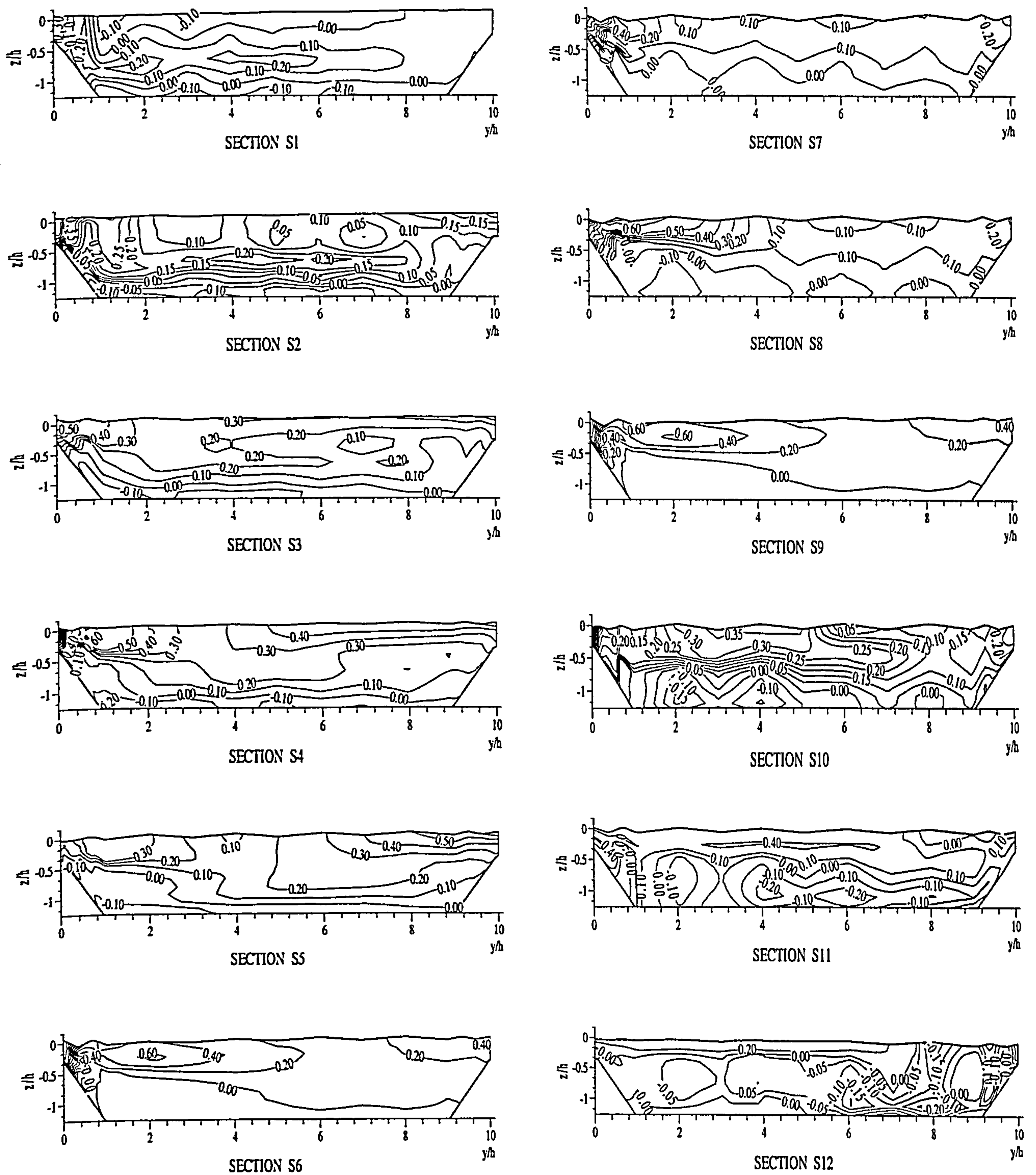
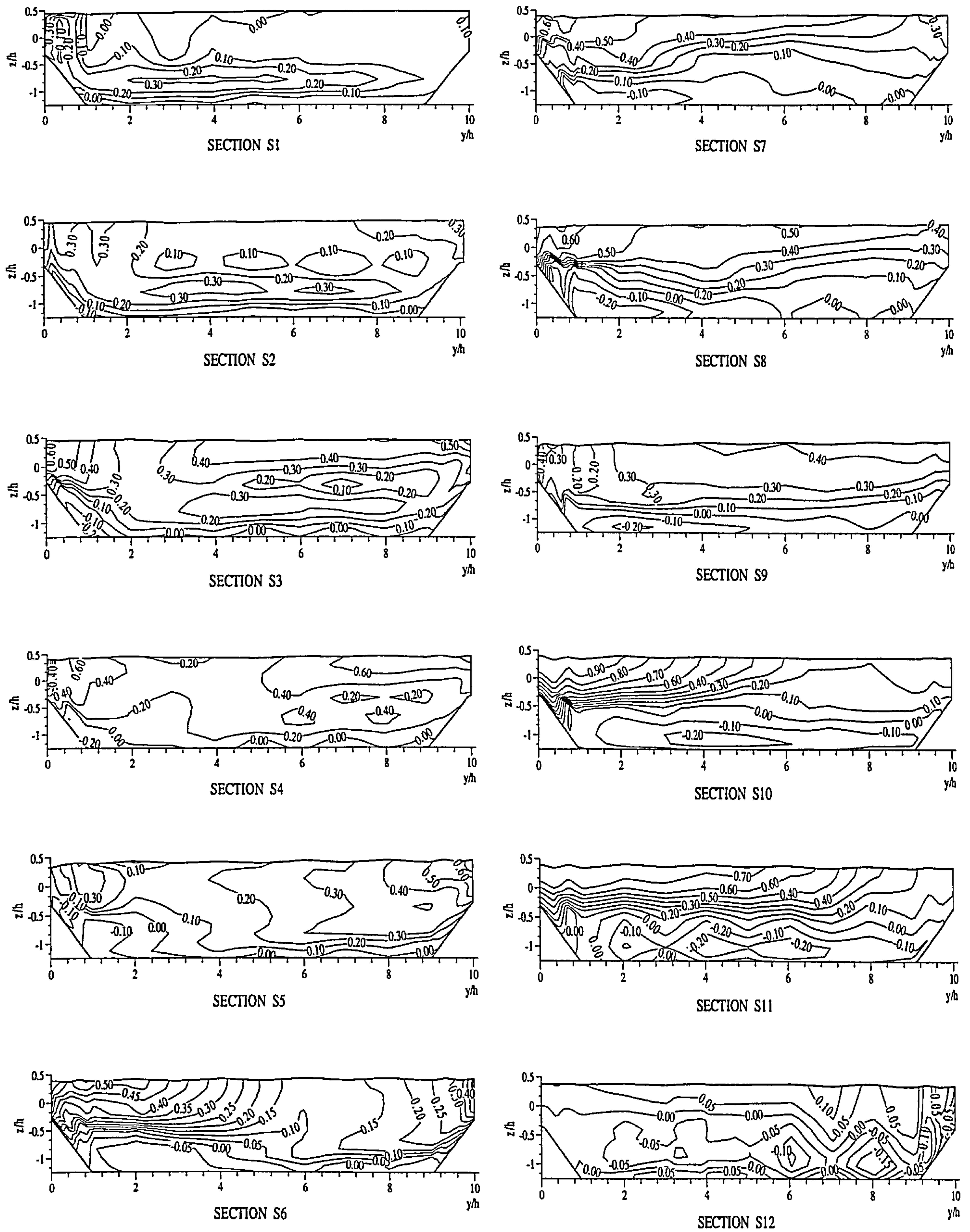


Figure 5.39: Predicted lateral velocity  $V$ , normalised by  $U_s$  for main channel in Case N Cross-over Block at  $Dr = 0.25$  at sections S1 to S12





**Figure 5.40:** Predicted lateral velocity  $V$ , normalised by  $U_s$  for main channel in Case N Cross-over Block at  $Dr = 0.45$  at sections S1 to S12



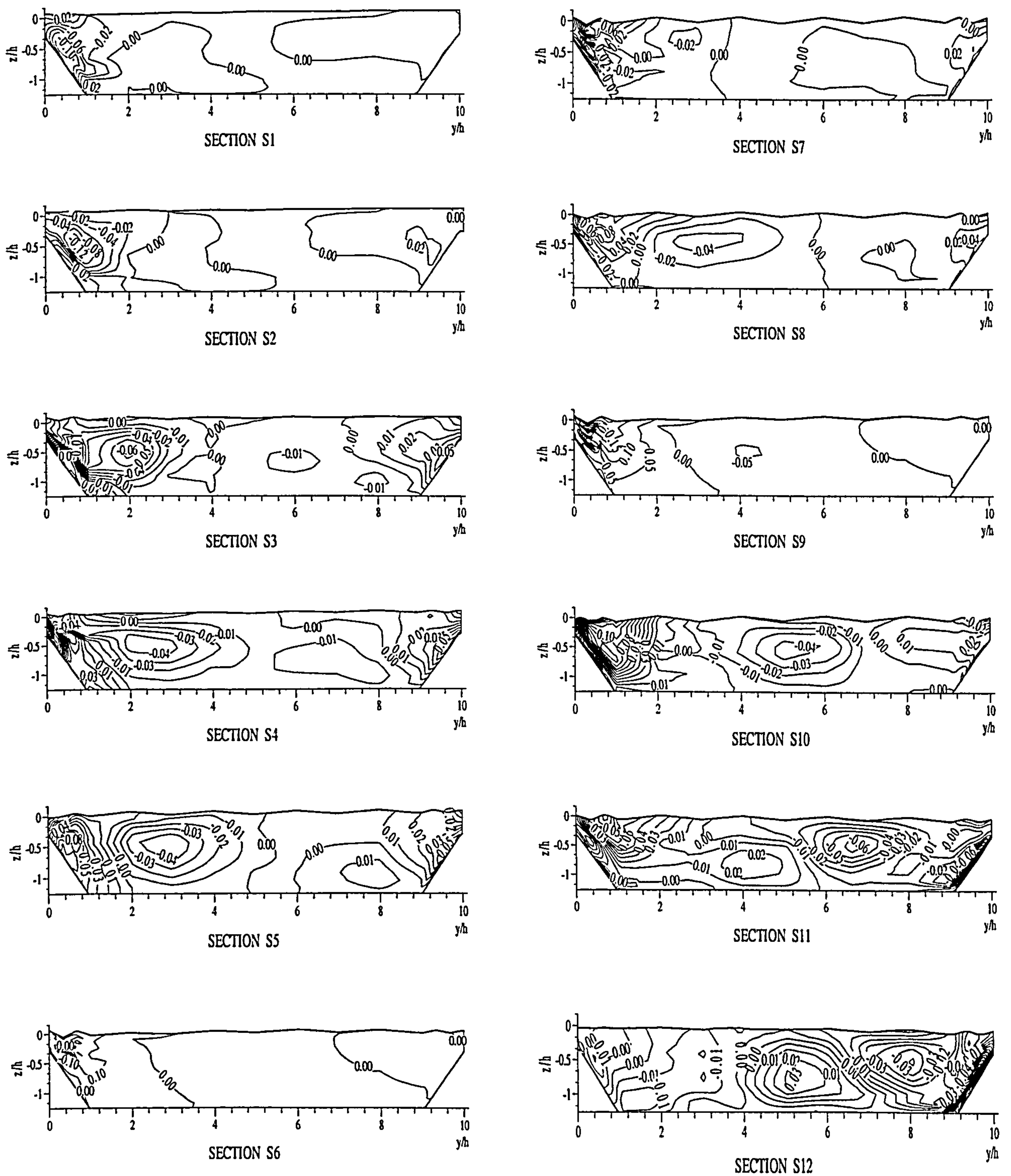


**Figure 5.41:** Predicted vertical velocity  $W$ , normalised by  $U_s$  for main channel in Case N Cross-over Block at  $Dr = 0.25$  at sections S1 to S12



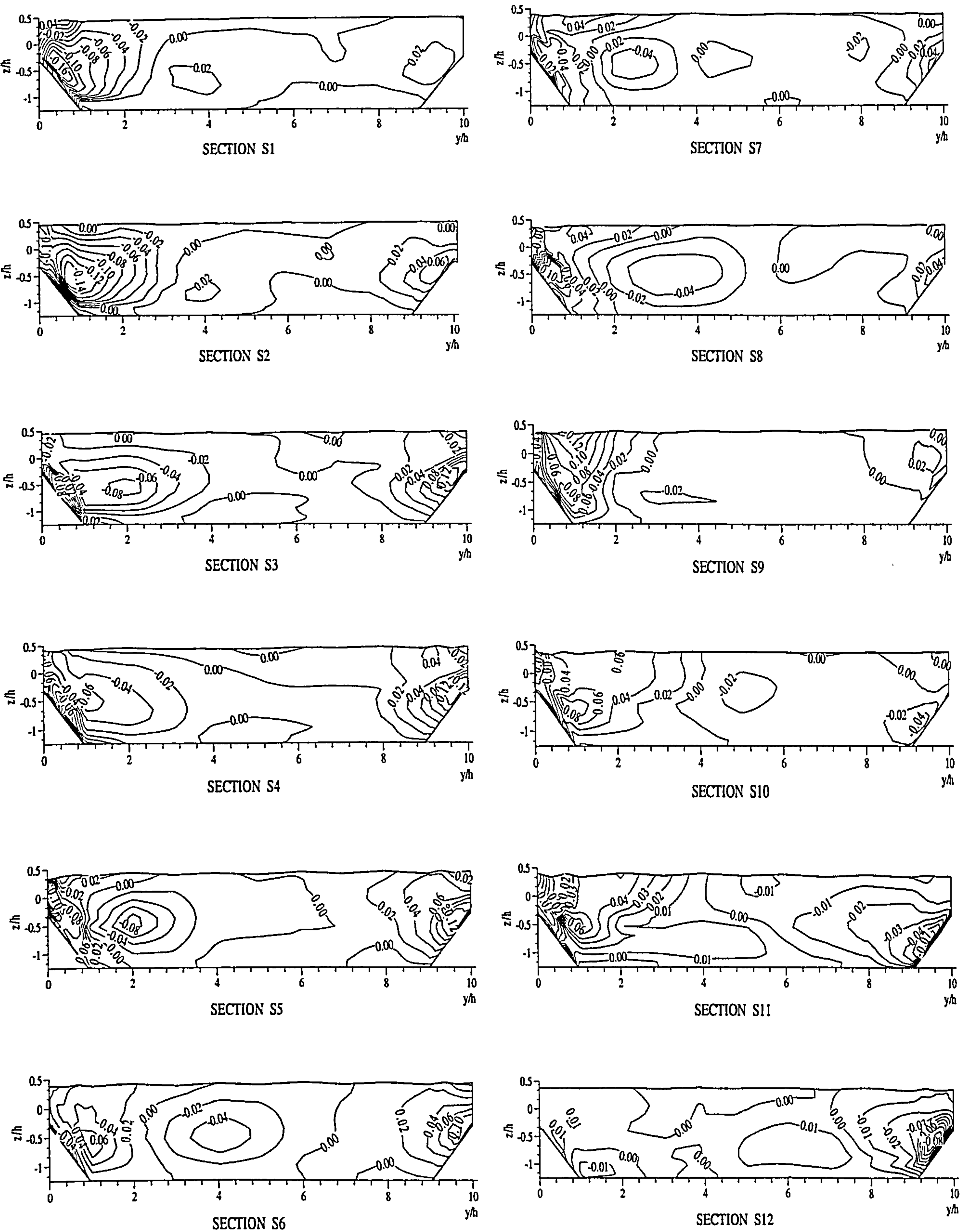


**Figure 5.42:** Predicted vertical velocity  $W$ , normalised by  $U_s$  for main channel in *Case N Cross-over Block* at  $Dr = 0.45$  at sections S1 to S12



### 5.9.3.3 Secondary Flow Vectors

Figures 5.43 and 5.44 show the predicted secondary vectors for  $Dr = 0.25$  and  $Dr = 0.45$  for sections S1 to S12 respectively. For the lower relative depth at the apex sections S1, as shown in Figure 5.43, there are multiple secondary cells. As the flow moves downstream to section S2, a small clockwise cell is observed at the inner side of the main channel and a large single clockwise cell can be seen near the bed. The single clockwise circulation at the inner side of the main channel then moves towards the channel centreline until section S6. At the mid point of the cross-over sections S7 to S9, the complicated secondary circulations appear below the bankful level. Although there was no clear pattern of secondary flow cell on the right hand side, the strong lateral velocity moves towards the outer bank direction, and, as a result, pushes the maximum velocity closer to the outer side of the main channel as shown in Figure 5.37. For sections S10 to S12, there are still a number of small-scale vortices appearing in the main channel although there are no blocks along the floodplain apex section. For the higher flow depth,  $Dr = 0.45$ , as shown in Figure 5.44, the secondary flow cell is shown to be more stable compared to the lower flow depth  $Dr = 0.25$ , especially the upstream bend apex section S1 and downstream bend apex section S12. The flow pattern is complicated by the emergence of numerous secondary flow cells, which create multiple diverging and converging flows within the main channel.

The flow in vegetated floodplain *Case N Cross-over Block* shows extremely complex behaviour compared to cases no block *L* and apex block *M*. The secondary flow pattern shows a quite distinct difference, both at the apex region and at the cross-over section. Firstly, as seen at the apex region, at section S1 the secondary flow patterns are not stable with multiple circulation cells being seen for both flow depths. This is due the large eddy effect generated by the blocks placed along the cross-over section. This large eddy is different in size for both relative flow depths with the higher flow depth generating the large eddy size (see Figures 5.36 (a) and (b)). Secondly in the cross-over region (sections S6 to S9), it can be seen that the circulation cells at the inner side of the main channel (left side) are quite different and strength compared to cases no block *L* and apex block *M*. This is due to the fact that the blocks along the cross-over section cause a reduction in the magnitude of the floodplain flow entering the main channel. The vortices and wakes effect caused by the blocks are also noticeable for good



portions of the main channel below the bankful level, which suggests that the flow in the main channel is not streamwisely dominant compared to cases no block  $L$  and cross-over block  $N$ .

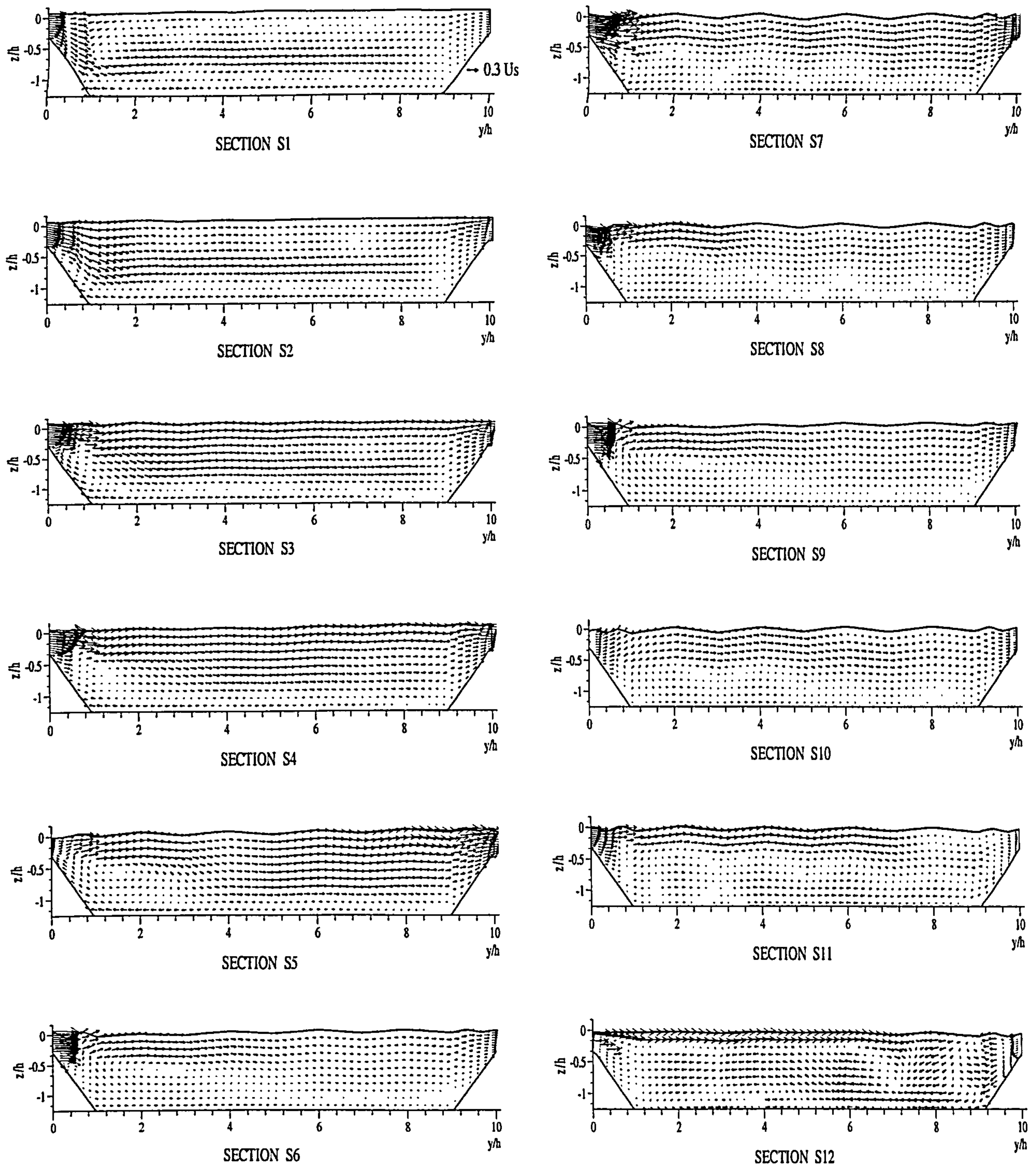


**Figure 5.43:** Predicted secondary flow vectors for main channel in *Case N Cross-over Block* at  $Dr = 0.25$  at sections S1 to S12



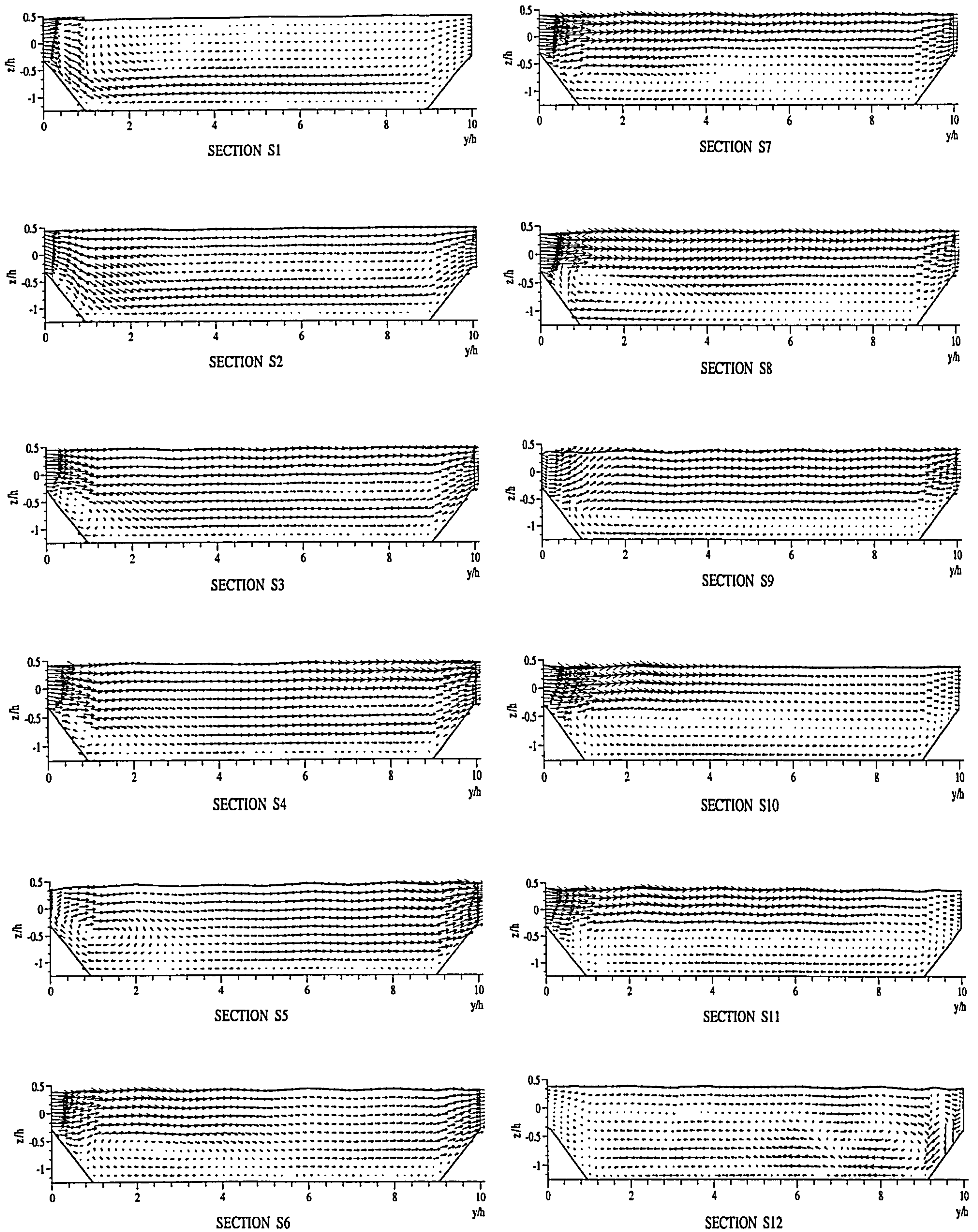


**Figure 5.44:** Predicted secondary flow vectors for main channel in *Case N Cross-over Block* at  $Dr = 0.45$  at sections S1 to S12



### 5.10 Boundary Shear Stress Distribution

The distribution of predicted boundary shear stresses ( $\tau_o$ ) on the wetted perimeter over the main channel was predicted for three cases namely no block *L*, apex block *M* and cross-over block *N*. Of these cases, the predicted of boundary shear stress were plotted for two different flow depths similar to the predicted velocity as described in previous section.

Figure 5.45 shows the predicted lateral boundary shear stress for two different relative depths,  $Dr = 0.25$  and  $Dr = 0.45$ , from sections S1 to S12 for *Case L No Block*. Both cases seem to have a similar pattern of boundary shear stress profile in the main channel, in which both of the local boundary shear stress values reach their maximum at the inner bank sidewall bend apex section, S1. Of that, the higher flow depth case remains larger in magnitude than that for the shallow flow depth. It can be seen that both patterns of boundary shear stress distributions in the main channel for shallow and higher overbank flow are generally similar but different in magnitude; with the magnitude of the boundary shear stress being larger for higher flow depths. These highest magnitudes of boundary shear stress occur near to the inner bank at the apex, section S1, and shift progressively to the outer side along the course of the main channel and appear near to the outer side of the bank. For the shallow flow depth, more wave-like behaviour can be seen along the inner side of the main channel for the shallow flow depth compared to the higher flow depth. This behaviour becomes wider as the flow goes downstream to section S6. The point of the highest boundary shear stress in the main channel roughly indicates the limit of the interaction of the floodplain flow with the main channel.

At the cross-over sections, S5 to S9, both shallow and higher relative depths show that the predicted boundary shear stresses are similar to each other. The boundary shear stress is higher at the edge of the inner and outer sides of the main channel than in the main channel cross-section. For the shallow flow depth, there is a slight abrupt reduction across the channel with high boundary shear stress along the right-hand bank of the channel and small boundary shear stress on the other side. This is because of the effect of flow crossing from the floodplain into the main channel at the cross-



over section and the mirror images of the boundary shear stress profile are attained at the consecutive bend apex sections (S1 and S12).

Having understood the internal flow behaviour for cases apex block *M* and cross-over block *N* as discussed previously, the predicted boundary shear stress over a half-meander wavelength were plotted in order to understand their behaviour especially near and behind the blocks along the upstream and downstream bend apex regions. Figures 5.46 and 5.47 show the predicted boundary shear stress distribution for different relative depths for apex block *M* and cross-over block *N* cases respectively. Figure 5.46 shows that, at the apex section, the boundary shear stresses are higher at the inner side of the main channel for both relative depths. However, as section S2 moves towards section S5, the boundary shear stress starts to decrease from the inner side of the main channel towards to the central part of the main channel. At the cross-over sections S6 to S9, as expected, both shallow and higher relative depths show that the boundary shear stresses are quite similar in pattern to *Case L No Block* and the mirror images of the predicted boundary shear stress distributions are attained at the consecutive bend apex sections (S1 and S12).

Figure 5.47 shows the lateral plots of the predicted boundary shear stress in the main channel for two different relative depths for *Case N Cross-over Block*. At the apex region sections S1 to S5, the boundary shear stresses are higher at the outer side of the main channel for both relative depths due to the blocks placed at the inner side of the floodplain bank apex region and due to the co-flowing turbulent shear between the main channel and the floodplain. These patterns are totally different compared to cases *L* and *M*, which show that the boundary shear stresses are higher at the inner side of the main channel in the apex region. Similarity, further downstream from the apex, at the cross-over region sections S6 to S9, the boundary shear stress remains higher at the outer side of the main channel (right side) but lower at the inner side for both flow depths. The lower magnitude of the boundary shear stress at the inner side (left side) is due to the flow-blocking by blocks at the cross-over section. Again, towards the downstream apex region sections S10 to S12, the boundary shear stresses are seen to be higher at the outer side of the main channel (left side). In general, the results show such features as the location of the minimum and maximum boundary shear stress for each traverse. This is important since the features relate to the flow exchange between the



floodplain and the main channel flows at the cross-over section in terms of disturbing and plunging floodplain flow into the main channel and of course the subsequent effect on the complex secondary flow caused by blocks placed along the cross-over region as described in the previous section.

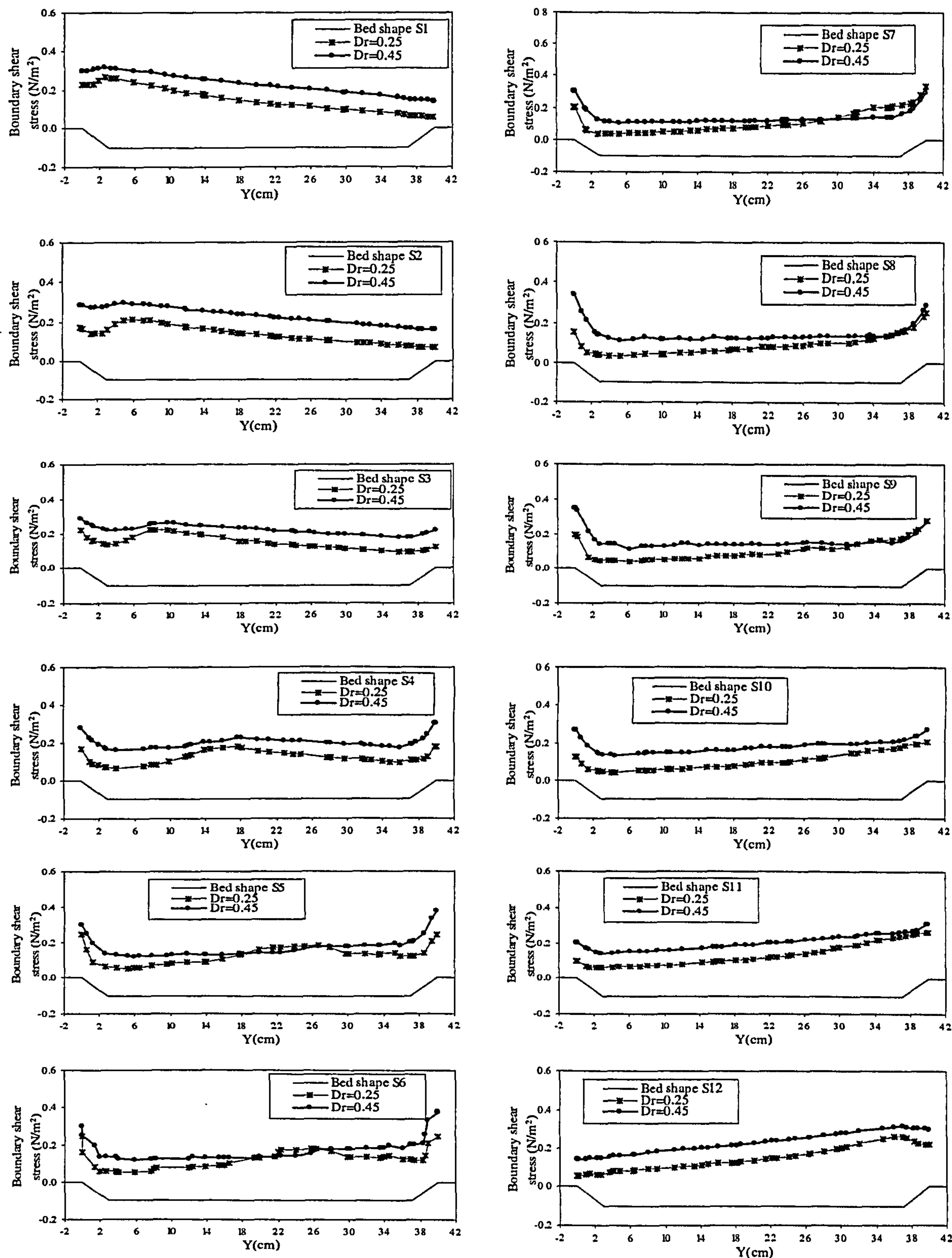


Figure 5.45: Predicted boundary shear stress for the main channel in *Case L No Block* for different relative depth,  $Dr$ , at sections S1 to S12



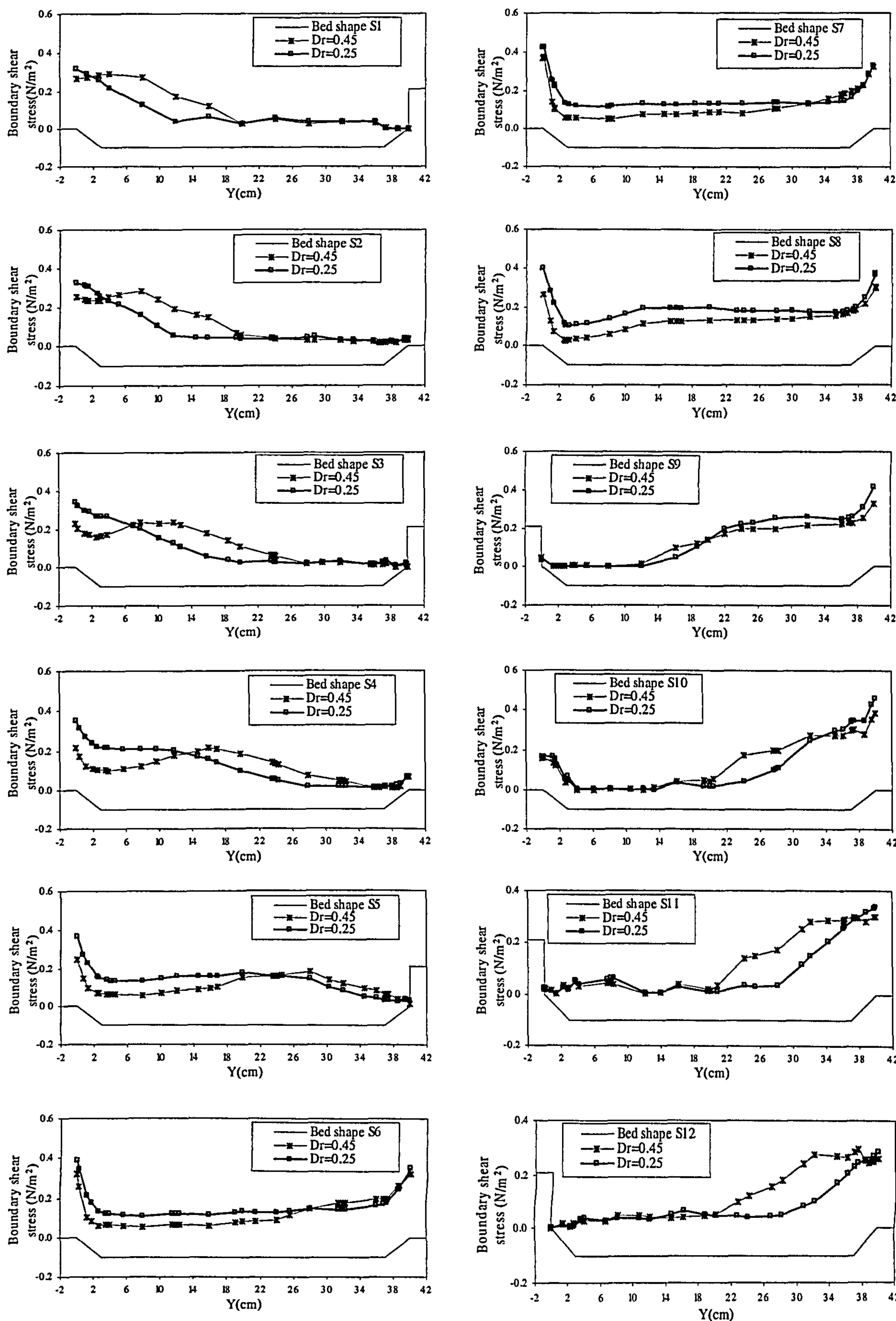


Figure 5.46: Predicted boundary shear stress for the main channel in *Case M Apex Block* for different relative depth,  $Dr$ , at sections S1 to S12



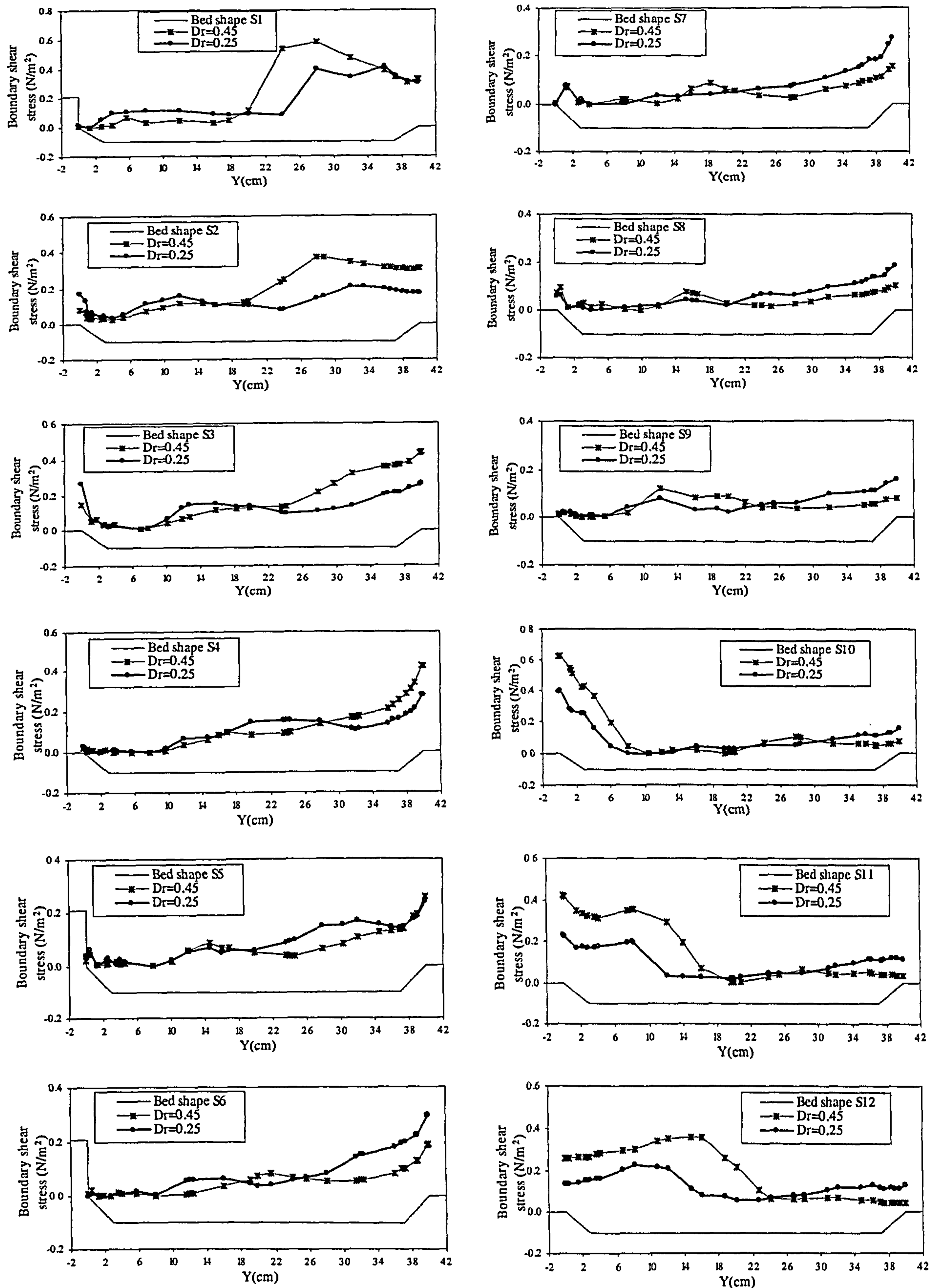


Figure 5.47: Predicted boundary shear stress for the main channel in *Case N Cross-over Block* for different relative depth,  $Dr$ , at sections S1 to S12



### 5.11 Sectional Averaged Discharges Distribution

The discharges in the main channel were averaged over the flow depth using Equation (5.32) in order to determine the averaged sectional discharge ( $Q_m$ ).

$$Q_m = \sum_{i=1}^{i=m-1} 0.5(u_{ai} + u_{ai+1}) \times \Delta h_a / m_i \quad (5.32)$$

where,

$Q_m$  = main channel sectional averaged discharge

$m_i$  = total number of predicted points (i) over the depth of the main channel section

$u_a(i)$  = velocity predicted at (i)th and (i+1)th points respectively and at a height of  $\Delta h_a$

$h_a$  = the height of the predicted water depth of the section

The results of the observations are as shown in Figures 5.48 to 5.50. Figures 5.48 and 5.49 show the sectional averaged discharge distribution for twelve prediction sections in various cases for  $Dr = 0.25$  and  $Dr = 0.45$  respectively. It is clearly seen that the magnitude of the discharge is reduced at the cross-over section for all cases at  $Dr = 0.25$ . The lowest sectional averaged discharge distribution at the cross-over section is for *Case N Cross-over Block* due to the continuous blocks placed along the floodplain cross-over area. The averaged sectional discharge profiles exhibit an almost symmetrical pattern (mirror image) at both of the bend apexes, while the velocities were substantially reduced at the cross-over sections, particularly at  $Dr = 0.25$ . This result provides a good indicator of the significant effect of “cross-over” flow plunging from the floodplain into the main channel. However, for a higher relative depth at  $Dr = 0.45$  the sectional discharge profile for *Case M Apex Block* is quite different to those for cases *L* and *N*. It is apparent that the sectional averaged discharges are distributed quite uniformly in the range of 0.025 – 0.035 m<sup>3</sup>/s from sections S5 to S8 within the cross-over section then slightly decreased at section S9 and start to increase again in the apex bed region of sections S10 to S12.



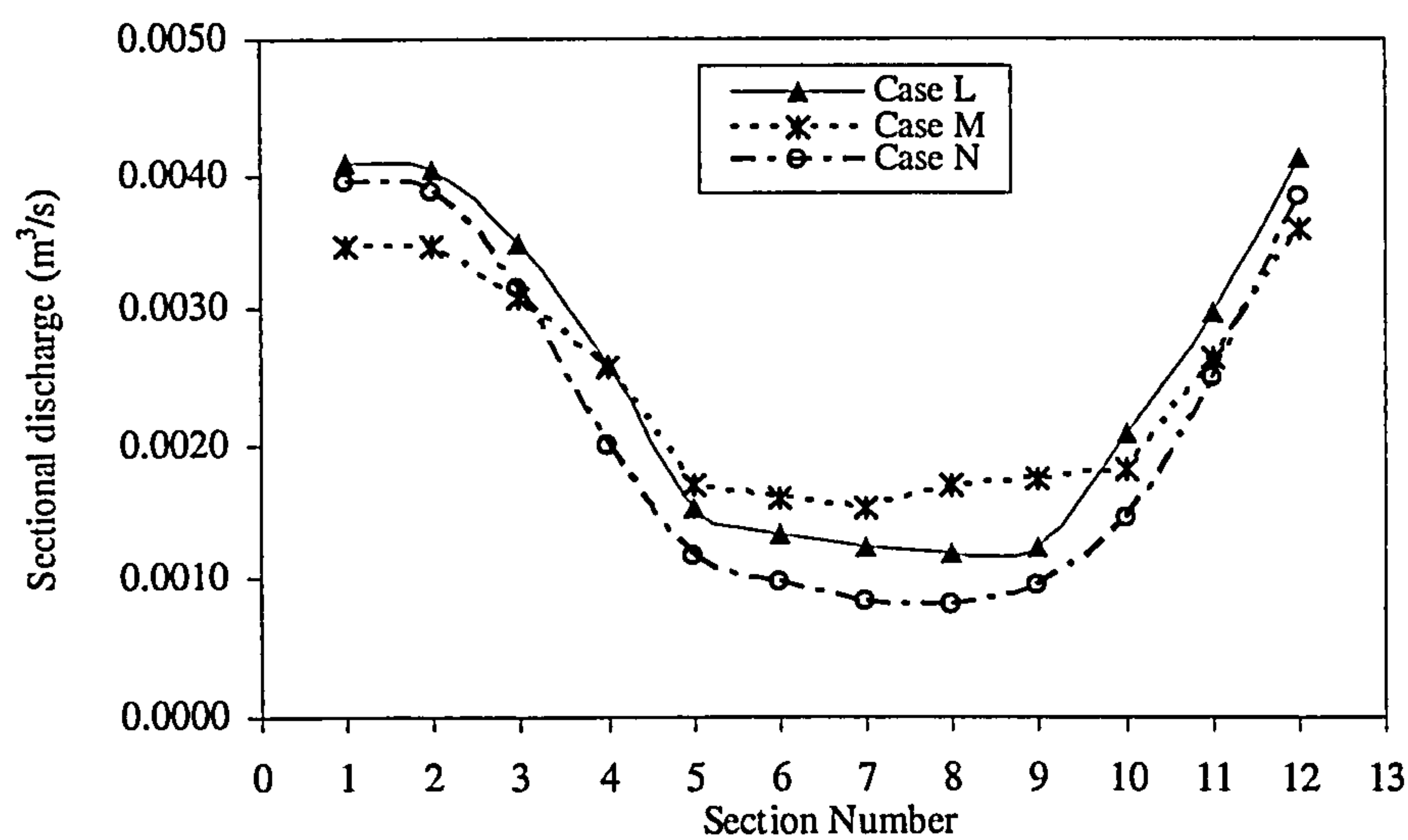


Figure 5.48: Variation of cross-sectional discharge in the main channel for cases no block *L*, apex block *M* and cross-over block *N* at  $Dr = 0.25$

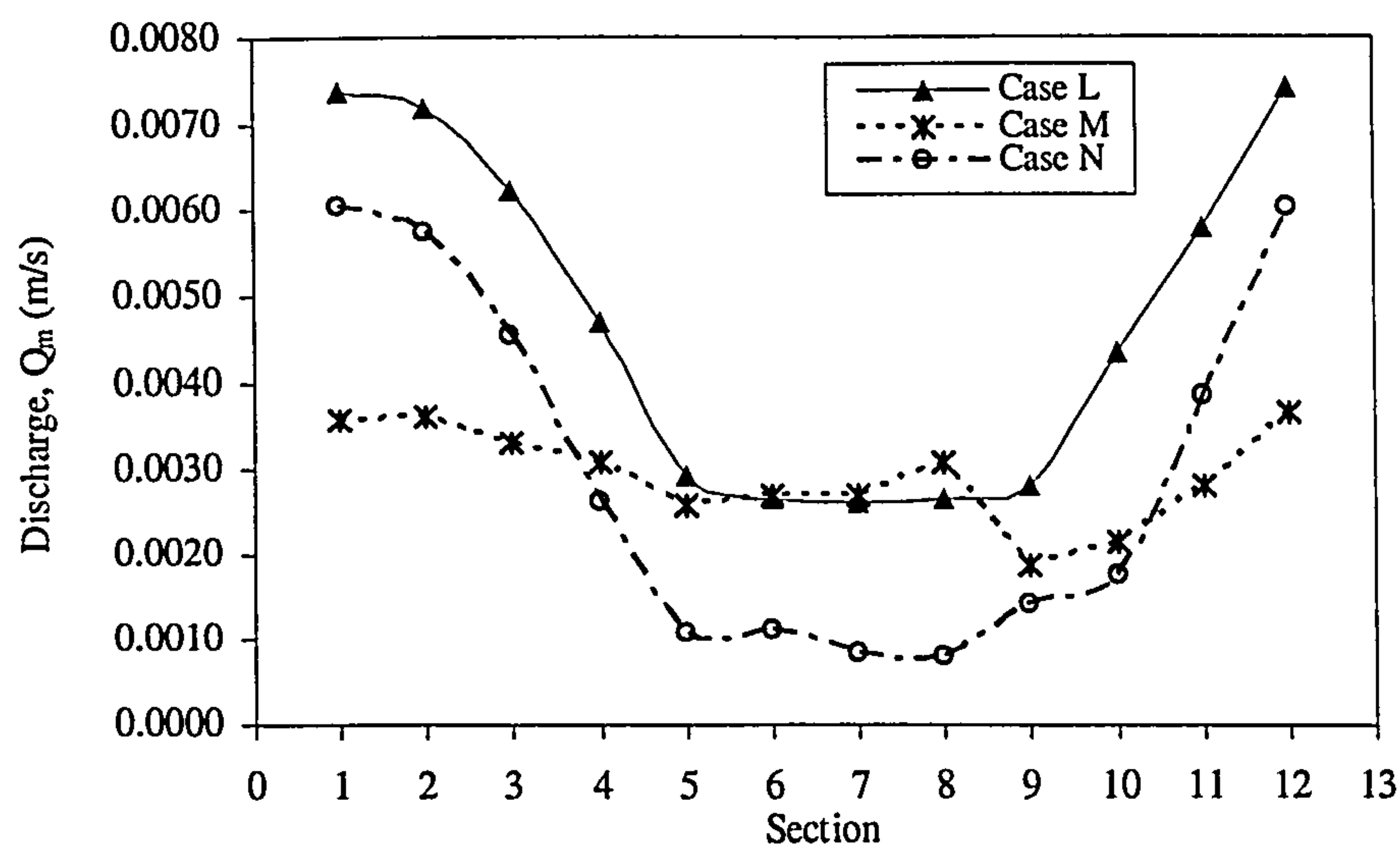


Figure 5.49: Variation of cross-sectional discharge in the main channel for cases no block *L*, apex block *M* and cross-over block *N* at  $Dr = 0.45$



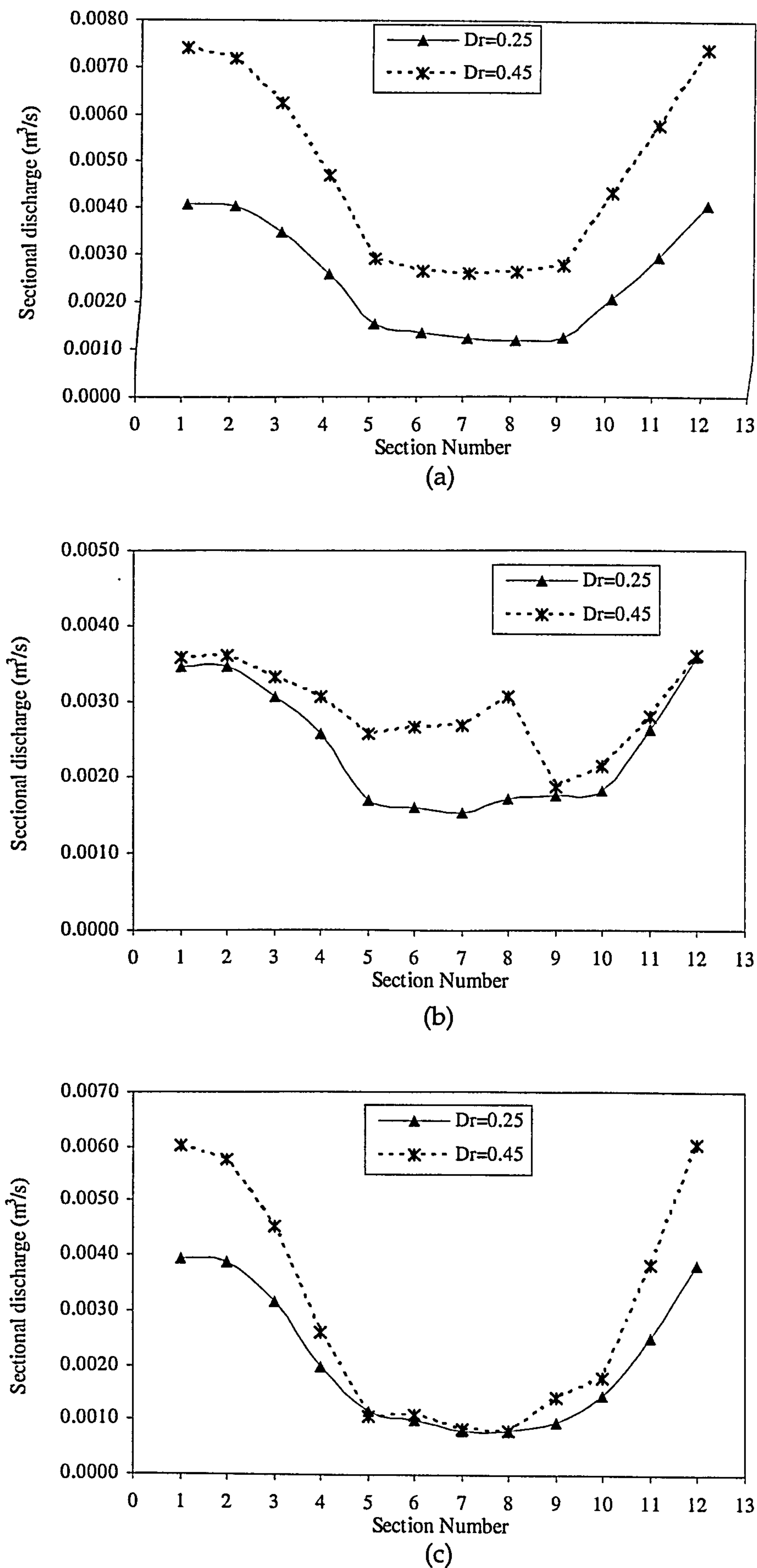


Figure 5.50: Variation of cross-sectional discharge in the main channel for different relative depth (a) Case L No Block (b) Case M Apex Block and (c) Case N Cross-over Block



### 5.12 Evaluation of Manning's $n$

In this section, the computed values of Manning's  $n$  were compared for cases with no blocks, apex blocks and crossover blocks and were considered in the light of the calculations in Chapter 4. Figure 5.51 shows a comparison between the computational results and calculated values of Manning's  $n$  for no blocks, apex blocks and cross-over blocks for  $Dr = 0.25$  and  $0.45$ . It is seen that good agreements of Manning's  $n$  are obtained when the computational simulation using Telemac in the case with no block, apex block and cross-over block were compared to the calculated values of Manning's  $n$  as in Chapter 4. Deviations from the line of perfect agreement showed that the relationship between computational Manning's  $n$  values by using the divided channel method and calculated values of Manning's  $n$  for two different relative depths for no blocks, apex blocks and cross-over blocks have most of the values falling within a limit of 10 %.

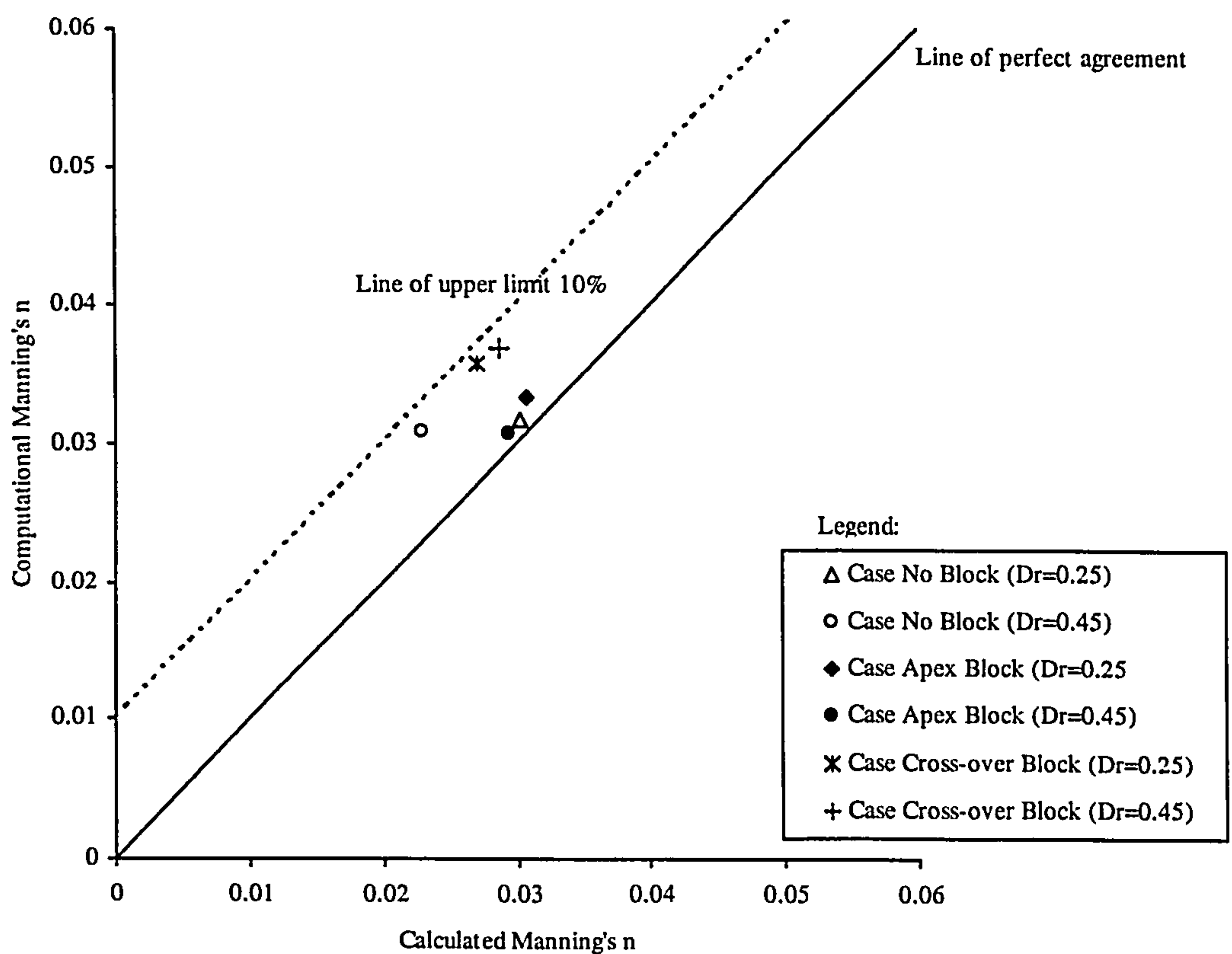


Figure 5.51: Comparison between simulation results of Manning's  $n$  values and calculated values of Manning's  $n$  for no block, apex block and cross-over block cases



### 5.13 Application of Projected Area Approach Velocity on Drag Force

In Chapter 4, the calculations of drag force over the weight component on one meander were discussed by using the average approach velocity. The value of  $F_D/w$  was greater than 1 for the higher density of blocks on the floodplain in certain cases. The reason for this might be that the approach velocity due to the project area of the block is much larger than the averaged velocity. Although the limited computation results for cases cross-over block  $N$  and apex block  $M$  for two different relative depths, this section will demonstrate the effect of the projected area approach velocity calculated from the predicted velocity on the drag force for the different vegetated floodplain cases being considered.

In the previous section, the vegetated floodplain cases show that the simulation results of depth-averaged velocity vector fields are different at the outer and inner edges of the meander belt depending on the placement of the blocks on the floodplain. Because of this, the computed projected area approach velocity is used to calculate the drag force and compared to the calculated average velocity as follows:

$$F_D = \frac{\rho C_D A_p v_p^2}{2} \quad (5.33)$$

where,

$\rho$  = water density

$C_D$  = the drag coefficient for the block ( $C_D = 1.85$  used in this study)

$v_p$  = projected area approach velocity

$A_p$  = projected area of the block in the streamwise direction

Figure 5.52 shows the plot of relative depth,  $Dr$ , versus  $F_D/w$  for cases apex block  $M$  and cross-over block  $N$  when the average velocity and projected area approach velocity are applied. It can be seen that the values of  $F_D/w$  for a lower relative depth of  $Dr = 0.25$ , are quite similar for both cases. However, for a higher relative depth of  $Dr = 0.45$ , it is clearly shown that the values of the drag force over the weight component are reduced by 22% and 28% for cases apex block  $M$  and cross-over block  $N$  respectively.



This shows the need to use the projected area approach velocity rather than the average velocity to predict the drag force over one meander wave length.

In addition, the correction parameter for the effect of block,  $\alpha$  was discussed in detail for each case for rectangular main channel cross-section in Chapter 4. It should be noted that this  $\alpha$  contains the main effect of  $v_p/v$ , and also some effects of the drag coefficient,  $C_D$ , and the interaction of block wakes with the main channel flow. Due to that, a similar way to calculate  $\alpha$  in Chapter 4 was carried out using both average velocity and computational approach velocity in order to see  $\alpha$  variations for trapezoidal main channel cross-section.

Figure 5.53 shows the relationships between  $\alpha$  and relative depth,  $D_r$  for cases apex block  $M$  and cross-over block  $N$  when the average velocity and computed projected area approach velocity were applied. When comparing  $\alpha$  values calculated by the averaged velocity with those obtained from the computational approach velocity, they agree reasonably well in deeper overbanks flows, but have a little discrepancy in the shallow water depth. Therefore, the correction factor  $\alpha$  can be used to estimate a stage-discharge rating curve even the averaged velocity is used as long as the  $\alpha$  value is calibrated well. This confirms that the concept of force balance with boundary friction factor and correction  $\alpha$  described in Chapter 4 appears to be reasonable.

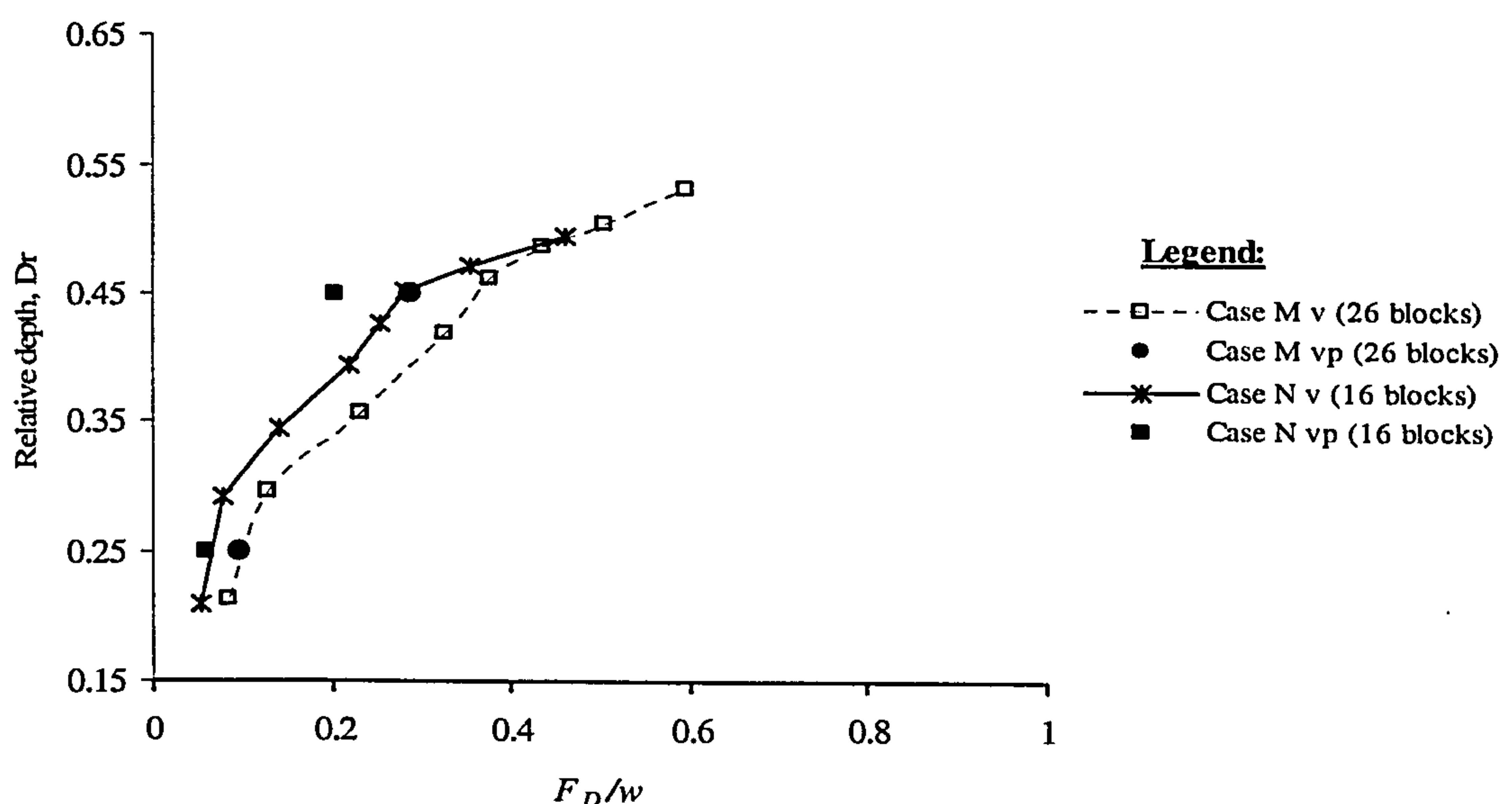
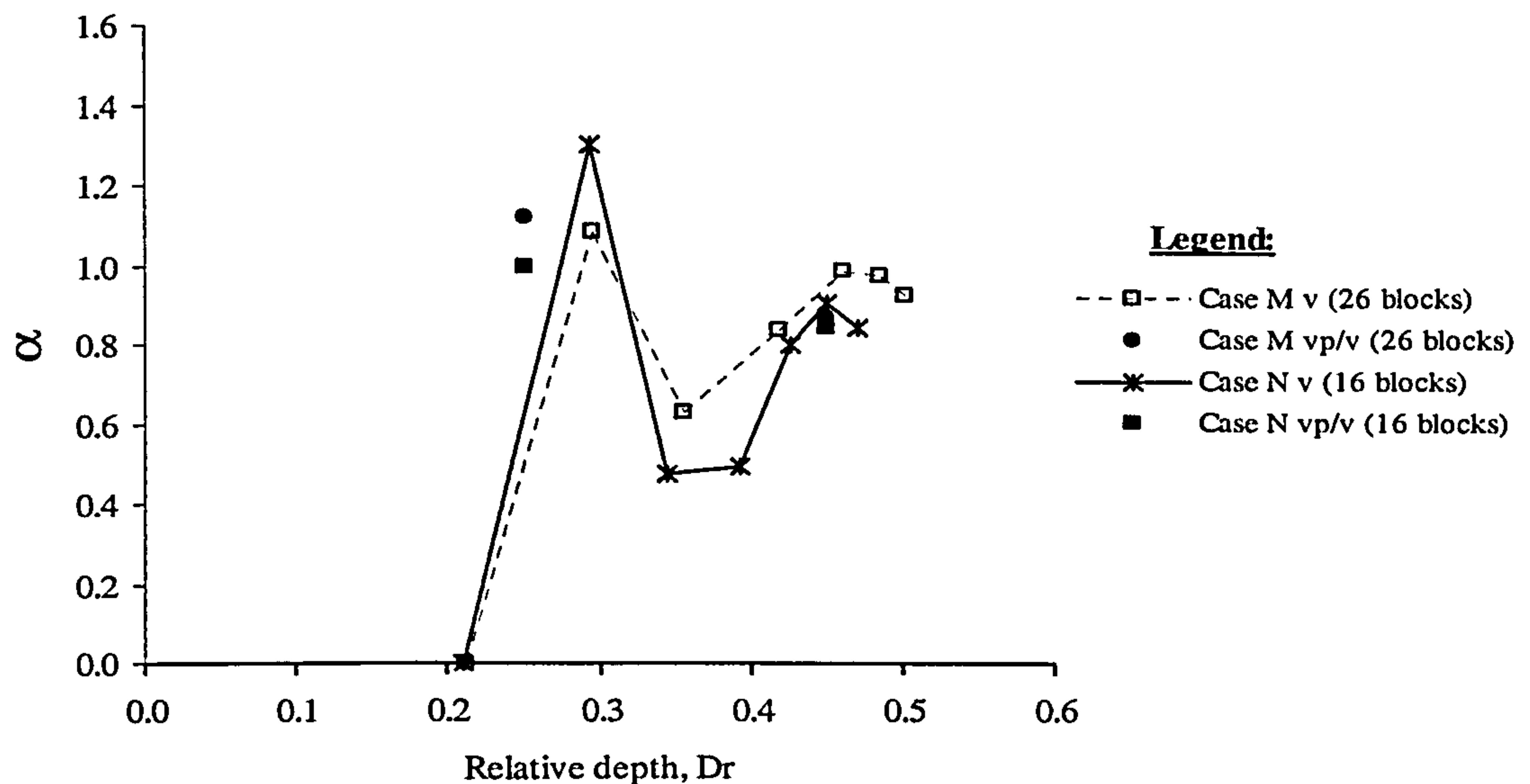


Figure 5.52: Comparison between the average velocity,  $v$  and the projected area approach velocity,  $v_p$  on relative depth versus  $F_D/w$  for cases apex block  $M$  and cross-over block  $N$  respectively





**Figure 5.53:** Comparison between the average velocity,  $v$  and the projected area approach velocity,  $v_p$  on  $\alpha$  versus relative depth for cases apex block  $M$  and cross-over block  $N$  respectively

## 5.14 Discussion of Results

This chapter firstly presented the comparisons and the validation of the computational results with the experimental data for the different flow cases. The methodology of this research into meandering compound channels with the present of vegetation makes comparisons with that of other authors difficult. Particular attention was paid to assessing the numerical model's ability to reproduce the important mean flow characteristics observed from the measurement data. In general, the computation using Telemac 3D used to predict the velocity for the case of overbank flow for a meandering channel with both non-vegetated and vegetated floodplains is in very good agreement with the measured data in the main channel. Also, reasonably good agreements between the measured and predicted boundary shear stress as well as the free-surface are observed in the main channel for non-vegetated and vegetated floodplains cases. The results show important differences between the flow characteristics in the non-vegetated and vegetated floodplain cases. The most significant and important of which is that the velocity and conveyance in the cases of the main channel with a vegetated floodplain is reduced compared to that in the non-vegetated floodplain case.



The depth-averaged velocity vector field for the non-vegetated floodplain case shows that the main channel flow generally follows the direction of the meander channel. The maximum velocity filament in the main channel stays close to the inner bank sidewall at the upstream apex and moves progressively to the outer bank as it approaches the downstream apex. However, the main channel flow deviates at an angle away from the meander streamline direction for higher flow depths. In the *Case M Apex Block*, the small velocity filament in the main channel occurs relatively near to the inner bank sidewall at the upstream apex bend and higher intensification of the vortices occurs behind the blocks at the outer bank as it approaches the downstream bend apex. However, for *Case N Cross-over Block*, along the cross-over section, the higher vortices occur near to the inner bank of the main channel behind the blocks and at the end of the cross-over section there are strong vortices produced by the blocks. Therefore, in general, the main channel flow structures are significantly different from those for the non-vegetated floodplain case.

The overall velocity magnitudes were found to be smaller for the vegetated floodplain cases as compared to the non-vegetated floodplain case. This reflects the significant importance of the flow resistance induced by the block roughness. The main channel velocity was also found to be greatly influenced by the arrangement of floodplain roughness. For the higher overbank flow, there are patterns of diverging and converging velocity vectors caused due to a series of blocks in the vegetated floodplain case. This indicates that large vortex interactions and wakes occurred within the main channel behind the blocks, which are strongly associated with the nature of the flow structures in a meandering channel for the vegetated floodplain cases.

The most interesting feature of the compound meandering channel flow is the behaviour of the secondary flow. The difference in flow structures for non-vegetated and vegetated floodplain flows in the main channel over a half wavelength is investigated by detailed numerical simulation. In addition, making the selected measurements also confirmed and clarified the originating and developing processes of flow for all the cases considered.

The secondary flow patterns are different for the *Case L No Block* and the cases apex block *M* and cross-over block *N*. For the non-vegetated floodplain, the number of



secondary flow cells in the main channel is attributed to the flow depth on the floodplain and the location of the section. In the vegetated floodplain cases, for higher flow depths, there are multiple secondary flow cells across the apex section in both vegetated floodplain cases. For the higher relative depth condition, it was particularly interesting to relate the flow mechanisms and its characteristics to the sediment transport rates in the vegetated floodplain cases due to the block arrangement in the same part of the floodplain in order to see which flow resistance was caused by the floodplain vegetation and which reduced the main channel streamwise velocity and bed shear stress. *Case N Cross-over Block* with continuous blocks along the cross-over section, particularly the vortices and wake extending directly across the cross-over section, are a feature of the secondary flows that have not been shown before. In general, *Case N Cross-over Block* with a roughened floodplain showed that the secondary flow cell is more vigorous in structure compared to *Case M Apex Block*. This subsequently leads to a larger energy loss.

In the *Case L No Block*, the maximum boundary shear stress in the main channel generally follows the maximum filament. It was noticeable that the maximum boundary shear stress in the main channel moves toward the convex side of the inner bank as the flow depth increases. The redistribution of the maximum boundary shear stress filament along the channel sections indicates that the shear interaction reduces with the increase of flow depth. The main channel boundary shear stress values in the vegetated floodplain cases apex block *M* and cross-over block *N* were found to be smaller in magnitude as compared to the non-vegetated floodplain *Case L No Block*. However, the boundary shear stress values vary in different locations across the main channel and depend directly on the arrangement of the blocks along the meandering channel.

The patterns of reduction in the sectional-averaged discharge are quite different between the non-vegetated and vegetated floodplain cases, where the lowest mean discharge can be seen for cases apex block *M* and cross-over block *N*. This reflects that the loss of energy due to the momentum exchange effect caused by the block arrangement is greatest for both vegetated floodplain cases. Also, a comparison of computational simulation and calculated Manning's  $n$  using Manning's equation shows that the usage of the computational results for no block, apex block and cross-



over block data agrees satisfactorily with the calculated results. The results show that values of Manning's  $n$  fall within 8% for higher relative depths and 3% for lower relative depths of the upper limits respectively when the Manning's  $n$  equation was compared using calculated values.

The calculations of the drag force over one meander wave length by using the average approach velocity show the imbalanced force due to the higher value of the drag force on a vegetated floodplain for higher relative depths. However, using the limited computational projected area approach velocity would give an appropriate prediction for the drag force over one meander wavelength. In addition, the concept of force balance with the boundary friction factor and the correction parameter  $\alpha$  has been well proved when the average velocity and computed projected area approach velocity were applied for cases apex block  $M$  and cross-over block  $N$  in the case of trapezoidal main channel cross-section.



# Chapter 6

## 6.0 Conclusions and Future Research Plans

Both experimental and computational investigations have been carried out to investigate the overbank flows in the non-vegetated and vegetated floodplain in compound meandering channels. Several series of experiments have been conducted at the Loughborough University Flume Facility to investigate the flow through rigid blocks for modelling the flow through rigid, unsubmerged vegetation on floodplains in a two-stage meandering channel. This present study had four main objectives:

- (1) To investigate the stage-discharge, flow resistance, drag force and bedforms in the non-vegetated and vegetated floodplain.
- (2) To carry out the influence of using different arrangements and vegetation density on the floodplain resistance to sediment transport.
- (3) To carry out further detailed analyses of mean flow mechanisms and secondary flow structures by considering the experimental data as well as Telemac computational results.
- (4) To assess the capability of the computational model to reproduce the important flow characteristics, flow mechanisms and boundary shear stress associated with non-vegetated and vegetated floodplains.

In Chapter 4, for all arrangements, the hydraulics data, such as stage-discharge, flow resistance, bedforms and sediment transport rate were collected at various relative depths varying from shallow overbank flow to high overbank flow. The data collected contributes to a better understanding of the flow characteristics and mechanisms induced by blocks on a floodplain and how they impinge on the main channel velocity and sediment transport rate behaviours in a meandering channel. In Chapter 5, the



fundamental flow structures in a meandering channel in the overbank flow case as well as in the meandering channels in vegetated floodplain cases have been elucidated through detailed velocity simulations and measurements in order to validate selected cases as discussed in Chapter 4. A summary of the main findings and general conclusions for some applications of the results to engineering matters are drawn from the present study and set out below.

- All experiments, both fixed-bed and mobile-bed channels, were carried out for different arrangements and densities of blocks on floodplains under quasi-uniform flow conditions. The fixed bed channel is more efficient in flow conveyance when compared to the mobile bed channels. Stage-discharge for both cases increases almost linearly with flow depth. However, the conveyance efficiency tends to become relatively similar in both cases as overbank flow becomes deeper. This indicates that the flow resistance in the compound channel has a minimum effect to the overall conveyance at high overbank flow. The fixed bed vegetated floodplain case suggests that the roughness elements might induce additional flow resistance to the floodplain flow, and in turn, increase the shear interaction which causes flow reduction in the main channel flow. However, in mobile bed cases, there is a tendency for the main channel flow resistance to increase because of a significant variation of bedform patterns with the increase of flow depth. The flows passing through these standing bedforms create flow separation, which in turn induced a higher flow resistance. The present study shows that the conveyance efficiency in the low density of *Case D Combined Apex and Cross-over Block*, is up to 25 % more than the higher density, and the efficiency is lower at the higher stage for the higher block density.
- All the values of Manning's  $n$  were found to be within the accepted range of Manning's  $n$  as reported by Chow (1959). It was noticed that a similar trend of flow resistance between apex block and cross-over block cases existed for the fixed bed case. However, the flow resistance for the apex block for the higher density of blocks is higher than those for the cross-over block cases. This indicates an increase in drag force as block density increases in the apex block case. The flow resistance for apex block *B1* is approximately 20% greater than



those for apex block cases *B2* and *B3* and all cross-over block cases. This is due to the values of Manning's  $n$  account for the effects of the flow and the vegetation density. This was clear by noticing the significant increase in the Manning's  $n$  values as the density of the blocks increases. Also, the effect of the blocks on flow depth was clearly observed for each arrangement. It was also noticed that the Manning's  $n$  values are more affected by the change in the density of the arrangement of the blocks. The results of this study also show a clear correlation between the value of Manning's  $n$  and the density of the block

arrangement given as  $(V_{den} = \frac{C_D \sum A_p}{AL})$ . With a similar main channel configuration, the lower density of blocks on the floodplain conveys water more efficiently compared to the higher density of blocks. The conveyance efficiency in the smooth floodplain channel is up to 50% greater than the roughened floodplain channel. The efficiency reduces as the overbank flow depth increases.

- The observation of the bedform changes showed that, for the case with no blocks for higher flow depth, ripples were seen in the main channel. This indicates that the flow resistance becomes more homogeneous at the high overbank flow depth. However, in the vegetated floodplain case, the results show that those arrangements of blocks show a significant variation of bedform patterns in the main channel, which are totally influenced by sediment movement in the main channel. This is very important because understanding the flow phenomenon happening behind the blocks, especially the bedforms' morphology, has implications for engineers when designing riverbed and riverbank protection schemes in vegetated meandering rivers.
- The flow depth at which sediment discharge starts to increase depends on the floodplain roughness. The roughness elements of the floodplain induce different flow resistance in the main channel, and, in turn, the velocity depends on roughness, but at higher overbank flow, the resistance due to the floodplain's roughness is less significant to the overall flow. Rameshwaran *et al.* (1999) gave the reason for the decrease in the sediment transport rate in a meandering compound channel. Relatively slow floodplain flow, compared



with the meandering channel flow, enters the main channel in the cross-over section, which reduces the velocity in the main channel by momentum transfer due to interfacial turbulence at the bankful level. This interfacial turbulence also interacts with the bed and develops irregular bedforms, which has been observed by Shiono *et al.* (2001), meaning that an increase in flow resistance in the main channel occurs, which results in a substantial reduction of the velocity in the main channel. In the present study, the sediment transport rate for *Case G Cross-over Block*, gives a better efficiency for conveying water and generally contributes a minimum amount to the sediment transport rates in the case of vegetation along the cross-over section. In general, the amount of sediment load migrating along the main channel is increased as discharge and flow depth increases except for *Case H Combined Apex and Cross-over Block*, which has the highest vegetated floodplain along both sides of the main channel in which sediment transport rates were smaller over the flow depths. That this due to the reduced velocity in the main channel can be proved by the bedform friction factor for higher overbank flow, which is seen to be higher at up to 300% for the rough combined apex and crossover floodplain block case. In general, all cases show higher percentages of bedform friction factor as the number of blocks increases, which agree with Lyness *et al.* (1998).

- A new method, based on the force balance over one meander for various block cases, was introduced by considering forces over one meander for quasi-uniform flow for predicting discharge in the vegetated floodplain case. According to this, by knowing the correction parameter for the effect of blocks,  $\alpha$ , water depth and geometry, the discharge can be worked out by using a successive approximations' method or the Newton Rapson Method for solving non-linear equations. It should be noted that this prediction equation was validated using limited computational velocity data. However, the present study gives a general idea of  $\alpha$  and, most importantly, it is easy to apply in both the flume and field when the value of  $\alpha$  is well-calibrated for stage-discharge estimation.



The computational investigations were carried out to understand the mean flow mechanisms and the secondary flow structures in the compound meandering channels. The experimental data was collected at the small-scale meandering channel model only for higher relative depths. The important observations, findings and the original contributions of this phase are now summarised.

- Non-vegetated floodplain *Case L No Block*, and vegetated floodplain cases apex block *M* and cross-over block *N* show that the streamwise velocity, secondary flow, free-surface elevations and bed shear stresses were predicted reasonably well for both flow depths. In the non-vegetated floodplain case it was noticed that the measured and the predicted primary and secondary flows and turbulent kinetic energy (*TKE*) confirm the vigorous interaction between the main channel and the floodplain, particularly in the cross-over region. The mean flow velocities ( $U$ ,  $V$  and  $W$ ), free-surface elevations and bed-shear stresses were predicted reasonably well. This implies that the turbulent stress terms in the momentum equations are not significant for the prediction of the mean flows. This also confirmed that the Telemac finite element model can be used to predict velocity and boundary shear stress in the main channel of a meandering channel river for overbank flow in both non-vegetated and vegetated floodplains, therefore Telemac can be used to solve practical river engineering problems such as bank erosion, local bed scour and sediment transport rates.
- The overall velocity magnitudes were found to be smaller for the vegetated floodplain cases as compared to the non-vegetated floodplain case. This reflects that flow resistance induced by the block roughness is significantly important. The main channel velocity was also found to be greatly influenced by the arrangement of the floodplain roughness. In general, the three-dimensional numerical model predicted the important flow features associated with vegetated floodplain cases of the compound meandering channels reasonably well. The minimum shearing of the main channel flow by the floodplain flow plunging into and over the main channel was observed from the cross-sectional distributions of the secondary flow vectors for *Case N Cross-over Block*. The small gradients of the streamwise velocity and vertical



velocity at the inner bankful level, particularly in the cross-over region, therefore the shear interaction between the floodplain flow and the main channel flow is significantly less taken place. However, there are distinct velocity difference between the upper layer and lower layer in the inner side of the main channel (i.e. slower flow in the upper layer and faster flow in the lower layer) even the large relative depth. This means that the flow in the lower layer is retardant, rather than acceleration by the upper layer flow in no block *L* and apex block *M*. The present study suggests that the planting of trees and shrubs along the cross-over section is the better way for planning and managing the development of vegetation on floodplains and confirms that any vegetation or arrangement located in the cross-over area can have a minimal impact on water level, flow resistance and sediment transport rate.

- This present study also confirmed that the projected area approach velocity would give an appropriate prediction for the drag force over one meander wavelength. In addition, the concept of force balance with the boundary friction factor and the correction parameter  $\alpha$  has been well-proved when the average velocity and computed projected area approach velocity were applied for cases apex block *M* and cross-over block *N* in the case of a trapezoidal main channel cross-section, especially for higher flow depth where the values of the drag force over the weight component are reduced by 22% and 28% for apex block *M* and cross-over block *N* cases respectively. This shows the need to use the projected area approach velocity rather than the average velocity to predict the drag force over one meander wave length.

It is felt that the flow structure in the vegetated floodplain in the overbank flow is now better understood and this will in turn lead to improved control of flows for these sorts of channels in engineering applications. Nevertheless, there are several important topics and factors which have not been dealt with here. For example, comprehensive studies should be carried out to obtain the best approach for estimating the drag force when dealing with a meandering compound channel in a vegetated floodplain. The present study shows that some arrangements and densities of blocks contribute a higher value for the drag force. This is due to the average velocity being used is higher in magnitude than the approach velocity in the projected area. This is confirmed by the



computational result. Continuation to this, correction coefficient  $\alpha$  is the parameter used to take into account the effect of the blocks. However,  $\alpha$  has been shown to vary in the fixed bed case for different arrangements of vegetated floodplain in meandering channels. Although the present study gives a general idea of  $\alpha$ , further work will be needed to verify the dependence of this term by obtaining more experimental, computational, or field data and to find a better way of quantifying the value of  $\alpha$  and its associations with other parameters to enable this approach to be used confidently and universally in all flow conditions. However, one of the main objectives of this thesis was to give a picture of the flow structure of non-vegetated and vegetated floodplains, in the case of overbank flow in a meandering compound channel this has been achieved. Nevertheless, the range of channels studied here is insufficient. Many parameters which could be the determinants for the flow structure, such as the channel aspect ratio, the wall roughness, the sinuosity of the floodplain banks and their relative phase to that of the main channel have not been investigated and must be of interest to those looking at the conveyance/transport of sediment and erosion/deposition. A further research programme exploring these parameters will give a more comprehensive understanding of these sorts of flow mechanisms, especially in the presence of vegetated floodplain roughness.



# References

- Ackers, P. (1991). "Hydraulic Design of Straight Compound Channels." *Report SR 381*, HR Wallingford Ltd, UK.
- Al-Romaih, J. S. (1995). "Stage-Discharge Assessment in Meandering Channels." *PhD Thesis*, University of Bradford, UK.
- Bathurst J. C., Thorne C. R., & Hey R. D. (1979). "Secondary Flow and Shear Stress at River Bends." *Journal of Hydraulics Division*, Vol. 105, No. 10, pp. 1277-1295.
- Biron, P. M., Richer, A., Kirkbride, A. D., Roy, A. G., & Han, S. (2002). "Spatial Patterns of Water Surface Topography at River Confluence." *Earth Surface Processes and Landforms*, Vol. 27, pp. 913-923.
- Bousmar, D. (2002). "Momentum Transfer between Main Channel and Prismatic or Non-Prismatic Floodplains." *PhD thesis, Universite' catholique de Louvain, Louvainla- Neuve*, Belgium.
- Bousmar, D., & Zech, Y. (1999). "Momentum Transfer for Practical Flow Computation in Compound Channels." *Journal of Hydraulic Engineering*, Vol. 125, No. 7, pp. 696-706.
- Brooks, A., & Hughes, T. (1982). "Streamline Upwind/Petrov-Galerkin Formulations for Convection Dominated Flows with Particular Emphasis on the Incompressible Navier-Stokes Equations." *Computer Methods in Applied Mechanics and Engineering*, Vol. 32, pp. 199-259.
- Bruce, R. M., Donald, F. Y. & Theodore, H. O. (1994). "Fundamentals of Fluid Mechanics." *John Wilay and Son, Inc*, New York.
- Cassells, J. (1998). "Hydraulic Characteristics of straight Mobile Bed Compound Channels with Uniform Sediment." *Ph.D Thesis*, University of Ulster.
- Casulli, V., & Stelling, G. S. (1998). "Numerical Simulation of 3D Quassi-Hydrostatic Free-Surface Flows." *Journal of Hydraulic Engineering*, Vol. 124, No. 7, pp. 678-686.
- Chan, T. L. (2003). "A Study of Sediment Transport in Two-Stage Meandering Channel." *Ph.D Thesis*, Loughborough University, U.K.
- Chow, V. T. (1959). "Open Channel Hydraulics." *McGraw-Hill Book Co.*, New York.
- Cruise, J. F., Singh, V. P., & Sherif, M. (2003). "Elementary Hydraulics."



- Chang, H. H. (1984). "Variation of Flow Resistance through Curved Channels." *Journal of Hydraulic Engineering*, Vol. 110, No.12, pp. 1772-1782.
- Chang, Y. C. (1971). "Lateral Mixing in Meandering Channels." *PhD thesis*, Univ. of Iowa, Iowa city, Iowa.
- Cokljat, D., & Younis, B. A. (1995). "Second-Order Closure Study of Open-Channel Flow." *Journal of Hydraulic Engineering*, Vol. 121, No. 2, pp. 94-107.
- Conti, C., Morandi, R., & Scaramelli, D. (2004). "Using Discrete Uniformity Property in a Mixed Algebraic Method." *Journal of Applied Numerical Mathematics*, Vol. 49, No. 3-4, pp. 355-366.
- Dalrymple, R. A. (1985). "Physical Modelling in Coastal Engineering." 1<sup>st</sup> ed. *University of Delaware*, Newark: Balkema.
- Dargahi, B. (2004). "Three-dimensional Flow Modelling and Sediment Transport in the River Klarälven." *Earth Surface Processes and Landforms*, DOI: 10.1002/esp.1071.
- Djordjevic, S. (1993). "Mathematical Model of Unsteady Transport and its Experimental Verification in Compound Channel Flow." *Journal of Hydraulic Research, IAHR*, Vol. 31, No. 2, pp. 229-248.
- Ervine, D. A., & Ellis, J. (1987). "Experimental and Computational Aspects of Overbank Floodplain Flow." *Transaction of the Royal Society of Edinburgh: Earth Sciences*, Vol. 78, pp. 315-325.
- Ervine, D. A., & Jasem, H. K. (1989). "Flood Mechanism in Meandering Channels with Floodplain Flow." *Proceedings of the XXIII IAHR Congress*, Ottawa, Canada, 21-25 August 1989, pp. B449-B456.
- Ervine, D. A., Willetts, B.B., Sellin, R. H. J., & Lorena, M. (1993). "Factors Affecting Conveyance in Meandering Compound Flows." *Journal of Hydraulic Engineering*, Vol. 119, No.12, pp. 1383-1399.
- Ervine, D. A., & Jasem, H. K. (1995). "Observations on Flows in Skewed Compound Flows." *Proc., Instn. Civ. Engrs.*, London, Vol. 112, No. 3, pp. 249-259.
- Ervine, D. A., Babaeyan-Koopaei, K., & Sellin, R. H. J. (2000). "Two-dimensional Solution for Straight and Meandering Overbank Flows." *Journal of Hydraulic Engineering*, Vol. 126, No. 9, pp. 653-669.
- Falconer, R. A., & Lin, B., (1997). "Three-dimensional Modelling of Water Quality in the Humber Estuary." *Water Research*, IAWQ 31(5).
- Fathi-Mghadam, M., & Kouwen, N. (1997). "Nonrigid, Nonsubmerged Vegetation Roughness on Floodplains." *Journal of Hydraulic Engineering*, Vol. 123, No. 1, pp. 51-57.
- Ferguson, R. I., Parsons, D. R., & Dunne, T. (2003). "Flow in Meander Bends with Circulation at the Inner bank." *Water Resources Research* 39, 2003WR001965.



- Ferziger, J., & Peric, M. (1996). "Computational methods for fluid dynamics." *Springer-Verlag*, Berlin Heidelberg New York.
- Fischer, H. B., List, E. J. Koh, R. C. Y., Imberger, J., & Brooks, N. H., (1979). "Mixing in Inland Waters." *Academic Press*, San Diego.
- Fukuoka, S., & Fujita, K. (1989). "Prediction of Flow Resistance in Compound Channels and Its Application to Design of River Courses." *Proc. JSCE*, Vol. 411, pp. 63-72 (in Japanese).
- Gerhart, P. M., & Gross, R. J. (1985). "Fundamentals of Fluid Mechanics." *Addison Wesley Publishing Co.*, Don Mills, Ontario.
- Greenhill, R. K., & Sellin R. H. J., (1993). "Development of a Simple Method to Predict Discharge in Compound Meandering Channels." *Proc. of Instn. of Civ. Engrs. Wat., Marit. & Energy*, Vol. 101, pp. 37-44.
- Henderson, F. M. (1966). "Open Channel Flow." *MacMillan Publishing Co.*, New York.
- Hervouet, J. -M. (2000). "TELEMAC Modelling System: an Overview." *Hydrological Processes*, Vol. 14, pp. 2209-2210.
- Hervouet, J. -M., & Van Haren, L. (1996). "Recent Advances in Numerical Methods for Fluid Flows." *Floodplain Processes*, Edited by M.G. Anderson, D.E. Walling and P.D. Bates, John Wiley and Sons Ltd, Chapter 6, pp. 183-214.
- Hicks, F. E. (1985). "Shear and Velocity Near a Sloped Bank in a Curved Channel." *MS thesis*, Univ. of Alberta, Edmonton, Alta., Canada.
- Hughes, S. A. (1993). "Physical Models and Laboratory Techniques in Coastal Engineering." *Singapore: World Scientific Publishing Co. Private Ltd.*
- James, C. S., & Wark, J. B. (1992). "Conveyance Estimation for Meandering Channels." *Report SR 329*, HR Wallingford Ltd, UK.
- James, C. S. (1994). "Evaluation of methods for Predicting Bend Loss in Meandering Channels." *Journal of Hydraulic Engineering*, Vol. 120, No. 2, pp. 245-253.
- James, C. S., & Myers W. R. C., (2001). "Conveyance of Meandering Channel with Marginal Vegetation." *Proc. of Instn. of Civ. Engrs. Wat., Marit. & Energy*, Vol. 148, pp. 97-106.
- Janin, J. -M., Marcos, F., & Denot, T. (1997). "Code Telemac3D-Version 2.2 Note Theorique.". *Tech. Rep. HE-42/97/049/B*, Electricite de France (EDF-DER), Laboratoire National d'Hydraulique.
- Jankowski, J. A. (1998). "A Non-Hydrostatic Model for Free Surface Flows." *PhD thesis*, University of Hannover, Germany.
- Jarvela, J. (2002). "Determination of Flow Resistance of Vegetated Channel Banks and Floodplains." *River Flow 2002*, Bousmar & Zsch (eds), pp. 311-318.



- Jordan, S. A., & Spaulding, M. L. (1993). "A Fast Algorithm For Grid Generation." *Journal of Computational Physics*, Vol. 104, No. 1, pp. 118-128.
- Kadlec, R. H. (1990). "Overland Flow in Wetlands: Vegetation Resistance." *Journal of Hydraulic Engineering*, Vol. 116, No. 5, pp. 691-706.
- Kamphuis, J. W. (1985). "On Understanding Scale Effect in Coastal Mobile Bed Models." In *Physical Modelling in Coastal Engineering*, R.A. Dalrymple, Ed., A.A. Balkema, Rotterdam, pp.141-162.
- Khamayseh, A., Kuprat, A., & Mastin, W. (1999) "Boundary Orthogonality in Elliptic Grid Generation." in *Handbook of Grid Generation*, eds. Joe Thompson et al., CRC Press, pp. 6.1-6.26.
- Kiely, G. (1990). "Overbank Flow in Meandering Compound Channels – The Important Mechanism." *International Conference on River Flood Hydraulics*. W. R. White. Chichester, England, John Wiley & Sons, pp. 207-217.
- Kiely, G. K., & McKeogh, E. J. (1993). "Secondary Currents Rotations during Flood Flow in Meandering Channels." *Advances in Hydro-Science and Hydro-Engineering*, Vol. 1, pp. 1215-1225.
- Knight, D. W., Yuan, Y. M., & Fares, Y. R. (1992). "Boundary Shear in Meandering Channels." *Proc. of Instn. of Symp on Hydr Res. in Nature and Laboratory*. (Ed. C. Jisheng) Yangtze River Scientific Research Institute, Wuhan, published by the Yangtze River Scientific Research Institute, China, Vol. 2, pp. 102-107.
- Knight, D. W., Yuan, Y. M., & Al-Hamid, A. A. I. (1994). "Boundary Shear Stress Distribution in Open Channel Flow." *Mixing and Transport in the Environment*, pp. 102-107.
- Knight, D. W., & Shiono, K. (1996). "River Channel and Floodplain Hydraulics." *Floodplain Processes*, M. Anderson, D. Walling, P. Bates, eds., John Wiley and Sons, pp. 139-181.
- Knight, D. W., & Brown, F. A. (2001). "Resistance Studies of Overbank Flow in Rivers with Sediment Using the Flood Channel Facility." *Journal of Hydraulic Research*, Vol. 39, No. 3, pp. 283-301.
- Kouwen, N., & Fathi-Moghadam, M., (2000). "Friction Factors for Coniferus Trees along Rivers." *Journal of Hydraulic Engineering*, Vol. 126, No. 10, pp. 732-740.
- Lane, S. N., Bradbrook, K. F., Richards, K. S., Biron, P. A., & Roy, A. G. (1999). "The Application of Computational Fluid Dynamics to Natural River Channels: Three-dimensional versus Two-dimensional Approaches", *Geomorphology*, Vol. 29, No. 1-2, pp.1-20.
- Launder, B. E., & Spalding, D. B. (1974). "The Numerical Computation of Turbulent Flows." *Comput. Methods Appl. Mech. Eng.*, Vol. 3, pp. 269-289.



- Launder, B. E., Reece, G. J., & Rodi, W. (1975). "Progress in the Development of a Reynolds Stress Turbulence Closure." *Journal of Fluid Mechanics*, Vol. 68, pp. 537.
- Leopold, L. B., & Langbein, W. B. (1966). "River Meander." *Scientific America*, Vol. 214, No. 6, pp. 60-70.
- Leopold, L. B., & Wolman, M. G. (1957). "River Channel Patterns: Braided, Meandering and Straight." *U.S. Geol. Survey Professional Paper 282-B*, pp. 39-85.
- Liriano, S. L., Marriott, M. J., & Day, R. A. (2001). "Experimental Observations of Obstruction on Floodplains." *Proc. Of the XXIX IAHR Congress*, Vol. 1, pp. 332-337.
- Li, R. M. & Shen, H. W. (1973). "Effect of Tall Vegetations on Flow and Sediment." *Journal of Hydraulic Division*, Vol. 99, No. 5, pp. 793-814.
- Lin, B., & Fleming, C. A. (2003). "Three-Dimensional Hydrodynamic Model for Free Surface Flow." *Journal of Hydraulics Research*, Vol. 41, No. 4, pp. 367-377.
- Liu, W., & James, C. S. (1997). "Effects of Floodplain Geometry on Conveyance of Meandering Compound Channels." *HR Wallingford Limited*, pp. 81-90.
- Lorena, M. (1992). "Meandering Compound Flow." *Ph.D Thesis*, University of Glasgow, Glasgow, U.K.
- Lyness, J. F., Myers, W. R. C., & O'Sullivan, J. J. (1998). "Hydraulics Characteristics of Meandering Mobile Bed Compound Channels." *Proc. of Instn. of Civ. Engrs. Wat., Marit. & Energy*, Vol. 130, pp. 179-188.
- McKeogh, E. J., & Kiely, G. K. (1989). "Experimental Study of the Mechanics of Flood Flow in Meandering Channels." *Proc. 23<sup>rd</sup> IAHR Congress*, pp. B491-B498.
- Melville, B. W. & Sutherland, A. J. (1988). "Design Method for Local Scour at Bridge Piers." *Journal of Hydraulic Engineering*, Vol. 114, No. 10, pp. 1210-1226.
- Morvan, H. (2001). "Three-dimensional Simulation of River Flood Flows." *PhD thesis*, Univ. of Glasgow, U.K.
- Morvan, H., Pender, G., Wright, N. G., & Ervine, D. A. (2002). "Three-dimensional Hydrodynamics of Meandering Compound Channels." *Journal of Hydraulic Engineering*, Vol. 128, No. 7, pp. 674-682.
- Muto, Y., & Shiono, K. (1998). "Three Dimensional Flow Structure for Overbank Flow in Meandering Channels." *Journal Hydroscience & Hydraulics Engineering*, Vol. 16, No. 1, pp. 97-108.
- Myers, W. R. C., Knight, D. W., Lyness, J. F., Cassells, J. B., & Brown, F. (1999). "Resistance Coefficients for Inbank and Overbank flows." *Proc. of Instn. of Civ. Engrs. Wat., Marit. & Energy*, Vol. 136, pp. 105-115.



- Myers, W. R. C., Lyness, J. F., & Cassells, J. B. (2000). "Influence of Boundary Roughness on Velocity and Discharge in Compound River Channels." *Journal of Hydraulic Research*, Vol. 39, No. 3, pp. 311-319.
- Nepf, H. M. (1999). "Drag, Turbulence and Diffusion in Flow Through Emergent Vegetation." *Journal of Water Resource Research*, Vol. 5, pp. 271-279.
- Nezu, I., & Rodi W. (1985). "Open-Channel Flow Measurements with a Laser Doppler Anemometer." *Journal of Hydraulic Engineering*, Vol. 112, No. 5, pp. 335-355.
- Naot, D., Nezu, I., & Nakagawa, H. (1993). "Hydrodynamic Behavior of Compound Rectangular Open Channels." *Journal of Hydraulic Engineering*, Vol. 119, No. 3, pp. 390-408.
- Naot, D., & Rodi, W. (1982). "Calculation of Secondary Currents in Channel Flow." *Journal of Hydraulic Division, Am. Soc. Civ. Eng.*, Vol. 108, No. 8, pp. 948-968.
- Nicholas, A. P., & McLelland, S. J. (2004). "Computational Fluid Dynamics Modelling of Three-dimensional Processes on Natural River Floodplains." *Journal of Hydraulic Engineering*, Vol. 130, No. 7, pp. 727-728.
- Noda, E. K. (1972). "Equilibrium Beach Profile Scale-Model Relationship." *Journal of Waterways Harbors and Coastal Divison*, WWWW4, pp. 511-528.
- O'Sullivan, J. (1999). "Influence of Planform and Boundary Roughness on Conveyance, Flow Resistance and Sediment Load Prediction in Meandering Channel." *Ph.D Thesis*, Ulster University, Ireland.
- Olsen, N. R. B. (2003). "Three-dimensional CFD Modelling of Self-Forming Meandering Channel." *Journal of Hydraulic Engineering*, Vol. 12, No. 5, pp. 366-372.
- Patel, V. C. (1965). "Calibration of Preston Tube and Limitations on its Use in Pressure Gradients." *Journal of Fluid Mechanics*, Vol. 23, pp. 185-208.
- Patra, K. C., & Kar, S. K. (2001). "Flow Interaction of Meandering Channel River with Floodplains." *Journal of Hydraulic Engineering*, Vol. 126, No. 8, pp. 593-604.
- Patra, K. C., Kar, S. K., & Bhattacharya, A. K. (2004). "Flow and Velocity Distribution in Meandering Compound Channels." *Journal of Hydraulic Engineering*, Vol. 130, No. 5, pp. 398-411.
- Petryk, S., & Bosmajian, G. I. (1975). "Analysis of Flow through Vegetation." *Journal of Hydraulic Division*, Vol. 101, No. 7, pp. 871-884.
- Preston, J. H. (1954). "The Determination of Turbulent Skin Friction by Means of Pitot Tube." *Journal of Royal Aeronautics Society*, Vol. 58, pp. 109-121.
- Rameshwaran, P. (1997). "Conveyance Prediction for Meandering Two-Stage Channel Flows." *Ph.D Thesis*, University of Aberdeen, U. K.



- Rameshwaran, P., & Naden, P. S. (2003). "Three-dimensional Numerical Simulation of Compound Channel Flows." *Journal of Hydraulic Engineering*, Vol. 129, No. 8, pp. 645-652.
- Rameshwaran, P. & Naden, P. S. (2004a). "Modelling of Turbulent Flow in Two-Stage Meandering Channels." *Proceedings of the Institution of Civil Engineers - Water Management*, Vol. 157, No. 3, pp. 159-173.
- Rameshwaran, P., & Naden, P. S. (2004b). "Three-dimensional Modelling of Free-Surface Variation in a Meandering Channel." *Journal of Hydraulic Research*, Vol. 42, No. 6, pp. 603-615.
- Rameshwaran, P., Spooner, J., Shiono, K., & Chandler, J. H. (1999). "Flow Mechanism in Two-Stage Meandering Channel with Mobile Bed." *Instn. Assoc. for Hydr Res. XXVIII Biennial Congress*, Graz, Austria, D6, 259.
- Rameshwaran, P., & Shiono, K. (2002). "Predictions of Velocity and Boundary Shear Stress in Compound Meandering Channel." *River Flow 2002, International Conference on Fluvial Hydraulics*, Vol. 1, pp. 223-231.
- Rameshwaran, P., & Shiono, K. (2003). "Computer Modelling of Two-Stage Meandering Channel Flows." *Proceedings of the Institution of Civil Engineers - Water and Maritime Engineering*, Vol. 156, No. 4, pp. 325-339.
- Rameshwaran, P., & Willets, B. B. (1999). "Conveyance Prediction for Meandering Two-Stage Channel Flows." *Proc. of Instn. of Civ. Engrs. Wat., Marit. & Energy*, Vol. 136, pp. 153-166.
- Rhoads, B. L. (1996). "Mean Flow Structure of Transport-Effective Flows at an Asymmetrical Confluence When the Main Stream is Dominant." In Ashworth, P. J., Bennett, S., best, J. L., & McLelland, S. M. (Eds.). "Coherent Flow Structures in Open Channels." *Wiley, Chichester*, pp. 459-490.
- Richardson, E. V., & Davis, S. R. (1995). "Evaluating Scour at Bridges." 3<sup>rd</sup> Ed. *Hydraulic Eng. Circular, No. 18 (HEC-18)*, Publication No. FHWA-IP-90-017, U. S. Department of Transportation, Washington, D. C. 132.
- Rodi, W. (1993). "Turbulence Models and their Application in Hydraulics." A. A. Balkema, Rotterdam, The Netherlands.
- Rouse, H. (1965). "Critical analysis of Open Channel Resistance." *Journal of Hydraulic Divison*, Vol. 91, No. HY4, pp. 1-25.
- Rouve, G., & Schroder, M. (1992). "One-dimensional vs. Two-dimensional Prediction of Compound Open Channel Flow." *Proceedings of the First International Conference on Hydro-Scinece and Engineering*, Washington, DC, USA, 7-11 June 1993, Edited by S. S. Y. Wang, pp. 1197-1205.
- Samuels, P. G. (1985). "Modelling of River and Floodplain Flow Using the Finite Element Method." *Technical Report SR61*, HR Wallingford, U.K.



- Sellin R. H. J. (1964). "A Laboratory Investigation into the Interaction between the Flow in the Channel of a River and That over Its Floodplain." *La Houille Blanche*, Vol. 7, pp. 793-802.
- Sellin, R. H. J., Irvine, D. A., & Willetts, B. B. (1993). "Behaviour of Meandering Two-Stage Channels." *Proc. Instn. Civ. Engrs Wat., Marit. & Energy*, Vol. 101, pp. 99-111.
- Sellin, R. H. J., & Willets, B. B. (1996). "Three-Dimensional Structures, Memory and Energy Dissipation in Meandering Compound Channel Flow." *Floodplain Processes*, Edited by M.G. Anderson, D.E. Walling, and P.D. Bates, *John Wiley & Sons*, Chapter 8, pp. 255-297.
- Shao, X., Wang, H., & Chen, Z. (2003). "Numerical Modeling of Turbulent Flow in Curved Channels of Compound Cross-Section." *Adv. In Water Resources*, Vol. 26, pp. 525-539.
- Shiono, K., & Knight, D. W. (1989). "Transverse and Vertical Reynolds Stress Measurements in a Shear Layer Region of a Compound Channel." *Proc. of the Seventh Symposium on Turbulent Shear Flows*, Stanford University, USA.
- Shiono, K., & Knight, D. W. (1990). "Mathematical Models of Flow in Two or Multistage Straight Channels." *Proc. Int. Conf. on River Flood Hydraulics*, pp. 229-238.
- Shiono, K., & Knight D. W. (1991). "Turbulent Open-Channel Flows with Variable Depth across the Channel." *Journal of Fluid Mechanics*, Vol. 222, pp. 617-646.
- Shiono, K., & Muto, Y. (1993). "Secondary Flow Structure for Inbank and Overbank Flows in Trapezoidal Meandering Channels." *Proc., 5<sup>th</sup> Int. Symp. of Refined Flow Modl. and Turb. Measu.*, Paris (September), pp. 645-652.
- Shiono, K., Muto, Y., Imamoto, H., & Ishigaki, T. (1993). "Flow Discharge Characteristics for Overbank Flow in Meander Channels." *Proc. of the 1<sup>st</sup> Int. Conf. on Hydro-Science and Engineering*, Washington D. C., pp. 1309-1316.
- Shiono, K., Muto, Y., Imamoto, H. & Ishigaki, T. (1994). "Flow Structure in Meandering Compound Channel for Overbank." *The Seventh International Symposium on Application of Laser Techniques to Fluid Mechanics*, Vol. 2, pp. 28.2.1-28.2.8.
- Shiono, K., Muto, Y., Knight, D. W., & Hyde, A. F. L. (1997). "Energy Losses Due to Secondary Flow and Turbulence in Meandering Channel with Overbank Flow." *Journal of Hydraulic Research*, Vol. 37, No. 5, pp. 641-664.
- Shiono, K., & Muto, Y. (1998). "Complex Flow Mechanisms in Compound Meandering Channels with Overbank Flow." *Journal of Fluid Mechanics*, Vol. 376, pp. 221-261.
- Shiono, K., Al-Romaih, J. S., & Knight, D. W. (1999). "Stage-Discharge Assessment in Compound Meandering Channel." *Journal of Hydraulic Engineering*, Vol. 125, No. 1, pp. 66-77.



- Shiono, K., Spooner, J., Rameshwaran, P., & Chandler, J. (2001). "Energy Losses in Meandering Channels with Flat Bed and Natural Beds for Overbank Flows." *Proc. Of the XXIX IAHR Congress*, Vol. 1, pp. 256-263.
- Shukla, D. R. (2006). "Three-dimensional Computational Investigations of Flow Mechanisms in Compound Meandering Channels." *Ph.D Thesis*, Loughborough University, U.K.
- Sinha, S. K. (1997). "An Algebraic Grid Generation Technique for Three-Dimensional Natural River Reaches." *Communication in Numerical Methodes in Engineering*, Vol. 13, pp. 475-485.
- Sofialidis, D., & Prinos, P. (1998). "Compound Open-Channel Flow Modeling with Nonlinear Low-Reynolds  $k$ - $\epsilon$  Models." *Journal of Hydraulic Engineering*, Vol. 124, No. 3, 253-262.
- Sofialidis, D., & Prinos, P. (1999). "Numerical Study of Momentum Exchange in Compound Open Channel Flow." *Journal of Hydraulic Engineering*, Vol. 125, No. 2, pp. 152-165.
- Spitaleri, R. M., & Micacchi, V. (1998). "A Multiblock Multigrid Grid Generation Method for Complex Simulations." *Mathematics and Computer Simulation*, Vol. 46, pp. 1-12.
- Spooner, J., & Shiono, K. (2003). "Modelling of Meandering Channels for Overbank Flow." *Proc. Instn. Civ. Engrs Wat., Marit. & Energy*, Vol. 156, pp. 225-233.
- Stein, C. J., & Rouve, G. (1989). "2D Depth-averaged Numerical Predictions of the Flow in a Meandering Channel with Compound Cross Section., *Hydrosoft*, Vol. 2, No.1, pp. 2-7.
- Toebes, G. H., & Sooky, A. A. (1967). "Hydraulics of Meandering Rivers with Floodplains." *Journal of Hydraulic Waterways and Harbours Division*, Vol. 93, No. 2, pp. 1053-1066.
- Tominaga A., Nezu I., & Ezaki K. (1989) "Experimental Study on Secondary Currents in Compound Open-Channel Flow." *Proc. of the 23<sup>rd</sup> IAHR Congress*, Ottawa, Canada, pp. A15-A22.
- Tominaga, N., & Nezu, I. (1991). "Turbulent Structure in Compound Open-Channel Flows." *Journal of Hydraulic Engineering*, Vol. 117, No. 1, pp. 21-41.
- Vanoni, V. A. (1977). "Sedimentation Engineering." *Chapter 6*, ASCE, New York
- Vectrino Velocimeter User Guide (2004), Nortek, Norway.
- Willetts, B. B., & Hardwick, R. (1993). "Stage Dependency for Overbank Flow in Meandering Channels." *Proc. Instn. Civ. Engrs Wat., Marit. & Energy*, Vol. 101, pp. 45-54.



- Willetts, B. B., & Rameshwaran, P. (1996). "Meandering Overbank Flow Structures." *Coherent Flow Structures in Open Channels*, John Wiley & Sons Ltd, Chapter 29, pp. 609-629.
- Wilson, C. A. M. E., Stoesser, T., & Olsen, N. R. B. (2004). "Validation of a 3D Computational Dynamics Code in Simulation of Meandering Compound Channel Flows." *Proceedings of Abstract and Papers of the 6<sup>th</sup> International Conference Hydro-Science and -Engineering*, Brisbane, May 31-June 3, Australia, Paper 416.
- Wilson, C. A. M. E., Bates, P. D., & Hervouet, J. -M. (2002). "Comparison of Turbulence Models for Stage-Discharge Rating Curve Prediction in Reach-Scale Compound Channel Flows Using Two-dimensional Finite Element Methods." *Journal of Hydrology*, Vol. 257, pp. 42-58.
- Wilson, C. A. M. E., Boxall, J. B., Guymer, I., & Olsen, N. R. B. (2003b). "Validation of a Three-dimensional Numerical Code in the Simulation of Pseudo-Natural Meandering Flows." *Journal of Hydraulic Engineering*, Vol. 129, No. 10, pp. 758-768.
- Wilson, C. A. M. E., Stoesser, T., Olsen, N. R. B., & Bates, P. D. (2003a). "Application and Validation of Numerical Codes in the Prediction of Compound Channel Flows." *Proc. Instn. Civ. Engrs Wat., Marit. & Energy*, Vol. 156, pp. 117-128.
- Wu, F. C., Shen, H. W., & Chou, Y. J. (1999). "Variation of Roughness Coefficients for Unsubmerged and Submerged Vegetation." *Journal of Hydraulic Engineering*, Vol. 125, No. 9, pp. 934-942.
- Wu, W., Rodi, W., & Wenka, T. (2000). "3D Numerical Modelling of Flow and Sediment Transport in Open Channels." *Journal of Hydraulic Engineering*, Vol. 126, pp. 4-15.
- Ye, J., & McCorquodale, J. A. (1997). "Depth-averaged Hydrodynamic Model in Curvilinear Collocated Grid." *Journal of Hydraulic Engineering*, Vol. 123, No. 5, pp. 380-388.
- Ye, J., & McCorquodale, J. A. (1998). "Simulation of Curved Open Channel Flow by 3D Hydrodynamic Model." *Journal of Hydraulic Engineering*, Vol. 124, No. 7, pp. 687-697.
- Yen, B. C., & Yen, C. L. (1983). "Flood Flow over Meandering Channels." *River Meandering* (ed. C.M. Elliott), pp. 554-561.
- Yu, L., Zhu, Y., & Righetto, A. M. (1997). "Hybrid Grid- A Specialized Mesh System for Full Three-dimensional Numerical Simulation in Natural Waters." *Mathematical Computation Modelling*, Vol. 26, pp. 81-95.
- Yuen, K. W. H., & Knight, D. W. (1990). "Critical Flow in a Two Stage Channel." *Proc., Int. Conf. on River Flood Hydr., Hydraulics Research Limited*, Wiley, New York, 267.